

AD-A257 801



# CONFERENCE PROCEEDINGS

①

## 8th Optical Fiber Sensors Conference

January 29 - 31, 1992

**Monterey Marriott**  
Monterey, CA

*Co-sponsored by:*  
**IEEE Lasers and  
Electro-Optics Society  
Optical Society  
of America**

IEEE Catalog #92CH3107-0

ISBN# Softbound 0-7803-0518-3

Casebound 0-7803-0519-1

Microfiche 0-7803-05205

Library of Congress #9177785

**DTIC**  
**S** **ELECTE** **D**  
**C**  
NOV 3 1992



**CONTRIBUTION STATEMENT A**

Approved for public release;  
Distribution Unlimited

# CONFERENCE PROCEEDINGS

---

## 8th Optical Fiber Sensors Conference

January 29 - 31, 1992

**Monterey Marriott**  
Monterey, CA

*Co-sponsored by:*  
**IEEE Lasers and  
Electro-Optics Society  
and  
Optical Society  
of America**

IEEE Catalog #92CH3107-0

ISBN# Softbound 0-7803-0518-3

Casebound 0-7803-0519-1

Microfiche 0-7803-05205

Library of Congress #9177785

---



92 1

10

92-27909



181100

44805

The papers in this book comprise the proceedings of the meeting mentioned on the cover and title page. They were reviewed and accepted for presentation by the OFS '8 Technical Program Committee. They reflect the authors' opinions and are published as presented and without change, in the interests of timely dissemination. Their inclusion in this publication does not necessarily constitute endorsement by the editors, the Institute of Electrical and Electronics Engineers, Inc.

Copyright and Reprint Permissions: Abstracting is permitted with credit to the source. Libraries are permitted to photocopy beyond the limits of U.S. copyright law for private use of patrons those articles in this volume. Instructors are permitted to photocopy isolated articles for noncommercial classroom use without fee. For other copying, reprint or republication permission, write to Director, Publishing Services, IEEE, 345 E. 47th St., New York, NY 10017. All rights reserved. Copyright ©1991 by the Institute of Electrical and Electronics Engineers, Inc.

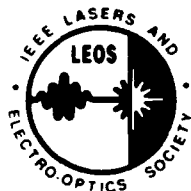
IEEE Catalog #92CH 3107-0

ISBN# Softbound: 0-7803-0518-3

Casebound: 0-7803-0519-1

Microfiche: 0-7803-0520-5

Library of Congress #9177785



# OFS'8 CONFERENCE COMMITTEE

## Conference Chair

**Fred Leonberger**  
*United Technologies Research Center,  
East Hartford, CT*

## Program Chair

**Anthony Dandridge**  
*Naval Research Laboratory, Washington, DC*

## PROGRAM COMMITTEE

**Kjell Bløtekjaer**  
*Norwegian Inst. of Technology, Norway*

**Jacek Chrostowski**  
*National Research Council Canada,  
Ottawa, Canada*

**Richard O. Claus**  
*Virginia Polytechnic Institute, Blacksburg, VA*

**Gordon W. Day**  
*National Institute of Standards and Technology, Boulder, CO*

**Shaoul Ezekiel**  
*MIT, Lexington, MA*

**Masamitsu Haruna**  
*Osaka University, Osaka, Japan*

**Kazou Hotate**  
*The University of Tokyo, Tokyo, Japan*

**David A. Jackson**  
*University of Kent at Canterbury, Kent, United Kingdom*

**Alan D. Kersey**  
*Naval Research Laboratory,  
Washington, DC*

**Byoung Yoon Kim**  
*Korea Adv. Institute of Science & Technology, Seoul,  
Korea and Stanford University, Stanford, CA*

**Kiyoshi Kurosawa**  
*Tokyo Electric Power Company Inc.,  
Tokyo, Japan*

**R.A. Lieberman**  
*Physical Optics Corporation, Torrance, CA*

**Anna-Grazia Mignani**  
*IROE-CNR, Firenze, Italy*

**William W. Morey**  
*United Technologies Research Center, East Hartford, CT*

**Juichi Noda**  
*NTT Opto-Electronics Labs, Ibaraki-ken, Japan*

**Daniel B. Ostrowsky**  
*University of Nice, Nice, France*

**Simon B. Poole**  
*University of Sydney, Sydney, Australia*

**Alan J. Rogers**  
*King's College, London, United Kingdom*

**Peter J. Samson**  
*BHP Central Research Labs, Australia*

**Glenn A. Sanders**  
*Honeywell, Inc., Phoenix, AZ*

**Pierre Sansonetti**  
*Bertin, Les Milles Cedex, France*

**Takeo Shiota**  
*Fujikura, Ltd., Chiba, Japan*

**Shigeru Tanaka**  
*Sumitomo Electric Industries, Yokohama, Japan*

**Moshe Tur**  
*Tel Aviv University, Tel Aviv, Israel*

**Eric Udd**  
*McDonnell Douglas Electronic Systems Company,  
Santa Ana, CA*

**Reinhard Ulrich**  
*Technische Universitat, Hamburg, Germany*

**Otto S. Wolfbeis**  
*Karl Franzens University, Graz, Austria*

Statement A per telecon Mr. Pilloff  
ONR/Code 1112LO  
Arlington, VA 22217-5000

11/2/92 JK

iii

DTIC QUALITY INSPECTED 5

### Accession For

DTIS GRA&I

DTIC TAB

Unannounced

Justification

By

Distribution/

Availability Code

Dist

Avail and/or  
Special

A-1



# OFS'8 INTERNATIONAL STEERING COMMITTEE

## Steering Committee Chairman

**Fred Leonberger**  
*United Technologies Research Center*  
East Hartford, CT

**Brian Outshaw**  
*University of Strathclyde, Glasgow, Scotland*

**Anthony Dandridge**  
*Naval Research Laboratory, Washington, DC*

**Byoung Yeon Kim**  
*Korea Advanced Institute of Science and Technology,  
Seoul, Korea and Stanford University, Stanford, CA*

**Herve C. Lefevre**  
*Photonetics, Marly-le-roi, France*

**Yoshihiko Ohtsuka**  
*Hokkaido University, Sapporo, Japan*

**Olivier Perniaux**  
*Centre Suisse D'Electronique et de Microtechnique S.A.,  
Switzerland*

**Scott Rashleigh**  
*Australian Optical Fiber Research Pty. Ltd.,  
Fyshwick, Australia*

**Annamaria Scheggi**  
*IROE-CNR, Firenze, Italy*

**George Siegel**  
*Rutgers University, Piscataway, NJ*

**Eric Udd**  
*McDonnell Douglas Electronic Systems Company,  
Santa Ana, CA*

**Toshihiko Yoshino**  
*Gunma University, Gunma, Japan*

## **ACKNOWLEDGEMENTS**

The 8th Optical Fiber Sensors Conference is sponsored by the IEEE Lasers and Electro-Optics Society and the Optical Society of America. Support has been provided by the following agencies:

*Air Force of Scientific Research*

*National Security Agency*

*Office of Naval Research*

*National Science Foundation*

# FOREWORD



**Tony Dandridge**  
**Chairman, OFS Technical Program Committee**

This conference is the eighth in the Optical Fiber Sensor (OFS) Series, the first being held in London in 1983. There has been considerable progress over the past nine years and recently a number of the technological hurdles which have slowed the development of this technology have been overcome. The number of commercially available fiber optic sensors is still growing, however workers in the fiber sensor area now have a better appreciation of the strengths of conventional sensor technology and realize the stiffness of the competition. However a number of workers in the user community, initially skeptical, are beginning to see the real advantages fiber optic sensor technology has to offer.

It has always been the OFS conference charter to publish original, significant research in the area of fiber optic sensors. As the technology matures it is natural that emphasis shifts towards applications-oriented research and development. Since the last OFS conference there have been a number of important demonstrations of fiber optic sensor technology - for example a 48 channel all optical towed array was successfully tested at sea by the U.S. Navy. In the area of fiber optic gyroscope progress has also been rapid towards the demonstration of the viability of this technology for wide ranging applications. As these areas mature a number of other applications- especially smart skins, are rapidly expanding. This gives opportunities for the development of new sensing and interrogation techniques.

There still appears to be growing interest in the area of fiber sensor research, the number of papers submitted to the conference was up by approximately 50% compared to the last two OFS conferences. The total number of accepted papers increased slightly by expanding the poster session, the number of oral papers remaining approximately the same. The increased number of submitted papers led to a substantially lower acceptance rate compared to recent OFS conferences. I think this has led to a higher standard, but unfortunately a number of interesting papers had to be rejected. I would like to emphasize as a committee we avoided placing papers in the poster session purely on scoring, the judgement was based on the suitability of the subject matter. A number of the highest rated papers were assigned to the poster session.

I would like to take this opportunity to thank the many people who have contributed to the success of the conference. Firstly I would like to thank the members of the technical program committee for undertaking both the solicitation and refereeing of the papers. I would like to give special thanks to those members who travelled to the committee meeting for their help, not only in lending their expertise in the first hand evaluation of the papers, but in their contributions in helping to organize the sessions. I would also like to praise the efforts of Fred Leonberger, Chairman of the International Steering Committee for his invaluable contributions in numerous areas. I would also like to thank Wendy Rochelle and the LEOS staff for their valuable help in organizing the conference. Finally I would like to thank the many scientists and engineers for their efforts in providing numerous original, high quality papers without which there would be no OFS conference.

**MONTEREY MARRIOTT**



# 8th OPTICAL FIBER SENSOR CONFERENCE AT A GLANCE

WEDNESDAY, JANUARY 29, 1992			
TIME	EVENT	CHAIR	LOCATION
7:30am - 5:30pm 8:20am - 8:30am 8:30am - 10:00am 10:00am - 10:30am	Registration <b>Opening Remarks</b> <b>Session W1: Sources</b> Coffee Break	B.Y. Kim	MM: San Carlos Foyer MCC: Steinbeck Forum MCC: Steinbeck Forum MM: San Carlos Foyer
10:00am - 5:00pm 10:30am - 12noon 12noon - 1:00pm	Exhibits <b>Session W2: Fiber Gyros</b> Lunch	S. Ezekiel	MM: San Carlos Foyer MCC: Steinbeck Forum MM: San Carlos III/IV
1:00pm - 3:00pm 3:30pm - 5:30pm 6:30pm - 8:00pm	<b>Session W3: Interferometry I</b> <b>Poster Session</b> Conference Reception	A. Kersey	MCC: Steinbeck Forum MM: San Carlos III/IV Monterey Bay Aquarium
THURSDAY, JANUARY 30, 1992			
8:00am - 5:30pm 8:00am - 10:00am 10:00am - 10:30am	Registration <b>Session TH1: Multiplexed &amp; Distributed Sensors</b> Coffee Break	K. Bløtekjaer	MM: San Carlos Foyer MCC: Steinbeck Forum MM: San Carlos Foyer
10:00am - 5:00pm 10:30am - 12noon 12noon - 1:30pm	Exhibits <b>Session TH2: Fiber Devices</b> Lunch	S. Poole	MM: San Carlos Foyer MCC: Steinbeck Forum MM: San Carlos III/IV
1:30pm - 3:00pm 3:00pm - 3:30pm	<b>Session TH3: Photonic Devices</b> Coffee Break	J. Noda	MCC: Steinbeck Forum MM: San Carlos Foyer
3:30pm - 5:00pm 7:30pm - 9:00pm	<b>Session TH4: Chemical And Environmental Sensors</b> <b>Post Deadline Session</b>	A.M. Scheggi	MCC: Steinbeck Forum MM: San Carlos III/IV
FRIDAY, JANUARY 31, 1992			
8:00am - 5:00pm 8:00am - 10:00am 10:00am - 10:30am	Registration <b>Session F1: Interferometry II</b> Coffee Break	D. Jackson	MCC: DeAnza III MCC: DeAnza III MCC: DeAnza III Foyer
10:30am - 12noon 12noon - 1:30pm	<b>Session F2: Smart Structures</b> Lunch	E. Udd	MCC: DeAnza III MCC: Serra II
1:30pm - 3:00pm 3:00pm - 3:30pm	<b>Session F3: Faraday Effect Sensors</b> Coffee Break	A. Rogers	MCC: DeAnza III MCC: DeAnza III Foyer
3:30pm - 5:00pm	<b>Session F4: Electromagnetic Sensors</b>	G. Day	MCC: DeAnza III

MM: Monterey Marriott  
MCC: Monterey Convention Center

# TABLE OF CONTENTS

## TECHNICAL PROGRAM

Wednesday, January 29

### W1: SOURCES

Chair: Byoung Yoon Kim

Advance Institute of Science and Technology, Seoul, Korea ..... 1

- W1.1: 1 kW Pulsed Fibre Laser For Time Division Multiplexed Sensor Systems  
P.R. Morkel, K.P. Jedrzejewski, E.R. Taylor, and D.N. Payne  
*University of Southampton, Highfield, Southampton, U.K.* ..... 2
- W1.2: Sagnac Interferometer Including A Recirculating Ring With An Erbium-doped Fibre Amplifier, J.T. Kringlebotn, and K. Bløtekjær, *Norwegian Institute of Technology, Trondheim, Norway*; C.N. Pannell, *Optical Fibre Group, University of Southampton, Southampton, U.K.* ..... 6
- W1.3: Interferometric Measurements Of Linewidth And Phase Noise Of An Er-doped Fiber Ring Laser, R.S. Weis, *U.S. Naval Academy, Annapolis, MD*; A.D. Kersey, and I.N. Duling, III, *Optical Techniques Branch, U.S. Naval Research Laboratory, Washington, D.C.* ..... 10
- W1.4: High Power, Broadband Light Source By Tandem Combination Of A Superluminescent Diode And An Er Doped Fiber Amplifier, N.S. Kwong, *Ortel Corporation, Alhambra, CA* ..... 14
- W1.5: 1.5- $\mu$ m Polarization-Insensitive Strained MQW Superluminescent Diode, O. Mikami, *University of Tokyo, RCAST, Tokyo, Japan* ..... 18
- W1.6: Optothermal Modulation Of Diode Lasers, D.J. Anderson, and J.D.C. Jones, *Heriot-Watt University, Riccarton, Edinburgh* ..... 22

### W2: FIBER GYROS

Chair: Shaoul Ezekiel, MIT, Lexington, MA ..... 26

- W2.1: (Invited) Progress In Interferometer and Resonator Fiber Optic Gyros, G.A. Sanders, R.-Y. Liu, L.K. Strandjord, *Honeywell Systems and Research Center, Phoenix, AZ* ..... 26
- W2.2: Fiber Optic Gyroscope With Single Mode Fiber Coll, S. Motohara, and A. Ohno, *Japan Aviation Electronics Industry, Ltd., Tokyo, Japan* ..... 30
- W2.3: Method To Reduce The Optical Kerr-Effect Induced Bias In An Optical Passive Ring-Resonator Gyro, K. Takiguchi, and K. Hotate, *RCAST, The University of Tokyo, Japan* ..... 34
- W2.4: Experimental Investigation On Direction Sensor Using A Fiber Optic Gyroscope With High Resolution, H. Kajoka, N. Ashizuka, T. Kumagai, and H. Nakai, *Hitachi Cable Ltd., Hitachi-city, Japan* ..... 38
- W2.5 Integrated 1.06  $\mu$ m Fiber Gyro Superfluorescent Source, W.K. Burns, and R.P. Moeller, *Naval Research Laboratory, Washington, DC*; E. Snitzer, *Rutgers University, Piscataway, NJ* ..... 42

### W3: INTERFEROMETRY I:

Chair: Alan Kersey, Naval Research Lab, Washington, DC ..... 46

- W3.1: (Invited) Interferometric Heterodyne Sensing, T. Yoshino, *Gunma University, Gunma, Japan* ..... 46
- W3.2: Noise-Resistant Signal Processing For Electronically Scanned White-Light Interferometry, R. Dändliker, E. Zimmermann, and G. Frosio, *University of Neuchâtel, Neuchâtel, Switzerland* ..... 53
- W3.3: Remote Fiber Optic Measurement Of Air Index With White Light Interferometry, D. Troughet, F.X. Desforges, P. Graindorge, and H.C. Lefèvre, *Photonetics, Marly-le-Roi, France* ..... 57

<b>W3.4:</b>	<b>Coherent FMCW Reflectometry Using A Piezoelectrically Tuned Nd:YAG Ring Laser,</b> S. Venkatesh, W.V. Sorin, D.K. Donald, and B.L. Heffner, <i>Hewlett-Packard Laboratories,</i> <i>Palo Alto, California</i> .....	61
<b>W3.5</b>	<b>High Spatial-Resolution And Sensitivity Interferometric OTDR,</b> M. Kobayashi, <i>NTT Technical</i> <i>Assistant and Support Center, Tokyo, Japan;</i> J. Noda, <i>NTT International Corporation, Tokyo,</i> <i>Japan,</i> and H.F. Taylor, <i>Texas A &amp; M University, College Station, TX</i> .....	65
<b>W3.6:</b>	<b>Fiber Optic Michelson Array With Passive Elimination Of Polarization Fading And Source</b> <b>Feedback Isolation,</b> M.J. Marrone, A.D. Kersey, and A. Dandridge, <i>Optical Sciences Division,</i> <i>Naval Research Laboratory, Washington, DC</i> .....	69
<b>W3.7</b>	<b>Utilisation Of Fiber Fabry-Perot Inter-ferometers For The Determination Of Heat Transfer</b> <b>Transients In Wind Tunnels,</b> S.R. Kidd, P.G. Sinha, J.S. Barton, and J.D.C. Jones, <i>Heriot-Watt</i> <i>University, Edinburgh, UK</i> .....	73

<b>POSTER SESSION</b> .....	<b>77</b>
-----------------------------	-----------

<b>P1:</b>	<b>High-power 0,82 <math>\mu</math>m Superluminescent Diodes With Extremely Low Fabry-Perot Modulation</b> <b>Depth,</b> S.A. Safin, A.T. Semenov, V.R. Shidlovski, N.A. Zhuchov, and Y.V. Kurnyavko, <i>J.E. Interface, Moscow, USSR</i> .....	78
<b>P2:</b>	<b>1.06 <math>\mu</math>m All-fiber Gyroscope With Noise Subtraction,</b> R.P. Moeller, and W.K. Burns, <i>Naval</i> <i>Research Laboratory, Washington, DC</i> .....	82
<b>P3:</b>	<b>Observation Of Backscatter-Induced CrossTalk In A Two-dimensional Frequency-Division</b> <b>Multiplexed Fibre Optic Gyro System,</b> W. Jin, and B. Culshaw, <i>Optoelectronics Division,</i> <i>University of Strathclyde, Scotland, UK</i> .....	86
<b>P4:</b>	<b>More Exact Measurement Of Gravitation Constant G By Using Fixed Precision Fiber Gyro,</b> M. Böhm, <i>Alcatel Sel, Stuttgart, Germany</i> .....	90
<b>P5:</b>	<b>Sensitive Fibre Optic Thermometer Using Cr:LISAF Fluorescence For Bio-Medical Sensing</b> <b>Applications,</b> Z. Zhang, K.T.V. Grattan, and A.W. Palmer, <i>Measurement and Instrumentation</i> <i>Centre, City University, London, England</i> .....	93
<b>P6:</b>	<b>Multipoint Temperature Monitoring In A Hazardous Environment,</b> M. Brenci, A. Mencaglia, and A.G. Mignani, <i>Istituto di Ricerca sulle Onde Elettromagnetiche del Consiglio Nazionale delle</i> <i>Ricerche, Firenze, Italy</i> .....	97
<b>P7:</b>	<b>Strain and Temperature Dependence of Elliptical Core Two-Mode Fiber Acousto-Optic</b> <b>Interaction,</b> J.O. Askautrud, H.E. Engan, <i>The Norwegian Institute of Technology,</i> <i>Trondheim, Norway</i> .....	101
<b>P8:</b>	<b>In-line Fiber Fabry-Perot Interferometer With High-Reflectance Internal Mirrors,</b> C.E. Lee, W.N. Gibler, R.A. Atkins, and H.F. Taylor, <i>Texas A&amp;M University, College Station, TX</i> .....	105
<b>P9:</b>	<b>Sensors For Structural Displacement Measurement,</b> S.R. Lang, J.M. Pauschke, and D.J. Ryan, <i>Northern Illinois University, DeKalb, IL</i> .....	109
<b>P10:</b>	<b>Remote Fiber - Optic Strain Sensing On Composites With Simultaneous Interferometric</b> <b>and Polarimetric Readout,</b> N. Fürstenau, and W. Schmidt, <i>German Aerospace Research</i> <i>Establishment (DLR) Institute for Flight Guidance, Braunschweig, Germany;</i> H.-C. Goetting, <i>Institute for Structural Mechanics, Braunschweig, Germany</i> .....	113
<b>P11:</b>	<b>Novel Fibre-optic Torsional Vibrometers,</b> T.Y. Liu, M. Berwick, and D.A. Jackson, <i>Applied</i> <i>Optics Group, University of Kent, Canterbury, Kent, UK</i> .....	117
<b>P12:</b>	<b>Developments In Elliptical Core Polarization-Maintaining Fiber,</b> G.E. Berkey, <i>Corning</i> <i>Incorporated, Corning, NY</i> .....	121

<b>P13:</b>	<b>Splitting Of The Second Order Mode Cutoff Wavelengths In Elliptical Core Fibers,</b> J. Blake, <i>Texas A&amp;M University, College Station, TX</i> ; M.C. Pacitti, and S.L.A. Carrara, <i>Centro Technico Aeroespacial, S.J. Campos, Brazil</i> .....	125
<b>P14:</b>	<b>Spatially-weighted Vibration Sensors Using Tapered Two-mode Optical Fibers,</b> K.A. Murphy, B.R. Fogg, and R.O. Claus, <i>Virginia Polytechnic Institute and State University, Blacksburg, VA</i> ; A.M. Vengsarkar, <i>AT&amp;T Bell Laboratories, Murray Hill, NJ</i> .....	129
<b>P15:</b>	<b>Fiber Optic Depolarizer,</b> D.R. Lutz, <i>3M Company, St. Paul, MN</i> .....	133
<b>P16:</b>	<b>High Performance Polarization Maintaining Optical Fiber Couplers,</b> E. Sasaoka, H. Suganuma, and M. Takagi, <i>Sumitomo Electric Industries, Ltd., Yokohama, Japan</i> .....	137
<b>P17:</b>	<b>Statistical Properties Of Fiber-Birefringence Models,</b> A.D. Kersey, M.A. Davis, and M.J. Marrone, <i>Optical Sciences Division, Naval Research Laboratory, Washington, DC</i> .....	141
<b>P18:</b>	<b>In-line Polarization Controller Based Upon A Recirculating Fiber Delay Line,</b> B.A. Ferguson, C.L. Chen, <i>Purdue University, West Lafayette, IN</i> .....	145
<b>P19:</b>	<b>Self Checking Fiber Coupled Optical Resolver,</b> R.W. Huggins, and C.R. Porter, <i>Boeing Defense and Space Group High Technology Center, Seattle, WA</i> .....	149
<b>P20:</b>	<b>Integrated Optics Pockels Cell As A High Voltage Sensor,</b> N.A.F. Jaeger, and F. Rahmatian, <i>The University of British Columbia, Vancouver, British Columbia, Canada</i> .....	153
<b>P21:</b>	<b>A Hybrid Coherent Fiber-Optic Probe For Remote Sensing Of Electro-Optic Effects In GaAs,</b> D.L. Mazzoni, K. Cho, S. Saddow, and C.C. Davis, <i>University of Maryland, College Park, MD</i> .....	157
<b>P22:</b>	<b>Fiber Optic Magnetic Field Sensors Using Metallic-Glass-Coated Optical Fibers,</b> Y.W. Bibby, <i>Wilkes University, Wilkes-Barre, PA</i> ; D.C. Larson, and S. Tyagi, <i>Drexel University, Philadelphia, PA</i> ; L.C. Bobb, <i>Naval Air Development Center, Warminster, PA</i> .....	161
<b>P23:</b>	<b>Interference Of The Faraday Coupled Signal With The Residual Mode Component In A Highly-Birefringent Optical-fibre Current Sensor,</b> W. Chu, D. Haldar, D. McStay, and A.J. Rogers, <i>King's College London, Strand, London, UK</i> .....	165
<b>P24:</b>	<b>A Novel Miniature Faraday Current Sensor Using a Bulk-optic-ring Sensing Element,</b> Y.N. Ning, B.C.B. Chu, and D.A. Jackson, <i>University of Kent, Canterbury, Kent, UK</i> .....	169
<b>P25:</b>	<b>The Performance Of A Fibre Optic Magnetic Field Sensor Utilizing A Magneto-Optical Garnet,</b> H. Sohlström, and K. Svantesson, <i>The Royal Institute of Technology, Instrumentation Laboratory, Stockholm, Sweden</i> .....	173
<b>P26:</b>	<b>Low-frequency Intensity Noise Reduction For Fiber-Optic Sensor Applications,</b> D.M. Dagenais, K.P. Koo, and A. Dandridge, <i>Naval Research Laboratory, Washington, DC</i> .....	177
<b>P27:</b>	<b>A Fibre Optic Frequency Shifter Utilising Stimulated Brillouin Scattering In Birefringent Optical Fibre,</b> R.P. Tatam, <i>Cranfield Institute of Technology, Cranfield, Milton Keynes, UK</i> ; C.J. Duffy, <i>Sowerby Research Centre, British Aerospace plc, Filton, Bristol, UK</i> .....	181
<b>P28:</b>	<b>Fibre Frequency Shifter Based Upon Stimulated Brillouin Scattering Generation In High Finesse Ring Resonators,</b> K. Kalli, D.O. Culverhouse, and D.A. Jackson, <i>University of Kent, Canterbury, Kent</i> .....	185
<b>P29:</b>	<b>Acoustically Scanned Delay For White-Light Interferometry,</b> E. Kolltveit, and K. Bløtekjær, <i>Norwegian Institute of Technology, Trondheim, Norway</i> .....	189
<b>P30:</b>	<b>Extrinsic Fabry-Perot Optical Fiber Sensor,</b> K.A. Murphy, M.F. Gunther, A. Wang, and R.O. Claus, <i>Virginia Polytechnic Institute and State University, Blacksburg, VA</i> ; A.M. Vengsarkar, <i>AT&amp;T Bell Laboratories, Murray Hill, NJ</i> .....	193
<b>P31:</b>	<b>A Novel Fibre Refractive Index Sensor Using Resonance Shift Phenomena,</b> G. Thursby, W. Johnstone, K. McCallion, D. Moodie, and B. Culshaw, <i>University of Strathclyde, Glasgow, Scotland, UK</i> .....	197



<b>P32:</b>	<b>Quadrature Polarization-State Delivery Through Optical Fiber For Polarimetric Sensors,</b> M. Johnson, and C. Pannell, <i>University of Southampton, Southampton, UK</i> .....	201
<b>P33:</b>	<b>An Optical Fiber Network For Analog Temperature And Pressure Sensing Purposes,</b> M.R.H. Voet, <i>Glöztz, Rheinstetten, Germany</i> ; F.X. Desforges, <i>Photonetics, Marly le Roi, France</i> ; A.R.F. Barel, <i>VUB, Brussels, Belgium</i> .....	205
<b>P34:</b>	<b>A Multiplexing Scheme For Optical Fibre Interferometric Sensors Using An FMCW Generated Carrier,</b> S.F. Collins, <i>Victoria University of Technology, Victoria, Australia</i> ; B.T. Meggitt, A.W. Palmer, and K.T.V. Grattan, <i>City University, Northampton Square, London, U.K.</i> .....	209
<b>P35:</b>	<b>Visibility And Bias Phase Noise In Fiber-optic Interferometers With An Output Polarizer,</b> M. Tur, and H.J. Shaw, <i>Ginzton Laboratory, Stanford University, Stanford, CA</i> .....	213
<b>P36:</b>	<b>Applications Of Fibre Optic Electronic Speckle Pattern Interferometers Using Laser Diode Sources,</b> H. Atcha, and R.P. Tatam, <i>Cranfield Institute of Technology, Cranfield, Bedford, UK</i> .....	217
<b>P37:</b>	<b>Novel Passive Compensation Technique Applied To A White Light Interferometric System,</b> D. Walsh, and B. Culshaw, <i>University of Strathclyde, Scotland, UK</i> .....	221
<b>P38:</b>	<b>Spurious Sidebands Of Signal Carriers In Fiber-optic Interferometric Sensors,</b> K.P. Koo, D.M. Dagenais, F. Bucholtz, and A. Dandridge, <i>Naval Research Laboratory, Washington, DC</i> .....	225
<b>P39:</b>	<b>Focus-sensing Characteristics Of A Monolithic 3-channel Laser Diode Array With Vertically Staggered Facets,</b> Y. Katagiri, Y. Suzuki, and H. Tanaka, <i>NTT Interdisciplinary Research Laboratories, Tokyo, Japan</i> .....	229
<b>P40:</b>	<b>An Integrated Silicon Micromechanical Interferometer,</b> A. Vadekar, W.P. Huang, and A. Nathan, <i>University of Waterloo, Waterloo, Ontario, Canada</i> .....	233
<b>P41:</b>	<b>A Fibre Optic, Low Coherence Laser Doppler Anemometer System For Determining Flow Velocity,</b> K. Weir, W.J.O. Boyle, A.W. Palmer, K.T.V. Grattan, and B.T. Meggitt, <i>Measurement and Instrumentation Centre, City University, Northampton Square, London, UK</i> .....	237
<b>P42:</b>	<b>Dual Aperture Single Mode Optical Fiber Laser Doppler Velocimeter,</b> M.D. Mermelstein*, and J.A. Blodgett, <i>Naval Resarch Laboratory, Washington, DC</i> .....	241

**Thursday, January 30**

**TH1: MULTIPLEXED AND DISTRIBUTED SENSORS**

Chair: Kjell Bløtekjær, *Norwegian Institute of Technology, Trondheim, Norway* .....245

<b>TH1.1:</b>	<b>(Invited) Recent Advances In Fiber Optic Distributed Sensing Systems,</b> A. Hartog, <i>York Sensors, Ltd., Chandler's Ford, UK</i> .....	246
<b>TH1.2:</b>	<b>Detection Of Localised Polarization Mode Coupling Using The Optical Kerr Effect,</b> V.A. Handerek, A.J. Rogers, and I. Cokgor, <i>King's College London, Strand, London, U.K.</i> .....	250
<b>TH1.3:</b>	<b>Structured Metal Coatings For Distributed Fiber Sensors,</b> L. Falco, and O. Parriaux, <i>Swiss Center for Electronics and Microtechnology, Research and Development, Neuchâtel, Switzerland</i> .....	254
<b>TH1.4:</b>	<b>An Ultra High Resolution Distributed Temperature Sensor,</b> D.A. Thorncraft, M.G. Sceats, and S.B. Poole, <i>University of Sydney, Sydney, Australia</i> .....	258
<b>TH1.5:</b>	<b>A Temperature Optical Fiber Sensor Network: From Laboratory Feasibility To Field Trial,</b> H. Fevrier, J. Hervo, S. Artigaud, A. Tardy, M. Jurczyszyn, and A. Derossis, <i>Alcatel Alsthom Recherche, Marcoussis, France</i> ; D. Bouilleret, <i>GEC Alsthom, DEM/DEA, Cedex, France</i> ; J.L. Pierrat, <i>GEC Alsthom, DEM/DTA, Cedex, France</i> .....	262

<b>TH1.6: Code-division Multiplexed Interferometric Array With Phase Noise Reduction And Low Crosstalk</b> , A.D. Kersey, A. Dandridge, and M.A. Davis, <i>Naval Research Laboratory, Washington, DC</i> .....	266
<b>TH1.7: An Improved TDM System Applied To The Multiplexing Of Silicon Microresonator Sensors Exhibiting Identical Characteristics</b> , Y.J. Rao, B. Culshaw, and D. Uttamchandani, <i>University of Strathclyde, Glasgow, UK</i> .....	270

## **TH2: FIBER DEVICES**

**Chair:** Simon B. Poole, *University of Sydney, Sydney, Australia* ..... 274

<b>TH2.1: (Invited) Application Specific Optical Fibres And Fibre Devices For Optical Fibre Sensors</b> , S.B. Poole, <i>Optical Fibre Technology Centre, University of Sydney, Australia</i> .....	274
<b>TH2.2: Optical Fibers In Sensor Applications: Designing For Mechanical Reliability</b> , G.S. Glaesemann, and R.M. Hawk, <i>Corning Incorporated, Corning, NY</i> .....	279
<b>TH2.3: Ultra-Wide Bandwidth Fiber Polarizer</b> , M. Takagi, Y. Kubo, E. Sasaoka, and H. Suganuma, <i>Sumitomo Electric Industries, Ltd., Yokohama, Japan</i> .....	284
<b>TH2.4: Polarization Mode Couplers Made By Photoinduced Grating For White-light Quasi-distributed Polarimetric Sensors</b> , J.J. Guerin, J.M. Maillard, and P. Sansonetti, <i>Bertin &amp; Cie, Cedex, France</i> .....	288
<b>TH2.5: Effect of Parasitic Birefringence Modulation In Interferometric Fiber Sensor Transducers</b> , A.D. Kersey, K.H. Wanser*, and M.A. Davis, <i>Optical Sciences Division, Naval Research Laboratory, Washington, DC</i> .....	292

## **TH3: PHOTONIC DEVICES**

**Chair:** Juichi Noda, *NTT Opto-Electronics Labs, Ibaraki-Ken, Japan* ..... 296

<b>TH3.1: (Invited) Integrated Optical Circuits For Fiber Optic Sensors</b> , P.G. Suchoski, <i>United Technologies Photonics, East Hartford, CT</i> .....	296
<b>TH3.2: A Fault Locator For Integrated Optics</b> , K. Iizuka, <i>ATR, (on leave of absence from the University of Toronto), Toronto, Canada</i> ; S. Fujii <i>ATR Optical and Radio Communications Research Laboratories, Kyoto, Japan</i> .....	297
<b>TH3.3: A Differential Measurement Technique For Optical Fibre Sensors Using Intensity Modulation</b> , R.I. MacDonald, and R. Nychka, <i>Telecommunications Research Laboratories (TRLabs), Edmonton, Canada</i> .....	301
<b>TH3.4: Optical Displacement Sensor By Focus Error Detection</b> , M. Shigehara, and Y. Hattori, <i>Sumitomo Electric Industries, LTD., Yokohama, Japan</i> .....	305
<b>TH3.5: Proposal Of Ultra-High Finesse, Bi-directional Vernier Based On Er-Doped Fiber Ring Resonator</b> , H. Okamura, and K. Iwatsuki, <i>NTT Transmission Systems Laboratories, Kanagawa, Japan</i> .....	309

## **TH4: CHEMICAL AND ENVIRONMENTAL SENSORS**

**Chair:** Anna Maria Scheggi, *IROE-CNR, Firenze, Italy* ..... 313

<b>TH4.1: (Invited) Fiber Optic Optrodes For Chemical Sensing</b> , M. Brenci, <i>Istituto di Ricerca</i> .....	313
<b>TH4.2: (Invited) Environmental Sensing</b> , R.A. Lieberman, <i>Physical Optics Corporation, Torrance, CA</i> .....	320
<b>TH4.3: Porous Fiber Optical Sensor For pH Measurement</b> , J.Y. Ding, M.R. Shahriari, and G.H. Sigel, Jr., <i>Rutgers - The State University of New Jersey, Piscataway, N.J.</i> .....	321
<b>TH4.4: New Optical Fiber Sensor For Oxygen Detection</b> , F. Baldini, M. Bacci, F. Cosi, A. Del Bianco, and A.M. Scheggi, <i>Istituto di Ricerca sulle Onde Elettromagnetiche del CNR, Firenze, Italy</i> .....	325

<b>TH4.5: Sensitivity Enhancement Of Evanescent Wave Immunoassay</b> , M. Yoshida, K. Shigemori, M. Sugimura, and M. Matano, <i>Daikin Industries, Ltd., Shiga, Japan</i> .....	329
<b>TH4.6: Long-distance Simultaneous Detection Of Methane And Acetylene By Using Diode Lasers In Combination With Optical Fibers</b> , K. Yamamoto, and H. Tai, <i>Tokyo Gas Co, Ltd., Tokyo, Japan</i> ; M. Uchida, and S. Osawa, <i>Hitachi Cable, Ltd., Ibaraki, Japan</i> ; K. Uehara, <i>Keio University, Kanagawa, Japan</i> .....	333

## Friday, January 31

<b>F1: INTERFEROMETRY II</b> Chair: Reinhard Ulrich, <i>Technische Universitat, Hamburg, Germany</i> .....	337
<b>F1.1: (Invited) Status Of Fiber Optic Acoustic Sensing</b> , A.M. Yurek, <i>Naval Research Laboratory Washington, DC</i> .....	338
<b>F1.2: Parallel-Wrapped Optical Fiber Interferometric Ellipsoidal Shell Acoustic Sensors</b> , D.A. Brown, and S.L. Garrett, <i>Naval Postgraduate School, Monterey, CA</i> .....	342
<b>F1.3: Detection Of Acoustic Emission In Cutting Processes By Fibre Optic Interferometry</b> , R. McBride, T. Carolan, J.S. Barton, W.K.D. Borthwick, and J.D.C. Jones, <i>Heriot-Watt University, Edinburgh, UK</i> .....	346
<b>F1.4: A High Frequency Fiber Optic Hydrophone</b> , A.B. Tveten, A. M. Yurek, and A. Dandridge, <i>Naval Research Laboratory, Washington DC</i> ; Y. Y. Chao, <i>University Research Foundation, Greenbelt, MD</i> .....	350
<b>F1.5: Experimental Performance Of A Miniature Fabry-Perot Fiber Optic Hydrophone</b> , P.J. Kuzmenko, <i>Lawrence Livermore National Laboratory, Livermore, CA</i> .....	354
<b>F1.6: An Interferometer Incorporating Active Optical Feedback From A Diode Laser With Application To Vibrational Measurement</b> , W.M. Wang, W.J.O. Boyle, K.T.V. Grattan, and A.W. Palmer, <i>Measurement and Instrumentation Centre, City University, Northampton Square, London, England</i> .....	358
<b>F1.7: Interfero-Polarimetric Fiber Optic Sensor For Both Pressure And Temperature Measurement</b> , M. Turpin, M. Brevignon, and J.P. Le Pesant, <i>Thomson-CSF LCR, Cedex, France</i> ; O. Gaouditz, <i>Sextant Avionique, Cedex, France</i> .....	362
<b>F2: SMART STRUCTURES</b> Chair: Eric Udd, <i>McDonnell Douglas Electronic Systems Co., Santa Ana, CA</i> .....	366
<b>F2.1: (Invited) Fiber Optic Based Smart Structures</b> , R. Measures, <i>University of Toronto</i> .....	366
<b>F2.2: Fiber Optic Fabry-Perot Sensors Embedded In Metal and In a Composite</b> , C.E. Lee, W.N. Gibler, R.A. Atkins, J.J. Alcoz, and H.F. Taylor, <i>Texas A&amp;M University, College Station, TX</i> .....	368
<b>F2.3: Passive Interrogation Of A Lead-Insensitive Two-Mode Elliptical Core Fiber Strain Sensor</b> , T.A. Berkoff, and A.D. Kersey, <i>Naval Research Laboratory, Washington, DC</i> .....	372
<b>F2.4: Grating-based, Two-mode Elliptical-core Optical Fiber Sensors</b> , A.M. Vengsarkar, <i>AT&amp;T Bell Laboratories, Murray Hill, NJ</i> ; J.A. Greene, B.R. Fogg, K.A. Murphy, and R.O. Claus, <i>Virginia Polytechnic Institute and State University, Blacksburg, VA</i> .....	376
<b>F2.5: Fiber Optic Sensors For Guy Wire Vibration Measurements</b> , P. L. Fuhr, and D.R. Huston, <i>University of Vermont, Burlington, VT</i> ; W.B. Spillman, Jr., <i>Catamount Scientific Inc., Vergennes, VT</i> .....	380

<b>F3:</b>	<b>FARADAY EFFECT SENSORS</b>	
	Chair: Alan Rogers, <i>Kings College, London, UK</i> .....	386
<b>F3.1:</b>	<b>(Invited) Optical Magnetic Field Sensors Using Iron Garnet Crystals</b> , M. Imaeda, Y. Kozuka, <i>NGK Insulators, Ltd., Nagoya, Japan</i> .....	386
<b>F3.2:</b>	<b>High Frequency Magnetic Field Sensors Based On The Faraday Effect In Garnet Thick Films</b> , R. Wolfe, E.M. Gyorgy, R.A. Lieberman, V.J. Fratello, and S.J. Licht, <i>AT&amp;T Bell Laboratories, Murray Hill, NJ</i> ; M.N. Deeter, and G.W. Day, <i>NIST, Boulder, CO</i> .....	390
<b>F3.3:</b>	<b>Submicroampere Per Root Hz, High Bandwidth Current Sensor Based On The Faraday Effect In Ga:YIG</b> , A.H. Rose, M.N. Deeter, and G.W. Day, <i>National Institute of Standards and Technology, Boulder, CO</i> .....	394
<b>F3.4:</b>	<b>High Frequency Response Of Fiber Current Sensors With Noncircular And Nonconcentrated Coils*</b> , R.W. Cernosek, <i>Sandia National Laboratories, Albuquerque, NM</i> .....	398
<b>F3.5:</b>	<b>Stabilized Sagnac Optical Fiber Current Sensor Using One Phase And Two Amplitude Modulations</b> , P.-A. Nicati, and P. Robert, <i>Laboratoire de Métrologie, Swiss Federal Institute of Technology of Lausanne, Lausanne, Switzerland</i> .....	402
<b>F4:</b>	<b>ELECTROMAGNETIC SENSORS</b>	
	Chair: Gordon Day, <i>National Institute of Standards and Technology, Boulder, CO</i> .....	406
<b>F4.1:</b>	<b>A High Resolution Three-Axis Fiber Magnetometer</b> , D.M. Dagenais, K.P. Koo, and F. Bucholtz, <i>Optical Sciences Division, Naval Research Laboratory, Washington, DC</i> .....	406
<b>F4.2:</b>	<b>An Optical Fiber Alternating - gradient Magnetometer</b> , L.C. Bobb, and H.D. Krumboltz, <i>Naval Air Development Center, Warminster, PA</i> ; P.M. Shankar, <i>Drexel University, Philadelphia, PA</i> .....	410
<b>F4.3:</b>	<b>Remote Fiber Optic AC Magnetometer</b> , A.R. Davis, S.S. Patrick, A. Dandridge, and F. Bucholtz, <i>Naval Research Laboratory, Washington, DC</i> .....	414
<b>F4.4:</b>	<b>A Fiber Optic DC And Low Frequency Electric Field Sensor</b> , S.T. Vohra, F. Bucholtz, and A.D. Kersey, <i>Naval Research Laboratory, Washington, DC</i> .....	418
<b>F4.5:</b>	<b>A New Scheme Of Fiber Optic Light Sensor For Detection Of Corona Discharges In Gas Insulated Power Apparatus</b> , K. Kurosawa, and W. Watanabe, <i>Tokyo Electric Power Company, Tokyo, Japan</i> .....	422
<b>F4.6:</b>	<b>Three Phase Current Measurement Using A Hybrid Current Sensing Technique</b> , D.A. Jackson, Y.N. Ning, C. McGarrity, <i>University of Kent, Canterbury, Kent</i> ; J.L. Santos, <i>University of Porto, Portugal</i> .....	426

**WEDNESDAY**  
**January 29, 1992**  
**MCC: Steinbeck Forum**

**W1: SOURCES**

**Chair:** Byoung Yoon Kim, *Advanced Institute of Science and Technology, Seoul, Korea*

**W2: FIBER GYROS**

**Chair:** Shaoul Ezekiel, *MIT, Lexington, MA*

**W3: INTERFEROMETRY I:**

**Chair:** Alan Kersey, *Naval Research Lab, Washington, DC*

## **W1.1      1 kW Pulsed Fibre Laser For Time Division Multiplexed Sensor Systems**

**P.R.Morkel, K.P.Jedrzewski\*, E.R.Taylor & D.N.Payne.**

Optoelectronics Research Centre  
University of Southampton  
Southampton  
SO9 5NH  
U.K.

tel: (703) 593145

fax: (703) 593142

**\* Permanent address**

Institute of Electronics Fundamentals  
Warsaw University of Technology  
Poland

### **Summary**

Q-switching of fibre lasers is an attractive means of converting the relatively low CW power of pump laser diodes into short, high intensity pulses for use in time-resolved sensor systems. Peak powers of 100W at  $1.06\mu\text{m}$  with 15ns duration have previously been reported<sup>1</sup> based on the use of Nd-doped alumino-silicate fibre as the gain medium. We report here the attainment of much higher powers in short pulses in a module specifically designed for high-resolution distributed sensor applications.

A multi-component neodymium-doped phosphate glass fibre is used as the amplifying element. The core material was Schott LG750 (1 wt%  $\text{Nd}^{3+}$ ) which was fabricated into a single-mode fibre using a rod-in-tube manufacturing technique described elsewhere<sup>2</sup>. Fibres fabricated with LG750 (a phosphate glass) as the core material have the advantage of higher emission cross-sections than those of silica-based fibres. In bulk form the emission cross-section<sup>3</sup> of LG750 is  $4 \cdot 10^{-20} \text{ cm}^2$  compared with Nd-doped silica fibres which have emission cross sections around  $1 \cdot 10^{-20} \text{ cm}^2$  [4]. This gives rise to higher gain in terms of dB/mW. A further advantage of the phosphate glass fibre is its high content of  $\text{Nd}^{3+}$  which permits very short fibre lasers to be constructed, an essential if short Q-switched pulses are required. High round trip gain combined with a short cavity gives rise to rapid power build up even when relatively large values of output coupling are used. The combination of rapid power build-up and relatively large output coupling enables short pulses to be obtained.

Fig. 1 shows the laser configuration. A 25mm length of fibre was potted in a silica capillary using conventional epoxy. The ends of the capillary were polished orthogonal to the optical axis and a dichroic dielectric coating was applied to one end of the capillary. The coating was >99% reflection at  $1.054\mu\text{m}$  with >90% transmission at 810nm. A 1mm glass slide was bonded to the other capillary end in order to displace the 4% Fresnel

reflection from the waveguide end in order to prevent premature oscillation of the high gain laser. An intra-cavity lens was used to collimate the fibre output onto a 30% reflection mirror which provided the laser output and round-trip feedback. A compact electro-optic integrated Q-switch was used to modulate the cavity loss. The overall cavity length (10cm) was dominated by the length of the Q-switching element. A 100mW single-stripe laser diode operating at 812nm was used as the pump source and was coupled into the fibre using conventional launch optics.

Fig. 2 shows the variation of output power and pulse duration (at sub 1kHz repetition rate) with the laser diode output power. Although it was not possible to determine the efficiency of coupling into the highly-doped fibre directly, measurements on a similar un-doped fibre indicated that up to 50% launch efficiency was possible. A peak power of  $1.06 \pm 0.05$  kW with 2ns duration was obtained. It is interesting to note that the pulse duration is only 2.5 times the cavity round trip period. The deviation of the power characteristic from an expected straight line at the higher pump powers is attributed to bleaching of the pump absorption of the fibre at these higher pump powers. This implies that a higher-still  $\text{Nd}^{3+}$  concentration in the fibre is desirable. Inset in fig. 2 is an oscilloscope trace of the output pulse shape at maximum pump power recorded with a high speed InGaAs photodetector.

Fig 3. Shows the variation of peak power and pulse duration as a function of repetition frequency at maximum pump power. Above 1kHz, lower-power, longer-duration pulses are observed as expected for a medium with a upper-level lifetime of  $\approx 300\mu\text{s}$ . This is due to the inability of the population inversion to reach its maximum equilibrium value in the time between Q-switch trigger pulses.

In summary, we have obtained 1.1kW peak power pulses with 2ns duration from a laser-diode pumped Nd-doped fibre laser. This is the highest power obtained to date from a diode-pumped fibre laser source. The laser is compact, robust and potentially inexpensive. Further increases in peak power are possible by shortening the cavity and the laser is potentially tunable. We believe this makes it ideal for a number of time-multiplexed sensor applications, particularly those based on OTDR, such as the Raman distributed fibre temperature sensor.

### Acknowledgements

Thanks are due to A.Hartog of York Sensor Ltd. for useful discussions. The work was supported by a U.K. government DTI/SERC LINK program in collaboration with York Sensor Ltd.

## References

- 1) W.L.Barnes et. al., "Q-switched and single polarisation diode-pumped Nd-doped fibre lasers", IEE coll. on "All fibre devices", London, June 1988.
- 2) E.R.Taylor et. al., "Application specific optical fibres manufactured from multicomponent glasses", MRS symposium, Vol. 172, pp. 321-327, Dec 1989.
- 3) Schott Laser glass catalogue.
- 4) W.L.Barnes, P.R.Morkel & J.E.Townsend, "Detailed characterization of  $\text{Nd}^{3+}$  doped  $\text{SiO}_2\text{-GeO}_2$  glass fibre lasers", Opt. Comm., Vol.82, No.3,4, pp 282-288, April 1991.

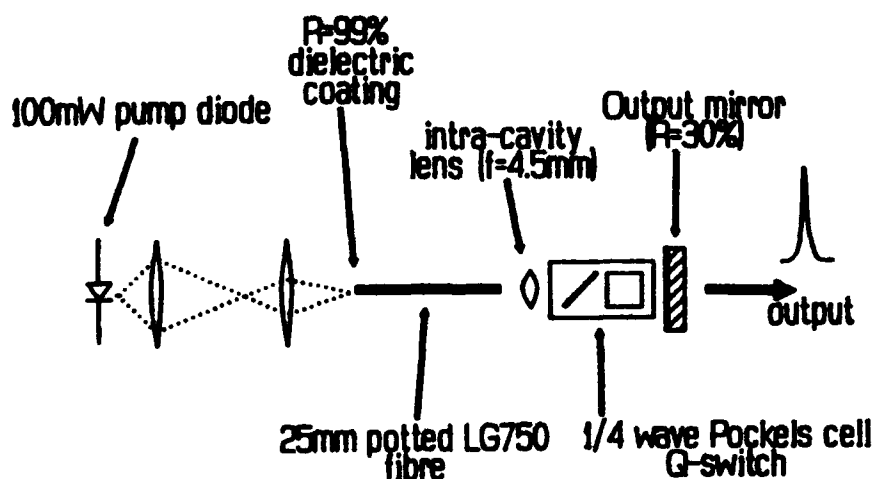


Fig. 1 Q-switched fibre laser configuration. Cavity length 10cm.



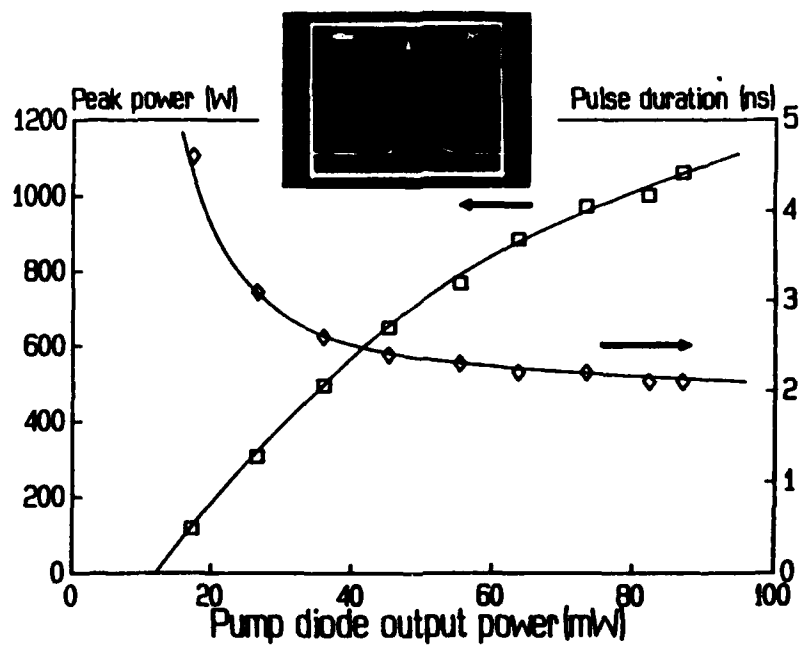


Fig. 2 Q-switched pulse peak power and duration variation with laser diode output power. Repetition frequency < 1kHz. Inset is the pulse shape at maximum pump power (87mW).

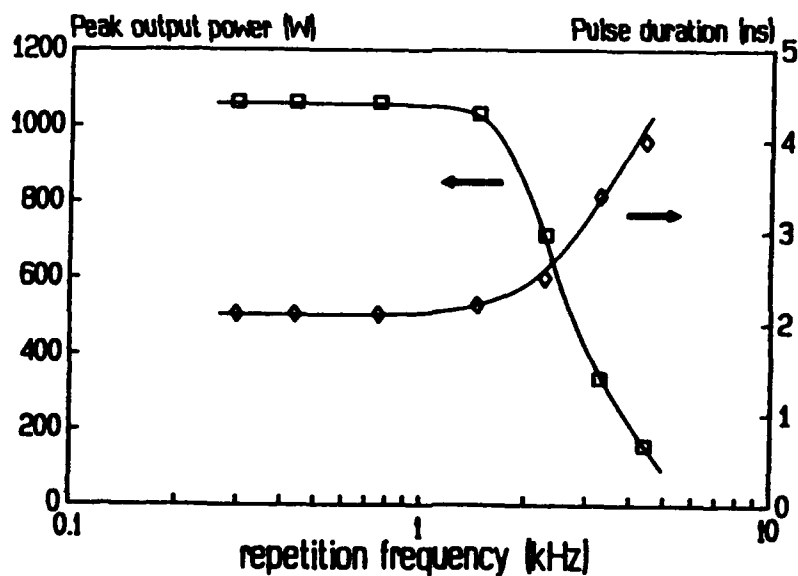


Fig. 3 Q-switched pulse peak power and duration variation with repetition frequency. Pump power 87mW.

## W1.2 Sagnac Interferometer Including A Recirculating Ring With An Erbium-doped Fibre Amplifier

*J. T. Kringlebotn and K. Bløtekjær*

University of Trondheim, Norwegian Institute of Technology,  
Division of Physical Electronics, Trondheim, Norway

and

*C. N. Pannell*

University of Southampton, Optical Fibre Group, Southampton, U. K.

### Introduction

The use of a Sagnac interferometer as an acoustic sensor has recently been demonstrated [1]. One reason for using a Sagnac interferometer is that the path imbalance is zero, such that no interferometric conversion of the source phase noise to intensity noise occurs. The low frequency response of a Sagnac interferometer increases with increasing loop length, and a very long length of fibre is needed to achieve high responsivity for acoustical frequencies. In this paper we present a scheme where we enhance the low frequency response using a recirculating ring within the Sagnac loop, as shown in fig. 1, thereby increasing the effective length of the Sagnac loop. To increase the number of recirculations an erbium-doped fibre amplifier is incorporated in the ring to compensate for both the coupling and the intrinsic losses of the ring. We also present the results of a noise analysis of a recirculating ring including a fibre amplifier, and show that the dominating noise in our sensor is the beat noise between the signal and the spontaneous emission produced by the fibre amplifier.

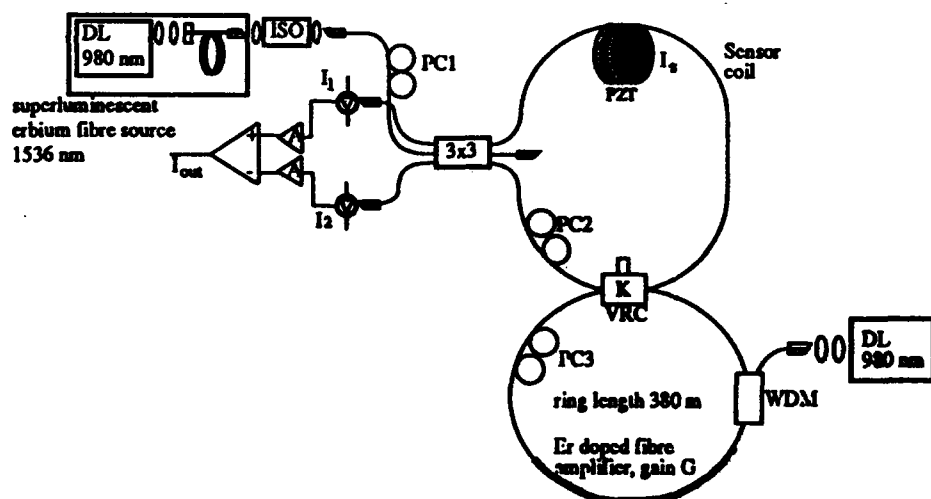


Figure 1. Experimental setup. PZT = piezo-electric transducer, VRC = variable ratio coupler, WDM = wavelength division multiplexer, PC = polarization controller, ISO = optical isolator and DL = diode laser. To prevent oscillation from the fibre end-faces, all ends were angle-polished.

### Theory

In the following theoretical analysis the source is assumed to be a single mode laser with a source linewidth much narrower than the linewidth of the erbium amplifier gain spectrum, and a frequency matching exactly the peak frequency  $\nu_0$  of this spectrum. We may therefore assume a constant amplifier gain  $G = G(\nu_0)$ . When the coherence time of the source  $\tau_{\text{coh}}$  is much smaller than the transit time  $\tau$  of the recirculating ring, the signal output current is a sum of contributions from Sagnac interferometers with increasing loop length:

$$I_s(t) = I_{s0}(t) + \sum_{m=1}^{\infty} I_{sm}(t) \quad (1)$$

where  $m$  is the number of circulations in the ring. The individual contributions  $I_{sm}(t)$  are given in ref. [1]. For a harmonic signal, the sum can be evaluated, and the total rms signal current as a function of frequency may be written:

$$I_{s,rms}(f) = \frac{\sqrt{6}}{9} A R P_0 \Phi \frac{(1-\delta_0)(1-K)^2 U}{K(1-U)} \sqrt{\frac{2(1-\cos[2\pi f\tau])}{1-2U\cos[2\pi f\tau]+U^2}} \quad (2)$$

where  $\Phi = \delta\beta L_s$  is the amplitude of the acoustically induced phaseshift in the sensor coil.  $\delta\beta$  is the amplitude of the acousto-optic modulation of the propagation constant and  $L_s$  is the length of the sensor coil.  $A$  is the amplification of the two detector currents,  $R$  is the responsivity of the detectors,  $P_0$  is the power coupled into the fibre and  $f$  is the acoustical frequency.  $\delta_0$  is the loss in the variable ratio coupler (VRC),  $K$  is the coupling coefficient of that coupler and  $U = (1-\delta_0) K G (1-L)$  is the roundtrip transmission which must be less than one, this being the threshold for laser oscillations in the ring.  $L$  is the loss in the ring. We have assumed that the sensor coil is short,  $L_s \ll c/f$ , and that the signal is weak,  $\Phi \ll 1$ . The linear response is a result of using a 3x3 coupler with subtraction of the two outputs, as shown in fig.1.

The output noise current spectrum is obtained as the Fourier transform of the autocovariance function of the output current, as in [2] and [3], but with the fibre amplifier incorporated as an additional noise source. We get three noise terms, the source induced noise as in [2] and [3], the signal-spontaneous beat noise and the spontaneous-spontaneous beat noise. Source induced noise will normally be the dominating noise, but should be cancelled in our differential detection scheme. The dominating noise term is then the signal-spontaneous beat noise. Shot noise is negligible in this setup. With a narrowband laser source there will always be some interferometric conversion of source phase noise due to coherent backscattering. This noise is negligible when using a broadband thermal like source. When  $\tau_{coh} \ll \tau$  we get for the signal-spontaneous beat noise:

$$S_{s,sp}(f) = \frac{2}{9} 2 R^2 P_0 \mu h\nu_0 (G-1) \cdot S_{\delta,s-sp}(f) \quad (3)$$

$\mu$  is the amplifier population inversion factor, which is assumed to be one, and  $h\nu_0$  is the ASE photon energy.  $\mu h\nu_0(G-1)$  is the ASE spectral power in one polarization state [4]. The factor  $2/9$  is due to the 3x3 coupler.  $S_{\delta,s-sp}(f)$  is a dimensionless transfer function for the recirculating ring, given by

$$S_{\delta,s-sp}(f) = \frac{(1-\delta_0)^2 K(1-K)}{1-U} \left\{ 1 + \frac{(1-K)U}{K} \left( \frac{(1-K)(U+1)}{K} + 2(U-\cos[2\pi f\tau]) \right) \right\} \quad (4)$$

This function has maxima at frequencies  $n \cdot 1/\tau$  where  $n = 0, 1, 2, \dots$

The noise equivalent phaseshift  $NE\Phi(f)$  is obtained by setting  $I_{s,rms}(f)$  in (2) equal to the rms noise current  $I_n(f) = A\sqrt{S_{s-sp}(f) B}$ , where  $B$  is the electrical bandwidth of the detection system. The result is

$$NE\Phi(f) = \frac{K(1-U)}{(1-\delta_0)(1-K)^2 U} \sqrt{\frac{6\mu h\nu_0(G-1)B S_{\delta,s-sp}(f)(1-2U\cos[2\pi f\tau]+U^2)}{P_0 2(1-\cos[2\pi f\tau])}} \quad (5)$$

## Experiment

The experimental setup is shown in fig. 1. Polarization controllers (PC) were used to control both the input polarization state, the reciprocity of the Sagnac interferometer and the birefringence inside the recirculating ring, this being essential to obtain maximum signal-to-noise ratio. Some meters of fibre were wrapped around a piezo-electric transducer (PZT) which was used to simulate the acoustical signal. As a source we first used a DFB laser with linewidth (FWHM) of 20 MHz designed to operate at 1536 nm. The wavelength of the DFB laser was temperature tuned to match exactly the peak of the erbium amplifier gain spectrum. Secondly, we tried a broadband superluminescent erbium fibre source with 2 nm linewidth (FWHM) (and maximum power 0.45 mW) to reduce the problem with coherent backscattering. The erbium fibre was the same as in the fibre amplifier and no wavelength tuning, and therefore temperature control, was needed to match the fibre source with the amplifier. The erbium amplifier linewidth (FWHM) is 4 nm.

## Results and discussion

Fig. 2a shows  $NE\Phi(f)$  when using the DFB laser. The three solid curves refer to different values of the coupling  $K$ , keeping the roundtrip transmission  $U$  close to one. Launched source power  $P_0 = 0.1$  mW. Fig. 2a also shows the measured  $NE\Phi(f)$  for a simple Sagnac interferometer without a recirculating ring, but with the same total length of fibre, which is seen to give the lowest  $NE\Phi$ ! In fig. 2b we plot  $NE\Phi(f)$  according to eq. (5) for the same source power  $P_0$  and the same values of  $K$ , assuming  $L = 0.37$ ,  $\delta_0 = 0.04$ ,  $\tau = 1.86$   $\mu$ s and  $U = 0.99$ , this being based on experiments with a pulsed source [4].  $NE\Phi$  for the simple Sagnac interferometer is assumed to be shot noise limited [1]. We observe a clear mismatch between the experimental results in fig. 2a and the theoretical curves in fig. 2b, even though the functional forms are similar. This is mainly due to the conversion of source phase-noise because of coherent backscattering associated with the use of the relatively coherent DFB-laser.

This problem should not be present when using the incoherent superluminescent erbium source. The experimental results with this source is shown in fig. 3a, again for different values of  $K$ , operating close to threshold. We see a decrease in  $NE\Phi$  by one order of magnitude which confirms the explanation given above. Fig. 3a also shows that using a Sagnac interferometer including a recirculating ring with a fibre amplifier decreases  $NE\Phi$  at low frequencies by at least a factor of 2 (at 10 kHz) compared to a simple Sagnac interferometer with the same total length of fibre. The corresponding theoretical curves are shown in fig. 3b, where the same parameters as in fig. 2b are used. However, in this case we can no longer assume a constant gain, and the expressions in (2) - (5) have been modified to include the frequency dependency of the gain. The mismatch is still about one order of magnitude. This is believed to be due mainly to a contribution of source induced noise because of a slight asymmetry in our differential detection scheme. We also see that the experiments exhibit higher noise at frequencies below 5 kHz. This is probably due to  $1/f$ -noise.

The signal frequency response was experimentally found to follow eq.(2), where the low frequency response is enhanced when increasing the roundtrip transission  $U$ . The discrepancy between theory and experiment is, therefore, due to the noise.

## Conclusion

We have shown that incorporating a recirculating ring with an erbium-doped fibre amplifier in a Sagnac interferometer used as acoustical sensor decreases the noise equivalent phaseshift at low frequencies compared to a simple Sagnac interferometer with the same total length of fibre. The noise penalty using a fibre amplifier in a recirculating ring is, however, quite high. The peak in the noise spectrum centred at  $f = 0$  is crucial for low frequency operation such as in our acoustical sensor, and therefore, the advantage of using the recirculating ring with fibre amplifier is limited. However, the active recirculating ring can be very useful in many other applications, for instance as an optical delay line [5]. We have also shown that a superluminescent fibre source is an almost

ideal source for sensor applications because of its incoherence and relatively high power. It is also a good source in combination with a fibre amplifier.

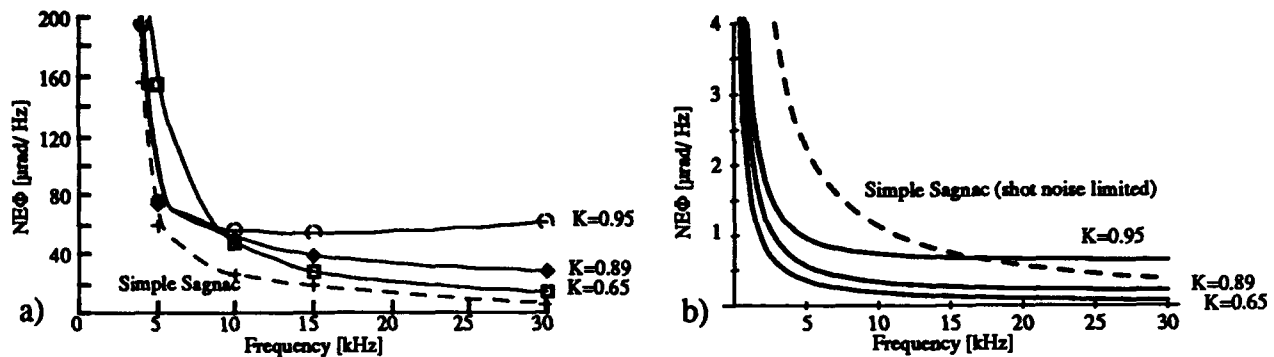


Figure 2. Noise equivalent phaseshift as a function of frequency at different coupling ratios  $K$ . The source is a DFB laser. a) experimental results, roundtrip transmission close to threshold. Results with a simple Sagnac loop interferometer without a fibre amplifier is also shown. b) theoretical results, signal-spontaneous beat noise limited. Roundtrip transmission  $U = 0.99$ , Shot noise limited noise equivalent phaseshift for a simple Sagnac loop interferometer is also shown.

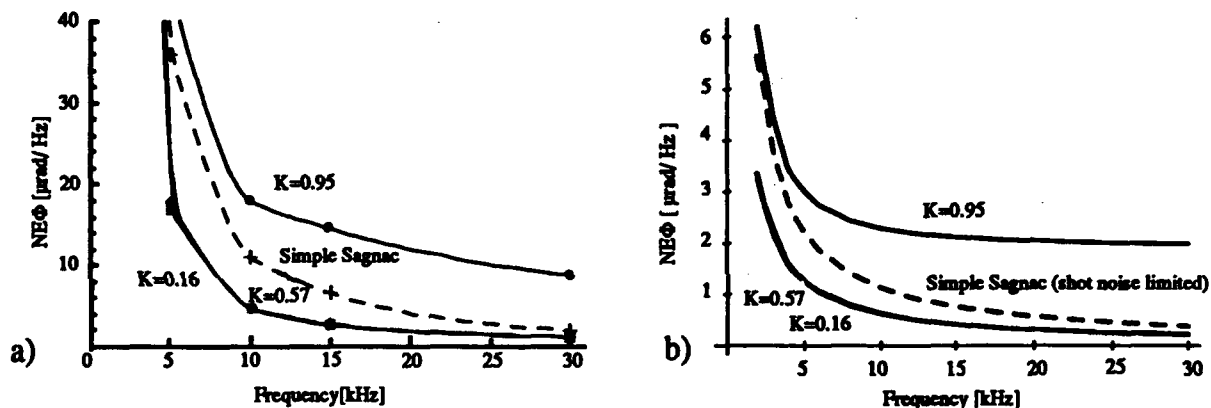


Figure 3. Same as 2, but with a superluminescent erbium source, a) experimental results, b) theoretical results.

## Acknowledgements

J. T. K. thanks D. N. Payne for the invitation to work in the ORC, and P. R. Morkel and R. I. Laming for fruitful discussions.

## References

1. K. Kråkenes and K. Bløtekjær, "Sagnac interferometer for underwater sound detection: noise properties", *Opt. Lett.*, **14**, 1152 (1989)
2. M. Tur, B. Moslehi and J. W. Goodman, *J. Lightwave Technol.*, "Theory of laser phase noise in recirculating fiber-optic delay lines", **3**, 20 (1985)
3. M. Tur, E. Shafir and K. Bløtekjær, *J. Lightwave Technol.*, "Source-induced noise in optical systems driven by low-coherence sources", **8**, 183 (1990)
4. A. Yariv, "Quantum Electronics", 2. ed., Wiley, pp. 293 (1975)
5. J. T. Kringlebotn, P. R. Morkel, C. N. Pannell, R. I. Laming and D. N. Payne, "Amplified fibre delay line with 27000 recirculations", submitted to *Electron. Lett.*

## W1.3 Interferometric Measurements Of Linewidth And Phase Noise Of An Er-doped Fiber Ring Laser

R. S. Weis

Electrical Engineering Department, U. S. Naval Academy  
Annapolis, Maryland 21402

A. D. Kersey and I. N. Duling, III

Optical Techniques Branch, Code 6570  
U. S. Naval Research Laboratory, Washington, D. C. 20375

**Abstract:** A measured linewidth of  $< 10\text{kHz}$  and a phase noise level of  $\sim 20 \mu\text{rad}/\sqrt{\text{Hz}}$  (measured with a 3m unbalanced interferometer) are reported for an Er-doped fiber ring laser with an intra-ring fiber birefringent spectral filter. The effects of acoustical and vibrational shielding on these measurements are also reported.

There is considerable interest in the development and application of doped fiber amplifiers and lasers in communications systems [1]. The use of such devices in fiber optic sensor systems is also of interest (e. g., broadband superfluorescent Nd and Er fiber sources for fiber gyroscopes [2, 3]). Single frequency fiber lasers are potentially useful sources for interferometric sensor applications. A number of single frequency fiber lasers have been demonstrated, most commonly utilizing a traveling-wave ring configuration [4—7]. The important laser characteristics for interferometric sensor systems are phase noise, linewidth, frequency stability, and tunability. In this paper, we report measurements of the linewidth and low-frequency phase noise of an Er-doped fiber ring laser with an intra-ring fiber birefringent spectral filter. Measurements of the low-frequency laser jitter ( $1/f$  FM noise) are reported for the first time. We also demonstrate that linewidths measured using the delayed self-heterodyne method are significantly broadened by laser FM noise due to acoustical perturbations of the laser and the delay fiber in the interferometer.

The ring configuration used for this work is shown in Fig. 1. The amplifier used was a BT&D EFA3000 which contains 20 m of Er-doped fiber, pumped by a 1480 nm diode laser. The Er-doped fiber is a single-mode  $\text{Al}_2\text{O}_3/\text{GeO}_2/\text{SiO}_2$ -cored fiber with a  $\text{LP}_{11}$  mode cutoff wavelength of  $\sim 1270$  nm. The Er concentration is  $\sim 300$  ppm. The fiber-pig-tailed Faraday rotator/polarizer (FR/P) combination (Isowave) ensured that the ring would be a unidirectional laser. The output coupler coupled 30% of the power out of the ring. The 2m and 8m sections of high birefringence fiber (York HiBi, 1mm beat length) were spliced together with an arbitrary alignment of their birefringent axes. The resultant wavelength selectivity can be seen in the modulation of the amplified spontaneous noise in Fig. 2, the laser's optical spectrum at about twice threshold. The observed wavelength could only be changed by discrete steps by changing the polarization controller (PC) in the ring. However, when the HiBi was heated very slightly the wavelength changed continuously and then "hopped" back to the starting wavelength when it began to approach the next discrete step. Single-mode operation was verified by observing the beat frequencies and the interference fringes from the 3m path imbalance Mach-Zehnder interferometer (see Fig. 3). The fringes from the interferometer were stable for periods on the order of 10 seconds, then would change discretely to a new state as the laser mode-hopped. The maximum output power of the ring laser was  $\sim 500 \mu\text{W}$ , with a slope efficiency  $\sim 2.5\%$ .

The phase noise was measured by introducing a 22 mrad signal at 2.25 kHz using a piezoelectric transducer in one arm of the 3m path-imbalance interferometer. The phase noise of the laser with no acoustical shielding was  $35 \mu\text{rad}/\sqrt{\text{Hz}}$ . The laser was then acoustically shielded. The phase noise at the same pump level (1.5 times threshold) decreased to  $22 \mu\text{rad}/\sqrt{\text{Hz}}$  (see Fig. 4 (a)). The measurement frequency and pump level of the laser are important parameters in the measurement because the relaxation oscillations varied from  $\sim 5\text{kHz}$  to  $\sim 15\text{kHz}$  and increase the noise floor near the measurement frequency.

The laser's linewidth was measured using the delayed self-heterodyne technique [8]. The degree of acoustical and vibrational shielding of both the long-path-imbalance interferometer employed and the laser made a large difference in the measured linewidth as demonstrated in Fig. 5. Curve *A* corresponds to the laser with no acoustical or vibrational shielding, curve *B* corresponds to the laser with improved vibration isolation, and curve *C* corresponds to both the laser and the long-path-imbalance interferometer acoustically shielded. Typical lineshapes corresponding to points on the curves are shown in Fig. 6. The line shapes did not depend on the pump current. As shown in Fig. 5, the line broadening due to higher levels of acoustically-induced noise increased slightly with delay length. The primary delay length dependence of the line broadening is due to low-frequency jitter ( $1/f$  FM noise). To investigate the frequency dependence of the FM noise, the phase noise shown in Fig. 4(a) was recalculated as FM noise and plotted as a function of frequency in Fig. 4(b). The FM noise is approximately  $1/f$  dependent for  $0 < f < 3$  kHz. The jitter is also the primary reason that once the laser and delay line were acoustically shielded, the measured linewidth was independent of the pump power [9].

In summary, measurements of the linewidth and low-frequency phase noise of an Er-doped fiber ring laser with an intra-ring fiber birefringent spectral filter were reported. Measurement of the low-frequency laser jitter ( $1/f$  FM noise) was also reported. Linewidths measured using the delayed self-heterodyne method were shown to be significantly broadened by laser FM noise due to acoustical perturbations of the laser and the delay fiber in the interferometer.

#### References

- [1] P. Urquhart, *IEE Proc., Part J*, vol. 135, pp. 385—407, 1988.
- [2] W. K. Burns, I. N. Duling, L. Goldberg, R. P. Moeller, C. A. Villareul, E. Snitzer, and H. Po, *Proc. Conf. on Optical Fibre Sensors, OFS'89* (Paris, France), Sept. 1989, pp. 137—142.
- [3] P. R. Morkel, *Proc. Conf. on Optical Fibre Sensors, OFS'89* (Paris, France), Sept. 1989, pp. 143—148.
- [4] P. R. Morkel, G. J. Cowle, and D. N. Payne, *Electron. Lett.*, vol. 26, pp. 632—634, 1990.
- [5] K. Iwatsuki, H. Okamura, and M. Saruwatari, *Electron. Lett.*, vol. 26, pp. 2033—2035, 1990.
- [6] D. A. Smith, M. W. Maeda, J. J. Johnson, J. S. Patel, M. A. Saifi, and A. Von Lehman, *Opt. Lett.*, vol. 16, pp. 387—389, 1991.
- [7] G. A. Ball, W. W. Morey, and W. H. Glenn, *IEEE Photon. Technol. Lett.*, vol. 3, pp. 613—615, 1991.
- [8] T. Okoshi, K. Kikuchi, and A. Nakayama, *Electron. Lett.*, vol. 16, pp. 630—631, 1980.
- [9] K. Kikuchi and T. Okoshi, *Electron. Lett.*, vol. 21, pp. 1011—1012, 1985.

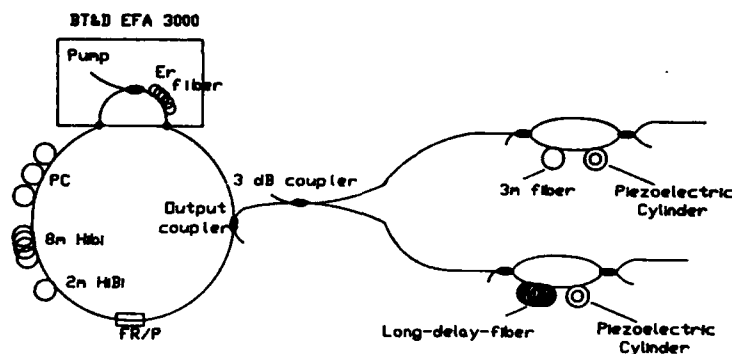


Fig. 1 Ring Laser Configuration. The lasing wavelength was controlled by the orientations of the polarization controller (PC) coils and the Faraday rotator/exit polarizer (FR/P) device.

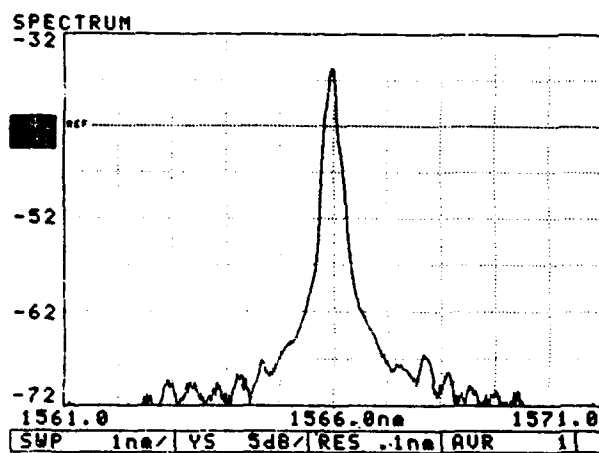


Fig.2 Optical spectrum of the ring laser at about twice threshold. The modulation of the amplified spontaneous emission is due to the intra-ring birefringent spectral filter which consisted of two lengths of HiBi and the the combined Faraday rotator/polarizer.

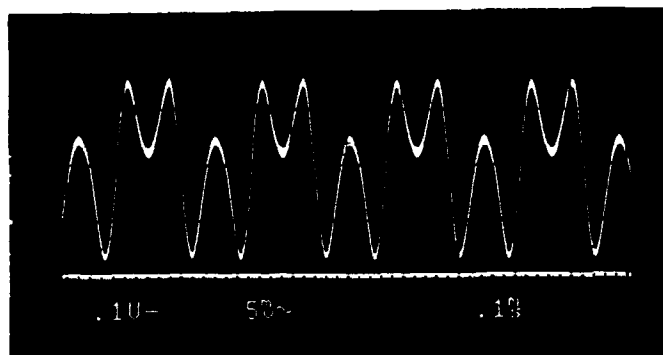
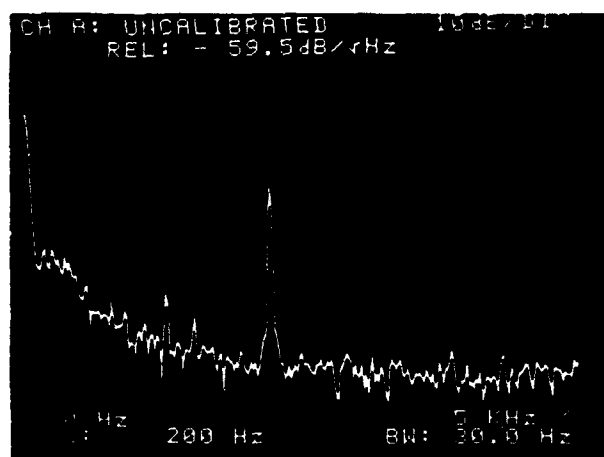
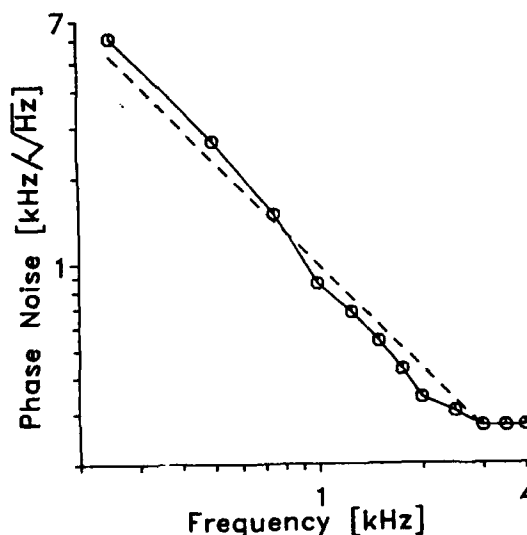


Fig. 3 Interference fringes observed with 3m path-imbalance Mach-Zehnder interferometer.



(a)



(b)

Fig. 4 (a) Phase noise measurement using 3m path-imbalance Mach-Zehnder interferometer. The peak at 2250 Hz is 22 mrad and is generated by a piezoelectric transducer in the long arm of the interferometer. (b) Phase noise of Fig. 4(a) recalculated as FM noise.



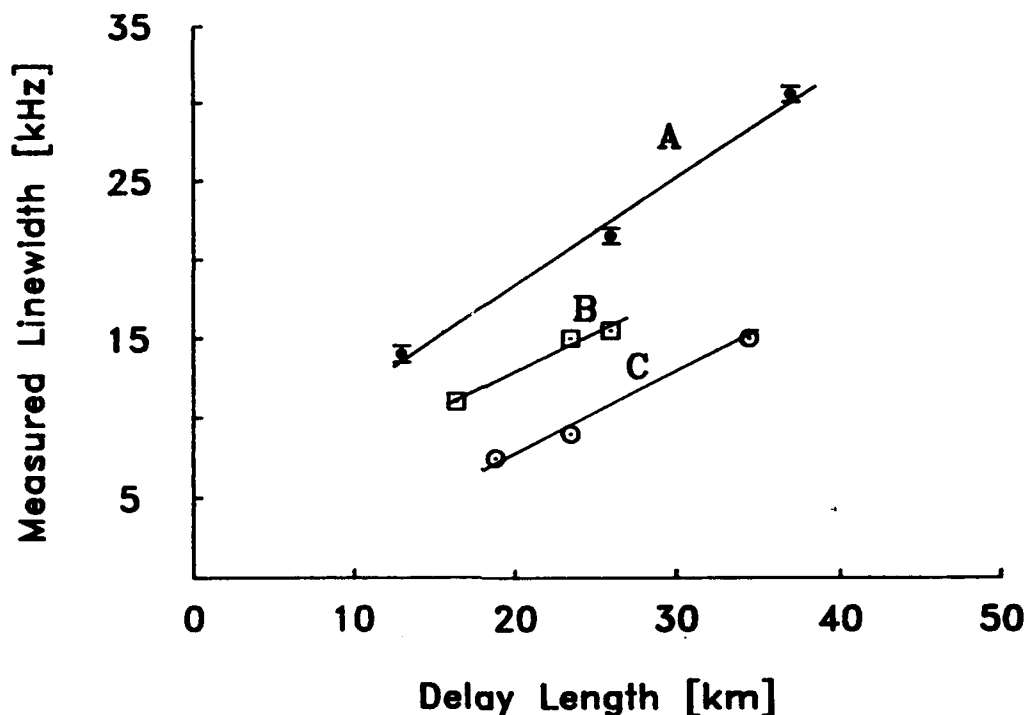
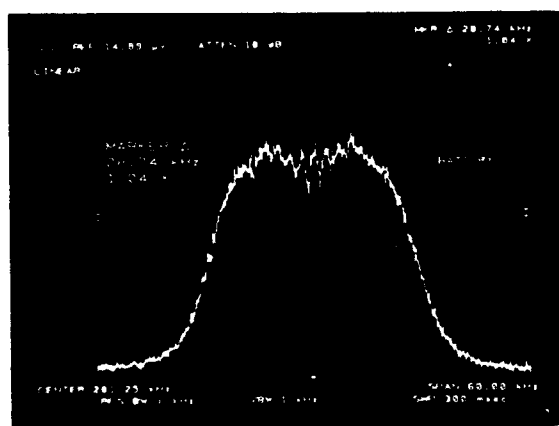
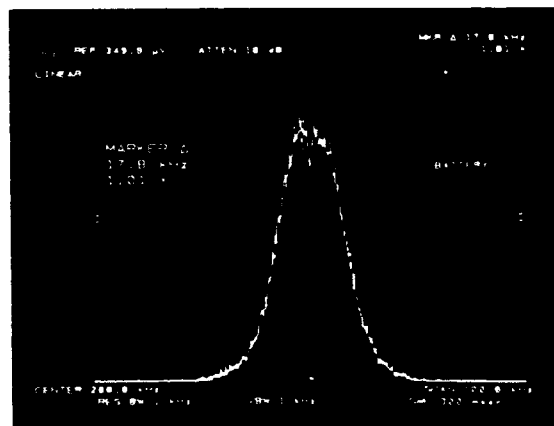


Fig. 5 Laser linewidth measured using the delayed self-heterodyne technique vs. the delay length of one of the interferometer arms. Curve A corresponds to the laser with no acoustical or vibrational shielding, curve B corresponds to the laser with improved vibration isolation, and curve C corresponds to both the laser and the long-path-imbalance interferometer acoustically shielded.



(a)



(b)

Fig. 6 Lineshapes observed under different acoustic conditions, (a) was observed with a delay length of 13 km with no acoustical or vibrational shielding of the laser (corresponds to the leftmost point on curve A of Fig. 5), (b) was observed with a delay length of 18.8 km with the laser and the delay fiber acoustically shielded (corresponds to the leftmost point of curve C in Fig. 5). The frequency span of (a) is 60 kHz and of (b) is 100 kHz.

## W1.4 High Power, Broadband Light Source By Tandem Combination Of A Superluminescent Diode And An Er Doped Fiber Amplifier

Norman S. Kwong

Ortel Corporation

2015 W. Chestnut St., Alhambra, CA 91803

Broadband light sources have been proven to be very useful in fiber gyro applications. In the past, the broad band light sources which have been used for fiber gyro applications are light emitting diodes (LED), superluminescent diodes (SLD), and superfluorescent fiber light sources (SFF). Let us compare these light sources performances at the 1550 nm wavelength. LEDs have a very wide spectrum ( $\sim 100$  nm FWHM), but very low fiber coupled power ( $\sim 10$   $\mu$ W.). SLDs have about 50 nm spectral width and about 1 mW fiber coupled power [1]. SFFs have high output power (typically a few mW depending on pump power) and very stable optical spectrum with respect to temperature variation. However, SFFs have undesirable twin peak characteristic (at 1532 and 1558 nm) in the fluorescence spectrum. At high output power, the peak at 1532 nm dominates and the resulting spectral width is very narrow ( $\sim 2$  nm) [2]. Recently, it has been shown that the spectral width at 1532 nm can be widened to 9 nm by using Al as a co-dopant [3,4].

We have found that the fluorescent peak at 1532 nm can be suppressed and the broad band fluorescent peak at 1558 nm can be enhanced by operating the EDFA in the gain saturation regime. Gain saturation is achieved by injecting a relatively low power ( $\sim 0.3$  mW) signal from an SLD into the EDFA. The resulting broadband light source has 20 mW output power, 21 nm spectral width and less than 7% spectral modulation.

The Er doped fiber used in the experiment is an Al-codoped (3 mole %  $\text{Al}_2\text{O}_3$ ) Er doped fiber produced by AT&T. The core diameter, Er concentration and cut-off wavelength of the fiber are 3.2  $\mu$ m, 400 ppm and 1.02  $\mu$ m respectively. The lengths of Er doped fiber is 12 m.

Fig. 1 shows the schematic diagram of the SLD-EDFA configuration. The spectrum of the SLD before the EDFA is shown in Fig. 2. The spectral width is seen to be 49 nm. The SLD-EDFA spectrum is shown in Fig. 3. The forward ASE spectrum without SLD input is also shown in Fig. 3 for comparison. The 980 nm pump power is 60 mW. The peak at 1532 is greatly suppressed due to gain saturation.

The coherence spectrum of the SLD-EDFA is shown in Fig. 4. The primary coherence peak is widened from 48  $\mu$ m to 120  $\mu$ m at the  $1/e^2$  point as compared to the original SLD coherence spectrum. This is due to the spectral width being reduced from 50 nm to 21 nm. The secondary coherence peak is basically the same as the original SLD, which indicates that the fiber amplifier does not introduce any

additional spectral modulation to the system. The output power of the SLD-EDFA versus input SLD power is shown in Fig. 5. For the given experimental conditions, the SLD power required to saturate the EDFA gain is only 0.2 mW.

As long as the SLD spectrum is broad and covers the entire EDFA fluorescent spectrum, the resultant SLD-EDFA spectrum is determined by the saturated gain spectrum of the EDFA. Therefore, SLD-EDFA enjoys the same spectral stability with respect to temperature as the SFF.

In conclusion, a light source with high power, broad spectrum, small spectral modulation and good spectral stability with temperature has been demonstrated. These characteristics are highly desirable for fiber gyro applications. The twin fluorescence peak problem is solved by operating the EDFA in the saturated region with an injected SLD signal.

#### Acknowledgement

The Er fiber used in the experiment are provided by D. Digiovanni of AT&T.

#### References

1. T.R. Chen, et.al., Appl. Phys. Lett. vol. 56, pp. 2502, 1990.
2. K. Iwatsuki, IEEE Photon. Technol. Lett., vol. 2, pp. 237, 1990.
3. K. Iwatsuki, IEEE Photon. Technol. Lett., vol. 3, pp. 281, 1991.
4. P.F. Wysocki, IEEE Photon. Technol. Lett., vol. 2, pp. 178, 1990.
5. M. Tachibana, et.al., Proc. Topical Mtg. on Optical Amplifiers and Their Applications, Paper MDI, Monterey, 1990.

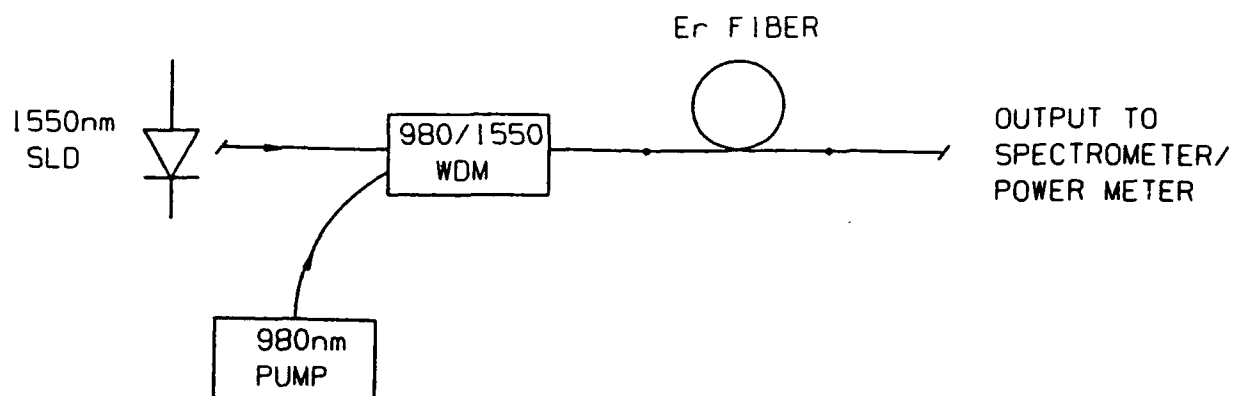


Fig. 1 Schematic diagram of superfluorescent fiber light source (SFF).

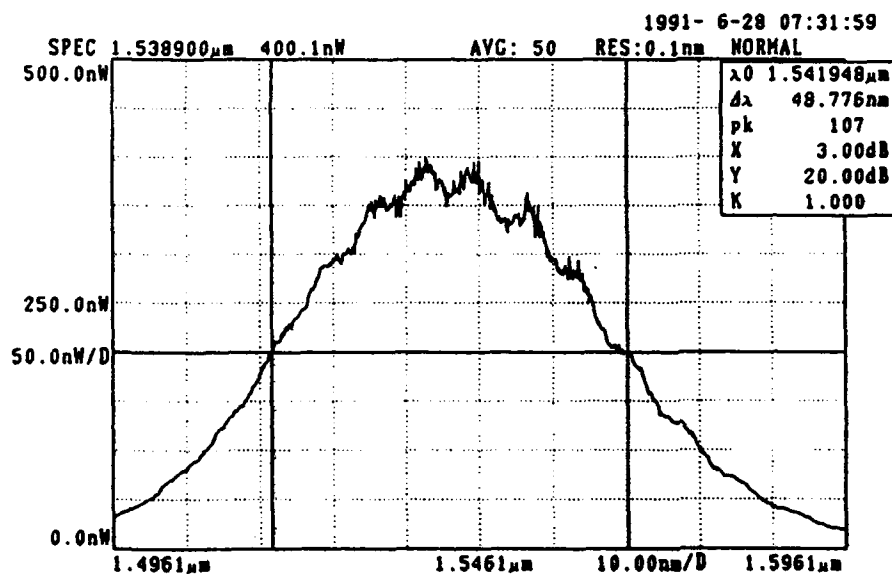


Fig. 2 SLD spectrum at 0.3 mW.

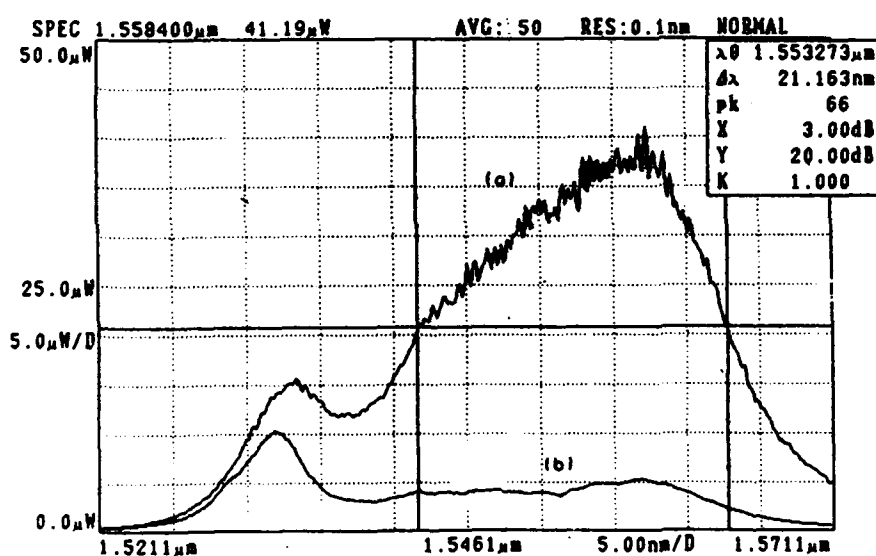


Fig. 3 (a) SLD-EDFA output spectrum at 20 mW, SLD input power is 0.3 mW.  
(b) SLD-EDFA output spectrum without SLD input (equivalent to forward ASE SFF).

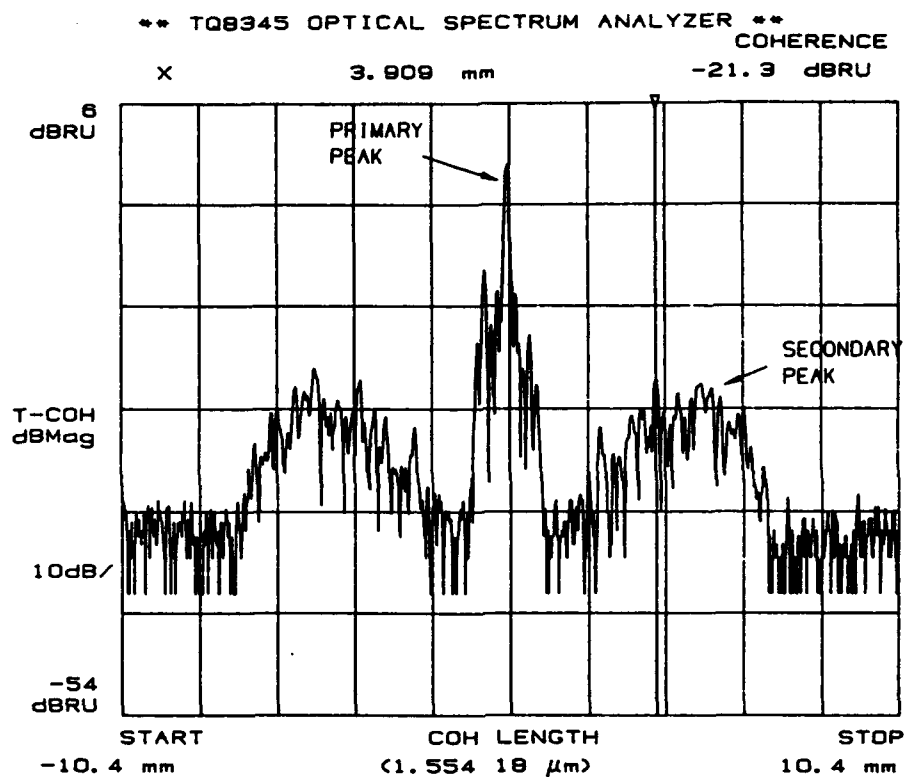


Fig. 4 Coherent spectrum of SLD-EDFA at 20 mW output power.

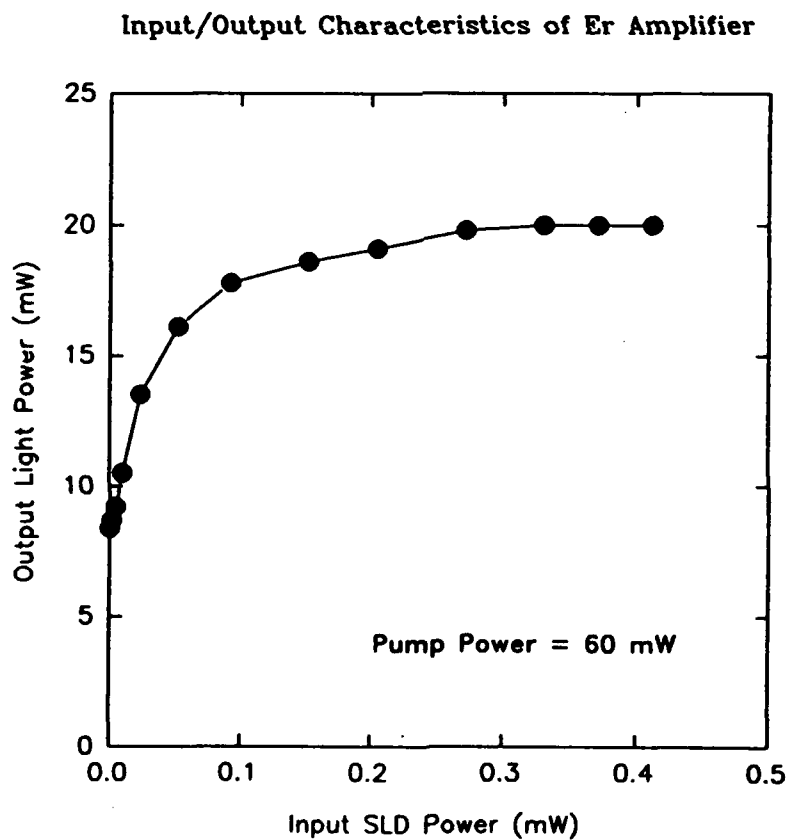


Fig. 5 SLD-EDFA outpower power vs. input SLD power.

## 1.5- $\mu\text{m}$ Polarization-Insensitive Strained MQW Superluminescent Diode

Osamu Mikami <sup>a)</sup>, Yoshio Noguchi <sup>b)</sup>, Katsuaki Magari <sup>b)</sup>  
and Yasuhiro Suzuki <sup>b)</sup>,

<sup>a)</sup> University of Tokyo, RCAST,  
4-6-1 Komaba, Meguro-ku, Tokyo, 153 JAPAN

<sup>b)</sup> NTT Opto-electronics Laboratories,  
3-1 Morinosato Wakamiya, Atsugi, 243-01 JAPAN

### Abstract

*Polarization-insensitive high-power superluminescent diodes emitting at 1.5- $\mu\text{m}$  were fabricated by using a tensile-strained-barrier MQW. Polarization dependence as low as 5 % and 3.8 mW optical power were obtained at 200 mA.*

### Introduction

Superluminescent diodes (SLDs) will prove to be optimum light sources in optical fiber gyroscopes and in optical time domain reflectometry (OTDR) applications because of their low coherence and high output power<sup>1)</sup>. Furthermore, their broad emission spectral width and consequently short coherence length can significantly improve system performance. We have already reported the fabrication of high-power and broad-spectral-width InGaAsP SLDs emitting at 1.3  $\mu\text{m}$  and 1.5  $\mu\text{m}$  <sup>2-5)</sup>. These SLDs have an inherent problem, however, in that the optical output powers differ greatly between the TE and TM modes. Polarization-maintained optical fibers and other polarization-control optical devices are therefore needed in optical sensor applications, but there have so far been no trials to fabricate polarization-insensitive SLDs.

Here we propose a novel approach using a tensile-strained-barrier multiple quantum well (MQW) active layer. Applying this active layer structure, we could realize polarization-insensitive SLDs with a power difference as low as 5% for all polarization angles. An optical output power of 3.8 mW and a spectral modulation of 3% were attained at an injection current of 200 mA.

### Approach and Device Structure

In conventional SLDs, optical power in the TE mode is usually higher than in the TM mode. This is mainly due to the different mode confinement factors for these modes, even though conventional bulk materials exhibit polarization-insensitive optical gain. Introducing tensile strain offers a promising way of achieving polarization-insensitive output power. The effectiveness of this approach derives from the fact the TM-mode gain can be enhanced, thus allowing a polarization-insensitive optical amplifier<sup>6,7</sup>). In strained MQW SLDs, tensile strain might be introduced into the well layers or into the barrier layers. We used the latter approach and obtained very promising results.

The active region structure is shown in Fig.1. The lattice constant of 10  $\text{In}_{1-x}\text{Ga}_x\text{As}$  ( $x=0.47$ ) wells was matched to that of the InP substrate. The thickness of the wells was 50 Å. The 11  $\text{In}_{1-y}\text{Ga}_y\text{As}$  ( $y=0.72$ ) barriers were mismatched to the InP substrate and had an internal strain of -1.7 %. The barrier thickness was also 50 Å. This active region was sandwiched between two InGaAsP waveguide layers with a bandgap wavelength of 1.28  $\mu\text{m}$ . The thickness of the upper and lower InGaAsP layers were 1000 Å and 500 Å, respectively. This device was grown by metal organic chemical vapor deposition (MOCVD) and was buried with InP current-blocking layers by liquid phase epitaxy (LPE). The stripe width was 1.5  $\mu\text{m}$ .

Suppression of the Fabry-Perot lasing mode for our conventional SLDs have been achieved by using a nonpumped bent-channel waveguide region<sup>2-5</sup>), but here we used a new suppression structure (Fig. 2). The bandgap of one part of the straight MQW active region was shifted to the longer wavelength by disordering, and this straight-channel waveguide region thus effectively worked as a nonpumped absorber. The strained MQW disordering was accomplished by a  $\text{SiO}_2$  cap annealing method<sup>8,9</sup>). The active region was 600  $\mu\text{m}$  long and the nonpumped disordered region was 300  $\mu\text{m}$  long.

### Characteristics

Output power over 3.8 mW was obtained at an injection current of 200 mA (Fig. 3). This power level is comparable to the 1.5- $\mu\text{m}$  high-power SLDs we reported recently<sup>3</sup>). The inset in this figure is the

emission spectrum observed at a 200mA injection current. The lasing mode was well suppressed by the nonpumped disordered MQW region, even though the absorber waveguide was straight. Spectral modulation was less than 3%. At an injection current of 200 mA, the optical power difference for all polarization angles was as low as 5% (Fig. 4).

### Summary

Polarization insensitive SLDs emitting at a wavelength of 1.5  $\mu\text{m}$  have been fabricated for the first time by using a tensile-strained-barrier MQW active structure. Polarization dependence as low as 5% was obtained with an optical power of 3.8 mW at an injection current of 200 mA. These novel SLDs should provide highly sensitive fiber gyroscopes and other optical sensor applications.

### Acknowledgement

The authors are very grateful to Minoru Okamoto for his cooperation in growth. We also thank Mitsuru Naganuma, Yoshihiro Imamura and Haruhiko Tsuchiya for their encouragement.

### References

- 1) W. K. Burns, C. L. Chen, and R. P. Moeller, IEEE/OSA J. Lightwave Technol. LT-1, p.98, 1983.
- 2) H. Nagai, Y. Noguchi and S. Sudo, Appl. Phys. Lett., 54, p.1719, 1989.
- 3) Y. Noguchi, H. Yasaka, O. Mikami and H. Nagai, J. Appl. Phys. 67, p.2665, 1990.
- 4) O. Mikami, Y. Noguchi and H. Yasaka, Appl. Phys. Lett., 56, p.987, 1990.
- 5) O. Mikami, Y. Noguchi, H. Yasaka, K. Magari and S. Kondo, IEE Proc. -J, 138, p.133, 1991.
- 6) M. Okamoto, K. Sato, H. Mawatari, F. Kano, K. Magari, Y. Kondo and Y. Itaya, to be published in IEEE J. Quantum Electron. 1991.
- 7) K. Magari, M. Okamoto, H. Yasaka, K. Sato, Y. Noguchi and O. Mikami, IEEE Photon. Technol. Lett., 2, p. 556, 1990.
- 8) T. Miyazawa, H. Iwamura, O. Mikami and M. Naganuma, Japan. J. Appl. Phys. 28, p.L1039, 1989.
- 9) Y. Suzuki, H. Iwamura, T. Miyazawa and O. Mikami, Appl. Phys. Lett., 56, p.19, 1990.



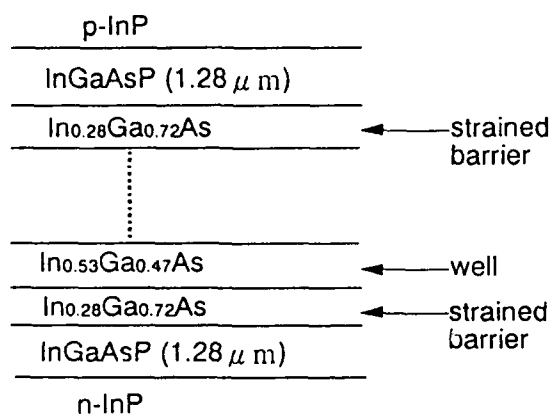


Fig. 1. Strained MQW structure.

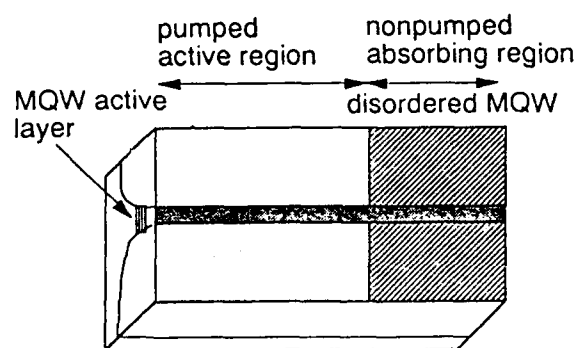


Fig. 2. SLD structure.

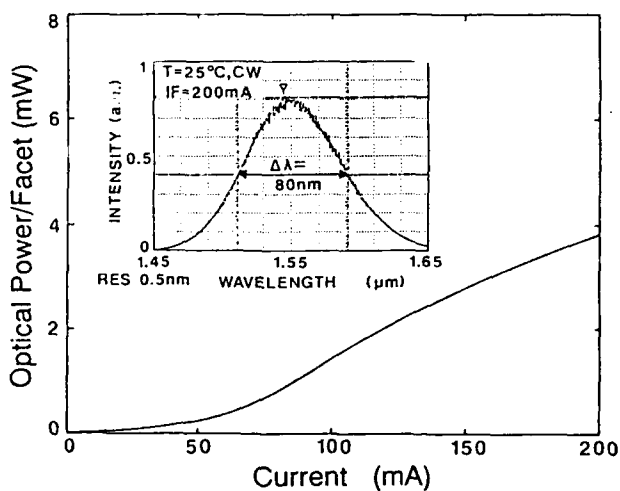


Fig. 3.  
Optical power vs. injection current.  
Inset shows emission spectrum.

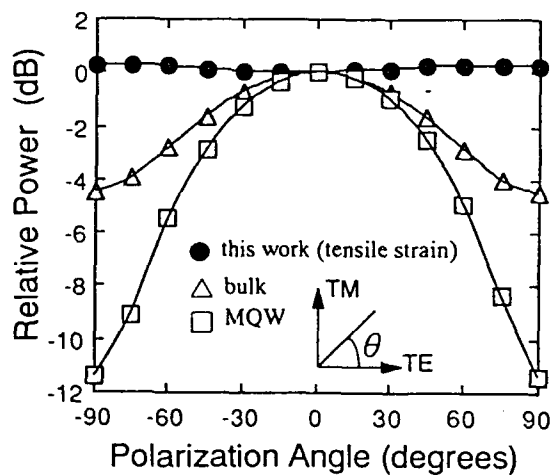


Fig. 4.  
Optical power vs. polarization angle.

## W1.6

## Optothermal Modulation Of Diode Lasers

D.J.Anderson and J.D.C.Jones

Physics Department, Heriot-Watt University, Riccarton, Edinburgh, EH14 4AS

### INTRODUCTION

Frequency modulation (FM) of diode lasers is the basic principle behind many signal processing schemes used for fibre optic sensors based on interferometry, and is most conveniently implemented by injection current modulation. Injection current induced frequency modulation also results in unwanted intensity modulation; the objective of optothermal modulation is to achieve optical frequency modulation without intensity modulation by heating the laser chip with an external pump laser.

### THEORY

The optical frequency shift,  $\Delta\nu$ , induced by injection current modulation can be shown to be<sup>(1)</sup>

$$\frac{\Delta\nu}{\nu} = \left[ \frac{1}{n_r} \cdot \frac{\partial n_r}{\partial \rho} \right] \Delta\rho + \left[ \alpha + \frac{1}{n_r} \cdot \frac{\partial n_r}{\partial T} \right] \Delta T \quad (1)$$

where  $n_r$  and  $\alpha$  represent the refractive index and linear expansion coefficient of the laser cavity respectively;  $\Delta\rho$  and  $\Delta T$  depict the excess charge carrier density and the temperature shift resulting from modulation of the injection current, and  $\nu$  is the mean optical frequency of the laser. The temperature effect,  $\Delta T$ , dominates the charge carrier effect,  $\Delta\rho$ , for current modulation frequencies  $< 1\text{MHz}$ <sup>(2)</sup>, which is the frequency range most relevant for our applications.

For the optothermal case, it can be shown that

$$\Delta\nu = c_1 \cdot \Delta\rho(x) - c_2 \cdot \Delta T(x) \quad (2)$$

where the magnitude of  $c_1$  and  $c_2$  are found from the formula used to describe the injection current induced frequency modulation, equation (1). However, in the optothermal case both the temperature modulation,  $\Delta T(x)$ , and charge carrier density modulation,  $\Delta\rho(x)$ , are a function of the position of the pump spot,  $x$ , relative to the centre of the active region output facet, and it can be shown that

$$\Delta T(x) = F(x) \cdot R \cdot \Delta P_{\text{pump}} \quad (3)$$

where  $R$  is the thermal resistance of the diode laser structure;  $\Delta P_{\text{pump}}$  represents the pump power incident on the diode facet and  $F(x)$  is a factor which depends on  $x$ , and is given by

$$F(x) = \left[ \underset{(a)}{k \cdot \eta \cdot \left( 1 - \frac{\lambda_p}{\lambda} \right)} + \underset{(b)}{k \cdot (1 - \eta)} + \underset{(c)}{(1 - k) \cdot \exp\left( -\frac{|x|}{d} \right)} \right] (1 - r) \quad (4)$$

where  $k(x)$  is the coupling coefficient of the pump radiation into the active region and is a gaussian function of the pump spot position  $x$ ;  $\eta$  represents the internal quantum efficiency;  $\lambda_p$  and  $\lambda$  are the pump and source wavelengths respectively;  $d$  depicts the thermal diffusion length and  $r$  represents the power reflectivity of the diode facet at the pump wavelength.

The factor  $F(x)$  contains three distinctive terms, (a) and (b) represent the pump photons injected into the active region creating electron-hole pairs that decay radiatively and non-radiatively respectively; whereas part (c) indicates the pump photons that are not coupled into the active region but still contribute to its heating.

The charge carrier density shift,  $\Delta\rho(x)$ , injected into the active region by the pump laser is assumed to be of the form

$$\Delta\rho(x) \propto k(x) \cdot \Delta P_{\text{pump}} \quad (5)$$

Optothermal induced amplitude modulation of the source laser diode is also assumed to be a function of both the charge carrier density and the temperature. The temperature modulates the threshold current,  $i_{th}$ , and hence the power output. The overall power modulation can be shown to be

$$\Delta P = k(x) \cdot \eta \cdot \frac{\lambda_p}{\lambda} \cdot (1 - r) \cdot \Delta P_{\text{pump}} - \epsilon \cdot \frac{i_{th}}{T_0} \cdot \Delta T(x) \quad (6)$$

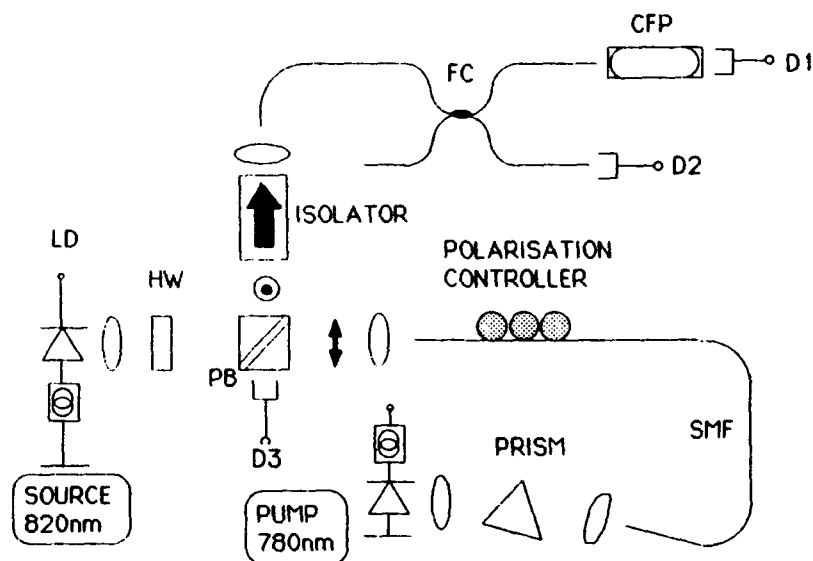
where  $\epsilon$  is the slope efficiency of the source diode laser and  $T_0$  is the characteristic temperature associated with the threshold current,  $i_{th}$ <sup>(3)</sup>.

Since both the coupling coefficient,  $k(x)$ , and the temperature shift,  $\Delta T(x)$ , are both functions of the pump spot position,  $x$ , it is possible to move the pump spot into a position where the charge carrier and thermal effects on output power become of approximately equal magnitude, but of opposite sign, such that the power modulation is minimised. The frequency modulation continues to be thermally dominated and hence remains of useful magnitude for the applications noted in the introduction.

## EXPERIMENT

An external diode pump laser, ( 780nm ), was intensity modulated via its injection current and coupled into a single mode fibre, see figure (1). The pump power reaching the source diode laser facet, ( 820nm ), was controlled with the combination of a fibre polarisation controller and a polarising beamsplitter. The polarisation of the two lasers were orthogonal which allowed the source diode laser radiation to be launched into a 3db fibre coupler in order that both the intensity and the optical frequency could be monitored. The optical frequency was monitored with a confocal interferometer. The pump spot, with a diameter of  $\sim 3\mu\text{m}$ , was piezoelectrically positioned on the facet of the source diode laser by transversely moving the output end of the fibre delivering the pump light. A dispersing prism was inserted at the input of the pump fibre to minimise reflections back to the source diode laser occurring at the pump laser.

The pump laser was intensity modulated at a frequency of 1kHz and the pump spot was moved away from the active region in a direction perpendicular to the junction of the source diode laser, both the frequency and power modulation of the source laser were monitored.



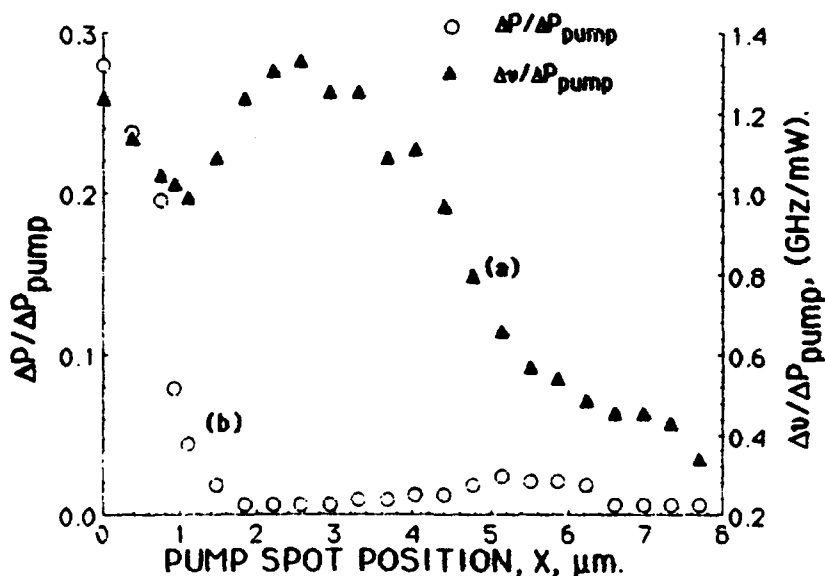
CFP: CONFOCAL FABRY-PÉROT, SMF: SINGLE MODE FIBRE, HW: HALF-WAVE PLATE  
FC: FIBRE COUPLER, PB: POLARISING BEAMSPLITTER, LD: LASER DIODE.

Figure 1. Experimental set-up.

## RESULTS.

The frequency shift,  $\Delta\nu$ , and the source laser power modulation,  $\Delta P$ , are normalised to the pump laser power,  $\Delta P_{\text{pump}}$ , and they are both displayed as a function of pump spot position,  $x$ , in graphs 1(a) and 1(b) respectively.

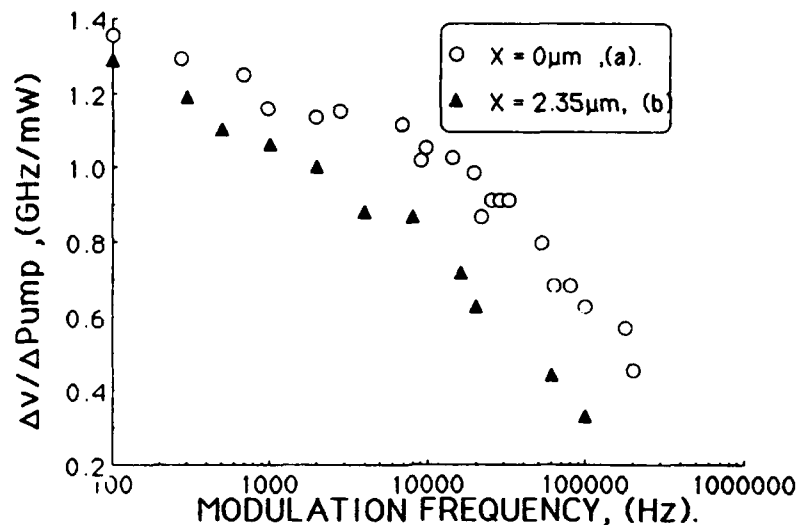
Graph 1 indicates a minimum in the power modulation, but still with useful frequency modulation, as predicted by the optothermal theory. The minimum in the power



Graph 1. Frequency and power shift as a function of pump spot position

modulation depth is less than 0.1 %/mW, when operating at  $1.7 i_{th}$ , and the frequency modulation at this point is about 1.33 GHz/mW.

The optothermal 3db frequency modulation bandwidth was measured to be  $\sim 80$ kHz when the pump spot was positioned on the active region and is shown in graph 2(a). When the pump spot is moved to a position where the intensity modulation of the source is at a minimum, the bandwidth was  $\sim 20$ kHz and is shown in graph 2(b).



Graph 2. Optothermal FM bandwidth for two pump spot positions.

## DISCUSSION AND CONCLUSION

It has been shown that optothermal modulation can be used to produce amplitudes of frequency modulation suitable for a number of signal processing schemes commonly used in fibre interferometers. Most importantly, it has been demonstrated that the concomitant intensity modulation is negligible, in contrast with the more commonly used injection current modulation. Hence, for example, it is possible to implement pseudo-heterodyne signal processing with almost complete carrier suppression. The modulation bandwidth is sufficient for most applications, but may be extended using equalisation techniques similar to those which we have discussed previously<sup>(4)</sup>.

## REFERENCES

1. M.Ito and T.Kimura, " Carrier Density Dependence of Refractive Index in AlGaAs Semiconductor Lasers ", IEEE J. Quantum Elect., 16, 9, 1980.
2. S.Kobayashi, Y.Yamamoto, M.Ito and T.Kimura, " Direct Frequency Modulation in AlGaAs Semiconductor Lasers ", IEEE J. Quantum. Elect., 18, 4, 1982.
3. H.Kressel and J.K.Butler, " Semiconductor Lasers and Heterojunction LED's", Academic Press, Chapter 8.3, pp275-280.
4. D.J.Anderson, J.D.C.Jones, P.G.Sinha, S.R.Kidd and J.S.Barton, " Scheme for Extending The Bandwidth of Injection Current Induced Laser Diode Optical Frequency Modulation ", J. Modern Optics, In Press.

## W2.1 Progress in Interferometer and Resonator Fiber Optic Gyros

(Invited)

G. A. Sanders, R.-Y. Liu & L. K. Strandjord  
Honeywell Systems & Research Center  
Phoenix, AZ

Fiber-optic gyroscopes (FOGs) have been under investigation worldwide for over fifteen years. The interferometer fiber-optic gyro (IFOG) which has received the most attention among the two most basic FOGs, has recently moved out of the purely research and development environment. Efforts now concentrate on productization of early products, environmental ruggedization, size and cost reductions, as well as further performance improvements. The resonator fiber-optic gyro (RFOG), on the other hand, is still in a purely research and development phase. RFOG development efforts, motivated by the potential for using nominally 30X less fiber to achieve comparable performance to the IFOG, are aimed at demonstrating its performance potential. Solutions to key error mechanisms such as polarization-related error mechanisms are now being demonstrated.

Several companies are now pursuing IFOG product developments for various applications. The most prevalent first application of the IFOG appears to be in the  $1^\circ/\text{hr}$  ( $1\sigma$ ) performance range; particularly for attitude heading reference systems (AHRS). Several successful flight tests have been reported.<sup>1-4</sup> Based on its inherent long life, low cost and its ability to meet the rather modest 1000 ppm scale factor requirements, an all-fiber open loop approach is being developed at Honeywell for AHARS applications. Three production contracts exist, one for usage on the Dornier 328 aircraft, the second for the Boeing 777 aircraft and the third for a Canadair application. The first of these systems is shown in figure 1. One major milestone in this application is the demonstration of bias performance over the entire temperature range, which has recently been reported.<sup>1</sup> Similarly IFOGs for military AHRS applications are now being productized.<sup>3</sup>

In the area of high performance IFOGs, several developers have reported navigation-grade or near navigation-grade performance over limited environments. Efforts such as the DARPA-sponsored GGP program,<sup>5</sup> where an IFOG-based IMU is coupled to a GPS receiver, are aimed at the demonstration of a  $0.01^\circ/\text{hr}$  IFOG over the military environment. While much attention has focussed on the IFOG bias issues and associated solutions, less discussion has centered around inherent features of the IFOG that enable the demonstration of navigation-grade scale factor performance. In particular, for the most commonly pursued loop closure techniques, i.e., serrodyne phase modulation<sup>6</sup> (Fig. 2) and the digital phase ramp<sup>7</sup>, the IFOG scale factor is inherently insensitive<sup>8</sup> to imperfections in the phase modulation.

One example of the IFOG tolerance to phase ramp imperfections is illustrated in figures 3, 4 and 5 for the case of serrodyne modulation of non- $2\pi$  amplitude.<sup>11</sup> For the ideal case of fixed  $2\pi$  amplitude and infinitely fast fall time, one can show that the servo adjusts the ramp slope,  $S$ , to impart a phase shift  $\Delta\phi = -\phi_s$  where  $\phi_s$  is the phase shift due to rotation. No errors are incurred in this case since the serrodyne frequency,  $F$ , used as the readout is strictly proportional to the rotation rate  $\Omega$  under this condition,

$$F = \frac{-\phi_s}{2\pi\tau} = \frac{-D\Omega}{\lambda n}$$

where  $D$  is the coil diameter,  $\lambda$  is the wavelength, and  $n$  is the fiber index.

Figure 3 shows the applied serrodyne voltage  $v(t)$  on the modulator for the case of a phase ramp of period  $T$  with arbitrary voltage height  $h$ . Figure 4 shows the resulting phase shifts  $\phi_1(t)$  and  $\phi_2(t)$  for the cw and ccw light waves traversing the sensing loop of transit time  $\tau$ . The phase difference  $\Delta\phi = \phi_1 - \phi_2$  is thus given by,

$$\Delta\phi = k[v(t) - v(t-\tau)] = \begin{cases} k[st - s(t-\tau)] = kst & 0 \leq t < T-\tau \\ k[st - h - s(t-\tau)] = k(st-h) & T-\tau \leq t < T \end{cases}$$

If one assumes a square wave bias modulation of  $\pi/2$  amplitude and subsequent digital demodulation<sup>8</sup>, then the servo assures equal average detected intensities,  $I$ , on each half cycle of the modulation (corresponding to the gyro being AC biased to the  $-\pi/2$  and  $\pi/2$  operating points). Thus,

$$\langle I(\pi/2) - I(-\pi/2) \rangle = 0$$

$$\text{where} \quad I(\pm\pi/2) = I_0[1 + \cos(\phi_s + kst \pm \pi/2)] \quad 0 \leq t < T-\tau$$

$$\text{and} \quad I(\pm\pi/2) = I_0[1 + \cos(\phi_s + k(st-h) \pm \pi/2 + 2\pi)] \quad T-\tau \leq t < T$$

where an arbitrary  $2\pi$  phase shift (see figure 5) has been added to the phase in the last term. We now assume that the intended serrodyne phase shift  $kst$  is close to  $-\phi_s (kst + \phi_s) \ll 1$  and that the reset amplitude  $kh$  is close to  $2\pi$  ( $kh - 2\pi \ll 1$ ).

Using the above equations to compute the time average fields

$$\langle I(\pi/2) - I(-\pi/2) \rangle = \frac{-2I_0[(\phi_s + kst)(T-\tau) + (\phi_s + kst - kh + 2\pi)\tau]}{T} = 0$$

Since  $ST = h$ , the above equation yields

$$\phi_s = \frac{-2\pi\tau}{T} = -2\pi F\tau \Rightarrow F = \frac{-\phi_s}{2\pi\tau}$$

Thus, as long as the reset amplitude is close to  $2\pi$  such that the gyro operates near  $\pm\pi/2$  (on the linear slope) the frequency  $F$  is not to first order affected by deviations of the serrodyne height from  $2\pi$ . This is a consequence of the errors during the main ramp interval of length  $(T-\tau)$  being  $\tau/(T-\tau)$  smaller and opposite sign than those during the flyback-affected interval of length  $\tau$ .

This intrinsic tolerance to phase ramp imperfections is responsible for the high performance scale factor data reported thus far in both the serrodyne<sup>10</sup> and digital phase ramp<sup>9</sup> cases where 15 ppm (see Fig. 6) and 10 ppm linearities have been reported.

Recent RFOG efforts<sup>12-21</sup> have focused on solutions to issues of optical backscatter<sup>13,14,19</sup>, polarization errors<sup>15-18</sup>, and the demonstration of high quality fiber-optic resonators<sup>19</sup>. Ezekiel et al<sup>21</sup> underscored the importance of the optical backscatter issue by showing that lock-in like behavior, similar to that of the RLG, results if the interference between the backscatter wave and the signal wave is not suppressed. Thus, use of a carrier suppressed phase modulation on one input wave is effective for this purpose. However, it was also pointed out that the intensity of the backscattered wave is a significant second error mechanism affecting the

scale factor performance. Hotate et al suggested the use of separate modulation and detection frequencies to address this issue,<sup>13</sup> which was experimentally demonstrated to the 860 ppm performance level.<sup>14</sup>

One of the major issues in the resonator FOG is that due to the unavoidable propagation of light in a second unwanted polarization state of the resonant sensing coil. As a result, the fiber resonator has a second resonance, in addition to the main resonance (used to sense rotation), that influences the rotation measurement. The frequency of this resonance relative to that of the main resonance changes with temperature<sup>15</sup>. Up to 1°/S bias drifts have been observed when the two resonances coincide. One method of suppressing this error is the use of single polarization fiber inside the ring; however, the extinction ratio requirements range from 40 dB for a 1°/hr gyro to 80 dB (not realizable in today's low-loss guided wave components) for a 0.01°/hr gyro performance.<sup>18</sup> Another approach is based on the use of a 90° rotation of the polarization in the loop.<sup>15,16</sup> This approach effectively makes the birefringence of the fiber, of which temperature changes caused the relative drift between resonances in the standard resonator, common to both resonant polarization states of the ring. In this way, a 90° rotation provides a temperature independent separation of the resonances.

Figure 7 shows a schematic of the first RFOG assembled using a 90° splice.<sup>17</sup> Results to date show a factor of 10 improvement in the bias stability over previous work, achieving 0.4°/hr bias stability over a 2 hour drift run (thermal compensation was used here so the data represents the repeatability of the compensated bias). However, these results were limited, as shown in the Allen variance plot in Figure 8, by random noise attributed to laser phase and amplitude instabilities. Improved results are expected with the implementation of standard laser stabilization techniques.

**Acknowledgement** The authors thank Gunter Stein for his contribution to the analysis of imperfect serrodyne modulation.

1. G. Weed, et al., Proc. SPIE, Vol. 1585, Fib. Opt. Gyros:15th Anniv. Conf., 1991.
2. W. Auch, et al., Proc. SPIE, Vol. 1585, Fib. Opt. Gyros:15th Anniv. Conf., 1991.
3. H. Gilles, et al., Proc. SPIE, Vol. 1585, Fib. Opt. Gyros:15th Anniv. Conf., 1991.
4. G. Pavlath, et al., Proc. SPIE, Vol. 1585, Fib. Opt. Gyros:15th Anniv. Conf., 1991.
5. W. Homer, 15th Biennial Guidance Test Symposium, Holloman AFB, 24-26, Sept., 1991.
6. A. Ebberg, et al., Optics Letters, Vol. 10, No. 6, 300-302, 1985.
7. H. Lefevre, et al., Proc. OFS'85, PSD 7, 1985.
8. H. Arditty, et al., Proc. OFS'89, Springer-Verlag, 131-136, 1989.
9. H. Lefevre, et al., Proc. SPIE, Vol. 1367, Fib. Opt. and Laser Sensors VIII, 72-80, 1990.
10. R.-Y. Liu, et al., Proc. SPIE, Vol. 1585, Fib. Opt. Gyros:15th Anniv. Conf., 1991.
11. Private communication with G. Stein of Honeywell Systems and Research Center.
12. R. Meyer, et al., Optics Letters, Vol. 8, No. 12, 644, 1983.
13. K. Hotate, et al., IEEE Photon. Technol. Lett., Vol. 2, No. 1, 75-77, Jan. 1990.
14. G. Sanders, et al., Proc. SPIE Vol. 985, Fib. Opt. and Laser Sensors VI, 202-210, 1988.
15. G. Sanders, et al., Proc. SPIE, Fib. Opt. and Laser Sensors VII, 1169, 372-381, 1989.
16. P. Mouroulis, Proc. SPIE, Fib. Opt. and Laser Sensors VII, 1169, 400-412, 1989.
17. L. Strandjord, et al., Proc. SPIE, Vol. 1585, Fib. Opt. Gyros:15th Anniv. Conf., 1991.
18. K. Hotate, et al., Proc. SPIE, Vol. 1585, Fib. Opt. Gyros:15th Anniv. Conf., 1991.
19. T. Kaiser, et al., Proc. SPIE, Fib. Opt. and Laser Sensors VIII, 1367, 121-126, 1990.
20. R. Dahlgren, et al., Proc. SPIE, Vol. 1585, Fib. Opt. Gyros:15th Anniv. Conf., 1991.
21. F. Zarinetchi, et al., Optics Letters, Vol. 11, No. 6, 401-403, June 1986.



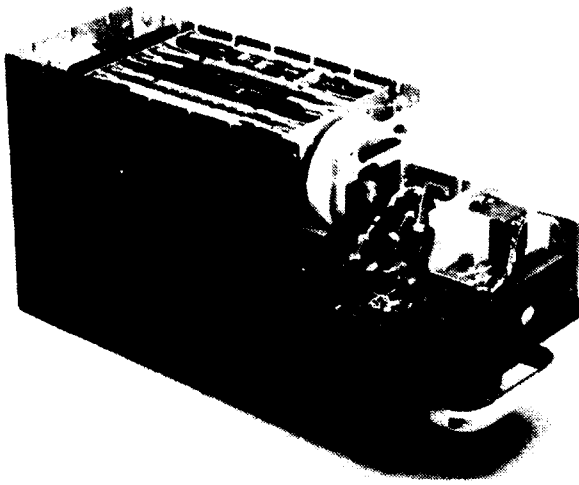


Figure 1

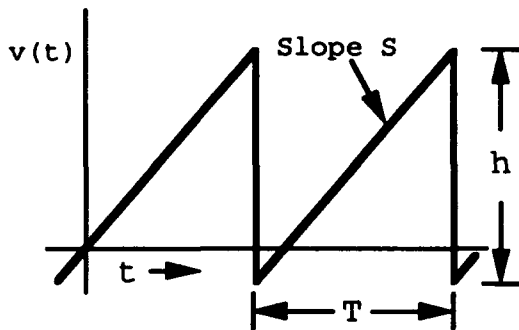


Figure 3

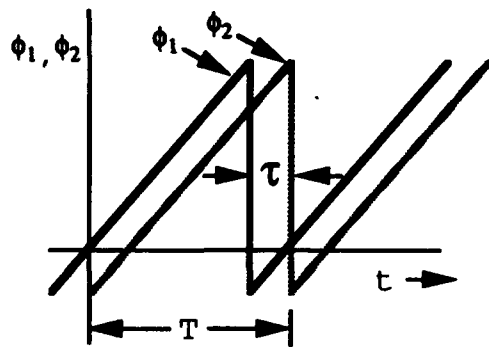


Figure 4

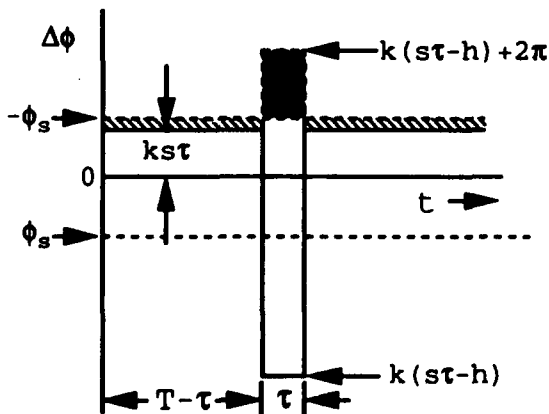


Figure 5

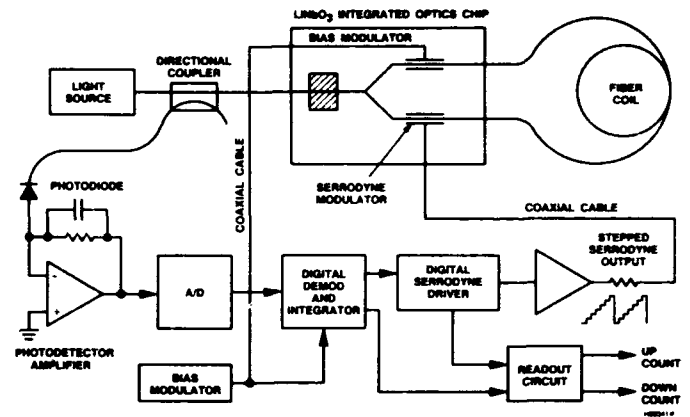


Figure 2

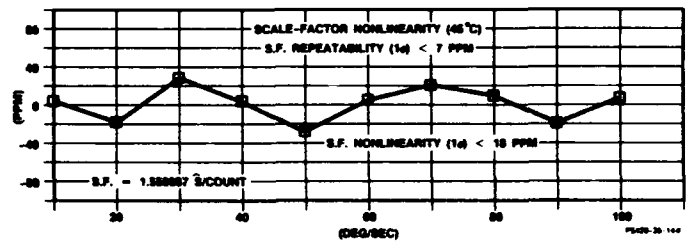


Figure 6

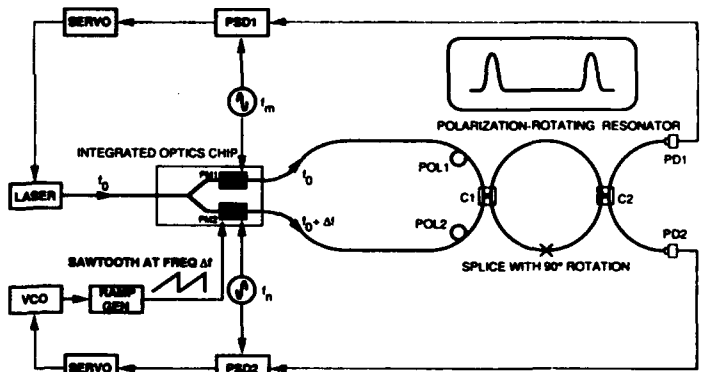


Figure 7

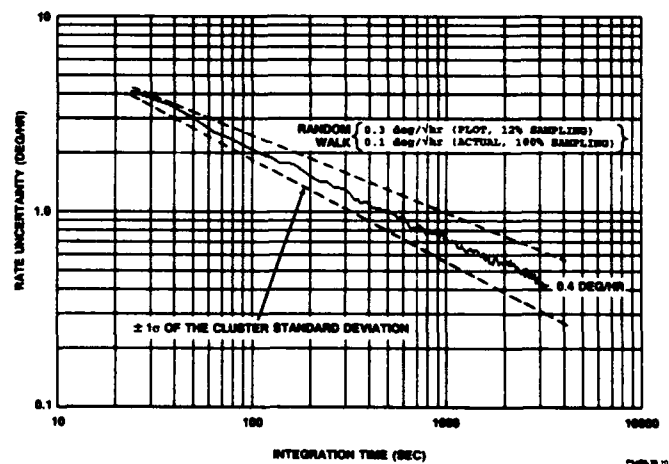


Figure 8

Shinji Motohara and Aritaka Ohno

*Japan Aviation Electronics Industry, Ltd.  
3-1-1 Musashino, Akishima-shi, Tokyo, Japan*

## 1. INTRODUCTION

Fiber optic gyros (FOGs) are all solid state devices, compact, lightweight and highly reliable. These merits have attracted much attention and developments have been energetically implemented mainly for aerospace applications.

The sensing loop of FOG has been conventionally constituted of polarization maintaining (PM) fiber. This fiber is more expensive than ordinary single mode (SM) optical fiber. It is currently an essential problem to be tackled. In the FOGs with sensing loops of low cost SM fiber, a depolarizer is inserted at one end of the coils. The performance of this type obtained under laboratory conditions has been reported (1). However, no evaluation under practical environmental conditions has been conducted to date. The authors evaluated and investigated the behavior of a FOG with SM fiber sensing loop under practical conditions. Through this study, an intermediate grade (3 degrees/hr  $1\sigma$ ) was achieved by resorting to a novel configuration of sensing loop.

## 2. THEORY

In FOGs with SM fiber coils, interference between X and Y polarizations in the coils. It is therefore very difficult to have a high precision. The reason is its excessively small phase difference between X and Y polarization. As a solution to this inconvenience, a light source with a low coherency, SLD for example, is used. The required phase difference  $\phi_p$  is given by the equation

$$\phi_p = \frac{L_c}{\lambda} \times 2\pi$$

where  $L_c$  is the coherent length,  $\lambda$  is the wavelength.

To produce a required phase difference, a system with LYOT type depolarizer is usually employed. However, there is great possibility of gyro errors due to the presence of a fiber of different kind at one end of the coil. The influence of the use of depolarizer is discussed here in terms of thermally induced nonreciprocity (2). With a depolarizer provided at a suitable position as shown in Fig. 1, the phase error  $d\phi$  generated in an interval of  $dl$  is determined by

$$d\phi = \left( \frac{d\beta}{dT} + \alpha\beta \right) \frac{\delta T}{\delta t} \times \tau dl$$

where  $\beta$  is the propagation constant,  $\alpha$  is the linear thermal expansion coefficient of fiber in the longitudinal direction,  $\tau$  denotes the time elapsed, after the clockwise light has passed the interval  $dl$ , till the counterclockwise light traverses the same interval.

$\tau$  can be expressed as follows:

$$\tau = \frac{n(2l - L)}{C}$$

where  $n$  is the refractive index of the optical fiber core.

Here letting  $n_p$  be the refractive index of PM fiber core,  $n_s$  be the refractive index of SM fiber core, and  $\phi_1$  and  $\phi_2$  be the phase error produced at the depolarizer and phase error at a position symmetrical to the center of the whole length of the fiber respectively, and  $\delta\phi$  be the difference between these errors, we obtain

$$d\phi_1 = k \left( \frac{dn_p}{dT} + \alpha n_p \right) \frac{\delta T}{\delta t} \times \frac{n_s(2l - L)}{C} dl$$

$$d\phi_2 = k \left( \frac{dn_s}{dT} + \alpha n_s \right) \frac{\delta T}{\delta t} \times \frac{n_s(2l - L)}{C} dl$$

Hence

$$\Delta\phi = d\phi_1 - d\phi_2$$

$$= \frac{k}{C} \times n_s \left\{ \underbrace{\frac{dn_p}{dT} - \frac{dn_s}{dT}}_{[1]} + \alpha(n_p - n_s) \right\} \underbrace{\frac{\delta T}{\delta t}}_{[2]} \times \underbrace{(2l - L)}_{[3]} dl$$

The first term of this equation represents the change in refractive index due to temperature change, the second term the temperature change rate, the third term the point where the phase error occurs.

One solution for reducing the phase error is to set  $l = L/2$ , that is to say, to locate the depolarizer at the center of the coil. However, it considerably degrades the design feasibility, so it is not the best strategy. To avoid this disadvantage, a system not using LYOT type depolarizer is designed as follows. A PM fiber is wound into each lead of the coil. In this system, light is propagated from a fiber of low birefringence (i.e., SM fiber) to the fiber of high birefringence. Consequently, polarization is maintained to some extent, though a little fluctuation may arise due to environmental perturbations. Besides, it is assumed that connection of PM fibers of the same length to both ends of the coil will result in better reciprocity and significantly reduced thermal nonreciprocity (Fig. 2). An essential parameter in the design of the system is the length of the PM fiber to be connected with coil. Letting  $\beta_{sx}$ ,  $\beta_{sy}$ ,  $\beta_{px}$ ,  $\beta_{py}$  denote respectively the propagation constant of SM fiber along the X and Y axes, and that of PM fiber along X and Y axes, we have the relationship :

$$\beta_{sx} = \beta_{px} > \beta_{sy} > \beta_{py}$$

The minimum phase difference between X and Y polarizations produced during propagation from the point A to B shown in Fig. 3 can be approximated by

$$\Delta\phi = (\beta_{sx} - \beta_{sy})l' - 2(\beta_{px} - \beta_{py})l$$

where  $l$  denotes the length of PM fiber,  $l'$  the length of SM fiber. The phase difference thus obtained must be sufficiently large so as not to cause interference, considering the coherent length of the light source used. This requirement is satisfied if

$$\Delta\phi > \frac{L_C}{\lambda} - 2\pi$$

Rewriting the above equation, we get

$$(\beta_{SX} - \beta_{SY})l - 2(\beta_{PX} - \beta_{PY})l > \frac{L_C}{\lambda} \times 2\pi$$

Hence the suitable length of PM fiber,  $l$ , is determined by

$$l < \frac{(\beta_{SX} - \beta_{SY})l}{2(\beta_{PX} - \beta_{PY})} = \frac{2\pi \times L_C}{2(\beta_{PX} - \beta_{PY}) \times \lambda}$$

A FOG of desirable precision is available, if a PM fiber of a length satisfying the above condition is connected to each end of coil.

### 3. EXPERIMENT

Fig. 4 illustrates the configuration of the FOG used in our experiments. FOG outputs are delivered through an open loop, using a lock-in amplifier as shown in Fig. 4. Fig. 5 indicates the bias stability in the range from  $-20^\circ\text{C}$  to  $+70^\circ\text{C}$  of a FOG of conventional configuration with a depolarizer at one end of the coils. In the experiments the temperature was changed at a rate of  $0.5^\circ\text{C}/\text{min}$ . The bias stability of the FOG with PM fiber used in the coils is given in Fig. 6. As known from Fig. 5, the output drift is large when the temperature changes, in the case of the configuration with a depolarizer. The bias stability of the FOG of the configuration proposed in this paper is shown in Fig. 7. As clearly demonstrated by comparing these figures, the new configuration presents a bias stability of the same level as that of PM fiber, insensitive to time-dependent perturbations such as temperature changes. Furthermore, bias periodical fluctuation is observed in Fig. 5, while it is suppressed in Fig. 7. For Fig. 6 and 7, these setups were did not protect against dew, therefore temperature range was set from  $0^\circ\text{C}$  to  $70^\circ\text{C}$ .

### 4. CONCLUSION

A low cost configuration with SM fiber has been presented here, with its analytical and experimental data. It has been demonstrated that the new configuration enables to achieve an intermediate grade FOG performance under practical conditions. The authors have intention, using this configuration, to investigate from now on the possibility of constructing a FOG of higher precision.

### 5. ACKNOWLEDGEMENT

The authors are grateful to Dr.K. Hotate of Tokyo University for precious suggestion for the analysis of the configuration described here.

### 6. REFERENCES

- (1) K. Böhm et al., Low drift fiber gyro using a superluminescent diode", Electronics Letters Vol.17 (10) p352 (1981)
- (2) D.M. Shupe, Thermally induced nonreciprocity in the fiber-optic interferometer", Applied Optics, Vol.19(5) p654 (1980)

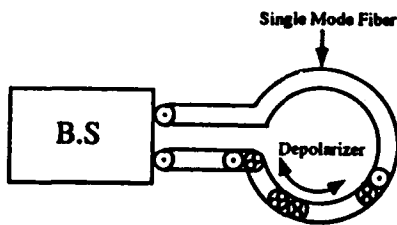


Fig.1

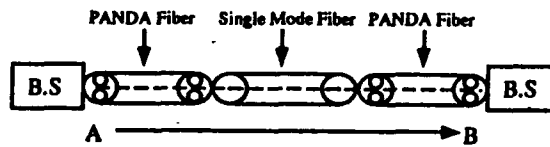


Fig.3

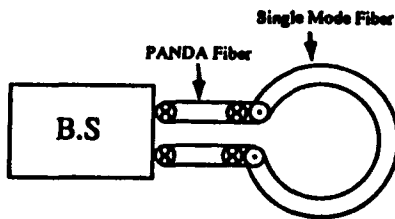


Fig.2

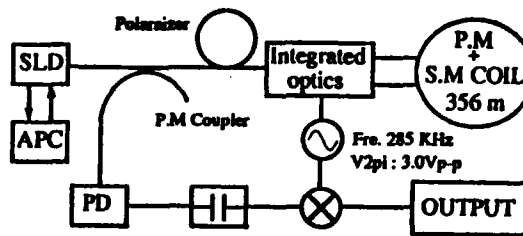


Fig.4

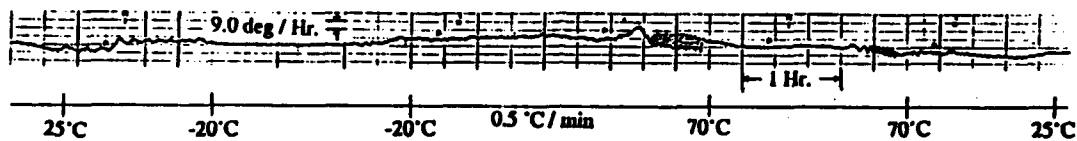


Fig.5 Bias Stability of Depol. Type (TC = 10s)

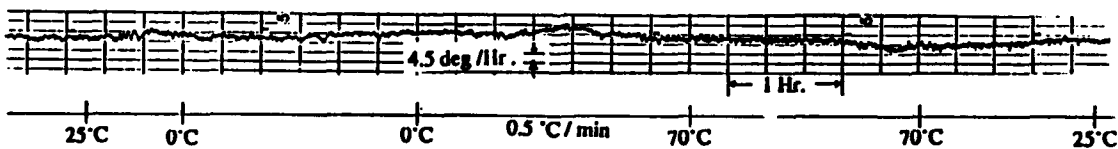


Fig.6 Bias Stability of PANDA Fiber Coil Type (TC = 10s)

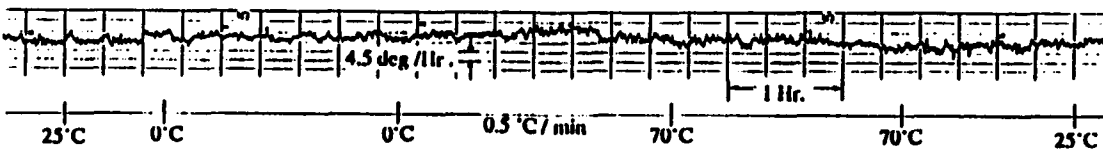


Fig.7 Bias Stability of Single Mode Fiber Coil Type (TC = 10s)

## **W2.3 Method To Reduce The Optical Kerr-Effect Induced Bias In An Optical Passive Ring-Resonator Gyro**

**Koichi TAKIGUCHI and Kazuo HOTATE**

**RCAST, Research Center for Advanced Science and Technology  
The University of Tokyo**

**4-6-1 Komaba, Meguro-ku, Tokyo 153, JAPAN**

**Telephone: +81-3-3481-4437, Facsimile: +81-3-3485-5135**

### **Abstract**

A novel method to reduce the optical Kerr-effect induced bias in the resonator-type gyro is presented. The bias is monitored by modulating light-source intensity, and fed back into one lightwave-intensity traveling in resonator to make it zero.

### **I. Introduction**

Optical Passive Ring-Resonator Gyro (OPRG), which utilizes a high finesse fiber ring-resonator, is expected to achieve a high performance using a much shorter length of a fiber loop than an interferometer-type fiber gyro. Through researches on the noise sources in OPRG [1]-[10], bias induced by optical Kerr-effect has been calculated to be one of the dominant noise sources [3]. This bias is proportional to the intensity difference between CW and CCW lightwaves in the resonator, as shown in Fig. 1. Even a small imbalance of 0.01 % between the two lightwaves produces a bias larger than the shot noise limit by 2 figures of magnitude in the high performance OPRG [3]. One method to reduce the bias is to modulate the input lightwave intensity into the resonator with a square wave, which has 50 % duty ratio and frequency of an integer times the resonator free spectrum range. However, requirements for the intensity modulator, such as the bandwidth and the extinction ratio, are rather severe [3].

In this paper, we present a novel and effective method to reduce the Kerr-effect induced bias in OPRG. First, the lightwave intensity into the resonator is slightly modulated by a low-frequency sinusoidal wave. The bias is obtained by synchronous detection with the modulation frequency, and is fed back into one lightwave intensity in resonator to make it zero.

### **II. Principle to reduce the Kerr-effect induced bias**

Figure 2 shows the experimental setup. Optical source is an LD-excited ring YAG laser ( $\lambda=1.3 \mu\text{m}$ ) with a spectrum linewidth of about 300 kHz including the jitter [11]. The resonator consists of polarization-maintaining fiber and coupler, and its length and diameter are 12 m and 0.1 m, respectively. The finesse is about 100. To suppress the polarization fluctuation induced bias [4], we adopted the resonator with a  $90^\circ$  polarization-axis rotation [5], [6]. The PZT is modulated by a 7 kHz sinusoidal wave to catch the resonance point by lock-in amplifiers (LIA's). The output of the detector D2 is fed back into the PZT through LIA2 to cancel the environmental fluctuations. Additionally, the laser frequency is controlled digitally combined with the normal analogue feedback to complement the shortcomings of the analogue

feedback in the low frequency region (partially digital-feedback scheme) [7]. Closed loop operation is adopted to remove the scale factor change. Accordingly, the rotation signal is obtained as the frequency difference between AOM1 and AOM2. Interference noise between the signal wave and the backscattering in the resonator [8] is reduced by a binary phase shift keying (b-PSK) modulation, by which the carrier component of CCW wave is eliminated [9].

The lightwave intensity into the resonator is slightly modulated with sinusoidal wave (angular frequency:  $k$ ) by using intensity modulator IM1. The modulation frequency  $k$  is much lower than that of the resonance point detection  $q$ . The difference output P3 between LIA1 and LIA2 contains the frequency  $k$  component which is produced by the Kerr-effect, when the average CW power  $I_{CW}$  is not equal to the average CCW power  $I_{CCW}$ . When  $I_{CW}=I_{CCW}$ , P3 does not contain the  $k$  component. These are illustrated in Fig. 3. Therefore, the Kerr-effect induced bias proportional to  $(I_{CW}-I_{CCW})$  is synchronously detected with LIA3, and the output P4 of LIA3 is fed back into the intensity modulator IM2 to make the intensity difference zero. The YAG laser has an intensity modulation function [11], which is used in the experiment in place of IM1. Moreover, AOM2 is used as the intensity modulator in place of IM2.

There may occur two questions on this method. One is that the intensity modulation itself by IM1 may cause an additional  $k$  component. The resonance characteristics of the resonator  $g(t)$  is given as follows.

$$g(t)=C_1\{1+C_2\sin(kt+\phi_k)\}\left[1-\frac{C_3}{1+C_4(f-f_0)^2}\right], (1) \quad f=f_0+f_w\sin(qt)+f_k\{1+C_2\sin(kt+\phi_k)\}+f_n, (2)$$

where  $C_i$  ( $i=1-4$ ),  $f_0$ ,  $f_w$ ,  $f_k$ ,  $f_n$ , and  $\phi_k$  are the constants, resonance frequency, frequency deviation of FM for detecting the resonance point, Kerr-effect induced bias, the offset from the resonance point, and the phase term of the intensity modulation, respectively. In Eqs. (1) and (2), the terms  $1+C_2\sin(kt+\phi_k)$  and  $f_k\sin(kt+\phi_k)$  represent the intensity modulation itself and the Kerr-effect induced  $k$  component, respectively. The demodulation output  $h(t)$  with frequency  $q$  is expressed, as the derivative of Eq. (1) with  $f$ , by

$$h(t)=2C_1C_3C_4\{f_n+f_k+f_kC_2^2/2+f_nC_2\sin(kt+\phi_k)+2f_kC_2\sin(kt+\phi_k)-f_kC_2^2\cos(2kt+2\phi_k)/2\}. (3)$$

In Eq. (3),  $f_n$  is small enough, because we adopt the closed loop operation. Therefore, the intensity modulation component itself (the fourth term of Eq. (3)) can be neglected compared with the Kerr-effect induced  $k$  component (the fifth term). We can detect the  $k$  component related only to the Kerr-effect at LIA3.

The other question is whether the difference between CW and CCW intensity can be obtained as P3, even though electronic gain for P1 and P2 is different each other. However, if both CW and CCW operation loops are closed, we can obtain it.

### III. Experimental results

Figure 4 (a) and (b) shows the OPRG output without and with

the Kerr-effect reduction method, respectively. The modulation frequencies for rotation sensing and the Kerr-effect detection are 7 kHz and 200 Hz, respectively. The intensity modulation index is set to be 3.2 %. The outputs of D1 and D2 are divided by the monitor output of the laser [11]. This division is also effective in eliminating the third term of Eq. (3). The time constant  $T_c$  for gyro output is 30 sec. The initial CW lightwave intensity in the resonator is about 55  $\mu$ W. The CW intensity is changed by 13  $\mu$ W using variable attenuator at the points indicated by the arrow in Fig. 4.

As shown in Fig. 4 (a), without this method, the bias changes by 90 Hz in agreement with theoretical value [3] in the order. However, Fig. 4 (b) clearly shows that this method can compensate the Kerr-effect bias induced by the intensity change.

We have already achieved the drift of about  $10^{-5}$  rad/s, which is limited by the Kerr-effect [2]. In the next step, we improve the drift by reducing the effect using this method.

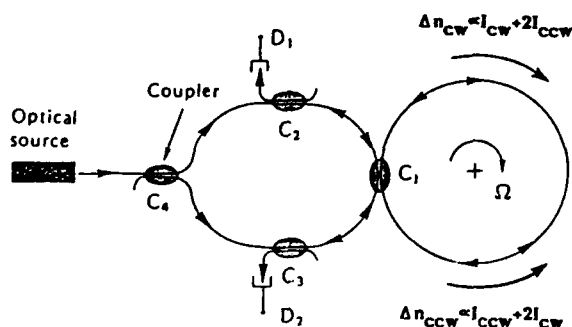
#### IV. Conclusion

We have presented the novel and effective method to reduce the optical Kerr-effect induced bias in OPRG. The experiments on basic operation to verify the validity of this method has been successfully performed. In the next step, we reduce the Kerr-effect induced drift by adjusting the parameters appropriately.

We would like to thank Dr. F. Suzuki and Dr. S. Yamasaki of Fujikura Ltd. for their help in fabricating the fiber resonator.

#### References

- [1] K.Hotate, *OFS'90* (Sydney), TU01.1, 11, Invited.
- [2] K.Hotate, K.Takiguchi, *Fiber Optic Gyros: 15th Anniv. Conf.* (Boston), 1585-14, Sept. 1991, Invited.
- [3] K.Iwatsuki, K.Hotate, M.Higashiguchi, *JLT*, LT-4, 645 (1986).
- [4] K.Iwatsuki, K.Hotate, M.Higashiguchi, *Appl.Opt.*, 25, 2606 (1986).
- [5] G.A.Sanders, R.B.Smith, G.F.Rouse, *SPIE OE/FIBERS'89* (Boston), 1169-74, 373.
- [6] K.Takiguchi, K.Hotate, *Photon.Tech.Lett.*, 3, 88 (1991).
- [7] K.Takiguchi, K.Hotate, *Photon.Tech.Lett.*, 3, July 1991.
- [8] F.Zarinetchi, S.Ezekiel, *Opt.Lett.*, 11, 401 (1986).
- [9] K.Hotate, K.Takiguchi, A.Hirose, *Photon.Tech.Lett.*, 2, 75 (1990).
- [10] K.Takiguchi, K.Hotate, *MOC'91* (Yokohama), L25, Oct. 1991.
- [11] User manual, Lightwave Electronics Co. (U.S.A.), Apr. 1988.

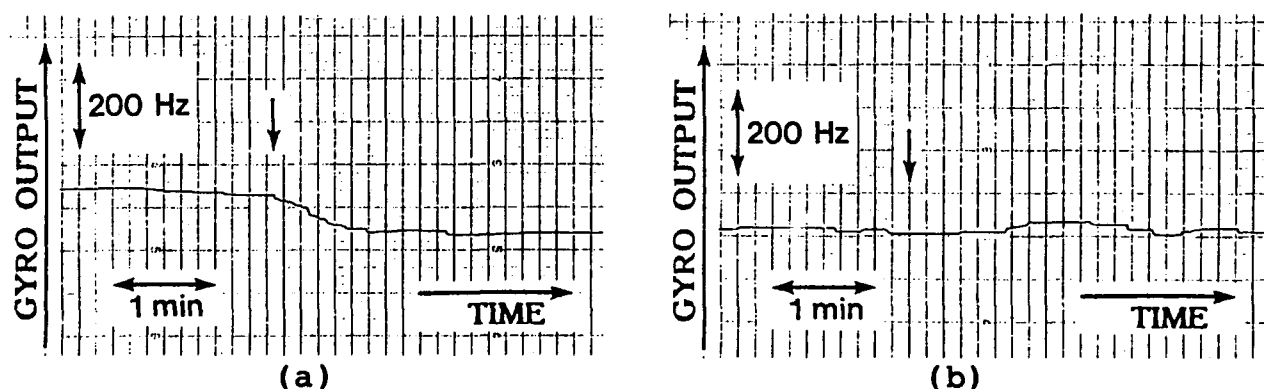
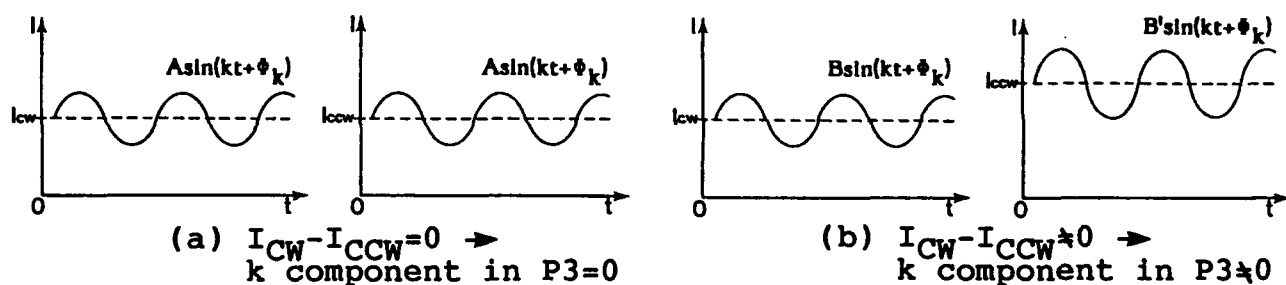
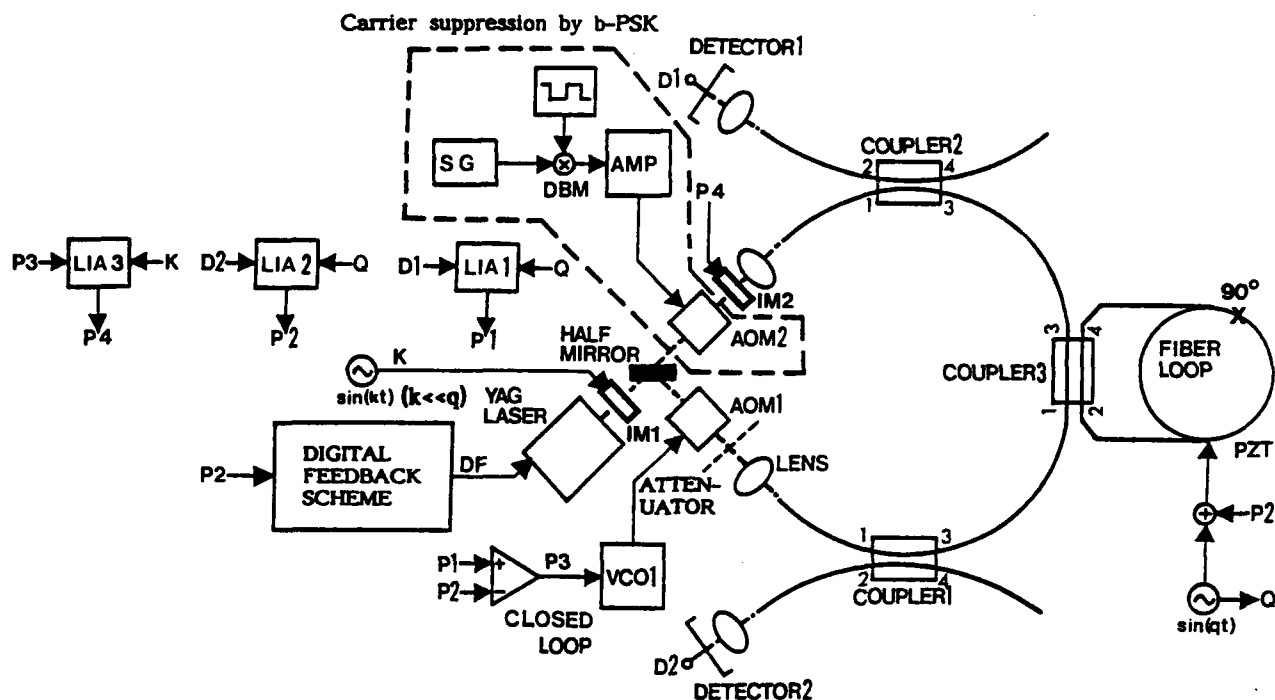


$$\Delta \Omega \propto (I_{cw} + 2I_{ccw}) - (I_{ccw} + 2I_{cw})$$

$$= I_{ccw} - I_{cw}$$

Fig. 1 Kerr-effect induced bias.





## W2.4 Experimental Investigation On Direction Sensor Using A Fiber Optic Gyroscope With High Resolution

H. Kajioaka, N. Ashizuka, T. Kumagai, and  
H. Nakai, *Hitachi Cable Ltd., Hitachi-city, Japan*

### 1. INTRODUCTION

A highly sensitive fiber optic gyroscope (FOG) is used as a geodesic compass. This FOG is based on an open loop and minimum reciprocal configuration with all polarization maintaining fiber (PFM) components. In this paper we present an experimental investigation on north-seeking accuracy by considering the rate resolution of the FOG.

### 2. PRINCIPLE

Figure 1 shows an example from the earth's rotation detection result. In the experiment, the fiber sensing coil is placed perpendicular to the horizon, and rotated vertically in many directions. When the loop pointed directly north, the output of the FOG decreased to nearly zero. Thus a highly sensitive gyroscope can be used as a geodesic compass. In an ideal case, the required rate resolution  $\delta \theta$  of the direction sensor is given as follows.

$$\delta \Omega = \delta \theta (\Omega_e \cos \theta_l) / (180/\pi) \quad (\text{deg/h}) \quad \dots \quad (1)$$

where  $\Omega_e$  is the earth's rotation rate, and  $\theta_l$  is the latitude. For example, when  $\theta_l$  is 37 degrees, and  $\delta \theta$  is 0.5 degrees then  $\delta \Omega$  is 0.1 deg/h.

### 3. HIGHLY SENSITIVE FOG

The FOG system is shown in Fig.2. The rate output of the FOG is shown in Fig.3. The noise level is about 0.1 deg/h and this value is near the shot noise level of 0.05 deg/h.

### 4. NORTH-SEEKING EXPERIMENT

Figure 4 shows a photograph of an optical geodesic compass prototype. This instrument consists of three parts: FOG, horizontal level stabilizer, and the rotating mechanism. Figure 5 shows one of the experimental results. In this experiment, the earth's rotation rate was measured every 36 degrees. Figure 6 shows the accuracy of the direction sensor, where the earth's rotation rate was measured every 36 degrees. According to this experiment, the north-seeking sensitivity of about 0.5 degrees agrees well with Eqn(1), considering that the rate resolution of the FOG is about 0.1 degrees per hour at an integration time of 5 seconds.

## 5. RESOLUTION IMPROVEMENT

Based on the above-discussed results, the most effective way to improve the north-seeking accuracy is to improve the rate sensitivity of the FOG. One way to do this is to make the scale factor as large as possible by using a longer PMF in the  $1.55\mu\text{m}$  region. Figure 7 shows the fiber length dependent north-seeking accuracy. The authors are presently investigating geodesic compass with a target accuracy of 0.05 degrees using 5 to 10 kilometers of PMF.

## 6. CONCLUSION

An optical gyrocompass with a north-seeking accuracy of 0.5 degrees has been developed by using a fiber optic gyroscope with a rate resolution of 0.1 degrees per hour with an integration time of 5 seconds. This showed that north-seeking accuracy is mainly determined by the rate resolution of the FOG. A longer PMF and a high power SLD in  $1.55\mu\text{m}$  wavelength region will be used to improve the accuracy of the direction sensor.

## 7. ACKNOWLEDGEMENT

The authors would like to thank T. Murakami and Y. Hotta of Santec corporation for their publicized discussion on a prototype optical gyrocompass.

## 8. REFERENCES

- (1) H. Kajioka et. al.: "Low loss polarization maintaining single-mode fibers for  $1.55\mu\text{m}$  operation," OFC '88, WA-5 New Orleans, 1988.
- (2) T. Kumagai et. al.: "Investigation of Low Zero Drift Optical Fiber Gyroscopes," Technical Report, IEICE of Japan, SANE 90-34, pp31-36 Sept. 1990.

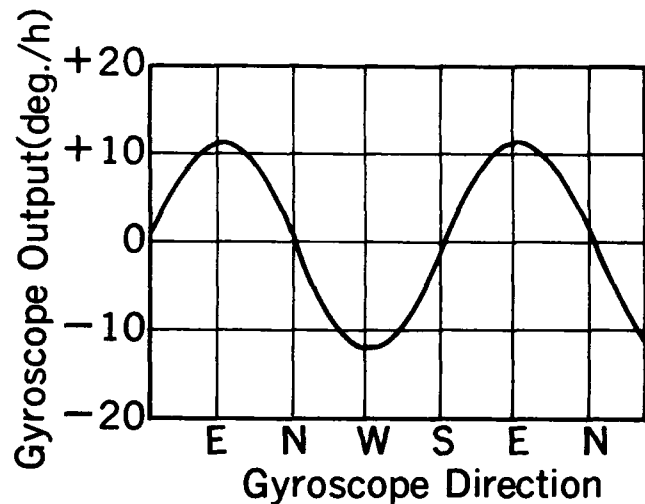
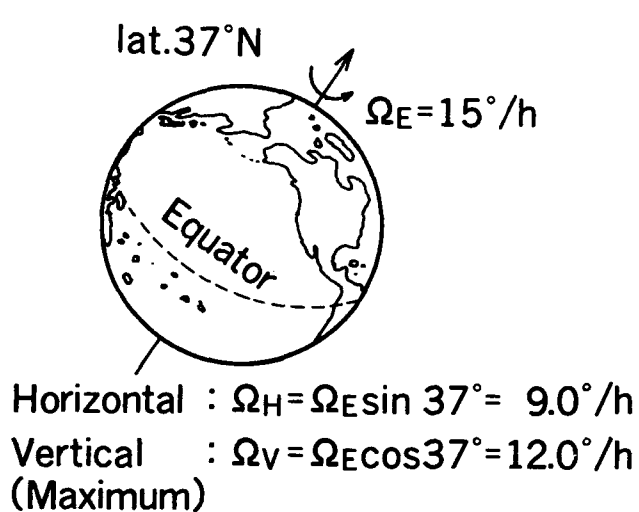


Fig. 1 Earth's rotation detection result

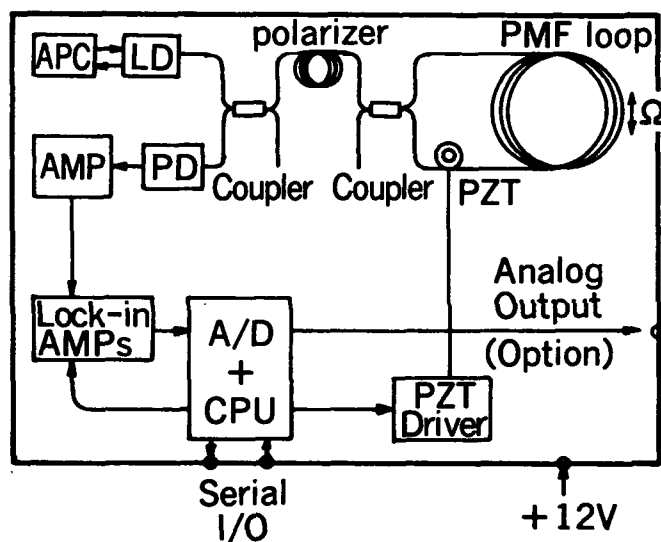


Fig. 2 Optical fiber gyroscope system

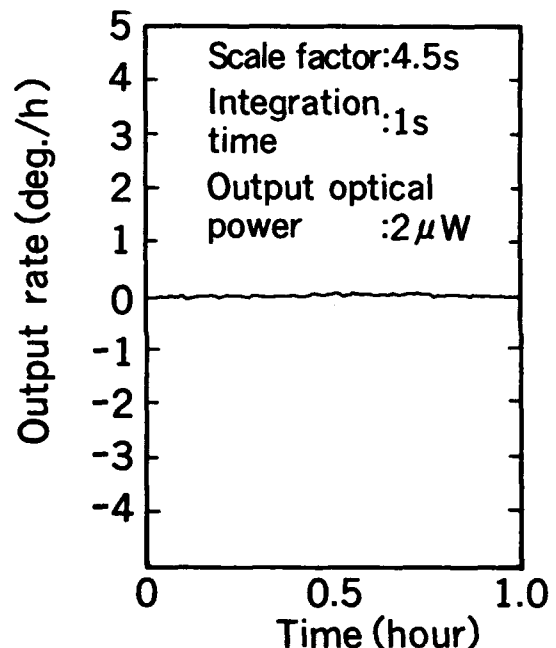


Fig. 3 Rate output of the Optical fiber gyroscope

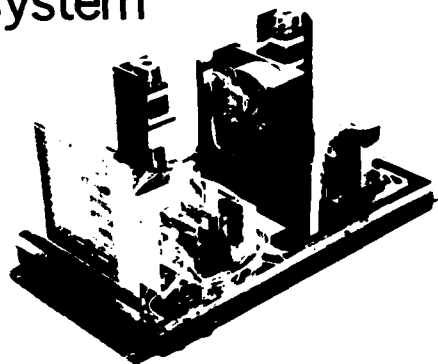


Fig. 4 Inner view of a prototype optical gyrocompass  
(Size : 520×320×300mm)

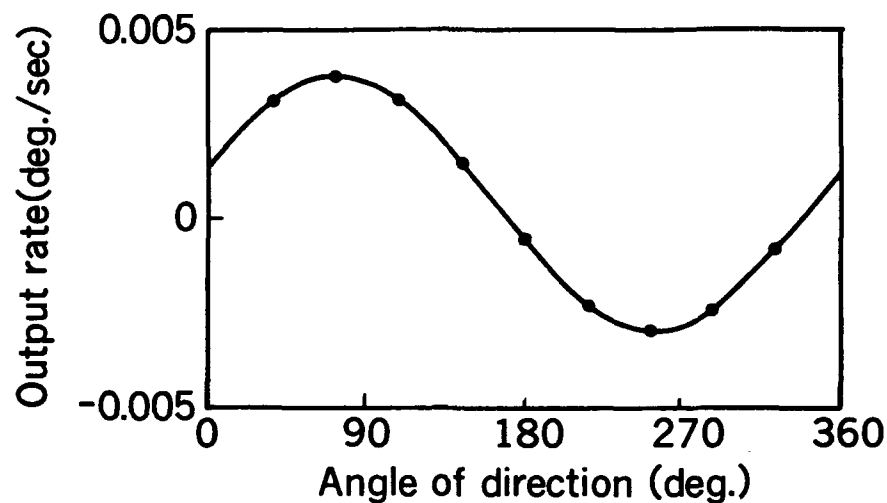


Fig. 5 An experimental result of earth's rotation rate.

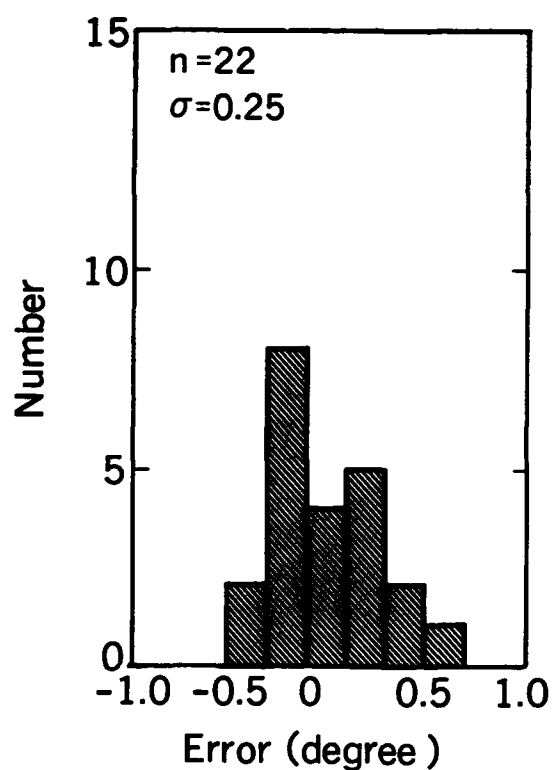


Fig. 6 The accuracy of optical gyrocompass

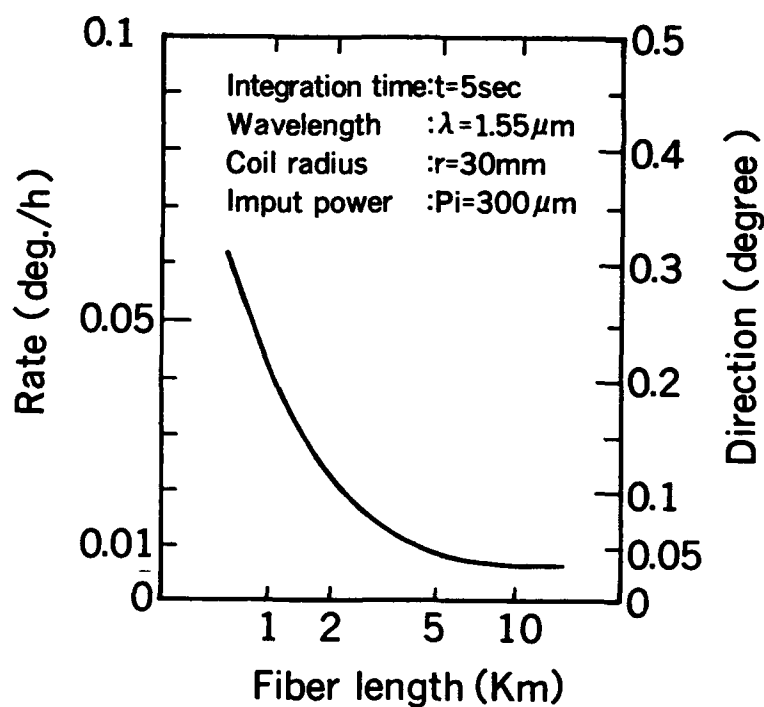


Fig. 7 Shot noise limited resolution

## **W2.5      Integrated 1.06 $\mu\text{m}$ Fiber Gyro Superfluorescent Source**

**W.K. Burns and R.P. Moeller  
Code 6570**

**Naval Research Laboratory  
Washington, DC 20375**

**and**

**E. Snitzer and G. Puc  
Rutgers University  
Piscataway, N.J. 28855**

There is great interest in using fiber superfluorescent sources in fiber optic gyroscopes as a replacement for semiconductor superluminescent diodes (SLD's). Potential benefits include higher available power, better wavelength stability with temperature, and improved lifetime. Multiclad Nd:fibers<sup>1</sup> pumped by a laser diode array offer high output powers in a single mode core, but are susceptible to lasing due to feedback.<sup>2</sup> This type of diode laser pumped source has been successfully employed in a fiber gyroscope using a backward pumping scheme.<sup>3</sup> In particular this approach avoided the backreflection of backwards going superfluorescent emission off the high reflectivity diode array facet.<sup>4</sup> In addition to concern about feedback and reflections one must consider the problem of source integration, such that an all-fiber source can be spliced into the gyro without bulk optic components.

We report an approach that deals with these issues by the use of a fiber coupled 1.06  $\mu\text{m}$  optical isolator between the active fiber output and the gyro, and by a novel samarium (Sm) doped fiber which couples the active fiber with the diode array. The Sm fiber is transparent at the 0.81  $\mu\text{m}$  pump and heavily absorbing at 1.06  $\mu\text{m}$ , thus providing isolation from the diode array facet. These components allow conventional forward pumping of the active fiber in a spliced, all-fiber configuration.

The Sm fiber has a construction similar to the multicladd Nd fiber, which in turn is similar to that of Ref. 1, used as the active fiber (Fig. 1). The inner core is  $\text{Al}_2\text{O}_3$  -  $\text{SiO}_2$  doped with 3 wt. % Sm and is made slightly larger in diameter than the Nd doped core of the active fiber. The  $45\text{ }\mu\text{m} \times 110\text{ }\mu\text{m}$   $\text{SiO}_2$  multimode core and the outer polymer layers are similar for each fiber. An absorption spectrum for the Sm preform (Fig. 2) shows an absorption at  $1.06\text{ }\mu\text{m}$  of 1.64 dB/cm. The corresponding loss at  $0.81\text{ }\mu\text{m}$ , measured in the fiber, was  $\sim 0.02$  dB/m. Thus adequate isolation can be obtained in a Sm fiber length of 0.5 m or less.

The fiber source configuration is shown in Fig. 3. The Sm fiber (1.6m) is butt coupled to a 0.5 W diode array. The Nd fiber (20m) is spliced to the Sm fiber (0.8 dB splice loss) and to the input fiber lead of a  $1.06\text{ }\mu\text{m}$  isolator (4 dB loss). The Nd doped fiber output power vs. diode array drive current is shown in Fig. 4. For this measurement the isolator was removed and the fiber output end index matched with index matching gel. Up to 24 mW at  $1.06\text{ }\mu\text{m}$  output was obtained for a pump input to the Nd fiber of  $\sim 230$  mW at  $0.81\text{ }\mu\text{m}$ . No lasing threshold was observed up to the maximum pump power available. Also shown in Fig. 4 for comparison is the output of an 8m length of Nd doped fiber where the Sm fiber is replaced by a dichroic mirror, and lens coupling of the diode array is employed. The pump input end of the Nd fiber had a facet reflectivity of 0.0027 and the fiber output end was index matched with index matching gel. In this case Rayleigh scattering in the fiber and the finite fiber rear facet reflectivity combined to give a lasing threshold near 160 mW of pump.

In contrast the reflectivity of the Nd-Sm interface is estimated to be less than  $10^{-6}$  for a core index difference between the Nd doped and Sm doped fibers of  $\leq 3.10^{-3}$ . Thus considering both the interface reflection and the attenuation of the back reflected signal, an isolation of  $\geq 60$  dB can be achieved. However as shown in Fig. 4 the rear facet reflectivity of the 8 m length without the Sm fiber

does increase the efficiency of the forward going superfluorescent emission compared to the 20 m length with the Sm fiber. The advantage of the less efficient case with the Sm fiber is that maximum power can be extracted without having to operate in the spectrally unstable region close to lasing threshold.

By utilizing a wavelength dependent absorption in a Sm doped fiber we have constructed an integrated superfluorescent source at 1.06  $\mu\text{m}$ . When this source is spliced to a fiber coupled 1.06  $\mu\text{m}$  isolator, all requirements are satisfied for a forward-pumped, fully integrated fiber superfluorescent source that exhibits high output power (up to 10 mW into the gyro) without lasing. We expect this source to provide vastly superior wavelength stability and lifetime then the previously used SLD's, for fiber gyroscope applications.

### References

- 1) H. Po, E. Snitzer, R. Tumminelli, L. Zenteno, F. Hakimi, N.M. Cho, and T. Haw, Proc. OFC'89, Houston, TX, 1989, Paper PD7.
- 2) I.N. Duling III et. al., IEEE J. Quantum Electron. **27**, 995 (1991).
- 3) K.A. Fesler, M.J.F. Digonnet, B.Y. Kim, and H.J. Shaw, Optics Lett. **15**, 1321, (1990).
- 4) K.A. Fesler, R.F. Kalman, M.J.F. Digonnet, B.Y. Kim, and H.J. Shaw, Proc. Soc. Photo-Opt. Instrum. Eng. **1171**, 346 (1990).

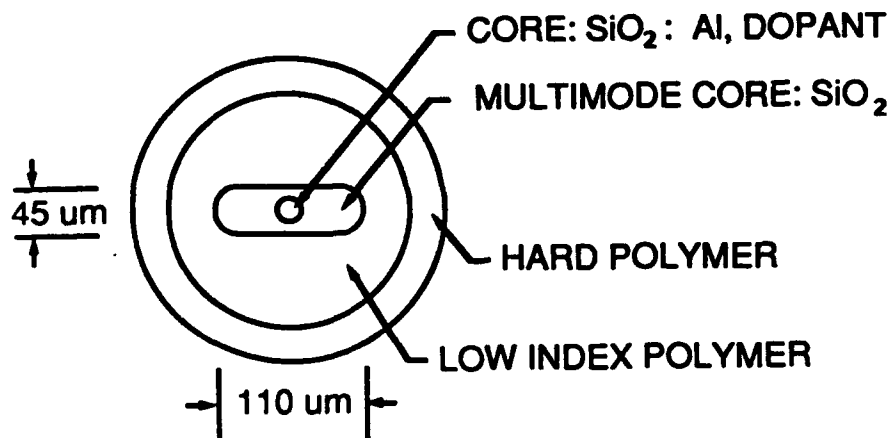


Fig. 1 Fiber geometry. Inner core dopant is either Sm or Nd.



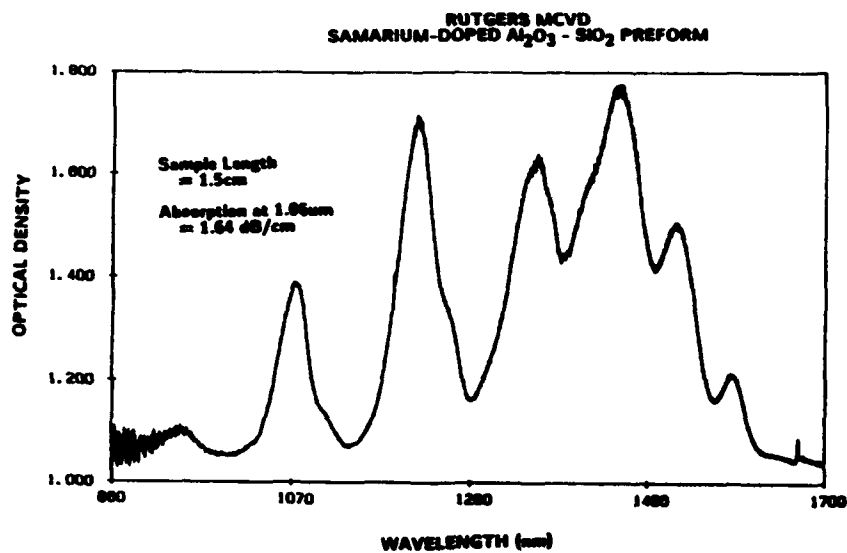


Fig. 2 Sm preform spectral absorption.

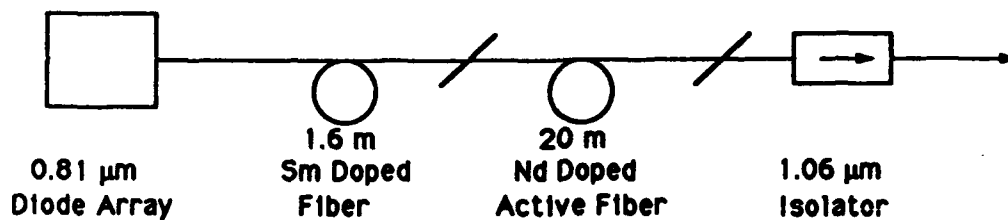


Fig. 3 All-fiber source configuration.

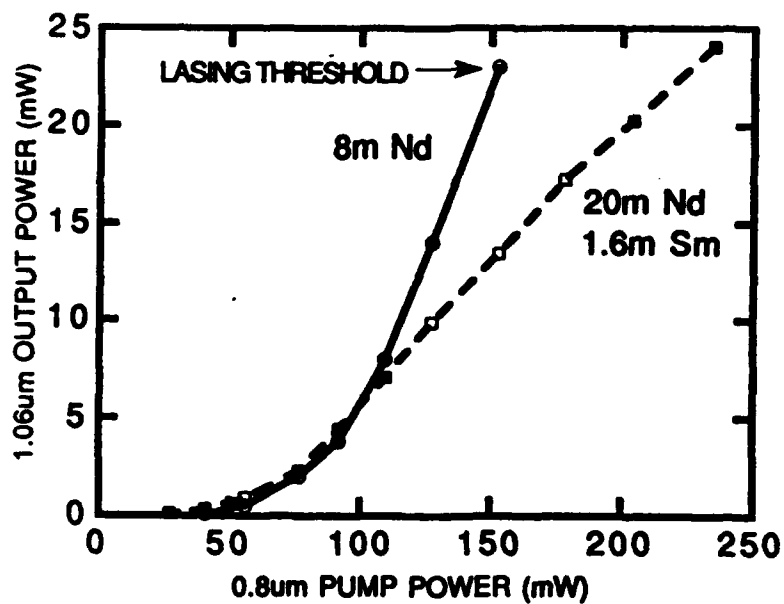


Fig. 4 Nd fiber output power vs. pump power for 20 m Nd/1.6 m Sm source and for 8 m Nd source.

### W3.1 (Invited)

## Interferometric Heterodyne Sensing

*Toshihiko Yoshino*

Department of Electronic Engineering, Gunma University  
1-5-1 Tenjin-cho, Kiryu, Gunma, Japan

### Abstract

The principle, advantages, related optical and electronic devices, applications to fiber sensors and measurement error sources of interferometric heterodyne sensing are described.

### I. Introduction

Optical heterodyne interferometry is an optical beat or in more general optical frequency modulation interferometry. Heterodyne interferometry can measure every parameter of an optical wave, i.e., phase, frequency, amplitude and polarization through the frequency-downed replica of the original wave. The most concern of heterodyne interferometry is, however, the application to optical phase and frequency detection. In the application, heterodyne interferometry offers several advantages over the conventional interferometry relying on the direct detection of interference intensity as follows:

- (1) real time detection
- (2) constant and linear scale factor detection
- (3) no signal fading
- (4) wide measurement range
- (5) detectability of sense
- (6) applicability of differential scheme
- (7) insensitivity to amplitude change

The advent of optical fiber and improvements on optoelectronic devices have made optical heterodyne a very powerful technique for interferometry.

### II. General principle

Consider an interferometer of Fig.1. The signal light having an instantaneous frequency  $\omega_s(t)$  travels through an optical pathlength  $L_s$  while the reference light having  $\omega_r(t)$  does through  $L_r$ . Letting A and B be the signal detection points, the interference signal at each point has the following instantaneous optical phase:

$$\Phi_A(t) = \int_0^{t+L_s/c} \omega_s(t)dt - \int_0^{t+L_r/c} \omega_r(t)dt, \quad (1)$$

$$\Phi_B(t) = \int_0^t \omega_s(t)dt - \int_0^t \omega_r(t)dt, \quad (2)$$

where  $c$  is the light velocity in vacuum. Detecting the difference between (1) and (2) yields

$$\Delta \Phi(t) = \Phi_A(t) - \Phi_B(t) = \int_t^{t+L_s/c} \omega_s(t) dt - \int_t^{t+L_r/c} \omega_r(t) dt. \quad (3)$$

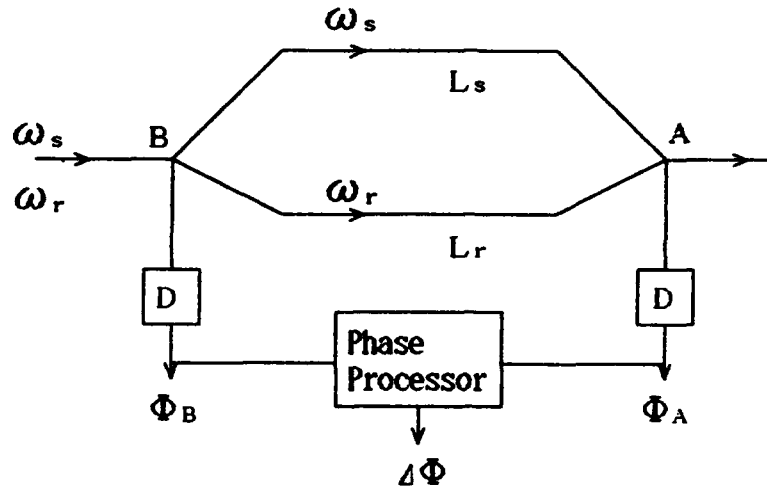


Fig.1 Schematic diagram for interferometric heterodyne sensing.

### III. Types of interferometric heterodyne sensing

#### (A) Intrinsic heterodyne sensing

In this case, the signal and reference lights have different constant frequencies with a constant frequency offset  $\Delta \omega$ , i.e.,  $\omega_s = \omega_0 + \Delta \omega$ ,  $\omega_r = \omega_0$  ( $\omega_0$ : light frequency). From (1) and (2),

$$\Phi_A(t) = \Delta \omega t + \omega_0(L_s - L_r)/c + \Delta \omega L_s/c, \quad (4)$$

$$\Phi_B(t) = \Delta \omega t, \quad (5)$$

and hence

$$\Delta \Phi = \omega_0(L_s - L_r)/c + \Delta \omega L_s/c, \quad (6)$$

$$\approx \omega_0(L_s - L_r)/c \text{ for } \Delta \omega L_s/c \ll 1. \quad (7)$$

The optical pathlength difference (OPD),  $L_s - L_r$ , is included in the beat signal (6) with the same scale factor as in the original optical wave. By means of a phase comparator, OPD is detected (Fig.2(a)). The absolute optical pathlength  $L_s$  is also involved in (6), but the scale factor is reduced by  $\Delta \omega / \omega_0$ . Time dependent changes in OPD, due to, e.g., Doppler effect, give rise to successive changes in the interference intensity, resulting in the beat frequency change by an amount of  $d[\Delta \Phi(t)/(2\pi)]/dt$ , which can be detected by a spectrum analyser or up-down counter.

#### (B) Pseudo heterodyne sensing

Laser frequency modulation (FM) in the presence of finite OPD leads to interferogram modulation, generally generating an optical beat. The beat frequency is related to the time delay between the reference and signal arms of the interferometer. Letting B be a pathlength-balanced point in Fig.1, then  $\Phi_B(t) = 0$ .

(B-1) Linear modulation:  $\omega_s(t) = \omega_r(t) = \omega_0 + \gamma t$

From (3),

$$\Delta \Phi(t) = \Phi_A(t) = \int_{t+L_r/c}^{t+L_s/c} [\omega_0 + \gamma t] dt$$

$$= [\gamma (L_s - L_r)/c]t + \omega_0 (L_s - L_r)/c [1 + (\gamma / \omega_0)(L_s + L_r)/2c] \quad (8)$$

$$\approx [\gamma (L_s - L_r)/c]t + \omega_0 (L_s - L_r)/c \text{ for } (\gamma / \omega_0)(L_s + L_r)/2c \ll 1. \quad (9)$$

The beat frequency is proportional to OPD, enabling the measurement of OPD (Fig.2(b)) [1,2]. As shown in (9), the phase bias of the beat signal is nearly proportional to OPD, e.g., when the frequency sweep rate  $\gamma$  is suitably small.

(B-2) Sinusoidal modulation :  $\omega_s(t) = \omega_r(t) = \omega_0 + \alpha \sin \omega_m t$

$$\Delta \Phi(t) = \Phi_A(t) = \int_{t+L_r/c}^{t+L_s/c} [\omega_0 + \alpha \sin \omega_m t] dt$$

$$= \omega_0 (L_s - L_r)/c + 2(\alpha / \omega_m) \sin[\omega_m (L_s - L_r)/2c] \sin[\omega_m \{t + (L_s + L_r)/2c\}], \quad (10)$$

which, if  $\omega_m (L_s - L_r)/2c \ll 1$ , is

$$\approx \omega_0 (L_s - L_r)/c + [\alpha (L_s - L_r)/c] \sin[\omega_m \{t + (L_s + L_r)/2c\}]. \quad (11)$$

The optical pathlength difference OPD is involved in both the bias and modulation components of  $\Delta \Phi(t)$ , which are detected from the output of an ac phase meter or from the spectral analysis of the high frequency components involved in the interference signal of  $\cos \Delta \Phi(t)$ .

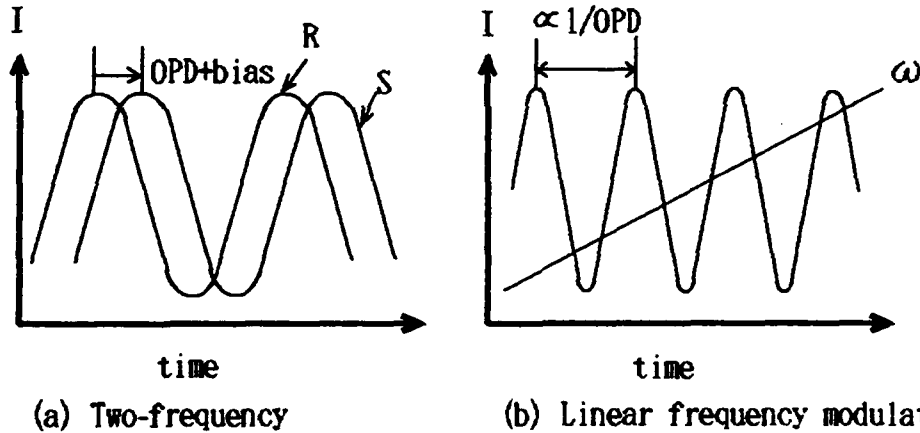


Fig.2 Beat signals in interferometric heterodyne sensing and relationship between interference intensity  $I$  and optical path difference OPD.

#### IV. Devices for interferometric heterodyne sensing

##### (1) Light sources

Axial and transverse Zeeman HeNe lasers at 633nm emit orthogonally polarized circular and linear polarization lights, respectively. The lasing frequency can be stabilized by a suitable feedback scheme [3]. Such lasers are now commercially available but can be home made by a simple modification of internal mirror HeNe lasers. The lasing frequency of laser diodes can be modulated by changing the injection current. Wide tuning without mode hopping is achieved by sweeping the cavity length of an external mirror coupled to a laser diode [4] or with distributed feedback (DFB) or cleaved-coupled-cavity ( $C^3$ ) laser diodes [5]. Two-frequency operation of laser diodes is investigated [6].

Cw dye lasers are capable of wide range frequency tuning.

## (2) Frequency modulators

Acousto-optic modulators using bulk Bragg cells are very common frequency shifters. The frequency converter from an ordinary to orthogonal-polarization two-frequency laser light is now commercially available. Electro-optic frequency shifters using  $\text{LiNbO}_3$  integrated optic waveguides have been developed [7,8]. PZT is often used for the phase modulation of single mode fiber. Old methods using rotating gratings or wavelength plates can be also applied.

## (3) Transmitters

Both fiberoptic and free space propagation of light are employed for interferometric heterodyne sensing. For the remote flexible propagation of orthogonal-polarization two-frequency light, polarization maintaining single mode fiber (PMF) is often used.

## (4) Detection electronics

The relevant electronics involve phase comparators, bandpass filters, gating and sampling circuits, double balanced mixers, frequency counters, spectrum analyzers, micro computers and so on. Analog schemes based on the rectification method or digital schemes based on the clock pulse method are usually used.

## V. Interferometric heterodyne fiber sensors

Many quantities are measured by using intrinsic or pseudo heterodyne interferometric fiber sensors (Table 1). The measurands reported so far involve

Table 1. Applications of interferometric heterodyne sensing to optical fiber sensors appeared in literatures. SMF, single mode fiber; PMF, polarization maintaining fiber.

Measurand	Sensor principle	Two-frequency	FM
Temperature	Elongation of SMF		[9]
	Retardation of PMF	[10]	[11]
	Birefringence of crystal	[12]	
Sound	Elongation of SMF	[13,14]	
Force (pressure, strain)	Elongation of SMF		[15]
	Retardation of SMF	[16]	
	Retardation of PMF	[17]	[18]
	Photoelastic effect of solid	[12]	
Displacement	Phase shift	[19,20]	
	Doppler effect	[21]	
Distance	Time delay		[5]
Gyro	Sagnac effect	[17,22,23]	[24]
Velocity	Doppler effect	[8,25]	
Magnetic field	Faraday effect of solid	[12,26]	
Current	Faraday effect of SMF	[27]	[28]
Voltage	Pockels effect of crystal	[12]	
Thickness	Ellipsometry	[29]	
Sensor multiplexing			[30-34]

temperature, sound, strain, pressure, rotation (gyro), displacement, distance, velocity, magnetic field, current, voltage and film thickness. The two-frequency heterodyne scheme is mostly used for the measurement of incremental values of phase or retardation. On the other hand, the FM heterodyne scheme is mostly used for the measurement of absolute values of them and also for sensor multiplexing and distributed sensing. Optical fiber is used for a sensor itself or an optical transmission line connecting between appropriate sensors and light sources or detectors. In the latter use in particular, the combination of transverse Zeeman lasers and PMF offers a very practical heterodyne sensing scheme, in which, with a simple differential scheme, stable and precise measurements of phase or retardation can be achieved even in unstable environments (Fig.3)[35].

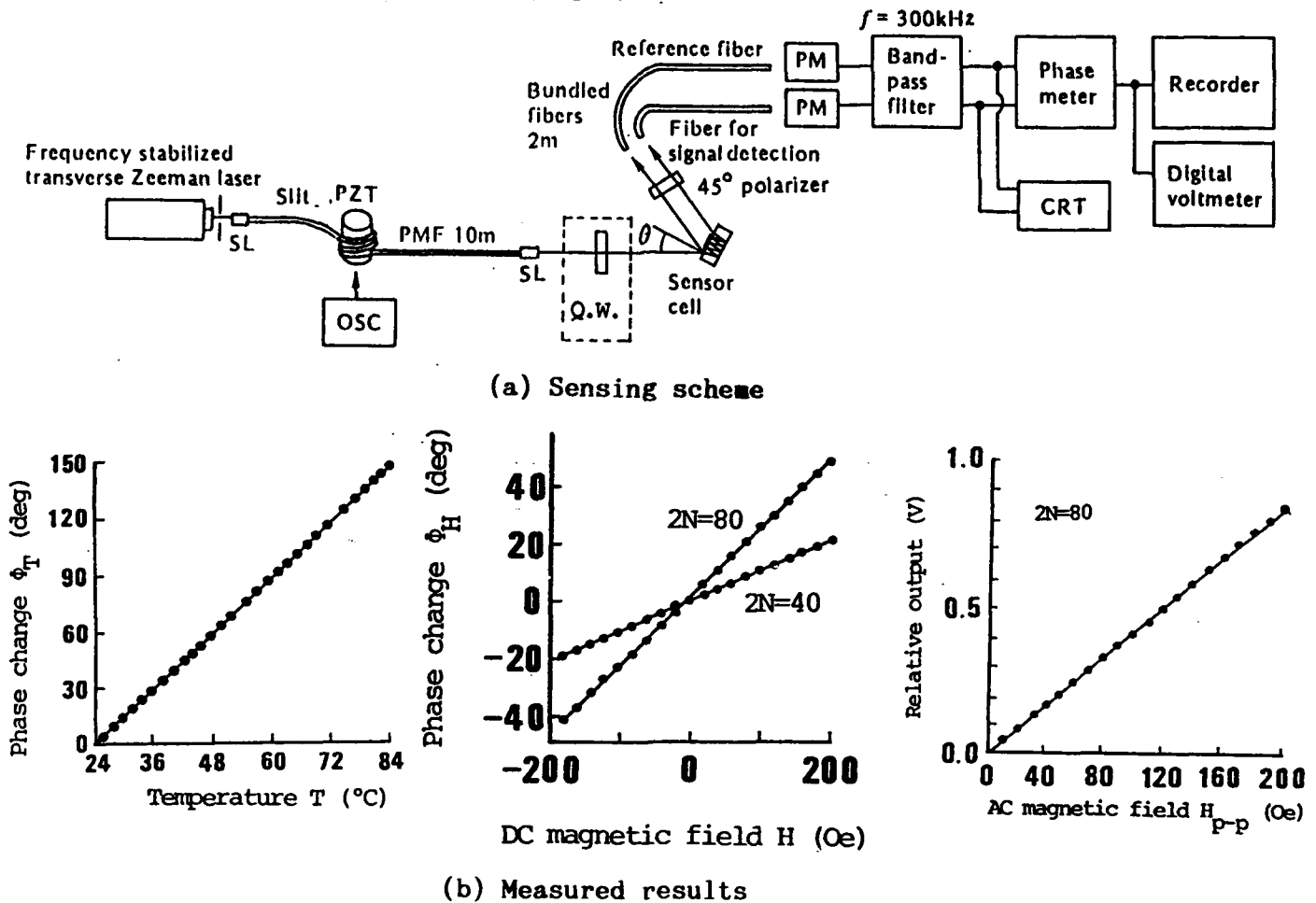


Fig.3. Differential heterodyne fiber sensing using retardation changes.

The phase meter output is stable against the fluctuations of laser beam position, surrounding air turbulence and variations of fiber coupling and laser power levels.  $2N$ : number of internal reflections within cell.

## VI. Considerations on measurement errors

### (1) Amplitude modulation

In phase detection, at least one full period of beat signal is necessary for signal processing, limiting the measurement speed. The light power change

during the period leads to phase measurement errors. For example, in the FM heterodyne methods using usual Fabry-Perot type laser diodes, the output power change is accompanied by frequency sweep. In order to decrease the measurement error, the intensity change has to be compensated by a suitable method, e.g., by analog dividing. Wide tuning without output power change is achieved with C<sup>a</sup> lasers[5].

### *(2) Two-frequency crosstalk*

If there is some crosstalk between two frequency components, additional beat signals are generated, leading to measurement errors, e.g., giving rise to a nonlinear relationship between real and output phase signals [36]. The crosstalk occurring at transverse Zeeman lasers are diminished by the precise alignment of applied magnetic fields and phase anisotropy axes involved in laser mirrors [37]. Some crosstalk occurs at optical coupling from a transverse Zeeman laser to PMF if there is an angular mismatch between their polarization axes. The first order crosstalk error due to it, however, can be eliminated by setting a frequency-mixing polarizer at a suitable azimuth [36,38].

### *(3) Frequency instability*

In heterodyne sensing, different laser frequencies travel optical paths of finite length so that a frequency instability involved causes phase measurement errors. In order to decrease the measurement errors, high stabilization of both the beat and laser frequencies is required. In the two-frequency heterodyne scheme, optical pathlength balancing is very effective for reducing such measurement errors, as discussed in [19]. Obviously, with poor coherence lasers, the modulation depth of beat signal becomes low and the phase detection error becomes considerable.

## **VII. Concluding Remarks**

Interferometric heterodyne sensing has been much investigated, in fiberoptic as well as free space optical sensors, because of its capability of the precise, stable, large dynamic range and linear scale measurements of optical phase and frequency. For the industrial practical uses of the sensing technology, cost down as well as performance improvements of related optoelectronic devices is desirable.

## **References**

- [1] I.P.Giles, D.Uttam, B.Culshaw and D.E.N.Davis: Electron. Lett. 19(1983)14.
- [2] T.Kubota, M.Nara and T. Yoshino: Opt. Lett. 12(1987)310.
- [3] N.Umeda, M.Tsukiji and H. Takasaki: Appl. Opt. 19(1980)442.
- [4] M.Nagata, M.Ohtaka and T.Kobayashi: Trans. IEICE J70-C (1987)379.
- [5] E.M.Strzelecki, D.A.Cohen and L.A.Coldren: 5th OFS(New Orleans, 1988)129.
- [6] S.Wakana, M.Shirasaki, Y.Furukawa and T.Inagaki: Appl. Phys. Lett. 50(1987)1547.
- [7] F.J.Leonberger, T.K.Findakly and P.G.Suchoski: 6th OFS(Paris, 1989)58.
- [8] M.Haruna and H.Nishihara: 5th OFS(New Orleans, 1988)305.

- [9]Y.Seki and K.Noda: 4th OFS(Tokyo,1986)227.
- [10]T.Yoshino: Kikai-no-Kenkyu[Japan] 36(1984)349.
- [11]M.Martinelli and L.De Maria: Opt. Lett.13(1988)779.
- [12]T.Yoshino and M.Nara: 2nd OFS(Stuttgart,1984)233.
- [13]J.A.Bucaro and T.R.Hickman: Appl. Opt.18(1979)937.
- [14]M.L.Henning and C.Lamb: 5th OFS(New Orleans,1988)84.
- [15]L.DeMaria, V.Gusmeroli and M.Martinelli: 6th OFS(Paris,1989)47.
- [16]T.Yoshino and T.Ose: Seisan Kenkyu[Japan] 35(1983)77.
- [17]T.Yoshino,T.Ose,H.Tai,T.Kubota and K.Kurosawa:4th IOOC(Tokyo,1981)312.
- [18]R.M.Taylor,D.J.Webb,J.D.C.Jones and D.A.Jackson:Opt.Lett.12(1987)744.
- [19]T.Yoshino and N.Yoshida: 5th IOOC/11th ECOC(Venice,1985)863.
- [20]N.Nakatani,T.Izumi,S.Asano,T.Yamada and T.Sakabe: Rev. Sci. Instrum.58(1987)2161.
- [21]A.Nagashima, N.Ohgi and M.Shimizu: 4th OFS(Tokyo,1986)15.
- [22]K.Hotate and S.Samukawa: Appl. Opt.29(1990)1345.
- [23]H.Koseki, Y.Imai and Y.Ohtsuka: 5th OFS(New Orleans,1988)168.
- [24]H.C.Lefevre, S.Fatoux, M.Papuchon and C.Pucech: SPIE 719(1986)101.
- [25]J.Knuhtsen, E.Olldag and P.Buchhave: J. Phy. E: Sci. Instrum. 15(1982)11.
- [26]S.C.Barlett, F.Farahi and D.A.Jackson: 7th OFS(Sydney,1990)85.
- [27]P.Ferdinand,C.Cahen,B.Dessus and J.L.Lense: 4th IOOC(Tokyo,1983) 114.
- [28]A.D.Kersey and M.A.Davis: 6th OFS(Paris,1989)285.
- [29]T.Yoshino and T.Hashimoto: CLEO (Baltimore,1987)306.
- [30]I.Sakai, G.Parry and R.C.Youngquist: 4th OFS(Tokyo,1986)47.
- [31]A.D.Kersey and A.Dandrige: 4th OFS(Tokyo,1986)55.
- [32]M.Tsubokawa, T.Higashi and S.Seikai: *The distributed fiber optic sensing handbook*, ed. J.P.Dakin (IFS Pub. Co.,1990)p.181.
- [33]R.B.Franks:ibid,p.103.
- [34]K.Kurosawa: S.Hattori and T.Yoshino:ibid,p.109.
- [35]T.Yoshino: 5th OFS(New Orleans,1988)40.
- [36]T.Hashimoto and T.Yoshino: 2nd Meeting on Lightwave Sensing Technology [Japan](Tokyo,1988) 113.
- [37]T.Yoshino: Jpn. J. Appl. Phys.18(1979)1503.
- [38]K.Kurosawa and T.Imai: 7th OFS(Sydney,1990)151.



## W3.2 Noise-Resistant Signal Processing For Electronically Scanned White-Light Interferometry

R. Dändliker, E. Zimmermann and G. Frosio  
Institute of Microtechnology, University of Neuchâtel  
Breguet 2, CH-2000 Neuchâtel, Switzerland, +41-38-20 51 21

Fiber optic sensors using white-light interferometry have been developed, among others, as absolute displacement sensors<sup>1</sup>, as strain or temperature sensors<sup>2</sup>. The main advantage of white-light interferometry, which uses broad band light sources with short coherence lengths rather than monochromatic sources, is the possibility to make absolute measurements. In the same manner, a broad band source allows to measure the absolute force from the induced birefringence in an optical fiber (Fig. 1). Scanning the interferogram in space, rather than in time, by a linear photodiode array (electronically-scanned interferometer) avoids moving parts and increases the mechanical stability of the system. In this paper, we present a new signal processing method for white-light interferometry which is fast, accurate, and extremely noise resistant. Theoretical results for the expected systematic and statistical errors will be compared with experimental results.

The goal of the signal processing is to determine the center position  $x_s$  of the white-light fringe signal shown in Fig. 2. This is achieved in two steps. First, by calculating the center of gravity of the signal power to better than half a fringe period. Second, by calculating the phase  $\Phi$  of the fringes, when their position is known to better than half a fringe period from the first step. The signal  $H(x)$  is sampled at the positions  $x_n = n \cdot b$ , where  $n$  is an integer with  $-N/2 \leq n \leq N/2$  and  $b$  is the center-to-center spacing of the photodiode array. The envelope of  $H(x)$  is given by the modulus of the coherence function. We calculate the total power  $A$  of the ac-part  $H_{ac}$  of the signal, its first moment  $B$  with respect to the origin  $x_{01} = 0$ , and the center of gravity  $x_{s1}$  of the fringe signal by

$$A = \sum_n [H_{ac}(x_n)]^2, \quad B = \sum_n n \cdot [H_{ac}(x_n)]^2, \quad x_{s1} = B/A. \quad (1)$$

Without noise one gets for the center position exactly  $x_{s1} = x_s$ , where  $x_{s1}$  and  $x_s$  are in general fractional values of the sample positions. In the presence of noise  $x_{s1}$  gets a systematic and a statistical error. To calculate these errors, the signal is written as  $H(x) = s(x) + g(x, \sigma)$ , where  $s(x)$  is the fringe signal without noise and  $g(x, \sigma)$  is a Gaussian noise with variance  $\sigma^2$ . The systematic error  $\Delta x_s$  between the calculated value  $x_{s1}$  and the real value  $x_s$  of the center of gravity is found to be approximately

$$\Delta x_s = x_{s1} - x_s \cong - (N+1) \cdot \frac{\sigma^2}{A_f} \cdot x_s, \quad (2)$$

where  $A_f$  is the total power of the ac signal without noise. For the statistical error  $\delta x_s$ , we find

$$\delta x_s \equiv \frac{2\sigma\sqrt{A_f}}{A_f + (N+1)\sigma^2} \left[ \Delta x_s^2 + \frac{12(N+1)x_s^2 + N(N+1)(N+2)}{24} \frac{\sigma^2}{A_f} + \frac{C_{f0}}{A_f} \right]^{1/2}, \quad (3)$$

where  $C_{f0}$  is the second moment of the ac signal power for  $x_s = 0$ . Note that  $A_f$  and  $C_{f0}$  depend only on the fringe signal and can be calculated for any particular shape of the envelope. For further calculations we have assumed a fringe signal with Gaussian envelope (Fig. 2), namely

$$s(x) = f_0(x) + f(x) = f_0(x) + m \cdot \exp \left[ -\frac{(x-x_s)^2}{\Delta x^2} \right] \cos \left[ \frac{2\pi x}{\Lambda} + \Phi \right], \quad (4)$$

with  $\Phi = -2\pi x_s/\Lambda$ , and where  $f_0$  is the dc-part of the signal,  $m$  is the visibility and  $\Lambda$  the period of the fringes,  $\Delta x$  is the width and  $x_s$  the center position of the Gaussian envelope.

Equations (2) and (3) show, that for  $x_s = 0$  the systematic error  $\Delta x_s$  vanishes and the statistical error  $\delta x_s$  becomes minimum. Therefore the accuracy can be improved by iteration. First, we calculate the center position  $x_{s1}$  of the signal as described above. Second, we take as new origin the sample position  $x_{02}$  next to the calculated  $x_{s1}$ . Thus, the new center position  $x_{s2}$  is close to zero. This procedure reduces both the systematic and the statistical error. The statistical error  $\delta x_s$  can further be reduced by limiting the number of samples  $(N+1)$  around the new origin  $x_{02}$ , however, the number of samples must be large enough to cover the whole range where the fringes are visible. Once the error for the center of gravity is smaller than half a fringe period  $\Lambda$ , the phase  $\Phi$  can be determined without ambiguity.

For the practical implementation we have introduced an optimum sampling concept, which is based on synchronous sampling using four samples per fringe period, i.e.  $b = \Lambda/4$ . Two local values are calculated per period, namely

$$S_n = \frac{1}{2} (s_{n-1} - s_{n+1}) \quad \text{and} \quad C_n = \frac{1}{2} \left\{ s_n - \frac{1}{2} (s_{n+2} + s_{n-2}) \right\}. \quad (5)$$

The local power of the ac signal is then given by  $F_n^2 = C_n^2 + S_n^2$  and  $F_n$  is a good approximation for the local value of the envelope. Using  $F_n$  in Eq. (1) instead of  $H_{ac}(x_n)$  to calculate the center position  $x_{s1}$ , the systematic error given in Eq. (2) is even reduced by a factor of 7/16. The phase  $\Phi$  of the fringe signal is determined with the help of the complex value  $C_n + i S_n = F_n \exp\{i n \pi/2\} \exp\{i \Phi_n\}$ , from which the local phase  $\Phi_n$  is obtained through

$$\Phi_n = \arg \{ (-i)^n (C_n + i S_n) \}. \quad (6)$$

Now, the phase  $\Phi$  is calculated as the average of the  $\Phi_n$  over as many periods as possible with a reasonable SNR. The center position of the fringes expressed in pixels is then  $x_\Phi = -2\Phi/\pi$ , since 4 pixels are equal to one fringe. This concept has been tested successfully by computer simulations.

For the experimental verification of this new signal processing method for white-light fringes applied to absolute force measurement from the induced birefringence in an optical fiber

(Fig. 1), we have replaced the optical fiber by a Soleil-Babinet compensator (SBC). The broadband source is a LED emitting at  $\lambda = 880$  nm with a spectral bandwidth  $\Delta\lambda$  of about 50 nm. The linearly polarized light is oriented at  $45^\circ$  with respect to the birefringence axes of the SBC. Therefore, two linear polarizations shifted in phase are obtained at the output. The beam is then enlarged to fill the whole aperture of the Wollaston prism (W). The retardation of the Wollaston varies linearly across its section. This causes the relative phase between the two orthogonal polarizations to change linearly across the beam section. Interference between this two polarizations is then obtained by a dichroic sheet polarizer (DSP) directly placed against the Wollaston output face. The transmitting axis of the DSP are oriented at  $45^\circ$  with respect to both polarizations to maximize the fringe contrast. The detector was a linear photodiode array of 512 pixels with a center-to-center spacing of  $25 \mu\text{m}$  and a line scan time of 30 ms. The Wollaston prism was designed to produce fringes of about  $100 \mu\text{m}$  separation. Therefore synchronous sampling with 4 pixels per period was obtained by the lens  $L_2$  for 1:1 imaging. By adjusting the distance between the lens  $L_2$  and the detector the imaging can be exactly adjusted, however, the results showed that this adjustment is not critical. The width of the envelope of the fringe signal was equal to about 15 fringes, which corresponds to  $\Delta x = 35$  pixels in Eq. (4). Figure 3 shows the relative systematic error  $\Delta x_s/x_s$  and the statistical error  $\delta x_s$  (for  $x_s = 0$  and  $N = 160$ ) as a function of the signal-to-noise ratio  $\text{SNR} = m^2/\sigma^2$ .

The experimental results for the calculated center of gravity  $x_{s2}$  (after one iteration) versus the Soleil-Babinet retardation are shown in Fig. 4. The statistical reproducibility was measured to be  $\delta x_{s2} \approx 10^{-3}$  pixels, which corresponds to a SNR of about 63 dB (Fig. 3). The observed oscillation of about 1/10 of a fringe around the linear fit has a periodicity of  $2\pi$  and was reproducible, but the cause could not be found yet. The experimental results for the calculated phase  $\Phi$ , expressed in numbers of pixels  $x_\Phi$ , are shown in Fig. 5. The linearity is nearly perfect and the statistical reproducibility was about  $10^{-4}$  pixels. The accuracy was measured for different SNRs. The results are shown in the Table below.

	SNR [dB]	63	51	43	31
center of gravity	$\delta x_{s2}$ [pixel]	0.005	0.016	0.04	0.18
	$\delta x_{s2}$ [fringe]	1/800	1/250	1/100	1/20
phase (zero fringe)	$\delta x_\Phi$ [pixel]	0.0003	0.0006	0.0008	0.004
	$\delta x_\Phi$ [fringe]	1/10000	1/6500	1/5000	1/1000

A signal processing method for white-light fringes, based on the calculation of the center of gravity of the average fringe power, has been presented. In addition, an optimum sampling concept has been developed, which is based on synchronous sampling with four samples per fringe period. This concept is particularly adequate for white-light fringes scanned by linear array detectors. The theoretical analysis and the experimental results show, that the proposed method is simple to operate, fast, accurate and extremely noise resistant. The method will be applied to measure the absolute force from the induced birefringence in an optical fiber.

## References

1. A. Koch and R. Ulrich, Fiber-optic displacement sensor with  $0.02 \mu\text{m}$  resolution by white-light interferometry, *Sensors and Actuators A*, Vol. 25-27, 201-207 (1991).
2. S. Chen, A. J. Rogers and B. T. Meggit, Electronically scanned optical-fiber Young's white-light interferometer, *Opt. Lett.*, Vol. 16 No. 10, 761-763 (1991).

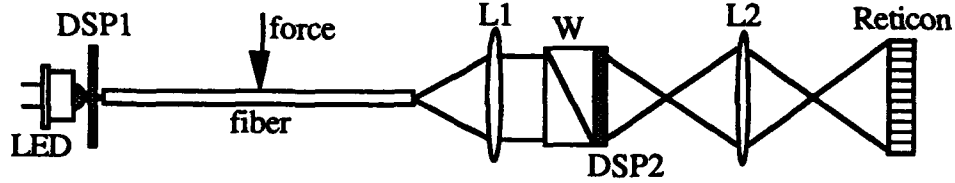


Fig. 1: Optical fiber sensor measuring the absolute force from the induced birefringence. L1 and L2: lenses; W: Wollaston prism; DSP: dichroic sheet polarizer.

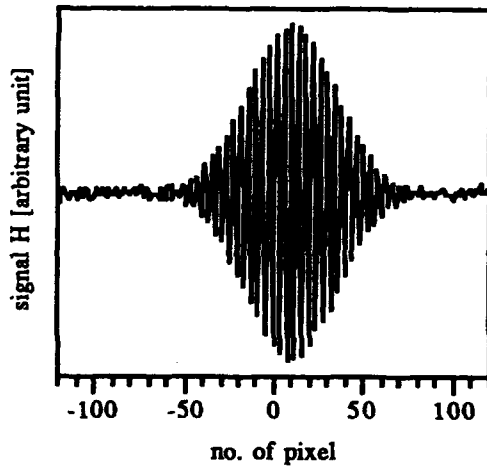


Fig. 2: White-light fringe signal for  $x_s = 10$ ,  $\Delta x = 35$ , and SNR = 35 dB.

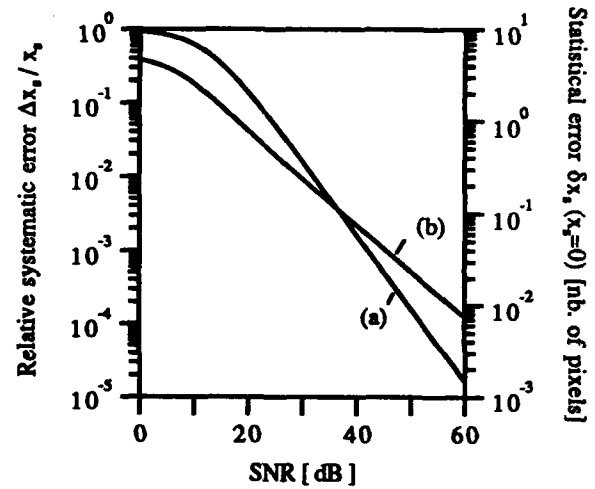


Fig. 3: Accuracy vs. SNR ( $\Delta x = 35$ ), (a) systematic error for  $N = 360$ , (b) statistical error for  $N = 160$ .

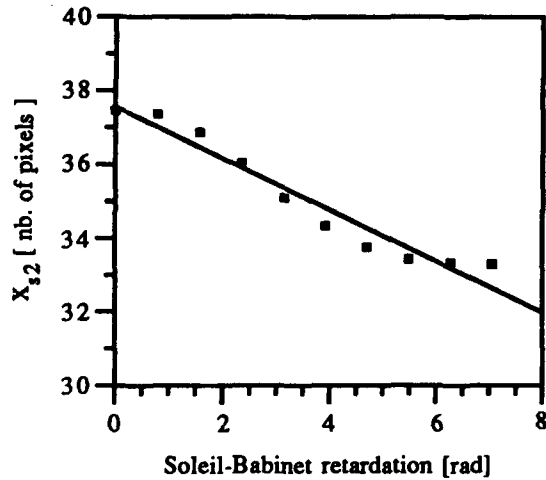


Fig. 4: Center of gravity  $x_{s2}$  (one iteration) vs. SBC retardation (SNR  $\approx 63$  dB).

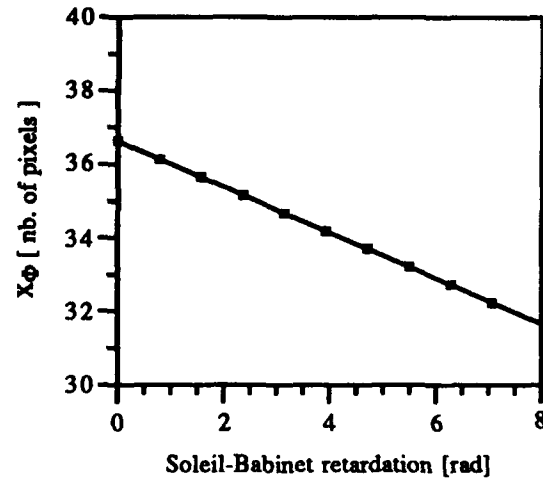


Fig. 5: Zero fringe position  $x_{\phi}$  (phase) vs. SBC retardation (SNR  $\approx 63$  dB).

### **W3.3 Remote Fiber Optic Measurement Of Air Index With White Light Interferometry**

**D. Trouchet, F.X. Desforges, P. Graindorge and H.C. Lefèvre**

**PHOTONETICS  
52, Avenue de l'Europe, 78160 Marly-le-Roi  
France**

#### **Abstract**

This paper describes a fiber optic system using white light interferometry to measure the refractive index of air with an accuracy of  $10^{-7}$ . This system will be used to improve the precision of a sub-micron linear positioning stage controlled with a coherent interferometer.

#### **Introduction**

White light interferometry is known as a very accurate technique for the remote measurement of physical measurands modifying the optical path of an interferometer [1]. In particular, we have previously developed a system for pressure sensing [2,3] and various publications have described the measurement of temperature [4], displacement [5] and fluid refractive index [6].

All these systems use two interferometers : a first sensing interferometer which produces a channelled spectrum with a periodicity that is proportional to the inverse of the optical path unbalance. This encoded spectrum is transmitted through a multimode fiber to a second readout interferometer that has an adjustable path unbalance. If the path unbalance of the readout interferometer is matched to the one of the sensing interferometer, a maximum of interference contrast is restored enabling to retrieve the corresponding value of the physical measurand.

We present a new system to measure the refractive index of air. It will be associated with a sub-micron linear positioning stage controlled with a coherent interferometer and currently developed by the University of Compiègne (France). The accuracy of such a positioning stage is actually limited by the change of the refractive index of air, which modifies the wavelength of the laser used in the coherent interferometer. This index change is a function of air pressure, temperature, humidity and gas composition.

According to the formulas given by B. Edlen [7] for the refractivity of standard air and taking into account the usual variations of atmospheric parameters, the air index has a mean value  $n = 1 + 2.67 \cdot 10^{-4}$  and its variation range is assumed to be  $\Delta n = \pm 2.5 \cdot 10^{-5}$ . The required accuracy ( $dn$ ) needed to achieve a measurement error of  $\pm 0.1 \mu\text{m}$  over a one meter long mechanical piece is  $dn = 10^{-7}$ .

#### **Description of the device**

As shown in Fig 1, this measurement system is composed of a sensing interferometer connected by two multimode fibers to an opto-electronic module which includes a light source, a readout interferometer, a CCD array and a microprocessor unit.

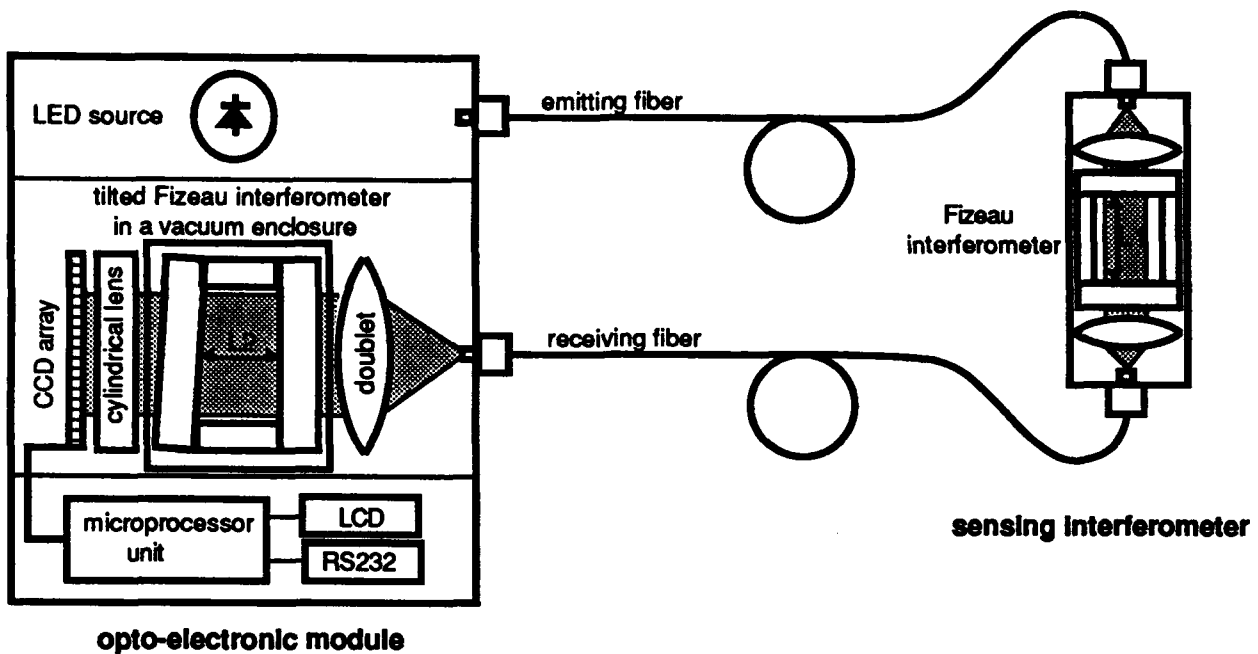


Figure 1 : Schematic set-up of the system

The sensing interferometer is a Fizeau interferometer made of two parallel and partially reflective plates and two spacers which ensure a constant distance  $L_1 = 40$  mm. The collimated incident beam is split into two transmitted and reflected beams which interfere and generate the channelled spectrum. The reflection coefficient of the partially reflective plates is about 40% to obtain a trade off between the low reflectance of a usual air-glass reflexion in a Fizeau interferometer and the multiple beam interference in a Fabry-Perot interferometer. The optical path unbalance  $\Delta$ , equal to  $2 n L_1$ , is a function of the refractive index of air. Therefore, a significant geometrical unbalance  $2 L_1$  is needed in order to achieve the required accuracy for the measurement of the index : anticipating a sensitivity of  $d\Delta = \lambda/100$ , we designed a sensing interferometer with  $2 L_1 = 80$  mm (i.e. about  $10^5 \lambda$  at  $0.85 \mu\text{m}$ ) to be able to detect index variation of  $10^{-7}$ . The mechanical arrangement of the Fizeau interferometer must ensure a great stability of the geometrical length between both plates (i.e. better than 4 nm) not to mask the variations of air index. All the optical components are made of zerodur and the semi-reflective plates have been contacted on the spacers. In this application, the Fizeau interferometer is used in a transmission set-up. Two 100-140 optical fibers are used to bring the light from the light source (emitting fiber) and to send it back to the readout interferometer (receiving fiber). An achromatic doublet collimates the beam delivered by the emitting fiber and a second one refocuses it on the receiving fiber.

The opto-electronic module is composed of the other components of the system. A LED solid state source emitting at a wavelength  $\lambda = 0.85 \mu\text{m}$  is connected to the emitting fiber. For readout, we use the technique of the tilted Fizeau interferometer that we have successfully developed for pressure sensor [2,3]. It consists of a wedge with two partially reflective plates (the reflection coefficients are also 40%) contacted at each extremity of a prismatic spacer, each component being made of zerodur. This device is placed in a vacuum enclosure to eliminate the air dependence. After passing through the sensing interferometer, the beam carrying the channelled spectrum is delivered by the receiving fiber and collimated by an achromatic doublet. It produces in the readout interferometer a spatial fringe pattern which can be analyzed with a linear CCD array. An additional cylindrical lens increases the amount of collected light. The fringe pattern is localized where the path unbalance of the

readout interferometer ( $\Delta = 2 L_2$ ,  $L_2$  being the variable geometrical length between both tilted plates) is equal to the one of the sensing interferometer :

$$\Delta = 2 L_2 = 2 n L_1$$

In practice, since there is a difference between the mean air index and the vacuum index, the average separation between both tilted plates has to be taken 11  $\mu\text{m}$  longer than the one of the sensing interferometer (i.e. 40.011 mm). The path unbalance corresponding to the full width of the spatial fringe pattern on the CCD array is about equal to 15 fringes ( $15 \lambda$ ). It depends on the coherence length of the light source. Its displacement due to air index variations is  $\pm 2.5$  fringes ( $2 \Delta n L_1 = \pm 2.5 \lambda$ ). The useful path unbalance range is thus 20 fringes ( $15 \lambda + 2 \times 2.5 \lambda$ ) corresponding to a geometrical length variation of 8.5  $\mu\text{m}$  in the tilted Fizeau interferometer. The wedge angle has been chosen equal to 1 mrad to get a sampling of 35 pixels per fringe and the video signal is then processed by the single-board 68010 microprocessor unit. The data measurement may be simply expressed in CCD pixels or converted in refractive index of air by calibration. It is displayed on an alphanumeric LCD and can be sent to the process controller through a RS232 interface.

### Experimental results

Fig. 2 is a photograph of the video signal delivered by the CCD array. It is composed of a fringe pattern modulating the coherence function of the light source (Fourier transform of its centered spectrum). The contrast of fringes (ratio between the fringe amplitude and the light background) is about 25% (the dark level is given by the extreme top pixels). Notice that the central fringe of the pattern is not as it could be expected a white fringe (two interferometers used in transmission) but a black fringe. It is due to the dispersion of air : the fringe position being given by the phase index ( $n_\phi$ ) and the coherence function position by the group index ( $n_g$ ) :

$$n_g = n_\phi \left( 1 - \frac{\lambda}{n_\phi} \frac{dn_\phi}{d\lambda} \right) \text{ with } \frac{dn_\phi}{d\lambda} = 5.3 \cdot 10^{-6} \mu\text{m}^{-1} \text{ around } \lambda = 0.85 \mu\text{m}$$

This yields a difference of about  $0.5 \lambda$  between the path unbalance relative to the fringe modulation ( $\Delta_\phi$ ) and the one of the coherence function envelope ( $\Delta_g$ ) :

$$\Delta_\phi - \Delta_g = 2 (n_\phi - n_g) L_1 = 2 \lambda \frac{dn_\phi}{d\lambda} L_1 = 0.43 \lambda$$

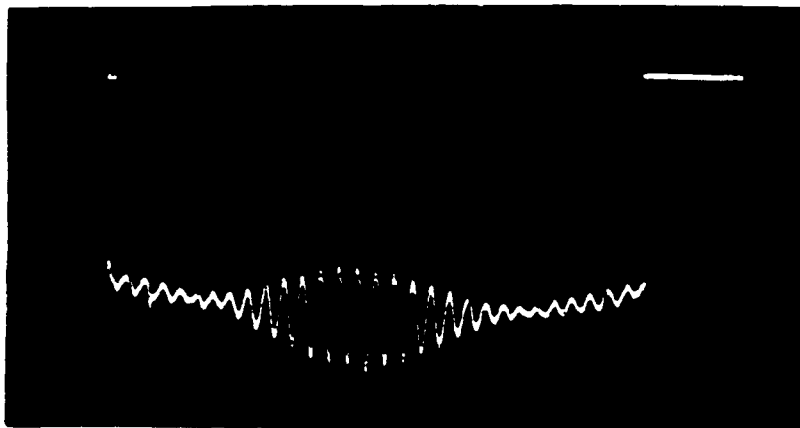


Figure 2 : video signal delivered by the CCD array

Fig. 3 shows the details of the central fringe. The CCD pixels look out of focus because of the shot noise during the exposition time of the photograph. A root mean square regression applied on this signal yields a short term sensitivity of about  $d\Delta = \lambda/3000$ , which is equivalent to an air index variation of  $3 \cdot 10^{-9}$ . This first experimental result is very encouraging since the wanted accuracy is  $10^{-7}$ . The system is now under test to evaluate more precisely its performance as a control measurement for sub-micron positioning.

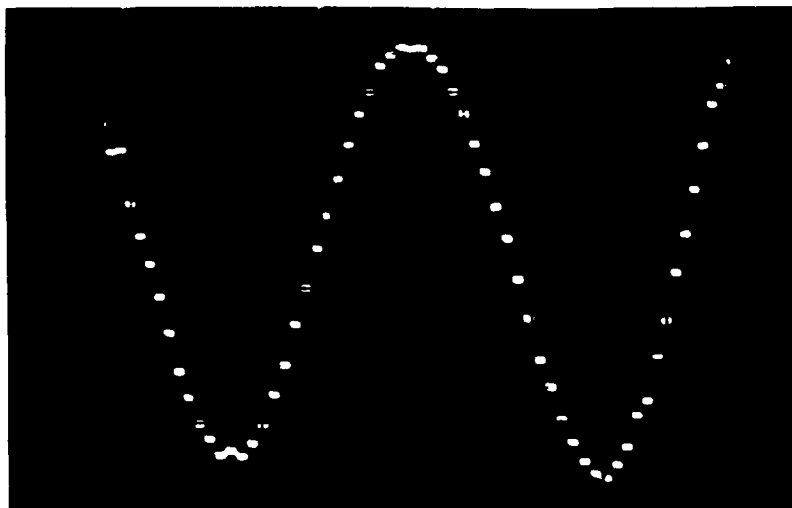


Figure 3 : Details of the black central fringe

### Conclusion

This system has demonstrated the feasibility of a high accuracy remote measurement of the refractive index of air based upon white light interferometry. It also shows that a tilted Fizeau interferometer associated with a CCD array gives a high visibility fringe pattern enabling a very accurate positioning. The combination of a cheap LED source, a readout interferometer with no moving part, and a microprocessor unit leads to a reliable and user-friendly system.

### Acknowledgments

We would to thank P. Bouchareine of *l'Institut d'Optique Théorique et Appliquée (IOTA)* and M. Bonis of *l'Université de Technologie de Compiègne (UTC)* for their collaboration in this program conducted under partial funding from the French Ministry of Research and Technology.

### References

- [1] See for example : H. C. Lefèvre, Proc. of OFS 7 (Sidney), 345-351, (1990).
- [2] D. Trouchet, B. Laloux and P. Graindorge, Proc. OFS 6 (Paris), 227-233, (1989).
- [3] D. Trouchet, P. Graindorge, F.X. Desforges, B. Laloux and H. C. Lefèvre, Proc. OPTO 90 (Paris), 359-362, (1990).
- [4] C. Mariller and M. Lequime, Proc. S.P.I.E., 798, (1987).
- [5] A. Koch and R. Ulrich, Eurosensors IV Conference, Karlsruhe, Germany, Paper B.8.2, (1990).
- [6] R. Bohm and R. Ulrich, Proc. OFS 7 (Sidney), 353-356, (1990).
- [7] B. Edlen, Metrologia 2,12 (1966).



### W3.4 Coherent FMCW Reflectometry Using A Piezoelectrically Tuned Nd:YAG Ring Laser

S. Venkatesh, W. V. Sorin, D. K. Donald and B. L. Heffner  
Hewlett-Packard Laboratories  
3500 Deer Creek Road, Palo Alto, California 94303

#### Summary

Coherent optical implementations of the FMCW technique [1] depend on the interferometric mixing of an optical signal probing the network under test with a reference signal obtained from the same source, whose carrier frequency is linearly, and phase-continuously, chirped [2]. Limitations on measurement range may be reduced by the choice of a laser source of long coherence length, as demonstrated in Ref. 3, but the temperature tuning employed in that particular case is relatively slow and inconvenient. A more serious problem is spatial resolution degradation due to residual nonlinearities in the frequency chirp, but this may be significantly reduced by incorporating a reference interferometer in the measurement system to track the nonlinearity and compensate for it [4]. This paper describes a coherent optical FMCW system that uses piezoelectric rather than thermal tuning of a source of long coherence length, in a fiberoptic network which includes a reference interferometer, triggering data capture by a system with a Fast Fourier Transform capability.

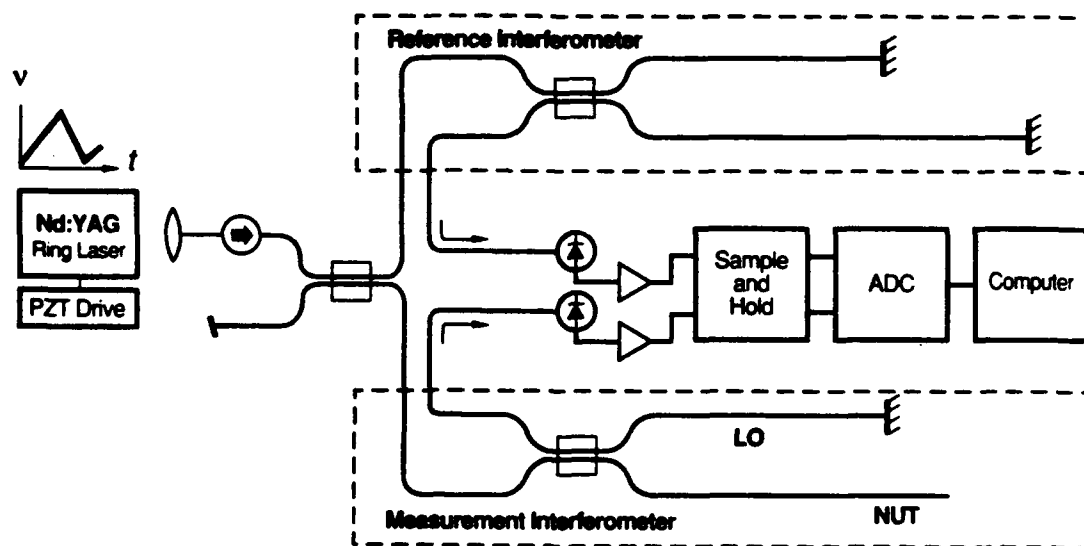
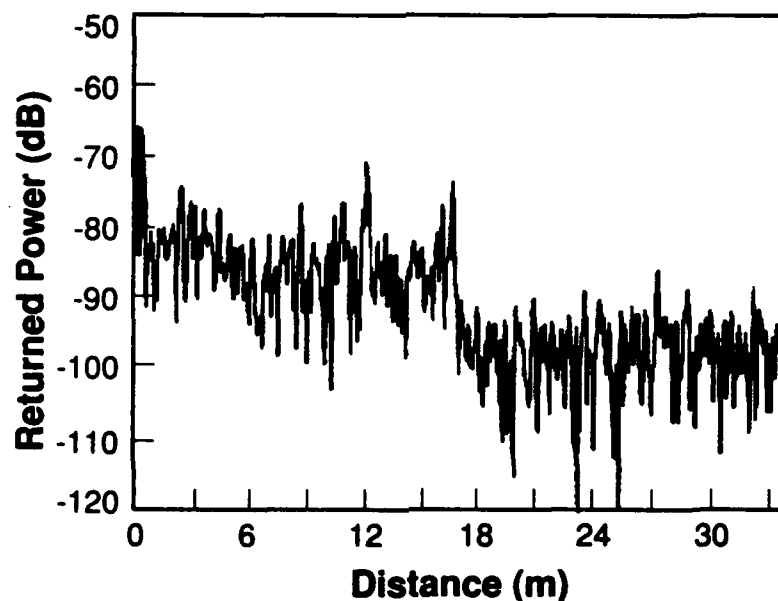


Figure 1. Experimental system for coherent optical FMCW measurements

The experimental arrangement is shown in Figure 1. The source is a bilithic, single-mode, Nd:YAG ring laser, tuned by piezoelectrically varying the gap between the two pieces making up the laser resonator [5]. Typical chirp rates used are of the order of a few tens of GHz/s. The chirped signal is passed through an isolator into a fused fiber coupler, which splits the signal into two portions. One portion enters the Michelson reference interferometer, shown in the upper part of the Figure. The output of this interferometer is used to trigger sample-and-hold circuitry at frequency intervals corresponding to its free spectral range of 1.476 MHz. The other portion of the chirped signal enters the measurement interferometer, also in the form of a Michelson, in which there is a "local oscillator" path (marked LO) to a mirrored fiber end, and a path to the network under test (NUT), which is either a single fiber, as shown, or a fused fiber coupler. The output from this interferometer is sampled, digitized, and Fourier transformed, to yield a beat frequency spectrum which is in fact the reflectometry signature of the network under test. Polarization controllers in both interferometers are not shown in Figure 1, but are present in the experimental system.

To observe Rayleigh backscatter, the laser was chirped through a frequency span of approximately 1.6 GHz, and data was collected from the measurement interferometer over approximately 75% of a single, 100 ms sweep. The network under test was a single length of fiber with its end-reflection well suppressed. A typical beat frequency spectrum, the result of a 1024-pt FFT, is shown in Figure 2.



**Figure 2.** FMCW beat signal from 17 m of fiber with suppressed end-reflection

The drop of 10 to 15 dB from the level of Rayleigh backscatter to the noise floor is seen to occur at about 17 m, corresponding to the end of the fiber. On the same vertical scale shown in this Figure, which expresses returned power relative to a 100% reflection, the normal

Fresnel reflection from the fiber tip would be a peak about 65 dB above the level of the Rayleigh backscatter. Experiments showed that averaging data from multiple measurements could reduce the noise of the noise floor, which is due to laser relative intensity noise, but had less effect on the fluctuation in the backscatter signal, which is largely due to a combination of polarization and coherence speckle noise.

To measure the limiting two-point resolution of this measurement system, a fused fiber coupler was spliced into the test arm of the measurement interferometer, and the lengths of the output fiber pigtails trimmed until the two corresponding peaks observed in the beat frequency spectrum were just resolved. The laser was chirped through approximately 6.1 GHz (about half the maximum possible with this laser without a longitudinal mode hop), at the same chirp rate as before, so 4096 data points could be collected from a single 400ms sweep. A magnified view of the relevant part of the measured spectrum is shown in Figure 3, on a linear scale.

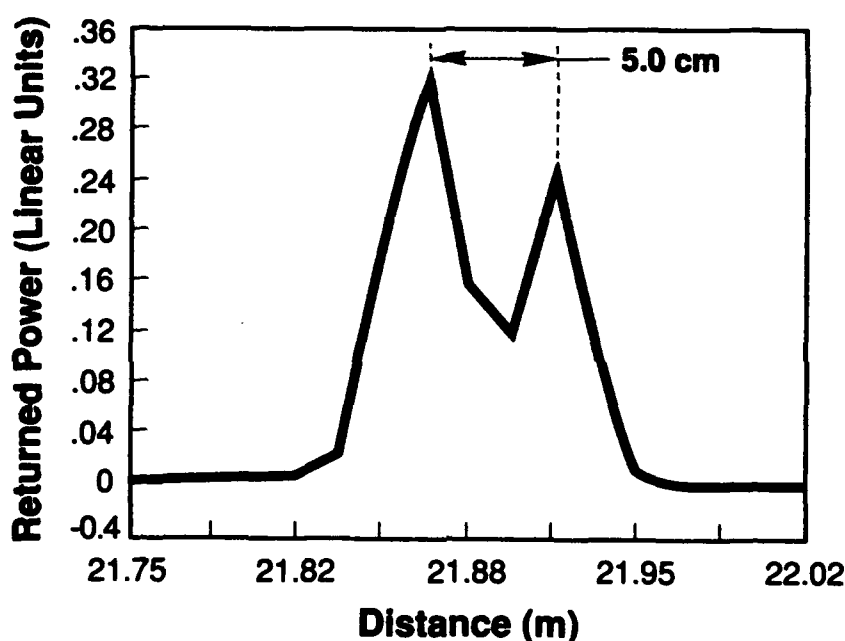


**Figure 3.** FMCW beat signal from a fiber coupler with output pigtails differing in length by 5 cm

Notice that the individual data points can be distinguished in this plot, and that the two peaks are only 3 data points apart, corresponding to a fiber length difference of 5 cm. The absolute minimum separation in a digitized output would be 2 data points, and that would only be achievable if the phase of the waveform being Fourier transformed were exactly the same at the first and last points of the sampled stream, which in general would not be the case. Notice too that this limiting resolution of 5 cm is achieved at the end of a fiber length of over 21 m, and could be achieved throughout the measurement range of 33.8 m without making adjustments to the experimental system (the maximum range is limited to one half of the path imbalance of the reference interferometer, whereas the resolution is limited only

by the frequency span of the chirp).

The experimental system described in this paper demonstrates the advantages expected of coherent optical FMCW reflectometry - principally, high sensitivity coupled with high resolution - in an implementation that overcomes some of the practical drawbacks of previous approaches. Problems remaining to be addressed before a fully practical solution is achieved include the reduction of coherence speckle and polarization noise, while the achievement of much finer resolution depends on the development of optical sources that can be chirped, without mode hopping, over much larger frequency spans.

**Acknowledgments** The authors gratefully acknowledge K W Chang for the optical isolator used in these experiments.

## 1 References

- [1] Hymans, A. J., and Lait, J.: "Analysis of a Frequency Modulated Continuous Wave Ranging System", *Proc. IEE*, 1960, **107B**, pp. 365-372.
- [2] Uttam, D., and Culshaw, B.: "Precision Time Domain Reflectometry in Optical Fiber Systems Using a Frequency Modulated Continuous Wave Ranging Technique", *IEEE/OSA J. Lightwave Technology*, 1985, **LT-3**, pp. 971-977.
- [3] Sorin, W. V., Donald, D. K., Newton, S. A., and Nazarathy, M.: "Coherent FMCW Reflectometry Using a Temperature Tuned Nd:YAG Ring Laser", *IEEE Photonics Technology Letters*, 1990, **2**, pp. 902-904.
- [4] Brinkmeyer, E., and Glombitza, U.: "High-resolution coherent frequency-domain reflectometry using continuously tuned laser diodes", *Technical Digest, OFC'91*, 1991, paper WN2, p. 129.
- [5] Trutna, W. R., and Donald, D. K.: "Two-piece, piezoelectrically tuned, single-mode Nd:YAG ring laser", *Optics Letters*, 1990, **15**, pp. 369-371.

## **W3.5 High Spatial-Resolution And Sensitivity Interferometric OTDR**

Masaru Kobayashi, Juichi Noda\*, and Henry F. Taylor\*\*

NTT Technical Assistant and Support Center  
Midori-cho, Musashino-shi, Tokyo 180

\*NTT International Corporation  
Roppongi 1-4-33, Minato-ku, Tokyo 106

\*\*Texas A & M University, Department of Electrical Engineering  
College Station, TX 77843-3128

### **1. INTRODUCTION**

Many kinds of silica-based glass waveguide circuits <sup>1</sup> and LiNbO<sub>3</sub> waveguides devices <sup>2</sup> have been proposed. These devices are highly potential for optical communication systems and optical sensor systems. To develop these waveguide devices, a diagnosing system for detecting fault locations and characterizing them is necessary. The interferometric optical-time-domain reflectometer (OTDR) is promising to apply to diagnosing the optical devices, because of high spatial-resolution and high sensitivity compared with conventional OTDR systems. The interferometric OTDR was based on the Michelson interferometer using a low-coherent light source <sup>3</sup>. The reflectance profile inside the optical components is described by the distribution of the interferometric signal power between the reflection light from the scattering centers and the reference light. The spatial resolution is determined by the coherence length of the light source. High spatial resolution up to 20 $\mu$ m has been reported in silica-based glass waveguide circuits using a superluminescent diode (SLD) <sup>4</sup>. The sensitivity was about -110dB which is sufficient for measuring reflection light from scattering centers or boundaries. However, this sensitivity is still insufficient for measuring Rayleigh scattering light in the optical waveguides. This paper presents the new interferometric OTDR to detect the Rayleigh scattering light.

### **2. SYSTEM STRUCTURE**

New interferometric OTDR system is composed of two interferometers as shown in Fig.1. One is a Mach-Zehnder (MZ) type interferometer composed of an SLD and two PANDA type polarization-maintaining fiber couplers (PANDA couplers) <sup>5</sup> for measuring reflectance profiles. The other is a Michelson (M) type interferometer composed of a distribution-feed-back laser-diode (DFB-LD) and a PANDA coupler for monitoring mirror translation. The output from the Michelson interferometer is used as a reference signal to the lock-in amplifier. The SLD has an output power of 14mW at 150mA injected current and a 40nm spectral band width at a center wavelength of 1.295 $\mu$ m. In the MZ interferometer, linearly polarized light from the SLD is divided by coupler<sub>1</sub> and transmitted into the sample and the optical delay line. The delayed light and the reflected light from the sample are combined by coupler<sub>2</sub> and detected with a balanced photodetector <sup>6</sup>. The balanced detector eliminates the intensity noise of the light source and doubles the interference signals

whose phases are opposite between the two combined outputs. The reflected light is transmitted through a fiber wound around a cylindrical piezo-electric transducer (PZT<sub>1</sub>) sinusoidally operated with  $f_p=10\text{kHz}$  frequency and phase-modulated. The reference light is frequency-shifted by  $f_d=2v/\lambda=15\text{Hz}$  with a Doppler effect produced by the mirror translation of  $v=10\mu\text{m/s}$ , where  $\lambda$  is the center wavelength of the SLD. The interferometric signal power of  $f=f_p+f_d$  frequency is measured by the lock-in amplifier with a narrow band width of 3Hz.

In the M interferometer a precise  $f=f_p+f_d$  frequency reference signal is produced in spite of the fluctuation induced in the mirror translation speed. The center wavelength of the DFB-LD is almost the same as that of the SLD and is  $\lambda=1.302\mu\text{m}$ . The DFB-LD light is divided into light reflected by the back of the mirror in the MZ interferometer and reference light reflected by another mirror butted to the fiber end face. The light reflected by the translated mirror is frequency-shifted by  $f_d$  and the reference light is phase-modulated with  $f_p$  frequency by PZT<sub>2</sub> operated by the oscillator used in the MZ interferometer. The  $f_p+f_d$  frequency signal filtered from the  $f_p\pm f_d$  frequency signal is used as the reference signal for the lock-in amplifier.

### 3. DETECTABLE LIMIT

To investigate the detectable limit, a reflectance profile was measured at the end face of the PANDA fiber without a sample as shown in Fig.2. The fiber was immersed in 1.458-refractive index liquid to reduce the return power from the fiber end face and the ghost peaks. The horizontal axis is the mirror position in free space and the position of the fiber end face is set at 0. The vertical axis is return power shown in log scale, calibrated so as to be -14.6dB by the return power of the fiber end face in free space. The return power of the fiber end face in the liquid is -60.7dB. The half band width of the signal corresponds to a spatial resolution of  $20\mu\text{m}$ . The detectable limit is -130dB by averaging the return power from the refractive index liquid.

### 4. BACKSCATTERING IN SINGLE MODE FIBERS

A distinct difference between the return power inside and outside the fiber was observed as shown in Fig.2. The peak in the fiber is discrete and the mean peak level is -118dB. Assuming that the Rayleigh scattering is isotropic and uniform, the return power  $R$  of the Rayleigh scattering over the length of the spatial resolution  $dl$  is expressed as  $R=S\alpha dl$ , where  $S$  is the recapturing factor and  $\alpha$  is the Rayleigh scattering loss coefficient<sup>7</sup>. The former coefficient is expressed as  $S=\Delta/2$  using relative refractive index difference  $\Delta$ . Substituting  $\Delta=0.3\%$ ,  $\alpha=1\times 10^{-4}$  (0.3dB/km loss), and  $dl=20\mu\text{m}$  in the equation, the return power is given as  $R=-117\text{dB}$ . This calculated value agrees well with the measured peak level. Therefore signals from the fiber are confirmed to be Rayleigh scattered light. This means that the present system can measure to a level about 10dB lower than the Rayleigh scattering level. This large dynamic range and high spatial-resolution can be used to characterize optical components.

## 5. POLARIZATION-MAINTAINING FIBER

A sample PANDA fiber is connected to the system with an angle of  $45^\circ$  between principle axes. With this alignment two orthogonal polarization modes of the sample fiber are excited. The two reflected light modes at the scattering points produce phase differences in proportion to the propagated length due to the modal birefringence of the PANDA fiber. When the phases of the two modes are the same, the interference signal between the reflected light and the reference light reaches maximum. When the phases are opposite, the signal reaches minimum. The resultant interference signal from Rayleigh scattering in the PANDA fiber is periodically modulated as shown in Fig.3. Since the periodicity of the modulation is  $L=2.0\text{mm}$ , a beat length  $L_b=2L/n=2.74\text{mm}$  ( $n=1.46$ ) and  $B=\lambda/L_b=4.7\times 10^{-4}$  ( $\lambda=1.3\mu\text{m}$ ) are obtained. The measured value agrees well with the value of  $4.9\times 10^{-4}$  obtained by other methods.

## 6. OPTICAL FIBER COUPLER

The reflectance profile in the PANDA fiber coupler connected to the system is shown in Fig.4. The coupler has a 3dB coupling ratio and a 0.5dB excess loss. The return power decreases gradually by about 5dB over a distance of 8.9mm. This 5dB drop approximately agrees with the sum of the coupling ratio and double the excess loss. In addition, the coupling length is estimated to be  $8.9\text{mm}/n=6.1\text{mm}$  ( $n=1.46$ ).

## 5. CONCLUSION

New interferometric OTDR for achieving high sensitivity close to the detectable limit has been demonstrated. The system is composed of a Mach-Zehnder interferometer for measuring the reflectance profile of optical waveguides with a balanced detector and a Michelson interferometer for monitoring the mirror translation speed exactly. Narrow band detection is realized by combination of two interferometers and high sensitivity of -130dB is achieved. Rayleigh scattered light of -118dB in the fiber can be measured with a spatial resolution of  $20\mu\text{m}$ . The modal birefringence in the PANDA fiber and the characteristics of the fiber coupler were measured successfully from the Rayleigh scattered reflectance profile.

## REFERENCES

1. M. Kawachi, Optical and Quantum Electronics 22, 391 (1986).
2. J. Noda, J. Opt. Commun. 1, 64 (1980).
3. K. Takada et al., J. Opt. Soc. Am. A 7, 857(1990).
4. H. Nagai et al., Appl. Phys. Lett. 54, 1719(1989).
5. I. Yokohama et al., Electron. Lett., 22, 929 (1986).
6. A. M. Yurek et al., J. Quantum Electron. 4, 522 (1986).
7. S. D. Personick, Bell Syst. Tech. J. 56, 355 (1977).

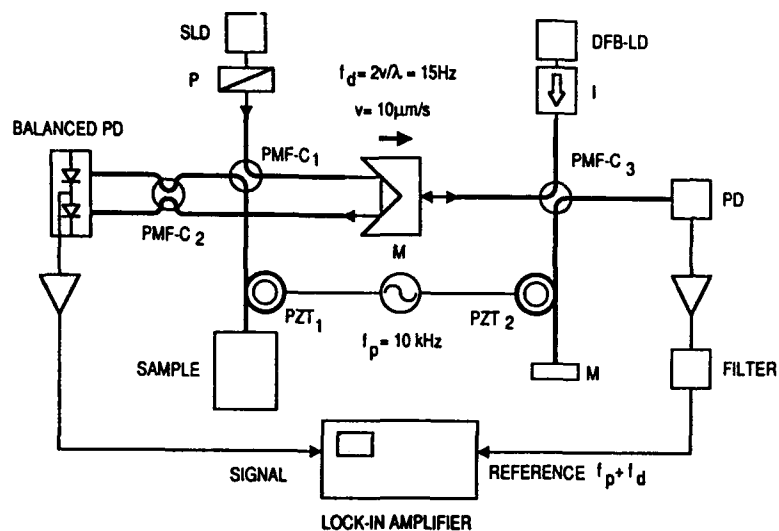


Fig.1 Interferometric OTDR composed of two interferometers.

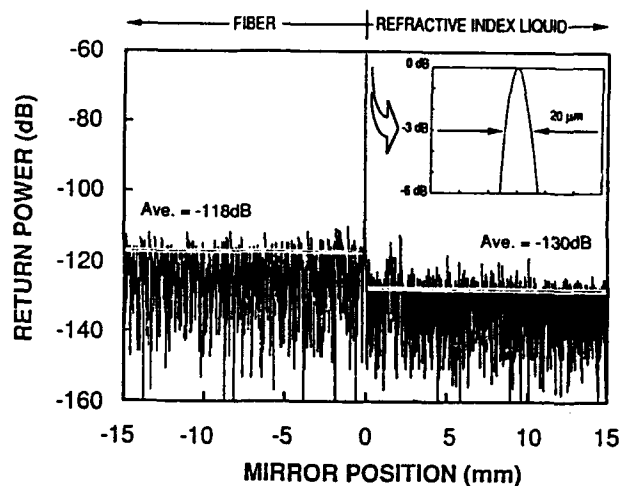
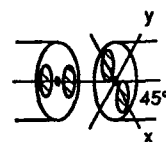
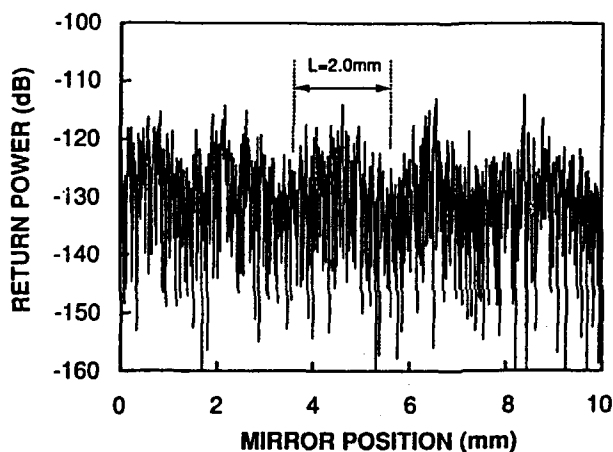


Fig.2 Reflectance profile at fiber end immersed in refractive index liquid.



$$L_b = 2L/n = 2.7 \text{ mm}$$

$$B = \lambda L_b = 4.7 \times 10^{-4}$$

Fig.3 Birefringent reflectance profile in PANDA fiber.

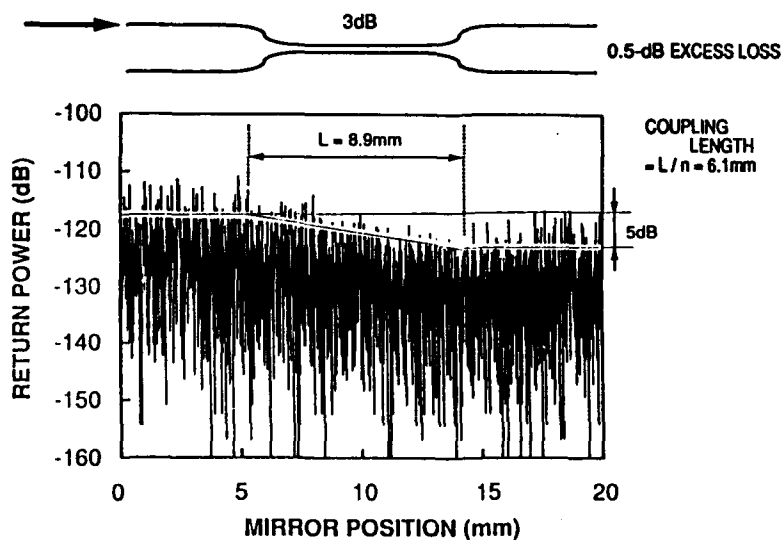


Fig.4 Reflectance profile in fiber coupler.



## **W3.6 Fiber Optic Michelson Array With Passive Elimination Of Polarization Fading And Source Feedback Isolation**

**M. J. Marrone, A. D. Kersey and A. Dandridge**

Optical Sciences Division, Code 6574  
Naval Research Laboratory  
Washington, DC 20375, USA

### **Abstract**

We report the operation of a fiber optic array of Michelson interferometric sensors using pigtailed Faraday-rotator/mirror devices for the passive elimination of polarization fading. The scheme also utilizes a polarization selective element in the input to provide isolation of the source from the reflective array.

**Introduction:** Recently, we reported the operation of a Michelson interferometer using a combination of bulk and fiber optic components which provides for the passive elimination of polarization-induced signal fading [1]. The method is based on the "orthoconjugate reflector" of Edge and Stewart [2] which consists of a  $45^\circ$  Faraday rotator followed by a plane mirror. For an optical beam which retraces its path in a fiber, Pistoni and Martinelli [3] demonstrated that the insertion of a Faraday rotator and mirror results in a state of polarization (SOP) at the exit which is orthogonal to the SOP at the entrance to the fiber. Wanser [4] proposed the use of nonreciprocal rotation elements in a Michelson configuration as a means of passive stabilization against polarization fading due to environmental birefringence perturbations. At the point of recombination the SOP from each of the interferometer arms is orthogonal to the common SOP at the entrance point and consequently they are aligned with each other to insure maximum fringe visibility.

In this paper, we describe the operation of an all-fiber version of the Michelson interferometer using Faraday-rotator/mirror (FRM) packaged devices for the birefringence compensation. The scheme uses a polarization selective element in the input fiber to provide isolation of the source from the strong optical signal returned from the Michelson configuration. We also report the results of an experimental four-sensor time-division-multiplexed array of Michelson interferometric sensors using FRMs to maintain polarization-independent operation of the array.

**Single Sensor Characterization:** In our previous work, light at the distal end of each arm of the interferometer was collimated through a tunable Faraday rotator to a plane mirror and recoupled back into the fiber after the return path through the rotator. For the fiber version of the FRM, it is noted that the principal components are already available in commercial in-line optical isolators. We have had fiber pigtailed FRMs fabricated by several isolator suppliers. Figure 1 shows the experimental arrangement for characterizing a single Michelson interferometer with pigtailed FRMs as the reflectors. Figure 2 shows packaged devices from Optics for Research (top) and Isowave (bottom). Each device consists of a  $1.3\ \mu\text{m}$  fiber, GRIN lens, Faraday rotating element and a dielectrically coated mirror. The total reflection efficiencies for these prototype devices, including recoupling back into the fiber, average 70% to 75%. For the characterization measurements, light from a  $1.3\ \mu\text{m}$  laser enters the system via a

3dB coupler and a fiber polarization beamsplitter (Sifam). The interferometer is a conventional fiber Michelson with the pigtailed FRMs fusion spliced onto both arms. Polarization controllers consisting of fiber fractional waveplates are incorporated in the input fiber ( $PC_1$ ) and in one arm of the interferometer ( $PC_2$ ) for investigating the birefringence properties of the system. A sinusoidal  $2\pi$  radian phase shift at 5kHz was applied to the piezoelectric fiber stretcher and the fringe visibility was monitored at the detector positions indicated on the diagram. At positions D1 and D2 the visibility variations with adjustment of both polarization controllers  $PC_1$  and  $PC_2$  were determined from oscilloscope traces (Figure 3) to be  $0.995 < V < 0.999$ . Because the SOP in the backward direction through the polarization beamsplitter is orthogonal to the SOP in the forward direction, this configuration has the added feature of providing isolation of the source from the strong optical return signal. The degree of isolation was measured by monitoring the interference signal at position D3. Relative to the signal at position D2 the isolation was -20.5 dB. One limitation to the isolation measured in this case is that the particular polarization beamsplitter used is not a completely symmetric 2X2 device. The orientation of the input lead was chosen for the best forward/backward operation. An improvement could be realized by inserting a fiber polarizer between the coupler and the beamsplitter. For these reasons, the 20.5 dB isolation is considered a minimum value for the isolation in this system.

**Four Sensor Array:** For a single sensor, a variety of schemes using polarization-diversity detection or active control of the input SOP have been proposed to overcome polarization-induced fading [5]. However, full optimization of the fringe visibilities of an array of sensors using polarization tracking will not be practical, in general, because the input SOP required to optimize the visibility of one sensor will not correspond to that required for another [6]. In order to demonstrate the use of the FRMs in a multi-element system, we constructed the four-sensor array shown in Figure 4. The array is based on the time-division-multiplexing scheme previously demonstrated in a ladder-type configuration of Mach Zehnder sensors [7]. Here the system employs Michelson sensors with pigtailed FRMs as the reflectors. This array topology has the advantage of using only  $N + 1$ , instead of  $2N$ , FRMs for  $N$  Michelson Sensors. An acousto-optic modulator (AOM) was used to obtain a pair of pulses of duration  $\tau$  and separation  $T$ . Fiber couplers of varying splitting ratios and FRMs with matching reflection efficiencies were selected to return pulses of nearly equal intensity through the polarization beamsplitter to the detector. Figure 5 shows a typical train of returned pulses. Figure 6 shows a pulse corresponding to a single sensor gated out of the array. A frequency-modulation was applied to the laser to generate an interference signal for the sensors. The fringe visibility was estimated to be  $> 0.95$  simultaneously for all of the sensors under birefringence perturbations induced manually in the fiber leads. This is the first demonstration of passive control of polarization-induced fading in an array of sensors. A related issue is polarization-induced phase noise. However, as expected in a sensor locked at maximum visibility [8], no significant polarization-induced phase changes were observed in this system.

**Conclusions:** We have demonstrated a scheme for simultaneously optimizing the fringe visibility ( $> 0.95$ ) of all the sensors in a four-element Michelson array. The scheme is completely passive and employs miniaturized all-fiber pigtailed components for practical sensor systems in remote applications. With the addition of a polarization-selective element in the input to the array the scheme also provides a source isolation of  $> -20$ dB from the reflected signal in the Michelson configuration.

## References:

1. A. D. Kersey, M. J. Marrone and M. A. Davis, "Polarization-Insensitive Fiber Optic Michelson Interferometer", *Electron. Lett.* 26, p. 518, 1991.
2. C. Edge and W. J. Stewart, "Measurement of Nonreciprocity in Single-Mode Optical Fibers", *Tech. Dig. IEE Colloq. on Optical Fiber Measurements*, No. 1987/55, 1987.
3. N. C. Pistoni and M. Martinelli, "Birefringence Effects Suppression in Optical Fiber Sensor Circuits", *Proc. 7th Int. Conf. on Optical Fiber Sensors*, p. 125, 1990.
4. K. H. Wanser, "Polarization Fade Free Michelson Interferometer Using Ordinary Non-Birefringent Optical Fiber", *SPIE Vol.* 891, p. 204, 1988.
5. A. D. Kersey, M. J. Marrone, A. Dandridge and A. B. Tveten, "Optimization and Stabilization of Visibility in Interferometric Fiber-Optic Sensors Using Input-Polarization Control", *J. Lightwave Technol.* 6, p. 1599, 1988.
6. A. D. Kersey, M. J. Marrone and A. Dandridge, "Experimental Investigation of Polarization Induced Fading in Interferometric Fiber Sensor Arrays", *Electron. Lett.* 27, p. 562, 1991.
7. A. D. Kersey, K. J. Williams, A. Dandridge and J. F. Weller, *Proc. 6th Int. Conf. on Optical Fiber Sensors*, p. 172, 1989 (Springer).
8. A. D. Kersey, M. J. Marrone and A. Dandridge, "Analysis of Input-Polarization-Induced Phase Noise in Interferometric Fiber-Optic Sensors and Its Reduction using Polarization Scrambling", *J. Lightwave Technol.* 8, p. 838, 1990.

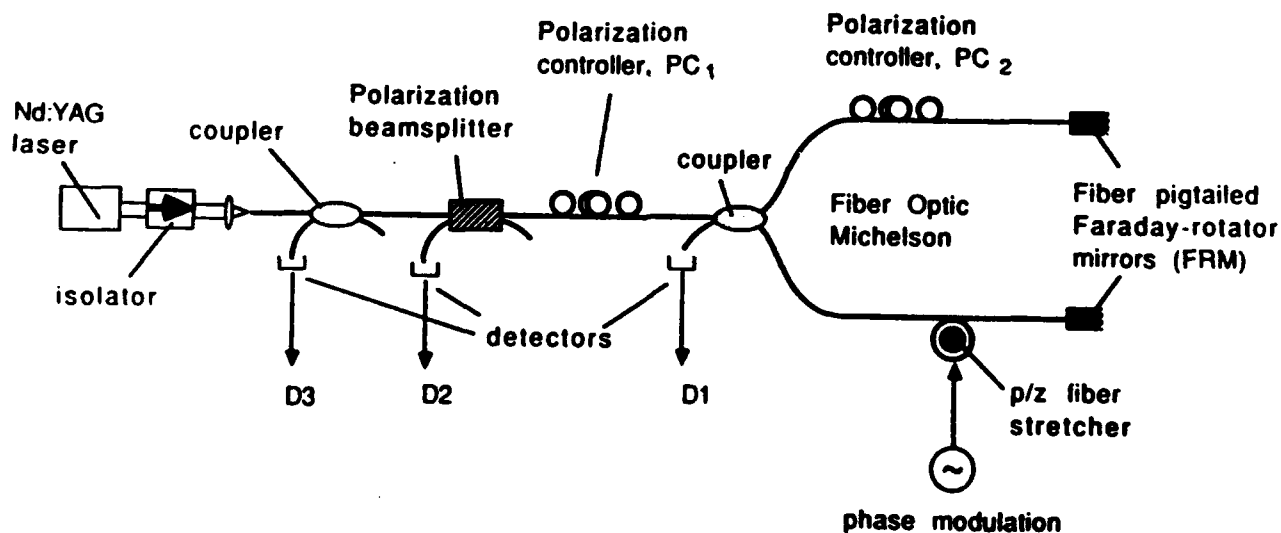


Figure 1. Experimental system for demonstrating polarization-independent Michelson interferometer with pigtailed FRMs.

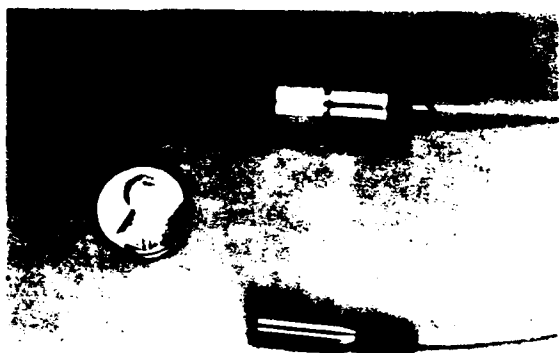


Figure 2. Packaged Faraday-rotator/mirror (FRM) devices Optics for Research (top); Isowave (bottom).

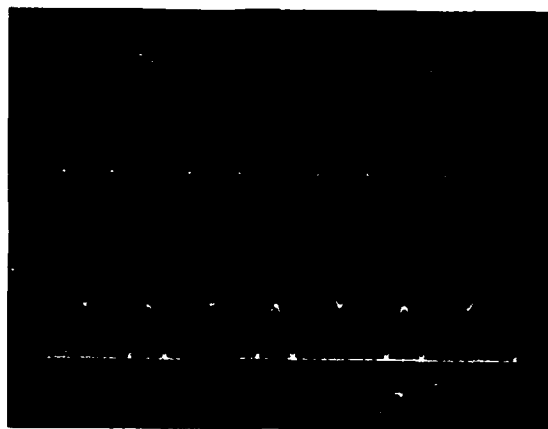


Figure 3. Fringe visibility  $0.995 < V < 0.999$  from Michelson interferometer with pigtailed FRMs.

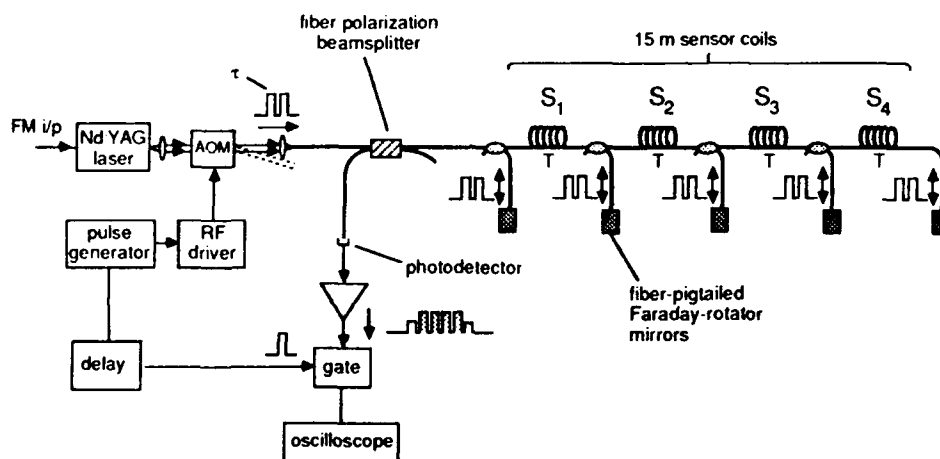


Figure 4. Four-sensor time-division-multiplexed array of Michelson interferometers with FRMs as the reflectors.

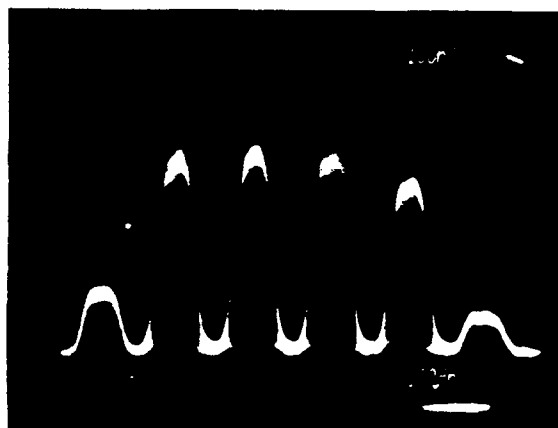


Figure 5. Output pulse train from time-division-multiplexed array of four Michelson sensors

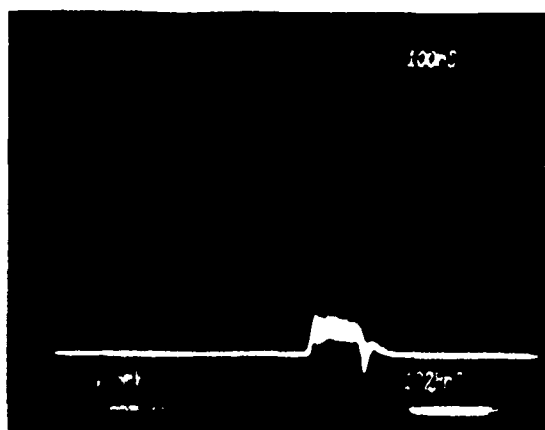


Figure 6. Gated output pulse from Sensor #3.

## W3.7 Utilisation Of Fibre Fabry-Perot Interferometers In The Determination Of Heat Transfer Transients In Wind Tunnels

S. R. Kidd, P. G. Sinha, J. S. Barton and J. D. C. Jones

Physics Department, Heriot-Watt University, Riccarton, Edinburgh, EH14 4AS, UK

### 1. INTRODUCTION

In this paper, we describe an interferometric optical fibre sensor that has been developed for the measurement of heat transfer rates. It has been developed for a specific application in which surface heat transfer rates need to be determined on ceramic model structures (e.g. turbine blades) subjected to short pulses of hot or cold gas flows in wind tunnel experiments. Heat pulse lengths vary from 10 to 1000 ms and cause surface temperature changes of up to 200 K. The wind tunnel environment provides gas flow speeds up to Mach 0.8 and gas temperatures 400 K above ambient, but also gives rise to pressure changes of 10 bar and significant levels of vibration.

Currently, heat transfer data on ceramic models are obtained using thin film platinum resistance thermometers [1].

The design specification for our sensor is a measurement bandwidth of 100 kHz, temperature resolution of 25 mK over a range of 50 K, spatial resolution of  $< 100 \mu\text{m}$  and a capability to work in the wind tunnel environment.

### 2. SENSOR CONSTRUCTION AND OPERATION

The sensor consists of a short length ( $\sim 3\text{mm}$ ) of single mode fused quartz optical fibre which has had a low reflectivity ( $\sim 10\%$ ) aluminium coating applied to each end. Alternatively, we have used  $\text{TiO}_2$  coatings to produce reflective fusion splices [2].

When suitably illuminated, the core of this structure forms a low finesse fibre Fabry-Perot (FFP) interferometer [3]. Because the reflectivities are low, higher order reflections are negligible, and the optical transfer function is similar to that of a two beam interferometer. Hence, the reflected intensity  $I$  is related to the optical phase difference  $\phi$  introduced by the cavity by [4].

$$I = I_0(1 + V \cos \phi)$$

where  $I_0$  is the mean return intensity,  $V$  is the fringe visibility and the optical phase difference can be expressed as

$$\phi = \frac{4\pi}{\lambda} \int_0^L n(x) dx$$

where  $\lambda$  is the vacuum wavelength of the illuminating light and  $n$  is the effective refractive index of the fibre core. A change in temperature,  $\Delta T$ , of the fibre core will produce an optical phase change  $\Delta\phi$  by changing the physical length (thermal expansion) and refractive index (thermo-optic effect) of the optical cavity, such that

$$\Delta\phi = \phi(T_0 + \Delta T) - \phi(T_0) = \frac{4\pi}{\lambda} \int_0^L (n\alpha + \beta) \Delta T(x) dx$$

where  $T_0$  is the initial temperature,  $\alpha$  is the thermal expansivity and  $\beta$  is the thermo-optic coefficient of the fibre and  $\Delta T(x)$  is the temperature change of an elemental section of length  $dx$ . By combining the above equations, it can be seen that by monitoring variations in the output intensity of the interferometer, the temperature change of the fibre core, integrated along its length, can in principle be determined.

In the measurement of heat transfer rates, the FFP sensing element is embedded in the test object with the fibre axis normal to the test surface and the outer (distal)

face of the fibre flush with the test surface, as shown in figure 1. The sensing element is connected to the optical source and detector assembly by a suitable length of single mode fibre. The inner (proximal) reflective face of the sensing element is spliced to this addressing fibre.

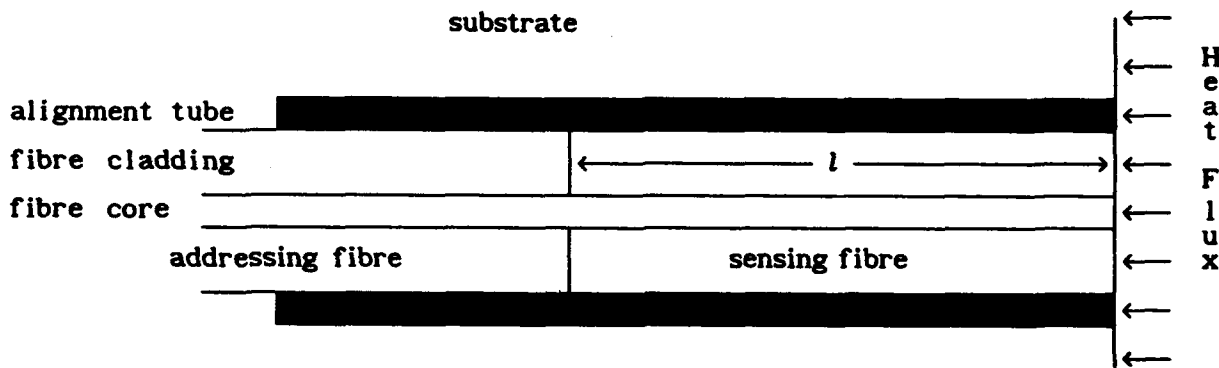


Figure 1. Arrangement of sensor, addressing fibre and substrate

To operate the sensor, a system comprising a laser diode source, launching optics to direct this light into fibre, a fibre directional coupler and a number of photo detectors are required. The arrangement of these components is shown in figure 2.

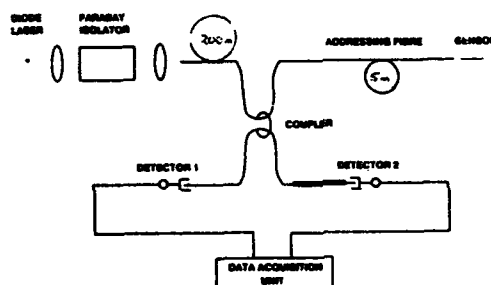


Figure 2. Arrangement of optics and fibres to operate a FFP sensor

The directional coupler splits the launched light into detector 2, (which serves as a laser intensity monitor) and the addressing fibre of arbitrary length. To date addressing fibre lengths of up to 200 m have been used successfully. The return signal from the sensor is split by the coupler and finally arrives at detector 1.

Linearisation of the sensor output signal can be performed via a number of different demodulation schemes. In cases where the overall phase change induced in the sensor is significantly less than one fringe, then homodyne processing of the signal by wavelength tuning of the laser diode source yields heat transfer data in a straightforward manner. When larger phase changes are expected, we have adopted a pseudo-heterodyne quadrature switching technique. Our implementation of this technique has previously been reported [5].

### 3. SENSOR EVALUATION

#### 3.1 Laboratory Evaluation

Initial evaluation of the sensors was carried in the laboratory using pulsed lasers to generate transient heat flux at the distal end of the sensing element. In these tests, the magnitude of the heat pulses was varied from  $40 \text{ kW m}^{-2}$  to  $18 \text{ MW m}^{-2}$ . The FFP's exhibited a typical response time of  $5 \mu\text{s}$  and noise floor of  $\sim 20 \text{ mK}$ . Full details of these tests have been reported elsewhere [6].

### 3.2 Transient Wind Tunnel Evaluation

Initial tests of the FFP sensors in a transient wind tunnel environment were carried out in a design variation of a shock tube, called a Ludwig Tube. This tube could provide pulses of gas for 20 ms at Mach 0.5 and 50 K below ambient room temperature. A schematic diagram of the tube is given in figure 3.

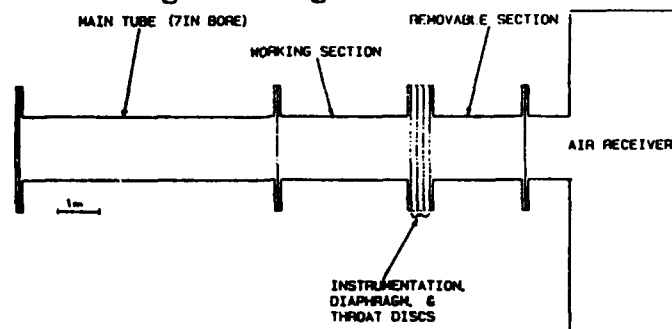
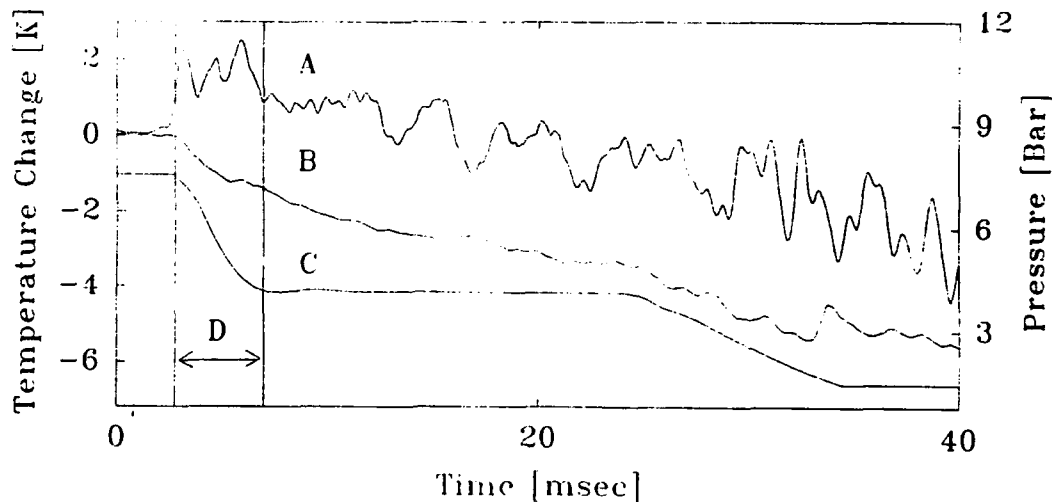


Figure 3. Schematic representation of a Ludwig Tube pulsed wind tunnel

The principle of operation is such that a diaphragm separates a high pressure gas supply at 10 bar (the main tube) from a low pressure region at a rough vacuum (the dump tank). When the diaphragm is ruptured, a rarefaction wave propagates into the main tube, is reflected from the far end and returns to the diaphragm position. The time taken for this cycle determines the run time of the tube and during this time, steady flow conditions are obtained in the working section.

Four multiplexed FFP sensors were embedded in a flat ceramic (Macor) plate, which served as our test object. The plate was also fitted with six thin film platinum resistance thermometers. The plate was mounted in the working section of the Ludwig tube, and measurements were made of the heat flux produced by the flow of the cold gas over the plate when the tube was operated. Figure 4 shows a typical experimental result, where data from an FFP, a resistance thermometer and a pressure gauge in the working section of the Ludwig Tube are all displayed. These data were used to calculate the heat transfer rate during the 20 ms run time of the tube. The resistance gauge yielded a value of  $52 \pm 1 \text{ kW m}^{-2}$  and the FFP data yielded  $53 \pm 6 \text{ kW m}^{-2}$ .



- A : Uncorrected output from an FFP of mean temperature  $\times 10$
- B : Surface temperature from platinum thin film resistance thermometer
- C : Pressure in working section of tube
- D : Duration of FFP pressure response

Figure 6. Data from a Ludwig Tube run

#### 4. DISCUSSION AND CONCLUSIONS

Heat flux data have successfully been derived in a wind tunnel experiment using a fibre Fabry-Perot interferometric sensor. Comparison of observed heat transfer rates between the optical sensor and a platinum thin film resistance gauge show that there is good agreement.

The sensitivity of the FFP to pressure variations is known to be influenced by the details of the mounting of the sensing fibre [7]. By using different adhesives and/or alignment tubes, it has been possible to reduce this pressure cross-sensitivity. Laser intensity noise was compensated for in the signal processing, and the frequency noise contribution is small for these short interferometers. Further sources of noise in the system include environmental noise in the form of vibration of the launch optics (which is responsible for the oscillations of the sensor signal in figure 4) and parasitic interferometers arising from small reflections at the termination of the end of the directional coupler arms, even though the reflection coefficients were reduced to  $\sim 10^{-5}$ . A fundamental and significant noise source arises due to coherent Rayleigh backscattering in the addressing fibre [8], and we shall describe procedures for its minimisation.

Our design of FFP has been shown to meet a demanding performance specification in a difficult working environment. It has demonstrated several advantages over thin film resistance thermometers. The FFP acts as a calorimeter and therefore yields heat flux directly; a thin film gauge measures surface temperature which is related to heat flux via an integral equation and hence requires complex signal processing. The FFP has high spatial resolution and thermal properties very similar to the blade material. The FFP provides a robust and relatively straightforward solution to a range of heat transfer measurement problems, and may be considered as an optical thermometer capable of wider applications in similarly hostile operating environments.

#### 5. ACKNOWLEDGEMENTS

This research was funded by the Ministry of Defence Royal Aerospace Establishment, Pyestock, Farnborough. P.G. Sinha also acknowledges the Association of Commonwealth Universities for additional funding. Thanks are due to Professor T.V. Jones, Oxford University, for supplying the Macor plate with its associated thin film gauges.

#### 6. REFERENCES

1. D.L. Shultz and T.V. Jones, "Heat transfer measurements in short duration hypersonic facilities," *NATO AGARD Report AG 165*, 1973
2. C. E. Lee, H. F. Taylor, A. M. Markus and E. Udd, "Optical Fibre Fabry-Perot Sensor," *Opt. Letts.*, vol 14, no 21, pp 1225-1227, 1989
3. A. D. Kersey, D. A. Jackson and M. Corke, "A Simple Fabry-Perot Sensor," *OptComm*, vol 45, pp 71, 1983
4. J.M. Vaughan, "*The Fabry-Perot Interferometer, History, Theory, Practice and Applications*," Adam Hilger, IoP Publishing Ltd, 1989
5. P.G. Sinha, D. Anderson, S.R. Kidd, H.J. Baker, J.S. Barton and J.D.C. Jones, "Compensation for Thermal Time Constant Induced Distortions in Current Induced Frequency Modulation of Diode Lasers," *Applied Optics Digest*, Proc. Applied Optics and Opto-Electronics, p289-290, IoP Publishing Ltd, Nottingham, September 1990
6. S.R. Kidd, P.G. Sinha, J.S. Barton and J.D.C. Jones, "Miniature Fast Response Fibre Optic Fabry-Perot Temperature Sensors," *Applied Optics Digest*, Proc. Applied Optics and Opto-Electronics, p41-42, IoP Publishing Ltd, Nottingham, September 1990
7. J.A. Bucaro, "Optical Fiber Sensor Coatings," *Optical Fibre Sensors*, NATO ASI Series E, No. 132, p321-338, Martinus Nijhoff, Dordrecht, 1987
8. A. M. Yurek, A. Dandridge, A. D. Kersey, "Coherent backscatter induced excess noise in reflective interferometric fibre sensors," *Proc. OFS* 1988



**WEDNESDAY**  
**January 29, 1992**  
**MM: San Carlos Ballroom**  
  
**POSTER SESSION**

# P1 High-power 0,82 $\mu\text{m}$ Superluminescent Diodes With Extremely Low Fabry-Perot Modulation Depth

S. A. Safin, A. T. Semenov, V. R. Shidlovski, N. A. Zhuchkov  
Yu. V. Kurnyavko

J. E. INTERFACE, USSR 123557 Moscow, Klimashina str., 9

Phones: (095) 253 50 10

124 06 18

Fax : (095) 253 68 89

## S U M M A R Y

Superluminescent diodes (SLD) are very attractive light sources for fiber optic sensors, especially for fiber optic gyros and microcavity sensors. SLD emits high-power low divergence beams with broad (up to 15 nm) spectrum width with coupling coefficient to single-mode fiber up to 25%[1]. However when output power exceeds 10 mW typical value of Fabry-Perot modulation depth is up to 20% even in antireflection-coated window structure. We developed AlGaAs/GaAs SLD with output power up to 15 mW and Fabry-Perot modulation depth about 1%.

One of the main feature of SLD over multimode laser diodes is lower power fluctuations. However strong increasing of SLD noise may be expected with increasing of output power[2]. So we also studied noise behavior of high power SLD and find noise saturation at high power levels.

Structure of devices is schematically scetched on Fig.1. LPE-grown structures with weak index guiding had three independently-pumped regions with length 250, 50 and 250  $\mu\text{m}$ . Reactive ion technique was used both for 4- $\mu\text{m}$  mesa and 50  $\mu\text{m}$  division gaps etching. Leakage resistance between different electrodes was typically 4-6 kOhms. Grounded absorber configuration was used[1]. Both regions 1 and 2 or only region 1 were pumped. Polyimide layer were used for electrical isolation.

Light-current characteristic of as-cleaved device is Shown on Fig.2 (curve 1). Only region 1 is pumped. With output power of 5 mW even in such devices Fabry-Perot modulation depth didn't exceed 3% for the most of samples, and spectrum FWHM was 15 nm.

Curve 2 on Fig.2 shows light-current characteristic and spectrum of SLD with less than 1% reflectivity coating of output facet. Output power increase at 3 times with respect to noncoated device (nearly the same, like in[1]). Nevertheless, extremely low Fabry-Perot modulation depth of about 1% is seen. This value is by the order of magnitude less that in[1] for the same power level. Note that the rear facet of the device remains uncoated.

For both coated and uncoated device degree of polarization of output radiation was not more then 10%.

The sensitivity of absorber section 3 when acts like photodiode was 0,4 mA/mW. This is nearly 2 times smaller than maximum theoretical sensitivity 0,7 mA/mW mainly due to incomplete absorption of incoming radiation from amplifier section. From this point high spectral modulation depth must be expected in contradiction with our results, especially for uncoated rear facet. We believe that small depth in our samples

is mainly due to weak index guiding in the structure.

Really, in amplifier region two effects have influence on refractive index profile in lateral direction. The first is decreasing of refractive index with carrier density increasing[3] and the second is increasing of the former due to temperature rise in active region. With optimum design of the mesa, especially the residual thickness of upper cladding layer outside of mesa, effective index step is enough to maintain stable confinement of radiation. By the other hand, in absorber only decreasing of refractive index due to photogenerated carriers takes place, thus leads to poor confinement.

The last effect leads to high lateral divergence of radiation in absorber region. Our measurements shows, that near field width of SLD is 5  $\mu\text{m}$  on output facet and nearly 40  $\mu\text{m}$  on rare facet. Evidently feedback effect from the back facet is negligible in this case even if it has no antireflection coatings.

As it was noted above, light-current characteristics were measured when only region 1 was pumped. The decreasing of output power by 10% was observed when the same total current flows through both sections 1 and 2. This effect may be caused by re-emission of photons by photoexcited carriers in section 2.

The other important characteristic of SLD is power fluctuations. Previous results [2] show that noise level of SLD with output power of 3 mW may exceed shot noise limit up to 20 dB. From the viewpoint of gaussian statistics[4], further increase of excess noise may be expected for high-power SLD. From the other point of view, some reduction of noise due to gain saturation effect may take place.

Fig.4 shows the dependence of SLD noise on and emitted power. Additionally theoretical dependence for noise on power is drawn. This was calculated as follows.

It can be shown[4], that gaussian statistics of SLD radiation leads to simple expression for SLD noise:

$$\langle dI \rangle^2 = 2eI(1+I/I_0), \quad I_0 = 2eMdv, \quad (1)$$

where  $e$  is elementary charge,  $I$  - photodetector current,  $dv$  - spectral bandwidth,  $M$  - number of spatially independent elementary sources, and factor 2 in expression for  $I_0$  is connected with depolarization of SLD emission.

It is seen that excess noise begin to saturate for output powers more than 8 mW. With output power of 15 mW noise is nearly twice less that calculated with (1). Qualitatively the same results were obtained for noncoated device when output power exceeds 3 mW. It can be seen from Fig.2, that noise saturation starts at linear part of light-current characteristics, where strong gain saturation take place.

For practical application coupling of SLD radiation to single mode fiber is important. The efficiency 20% was obtained for tapered microlens polarization maintain single-mode fiber. Modules had dual-in-line 14 pins package. SLD with heatsink was established on Peltier cooler. High precision thermoresistor was used for temperature stabilization. Excellent output power stability was obtained in ambient temperature range from -60 C to +60 C.

In conclusion, high power and extremely low Fabry-Perot

modulation depth SLD and modules are developed. Maximum power of 15 mW with 150 mA injection current and 15 nm spectral FWHM with 1% Fabry-Perot modulation depth are achieved. Output power of single-mode fiber pigtail module is 3 mW. Noise saturation at high power level due to gain saturation is found. The results show that optimum design of SLD structure lead to high performance of devices with simple mesa structure without output windows and only one antireflection coated facet.

## R E F E R E N C E S

1. N. S. K. Kwong, K. -Y. Law, N. Bar-Chaim. IEEE J. of Quantum Electron., v. QE-25, N 4, p. 696-704 (1989).
2. A. M. Yurek, H. F. Taylor, L. Goldberg, J. F. Weller, A. Dandridge. IEEE J. of Quant. Electron., v. QE-22, N 4, p. 522-527 (1986).
3. P. G. Eliseev. In: Introduction to physics of injection lasers. Moscow, Nauka, 1983 ( in Russian ).
4. Ya. Perina. In: Coherence of light. Moscow, Mir, 1974 ( In Russian ).

## F I G U R E C A P T I O N S

- Fig. 1. SLD structure. a - metal contact, b - polyimide layer, c, e - upper and lower cladding layers, d - active layer, f - n-type substrate, g - p<sup>+</sup>-contact layer.
- Fig. 2. Light-current characteristics of SLD before (1) and after (2) output facet coating.
- Fig. 3. Spectrum of SLD at 15 mW output power.
- Fig. 4. Relative noise versus output power dependence for SLD with coated facet.  $dI_{sh}$  - shot noise level.  $f = 10$  MHz.

FIG. 1.

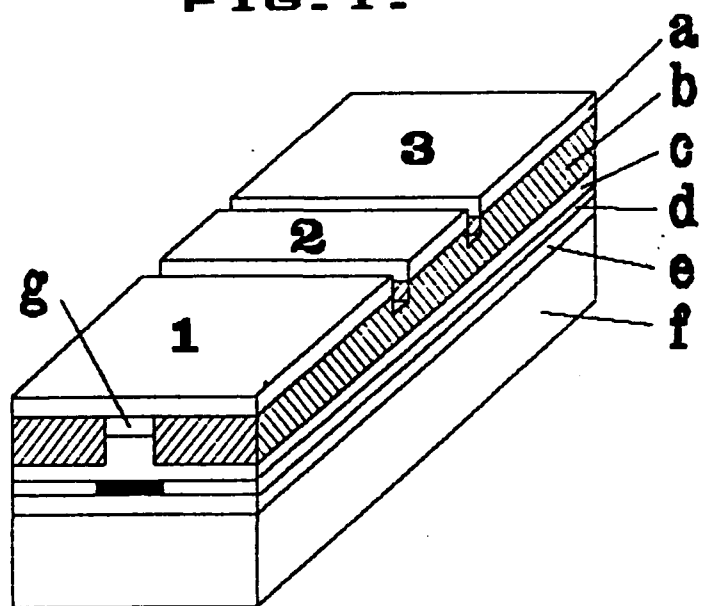


FIG. 2.

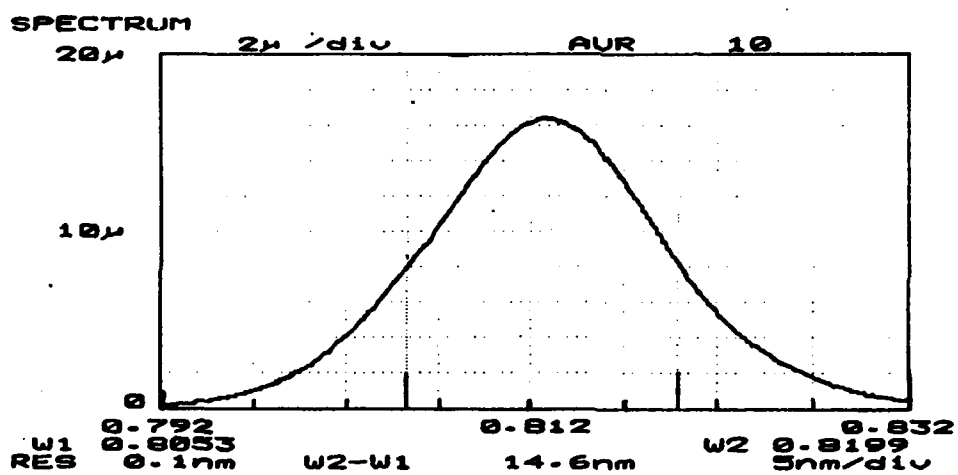
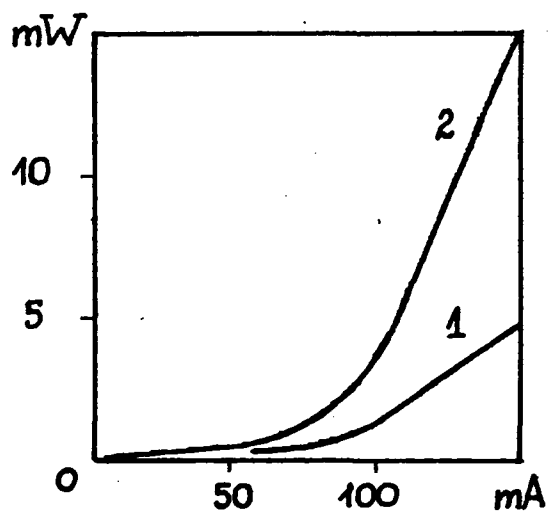


FIG. 3.

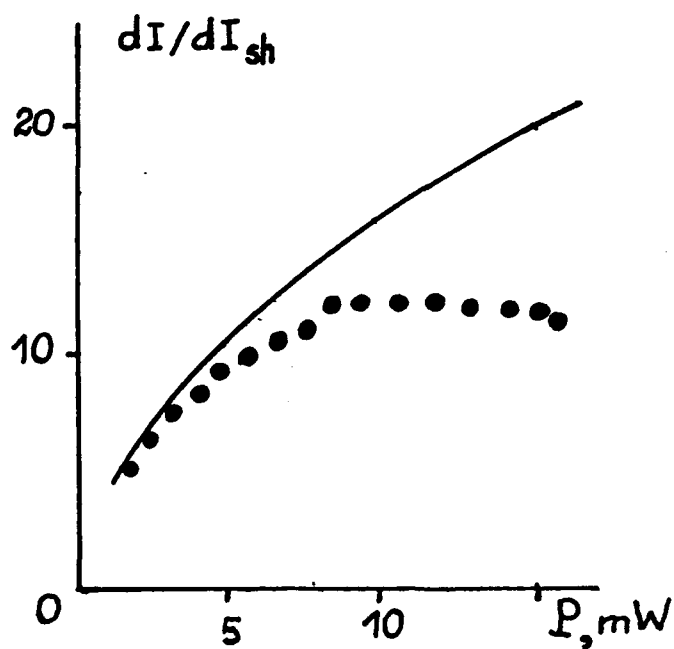


FIG. 4.

R.P. Moeller and W.K. Burns

Code 6570

Naval Research Laboratory

Washington, D.C. 20375-5000

There is great interest in using fiber superfluorescent sources in fiber gyroscopes as a replacement for semiconductor superluminescent diodes (SLD's). Potential benefits include higher available power, better wavelength stability with temperature, and improved lifetime. Multicore Nd:fibers<sup>1</sup> pumped by a laser diode array offer high output powers in a single mode core, but are susceptible to lasing due to feedback.<sup>2</sup> This type of diode laser pumped source has been successfully employed in a fiber gyroscope using a backward pumping scheme to avoid feedback.<sup>3</sup> We report a fiber gyro using a similar source, but are able to forward pump it with the use of an optical isolator. The gyro utilizes all spliced fiber components after the source fiber. Excess noise<sup>4,5</sup> has been an issue with fiber broadband sources due to their somewhat narrower (compared to SLD's) emission spectrum. We demonstrate an intensity noise subtraction scheme which is successful in removing most of the excess noise.

The gyro configuration is shown in Fig. 1. We use a 0.5W diode array pump (0.81 $\mu\text{m}$ ), which is focused into the end of the Nd doped active fiber through a dichroic mirror. This dichroic mirror isolates the backward 1.06  $\mu\text{m}$  emission from the diode array facet. The multicore (multimode pump, single mode at 1.06  $\mu\text{m}$ ) Nd doped fiber had a structure similar to the fiber of Ref. 1 and was fabricated by E. Snitzer at Rutgers University. The active fiber was spliced to the pigtail of a 1.06  $\mu\text{m}$  isolator (-4 dB insertion loss), which in turn was spliced to the input coupler of the open loop gyro. After this point all

the fiber in the gyro loop was polarization preserving fiber. The splices on each side of the isolator had insertion losses of  $\sim 1$  dB each and the gyro circuit insertion loss was 22.5 dB. The fiber coil was 1 km long, and quadrupole wound on a 16 cm radius.

Typical operating numbers were 6mW of  $1.06 \mu\text{m}$  source input to the gyro first coupler, which produced  $35 \mu\text{W}$  at the gyro detector, for 140mW of pump power at  $0.81 \mu\text{m}$ . The measured random walk coefficient for the gyro was  $7.3 \cdot 10^{-4} \text{ deg}/\sqrt{\text{hr}}$ , in good agreement with the calculated value<sup>5</sup> from the spectral width (6.8nm)  $6.7 \cdot 10^{-4} \text{ deg}/\sqrt{\text{hr}}$  (20  $\mu\text{A}$  detector current).

Since our gyro is in the excess noise limited regime we employed an intensity noise subtraction approach to reduce the excess noise. Intensity noise subtraction was used<sup>6</sup> to remove excess noise from an SLD source, but has not been reported as part of a fiber gyro. The experimental configuration for the intensity noise subtraction is shown in Fig. 2. A fiber polarizer was spliced to the unused lead of the input coupler, aligned such that its transmission axis is parallel to the transmission axis of the gyro polarizer. The noise signal is then delayed through 1 km of ordinary single mode fiber, equivalent to the length of the gyro coil. Both signals are then detected and amplified. At this point, with the gyro phase modulator drive off, a simple DC subtraction was carried out. In Fig. 3a we show the experimental signal to noise ratios (SNR), with and without noise subtraction, compared to shot and excess noise theory.<sup>5</sup> 14 dB (ele.) of noise improvement was obtained.

However an operating fiber gyro has an AC modulated output signal, whereas our noise signal is DC. Since the levels must be balanced for effective noise subtraction we modulate the AC coupled noise signal by mixing with the DC coupled gyro signal in a multiplier, and then subtract this modulated noise signal from the gyro signal. These operations are indicated by the signal and noise traces shown in Fig. 2. The output of the subtracter is then

demodulated in a lock-in amplifier. In Fig. 3b we show the experimental random walk coefficients compared to excess and shot noise theory. The results show that a factor of 3 improvement in the random walk coefficient was obtained using noise subtraction, reducing the previous value to  $2.5 \cdot 10^{-4} \text{ deg}/\sqrt{\text{hr}}$ .

We have demonstrated a  $1.06 \mu\text{m}$  fiber gyroscope that allows new, high levels of input power in an all fiber configuration. A novel intensity noise subtraction technique largely overcomes excess noise due to the source bandwidth. Although we have demonstrated this technique with an open loop gyro, the approach should also be applicable to closed loop gyros.

## References

1. H. Po et. al. Proc. OFC'89, Houston, TX, 1989, Paper PD7.
2. I.N. Duling III et. al., IEEE J. Quantum Electron, **27**, 995 (1991).
3. K.A. Fesler, M.J.F. Digonnet, B.Y. Kim, and H.J. Shaw, Optics Lett. **15**, 1321 (1990).
4. P.R. Morkel, R.I. Laming and D.N. Payne, Electron. Lett. **26**, 96 (1990).
5. W.K. Burns, R.P. Moeller, and A. Dandridge, IEEE Photonics Tech. Lett. **2**, 606 (1990).
6. A.M. Yurek, et al., IEEE J. Quantum Electron. **QE-22**, 522 (1986).

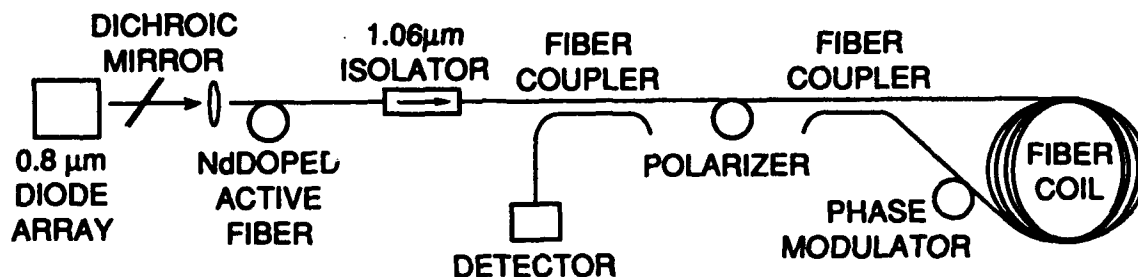


Fig. 1 Configuration of the fiber gyroscope.



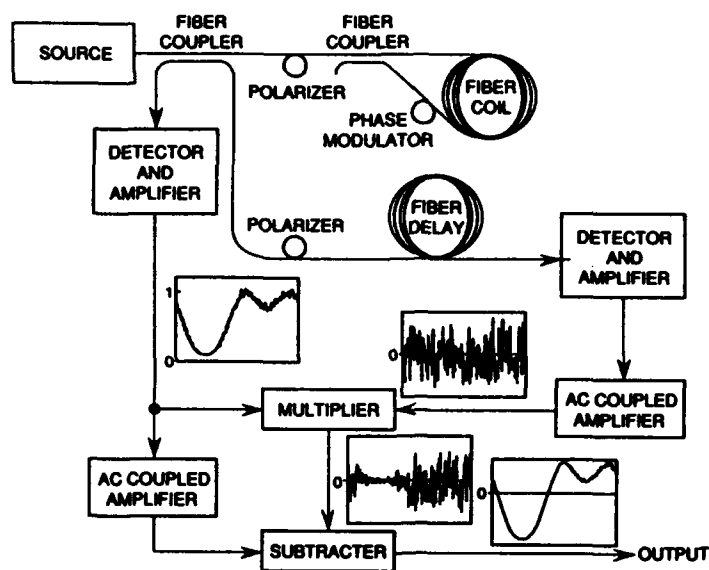


Fig. 2 Optical and electronic configuration for the intensity noise subtraction experiment.

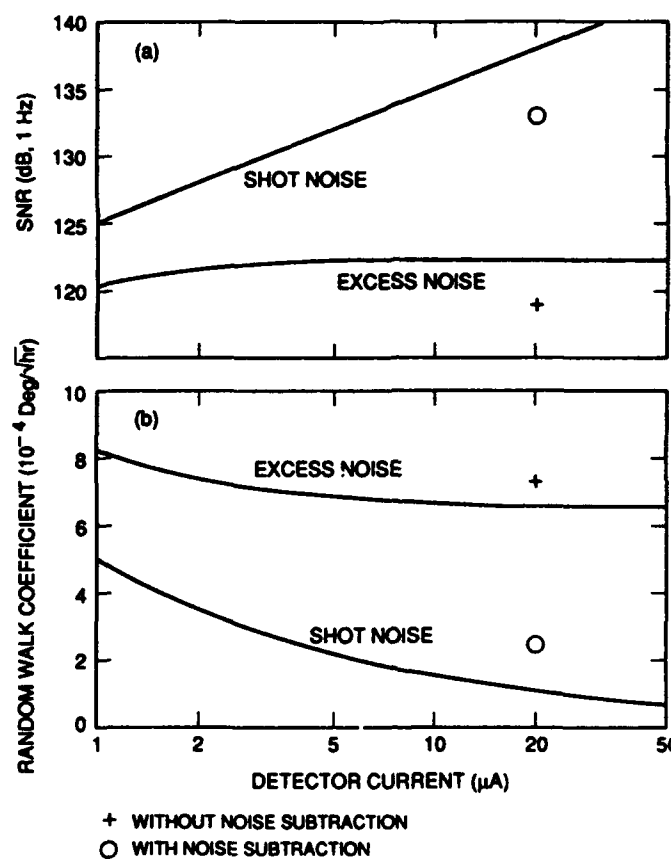


Fig. 3 Experimental data for SNR (a, phase modulator off) and random walk coefficient (b, phase modulator on).

# P3 Observation Of Backscatter-Induced CrossTalk In A Two-dimensional Frequency-Division Multiplexed Fibre Optic Gyro System

Wei Jin and Brian Culshaw

Department of Electronic and Electrical Engineering, University of Strathclyde, Glasgow G1 1XW, Scotland, UK

**ABSTRACT:** Backscatter induced crosstalk noise of about  $5^\circ/\text{hr}$  was observed in a 2-D FDM FOG system. It can be reduced to below  $0.2^\circ/\text{hr}$  by proper choice of modulation depth and frequency.

**INTRODUCTION:** Most gyroscope applications involve the use of a cluster of instruments measuring rotations along orthogonal axes. For such systems clearly a network of individual gyroscopes may be used. However, there are obvious potential economies in components when all the gyroscopes in a cluster are energised from a single source[1].

However the use of a single source for several gyroscopes does introduce the possibility of crosstalk between the signals detected from each of the gyroscopes. For a Frequency-Division Multiplexed (FDM) fibre gyro system with a single detector, crosstalk may be introduced by the effects of residual coherence, signal feedback into the light source or from first or second order backscatter[2][3][4]. This paper concentrates on examining, theoretically and experimentally, the characteristics of first order backscatter induced crosstalk in a 2-D FDM FOG system.

**THEORY:** Fig.1 shows 2-D FDM FOG system. If signals from the two gyro loops do not interfere with each other and modulation frequencies ( $\omega_1$  and  $\omega_2$ ) of the two bias modulator (PM1 and PM2) satisfy certain relations, the system will act as a two-dimensional gyro system[2].

The backscattering waves from one gyro loop will interfere with the signal waves from the other loop and this may induce serious crosstalk. For a light source with coherence length much shorter than the lengths of the gyro loops, this particular kind of crosstalk can be considered as a result of interference between signal waves from one gyro loop and scattered waves from two particular sections of the other gyro loop, each a coherence length  $L_c$  in length which travel nearly the same optical path as the signal waves of the former gyro. The amplitude of light scattered from each of these particular sections, relative to the primary beams, can be assumed as  $\delta = (\alpha S L_c)^{1/2}$ , where

$\alpha$  is the Rayleigh scattering loss,  $S$  represents the fraction of light which is reguided in the backward direction. The backcattering can thus be modelled by point scatters  $P_{ij}$  ( $i=1,2$  corresponds to gyro 1 or gyro 2;  $j=+, -$  correspond to

CW or CCW propagation) situated at a distance  $l_{ij}/2$  ( $l_{ij} < L_c$ ) from those points (A, A' or B, B') where the scattering waves travel through exact the same distance as the signal waves (see Fig.1). Variations in phases  $\beta l_{ij}$  ( $\beta$  is

the propagation constant) of the scattering waves due to perturbations of the source or coils are the cause of backscatter-induced crosstalk. By denoting the coupler detuning from ideal 50/50 as  $\Delta_i$  where  $\Delta_i = 1 - 2K_i$  where  $K_i$  is the

coupling ratio of the loop coupler of gyro  $i$ , assuming the two fibre gyro routes have similar length and the lead length in both gyros is much shorter than the loop length, and phase modulator at one end of loop  $i$  produces a phase modulation  $\phi_i(t) = \phi_{0i} \sin \omega_i t$ , The RMS value of the first order

backscatter induced crosstalk detected at frequency  $\omega_1$  under the condition of  $\omega_1/\omega_j \neq k/1$  ( $k, l = 1, 2, \dots$ ) can be expressed as[5]

$$\begin{aligned} I_{\omega_1}^{\text{In-phase}} &= A/2 \{ ((1-\Delta_j)^2 + (1+\Delta_j)^2 J_0^2(2\phi_{oj} \cos \omega_j \tau_j / 2)) \\ &\quad J_1^2(\phi_{oi}) \sin^2(\phi_{si}/2) \sin^2 \omega_1 \tau_i / 2 \}^{1/2} \end{aligned} \quad (1)$$

$$\begin{aligned} I_{\omega_1}^{\text{Quadrature}} &= A/2 \{ ((1-\Delta_j)^2 + (1+\Delta_j)^2 J_0^2(2\phi_{oj} \cos \omega_j \tau_j / 2)) \\ &\quad J_1^2(\phi_{oi}) \cos^2(\phi_{si}/2) \cos^2 \omega_1 \tau_i / 2 + (1+\Delta_i)^2 \cos^2 \phi_{sj} / 2 \\ &\quad J_0^2(\phi_{oj}) J_1^2(2\phi_{oi} \cos \omega_j \tau_j / 2) \}^{1/2} \quad (i=1, 2; j=2, 1) \end{aligned} \quad (2)$$

where  $A = I_0 \exp(-\alpha L_i) \delta(1-\Delta_i)^{1/2}$ ,  $I_0$  is the output intensity of the source, and  $L_i$  and  $\tau_i$  are length and loop delay of the  $i^{\text{th}}$  gyro loop.

It can be seen that the in-phase component at frequency  $\omega_1$  is proportional to  $J_1(\phi_{oi})$  and can therefore be nulled by suitable choice of modulation frequencies and depths. With  $\phi_{oi}$  set at a zero of  $J_1(\phi_{oi})$ , the Sagnac signal can be maximized by choosing a modulation frequency corresponding to  $\omega_1 = 2/\tau_i \arcsin(1.84/2\phi_{oi})$ . This is also true for the quadrature component if low modulation frequencies are used because for  $\omega_1 \tau_j \ll 1$ ,  $J_1(2\phi_{oi} \cos \omega_j \tau_j / 2) = J_1(2\phi_{oi})$ , which is near zero when  $J_1(\phi_{oi})$  is nulled. It should be pointed out that the backscatter-induced crosstalk can not be nulled even if an ideal 50/50 coupler is used. This is the main difference from the backscattering noise[6]. The dependence of the two components on the Sagnac phase is also of importance since at low rotation rates, the in-phase component is negligible. Therefore adjustment of the reference phase of the lock-in amplifier is required to reduced the effect of large quadrature component which may also be eliminated by using a modulation frequency corresponding to the eigen-frequency,  $\omega_1 = \pi/\tau_i$ .

**EXPERIMENTS:** Experiments were performed to observed the backscatter-induced crosstalk. As shown in Fig.1, a STC LC51/19 laser diode was used as a common source and a Sifam fibre polarizer (35 dB extinction ratio) were used as common polarizer. The loop coupler of gyro 1 is a polished one and is tunable from 0-70% coupling. Other couplers are all of fused type with fixed coupling ratio of about 50/50. Two fibre coils was wound in a quadrapole winding and have similar length of about 700 meters. Two PZT phase modulators (PM1 and PM2) were positioned in the ends of the two fibre loops respectively and three polarisation controllers (PCs), one in the input end of the polarizer and one in each of the coils, were used to adjusted the input polarisation state and the polarisation states within the coils. The output signal was detected by a GM5 photodetector and then filtered and monitored, at the modulation frequency  $\omega_1$  of gyro 1, through a lock-in amplifier. The lock-in amplifier has dual outputs and can therefore monitor both Sagnac and quadrature signals simultaneously. During the experiments, all the parameters of gyro 2 were fixed ( $\omega_2 = 2\pi \cdot 31.5$  kHz,  $\phi_{o2} = 0.92/\sin(\omega_2 \tau_2 / 2)$  and  $\Delta_2 = 0$ ) to maximise the Sagnac signal whilst the parameters of gyro 1 were tuned ( $\omega_2 = 26$  kHz or 144 kHz,  $\phi_{o1}$  vary from 0 to 9 rads and  $\Delta_1$  from 0 to 1). The in-phase crosstalk noise is not observable when  $\phi_{o1}$  vary from 0-9 rads or coupling ratio detuning  $\Delta_1$  vary

from 0-1 due to very low rotation rate (earth rotation). The variation of quadrature components with modulation depth  $\phi_{01}$  (when  $\Delta_1=0$ ) is shown in Fig.

2. A maximum noise of about  $5^\circ/\text{hr}$  was observed at  $\phi_{01} = 1.8$ , the noise is reduced to below  $0.2^\circ/\text{hr}$  (limited by laser intensity noise) at  $\phi_{01} = 3.8$  and  $7.0$  respectively which correspond to the first and second zeros of the first order Bessel function. This is similar to the scattering noise[6]. The variation of scattering-related noise with coupling ratio detuning  $\Delta_1$  is shown in Fig.3 which corresponds to the summation of the backscattering noise[6] and backscatter-induced crosstalk (see Eq.(2)). Both in-phase and quadrature components of the scattering related noise at the eigenfrequency (144kHz) of gyro 1 are below  $0.2^\circ/\text{hr}$  and shown in Fig.4.

**CONCLUSIONS:** In conclusion, we have observed the backscatter-induced crosstalk noise in a 2-D FDM FOG system. At low rotation rates, the in-phase components is negligible, however the quadrature noise is as high as  $5^\circ/\text{hr}$ . The noise can be reduced to below  $0.2^\circ/\text{hr}$  either by proper choice of the modulation depths or by using a modulation frequency corresponding to the eigenfrequency of the gyroscope.

**ACKNOWLEDGEMENTS:** The authors would like to thank J.M. Mackintosh, D. Platt for their help in building the gyro system and D. Uttamchandani, P. Bradley and J. S. Liu for their help during the experiments.

#### References

1. A.D. Kersey et al, SPIE Vol.838, Fibre Optic and Laser Sensors, 1987.
2. W. Jin et al, Proc. 1st international Symposium on Inertial Technology in Beijing, China, May 15-18, 1989.
3. W. Jin and B. Culshaw, Symposium Gyro Technology, Stuttgart, Germany, 1990.
4. W. Jin and B. Culshaw, to be presented at Fiber Optic Gyros: 15th Anniversary Conference, SPIE OE/FIBERS, Sept 3-6, Boston, USA, 1991.
5. W. Jin and B. Culshaw, to be submitted for publication.
6. J. M. Mackintosh, PH.D thesis, University of Strathclyde, July, 1988.

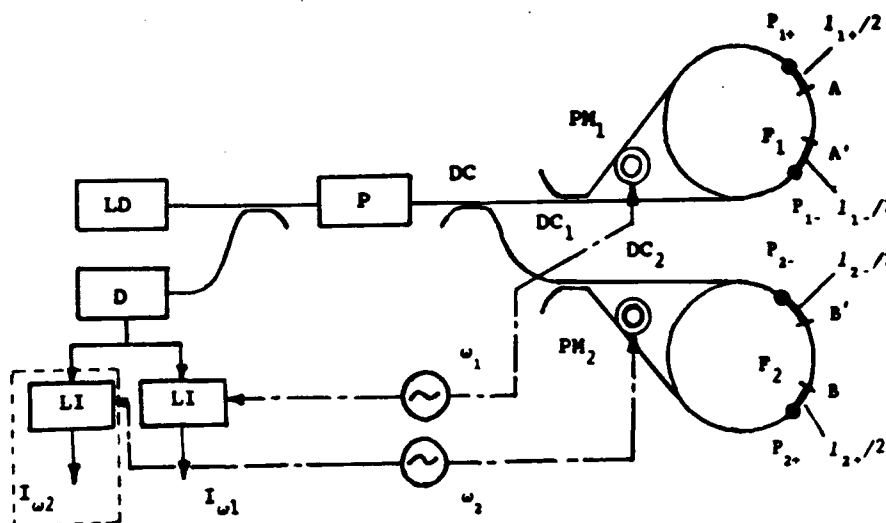


Fig.1 2-D FDM FOG system. LD: laser diode, D: detector, LI: lock-in amplifier, DC, DC1 and DC2: Directional couplers, P: polarizer, PM1 and PM2: phase modulators, F1 and F2: fibre loops,  $P_{ij}$ : point scatterers

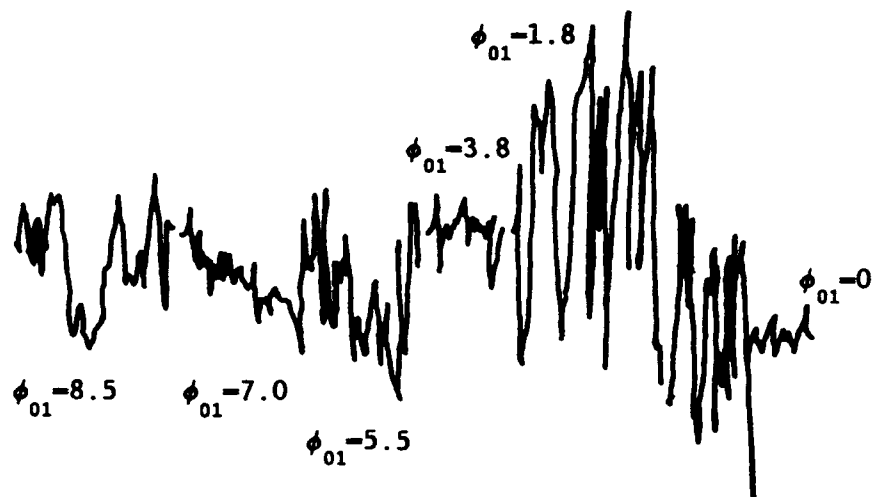


Fig.2 Variation of quadrature noise with  $\phi_{01}$  ( $\omega_1=2\pi\cdot 26\text{kHz}$ ,  $\Delta_1=0$ )

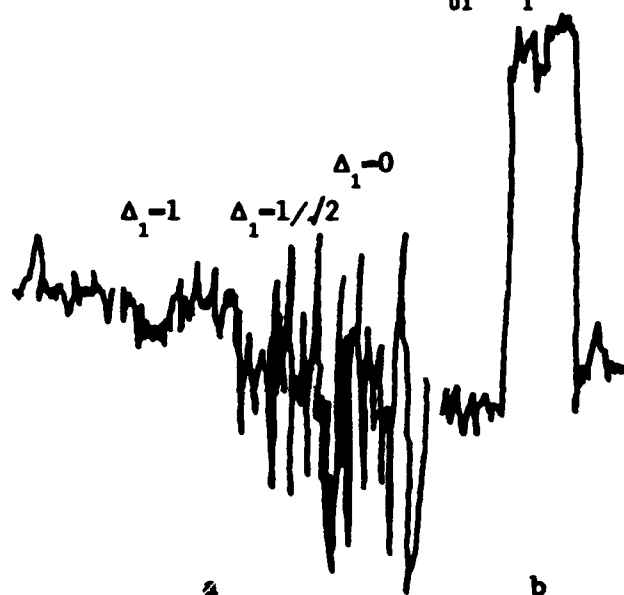


Fig.3 (a) Variation of quadrature noise with  $\Delta_1$  ( $\phi_{01}=-1.8$ )  
(b) Sagnac signal  $5^\circ/\text{hr}$  ( $\Delta_1=0$ ,  $\phi_{01}=-1.8$ )

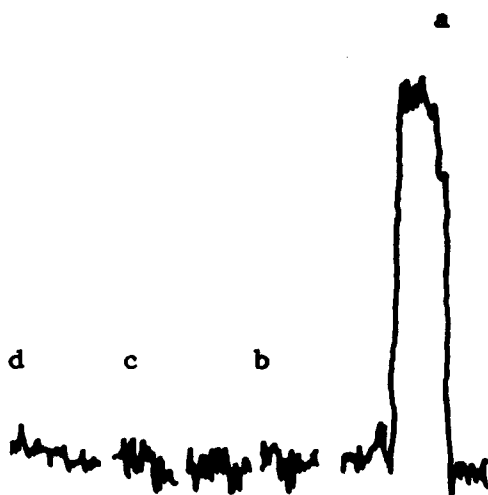


Fig.4 Noise levels with eigenfrequency modulation  
(a) Sagnac signal  $5^\circ/\text{hr}$   
(b) quadrature noise with  $\Delta_1=1/2$   
(c) quadrature noise with  $\Delta_1=1$   
(d) noise when laser was OFF

## P4 More Exact Measurement Of Gravitation Constant G By Using Fixed Precision Fiber Gyros

M. BÖHM  
ALCATEL SEL  
STUTTGART, GERMANY

Precise measurement of instantaneous earth rotation rate can serve several purposes, amongst them determination of torsional oscillations of earth and more exact derivation of the gravitation constant G.

The knowledge of torsional oscillations of earth may be of value for a number of research areas like earthquakes, volcanos, clima and exploration.

G is given with rather limited accuracy ( $6,67 \cdot 10^{-11} \text{ N m}^2 \text{ kg}^{-2}$ ) in view of present precision measurement techniques. It has been suggested that G can be described by (fig.1)

$$G = \left( \frac{3 \cdot 10^3}{8} \frac{m_e}{m_u} \right) \frac{\omega_1 \omega_2}{\xi_{\text{mol}}}$$

with

$m_e$  = electron mass

$m_u$  = atomic mass unit

$\omega_1$  = rate of yearly earth rotation

$\omega_2$  = rate of daily earth rotation

$\xi_{\text{mol}}$  = molar gas mass density

It is proposed to utilize fixed precision fiber-optic rate sensors for measuring the daily earth rotation profile with seven digits accuracy in order to determine possible error sources in conventional methods of G-determination (torsional balance) by  $\omega_2$ -variations during a 24 h - period.

The basic approach is to gain three digits (a factor of  $10^{-3}$ ) by increasing integration time and utilizing a number of fiber gyros colocated or arranged as a two- or three-dimensional array.

A gyro array (fig.2) allows for compensating statistical variations of the single sensors and thus increase the accuracy of measurements despite the errors of the individual sensors.

A vertical array - e.g. a linear one - is to be used for comparison with the results of a horizontal one.

A supplementary approach is to utilize the well known average rotation rate of earth for comparison with the actual fiber gyro outputs and thus compensate unidirectional gyro drifts. This is expected to provide a further digit, totalling in a rate accuracy of  $1,5 \cdot 10^{-6}$  degree/h. The increase of accuracy in daily earth rotation rate ( $\omega_2 = 7,29256 \cdot 10^{-5} \text{ s}^{-1}$ ) measurement requires to also consider the yearly earth rotation rate ( $\omega_1 = 1,99198 \cdot 10^{-7} \text{ s}^{-1}$ ), which is about three per mille of the daily rate.

This drift compensation is to be performed for each individual sensor of an array in order to avoid undefined errors.

In addition, the zero bias has to be compensated for each sensor of an array also individually by comparing the respective sensor outputs after 12 hours (180°) each.

A final approach would be to perform G measurements utilizing a conventional precision torsion balance colocated with a fiber gyro array in a temperature-controlled environment with different temperatures in sequence. The comparison of results is expected to not just provide a more exact value of G, but also to reveal at least two key error sources in conventional G-measurement techniques.

These error sources are expected to be

- temperature variations
- variations of measurement device altitude above sea level

Another error source, in addition to effects caused by sun and moon, might be Coriolis effects (fig.3).

Bu23



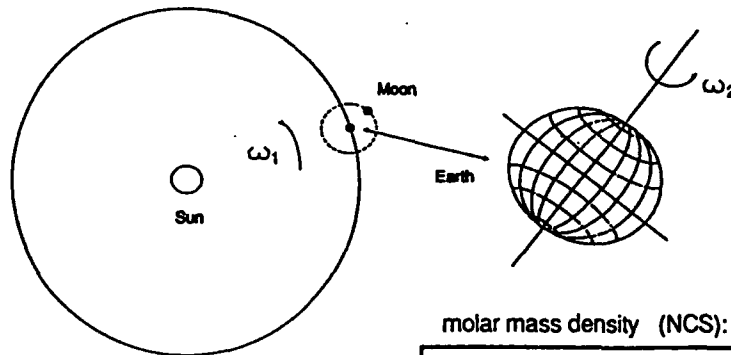
## G As A Function Of Earth Motion



$$\omega_1 = 1,992 \cdot 10^{-7} \text{ s}^{-1}$$

$$\omega_2 = 7,293 \cdot 10^{-5} \text{ s}^{-1}$$

$$m_\odot = 9,11 \cdot 10^{31} \text{ kg}$$



Gravitation Constant

$$G = 6,672 \cdot 10^{-11} \text{ N m}^2 \text{ kg}^{-2}$$

$$G = \left( \frac{3 \cdot 10^3}{8} \frac{m_\odot}{m_u} \right) \cdot \frac{\omega_1 \omega_2}{g_{\text{mol}}}$$

Note:

Result is 4 %  
above accepted  
value. Comment  
see text and next  
figure.

molar mass density (NCS):

$$g_{\text{mol}} = \frac{N_A m_u}{V_{\text{mol}}} \text{ kg m}^{-3}$$

$$N_A = 6,022 \cdot 10^{23} \text{ mol}^{-1}$$

NCS = Nuclear Charge System

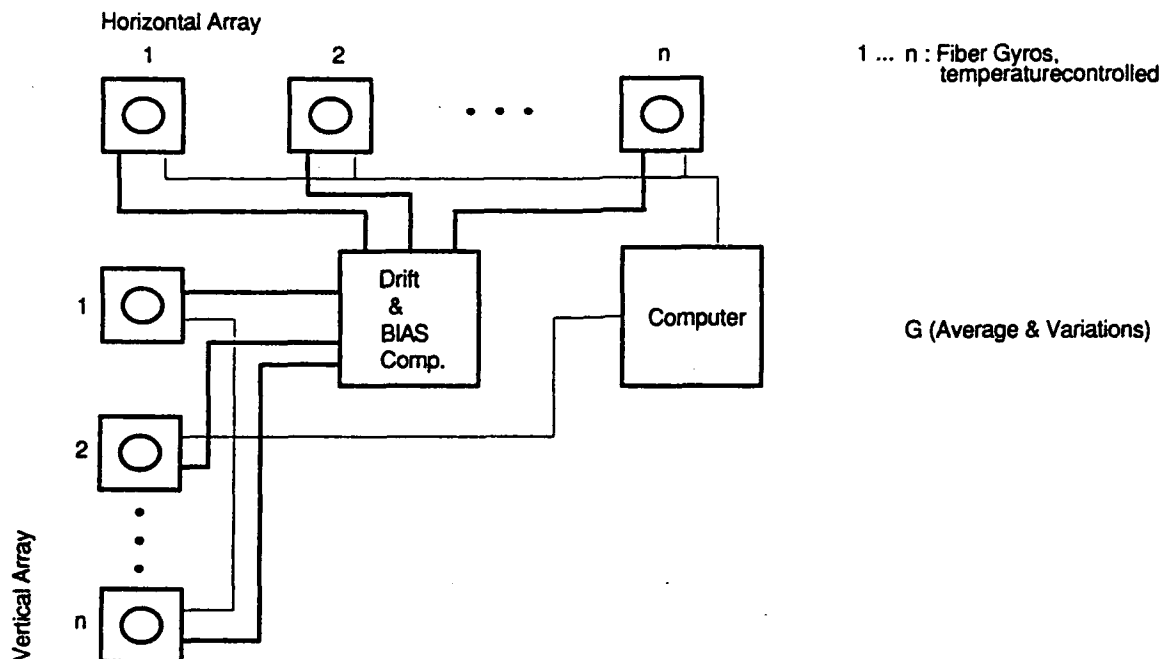
$$V_{\text{mol}} = 22,414 \cdot 10^{-3} \cdot \text{m}^3 \text{ kmol}^{-1}$$

$$m_u = 1,6606 \cdot 10^{-27} \text{ kg}$$

SEL

ALCATEL

# Fiber Gyro Array



2

Soft

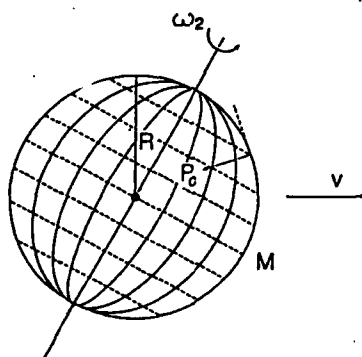
SEL

ALCATEL

# Gravity-A Coriolis Force ?



$$G = g \frac{R^2}{M} = 2 B (v \omega_2) \frac{R^2}{M}$$



Acceleration on  
earth surface

$$g = \underbrace{2 \omega_2 \cdot v}_{\text{Coriolis-Acceleration}} \cdot \underbrace{B}_{\text{Correction}}$$

$$P_c = m_u \cdot g$$

- $g = 9,81 \text{ m s}^{-2}$
- $m_u = \text{Atomic Mass Unit}$
- $v = 10^{-4} \text{ m s}^{-1} \text{ (} 0,994 \cdot 10^{-4} \text{ m s}^{-1} \text{)}$
- $\omega_2 = 7,293 \cdot 10^{-5} \text{ s}^{-1}$
- $B = 2,25 = \frac{9}{4} = \frac{9}{3} \cdot 2 \cdot 0,375$

3



## Sensitive Fibre Optic Thermometer Using Cr:LiSAF Fluorescence For Bio-Medical Sensing Applications

Zhiyi Zhang, K.T.V. Grattan and A.W. Palmer

Measurement and Instrumentation Centre,  
Dept. of Electrical, Electronic and Information Engineering,  
City University,  
London EC1V 0HB, England.

### INTRODUCTION

There has been considerable interest in the development of fibre optic temperature probes for bio-medical applications. The dielectric property of the fibre optic probe is essential for some applications, e.g., the monitoring of the human body temperature during treatment employing rf or microwave heating and for use with C.T. scanners using large electro-magnetic fields. The potentially high measurement sensitivity of fibre optic probes can cater for the particular requirement to monitor slight body temperature variance and their small size and flexibility also make such probes valuable for bio-medical applications.

An extensive review of fibre optic techniques for temperature measurement has been presented by one of the authors [1], and one of the more successful schemes is that based on fluorescence lifetime. Apart from the high measurement sensitivity achievable, the measurement of temperature using the fluorescence lifetime of appropriate materials has a significant advantage in that it is independent of an accurate measurement of light intensity. Therefore, the corresponding fibre optic probe can be free of the impact of fibre sterilising and bending, and be potentially robust enough for harsh day-to-day usage. An early proof-of-principle demonstration of a optical temperature probe using the fluorescence decay of ruby was presented by Sholes and Small [2] with a bulky optical configuration, and lately various probes using the fluorescence lifetime with a fibre optic configuration have been developed [3-7] together with the introducing of new signal processing schemes [7,8]. Herein, a highly sensitive fibre optic temperature probe based on the fluorescence lifetime of a newly developed laser material, Cr:LiSAF ( $\text{Cr}^{3+}$ -doped  $\text{LiSrAlF}_6$ ) is presented over temperature range from  $10^\circ\text{C}$  to  $100^\circ\text{C}$ . The material may be pumped with light from a solid state laser diode operating in the visible region.

### EXPERIMENTAL SYSTEM SETUP

Figure 1 is the schematic representation of the thermometer. The absorption spectrum of Cr:LiSAF spans the region from the UV to that near 750nm, with a peak falling between 600nm and 700nm [9], and thus a visible laser diode with lasing wavelength at 670nm and 1mW of optical power output can efficiently pump the Cr:LiSAF sample used as sensor element, to induce a fluorescence response from the sample with a sufficiently high signal-to-noise ratio to be detected. The long-pass filter placed before the photodetector, shown in Figure 1, is used to cut off the unwanted pumping light which would otherwise fall on the detector

stage and thus it allows only the fluorescence response, which ranges from 700nm to farther into the infrared, to be detected.

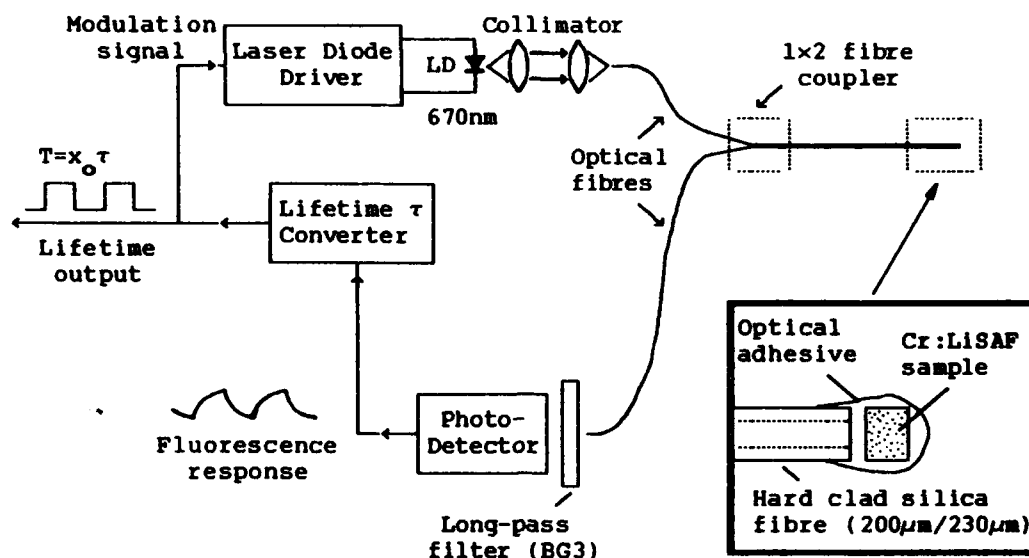


Figure 1 Schematic of the thermometer.

As indicated in Figure 1, the signal processing module, the 'lifetime  $\tau$  converter,' works in a feedback loop. Its output, a TTL compatible square-wave signal, is also used as the modulation signal to intensity-modulate the pumping light. The induced fluorescence response is fed back to the module, to regulate the modulation frequency and make its period fit to the measured fluorescence lifetime. Then, the square-wave lifetime output is obtained with its period proportional to the measured fluorescence lifetime. By using such a signal processing scheme, a high degree of resolution in the fluorescence lifetime measurement can be achieved. A detailed discussion of this signal processing scheme was presented in the previous work of the authors [8].

The configuration of the temperature probe is also depicted in Figure 1. The size of the Cr:LiSAF sample is about  $0.5 \times 0.6 \times 0.5 \text{ mm}^3$ . It is housed, using optical adhesive, on the sensor port of a 1x2 bidirectional fibre coupler made from 200 $\mu\text{m}$  hard clad silica fibre.

### EXPERIMENTAL RESULTS

The calibration of the thermometer was undertaken in a water bath in the region 0-100°C. The calibration curve of the fluorescence lifetime against temperature is depicted in Figure 2, together with that of the corresponding normalised fluorescence intensity. It shows that the Cr:LiSAF fluorescence lifetime decreases monotonically with the temperature increase, though it is rather insensitive to temperature variance around 0°C or below. Beyond about 5°C, the fluorescence lifetime drops more and more sharply with temperature increase. That indicates that the absolute value of the temperature sensitivity of the Cr:LiSAF fluorescence lifetime increases with temperature increase. The

significance of such a sensitivity increase is shown clearly in Figure 3, with, for comparison, the case of ruby, which was used in several optical thermometer schemes based on fluorescence lifetime [2,6,8]. The relative sensitivities of the two materials may be calculated from the following formula:

$$\text{Relative sensitivity} = (\Delta\tau/\tau)/\Delta\text{Temp} ;$$

$\tau$  is the fluorescence lifetime;  $\Delta\tau$  and  $\Delta\text{Temp}$  are increments of the fluorescence lifetime and temperature respectively.

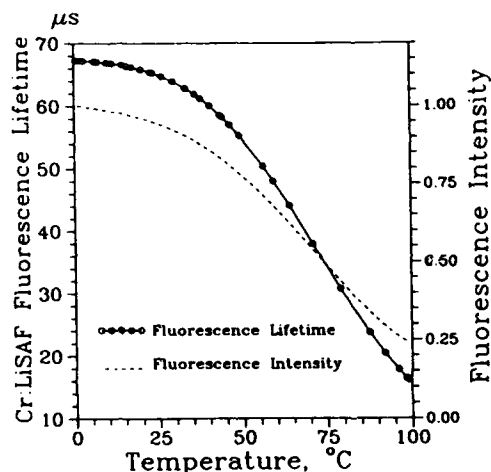


Figure 2 Fluorescence lifetime (solid line) and fluorescence intensity (dashed line) as functions of temperature.

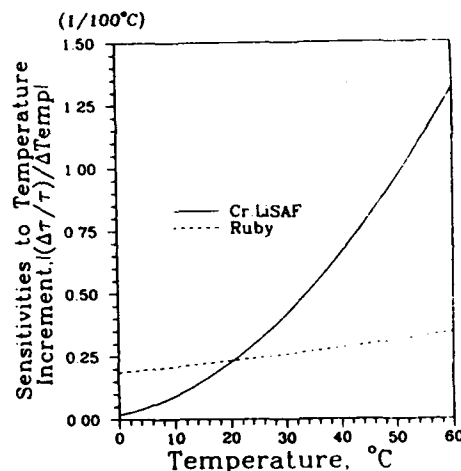


Figure 3 Relative sensitivities of Cr:LiSAF and ruby over the range showed.

With 0.7s response time, the standard deviations of consecutive measurements and the sensitivities of the lifetime to temperature at typical temperature points are listed in Table 1.

Table 1. Standard deviations of consecutive measurements in the laboratory, and sensitivities of fluorescence lifetime to temperature.

Temperature °C	$\sigma_{n-1}$	Sensitivity ns/°C
10	0.023 °C	-62.9
20	0.0095 °C	-151.6
30	0.0052 °C	-278.2
35	0.004 °C	-355.6
36	0.0039 °C	-372.3
37	0.0037 °C	-389.3
40	0.0032 °C	-442.6
50	0.0022 °C	-644.9
60	0.0016 °C	-885.1

## DISCUSSION

From the data listed in Table 1, under laboratory conditions the standard deviation of the measurements recorded is better than 0.01°C, within the 20°C and 50°C region, the temperature region most concerned in biological

applications. This is the best result by way of sensitivity that has been achieved from the authors' testing of a variety of fluorescent materials, e.g., Nd:YAG, Nd:glass and ruby, in this particular temperature region. That is mainly due to the significant increase of the temperature sensitivity of the Cr:LiSAF fluorescence lifetime, particularly beyond 20°C, (with reference to Figure 3). The comparatively short lifetime, from ~67μs at 0°C to ~48μs at 60°C, (long enough to be measured without requiring special high frequency electronic components for signal processing) also yields the better performance from Cr:LiSAF. For example, the ruby fluorescence lifetime is about 50 times longer than that of Cr:LiSAF. That means that within a same period of time, about 50 times as many measurements may be made using Cr:LiSAF as are made using ruby, using a scheme making one measurement per period. Simply by the means of data average processing, with the same response time, the standard deviation of measurements in the case of Cr:LiSAF over a fixed time response period can be expected to be much less.

To improve further the performance of the thermometer, experiments were carried out to coat the Cr:LiSAF sample (shown in Figure 1) with proper dielectric reflecting material, such as titanium dioxide. With the coating, the effect of the excitation light could be amplified by multiple reflection and more fluorescence collected. Furthermore, the coating can stop the bright excitation light spreading out into the patient on whom the measurement is to be made.

The material is not particularly suitable for use beyond 100°C due to the further shorting of the lifetime [10] and the reduction in the emitted fluorescence intensity (shown in Figure 2). Other materials are being studied for use in higher temperature regions.

#### ACKNOWLEDGEMENT

The authors are pleased to acknowledge the support of SERC for this work.

#### REFERENCES

1. Grattan, K T V, Measurement and Control, Volume 20, July, 32-9, 1987.
2. Sholes, R R, and Small, J G, Rev. Sci. Instrum. 51(7), July, 882-4, 1980.
3. McCormack, J S Electron Letts, 17, 630-1.
4. Grattan, K T V, and Palmer, A W, Rev. Sci. Instrum. 56, 1784, 1985
5. Grattan, K T V, Palmer, A W, and Willson, C A, J. Phys. E: Sci. Instrum. 20, 1201-5, 1987.
6. Grattan, K T V, Selli, R K, and Palmer, A W, Rev. Sci. Instrum. 59(8), August, 1328-35, 1988.
7. Bosselmann, Th, Reule, A, and Schröder, J, Proc. 2nd Optical Fibre Sensors Conf., Stuttgart, 151-4, 1984.
8. Zhang, Z, Grattan, K T V, and Palmer, A W, Rev. Sci. Instrum. 62(7), July, 1735-42, 1991.
9. Payne, S A, Chase, L L, Smith, L K, Kway, W L, and Newkirk, H W, J. Appl. Phys. 66(3), 1051-6, 1989.
10. Stalder, M, Chai, B H T, and Bass, M, The Advanced Solid State Lasers Topical Meeting, Hilton Head Island, SC, March 18-20 1991.

## P6 Multipoint Temperature Monitoring In A Hazardous Environment

Massimo Brenci, Andrea Mencaglia and Anna Grazia Mignani  
*Istituto di Ricerca sulle Onde Elettromagnetiche (IROE)  
of the Consiglio Nazionale delle Ricerche (CNR)  
via Panciatichi, 64 - I-50127 Firenze, Italy*

### ABSTRACT

The described work concerns the study of a fiberoptic alarm system for a real-time temperature profiling in hazardous environments. Such a system comprises twelve fiberoptic temperature sensors which are interrogated by using an OTDR technique.

### 1. INTRODUCTION

The possibility of performing remote-detection measurements in hostile environments and of achieving continuous monitoring of a large number of parameters, is often essential. Among the various physical and chemical quantities measured by optical fibers, heat and temperature monitoring is essential for industrial process control, engine monitoring, medical and biomedical instrumentation. In such applications measurements can be required to be made at a number of locations; then it becomes desirable to connect numerous sensors into a simple optical fiber network, which are located remotely from the signal processing site.

There have been a number of different approaches to sensor multiplexing which have been systematically overviewed by R. Kist<sup>1</sup>. Among these, the Optical Time Domain Reflectometry (OTDR) technique, seems particularly suitable to combine a number of reflective microswitches.

This paper describes a fiber-optic alarm system allowing a remote monitoring of twelve reflective sensors which are sensitive to the temperature variations.

### 2. WORKING PRINCIPLE OF THE SENSOR

The working principle of the sensor we have realized is well known, since it is based on the deformation of a bimetallic strip with the temperature. According to this principle, microswitches have been already proposed<sup>2</sup>. However, our device differs from such microswitches, making use of a novel design which can permit measurements of temperature in a wide range (tens of degrees).

The basic design of the sensor is sketched in Fig. 1. Two quarter-pitch microlenses are

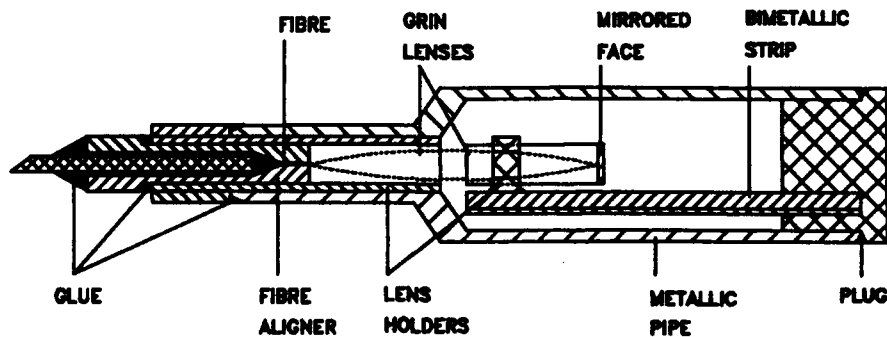


Figure 1 - Sketch of the sensor probe

used: the first one is connected to the illuminating fiber, while the other one, having a reflecting coating applied on the external face, is placed on a bimetallic strip. Light coming from a fiber is focussed by the first microlens, passes through the second microlens, is then reflected by the reflecting coating, and is collected by the same fiber after it has passed a second time through the microlenses.

For an estimation of the behavior of such an optical system<sup>3</sup> reference is made to the model shown in Fig.2. On the basis of trigonometric considerations, the coordinates  $(r_o, \Theta_o)$  of a meridional ray coming out from the optical system is related to the coordinate  $(r_i, \Theta_i)$  of the entering ray by the equation:

$$\begin{aligned}\tan\theta_o &= \tan\theta_i - 2 \cdot h \sqrt{A} \tau_i - (n_o/n_i) \cdot A \tau_i (D - h \tan\alpha) \cdot (2 - \tan^2\theta_i) \cdot \\ &\quad \cdot [1 + A \tau_i^2 \{1 - (n_o^2/(4 \cdot n_i^2) \cdot (2 - \tan^2\theta_i)^2)\}]^{-1/2} \\ r_o &= r_i \cdot k \sqrt{[1 + A \tau_i^2 (1 - k^2)]^{-1/2}} \\ k &= (2 + \tan^2\theta_i) / (2 - \tan^2\theta_i)\end{aligned}$$

where:  $\sqrt{A}$  = the quadratic gradient constant of the GRIN-rods,  
 $n_o$  = the refractive index on the GRIN-rod axis,  
 $n_i$  = the refractive index of the interposed medium,  
 $D$  = the longitudinal separation between microlenses.  
 $h$  = axial separation between microlenses  
 $\alpha$  = angular misalignment between microlenses

the following approximations can be introduced:

$$\begin{aligned}h \tan\alpha &< D \\ \tan^2\theta_i &< 1 \\ A \tau_i^2 &< 1 \\ k &\approx 1 - (\tan\theta_i - \tan\theta_o) \cdot (\tan\theta_i + \tan\theta_o) / 2 \approx 1\end{aligned}$$

thus obtaining

$$\begin{aligned}\theta_o &\approx \theta_i - 2 \cdot h \sqrt{A} - 2 \cdot A \tau_i \cdot D \cdot n_o/n_i \\ r_o &\approx r_i\end{aligned}$$

it thus follows that:

- the coordinate  $r_o$  of the output ray undergoes only small variation with respect to the coordinate  $r_i$  of the input ray; thereby, practically all the rays injected by the optical fiber into the optical system, leave the system (after having gone twice through it) in correspondence of the same position in which they are injected,
- the coordinate  $\Theta_o$  is dependent on the lateral displacement  $h$ .

For an evaluation of the response (output power/input power) of the microswitch as a function of the lateral displacement  $h$ , a Gaussian far field of the optical fiber is assumed, and

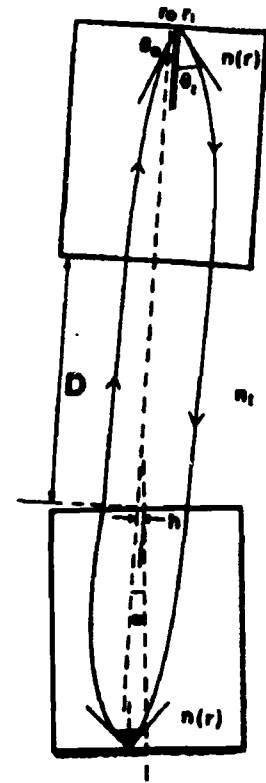


Figure 2 - Model of the optical system

a 100x100 grid, covering the ranges  $\{-R_r, +R_r\}$  and  $\{-\Theta_r, +\Theta_r\}$ , is considered. The numerical integrations of the illuminating light power distribution in the domains  $\{|\Theta_i| \leq \Theta_r, |r_i| \leq R_r\}$  and  $\{|\Theta_o| \leq \Theta_r, |r_o| \leq R_r\}$  give, respectively, the illuminating and the backreflected light power. By utilizing  $D=0.5$  mm and  $0 \leq h \leq 300$   $\mu$ m the integrations give the results which are displayed in Fig.3 (dotted line).

### 3. EXPERIMENTAL REALIZATION OF THE PROBE

Each probe makes use of a 50/125 graded-index fiber and two Selfoc GRIN rods (Nippon Sheet Glass Co., SLW-1.8-0.25p-0.83, having  $\sqrt{A}=0.337$  mm<sup>-1</sup> and  $n_0=1.599$ ). The dimensions of the bimetallic strip are 16x3x1 mm, and the alignment of the microlenses has been performed at room temperature.

The behavior of the sensors have been experimentally measured by varying the lateral displacement,  $h$ ; a typical result is displayed in Fig.3 and compared with the calculated one.

For calibration purpose each probe has been dipped into a thermostated bath and the response vs. lateral displacement  $h$  has been measured. Figure 4 shows a typical calibration curve in the 20-60° C range. A resolution of  $\approx 0.2$  °C, has been achieved.

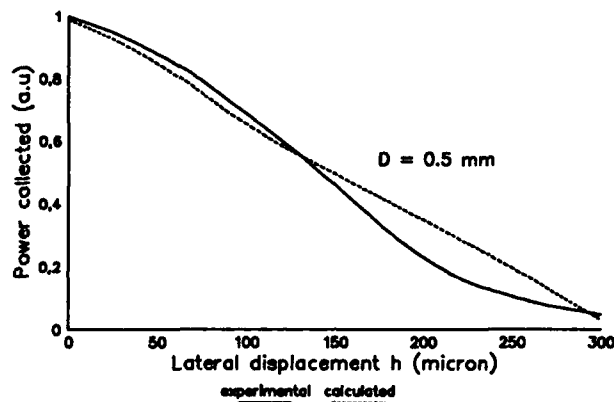


Figure 3 - Behavior of the response of the device vs the lateral displacement

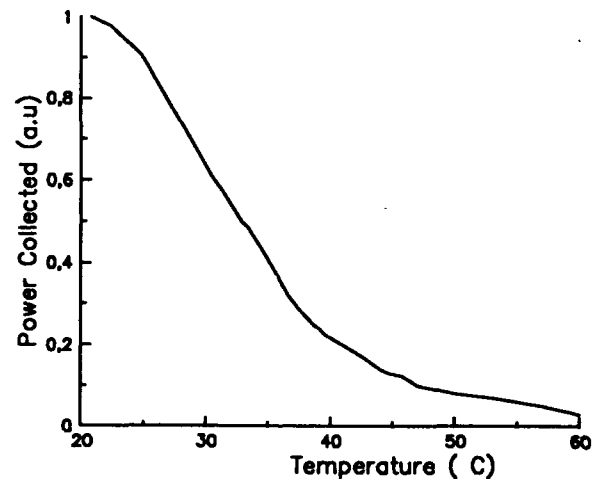


Figure 4 - Typical calibration curve

### 4. MULTIPLEXING

Twelve temperature sensors have been combined according to a reflective-tree basic topology which has been constructed using eight "Gould" fiber directional couplers (one 2x2, two 1x3, and six 1x2). The fibers connecting the sensors have such a length so that the optical paths (electrooptic unit - sensor) differ about 40 cm from each other.

The sensors are interrogated by using a Time Division Multiplexing technique. For such a purpose an "Opto-Electronic" millimeter resolution OTDR system has been used. The photograph of Fig. 5 shows a temperature profile which has been measured by applying the sensors on the surface of a heated body. In spite of the great number of both sensors and couplers the signal levels are high, since the sensors are reflective-type. This could make possible to increase the number of sensors up to several tens.

## 5. CONCLUSIONS

A fiberoptic network prototype has been tested for monitoring a number of temperature sensors. The temperature profile of a heated body, which was located in a hazardous environment, has been measured.

Insertion losses of both couplers and sensors are usually a critical parameter in this kind of networks, since they limit the number of the allowed sensors. Twelve sensor have been addressed in our system. However, the performed measurements show to be possible addressing a much larger number of sensors.

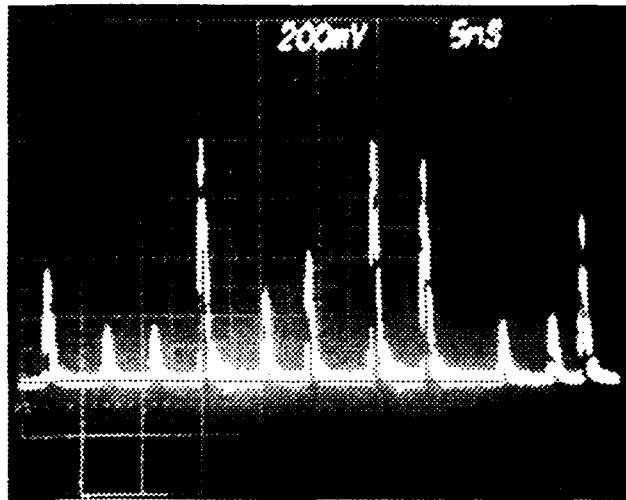


**Figure 5 - Response of the sensors**

## **Acknowledgements**

This work has been developed under the "Progetto Finalizzato" on Electrooptical Technologies of the National Research Council (CNR) of Italy.

## REFERENCES

1. R. Kist, "Point Sensor Multiplexing Principles", in *Optical Fiber Sensors: Systems and Applications*, edited by B. Culshaw & J. Dakin, Vol. II, Chap. 14, Artech House Inc., Norwood, Ma (1989).
2. J.D. Place, "Optical Control and Alarm Switches for the Process Industries", *Proc. Conf. PROMECON*, pp 157-63, London, 19-22 June 1984.
3. G. Conforti, M. Brenci, A. Mencaglia, A. G. Mignani, "Fiber-Optic Thermometric Probe Utilizing GRIN Lenses", *App. Opt.*, **28**, 3, pp 577-80 (1989).



## P7 Strain and Temperature Dependence of Elliptical Core Two-Mode Fiber Acousto-Optic Interaction

Jan Ove Askautrud and Helge E. Engan

Division of Physical Electronics, The Norwegian Institute of Technology,  
N-7034 Trondheim, Norway.

### Introduction.

The unique characteristics of elliptical core two-mode optical fibers make new solutions available within the field of fiberoptic sensors [1]. Their optical propagation characteristics under static perturbations have been examined in detail [2].

Such fibers have also proved suitable in all-fiber device development, where intermodal couplers [3], mode filters [4] and acousto-optic frequency shifters [5] have been demonstrated. In addition these fibers have recently been suggested for smart structure applications [6].

Fiber characterization and system development work often require strict control of the modal energy distribution. This can to some extent be achieved by proper excitation conditions or with static microbend couplers. In our experience, however, the acousto-optic modal coupler [5] provides excellent means for modal control.

Within this context we found it rewarding to investigate the strain and temperature dependencies of the condition for phase-matched coupling in the acousto-optic interaction. In this paper we present experimental results and compare them with theoretical considerations.

### Longitudinal strain.

The ideal acousto-optic mode coupler giving complete mode conversion should satisfy the condition for phase-matched coupling exactly, i.e. the acoustic wavelength,  $\lambda$ , should equal the optical beatlength,  $L_B$ . Any deviation from this condition resulting from fiber strain or temperature changes causes incomplete mode conversion. Such effects can be counteracted by tuning the acoustic frequency to satisfy the new phase-matching condition. With strain this can be expressed as;

$$\delta\lambda(\text{strain}+\text{frequency}) - \delta L_B(\text{strain}) \quad (1)$$

The term on the right hand side expresses the change in optical beatlength due to longitudinal strain and was calculated by Blake & al.[7]. We obtain the term on the left hand side by expressing the acoustic wave as a sum of two components according to Mott [8] as;

$$\lambda^2 = \lambda_a^2 + \lambda_t^2 \quad (2)$$

Here,  $\lambda_a$  is a low-frequency approximation obtained from the dispersion equation for the acoustic flexural wave and  $\lambda_t$  is an additional term due to the longitudinal tension. These can be expressed as

$$\lambda_a^2 = \frac{\pi R C_{\text{ext}}}{f}, \quad \lambda_t^2 = \frac{T}{\rho f^2} \quad (3)$$

where  $R$  is the fiber radius,  $C_{\text{ext}}$  is the extensional wave velocity for bulk fused silica,  $T$  is the longitudinal tension,  $\rho$  is the density and  $f$  is the acoustic frequency. Equation (1) may be differentiated with respect to strain and acoustic frequency using the relations

$$\frac{\delta R}{R} = -\nu \frac{\delta l}{l}, \quad C_{\text{ext}} = \sqrt{\frac{Y}{\rho}}, \quad Y = Y_0(1 + k_1) \frac{\delta l}{l} \quad (4)$$

where  $\nu$  is Poisson's ratio,  $Y_0$  is Young's modulus under strain-free conditions and  $k_1$  is the strain coefficient of Young's modulus. Substituting Eqs. (2)-(4) into Eq. (1) we find that the change in acoustic frequency necessary for maintaining phase-matched operation can be written in terms of the applied strain;

$$\frac{\delta f}{f} = \left( \frac{1 + k_1}{2} - 2\nu - 2K(\nu) + \frac{Y}{\rho \pi R C_{\text{ext}} f} \right) \frac{\delta l}{l} \quad (5)$$

i.e. for a small change in acoustic frequency it is linearly dependent on the elongation. At low acoustic frequencies its change with strain depends mainly on the longitudinal strain. The absolute frequency shift per unit strain increases with increasing acoustic frequency. The relative frequency shift, however, decreases with increasing acoustic frequency.

To verify this theoretical expression the frequency-strain relationship was measured experimentally using the setup shown in Figure 1. The acousto-optic interaction is in the stripped fiber region. The arrangement for stretching the fiber is not shown. The acoustic transducer was driven by a swept frequency generator while the frequency spectrum in the interference signal at the output was examined. The peak in this spectrum gives the optimum phase-matching condition. Figure 2 shows the results obtained with two different fibers and compared with theoretical curves. For the LTI fiber we have  $\delta f/f \approx 12\delta l/l$  and for the York fiber we have  $\delta f/f \approx 5\delta l/l$ . The agreement between experiment and theory is good.

### Temperature.

The temperature dependence of the optical beatlength was calculated by Blake & al. as well [7]. In order to obtain the change in acoustic wavelength, we require the temperature coefficient of the extensional wave velocity or of Young's modulus. Data is scarce and we have used the temperature coefficient of the relative delay for shear waves in bulk fused silica [9] to obtain an estimate for the temperature coefficient of the extensional wave velocity of about  $80 \times 10^{-6} / ^\circ\text{C}$ . Equating the change in optical beatlength to the change in acoustic wavelength we obtain the following relation;

$$\frac{\delta f}{f} = (k_c - 2\alpha - \frac{2df(\nu)/d\nu}{f(\nu)} \nu(\alpha + \zeta)) \delta T \quad (6)$$

where  $k_c$  is the temperature coefficient of the extensional wave velocity.  $\alpha$  is the linear thermal expansion coefficient and  $\zeta$  is the thermo-optic coefficient with typical values  $4 \times 10^{-7} / ^\circ\text{C}$  and  $1 \times 10^{-5} / ^\circ\text{C}$ , respectively.

The expression is dominated by the acoustic term. As an example, a frequency change of about 15 KHz is required at an acoustic frequency of 3.75 Mhz (LTI PMF 820 fiber) to compensate for a temperature change of  $50^\circ\text{C}$ . The accuracy of the experimental results shown in Figure 3 is not very good, but it is confirmed that an increase in temperature requires an increase in acoustic frequency to maintain phase-matched operation.

## Conclusions.

The temperature and strain dependencies of the optimum phase-matching condition have been determined for an acousto-optic mode coupler. Good agreement was found between theory and experiment in the case of applied longitudinal strain. The application of longitudinal strain alters the optimum frequency significantly. This indicates that stretching may be a potential tuning mechanism for such devices. The experimental accuracy limits our conclusions somewhat as regards the temperature dependence. In both cases the polarization dependence was found to be within experimental accuracy.

The results have implications for the stability of the modal energy distribution in few-mode fiber systems using mode couplers. A particular concern in acousto-optic frequency shifters is the suppression of the remaining carrier and spurious sidebands. Any deviation from the phase-matching condition should be minimized in order to optimize the spectral purity of the frequency shifter.

## References.

- [1] B.Y. Kim, J.N. Blake, S.-Y. Huang and H.J. Shaw, *Opt.Lett.*, Vol 12, No 9, pp 729-31, 1987.
- [2] S.-Y. Huang, J.N. Blake and B.Y. Kim, *IEEE-JLT*, Vol 8, No 1, pp 23-33, 1990.
- [3] H.G. Park and B.Y. Kim, *Electron.Lett.*, Vol 25, No 12, pp 1688-95, June 1989.
- [4] B.Y. Kim, Paper ThBB1-1, pp 146-149, *OFS-88*, New Orleans.
- [5] B.Y. Kim, J.N. Blake, H.E. Engan and H.J. Shaw, *Opt.Lett.*, Vol 11, No 6, pp 389-91, 1986
- [6] K.A. Murphy, M.S. Miller, A.M. Vengsarkar and R.O. Claus, *IEEE-JLT*, Vol 8, No 11, 1990.
- [7] J.N. Blake, S.-Y. Huang, B.Y. Kim and H.J. Shaw, *Opt.Lett.*, Vol 12, No 9, pp 732-34, 1987.
- [8] G. Mott, *J.Acoust.Soc.Am.*, Vol 53, No 4, pp 1129-1133, 1973
- [9] A.L. Zijlstra and C.M. van der Burgt, *Ultrasonics*, Vol. 5, p 29, 1967

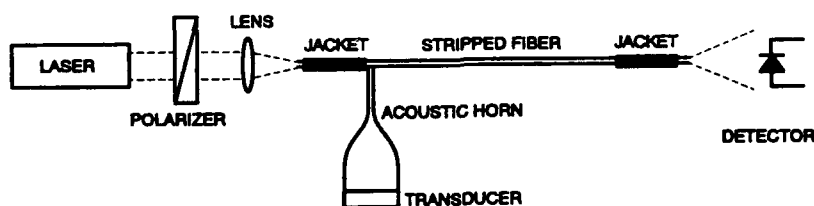


**Figure 1.** Schematic of the experimental setup  
(optical wavelength: 633 nm)

**Figure 2. Strain- (A)  
frequency relationship.**

(A) YORK HB 800 fiber  
(B) LTI PMF 820 fiber.

The line shows the  
theoretical curve.

Parameters:

$$R = 62.5 \mu\text{m}$$

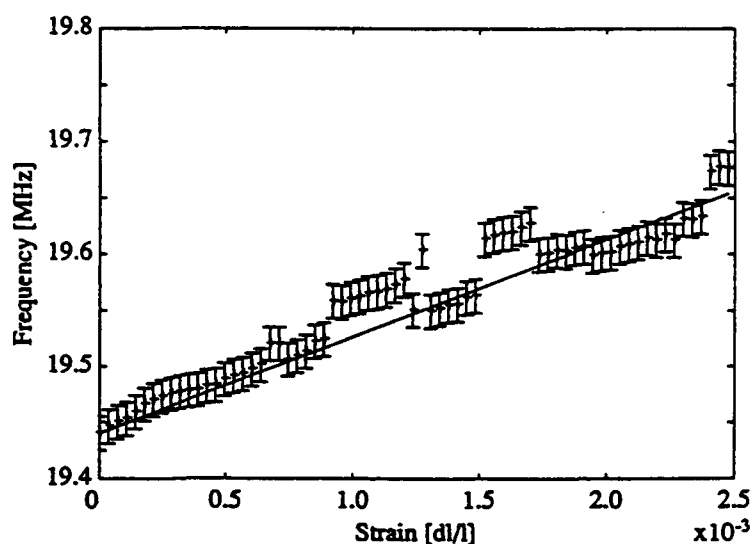
$$C_{\text{ext}} = 5760 \text{ m/s}$$

$$\rho = 2200 \text{ kg/m}^3$$

$$Y = 7.69 \times 10^{10} \text{ N/m}^2$$

$$k_1 = 5.75$$

$$\nu = 0.17$$



(B)

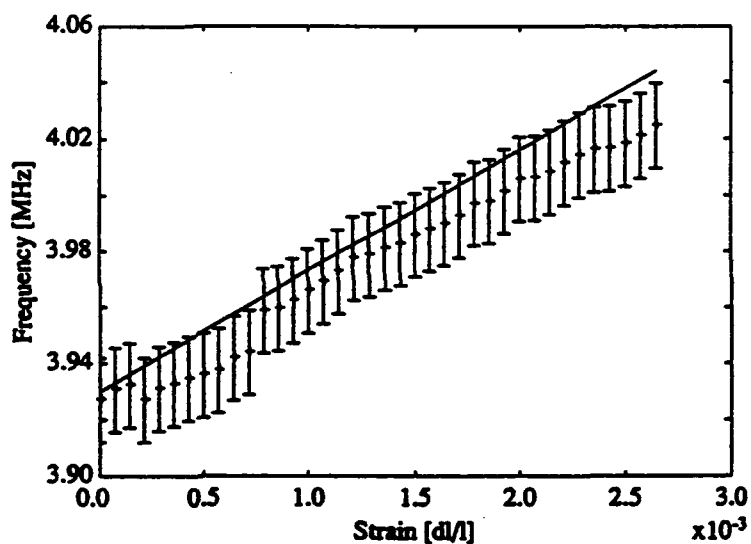
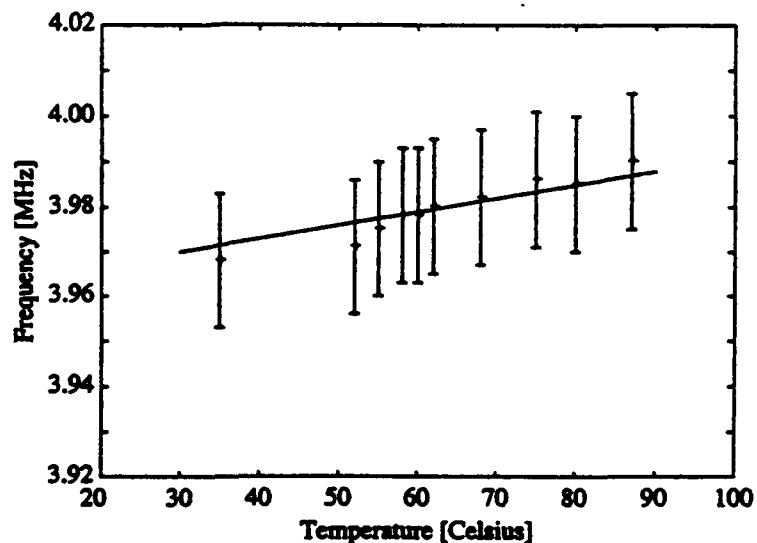


**Figure 3. Temperature-  
frequency relationship.  
LTI PMF 820 fiber.**



## In-line Fiber Fabry-Perot Interferometer With High-Reflectance Internal Mirrors

C. E. Lee, W. N. Gibler, R. A. Atkins, and H. F. Taylor

Department of Electrical Engineering

Texas A&M University

College Station, Texas 77843

Operation of fiber Fabry-Perot interferometer (FFPI) temperature sensors from  $-200^{\circ}\text{C}$  to  $+1050^{\circ}\text{C}$  has been demonstrated [1]. These sensors used internal mirrors produced by a fusion splicing technique. Internal-mirror FFPIs have been embedded in graphite-epoxy composites and polymers, where they were used to sense temperature [2] and ultrasonic pressure [3].

Previous work on internal mirror fiber devices has utilized single-layer dielectric mirrors, with maximum reflectances of less than 10% for the individual reflectors. In this paper, the use of multilayer films to obtain mirror reflectances of greater than 85% in a FFPI is reported, and data for a thermally tuned interferometer are compared with model calculations. Enhancement of sensor sensitivity through the use of high-finesse interferometers is discussed, as are potential applications of internal mirror FFPIs in communications.

The experimental arrangement for testing a FFPI is shown in Fig. 1. Light from a fiber-pigtailed  $1.3\text{ }\mu\text{m}$  distributed feedback laser is coupled into an input port of a fiber directional coupler through an in-line Faraday isolator. The FFPI is spliced to one output port of the coupler. Transmittance and reflectance of the FFPI are monitored using power meters. Reflections from fiber ends are suppressed using index matching gel.

Internal mirrors for the FFPI were produced by a fusion splicing technique [1] in Corning single-mode silica fiber. Multilayer films for the mirrors were deposited in a dc planar magnetron sputtering system. A seven-layer quarter-wave  $\text{TiO}_2/\text{SiO}_2$  stack on a cleaved fiber end gave a reflectance of 93%. The first mirror for the FFPI was produced by splicing a coated fiber end to the cleaved end of a

second, uncoated fiber. The mirror reflectance after splicing had decreased to 86%. Next, the fiber was cleaved a distance beyond the mirror corresponding to the desired interferometer cavity length. Another coated fiber was then spliced to the cleaved fiber end to produce the second mirror.

The dependence of the reflectance and transmittance of the FPPI on phase shift in the interferometer was characterized by thermal tuning. The FPPI and a thermocouple were inserted in a quartz tube, which was positioned in a hole in a copper block with embedded heating elements. The reflected and transmitted optical power and the thermocouple reading were recorded as the assembly was slowly heated. The refractive index of the fiber mode is, to a good approximation, a linear function of temperature in the  $120^{\circ} - 140^{\circ}\text{C}$  range where the measurements were made [1]. Thus, the thermal tuning response curves give the dependence of reflected and transmitted power on round-trip phase shift in the interferometer. The results are shown in Fig. 2 for a 9.5 mm long interferometer. The calculated curves [4] in Fig. 2 utilize values for the mirror reflectance  $R = 86\%$  and the mirror excess loss  $A = 7.2\%$ . The reflectance value used in the calculations was determined from the observed value of 21 for the finesse.

An alternative way of testing FPPIs makes use of thermal tuning of the frequency during a laser pulse to produce a spectral response curve. Fig. 3 shows the reflectance vs. time of the FPPI in response to a 20 mA, 750 nsec square pulse superimposed upon a dc bias of 25 mA for the DFB laser. The response peaks are farther apart near the end of the laser pulse because the chirp rate is a decreasing function of time.

Much better sensitivity to changes in temperature, pressure, strain, or other parameters of interest can be obtained in high-finesse FPPIs than in sensors with low-reflectance internal mirrors reported earlier [1-3]. To achieve high sensitivity, the sensor must be operated near the maximum slope of the  $R_{\text{FP}}$  vs. phase-shift curve. To achieve maximum sensitivity in practice, the laser frequency can be thermally tuned by changing the bias current. Our calculations indicate that, in comparison with an interferometer with mirror reflectances of 2% reported earlier [1], the high-finesse

interferometer increases the maximum sensitivity to temperature or other parameters of interest by a factor of about 25.

In line fiber Fabry-Perot interferometers are also of interest for use as filters and discriminators in frequency-shift-key fiber communications systems [5]. A finesse as high as 500 was reported for an FFPI in which multilayer dielectric mirrors were epoxied to the ends of a polished fiber [6]. The internal mirror FFPIs can also be used in this manner, with a piezoelectric fiber stretcher for tuning. However, higher mirror reflectance values (to give a higher finesse) and lower mirror excess loss (to reduce the insertion loss of the FFPI) will be needed before the internal mirror devices can be competitive in this application.

In conclusion, internal fiber mirrors with high reflectance (86%) and moderate excess loss (7.2%, or 0.33 dB) have been produced by a fusion splicing technique. The mirrors consist of a 7-layer  $\text{TiO}_2/\text{SiO}_2$  stack deposited in a magnetron sputtering system. A finesse of 21 was observed in a Fabry-Perot interferometer using these mirrors. The data agree well with model calculations. A sensitivity enhancement by a factor of 25 over earlier sensors using low-reflectance internal mirrors is calculated.

#### REFERENCES

1. C. E. Lee, R. A. Atkins, and H. F. Taylor, Opt. Lett. 13, 1038 (1988)
2. C. E. Lee, H. F. Taylor, A. M. Marcus, and E. Udd, Opt. Lett. 14, 1225 (1989).
3. J. J. Alcoz, C. E. Lee, and H. F. Taylor, IEEE Trans. Ultrason. Ferroelec. Freq. Contr. UFFC-37, 302 (1990).
4. M. Born and E. Wolf, Principles of Optics (Pergamon Press, New York, 6th ed., 1980), p. 329.
5. I. P. Kaminow, IEEE J. Select. Area in Commun. 8, 1005 (1990).
6. J. Stone and D. Marcuse, J. Lightwave Technol. LT-4, 382 (1986).

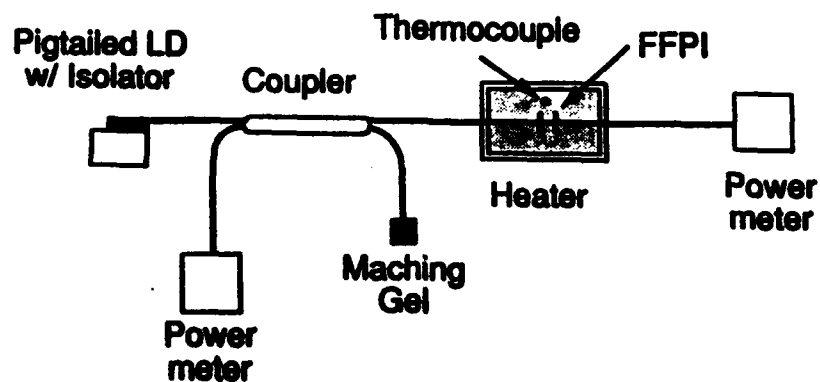


Fig. 1 Experimental Arrangement.

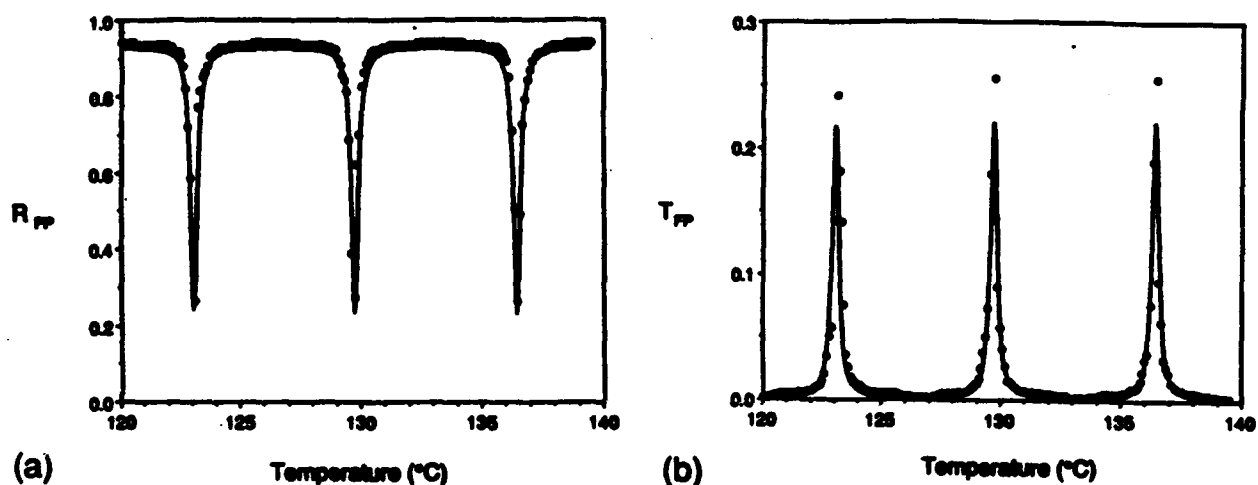


Fig. 2 Temperature dependence of (a) reflectance and (b) transmittance of internal mirror FFPI. Solid and dotted line indicate the calculated and measured data respectively.

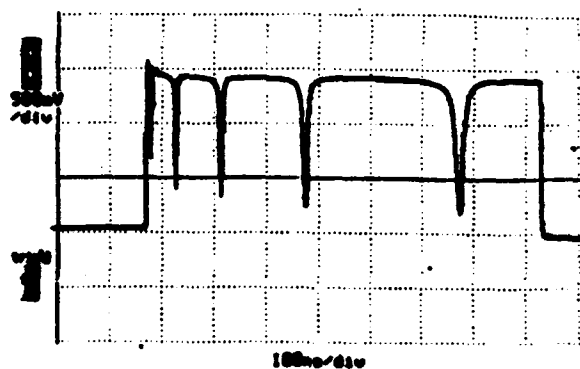


Fig. 3 Oscilloscope trace showing temporal response of FFPI reflectance to a chirped laser pulse.



S.R. Lang<sup>†</sup>, J.M. Pauschke<sup>‡</sup>, D.J. Ryan<sup>†</sup><sup>†</sup> Department of Electrical Engineering<sup>‡</sup> Department of Mechanical Engineering

Northern Illinois University

DeKalb, IL 60115

**Abstract.** Displacement measurements in large-scale structures are used to characterize structural response to dynamic excitation. A review of the current applicable sensor technologies presents alternatives to the traditional accelerograph method for obtaining those displacements.

## 1.0 Introduction

The dynamic response of a large-scale structure (e.g., building, bridge, or dam) due to wind, impact, extreme, or seismic loads is often expressed in terms of the acceleration, velocity, and displacement of the structure. Acceleration gives the forces acting on the structure and the velocity characterizes the vibrational energy. To assess the response of a structure for safety, structural integrity, and damage evaluation, accurate measurement of the displacement of the structure is needed. For example, in a building, displacements are used to determine the overall global response, mode shapes and amplitudes, interstory drift (relative horizontal movement of one floor with respect to another floor), stresses and strains, component (beam or column) failures, gaps between adjacent elements, torsion (twist or rotation of a building floor about a vertical axis) and overturning (bending of a building about a horizontal axis). Interstory drift is used for structural and nonstructural damage assessments. For example, a typical 20 story building may have a relative displacement of the roof with respect to the base of the structure of tens of centimeters [1] and the interstory drift between each adjacent floor may be several centimeters per floor. Figure 1 shows a typical building frame displacement profile during dynamic excitation.

Transducers which record structural accelerations are called accelerometers and are currently the most widely used method to record the response of structures to time-varying loads. Accelerometers utilize a spring-mass-damper system. The acceleration is found by measuring the relative motion of the mass with respect to the case of the instrument. To ensure that the instrument measures acceleration, the natural frequency of the accelerometer is high compared to the frequency of the vibrating structure. For example, if an accelerometer has a natural frequency of approximately 100 Hz, it will accurately measure accelerations in the range from 0 to 33 Hz [2], which is the range of practical interest in structural studies. Based on the dynamic characteristics of the building, triaxial accelerometers, which record motion in three directions, are placed at various floor locations throughout the building as shown in Figure 2. As a minimum, an instrumented building will have two accelerometers to record the relative horizontal motion of the building roof with respect to the base (e.g., one accelerometer at the roof and another at the base). Current triaxial force balance accelerometers digitally sample data and store the acceleration records in solid state memory, with a recording capacity of 30 minutes. The instrument is triggered when the acceleration exceeds a predetermined threshold.

Acceleration is the simplest component of structural motion to record and provides much valuable information about the forces acting on the structure. Acceleration alone, however, may not produce correct displacements due to nonlinear structural properties. Moreover, torsion and strain are becoming more widely used to determine structural response. To obtain structural displacements, the recorded structural acceleration data must be analytically manipulated (filtered and doubly integrated). Although integration is an error diminishing process, this is still a relatively imprecise way to obtain displacements and the accuracy is questioned. Consequently, the development of a sensor which can directly measure displacements can lead to a more durable, robust, and affordable instrument which provides more accurate and reliable estimates of structural response.

## 2.0 Techniques for the Measurement of Structural Displacement

As mentioned above, accelerometers are currently used to measure structural displacements. Other technologies currently exist, however, which enable displacements to be measured in terms of the following physical quantities: acceleration recorded by sensors other than the traditional force balance type, directly as displacements vibrational frequency content, or strain. These technologies and the various sensor types available to record the various physical parameters are summarized in Table 1 and discussed below.

## **2.1 Acceleration Measurement**

One possible solution to improve the accuracy of derived structural displacements is to improve the accuracy of the initial measurement by using a more sensitive accelerometer such as a fiber optic or silicon micromachined sensor. Several designs of fiber optic accelerometers have shown great resolution and dynamic range. One fiber optic accelerometer listed in Table 1 uses a nonlinear displacement to strain conversion which is highly accurate in recording frequencies down to DC [3]. The ability to record frequencies down to DC is important since large-scale vibration typically takes place in the frequency range of 0 - 33 Hz. The displacements obtained by fiber optic accelerometers, with their added accuracy and frequency range, would be more precise than the force balance accelerometers currently in use. While these accelerometers have great sensitivity, they are much more complex than the traditional accelerometers and require an interferometer and a lock-in amplifier.

Recent advances have also been made in the area of silicon micromachined accelerometers [4]. While not using optical techniques, the size and resolution of these accelerometers make them particularly valuable, as indicated in Table 1. Due to their low cost, many more of these silicon accelerometers could be placed throughout a structure than traditional accelerometers thus giving more detailed response information. In addition, it is possible that the silicon accelerometers could be combined with other technologies to produce an accurate and compact structural displacement sensor.

## **2.2 Displacement Measurement**

Measuring displacement directly would eliminate the error caused by the filtering and integration of acceleration records. Table 1 lists a number of excellent optical techniques for the measurement of macroscopic displacements which have been recently developed. These techniques all require a fixed frame of reference. The displacement sensor must remain fixed with respect to the displacement being measured. In a large-scale structure, it is not always possible to place the sensor in a separate frame of reference, but it is possible that relative movement can be transduced into a linear displacement that can be measured by one of the highly accurate optical techniques. The optical technique chosen depends on how the structural movement is transduced.

In order to measure large displacements, an optical potentiometer arrangement could be used [5]. The signal level received at the detector at each end of the fluorescent fiber is dependent upon the attenuation, which is a function of the distance from source to detector. A particular application would require a fiber which is tens of centimeters long so that there is attenuation between the source and detector.

A technique which is similar to the color modulating filter method for measuring macroscopic displacements of these structures is the general neutral density filter [6]. The reflectivity of the surface would vary linearly along the length of the filter. When the filter is placed in the path of an optical fiber, the intensity of the light reflected varies. The color modulation and neutral density methods are more compact than the optical potentiometer, but the resolution is not as great. Depending on the application, this tradeoff may be acceptable.

Two techniques which can measure small strokes with micron resolution are differential absorption [7] and the micromechanical frequency encoded sensor [8]. The differential absorption method only modulates light whose wavelength coincides with the absorption band of the doped glass. A reference channel can be added by using another wavelength that is not near the absorption band making the method more reliable. The micromechanical frequency encoded sensor is capable of measuring larger displacements with approximately the same micron resolution.

The displacement measurement techniques described all have their relative merits. Each method may be applicable depending on its specific use. For example, the techniques for measuring larger displacements may be useful to directly record movement in bridges. It is more likely, however, that they could be used in conjunction with other technologies, such as accelerometers, to improve the accuracy of the measured displacements.

## **2.3 Vibration Measurement**

The optical techniques which measure vibration with excellent accuracy are speckle modulation and position sensitive photodetector. Speckle modulation uses a length of multimode fiber as the sensing element. Disturbances are applied along the length of the fiber, changing the speckle pattern. The output is spatially filtered to convert it into intensity modulation [9]. The output represents the Fourier magnitude spectrum of the input disturbance. If the phase information is also recorded, the time domain waveform can be reproduced. Another method which has the capability of measuring vibration amplitude uses a position sensitive differential photodetector [10]. A plastic

optical fiber is used to direct light onto the differential photodetector. The vibration amplitudes can be derived by determining the amount of light being detected by each side of the photodetector. The difficulty in using this type of sensor is that it is designed to measure small vibration amplitudes on machines and other equipment, rather than larger displacements of bridges and buildings.

#### **2.4 Strain Measurement**

The direct measurement of displacement may not be possible in certain situations, but the strain may be measured. For example, the strain can be induced on an optical fiber by a microbend sensor and detected using a Mach-Zehnder interferometer. The data produced by several microbend sensors throughout a structure can be easily multiplexed and collected at a central point for analysis.

#### **3.0 Summary**

Knowledge of displacements is important to assess the response of large-scale structures to dynamic excitation. Since displacement measurements can yield important information about mode shapes and amplitudes, interstory drift, and torsion, a more reliable and accurate method for determining them is needed.

The review of the technologies presently available to measure structural displacement has been presented in four categories. Since a more accurate accelerometer would yield better displacement results, the highly sensitive fiber optic and micromachined silicon accelerometers were examined. Optical techniques for the measurement of displacement were considered. Several of the methods, although simple, maintained a high level of resolution. The possibility of using fiber optic technology to measure a quantity such as strain in a structure and then extrapolating the displacements was also considered. Future research will be concentrated on attempting to combine the best features of each method in order to design an accurate sensor capable of recording the displacements of structures during dynamic excitation.

#### **4.0 References**

- [1] R. L. Wiegel, ed., *Earthquake Engineering*, (Prentice-Hall, Englewood Cliffs, NJ, 1970).
- [2] W. T. Thomson, *Theory of Vibration with Applications*, Third Ed., (Prentice-Hall, Englewood Cliffs, NJ, 1988), Sec. 3.11.
- [3] F. Bucholtz, A. D. Kersey, A. Dandridge, "DC Fibre-Optic Accelerometer with Sub-g Sensitivity", *Elect. Lett.* 22(9), 451 (1986).
- [4] W. Henrion, L. DiSanza, M. Ip, S. Terry, H. Jerman, "Wide dynamic range direct accelerometer", *IEEE Solid State Sensor and Actuator Workshop Technical Digest*, 153 (1990).
- [5] M. F. Laguerre, "Optical potentiometer using fluorescent optical fiber for position measurement", *Appl. Opt.* 28(23), 5144 (1989).
- [6] R. A. Pinnock, P. Extance, R. J. Hazelden, S. J. Pacaud, C. P. Cockshott, "Colour-modulation optical displacement sensors", *Fiber Optics '87*, L. R. Baker, ed., *Proc. SPIE* 734, 238 (1987).
- [7] E. Theocharous, "Differential absorption displacement transducer", *J. Phys. E*, 18, 253 (1985).
- [8] G. Grosch, "Hybrid Fiber-optic/Micromechanical Frequency Encoding Displacement Sensor", *Sensors and Actuators*, A21-A23, 1128 (1990).
- [9] P. Martin, G. LeBoudec, L. B. Jeunhomme, "Integrating Fiber Optic Vibration Sensor", *Fiber Optic and Laser Sensors VI*, E. Udd and R. P. DePaula, ed., *Proc. SPIE* 985, 344 (1988).
- [10] V. T. Chitnis, S. Kumar, D. Sen, "Optical Fiber Sensor for Vibration Amplitude Measurement", *J. Lightwave Tech.* 7(4), 687 (1989).

Table 1. Technologies for the measurement of structural displacement.			
Sensor Type	Description	Specifications	Comments
<b>Accelerometers</b>			
Fiber Optic	Strain detected by interferometry	Sensitivity: $< 1 \mu\text{g}$ Dynamic Range: $> 120 \text{ dB}$	High accuracy; Requires complex optics; Requires double integration to get displacement
Micromachined Silicon	Electromechanical microscopic cantilever beam	Sensitivity: $< 1 \text{ ng}$ Dynamic Range: $> 120 \text{ dB}$	IC packaging; High sensitivity; Requires double integration to get displacement
Force Balance	Mass-spring-damper system	Sensitivity: approx. $0.1 \text{ mg}$ Dynamic Range: $> 60 \text{ dB}$	Standard technology; Requires double integration to get displacement
<b>Linear Displacement</b>			
Optical Potentiometer	Fluorescent fiber	Resolution: $< 1 \text{ mm}$ Dynamic Range: $> 65 \text{ dB}$	Direct measurement of displacement; Simple design; Large displacement capability; Requires fixed frame of reference
Color Modulating Filter	Color filter wedge placed in light path	Resolution: 1% of filter length	Direct measurement of displacement; Simple design; Low resolution; Requires fixed frame of reference
Differential Absorption	Gradient doped attenuator placed in light path	Resolution: $< 5 \mu\text{m}$ Dynamic Range: $> 74 \text{ dB}$	Direct measurement of displacement; Simple design; High resolution; Reference channel possible; Requires fixed frame of reference
Micromechanical Frequency Encoded	Displacement detection by microvibrator array	Resolution: $< 5 \mu\text{m}$ Dynamic Range: $> 85 \text{ dB}$	Direct measurement of displacement; High cost; High resolution; Requires fixed frame of reference
<b>Vibration</b>			
Speckle Modulation	Vibration distorts mode structure in optical fiber	Freq. Range: $10 - 1000 \text{ Hz}$	High cost; Used for small amplitude vibration environments
Position Sensitive Photodetector	Detector array maps vibratory movement of light source	Freq Range: $.5 - 100 \text{ kHz}$ Sensitivity: $.5 \text{ \AA} \cdot \text{Hz}^{-1/2}$ @ $1 \text{ kHz}$ Dynamic Range: $80 \text{ dB}$	Requires post-processing to determine displacement; Measures vibration amplitudes
<b>Strain</b>			
Microbend	Sawtooth transducer distorts mode structure in optical fiber	Sensitivity: approx. $1 \mu\text{m}$	Applicable in high stress areas such as joints or beam-column connections; Requires knowledge of correlation between strain and displacement

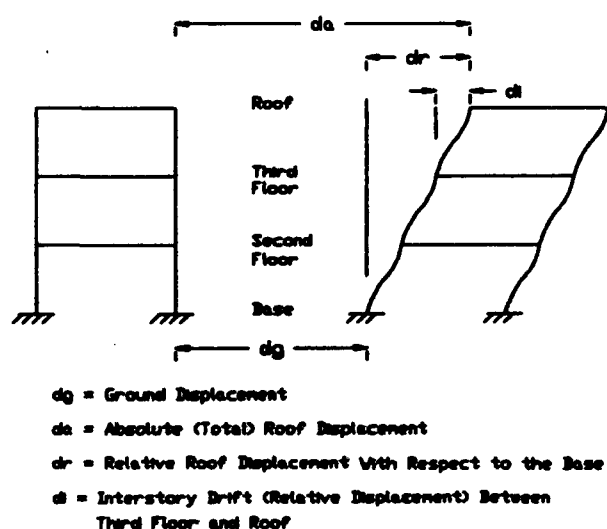


Figure 1. Typical building displacement profile.

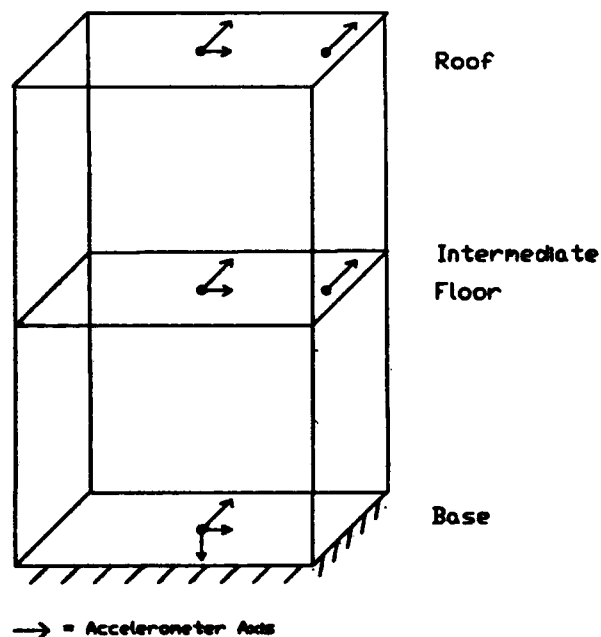


Figure 2. Instrumentation scheme for a typical building.

# P10 Remote Fiber - Optic Strain Sensing On Composites With Simultaneous Interferometric and Polarimetric Readout

N. Fürstenau, W. Schmidt, H.-C. Goetting\*  
 German Aerospace Research Establishment (DLR)  
 Institute for Flight Guidance  
 \*Institute for Structural Mechanics  
 Flughafen, D-3300 Braunschweig, Germany

## Summary

In preparation of fiber - optic strain measurements on an aircraft wing the performance of an interferometric strain gauge is investigated. A double - polarization Michelson-interferometer is employed for remote sensing of the bending induced surface strain (up to  $2500 \mu\epsilon$ ) of plates made from Carbon fiber composites (CFRP). Figure 1 shows the arrangement of a surface adhered fiber - optic strain gauge (OSG) with reference (R) and sensing arm (S) of equal length fixed nearby a conventional resistive gauge (ESG). The fiber jacket is removed in the sensing region.  $l$  = distance between the supports = 65 mm,  $L$  = length of sensitive fiber section = 44.4 mm  $\geq L_{fi1,2}$  = adhesive covered sections with different lengths for different experiments  $i$ ,  $2h$  = thickness of plate = 1 mm. The double-polarization method is employed for eliminating the ambiguity in fringe counting [1]. Fig. 2 shows a schematic of the experimental setup. A linearly polarized wave from a 1 mW HeNe laser (L) is guided to the interferometer via 5 m of cabled polarization maintaining input fiber which is connected to the input arm of a conventional 3 dB directional coupler via a NTT-FC single mode connector. A polarizing beam splitter (PB) splits the collimated (G) output wave into two orthogonally polarized interference signals (horizontal H, vertical V) with different phase offset ( $\Phi_H$ ,  $\Phi_V$ ) which are guided to photodiodes via multimode fibers (MF):

$$(1) \quad P_{H,V} = \frac{P_0 T_{H,V}}{4(1 + \mu_{H,V})} (1 + \mu_{H,V} \cos(\Delta\Phi + \Phi_{H,V}))$$

$P_0$  = input power,  $T$  = interferometer transmissivity,  $\mu$  = fringe contrast,  $\Delta\Phi$  = measurand induced phase shift of the light wave in the sensing arm. The offset difference ( $\Delta\Phi_{HV} = \Phi_H - \Phi_V$ ) can be adjusted for the H- and V- signals to be in quadrature. It depends on the polarization states of the input and output fibers, the length of the interferometer arms, and the fiber birefringence. Usually two rotatable fiber squeezers ( $PC_{1,2}$ ) in the input and output arm of the interferometer are sufficient to adjust the desired  $\Delta\Phi_{HV}$ . Besides fringe counting by means of an up-down counter (Co) a simultaneous polarimetric signal is derived employing the birefringence induced variation of  $\Delta\Phi_{HV}$  under bending of the CFRP-plate. This analog signal allows for unambiguous

initialization of the incremental readout over the full measurement range if the variation  $|\delta(\Delta\Phi_{HV})| < \pi$ . Moreover a linear dependence of  $\Delta\Phi_{HV}$  on the birefringence  $\beta$  is required which is expected under certain conditions [2]

$$(2) \quad \Delta\Phi_{HV} = 2 \beta_f L_f$$

$\beta_f$  is the transverse force (f) induced birefringence [3] due to shear stress acting on those fiber sections  $L_f < L$  which are covered by the adhesive ( $b_f \sim f \sim$  displacement H). With  $L_f$  in the order of 1 cm a birefringence variation of  $\delta\beta_f \sim 1$  rad/cm is required for initialization over the full measurement range.  $\Delta\Phi_{HV}$  is measured via time measurement ( $T_{HV}$ ,  $T_{HH}$ ) between successive fringes of the two interference signals. The symmetrized H- and V- signals of the readout electronics (RE) are fed into a separate control unit (CU) which produces start and stop pulses for a 100 kHz clock. A plastic housing encloses the optical components of the interferometer. The balanced interferometer arms are protected by means of a silicone tube between the housing and the CFRP - sample.

The scale factor relating the number of half fringes to the bending of the CFRP - sample is given by  $S = G S_H$  with gauge factor  $G = \Delta\Phi / \Delta L = \Delta\Phi / \epsilon / L$  and strain - displacement sensitivity  $S_H = \Delta L / H$  ( $\epsilon$  = relative strain  $\Delta L / L$ ). Following [4] G is obtained as  $G = 1.318 \text{ deg}/\mu\epsilon / \text{mm} = 3.66 \text{ } 2\pi\text{rad}/\mu\text{m}$  (index of refraction  $n = 1.458$ , Poisson ratio  $\nu = 0.16$  and photoelastic constants  $p_{11} = 0.113$ ,  $p_{12} = 0.242$ ).  $S_H$  is derived by integrating the surface strain  $\epsilon(z) = \sigma(z) / E$  along the S-fiber between  $z = 0$  and  $L$  (Youngs modulus  $E_{CFRP} = 2.5 \cdot 10^{10} \text{ Pa}$ ). Employing the well known equation for the deformation of an elastic bar under a central force F we get  $S_H = \Delta L / H = 12 h L (1 - L/2) / l^3 = 41.5 \pm 1 \mu\text{m}/\text{mm}$ . The theoretical scale factor is then obtained as  $S = 304 \pm 10 \text{ counts}/\text{mm}$ . Figure 3 shows the experimental results of the simultaneously measured strain-displacement characteristics obtained with the fiber-optic strain gauge and the resistive one. The CFRP-plate is bent under an external force employing the computer-controlled motor-driven (MC, fig.2) translation stage. The stage moves up to  $H \sim 2.6 \text{ mm}$  and back to the initial position  $H = 0$ , stopping after each  $10 \mu\text{m}$  for automatic readout of the position encoder and the interferometer-up-down counter. The linear fit to the data yields a displacement sensitivity of  $S_{exp} = \Delta\Phi / H = 306.7 \text{ counts}/\text{mm}$  (standard error 0.04) in good agreement with the theoretical value. The maximum fiber strain corresponding to  $N_{max} = 810 \text{ counts}$  is  $0.25 \% = 2500 \mu\epsilon$ . The above value yields a gauge sensitivity  $G = S_{exp} / S_H = 7.39 \cdot 10^{-3} \text{ counts}/\mu\epsilon / \text{mm} = 1.33 \text{ deg}/\mu\epsilon / \text{mm}$ , in agreement with the value measured by Valis et.al. [5], within our experimental uncertainty of  $0.03 \text{ deg}/\mu\epsilon / \text{mm}$ . Figure 4 displays the residuals of the least squares fit to the experimental data. It can be seen that the hysteresis of the OSG is not significantly larger than the 1 count ( $0.14 \mu\text{m}$ ) resolution, corresponding to  $0.1\text{-}0.2 \%$  (with

respect to  $N_{\max}$ ). The deviation from linearity at low strain values is due to a difference between the true bending of the plate and the displacement read from the incremental encoder.

Figure 5 shows two results of simultaneous strain and phase measurements, demonstrating a nearly linear dependence of  $\Delta\phi_{HV}$  on the fiber strain for two different lengths  $L_f$ . The curve with the small slope corresponds to the case with the fiber fixed at the end points of the sensitive section only ( $L_f=8.5\text{mm}$  of cement covering the sensitive fiber section). The linear fit to the data yields  $\Delta\phi_{HV}/2\pi\text{rad} = 0.72-2.72 \cdot 10^{-4} \Delta L/\text{COUNTS}$ . The large slope curve is obtained with  $L_f=22\text{mm}$  covered by the cement. In agreement with (2)  $\Delta\phi_{HV}$  exceeds  $\pi$  already at a strain of 320 counts. The fit yields  $\Delta\phi_{HV}/2\pi\text{rad} = 0.65-1.03 \cdot 10^{-3} \Delta L/\text{COUNTS}$ . Based on (2) and the linear dependence of  $\beta_f$  on  $H$  the two measurements can be used for obtaining an estimate of the shear stress induced birefringence at a certain displacement  $H$ . Employing the parameter values of the linear fits to the data we get  $\beta_f \approx 0.5 \text{ rad/cm}$  for  $\Delta L = 300$  counts (corresponding to  $H=1\text{mm}$ ). Small periodic deviations from the linear behavior are thought to be due to imperfect polarization splitting and mode coupling. It is expected that better optical components, careful polarization adjustment and improvements of the phase measurement unit will improve the polarimetric signal.

As a first test of the system outside the optics-laboratory, strain measurements under longitudinal stress are performed on CFRP-samples employing a hydraulic force frame. Fig.6 shows the simultaneously obtained strain-displacement characteristics of the optical and electrical strain gauge. The measurement procedure is the same as described above. The maximum displacement corresponds to  $\epsilon \approx 0.2 \%$ . Despite vibrational disturbance corresponding to  $\pm 1$  fringe the OSG in the fringe counting mode yields the correct linear characteristic and compares favorably with the electrical gauge. The increased noise is due to the inductive position encoder.

- [1] N. Fürstenau, "Double-Polarization Interferometer For Digital Force Sensing by Fiber Tension Bending", Optics Letters, vol.13 (1988) 242-244
- [2] N. Fürstenau, "Performance of the double-polarization method in interferometric digital force sensing by fiber-tension bending", SPIE-Proc. vol.891, (1988) pp 209-214
- [3] S.C.Rashleigh, "Origins and Control of Polarization Effects in Single-Mode Fibers", J. Lightwave Technology LT-1 (1983) 312
- [4] C.D.Butter, G.B.Hocker, "Fiber Optics Strain Gauge", Appl. Optics, 17 (1978) 2867-2869
- [5] T.Valis, E.Tapanes, R.M.Measures, "Localized Fiber-Optic Strain Sensors Embedded in Composite Material", SPIE Proc. vol. 1170 (89) 495-504

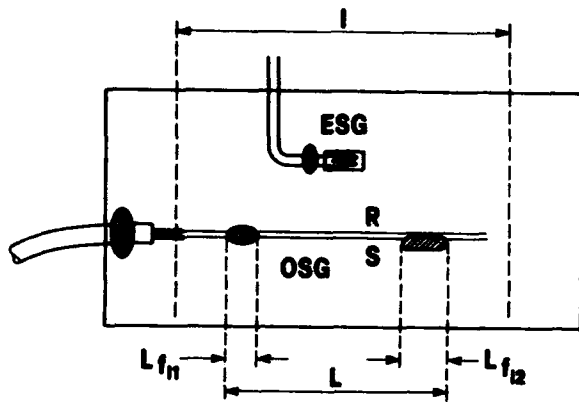


Figure 1: CFRP - plate with optical (OSG) and electrical (ESG) strain gauge.

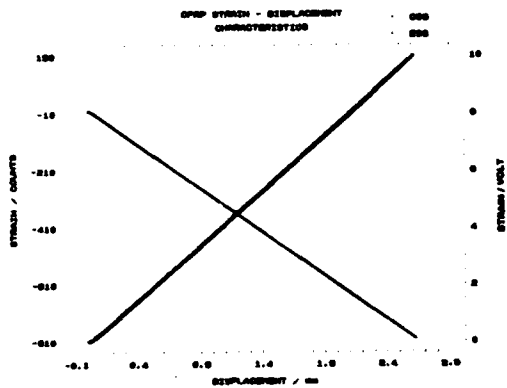


Figure 3: Strain-displacement characteristics under plate bending. OSG: neg. slope, left ordinate; ESG: pos. slope, right ordinate.

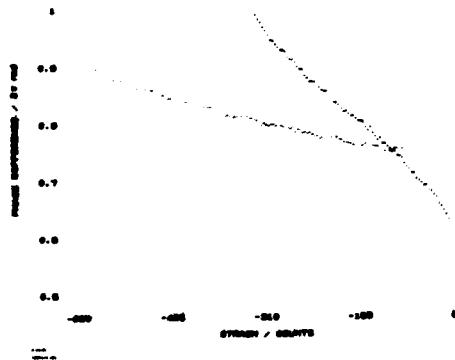


Figure 5: Polarimetric readout. Phase difference  $\Delta\phi_{HV}$  via fiber strain for  $L_f=8.5$  mm (small slope) and 22 mm (large slope).

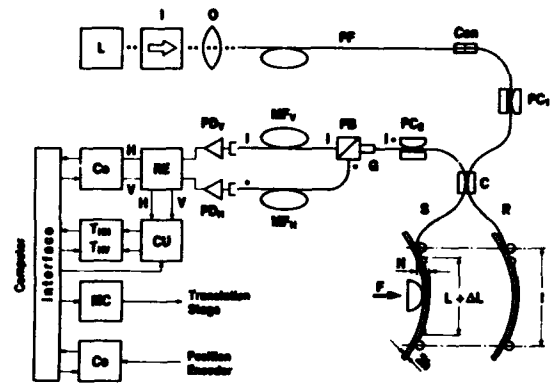


Figure 2: Experimental setup. For explanation see text.

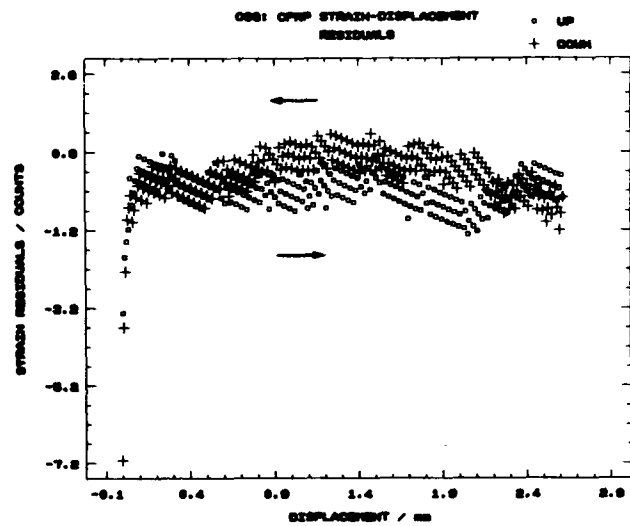


Figure 4: Residuals of linear fit to OSG - data.

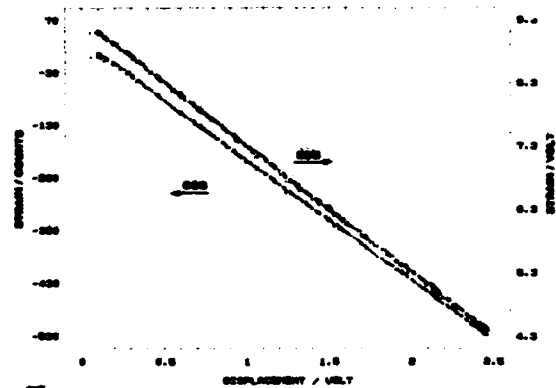


Figure 6: Strain - displacement characteristics under longitudinal stress employing hydraulic force frame.



T. Y. Liu\*, M. Berwick, D. A. Jackson

Applied Optics Group, Physics Laboratory, University of Kent, Canterbury, Kent CT2 7NR, UK.

\* Permanent address: Shandong Laser Institute, Jining, Shandong, P.R.CHINA

**Introduction and principles**

Although bulk optic torsional vibrometers are commercially available [1], similar sensors based on optical fibre technology have not been reported, to our knowledge. Fibre-optic torsional vibrometers represent a class of extrinsic fibre-optic sensor [2]. We have developed two new fibre-optic sensors which may be classified as either differential or reference instruments. These are based on the Laser Doppler principle and are fabricated with single mode fibres and associated components. The major advantage of basing the instrument on optical fibres is that it allows both a flexible light guide between the optical source and processing electronics and the possibility of a miniature but rugged lightweight probe to be deployed in the measurement volume, greatly enhancing the applicability of the technique. The instrument can be used conventionally in a 'line of sight mode' or deployed in inaccessible areas. It would be feasible to design a probe which could be mounted inside an engine to monitor the rotation of internally mounted shafts etc. The differential mode, like bulk torsional vibrometers, has the advantage of direction independent instantaneous measurement. The reference mode has similar applications and the advantage that measurements can be made with significantly lower optical power when compared to the differential mode.

When two parallel monochromatic laser beams, with intensities  $E_{01}^2$  and  $E_{02}^2$  respectively, illuminate a rotating object as shown in Figure 1(a) the frequency of the backscattered light from each beam will be Doppler shifted. The shifts  $\Delta v_1$  and  $\Delta v_2$  are described by,

$$\Delta v_1 = - \frac{2\omega R_1 \cos \alpha_1}{\lambda} \sin \theta \quad ; \quad \Delta v_2 = - \frac{2\omega R_2 \cos \alpha_2}{\lambda} \sin \theta \quad (1)$$

where  $\omega$  is the angular frequency of the rotating object,  $R_1$ ,  $R_2$ ,  $\alpha_1$  and  $\alpha_2$  are as shown in figure 1(a) and  $\theta$  is the angle between the light beams and the direction of the shaft axis. The geometry is such that the backscattered beams are perpendicular to the axis,  $\sin \theta = 1$ . When these two backscattered beams are mixed and interfere, their beat frequency  $\Delta v$  can be expressed as :

$$\Delta v = \Delta v_2 - \Delta v_1 = \frac{2\omega d}{\lambda} \quad (2)$$

Clearly this is only dependent on the angular rotation frequency  $\omega$ , the beam separation  $d$  and the laser wavelength  $\lambda$ . It is independent of both the shape of the rotating object and the direction of the parallel illuminating beams. Non-torsional vibration modes will contribute equal components to  $\Delta v_1$  and  $\Delta v_2$ , hence  $\Delta v$  is independent of translational motion of the rotating object. Figure 1(a) also shows a fibre-optic implementation of the torsional vibrometer. The system is basically a fibre optic Michelson interferometer with two auto collimating probes (figure 1(b)) mounted at the distal ends of the fibre. The signals returned from the probes will consist of both light backscattered from the rotating object and light internally reflected from the fibre ends and lens surfaces. The internally reflected light may be reduced by using angled fibre-ends and anti-reflection coatings. Assuming a single source of internally reflected light the resultant photodetector current output  $I_{pd}$  can be expressed by,

$$I_{pd} \propto (r + \rho)(E_{01}^2 + E_{02}^2) + 2\rho E_{01} E_{02} \cos(\Delta v t + \Delta \phi_{21}) + 2\sqrt{r\rho(E_{01}^2 + E_{02}^2)}(E_{01} \cos(\Delta v_1 t + \Delta \phi_{01}) + E_{02} \cos(\Delta v_2 t + \Delta \phi_{02})) \quad (3)$$

where  $\rho$  is the backscattering intensity coefficient, which is dependent on the object's surface properties,  $r$  is the reflected intensity coefficient and  $\Delta \phi_{ij}$  ( $i, j=0,1,2$ ) is the phase of each signal. Ignoring the dc term, the detector current output comprises two terms containing information about the velocities of locations (1) and (2) and a third term containing the beat frequency signal resulting from the mixing of backscattered light. The strengths of these signals depends on the relative power levels of the reflected and scattered light. In the limit where  $r \ll \rho$ , the photodetector output contains the beat frequency component, which is independent of beam direction. For the condition  $r \gg \rho$  the photodetector current essentially contains only the two individual backscattered frequency shifted components  $\Delta v_1$  and  $\Delta v_2$ . These may be electronically combined to give the beat frequency. From Figure 1(a),

$$\Delta v = \Delta v_{R+} = |\Delta v_2| + |\Delta v_1| \quad (|R_i \cos \alpha_i| \leq d, i = 1 \text{ and } 2) \quad (4a)$$

$$\Delta v = \Delta v_{R-} = ||\Delta v_2| - |\Delta v_1|| \quad (|R_i \cos \alpha_i| \geq d, i = 1 \text{ or } 2) \quad (4b)$$

The condition given by equation (4a) is that the two illuminating optical beams are on opposite sides of a line parallel to them which passes through the centre of the rotating object. The condition given by equation (4b) is that the two beams are both on the same side of the centre line. Thus, the relative positions of the two beams must be known to determine which 'mixed' frequency corresponds to  $\Delta v$ . Thus this system may be operated in two

regimes:

(i) A reference mode when  $r \gg \rho$ , where unambiguous data can only be recovered if the system is set up to fulfil condition (4b) and (ii) A differential mode when  $r \ll \rho$ , in this mode of operation any frequency shifts arising as a result of relative motion between the shaft and probes are not detected.

### Experimental

As shown in figure 1(b), the probe comprises two lenses. The first lens is used to expand the beam radius and collimate it into a parallel beam, the second is used to focus the illuminating beam onto the object. These lenses also collect the scattered light and focus it back into the optical fibre. When a Gaussian beam is brought to a focus by a lens the focused spot has a minimum diameter ( $2\omega_0 = 2f_2\lambda/\pi\omega$ ) termed the beam waist [3]. This strongly influences the system performance. The finite diameter of the beam at the object's surface gives rise to a spread in the observed Doppler shift of the backscattered light. The resolution of the system is limited by the resulting spectral linewidth of the Doppler signal. The 'length' of the waist determines the tolerance of the system to fluctuations in received backscattered power due to changes in the working distance. The waist diameter also influences the required laser power as this determines the power density at the illuminated object surface, and hence the scattered light power. The probe must therefore be designed with a light gathering power (N.A.) sufficient to collect the backscattered light with an adequate S/N ratio. In our experiments the first lens is a micro ball lens with a diameter of 3mm and focal length of 1.64mm. The second lens is of 30mm focal length. The optical fibre has a mode diameter of  $\sim 5\mu\text{m}$ , hence the theoretical beam waist diameter is approximately  $66\mu\text{m}$ . The probe diameter is 5mm and beam separation is 12.55mm. The  $1/e^2$  intensity diameter at the centre of  $L_1$  is  $\sim 400\mu\text{m}$ , hence with suitable microlenses the diameter of each probe could be  $< 1\text{mm}$  allowing a beam separation as small as 1mm.

**Reference mode:** In this configuration the distal ends of the fibre coupler output arms were approximately perpendicularly cleaved. This provides a relatively strong reflection to form the reference beam ( $r \sim -15\text{dB}$ ). With the probe design stated above, working distances in the range 25 mm to 35 mm were usable. The target was a disc with a coarsely polished surface ( $\rho \sim -60\text{dB}$ ), mounted in a precision high speed drill. Disc diameters in the range 30 mm to 75 mm were available for investigation. The detector spectrum contained the two individual frequency shifted components, however it was not possible to observe the differential beat signal. Good quality signals could be obtained with input powers as low as  $130\mu\text{W}$ . Furthermore, experiments were also carried out with different rough films attached to the rotating disc's surface. The grain size of the films ranged from  $0.3\mu\text{m}$  to over  $200\mu\text{m}$ . Rotation speeds from 3000 to 19000 rpm were used. The detector output spectrum was observed and for all the surfaces the shifted signal levels were always in excess of 20dB above the noise floor. Figure 2 shows a spectrum obtained from a surface of  $\sim 200\mu\text{m}$  black grains (P60 grit emery cloth).

**Differential mode:** In order to obtain a beat signal it was necessary to attach reflective tape ( $\rho \sim -35\text{dB}$ ) to the surface of the rotating disc and to inject the maximum power possible into the system. Similar tape is used with the commercial unit. Figures 3(a,b) show spectra obtained from the detector output. Each spectrum contains the two backscattered light frequency shifts and their beat frequency. To satisfy the condition  $\rho \gg r$ , it was necessary to use the reflective tape (increase  $\rho$ ) and to reduce the internally reflected light (decrease  $r$ ). Figure 3(a) shows the spectrum obtained when the fibre ends are simply cleaved perpendicular to the fibre axes. Clearly the individual frequency shifts ( $\Delta\nu_1$  and  $\Delta\nu_2$ ) are the dominant spectral components. Figure 3(b) shows the spectrum under similar conditions (except increased detector gain) with fibre end angles  $\sim 8^\circ$  to the perpendicular, reducing  $r$  by  $\sim 30\text{dB}$ . Clearly the beat frequency ( $\Delta\nu$ ) is now the dominant spectral component. From figure 3(b), the ( $-3\text{dB}$ ) linewidths of the individual frequency shifts are each  $\sim 0.2\text{MHz}$ . This is consistent with the geometrically induced linewidth arising from a disc position  $\sim 5\text{mm}$  from the waist. The beat frequency ( $-3\text{dB}$ ) linewidth is  $\sim 0.33\text{MHz}$  with centre frequency  $13.34\text{MHz}$ . Measurements of the beat frequency were made for angular frequencies in the range 3200 to 19000 rpm. Figure 4 shows a graphical comparison between the theoretical and experimental values of beat frequency versus disc angular frequency. The maximum deviation between theoretical and experimental beat frequency values is 0.8% over this range. The principal source of error is thought to be inexact parallel alignment of the two beams.

**Measurement of torsional 'jitter':** Monitoring the 'jitter' on a rotating shaft is an important factor in diagnosing wear and preventing potentially catastrophic failure. If the angular frequency of the object is not constant then the instantaneous Doppler frequency shift will vary. The maximum excursion of the observed shift frequency from its mean value is then a direct measure of the amplitude of the 'jitter' in the rotation. The jitter may be monitored, in either mode, by observing the beat frequency as before. The results presented in figure 5 demonstrate the measurement of jitter using a fibre-optic torsional vibrometer in the differential mode. The rotating object was a disc

driven by a D.C. motor. Reflective tape was again attached to the disc. The drive signal comprised a large D.C. current onto which was superimposed a variable low frequency A.C. component to introduce a controlled amount of jitter. Figure 5 is a plot of the apparent (-3dB) linewidth of the observed beat frequency, against the applied A.C. amplitude.

#### References:

1. Product Data: Torsional Vibration Meter: type 2523. Bruel & Kjaer, DK-2850 Naerum, Denmark.
2. D.A.Jackson, J.D.C.Jones 'Extrinsic fibre-optic sensors for remote measurement: part two' Optics and Laser Technology, Vol.18 No 6, pp 299-307, December 1986.
3. H. Kogelnik and T. Li, 'Laser beams and resonators.' Applied Optics, Vol. 5 No.10, pp 1550-66, October 1966.

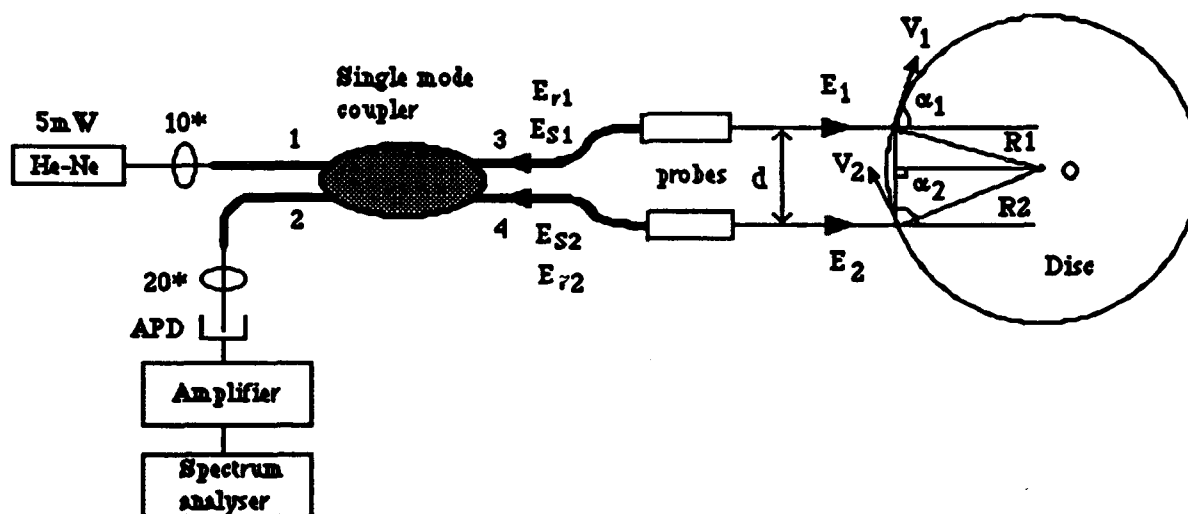


Figure 1(a): Schematic arrangement of fibre-optic torsional vibrometer.

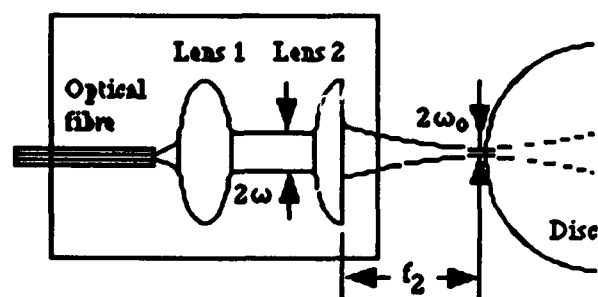


Figure 1(b): Arrangement of the probes.

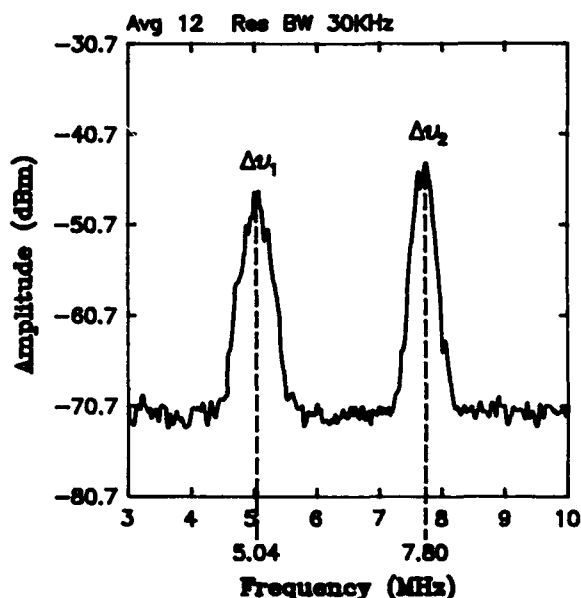
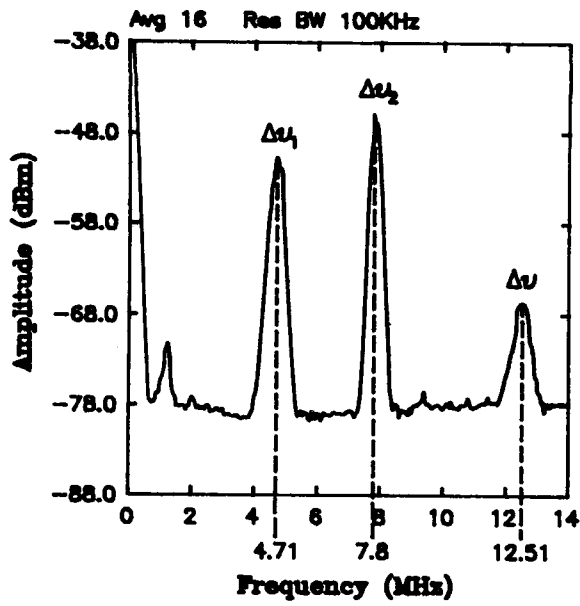
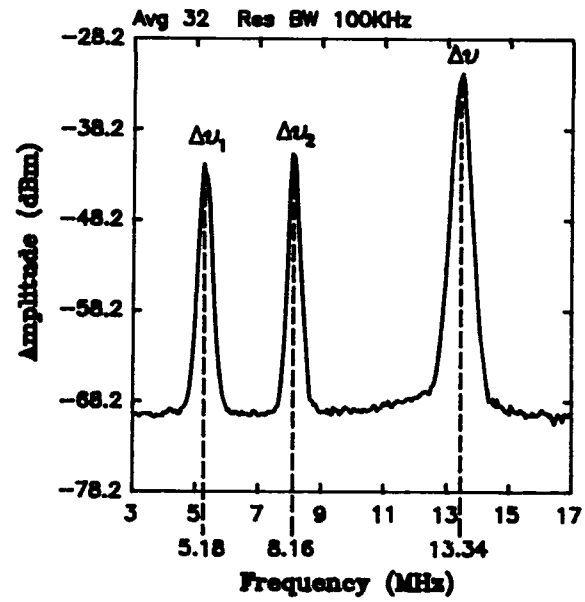


Figure 2: Typical spectrum with fibre-optic torsional vibrometer operating in the reference mode:  
(130μW illuminating power and black surface ~240μm grains)



[a]:  $r \approx -15\text{dB}$  and  $\rho \approx -35\text{dB}$



[b]:  $r \approx -45\text{dB}$  and  $\rho \approx -35\text{dB}$

Figure 3: Spectra for system operating in differential mode.

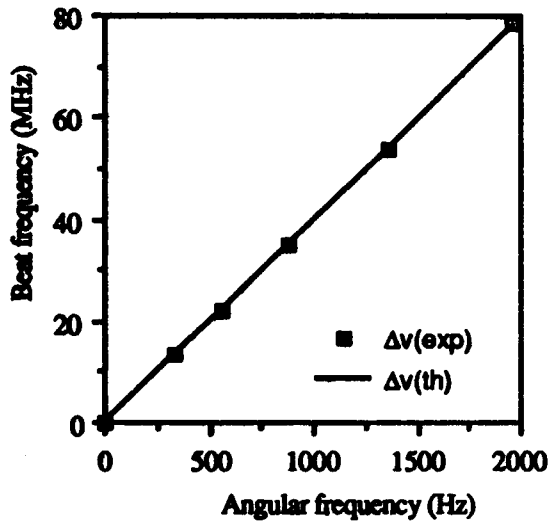


Figure 4: Comparison between experimental and theoretical values of the beat frequency versus angular frequency

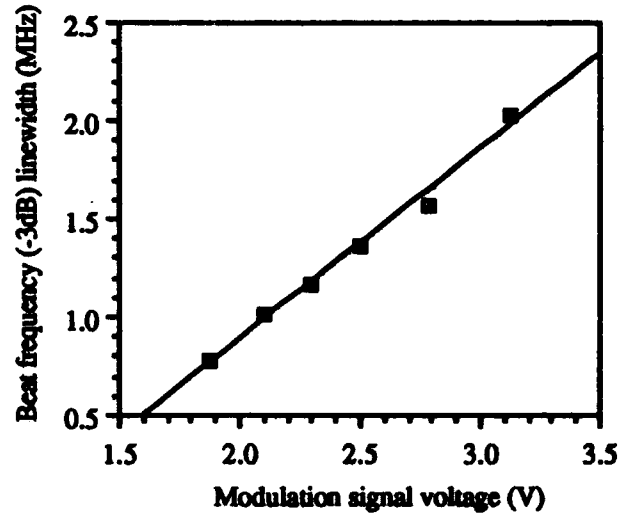


Figure 5: Graph of the modulated (-3dB) linewidth of the beat frequency versus modulation signal voltage

## P12    Developments In Elliptical Core Polarization-Maintaining Fiber

George E. Berkey

Corning Incorporated  
Corning, New York 14831

Polarization maintaining (PM) optical fibers are showing promise in a new generation of gyroscope applications and other fiber optic sensing systems. One of the key obstacles to making in-roads in these applications remains the long-term cost of the PM fiber. This paper describes the properties of an elliptical core fiber expected to meet the long term cost requirements for these applications.

The simplicity of the elliptical core design lends itself to ease of manufacture. A manufacturing process to make elliptical core fiber is currently under development at Corning that allows for efficient manufacturing rates, blank size, draw speeds, and yield selects.

The main factors which control the elliptical core fiber's performance are core delta, degree of ellipticity (aspect ratio), and polymer coating. Figure 1 shows the relationship of beat length versus weight % germania (delta) for a germania-doped core with a constant aspect ratio of 4. The beat length potential is fundamentally linked to the germania concentration of the core. The beat length for any given core delta though is strongly influenced by ellipticity. The optimum degree of ellipticity is between 5 and 6. Higher degrees of ellipticity do not improve the beat length and appear to make the fiber more bend sensitive.

The fiber design consists of a germania-doped silica core and a silica cladding. A spectral attenuation curve of an elliptical core fiber optimized for 780nm operation is shown in figure 2. This fiber is made by the outside vapor deposition (OVD) process is shown in figure 2. It consists of a core with a nominal 40 weight %  $\text{GeO}_2$  and a cut-off of 700nm. The beat length is .8mm. Figure 3 shows typical h-parameter temperature performance for a 110m length on a 60mm coil diameter (aluminum spool) at 5 grams wind tension. The developmental fiber O.D. was 80 microns with a dual acrylate coating O.D. of 175 microns. Feasibility of making couplers from elliptical core fiber with low excess loss and high extinction ratios has been demonstrated using Corning's multicladd coupler process.

# Beatlength vs Core Composition

(Core Ellipticity of 4)

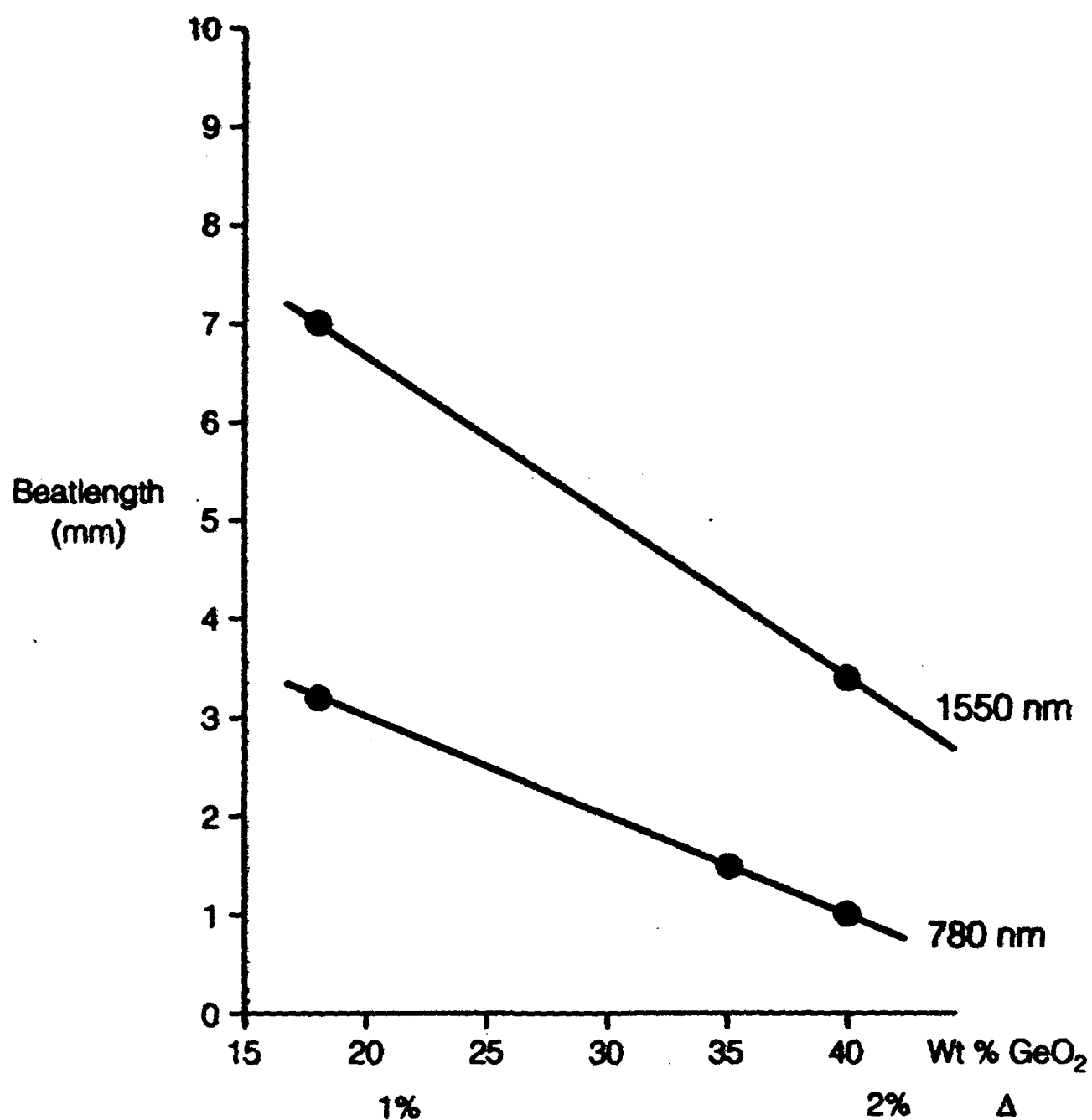


Figure 1

# Attenuation

0-3362-4

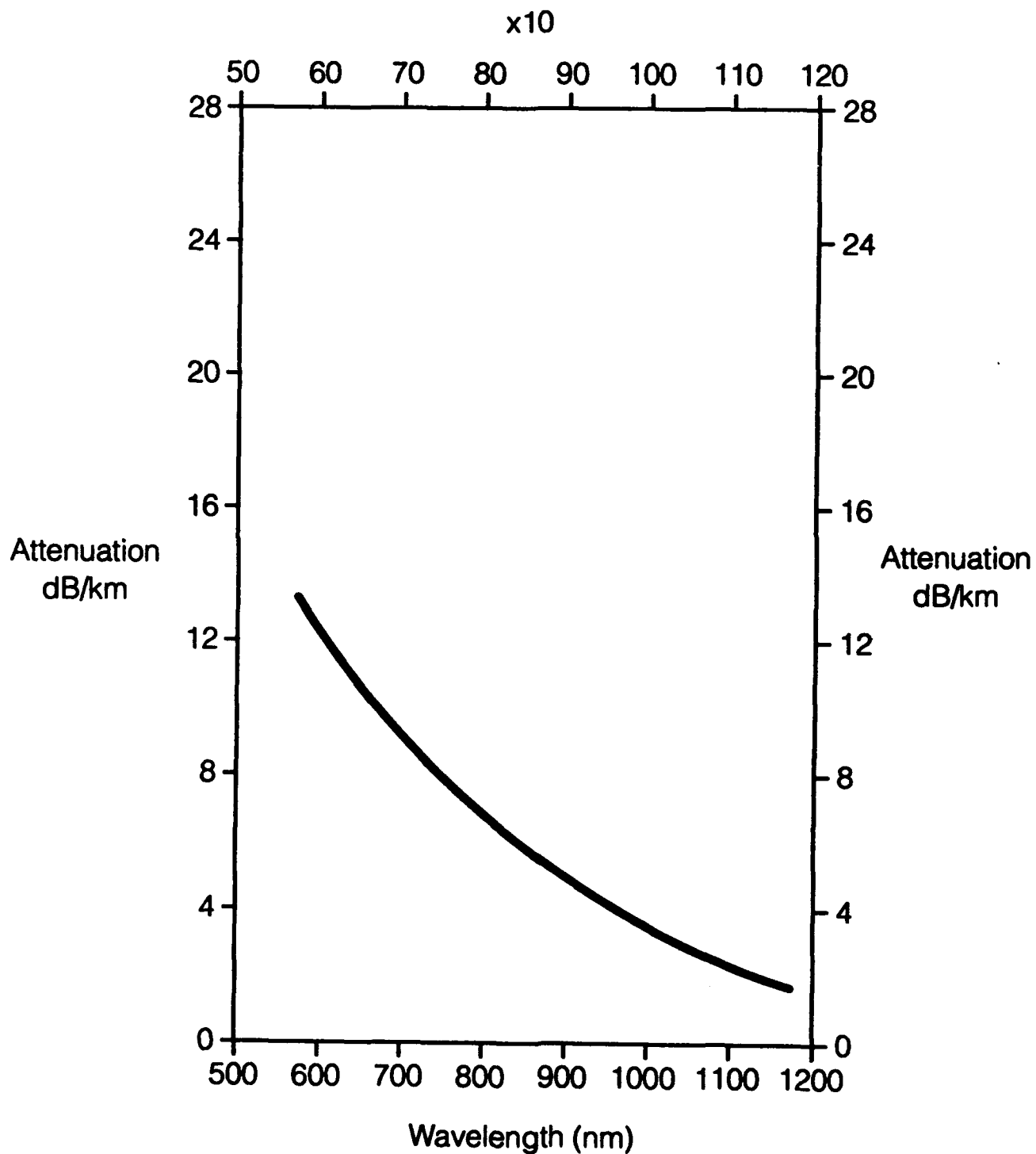


Figure 2

# h-parameter vs Temperature at 820 nm

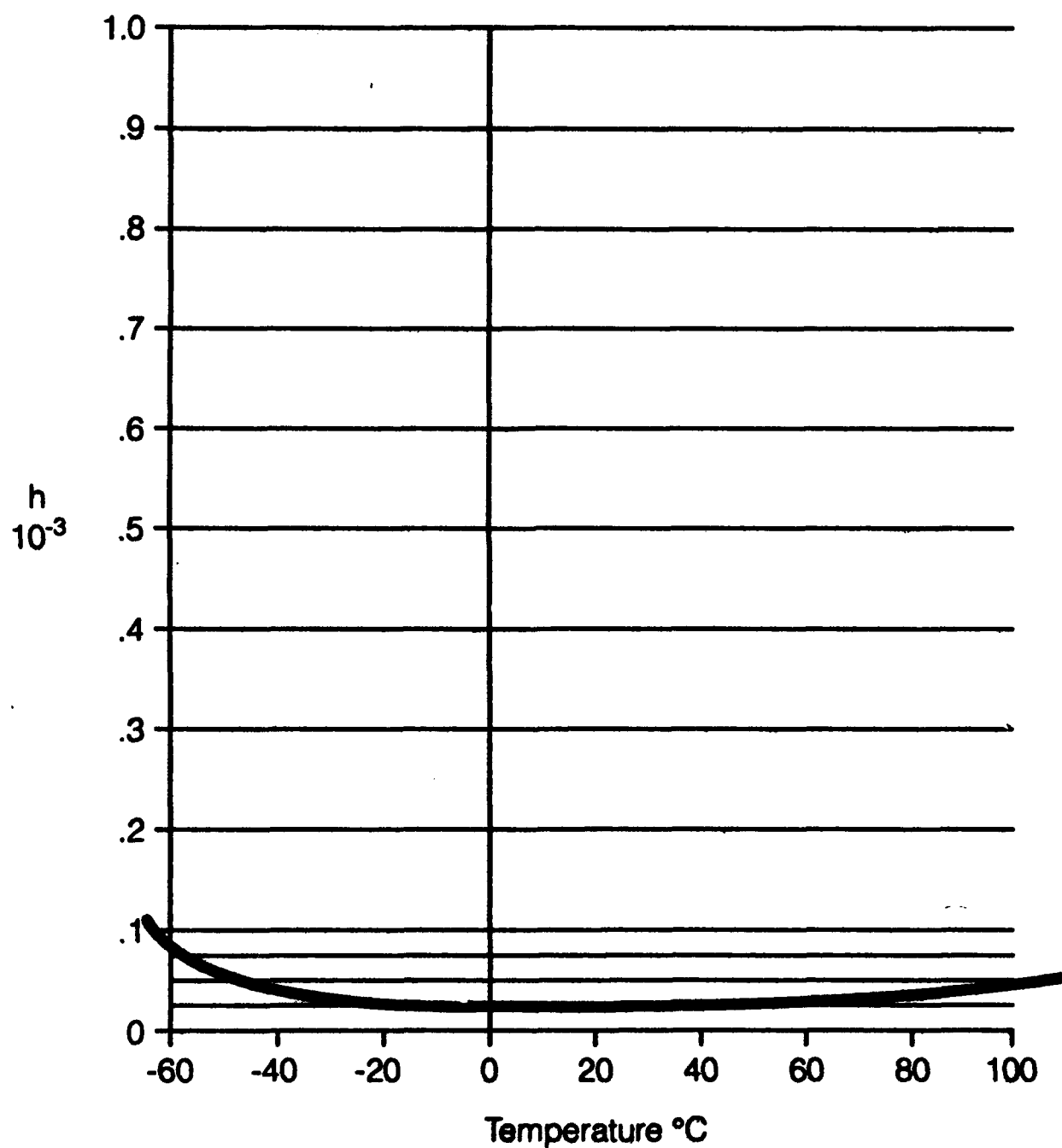


Figure 3



# **P13 Splitting Of The Second Order Mode Cutoff Wavelengths In Elliptical Core Fibers**

**J. Blake**  
Texas A&M University  
College Station, TX. 77843

**M. C. Pacitti and S. L. A. Carrara**  
Centro Technico Aeroespacial  
S. J. Campos, SP Brazil

## **Abstract**

A simple relation is reported for calculating the splitting of the cutoff wavelengths of the  $LP_{11}^{\text{even}}$  and  $LP_{11}^{\text{odd}}$  modes in elliptical core fibers. The results match experimental observation.

## **Introduction**

Many attempts have been made to calculate the modal behavior of elliptical core step index optical fibers[1]-[7]. Recent activity in two-mode fibers has heightened interest in these calculations. However, the most important modal characteristics for two-mode fiber applications, namely the splitting of the cutoff wavelengths of the even and odd second order modes, the beat lengths between the first and second order modes, and the wavelength at which the first and second order modes propagate with the same group velocity have not been accurately predicted. These calculations are far more difficult than predicting the general mode behavior since the results depend on the difference in propagation constants between two modes. Small errors in individual mode calculations become large errors in calculating these quantities.

In this paper, we report a simple model that accurately predicts the cutoff wavelengths of the  $LP_{11}$  modes. The splitting of the cutoff wavelengths between the even and odd  $LP_{11}$  modes matches the experimental evidence.

## **$(1+r^3)^{-1}$ approximation of the mode field**

The procedure for calculating the propagation constants of the modes in elliptical core fibers is the variational method adopted by Snyder and Love in their text, *Optical Waveguide Theory*[8]. The idea is to guess the form of the field distribution of the mode of interest and perform appropriate integrals to compute the propagation constant. (The scalar wave equation is assumed; thus accuracy is maintained provided  $\Delta$ , the normalized refractive index difference is small). Assuming proper field symmetries are used, this method always yields a propagation constant value lower than the true value. Equality holds when the field distribution is correctly chosen. The error in the calculated propagation constant is second order in the field error, however, for the purposes of calculating any differences between two modes, the error becomes first order in field distribution errors. Thus, for our purposes it is imperative that accurate field distributions are chosen.

We have found that describing the field of the second order mode near to cutoff by the expression

$$E_{11}(x,y) = \frac{x/a}{1+(x/a)^3+(y/b)^3} \quad (1)$$

is very accurate. Here  $a$  and  $b$  are parameters to be adjusted to maximize the calculated propagation constant. Applying this field to the case of a circular core step index fiber yields a cutoff value of  $V = 2.44$ . ( $V$  has its usual meaning and the second order modes are exactly cutoff at 2.405 for circular core fibers). This description of the field is much more accurate than the hermite gaussian approximation near to cutoff. It becomes less accurate than the gaussian approximation at about  $V = 2.9$ .

As an aside we note that using the form for the fundamental mode

$$E_{01}(x,y) = \frac{1}{1+(x/a)^3+(y/b)^3} \quad (2)$$

also yields a much better approximation than the gaussian field distribution for low  $V$  values. Tables 1 and 2 show comparisons between the exact results, the hermite gaussian results and the  $(1+r^3)^{-1}$  results for the first and second order modes of circular core step index fibers. The value of  $U$  is tabulated against  $V$  for easy comparison. ( $U$  has its conventional meaning)

#### Cutoff wavelength predictions

Analysis of the  $(1+r^3)^{-1}$  dependent field yields the following results for the second order modes:

- i) The field ellipse major to minor axis ratio ( $a/b$ ) is approximately the square root of the core ellipse major to minor axis ratio. This result is similar to that predicted by Snyder and Love for the infinite elliptical parabolic refractive index profile[8].
- ii) The cutoff wavelength of the even and odd second order modes are predicted to within 2% accuracy using  $V_{\text{eff}} = 2.4$  independent of fiber core ellipticity (up to 3:1) when  $V_{\text{eff}}$  is defined as

$$V_{\text{eff}} = \frac{4}{3+A/B} V_{\text{circ}} \quad (3)$$

where either *a)*  $A$  and  $B$  are the major and minor axes of the core ellipse and  $V_{\text{circ}}$  is the usual  $V$  number calculated using the major axis of the ellipse as the core diameter or, *b)*  $A$  and  $B$  are the minor and major axes of the core ellipse and  $V_{\text{circ}}$  is calculated using the minor axis of the ellipse as the core diameter. Situation *a)* describes the  $LP_{11}^{\text{even}}$  mode cutoff and situation *b)* describes the  $LP_{11}^{\text{odd}}$  mode cutoff. (The  $LP_{11}^{\text{even}}$  mode is defined to have the longer wavelength cutoff). Equation (3) can also be accurately used to describe the propagation behavior of the second order modes near to cutoff.

Using this derivation for the second order mode cutoffs yields the following formula describing the splitting of the cutoff wavelengths of the second order modes in elliptical core fiber:

$$\frac{\lambda_{\text{cutoff even}}}{\lambda_{\text{cutoff odd}}} = \frac{3A/B+1}{3+A/B} \quad (4)$$

The ratio of the even and odd second mode cutoff wavelengths versus A/B is plotted in figure 1.

Experimental verification of this result consists of two fiber samples. A Polaroid fiber having core ellipse 4.1 x 2.2 microns has a predicted ratio of the cutoff wavelengths of 1.35 and a measured ratio of 1.3[9]. A (Brazilian) Telebras fiber having core ellipse 8 x 3 microns has a predicted ratio of the cutoff wavelengths of 1.59 and a measured ratio of 1.63. The measured values agree with the theoretical values within experimental error (measured cutoff wavelengths and refractive index profile).

### Conclusions

We have reported a simple relation describing the propagation characteristics of the even and odd second order modes near to cutoff in elliptical core fibers and have accurately predicted their cutoff wavelengths. The relation is good enough to also accurately predict the splitting of those cutoff wavelengths. The predicted value of the even second order mode cutoff wavelength closely agrees with the prediction of reference [3] for low values of fiber core ellipticity and with the predictions of references [6], and [7] for high values of fiber core ellipticity.

### References

- [1] C. Yeh, J. Appl. Phys. 33, 3235 (1962)
- [2] C. Yeh, Optical and Quantum Electronics, 8, 43 (1976)
- [3] S. R. Rengarajan and J. E. Lewis, Electron. Lett. 16, 263 (1980)
- [4] K. S. Chiang, Optical and Quantum Electronics, 16, 487 (1984)
- [5] A. W. Snyder and X. Zheng, J. Opt. Soc. Am A, 3, 600 (1986)
- [6] A. Kumar, and R. Varshney, Opt. Lett. 14, 817 (1989)
- [7] J. Shaw, A. Vengsarkar, and R. Claus, Opt. Lett. 16, 135 (1991)
- [8] Snyder and Love, *Optical Waveguide Theory* Chapman and Hall (1983)
- [9] J. Blake, Ph.D. Thesis, Stanford University (1988)

V	$U_{\text{exact}}$	$U_{\text{gaussian}}$	$U_{\text{new}}$
1.2	1.134	1.168	1.156
1.4	1.262	1.293	1.274
1.6	1.367	1.393	1.371
1.8	1.454	1.475	1.457
2.0	1.528	1.545	1.533
2.2	1.591	1.605	1.603
2.4	1.645	1.659	1.665
2.6	1.693	1.706	1.725

V	$U_{\text{exact}}$	$U_{\text{hermite}}$	$U_{\text{new}}$
2.4	2.405	2.492	2.413
2.6	2.535	2.594	2.542
2.8	2.636	2.679	2.662
3.0	2.720	2.752	2.774
3.2	2.788	2.818	2.881
3.4	2.849	2.876	2.983
3.6	2.903	2.929	3.081
3.8	2.952	2.978	3.175

**Table 1**

Comparison of U vs. V for the fundamental mode of a circular core fiber between the exact results, the gaussian field approximation, and our new approximation.

**Table 2**

Comparison of U vs. V for the second order mode of a circular core fiber between the exact results, a hermite gaussian approximation, and our new approximation.

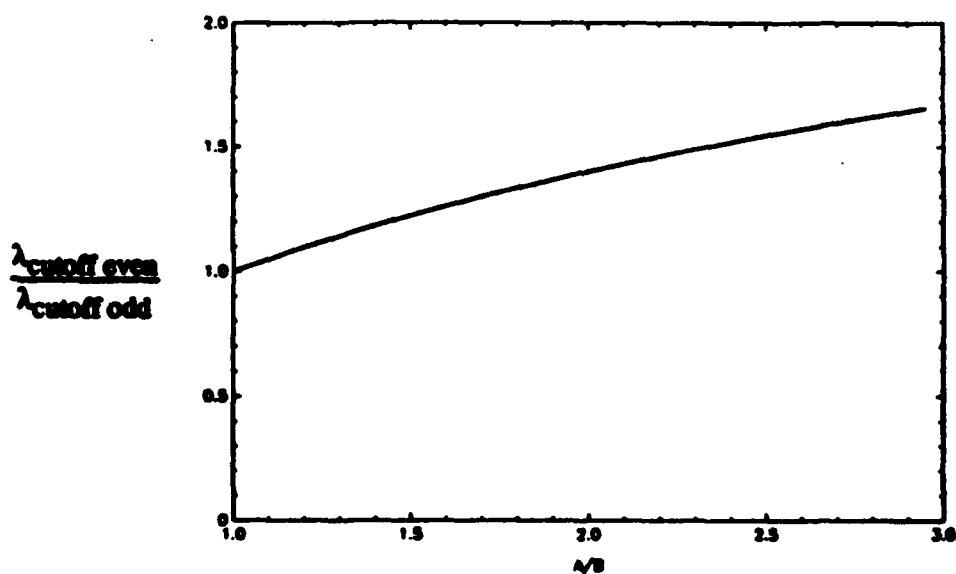


**Figure 1**

Ratio of the even to odd second order mode cutoff wavelengths as a function of the fiber core ellipse aspect ratio.

# P14      Spatially-weighted Vibration Sensors Using Tapered Two-mode Optical Fibers

**Kent A. Murphy, Brian R. Fogg, and Richard O. Claus**

Fiber & Electro-Optics Research Center, Bradley Department of Electrical Engineering  
Virginia Polytechnic Institute and State University, Blacksburg, VA 24061-0111.

**Ashish M. Vengsarkar**

AT&T Bell Laboratories, 600 Mountain Avenue, Murray Hill, NJ 07974

Two-mode elliptical-core (e-core) fibers have been used as efficient vibration sensors when operated in the linear region.<sup>1</sup> Such ruggedized e-core sensors can perform as vibration-mode filters when placed appropriately along the vibration antinodes of the beam.<sup>2</sup> We report the development of distributed modal sensors using optical fiber techniques. The variable sensitivity of the fiber sensors has been achieved by utilizing the feature that the differential propagation constant in a two-mode fiber is directly dependent on the normalized frequency (or, V-number). Tapering the fiber changes the V-number and hence can change the sensitivity of the sensor along its length. We show that these sensors are fiber optic analogs of shaped, piezo-electric modal sensors that have emerged recently in the area of structural control<sup>3</sup> and demonstrate their applications for clamped-free one-dimensional beams.

The fiber sensor operates on the principle of differential phase-modulation between the  $LP_{01}$  and  $LP_{11}^{even}$  modes. The output signal from a two-mode fiber sensor is sinusoidal and can be expressed as

$$I(t) = I_0 + I_m \cos[\phi(t)], \quad (1)$$

where  $\phi$  is the phase difference between the  $LP_{01}$  and the  $LP_{11}^{even}$  modes and can be written as

$$\phi(t) = \int_0^L \Delta\beta(x) \epsilon(x, t) dx, \quad (2)$$

where  $\epsilon$  is the strain experienced by the fiber,  $\Delta\beta$  is the difference in the propagation constants of the  $LP_{01}$  and the  $LP_{11}^{even}$  modes, and  $x$  denotes the longitudinal direction along the fiber axis. In Eq. (2), the explicit dependence of  $\Delta\beta$  on  $x$  implies that the strain sensitivity can be a function of the length along the beam. In order to evaluate the vibration modes of the beam, we express strain as

$$\epsilon(x, t) = \frac{\partial^2 y(x, t)}{\partial x^2}, \quad (3)$$

where  $y(x, t)$  denotes the deflection of the beam away from its equilibrium point. To analyze a sensor fabricated from tapered two-mode fibers, the differential propagation

constant,  $\Delta\beta$ , should now be considered to be an explicit function of  $x$ . Substituting Eq. (3) into (2) and integrating by parts leads to the equation

$$\phi(t) = \eta_n(t) \left( Q(a,b) + \int_a^b \Delta\beta''(x) \psi_n(x) dx \right), \quad (4a)$$

where

$$Q(a,b) = [\Delta\beta(x) \psi'_n(x)]_a^b - [\Delta\beta'(x) \psi_n(x)]_a^b \quad (4b)$$

and the primes indicate spatial derivatives with respect to  $x$ . The key to the weighted sensing approach is that the mode shapes are orthogonal, i.e.,

$$\int_0^L \psi_m(x) \psi_n(x) dx = \delta_{mn}, \quad (5)$$

where  $\delta_{mn}$  is the Kronecker delta and  $L$  is the length of the beam. Comparing Eqs. (4a) and (5) leads one to pick a possible weighting function given by  $\Delta\beta''(x) = \psi_m(x)$ . Except for the contributions of  $Q(a,b)$ ,  $\phi(t)$  would filter out all but the  $m$ th mode for a fiber sensor spanning the entire length of the beam. In Fig. 1 we have considered a taper with the minimum radius of the fiber,  $a_{\min} = 1 \mu\text{m}$  and the maximum radius,  $a_{\max} = 1.15 \mu\text{m}$  with a linear taper over the length of the beam. A direct superposition of the vibration-mode shapes and the  $\Delta\beta''(x)$  function for different taper profiles thus shows good correlation.

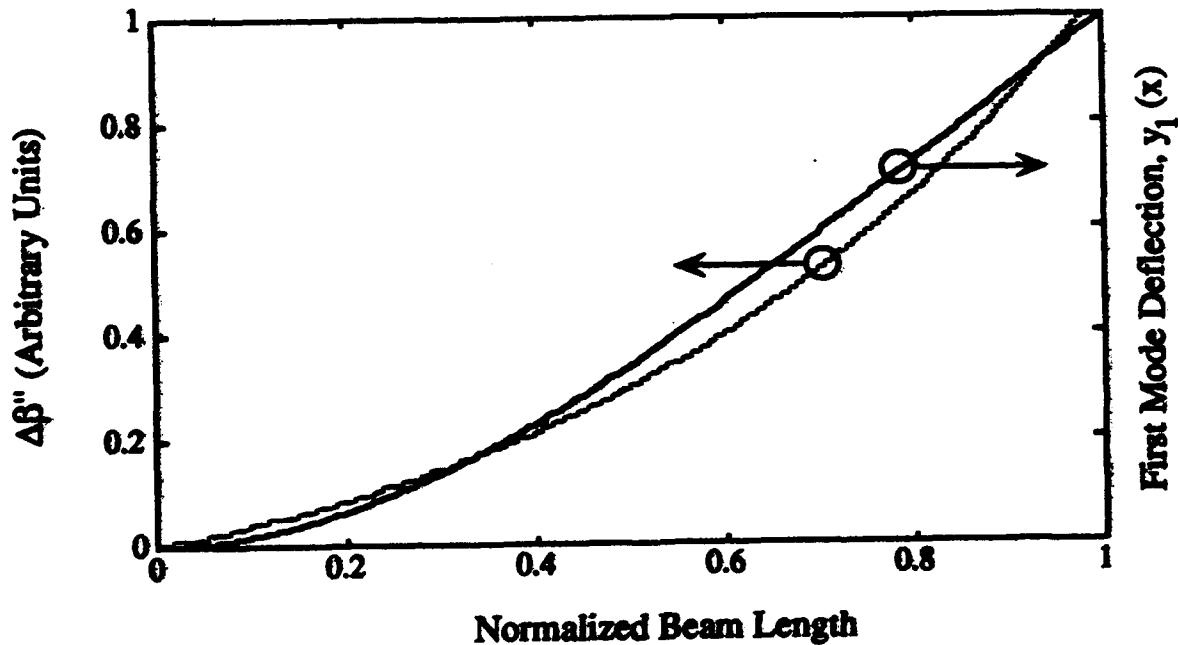


Fig. 1. Superposition of weighting function and first-vibration-mode shape as a function of normalized beam length. Linear fiber taper and a clamped-free beam.  $a_{\min} = 1 \mu\text{m}$ ,  $a_{\max} = 1.15 \mu\text{m}$ . Theoretical values obtained for circular-core fibers.

A conventional e-core sensor was adhered to a clamped-free beam. Output signals from piezo-electric patches attached to the beam were compared to the signals obtained from the fiber sensor. The first three modes of vibration of the beam were excited and the outputs from the fiber optic sensor and the piezo-electric patch were monitored. In Fig. 2 (a), we show a fast Fourier transform (FFT) of an oscilloscope waveform which shows that the sensor enhances the first mode of vibration in comparison with the piezo-electric sensor, and picks up other modes of vibration fairly well, with reduced sensitivities on the order of 2 and 4 dB for the second and third modes, respectively. A weighted fiber sensor with a taper that matches the  $\Delta\beta''(x)$  function to the first mode of the clamped-free beam was fabricated on a draw tower by varying the preform-feed and fiber-pull speeds as well as controlling the temperature of the furnace. The tapers could also be made on a coupler station used conventionally for fabricating fused-biconical-tapered couplers. The weighted fiber was attached to another clamped-free beam between the same endpoints as in the conventional case described above. Results obtained from the weighted fiber sensor are shown in Fig. 2 (b). The FFT's of the fiber sensor and the piezo-electric patch show that the second mode has been suppressed by 7 dB and the third mode by 12 dB in comparison to the piezo-electric sensor output.

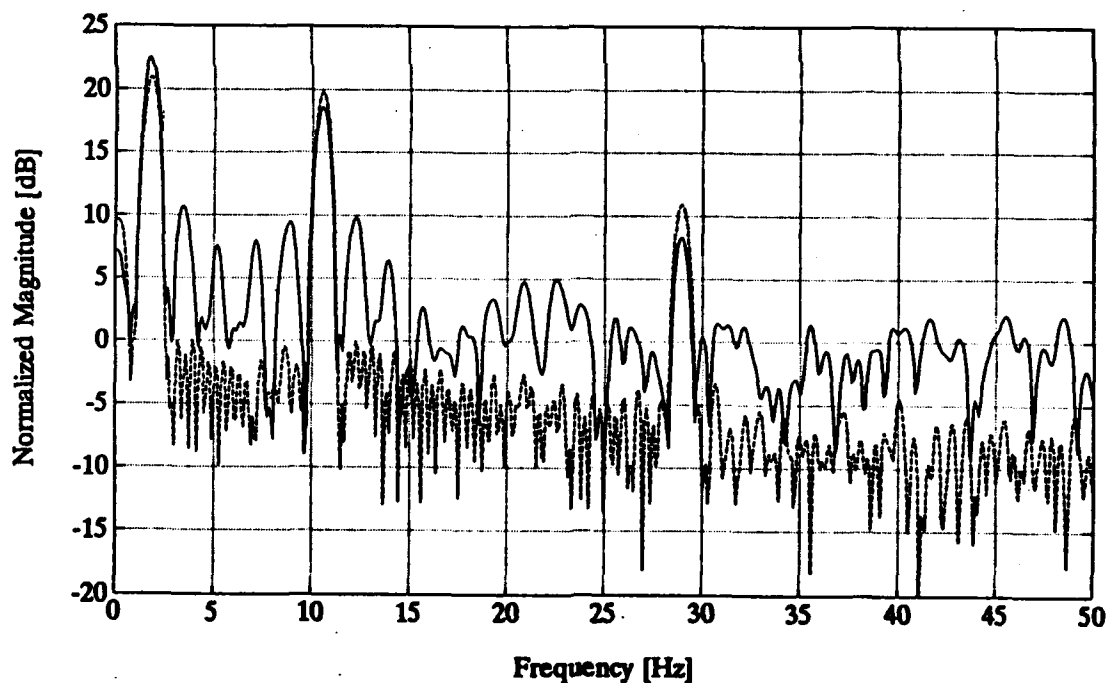


Fig. 2 (a). Fast Fourier transform of output signals for clamped-free beam. Conventional e-core fiber sensor and piezo-electric sensor comparison. Solid line: Fiber sensor. Dotted line: Piezo-electric sensor.

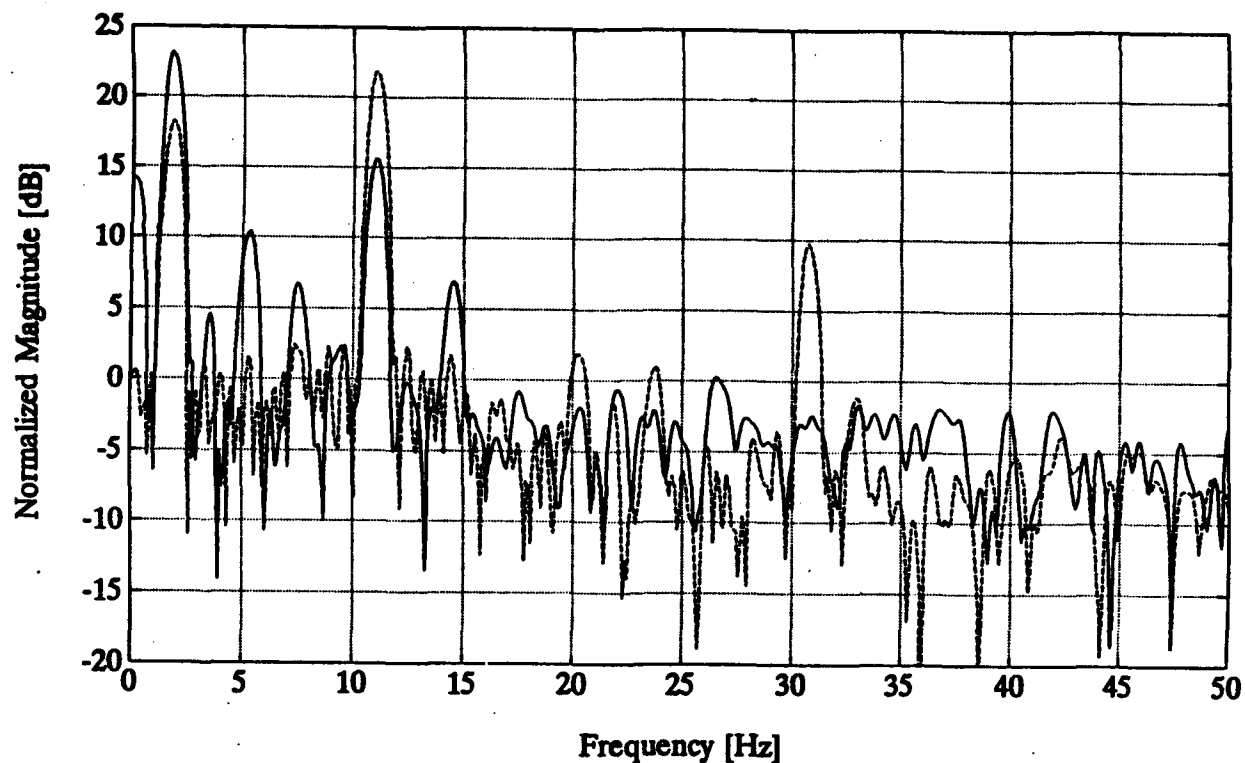


Fig. 2 (b). Fast Fourier transform of output signals for clamped-free beam. Tapered fiber sensor and piezo-electric sensor comparison. Solid line: Fiber sensor. Dotted line: Piezo-electric sensor.

We have demonstrated, for the first time to our knowledge, the use of spatially distributed fiber optic sensors with intrinsic weighting functions for selective vibration modal analysis. Modal suppressions of 7 and 12 dB were obtained for the second and third modes of vibration, respectively, for a clamped-free beam.

## References

1. K. A. Murphy, M. S. Miller, A. M. Vengsarkar, and R. O. Claus, "Elliptical-core, two-mode, optical fiber sensor implementation methods", *J. Lightwave Technol.*, **8**, 1688 - 1696 (1990).
2. A. M. Vengsarkar, B. R. Fogg, W. V. Miller, K. A. Murphy, and R. O. Claus, "Elliptical-core, two-mode optical fibre sensors as vibration mode filters", *Electron. Lett.*, **27**, 931-932 (1991).
3. C. -K. Lee and F. C. Moon, "Modal sensors/actuators", *J. Appl. Mechanics*, **57**, 434 - 441 (1990).



Dr. Dale R. Lutz - Member, IEEE/LEOS  
 3M Company, Fiber Optics Laboratory  
 3M Center, 260-5B-08, St. Paul, MN 55144-1000

**Background:** In a recent paper, Burns and co-workers noted that:

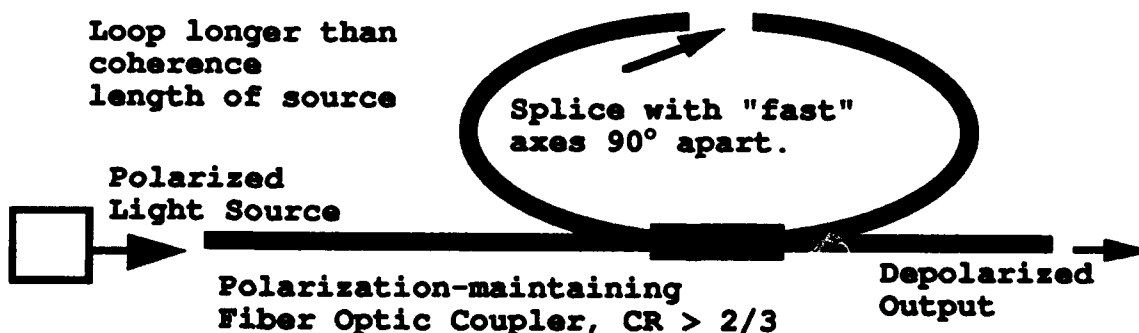
"In many fiber-optic applications, a definite state of optical polarization is required at the end of a long fiber run. This occurs in coherent communications on mixing with a local oscillator and in fiber sensors to avoid input lead polarization noise and polarization fading." One practical way around this problem is "... the use of depolarized light, which will always remain depolarized independent of fiber birefringence."[1.]

This paper describes a simple, passive device for depolarizing light from a polarized source (e.g., a semiconductor laser) in fiber optic sensor systems.

**Theory:** Unpolarized light "shows no preferential directional properties when resolved in different directions at right angles to the direction of propagation."[2.] This is equivalent to having two collinearly-propagating orthogonally polarized beams (e.g., horizontally and vertically linearly polarized light beams) of equal amplitude which add incoherently. That is, the phase shift between their instantaneous electric fields varies randomly and quickly on the timescale of the measurement, so the instantaneous net polarization states at the detector average out or "cancel" over the measurement period.

A passive fiber optic depolarizer based on this principle is shown schematically in Figure 1 below.

**Figure 1 - Depolarizer Concept**



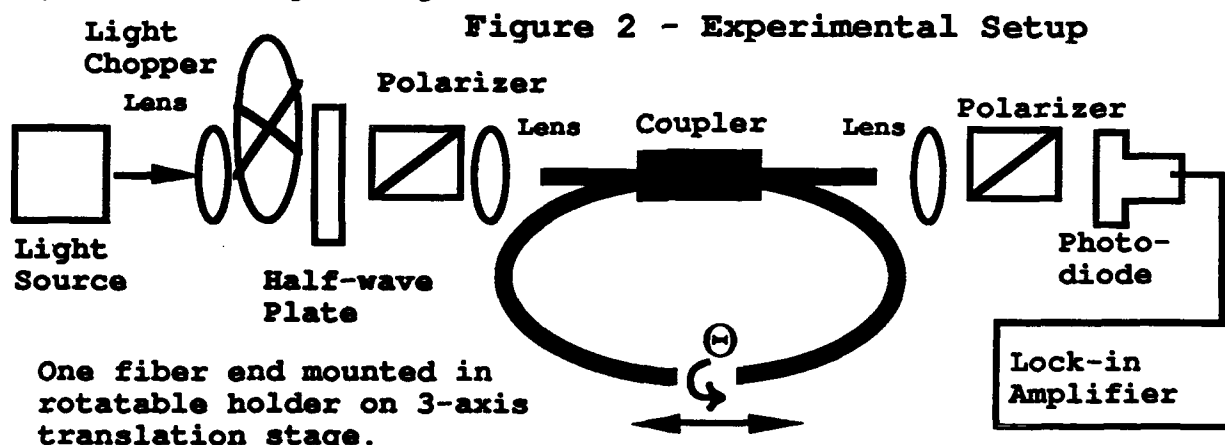
It consists of a polarization maintaining, 2x2 fiber optic coupler (made from high birefringence optical fiber), with an asymmetric splitting of the output light intensities (preferably with a coupling ratio (CR) > 2/3), having one "input" and one "output" fiber lead spliced or connected together such that the "fast" birefringence axes of the two fiber leads are oriented at 90° with respect to each other at the splice point. This splicing will form one

recirculating (i.e., recursive) loop in the optical path. The "output" fiber lead selected to form the loop is the one which gives the greatest light output when light is injected into the chosen "input" port, in order to maximize the amount of light which gets recirculated through the loop. An equation can be derived which shows that for the worst case the net polarization of the output is:

$$\text{net polarization} = (1 - \text{CR}) - (\text{CR})^2 \sum_{m=0}^{\infty} (-1)^m (1 - \text{CR})^m = (2 - 3\text{CR}) / (2 - \text{CR}).$$

The degree of polarization,  $P$ , is the absolute value of the expression above. Solving for net polarization = 0, we find that  $\text{CR} = 2/3 = 0.67$ . This predicts that a polarization-maintaining fiber optic coupler with a 70/30 splitting ratio, assembled as shown above in Figure 1, with low optical loss in the loop, should produce completely depolarized output. When the angle between the two "fast" birefringence axes is less than  $90^\circ$ , a higher coupling ratio into the loop will be required for complete depolarization. This behavior is qualitatively verified in the experimental data given below.

Experiment: To test the effect of varying the coupling ratio and the relative angle of the fiber birefringence axes at the splice point in the loop, the experimental setup in Figure 2 was assembled.



The selected polarization-maintaining coupler had a coupling ratio which varied strongly with wavelength in the region 750 nm - 1000 nm, as shown in Figure 3(a). The four fiber leads of the coupler were each about 1 meter long. One "input" and one "output" lead were brought together such that their cleaved endfaces almost touched, allowing light to be transmitted through air from one fiber into the other, thus forming a recirculating loop path for light which entered the coupler through the other "input" lead. One fiber end was mounted in a rotatable fixture on a translation stage, thereby allowing the relative orientations of the "fast" birefringence axes of the fiber ends to be varied through some arbitrary

angle ( $\Theta$ ) and allowing the loop to be opened and closed by translating one fiber. Rotatable polarizers were placed in the optical path at the input and output of the fiber system, in order to measure the polarization extinction ratio under various test conditions. The light source consisted of an arc lamp, which had a coherence length less than a few millimeters and significantly less than the length of the two 1 m long fiber leads making up the loop. A filter wheel allowed any one of a series of 10 nm bandpass interference filters to be placed immediately before the photodetector, so that only light experiencing a narrow range of coupling ratio values was monitored at a given time. The input light was first aligned with its polarization direction matching one of the birefringence axes of the input fiber by iterating the position of the input and output polarizers, with the loop open and no bandpass filters in the beam, until the input polarizer position yielding the maximum extinction ratio (ratio between the maximum signal and minimum signal obtained when rotating the output polarizer) was found. The extinction ratio was then measured as a function of wavelength, first with the loop open, then at a series of relative orientation angles of the "fast" birefringence axes at the "splice point" with the loop closed. This data is shown in Figure 3(b). The extinction ratio data is presented in terms of decibels (dB), where

$$\text{dB} = 10 \log(\text{extinction ratio}).$$

The open loop data shows that the output light was linearly polarized with an extinction ratio of better than 1000:1 (greater than 30 dB, except at 840 and 850 nm, where weak arc lamp output and system noise limited the dynamic range of the measurement to 28 dB). The series of closed loop measurements shows that the output light is more depolarized at wavelengths which have higher coupling into the loop. They also show that, for a given wavelength (i.e., coupling ratio), as the angle between the "fast" axes at the "splice point" approaches 90°, the output light becomes increasingly depolarized (dB approaches 0) until, for coupling ratios greater than 2/3, the output may pass through a completely depolarized state and become "repolarized" in the orthogonal direction (negative dB value). In this data, the coupling ratio required for complete depolarization is greater than 2/3, primarily due to the large optical loss at the air gap between the optical fiber endfaces at the "splice point".

A similar experimental system to that described above (Figure 2) using a Sharp LTO15MDO laser diode source and a coupler having CR = 0.48 was also studied. Measurements of the Stokes parameters ( $s_0, s_1, s_2, s_3$ ) [2.] with the aid of a Babinet-Soliel compensator [3.] permitted calculation of the degree of polarization (P) [2.], yielding the results below. (Note: Stokes parameter intensity differences are given in terms of photodiode currents, as measured by a lock-in amplifier.)

	$s_0$	$s_1$	$s_2$	$s_3$	$P$
open loop	4.63 nA	-4.59 nA	0.040 nA	0.350 nA	0.986
closed loop	8.45 nA	-5.07 nA	0.070 nA	0.300 nA	0.601

Thus, closing the loop reduced the degree of polarization of the output from 99% to 60% for this relative orientation of the birefringence axes of the loop fibers.

Figure 3(a) - Open-Loop Transmitted Light Fraction (1 - CR) vs. Wavelength

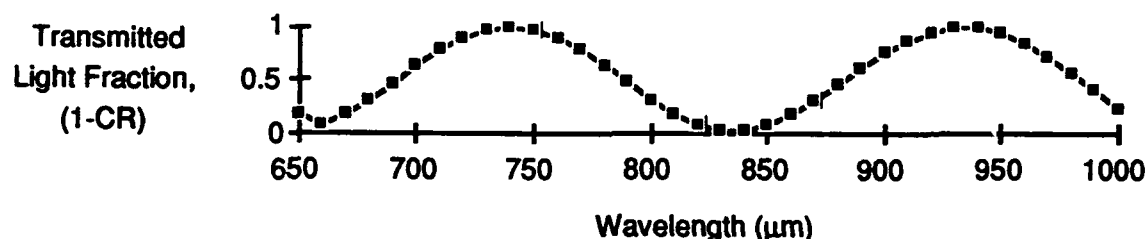
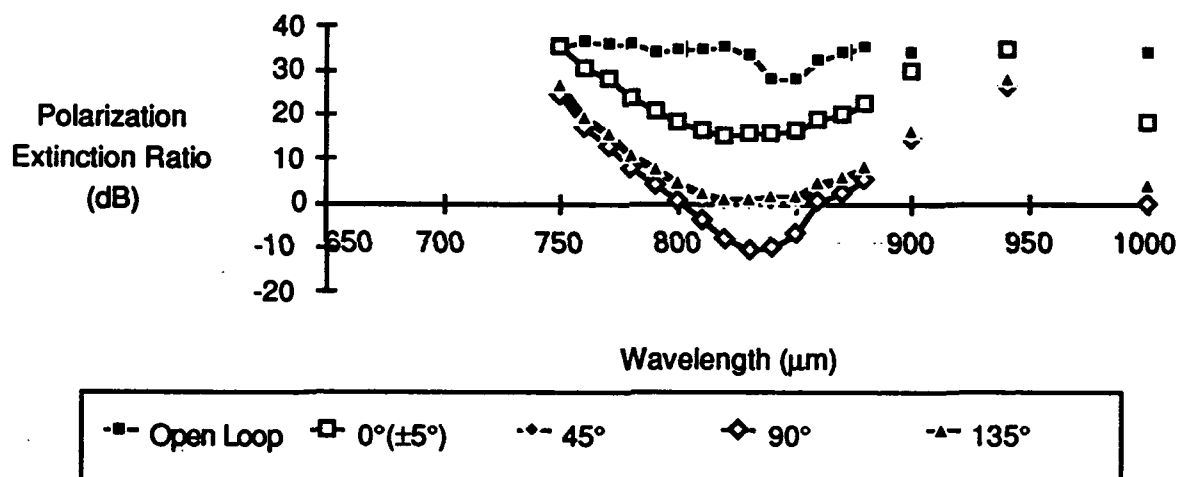


Figure 3(b) - Polarization vs. Relative Angle of Birefringence Axes



**Acknowledgements:** The author would like to thank J. R. Onstott for suggestions on the experimental setup, R. E. Budewitz for assistance in performing the measurements, and G. R. Olson and B. K. Nelson for making and characterizing the couplers.

#### References:

1. W. K. Burns et al., "Depolarized Source for Fiber-optic Applications", Opt. Lett., vol. 16, 381 (1991).
2. M. Born and E. Wolf, Principles of Optics, Third (Revised) Edition, Pergamon Press, 544-555 (1965).
3. E. Hecht, Optics, Second Edition, Addison-Wesley Publishing Company, Inc., 304 (1987).

# P16 High Performance Polarization Maintaining Optical Fiber Couplers

Eisuke SASAOKA , Hiroshi SUGANUMA , Masahiro TAKAGI

SUMITOMO ELECTRIC INDUSTRIES, Ltd.

1, Taya-cho, Sakae-ku, Yokohama, 244 Japan

## 1. Introduction

Polarization maintaining optical fiber couplers (PM couplers) are indispensable components for optical fiber sensors and coherent optical communication systems. There are two coupler fabrication methods. One is a polishing method and the other is a fusion elongation method. The polishing method has advantages in excess loss and crosstalk, but has some problems in mechanical and thermal stability<sup>(1)</sup>. As for the fusion elongation method, low loss was hard to achieve consistently without special treatments<sup>(2)</sup>. An improved fabrication condition realizes PM couplers which maintain low excess loss (about 0.1dB) and low crosstalk (less than -20dB), even in harsh conditions.

## 2. Coupler fabrication

The optical fiber used for coupler fabrication is PANDA type PM fiber for 0.85 $\mu$ m wavelength range, characteristics of the fiber are shown in Table 1. Birefringent axes of two fibers were aligned parallel before fusion and the fusion condition was optimized to achieve low excess loss. Couplers were elongated until the monitored splitting ratio reached 50%. After elongation, couplers were packaged into 3x3x50mm silica glass cases. The photograph of a packaged PM coupler is shown in Fig.1. A bonding method and materials were carefully selected so as not to induce anisotropic stress to bare fibers and cause crosstalk degradation.

## 3. Coupler characteristics

Coupler characteristics were evaluated using a LED light source whose center wavelength was 839nm and whose polarization direction was matched to an X-axis of the fiber. Characteristics of a typical coupler are listed in Table 2. Low loss of 0.08dB

and low crosstalk of -29.5/25.3dB(through/ splitting ports) were obtained. Low loss and low crosstalk couplers are highly reproducible. After the fabrication of 20 couplers, the excess loss mean value was 0.09dB and the mean value of crosstalk was -25.2/22.1dB(through/splitting ports). Stability of the coupler characteristics against temperature change from -40 to +70 centigrade was confirmed. Fig.2 shows splitting ratio and excess loss stability against temperature change. The maximum splitting ratio fluctuation was 0.8% and the maximum excess loss was 0.18dB, both of which are sufficiently low. Fig.3 shows crosstalk dependence on temperature. Sufficiently low crosstalk of -22dB, even at -40 centigrade, was confirmed. Following the temperature test, a humidification test and a vibration test were conducted for the coupler. In the four days of humidification testing, the coupler was placed in a chamber of 95% relative humidity and 60 centigrade temperature. The vibration test was conducted in a constant acceleration condition. During the test, acceleration was kept at 3G and frequency was swept from 15 to 50Hz. Vibration was applied to the coupler for 4 hours in each of three orthogonal directions. After these tests, no significant change of characteristics was observed.

#### 4. Conclusion

PM couplers with low excess loss and low crosstalk were fabricated with an optimized fusion elongation method. Their reliability in harsh conditions was confirmed.

#### References

- (1) J.NODA , K.OKAMOTO , Y.SASAKI , "Polarization-Maintaining Fibers and Their Applications" , J.Lightwave Tech.,vol.LT-4 pp1071-1089 , 1986
- (2) I.YOKOHAMA , K.CHIDA , J.NODO , "Low excess loss conditions of polarization-maintaining fiber couplers" , Appl.Opt. vol.27,No.23 , pp4807-4813 , 1988

**Table 1. Characteristics of the PM fiber for coupler fabrication**

refractive index difference	0.34%
core diameter	5.9 $\mu$ m
clad diameter	124.4 $\mu$ m
cutoff wavelength	0.82 $\mu$ m
crosstalk(2m long fiber)	-45.0dB

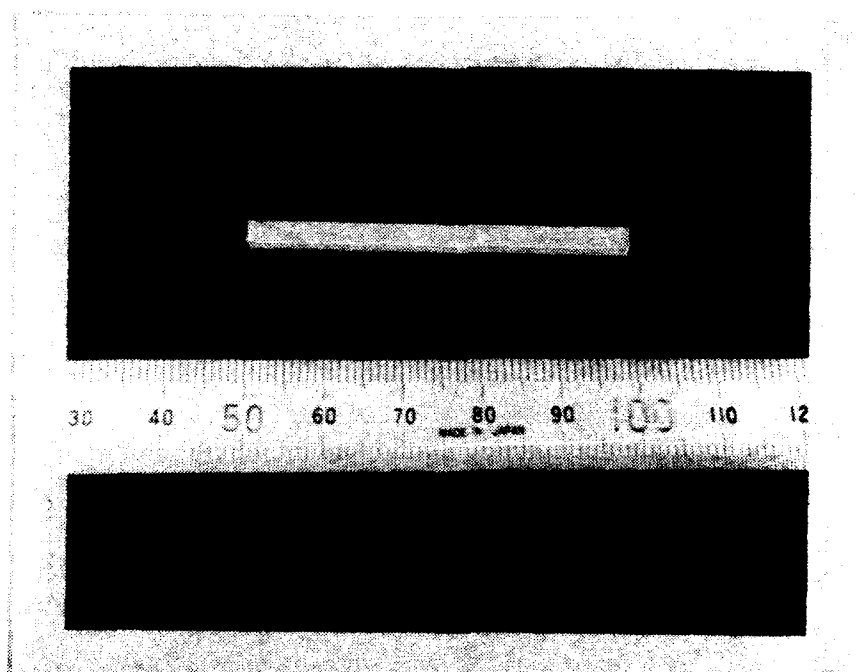


**Fig.1. Photograph of a packaged PM coupler**

**Table 2. Characteristics of typical coupler**

splitting ratio		50.6%
excess loss		0.08dB
crosstalk	(through port)	-29.5dB
	(splitting port)	-25.3dB

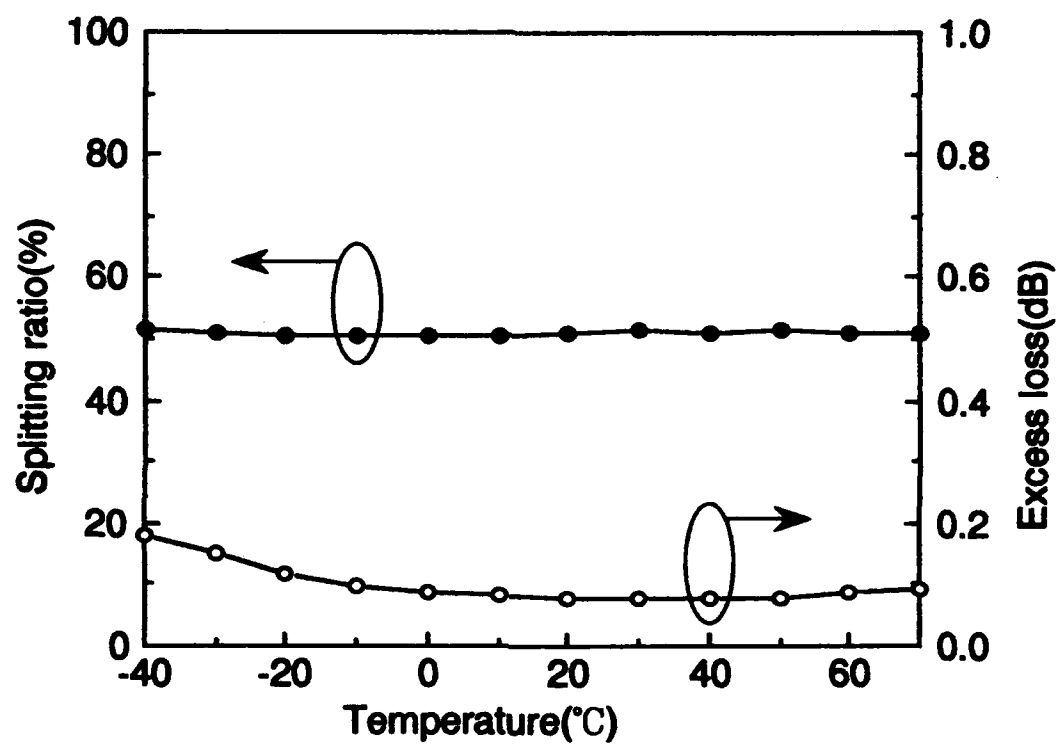


Fig.2. Temperature characteristics  
(Splitting ratio and Excess loss)

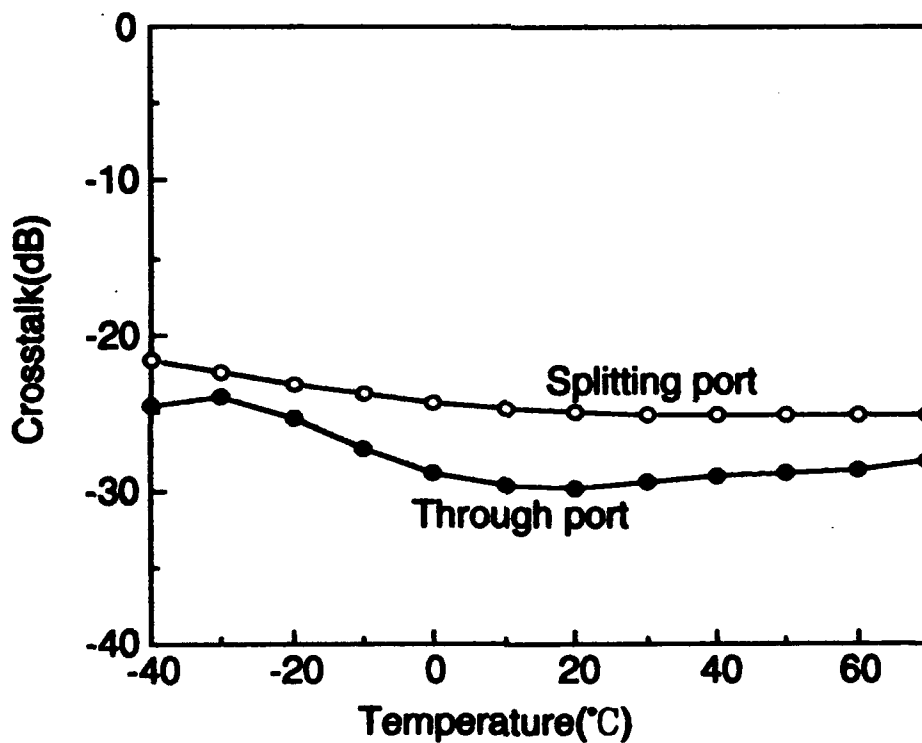


Fig.3. Temperature characteristics  
(Crosstalk)



## P17 Statistical Properties Of Fiber-Birefringence Models

A. D. Kersey, M. A. Davis and M. J. Marrone

Optical Sciences Division, Code 6574  
Naval Research Laboratory  
Washington, DC, 20375  
U.S.A.

### Abstract

We report the results of an experimental investigation of the statistical nature of the parameters of three different models which can be used to describe the lumped birefringence effects and polarization evolution in fiber systems.

**Introduction:** The evolution of polarization in single mode fiber systems is important in many applications, including coherent communications, and interferometric sensors. Two-beam interferometric fiber sensors experience polarization-induced fading (PIF) of the interference signal when the states of polarization (SOP) of the two beams at the point of recombination become orthogonal [1]. Recently, we investigated the probability functions associated with polarization induced fading effects in fiber interferometers. This information is useful for determining the necessity for polarization control and diversity detection techniques in various sensor systems, particularly where arrays of sensors are of interest. In this paper, we report the results of a continued investigation of the statistical nature of models which can be used to describe birefringence in fiber systems. We confirm by direct polarimetric measurements the probability functions for an elliptical birefringence description of a fiber link under random perturbation inferred in a previous publication [2]. The work presented here provides a more complete interpretation of the birefringence models used.

**Birefringence Models:** When conventional low birefringence fiber is used in the sensing element of an interferometer, randomly distributed bends, kinks and twists combined with fiber coils lead to a complex concatenation of birefringence effects which can vary in an unpredictable way with environmental perturbations of the system. In order to analyze the net SOP changes in such a system, two models are commonly used; a) a single elliptical birefringence element [3], and b) a combination of linear retarder and rotator [4], as shown in Figure 1.a and 1.b. respectively. These models have proved useful in describing polarization changes in fiber optic sensor systems, particularly interferometric sensors, fiber gyroscopes, polarimetric sensors and Faraday rotation sensors. A third model comprising three fixed operators; linear retarders with azimuths  $0^\circ$  and  $45^\circ$ , followed by a rotator (Figure 1.c.) can also be utilized to describe the net SOP evolution through an arbitrary fiber length. This model is interesting, as it is most simple to computationally model; the three birefringent components are described by three mutually orthogonal rotational operators in the Poincare sphere [5] representation of polarized light. It should be noted that in all cases the models reduce to a three angle-parameter description of the equivalent birefringence.

In order to model the variation of SOP in fiber optic systems such as interferometric sensors, and in particular multiplexed arrays, it is useful to understand the statistical properties of the birefringence models described above. We have experimentally studied the statistical behavior of the parameters involved in each of these models using polarimetric determination of changes in SOP. We assume monochromatic source light, and fiber lengths short enough to

lead to minimal polarization mode group delay effects, as is generally the case in sensor systems where fiber length are  $< 100$  m. For a given length of fiber, environmental perturbation of randomly distributed birefringence effects along the fiber result in an output SOP which varies randomly; in the Poincare sphere representation of polarized light this can be modeled by a random SOP on the surface of the sphere, with all states having equal probability. It can be shown that this translates into probability density functions for the Stokes parameters of the output SOP,  $S_1$ ,  $S_2$  and  $S_3$ , being uniform over the interval  $-1 \leq S_j \leq +1$ .

**Experimental:** Measurements of the polarization evolution in a length of fiber were made using a simple polarimetric system which allowed the Stokes vectors of the output light to be measured for three input SOPs; horizontal linear,  $45^\circ$  linear, and left circularly polarized, corresponding to the input vectors  $\{S_1, S_2, S_3\}$ ;  $\{1, 0, 0\}$ ,  $\{0, 1, 0\}$  and  $\{0, 0, 1\}$  respectively. The nine measurements fully characterise the net polarization change through the fiber, and can be used to infer the three parameters of any of the above birefringence models used to describe the fiber. In order to vary the birefringence properties of the fiber, multiple fiber fractional waveplates (FFWP) [6] were incorporated along its length. Other bends, loops and coils of differing diameters were also randomly located along the fiber to provide further randomization of the birefringences. Measurements were made using PC data acquisition, which recorded all the measurements, calculated the birefringence parameters and reduced the data to yield probability distributions. The experiments involved 1000 complete sets of measurements of a given fiber. The results reported here were obtained using an approximately 50 m length of fiber. Measurements have also been conducted using a shorter length of fiber, and showed the same distribution functions as for the longer length.

**Results:** Figure 2 shows the distribution in the output Stokes vectors  $S_1$ ,  $S_2$ , and  $S_3$  (for a particular input SOP) for 1000 random variations of the FFWPs distributed along the fiber. The clearly observable uniform distribution of each vector over the  $-1$  -  $+1$  interval indicates the output SOP generated was a randomly varying state, with all states having equal probability. Figures 3 - 5 show the distribution functions of the three birefringence parameters associated with each of the three models shown in Figure 1. Figure 3.a-c shows the single elliptical birefringent element parameters. As shown in Figure 1, the angles  $2\psi$  and  $2\alpha$  represent the spherical coordinates of the operator in the Poincare sphere representation, whereas  $\Omega$  is the magnitude of the vector, or the retardance of the elliptical element. As can be seen, the results show a uniform distribution in  $2\psi$  (longitude), and a  $\cos(2\alpha)$  form of distribution in  $2\alpha$  (latitude). It can be shown that this combination of probability density functions give rise to a random eigenstate of the elliptical retarder which has an equal probability for all states over the surface of the sphere. The measured distribution in  $\Omega$  (Fig. 3.c) exhibits a form which fits a  $\sin^2(\Omega/2)$  dependent probability density function. This result was previously observed from data inferred from measurements of the visibility of a fiber interferometer using depolarized input light [2]. The results shown in Figure 3.c validates this prior work using direct polarimetric measurement. Figures 4.a - c, and 5.a - c show the distributions in the parameters associated with the two-element and three-element models respectively. Fig 4.a, shows a uniform distribution in  $2\theta$ , which describes the azimuth of the linear retarder, whereas the retardance,  $\delta$ , exhibits a  $\sin(\delta)$  dependent distribution. The circularly birefringent element, or rotator magnitude  $\rho$  is characterized by a uniform distribution. Finally, the three-element model of Fig. 1.c produces distributions two of which are uniform ( $\beta_1$  and  $\beta_3$ ) and one which is characterized by a  $\cos \beta_2$  form, as shown in Figure 5.a-c. Computer simulations of each model have been carried out using the probability density functions for each of the parameters as shown in Figures 3-5, and confirm the experimental results obtained.

**Conclusions:** The results of an experimental investigation of the statistical nature of the parameters of birefringence models which can be used to describe conventional low birefringence optical fiber subjected to random perturbation has been presented. The results obtained are useful for modeling, characterizing and predicting the polarization-related behavior of fiber sensor systems based on low-birefringence fiber.

This work is supported by the U.S. Office of Naval Technology.

### References:

1. D. W. Stowe, D. R. Moore and R. G. Priest, "Polarization fading in fiber interferometric sensors," J. Quantum Electron., QE-18, p.1644, 1982.
2. A. D. Kersey, M. J. Marrone and M. A. Davis, "Statistical Modeling of Polarization Induced Fading in Interferometric Fiber Sensors", Electron Lett., 27, p. 481, 1991.
3. A. D. Kersey, M.J. Marrone, A. Dandridge and A.B. Tveten, "Optimization and stabilization of visibility in interferometric fiber sensors using input polarization control", J. Lightwave Technol. 6, p. 1599, 1988.
4. A. J. Rogers, "Polarization properties of monomode optical fibers: The use of P.O.T.D.R to determine spatial distributions", Fiber Optic Rotation Sensors, Ed. Ezekiel and Arditty, p. 208, 1982 (Springer-Verlag)
5. M. Johnson, "Poincare sphere representation of birefringent networks," Appl. Optics, 20, p. 2075, 1982.
6. H. C. Lefevre, "Single-mode fibre fractional wave devices and polarization controllers," Electron. Lett., 16, p. 778, 1980.

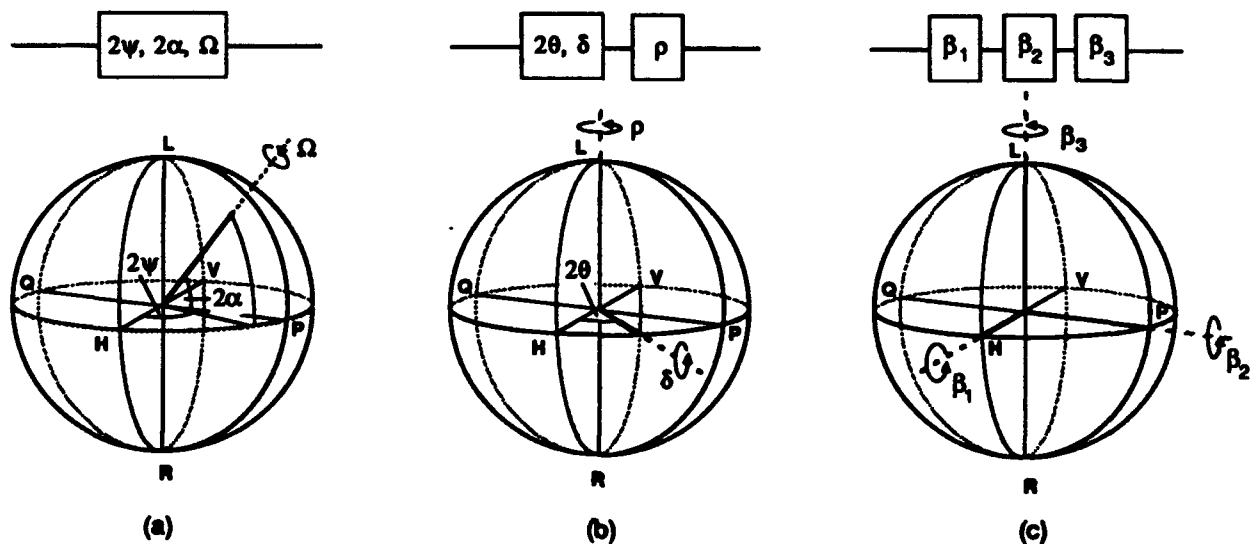


**Figure 1. Birefringence models: (a) single elliptical element, (b) linear retarder and rotator, and (c) three fixed elements.**

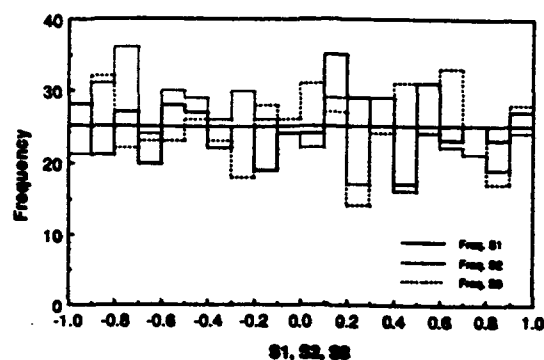


**Figure 2.** Experimentally observed distributions in the Stokes vectors  $S_1$ ,  $S_2$  &  $S_3$   
( $S_j \rightarrow S_j + \Delta S_j$  with  $\Delta S_j = 0.1$  for  $S_j = -1$  to  $0.9$ )

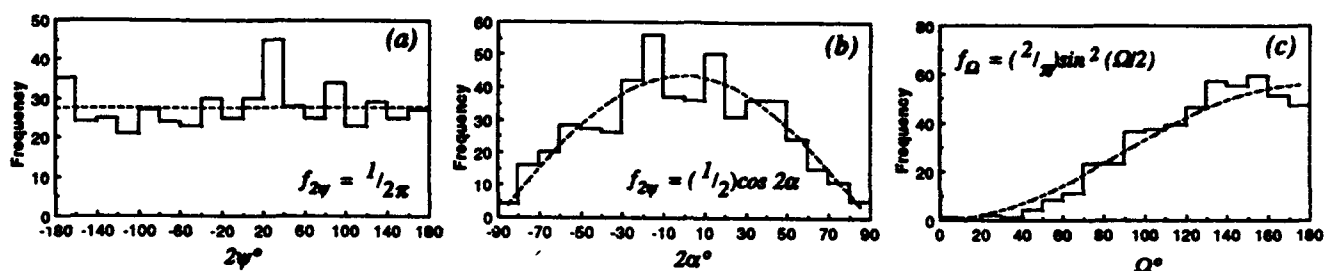


**Figure 3** Experimentally observed distributions in the single elliptical element parameters:  
(a)  $2\psi$  ( $2\psi \rightarrow 2\psi + \Delta 2\psi$  with  $\Delta 2\psi = 20^\circ$  for  $2\psi = -180$  to  $170^\circ$ )  
(b)  $2\alpha$  ( $2\alpha \rightarrow 2\alpha + \Delta 2\alpha$  with  $\Delta 2\alpha = 10^\circ$  for  $2\alpha = -90$  to  $80^\circ$ )  
(c)  $\Omega$  ( $\Omega \rightarrow \Omega + \Delta\Omega$  with  $\Delta\Omega = 10^\circ$  for  $\Omega = 0$  to  $170^\circ$ )

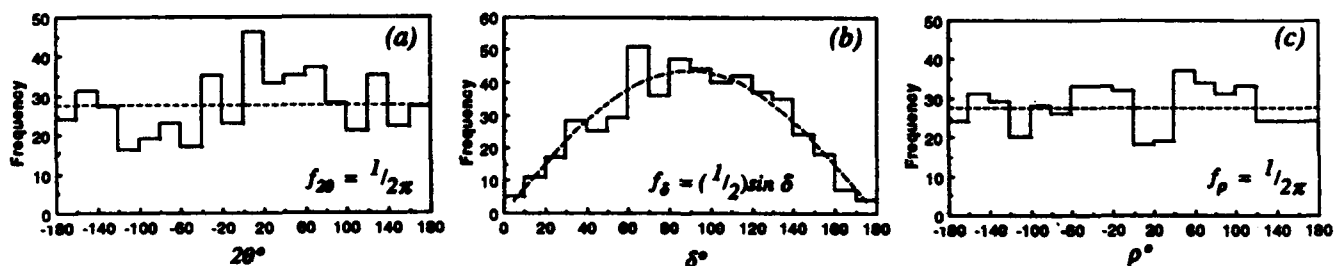


**Figure 4** Experimentally observed distributions in the linear retarder/rotator model parameters:  
(a)  $2\theta$  ( $2\theta \rightarrow 2\theta + \Delta 2\theta$  with  $\Delta 2\theta = 20^\circ$  for  $2\theta = -180$  to  $170^\circ$ )  
(b)  $\delta$  ( $\delta \rightarrow \delta + \Delta\delta$  with  $\Delta\delta = 10^\circ$  for  $\delta = 0$  to  $170^\circ$ )  
(c)  $\rho$  ( $\rho \rightarrow \rho + \Delta\rho$  with  $\Delta\rho = 20^\circ$  for  $\rho = -180$  to  $170^\circ$ )

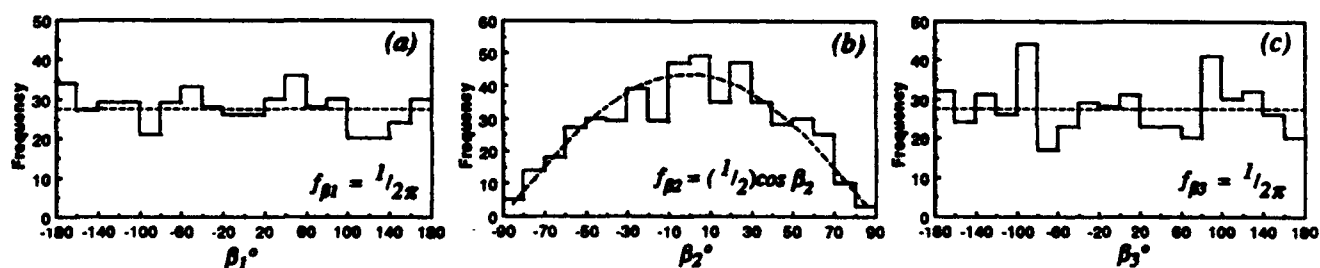


**Figure 5** Experimentally observed distributions in the three-element model parameters:  
(a)  $\beta_1$  ( $\beta_1 \rightarrow \beta_1 + \Delta\beta_1$  with  $\Delta\beta_1 = 20^\circ$  for  $\beta_1 = -180$  to  $170^\circ$ )  
(b)  $\beta_2$  ( $\beta_2 \rightarrow \beta_2 + \Delta\beta_2$  with  $\Delta\beta_2 = 10^\circ$  for  $\beta_2 = 0$  to  $170^\circ$ )  
(c)  $\beta_3$  ( $\beta_3 \rightarrow \beta_3 + \Delta\beta_3$  with  $\Delta\beta_3 = 20^\circ$  for  $\beta_3 = -180$  to  $170^\circ$ )

## In-line Polarization Controller Based Upon A Recirculating Fiber Delay Line

B. A. Ferguson and C. L. Chen  
School of Electrical Engineering  
Purdue University  
West Lafayette, IN 47907-1285

### I. Introduction

Many single-mode fiber coherent communication and sensing systems find a need for polarization control either for increased performance or for signal processing. In the past, most systems achieved polarization control either through in-line fractional wave polarization controllers or through the use of bulk optic polarization components [1]. In this work, we present a new approach to in-line polarization control through the use of a recirculating fiber delay line (RDL) system. The proposed device is less bulky than comparable fractional wave devices and shows potential for integrated optic implementation. It has the added advantage of having considerable polarization effect controllability, and thus its use may extend beyond simple polarization state azimuth control. The theoretical development for this system is contained elsewhere [2]; in this presentation we will concentrate on the experimental confirmation of its operation as a polarization rotator.

### II. Theoretical Considerations

We model the transfer matrix of a recirculating delay line system to reflect the transmission and coupling of two polarization states of the optical fiber in the usual fashion. The system is described by a Jones matrix,  $H$ , for the system. The matrix  $H$  is dependent upon the operating parameters of the system, including the splice misalignment angle  $\theta_s$ , birefringence delays  $d_1$  and  $d_2$ , and feedback phase delay  $\beta L$ , as well as the directional coupler intensity coupling coefficient  $\kappa^2$ , as well as loss in the coupler and splice (See Figure 1).

If we adjust the birefringence delays  $d_1$  and  $d_2$  such that the  $d_1 \pm d_2$  are even integer multiples of  $\pi$ , the eigenmodes of  $H$  become circularly polarized fields [2, 3]. The eigenvalues are of unit magnitude and are represented as  $\exp(j\rho_1)$ ,  $\exp(j\rho_2)$ . Since a linearly polarized field may be decomposed into circularly polarized fields, this suggests that, given linearly polarized input light, the output would remain linearly polarized, although rotated. For a linearly polarized input, oriented at an angle  $\theta_{in}$  with respect to the  $x$  axis, the output of the system with circularly polarized eigenmodes is a linearly polarized field oriented at an angle  $\theta_{out} = \theta_{in} - (\rho_1 - \rho_2)/2$ . Thus, the polarization has been rotated by an amount dependent upon the splice misalignment angle  $\theta_s$ , the directional coupler intensity coupling coefficient  $\kappa^2$ , and the phase delay  $\beta L$ . For a fixed system,  $\theta_{out}$  may be varied by varying  $\beta L$ .

### III. Experimental Study

The experimental setup is diagramed in Figure 1. The system studied experimentally is characterized by  $\kappa^2 = 0.66$  and  $\theta_s = 30^\circ$ . Normal, unadjusted operation results in the presence of two resonances in the output curve, due to the excitation of both of the undetermined orthogonal eigenmodes by a generic input. Using circularly polarized input light, the birefringence delays  $d_1$  and  $d_2$  are adjusted until a single resonance is displayed, thus indicating truly single resonance operation on a circularly polarized eigenmode. This is displayed in Figure 2b, where the experimental output intensity is displayed as a function of the feedback length  $\beta L$ . Two orthogonal polarization signals, obtained through the use of a polarizing beamsplitter, are displayed in

this figure. Figure 2a displays the simulated output for this situation. The input is then switched to linearly polarized light and measurements are made of the output visibility and polarization orientation relative to some starting value. For linearly polarized input and the RDL adjusted for circularly polarized eigenmodes, it is expected that both counter-revolving circularly polarized eigenmodes will be excited, thus resulting in two resonances in the output curves due to the different eigenvalues (total propagation delays) of the two system eigenmodes. The output of the system for linearly polarized input is displayed in Figure 3b. The simulated output is shown in Figure 3a. Two resonances are clearly visible in each of these figures. An inspection of Figure 3b reveals that the orientation of the linearly polarized light is rotated as  $\beta L$  is varied. From the relative intensities of the two channels, it is possible to infer a polarization rotation of approximately 35 degrees as  $\beta L$  is rotated. The low amount of rotation is believed to be due to excessive loss, especially at the splice. Computer simulations indicate that very low loss systems may be expected to allow over 90 degrees rotation as  $\beta L$  is varied.

As a test of the polarization preserving properties of this system, the output polarization angle and visibility of the system are measured as a function of input polarization angle. The result is shown in Figure 4. These measurements were made at a setting on the curve of Figure 3a corresponding to  $\beta L = \pi / 2$ . Note that the output orientation angle tracks the input angle, and that the visibility (determined with an analyzer) is always greater than 0.95. This indicates that the system functions as a polarization preserver and its performance is independent of  $\theta_{in}$ .

#### IV. Conclusions

A new in-line polarization controller utilizing feedback is proposed and demonstrated. The use of a recirculating delay line with a splice in the feedback loop is shown to have considerable promise as a polarization control device. The control of the eigenmode structure of such a system is demonstrated, as is its use as a polarization rotator. A version of this device can be envisioned with electro-optic birefringence control sections replacing the mechanical squeezers and PZT fiber stretchers, thus indicating promise for electro-optic implementation.

#### Acknowledgements

This work has been supported by a grant from the Indiana Corporation for Science and Technology, and by the AT&T Bell Laboratories Foundation.

#### References

1. H. C. Lefevre, "Single-mode Fibre Fractional Wave Devices and Polarisation Controllers," *Electronics Letters*, vol. 16 n20, pp. 778-780, September, 1980.
2. B. A. Ferguson and C. L. Chen, "Polarization Effect Controllability in Recirculating Delay Line Systems," *submitted to Applied Optics*.
3. Z. K. Ioannides, R. Kadiwar, and I. P. Giles, "Polarization Mode Coupling in Highly Birefringent Optical-Fiber Ring Resonators," *Optics Letters*, vol. 14 n10, pp. 520-522, May, 1989.

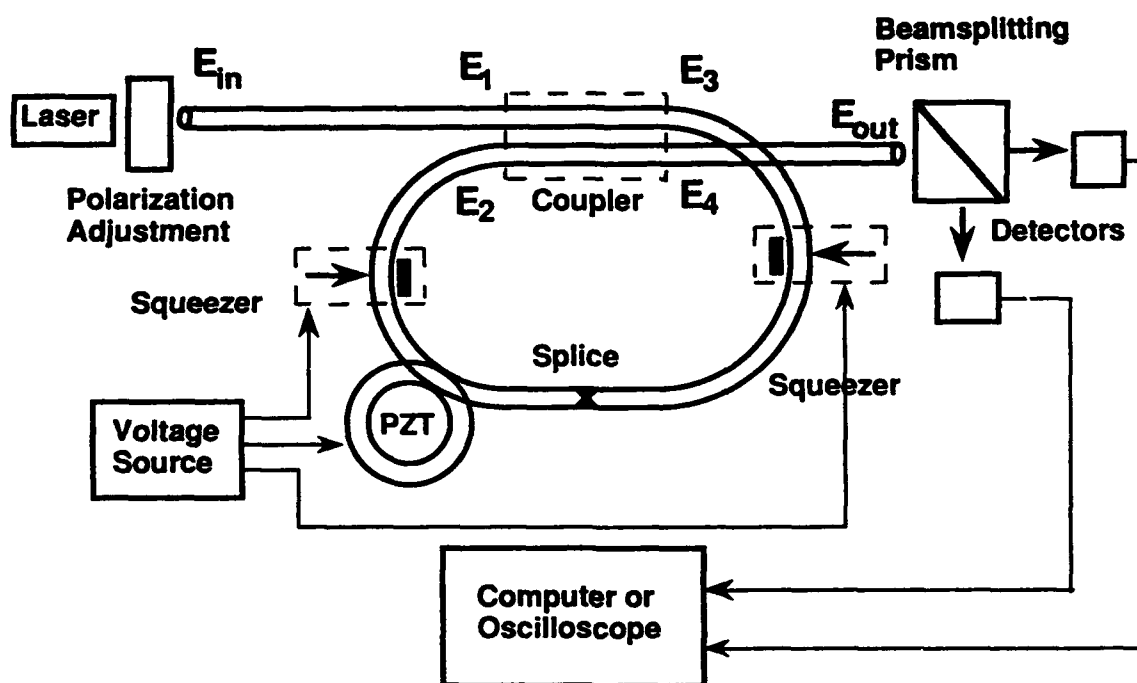
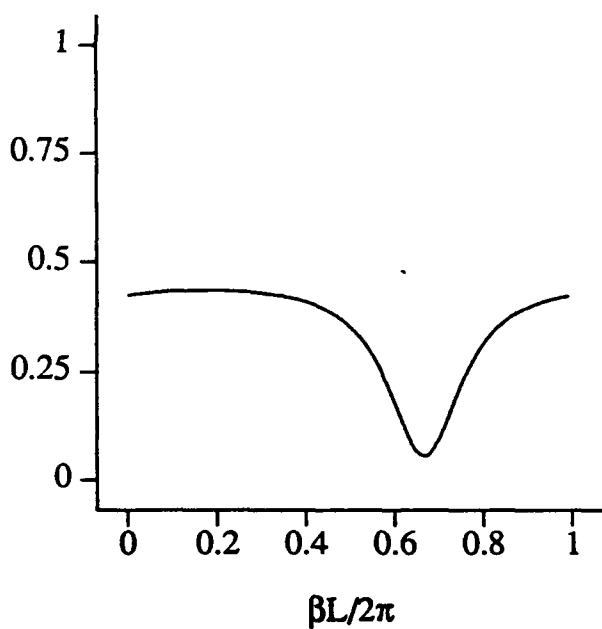
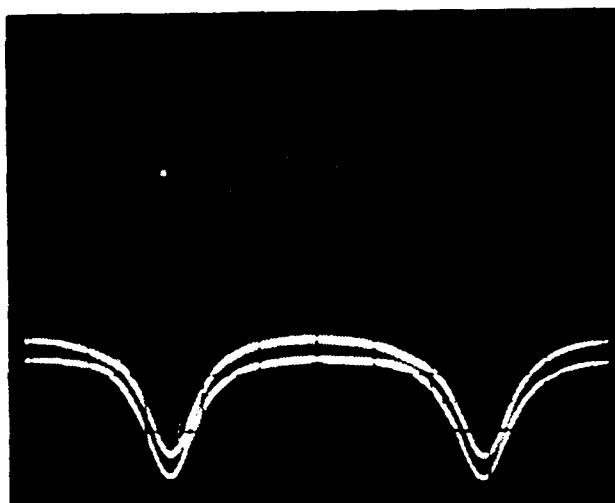


Figure 1. Schematic of the fiber polarization control system under study.



(a)



(b)

Figure 2. Output of system adjusted for circular eigenmodes given circularly polarized input light: a) simulation result (2 curves superimposed) b) experimental result.

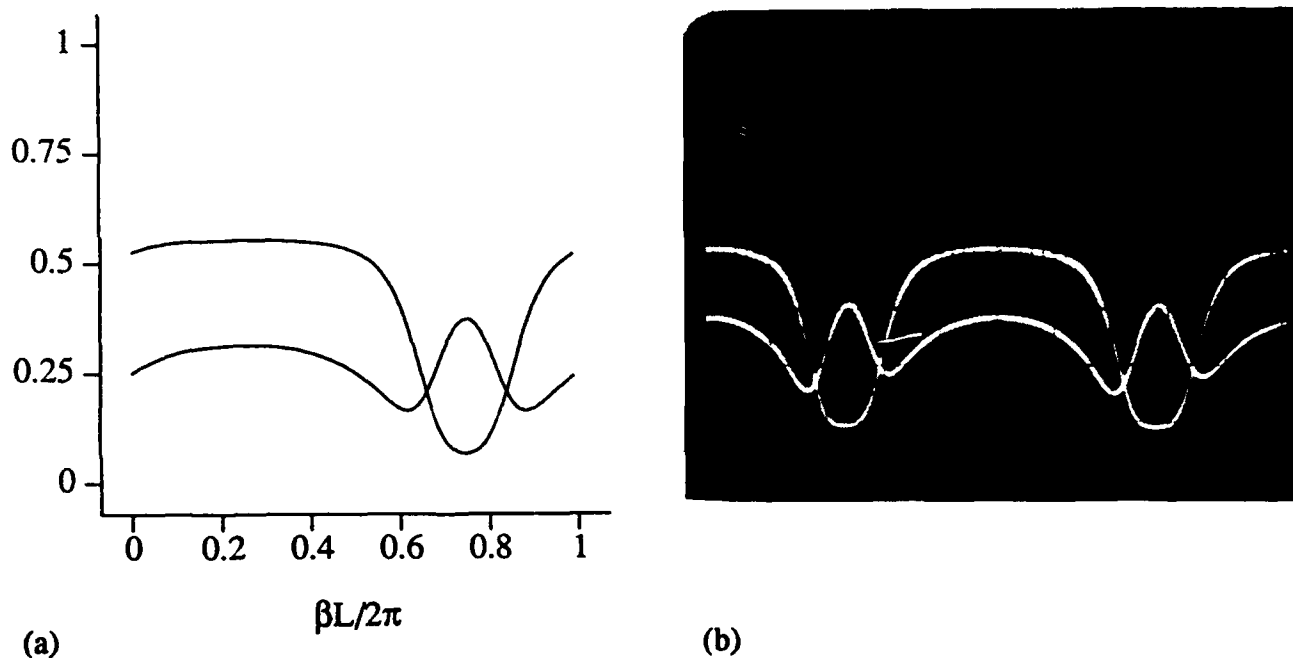


Figure 3. Output of system adjusted for circular eigenmodes given linearly polarized input light at  $\theta_{in} = 40^\circ$ : a) simulation result b) experimental result.

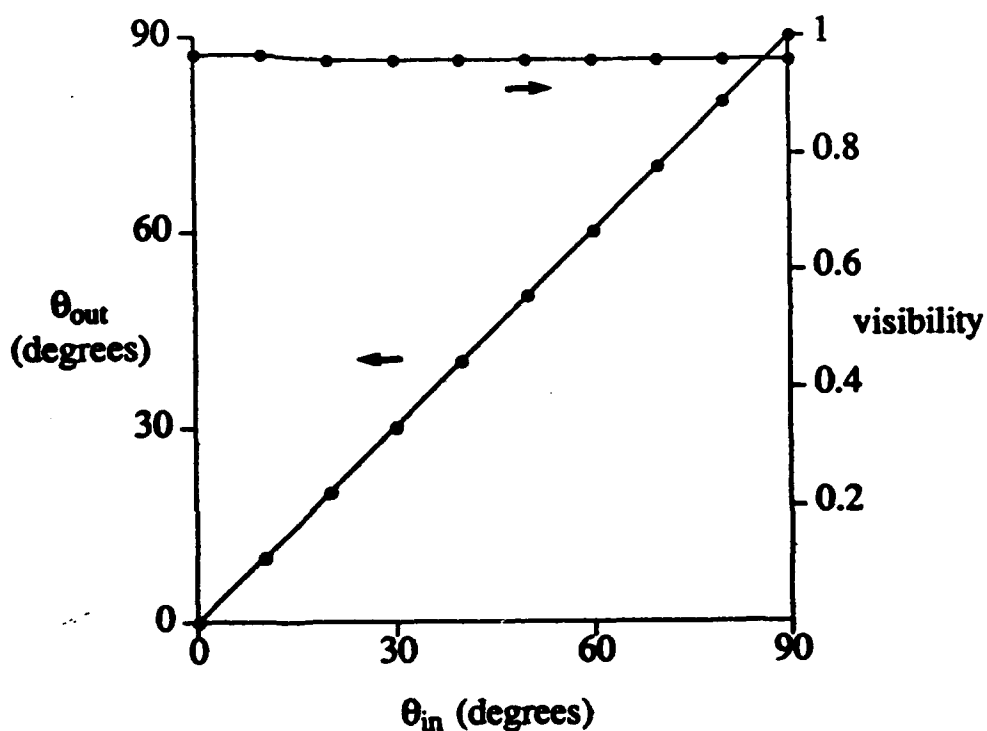


Figure 4. Output polarization state as a function of input polarization angle. Both the relative output polarization angle and output visibility are displayed as a function of input polarization angle  $\theta_{in}$ .



R. W. Huggins and C. R. Porter

Boeing Defense &amp; Space Group High Technology Center

P.O. Box 3999, Seattle WA 98124-2499

**ABSTRACT**

Position sensors for flight-critical airplane applications must indicate when a malfunction occurs. A fiber coupled resolver using residue number arithmetic encoding which satisfies this requirement has been demonstrated and will be described.

**INTRODUCTION**

An essential feature of a position measuring system used in flight-critical airplane applications is that if the system ceases to indicate the true value of the parameter being measured, this fact should be indicated to the operator or to the controlling computer. In the case of conventional rotary or linear variable differential transformers, signals corresponding to either the sine and cosine of the angle being measured or to the amplitude and the complement of the displacement are transmitted to the signal processing electronics. Fault-free operation is indicated by a constant sum of either the square of the sine and cosine, or the displacement and its complement. If the present electromagnetic resolvers are to be replaced by passive fiber coupled resolvers, the fiber coupled resolvers must have identical or improved performance characteristics. While most characteristics are being duplicated, the self checking feature is proving difficult to implement.

Various intensity modulated encoding schemes have been used in optical fiber coupled resolvers developed for aerospace applications. One method of encoding uses an optical code plate with multiple binary tracks<sup>1,2,3</sup>. A second method uses a single track whose density varies monotonically with position<sup>4,5</sup>, and a third

method uses multiple analog tracks with a modified weighted number system encoding<sup>6</sup>. Of the above, only the method described in reference 5, which is the optical equivalent of the linear variable differential transformer, is self checking. The drawbacks of this scheme are that it is optically complex, and that three fibers are required.

In the work to be described, the weighted number system encoding used in the multiple analog track sensor described in reference 6 has been replaced by a modified residue number system encoding. While this method of encoding requires an additional track, it has the property that an error in any track leading to an incorrect indication of position will be flagged as such.

**RESIDUE NUMBER SYSTEM ENCODING**

The residue numbering system uses  $n$  pairwise relatively prime (the greatest common divisor is 1) bases  $m_1, m_2, \dots, m_n$ . Any integer  $X$  up to  $M = m_1 \times m_2 \times \dots \times m_n$  is represented by another set of numbers (residues)  $r_1, r_2, \dots, r_n$  where the residues are defined by  $X = q_i m_i + r_i$ ,  $i = 1, 2, \dots, n$ . The values of  $q_i$  are chosen such that  $0 \leq r_i < m_i$ . As an example, in an  $n = 3$  system in which  $m_1 = 2$ ,  $m_2 = 3$ , and  $m_3 = 5$ , the number thirteen is represented by 113. If a redundant modulus  $m_r$  is added to the number base such that  $m_r$  is greater than  $m_n$  and satisfies the pairwise relatively prime condition, the integer calculated from the residues  $r_1, r_2, \dots, r_n, r_r$  must lie within the range 0 to  $M - 1$ . If conversion from a group of residues gives a number outside the range 0 to  $M - 1$ , an error has occurred. A more detailed description of residue arithmetic and error detection properties can be found in reference 7.

An example of a residue number encoded linear code plate with four width-modulated tracks is shown in Figure 1. The moduli used are 3, 4, and 5 with a modulo 7 redundant track giving a range of 0 - 59. The code plate is interrogated by four lines of light each having a length equal to the maximum width of the appropriate track as described in reference 6.

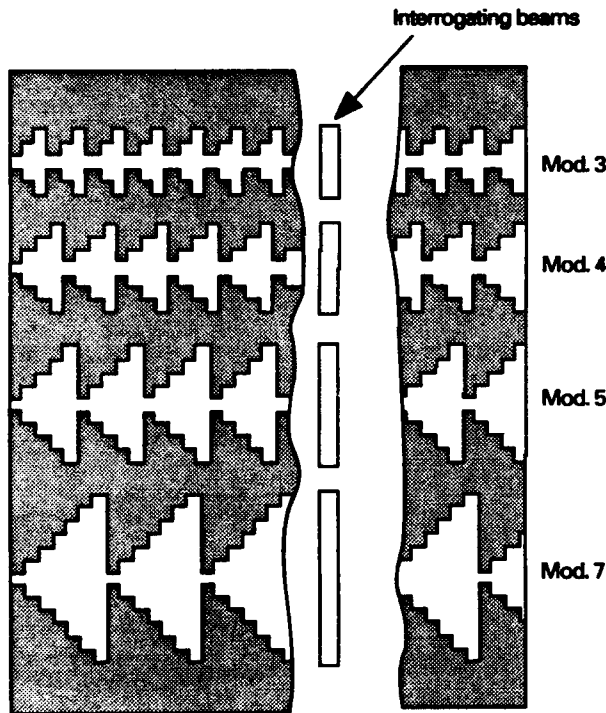


**Figure 1. Residue Number System Encoded Code Plate**

Two problems are encountered in the interrogation of a code plate such as that shown in Figure 1. First, the transition between the maximum and minimum widths places severe requirements on the width and line shape of the interrogating beam, and second, errors will generally be indicated during transitions between integral steps since the track transitions will not occur simultaneously. The first difficulty can be overcome by reflecting the tracks as in reference 6 without loss of the error detecting properties of the encoding. For example, the counting sequence of the modulo 3 track becomes 0,1,2,2,1,0,0... and so on. The only drawback is that the Chinese remainder theorem<sup>7</sup> can no longer be used to decode the number, and a lookup table has to be used. The second problem

of the nonsimultaneous transitions can be overcome by the addition of a binary strobe track such that the data are decoded only when the strobe track is high. Since the peak width of the strobe track is always constant, the strobe track can also serve as an intensity reference. A section of a linear code plate with modulo 3, 4, 5, and 7 tracks and a binary strobe track is shown in Figure 2.

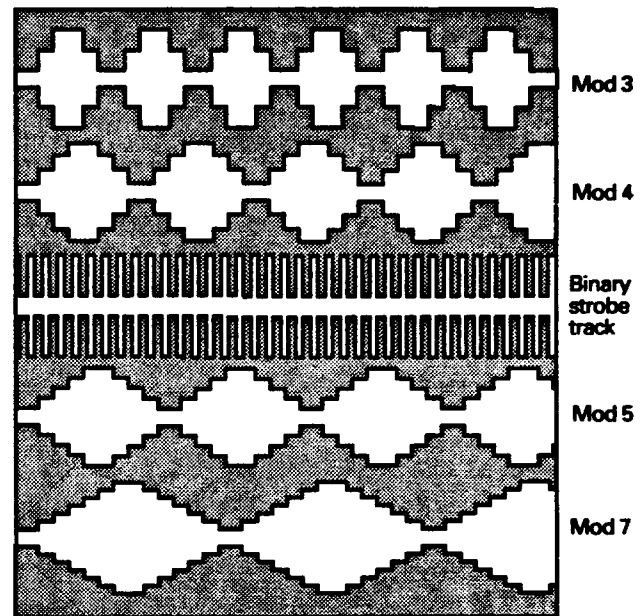


**Figure 2. Modified Residue Number System Encoded code Plate With Strobe**

## OPTICAL INTERROGATION AND SIGNAL PROCESSING

Interrogation of the code plate is identical to that described in reference 6, and is shown in Figure 3. Light from a broadband source is transmitted to the resolver along the outgoing optical fiber. Inside the resolver, the light is focused into a line across the code plate by a spherical - cylindrical lens combination. After passing through the code plate, the light is refocused on to the return fiber by a second cylindrical - spherical lens combination, and thence to the detector. Wavelength division multiplexing of the five tracks is achieved by locating five pass-band interference filters in front of the tracks as shown. Although this introduces an immediate

7 dB insertion loss, the loss is lower than that which is currently being achieved using diffracting optics<sup>1</sup>. The detector is a flat field spectrograph with an array detector, and signal processing consists of normalization, level detection and reference to lookup table. If the combination of residues is not found in the lookup table, an error is indicated

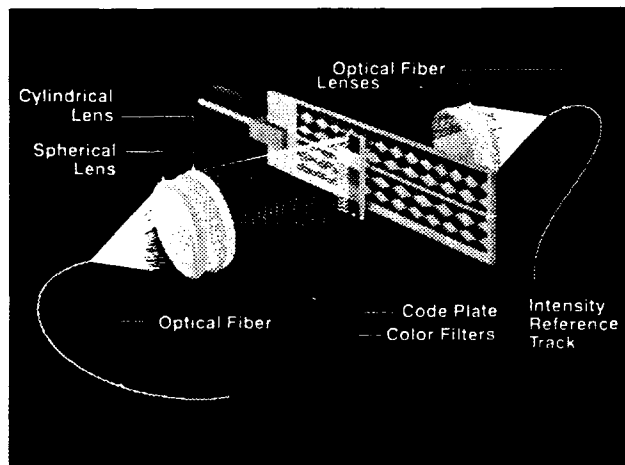


Figure 3. Sensor Optical System

## RESULTS

The error detection concept has been demonstrated using the prototype rotary sensor described in reference 6 with a 0 to 90 degree residue number encoded code plate having tracks of modulo 5,7,8 and 9 as shown in Figure 4. The detector voltage outputs corresponding to the four tracks over the angle range 0 to 10 degrees are shown in Figure 5. In order to demonstrate the error detecting capability, an error in one of the threshold levels was deliberately introduced, and the resultant transfer function is shown in Figure 6. Errors are indicated by a number of less than 0. The resolution of this particular code plate was 0.4 degrees, but higher resolution code plates are being developed.

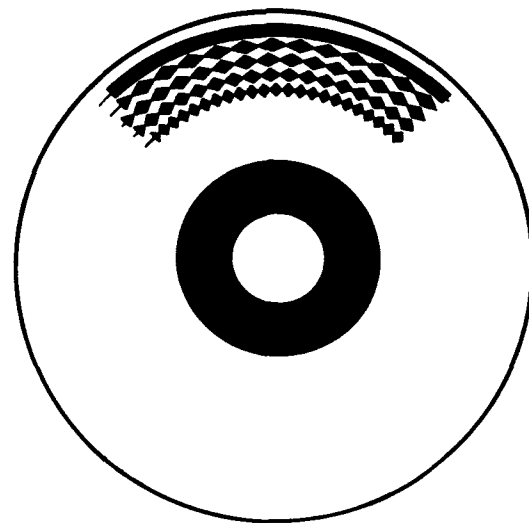


Figure 4. Rotary Residue Number System Encoded Code Plate (Negative)

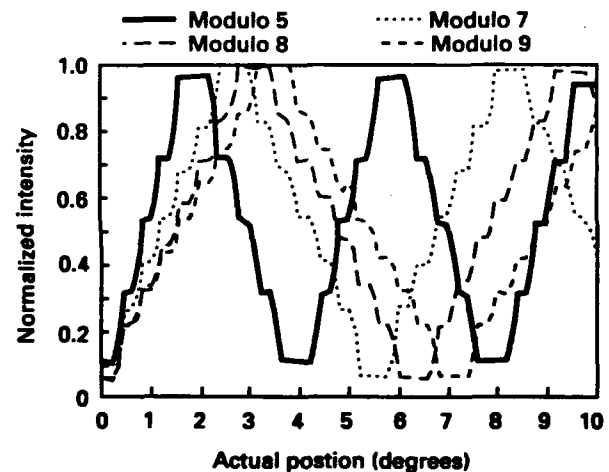


Figure 5. Detector Outputs from Code Plate Shown in Figure 4.

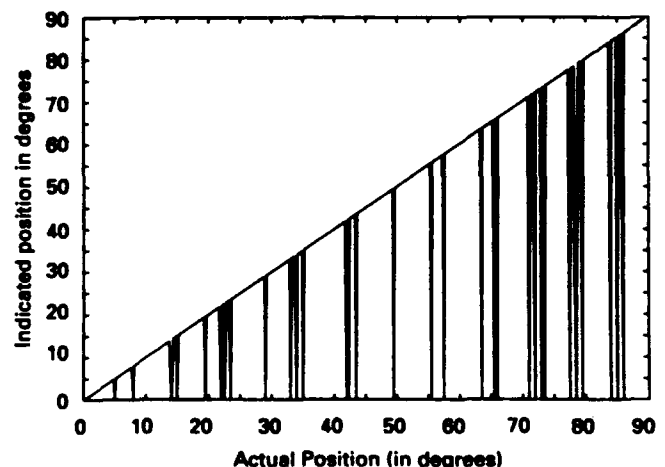


Figure 6. Example of Error Detection Capability

## ACKNOWLEDGEMENTS

The authors would like to thank Ted Houk for useful discussions concerning residue number arithmetic, and Scott Schaumburg for developing the computer programs used in demonstrating the concept. The authors would also like to thank John Rankin, Vicki Grimmert and Jeannette Jolley for graphic support.

## REFERENCES

1. P. T. Gardiner and R. A. Edwards, "Fiber Optic Position Sensors for Aircraft Flight Control Systems," Fiber Optic Sensors in Perspective Workshop, University of Strathclyde, July, 1987.
2. N. E. Lewis, and M. B. Miller, Wavelength Division Multiplexed Fiber Optic Sensors for Aircraft Applications," Proc. SPIE Vol. 989, pp. 29 - 37 (1988).
3. D. Varshneya, and W. L. Glomb Jr., "Applications of Time and Wavelength Division Multiplexing to Digital Optical Code Plates," Proc. SPIE Vol. 838, Fiber Optic and Laser Sensors (1987).
4. R. W. Huggins, E. C. Goldstick, and B. VanDeventer, "Fiber Coupled Analog Rotary Position Sensor," Proc. 6th International Optical Fibers Sensors Conference, OFS'89," Ed. Ardity, Dakin and Kersten, Springer-Verlag (1989).
5. G. E. Miller, "Application of Analog Fiber Optic Position Sensors to Flight-Control Systems," Proc. SPIE. Vol. 1367 Fiber Optic and Laser Sensors VIII pp. 165 - 173 (1990).
6. R. W. Huggins, "Multi-analog track fiber coupled position sensor," Proc. SPIE. Vol. 1367, Fiber Optic and Laser Sensors VIII, pp 174-180 (1990).
7. N. S. Szabo and R. I. Tanaka, "Residue Arithmetic and Its Applications to Computer Technology," McGraw Hill, 1967.

## **P20      Integrated Optics Pockels Cell As A High Voltage Sensor**

**Nicolas A. F. Jaeger and Farnoosh Rahmatian**  
**The Department of Electrical Engineering**  
**The University of British Columbia**  
**Vancouver, British Columbia, Canada**

***Abstract*** - The theory of operation of the integrated optics Pockels cell, for use as a high voltage sensor, is described. The results of measurements on various samples for bias, extinction ratio, and piezoelectric resonance are presented.

### **Introduction**

The measurement of voltage and current by optical means offers several advantages over the more conventional PTs and CTs used by the power industry, e.g., their immunity to electromagnetic interference, their non-intrusive nature, and their inherent insulating properties [1]. Integrated optics and fibre optics based sensors offer the further advantages of being small, inexpensive, and, in some cases, having higher frequency responses [2]. In this paper we discuss one such device, based on the integrated optics version of the Pockels cell [3], being developed at the University of British Columbia. This version of the Pockels cell is an immersion type device, by which we mean that it simply measures the electric field in which it is immersed without the use of special electrodes, capacitive dividers, or other sensing elements. However, there are restrictions on the orientation of the electric field with respect to the sensor, therefore, it is best suited to measure voltage in systems having a fixed geometry, e.g., in SF<sub>6</sub> gas insulated transmission lines.

### **Theory**

The integrated optics Pockels cell discussed in this work is constructed using a stripe waveguide fabricated in a Y-cut substrate of lithium niobate. The waveguide is formed by the in-diffusion of a titanium stripe lying parallel to the Z crystallographic axis of the substrate. The width and thickness of the titanium stripe are chosen so as to result in a waveguide supporting one TE like and one TM like mode after it has been diffused into the substrate. After the titanium in-diffusion the substrate is covered with an optical buffer layer of silicon dioxide. Finally, the ends of the waveguide are polished to allow efficient end-fire coupling of light to and from polished optical fibres.

Linearly polarized light is coupled into the waveguide from a polarization maintaining fibre. The fibre is oriented so as to couple equal amounts of light into both the TE and TM like modes of the waveguide. This alignment is substantially at 45° to the X and Y crystallographic axes of the lithium niobate. Interrogation of the output is by a second polarization maintaining fibre supporting two orthogonal modes. This second fibre is also aligned with its polarization axes at 45° to the X and Y axes of the crystal. Figure 1a is an isometric view of the Pockels cell, with fibre attached, and figure 1b illustrates the polarization axes alignment for the fibre and waveguide in the plane where the two meet.

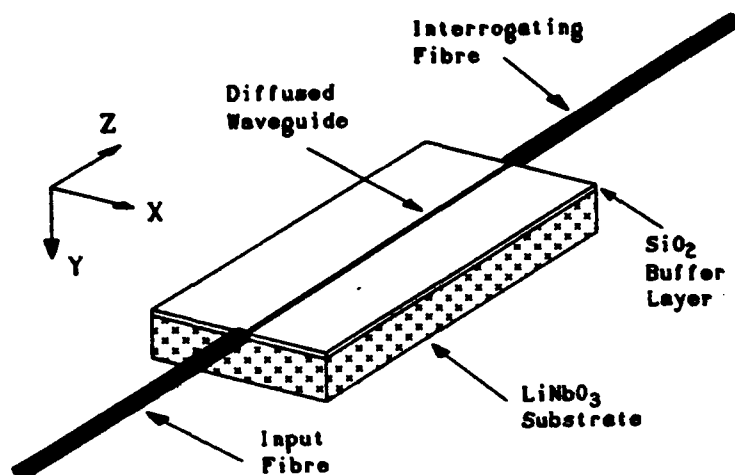


**Figure 1a.**

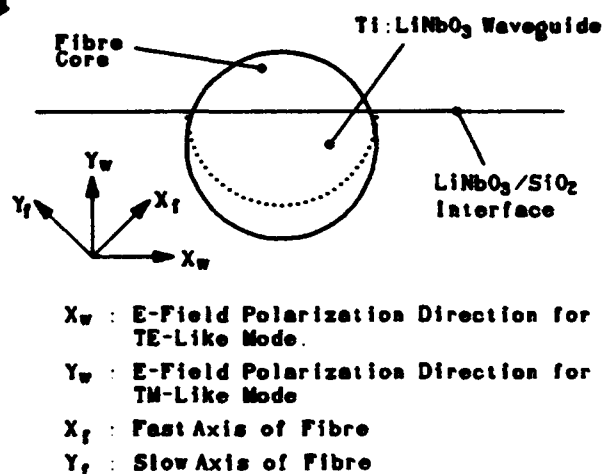


**Figure 1b.**

Once light has been launched into the waveguide the TE and the TM like modes propagate with slightly different phase velocities resulting in a polarization state at the output that depends on the waveguide's length. It is, therefore, possible to bias the integrated optics Pockels cell. Ideally, for small signal linear operation, the length of the waveguide is chosen so as to result in circularly polarized light when no external field is applied. The interrogating fibre measures the polarization state of the output of the waveguide by sensing the optical powers that are parallel to both the major and minor axes of the polarization ellipse. This information is transmitted to an opto-electronic conversion unit in the two modes of the interrogating fibre. In this manner the integrated optics Pockels cell measures the total instantaneous power at the output, allowing the output signal to be normalized and, in turn, making the device less sensitive to mechanical vibrations.

Choosing a Y-cut substrate with propagation in the direction of the Z axis has several advantages. One is that the mode profiles of the two modes are essentially equivalent so that the polarization state is virtually constant across the entire output plane. Also, there is no surface waveguide formation during the diffusion cycle. Additional advantages are gained by applying the electric field parallel to the Y crystallographic axis. Firstly, the piezoelectric resonances depend primarily upon the X and Y dimensions of the crystal, as opposed to the Z dimension. Secondly, it is the intrinsic phase difference between the TE and TM like modes that is responsible for our ability to bias the device and it is their phase velocities that are changed by applying the electric field parallel to the Y axis; this is not the case for a field applied parallel to the X axis.

For the ordinary refractive index of lithium niobate it is well known that the change in index is given by  $\Delta n = \pm n_o^3 r_{22} E_y / 2$  (see for example [4]), where  $n_o$  is the ordinary refractive index of lithium niobate,  $E_y$  is the electric field parallel to the Y axis in the crystal,  $r_{22}$  is the relevant electro-optic coefficient, and the sign depends on the axis (X or Y). Ideally, we can express the powers parallel to the major and minor axes of the polarization ellipse each in the form  $P_0 [1 \pm \cos(2\pi n_o^3 r_{22} E_y L / \lambda_o + \phi_i)] / 2$ , where  $L$  is the length of the waveguide,  $\lambda_o$  is the light's wavelength (here 670 nm),  $\phi_i$  is the intrinsic phase difference or bias, and  $P_0$  is the total power at the output. Hence, the output signal can be normalized with respect to the total output power. The output signal can thus be expressed as

$$S = \frac{1 \pm \cos(2\pi n_o^3 E_y L + \phi_i)}{2}$$

### Experimental Results

A 16.2 mm long sample, nominally 0.4 mm thick, was prepared. In it a titanium layer 55 nm thick was photo-lithographically formed into stripes and in-diffused for 6 hours at 1050°C. The sample was then covered with a 600 nm thick silicon dioxide optical buffer layer. Figure 2 shows the measured transfer function of one of the devices fabricated in the sample. It has a bias of 95° and an extinction ratio > 20 dB. The electric field,  $E_y$ , needed to create a relative change in phase of  $\pi$  radians between the two modes was measured to be 270 V/mm, the corresponding theoretical value was calculated to be 260 V/mm.

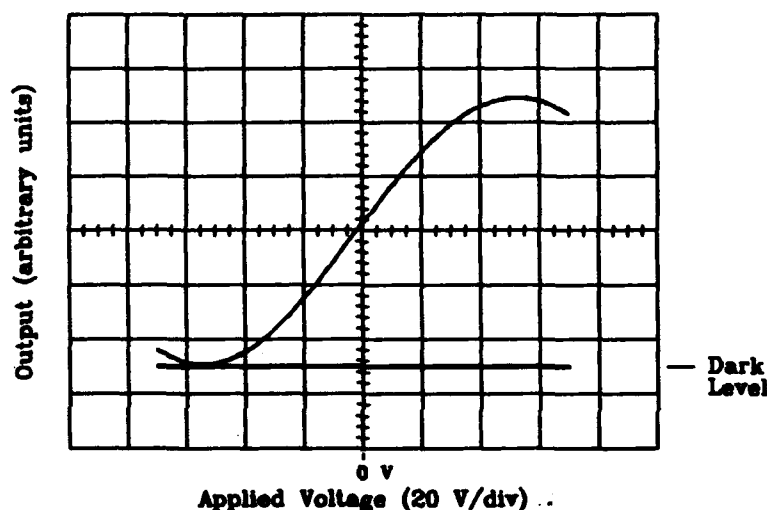
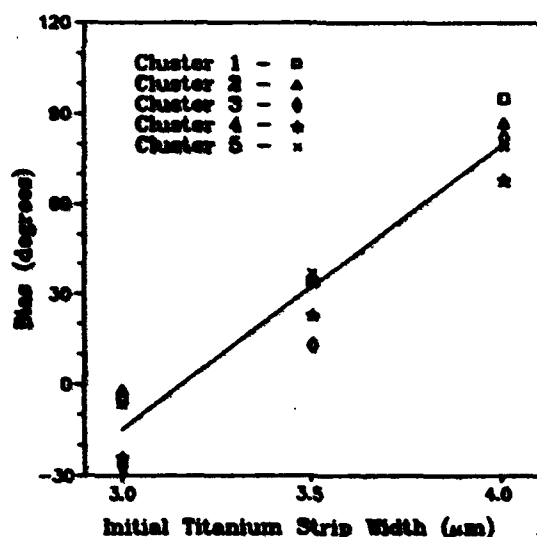


Figure 2.

While the integrated optics Pockels cell can be biased by controlling its length we conducted an experiment to study the effect of the pre-diffusion titanium stripe width on the bias of our devices. Our sample contained many devices with titanium stripe widths of 3.0, 3.5, and 4.0  $\mu\text{m}$ . The devices were formed in clusters in which the individual devices were separated by 100  $\mu\text{m}$  and the clusters were 1.5 mm apart. The measured biases are shown in figure 3. While the values of the bias for a particular stripe width vary by about 30° there is clearly an increase with width. The slope of the least squares fit line is 93°/ $\mu\text{m}$ . Similar measurements on devices 13.5 and 28.5 mm long gave phase changes of 63 and 120°/ $\mu\text{m}$ , respectively. These values give a change in phase per unit width per unit length between 4.2 and 5.7°/ $\mu\text{m}/\text{mm}$ . Presumably, these variations are due to slight differences in the way the samples were prepared. Still, we feel that it would be both possible and practical to prepare, on a sample, a range of devices with varying stripe widths from which one with an appropriate bias could be chosen.

Measurements of the piezoelectric resonance, for the lowest order mode, for a number of samples of different widths (X axis) and lengths (Z axis) indicated that, as expected for long thin devices, it is determined primarily by the sample's width. For our samples the resonant frequency is given by  $f_r \approx 3.4/w$  MHz, where  $w$  is the width in millimetres and is much greater than the thickness. The integrated optics Pockels cell should, therefore, be able to offer

bandwidths in the tens of megahertz making it suitable for high speed monitoring applications and time resolved fault location.



**Figure 3.**

### Summary

We have presented the theory of operation and measurement results, bias and extinction ratio, for the integrated optics Pockels cell as a high voltage sensor. We have shown that while it can be biased by controlling its length, one of a number of devices, having different widths, fabricated on a single substrate should have an appropriate bias. Measurements of the piezoelectric resonance have further shown that these devices can be fabricated with large bandwidths, perhaps making them useful for new applications such as time resolved fault location.

### Acknowledgements

The authors wish to thank the Science Council of British Columbia and the Natural Sciences and Engineering Research Council of Canada for their support of this work.

### References

1. G.A. Massey, D.C. Erickson, and R.A. Kaldec, "Electromagnetic field components: Their measurement using linear electrooptic and magneto optic effects," *Appl. Opt.*, vol 14, no. 11, pp. 2712-2719, 1975.
2. N.A.F. Jaeger and L. Young, "High-Voltage Sensor Employing an Integrated Optics Mach-Zehnder Interferometer in Conjunction with a Capacitive Divider," *J. Lightwave Technology*, vol. LT-7, no. 2, pp. 229-234, 1989.
3. N.A.F. Jaeger, "Integrated Optics Pockels Cell Voltage Sensor," U.S. Patent # 5,029,273, July 2, 1991.
4. I.P. Kaminow, *An Introduction To Electrooptic Devices*, Academic Press, Inc., Orlando, Florida, 1974.



## **P21     A Hybrid Coherent Fiber-Optic Probe For Remote Sensing Of Electro-Optic Effects in GaAs**

by

David L. Mazzoni, Kyuman Cho, Stephen Sadow, and Christopher C. Davis

Electrical Engineering Department  
University of Maryland  
College Park, MD 20742

### **Summary**

It is well known that GaAs has a large electro-optic (EO) coefficient. Therefore, GaAs integrated circuits and devices can be probed optically through the electro-optic effects produced by steady or transient voltages in the circuit. For example, Bloom et al <sup>(1)</sup> have shown that noninvasive electro-optic sampling of microwave circuits is useful for measuring device parameters. GaAs circuits can be tested using a transmission line formed on an electro-optic substrate. EO crystals are placed close to the device under test, and a sampling beam probes the crystal to measure the fringing fields of the transmission line. Unfortunately, this technique has limitations since the transmission line and crystal disturb the fields in the device under test. Techniques for non-perturbing in situ measurements, such as those investigated by Bloom, are more desirable since an external crystal is not required.

We have developed a coherent fiber-optic probe that is ideal for measuring birefringence in a remote sample. By utilizing a single fiber carrying two orthogonally polarized beams to a remote sensing section, the fading problem common to interferometers with separate beam paths is minimized. We employ phase locked loop detection which is insensitive to slowly varying phase shifts while at the same time being simple and inexpensive. Such sensors are ideal for the remote sensing of parameters in hostile environments or where electromagnetic fields can interfere with traditional sensors<sup>(2)</sup>.

In our implementation of a coherent hybrid sensor, in order to minimize phase and polarization drifts that occur when independent signal and reference arms are used in an interferometer, we have combined two orthogonally polarized beams into a single fiber, thereby minimizing common-mode effects. In addition, to avoid operating point drift that plagues homodyne detection schemes, we have used a true heterodyne scheme in which these two orthogonally polarized beams are at different frequencies. A single mono-mode fiber acts to deliver and return the beams to/from a remote sensor element. In GaAs circuit characterization the semiconductor substrate becomes the sensor element. It induces

a phase shift between the orthogonally polarized components of the beam penetrating the substrate. The beam is reflected off the back surface of the substrate into the fiber. The detection optics and electronics can be located in a benign location at the input end of the fiber. This type of single fiber system is relatively invulnerable to environmental effects since any perturbation affects both beams in the fiber, and any common mode signals can be suppressed in the detection electronics.

A diagram of the fiber sensor is shown in Figure 1. A 35 mW single mode diode pumped  $1.3\mu\text{m}$  Nd-Yag laser is used as a signal source. The beam is optically isolated and passes through a 40 MHz Acousto-Optic modulator (AOM) that produces two beams, one of which is shifted in frequency by 40 MHz from the fundamental. The beams enter an arrangement of mirrors and  $\lambda/2$  waveplates that align the beams with the first polarization sensitive beam splitter (PSBS1). One of the beams is also rotated  $90^\circ$  with respect to the other so that two collinear orthogonally polarized beams emerge from PSBS1. These beams are injected into a single mode fiber through a 3dB coupler. One of the coupler output beams is lost into index matching fluid, while the other output beam continues to the sensing end. A 0.29 pitch graded index (GRIN) lens is epoxied to the end of the fiber with a focal point 5 mm from the GRIN lens. The GRIN is positioned above the GaAs sample for maximum reflection. A computer controls an XYZ positioner that scans the GRIN above the GaAs device. The local electric field in the GaAs modulates the birefringence of the substrate and induces a phase shift between the orthogonal components of the probe beam. The beam is reflected back into the fiber and returns through the 3dB coupler, a  $\lambda/2$  waveplate, and polarizing beam-splitter PSBS2 before reaching the detection photodiodes. The phase shift induced by the GaAs is detected by placing the output beam splitter (PSBS2) at  $45^\circ$ , so that the two orthogonal components of the beam mix. Final detection occurs at a balanced mixer using two wideband photodiodes. Common mode amplitude noise is suppressed by differentially amplifying the signals from these two photodiodes.

The output of the differential amplifier following the diodes in Fig.1 is

$$I_{diff} \propto \cos(\Delta\omega t + \Delta\phi_s - \phi_m) \quad (1),$$

where  $\Delta\omega = \omega - \omega'$  is the AOM excitation frequency,  $\phi_m$  is the induced phase shift, and  $\Delta\phi_s$  is the static phase term. The signal modulation is present in  $\phi_m$  and is directly detected in the PLL stage. The  $\Delta\phi_s$  above represents a static phase shift due to differing path lengths, thermal expansion and contraction of the optical components, and other slowly varying effects. Heterodyne detection is immune to these pseudo-static phase perturbations. Direct PLL detection does not require a stable source since a voltage controlled oscillator is locked to the carrier. Although other schemes exist for heterodyne detection <sup>(3)</sup>, they often require complicated techniques and are usually not as sensitive as true heterodyne methods. <sup>(4)</sup>

The simplicity of the detection electronics using the direct PLL method is evident from Figure 1. The 40 MHz phase modulated signal from the photodiodes is amplified in a wide-band differential amplifier (ComLinear CL231). Using two diodes in a balanced detector arrangement improves the SNR by 3 dB – in addition, balanced detection suppresses amplitude noise from the laser. In Figure 1 the phase modulation is detected in a discrete 40 MHz PLL employing a limiter/AGC, doubly balanced mixer, 40 MHz VCO, and an active loop filter. Phase demodulation is achieved by mixing the differential amplifier output with the VCO output. The mixer output is filtered and is used to form the VCO control voltage that keeps the VCO frequency locked to the incoming RF carrier. The VCO control voltage also contains the demodulated phase signal, which is further amplified before the output signal is displayed on an oscilloscope or dynamic signal analyzer. This detection scheme is elegant and does not require any specialized or expensive components, making the sensor desirable for commercial applications.

Figure 2 shows the result obtained in scanning the fiber probe in one dimension perpendicular to 3 different gold stripline features on the surface of a GaAs (100) wafer. All three striplines were excited with a 4 kHz signal at 5V. The wafer underside was gold coated for enhanced reflection and used as a ground plane. At each of the outer electrodes the rising signal is due to the increase in electric field intensity adjacent to the gold striplines. In principle, this plot shows the electric field profile in the GaAs surrounding the electrodes. The results of Figure 1 show rough edges on the gold strips caused by wet chemical etching of the wafer, and this data is exactly reproducible. Furthermore, this technique can show extremely small variations in such things as conductor width, doping density, epitaxial layer differences, surface impurities, and defects in the GaAs.

Figure 3 shows a spectrum analyzer plot of the sensor signal obtained with a 5V signal on the stripline. A signal to noise ratio of at least  $45\text{dBV}^2$  is shown indicating that minimum sensitivities down to  $\sim 7\text{mV}/\sqrt{\text{Hz}}$  can be achieved.

This research is supported by the U. S. Army Medical Research and Development Command through Contract DAMD-90-Z-0052. Stephen Sadow is also at Harry Diamond Laboratories, Adelphi MD.

### References

- [1] B. H. Kolner, D. M. Bloom, IEEE J. Quantum Electronics, **QE-22**, no.1 (January 1986).
- [2] D. L. Mazzoni, K. Cho, C. C. Davis, Optics Letters, **16** no.8 (April 1991)
- [3] T. Okoshi, IEEE J. Lightwave Technol., **LT-3** no.6, (December 1985).
- [4] I. M. I. Habbab, and L. J. Cimini, Jr., IEEE J. Lightwave Technol., **6-10**, (October 1988).

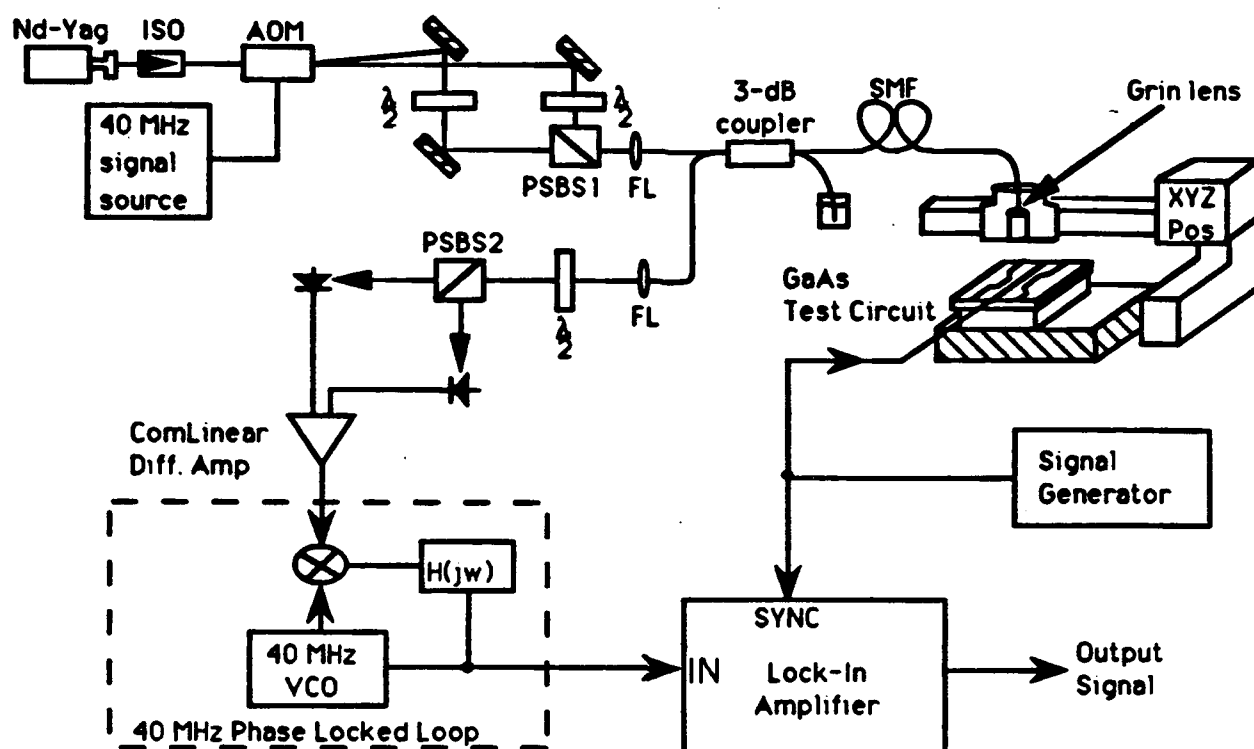


Figure 1. Coherent Hybrid Fiber-Optic Sensor

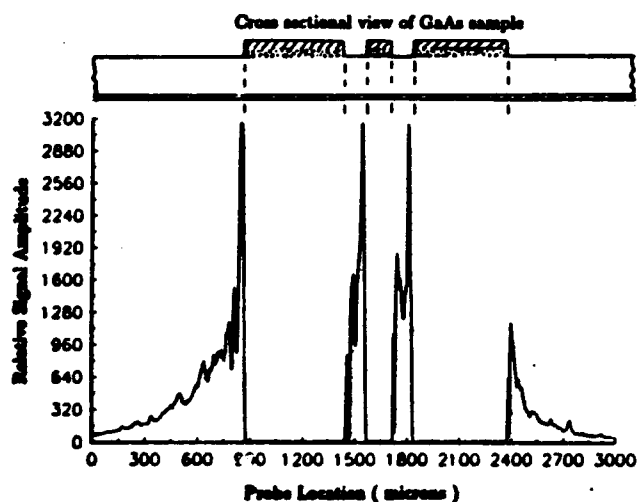


Figure 2  
GaAs Scan Results

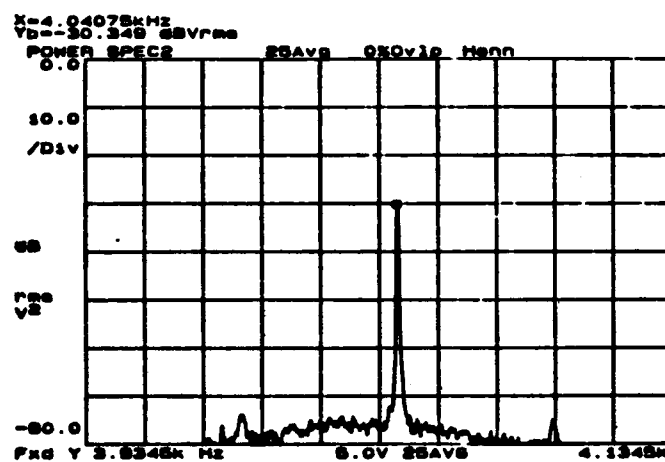


Figure 3  
Signal Power Spectrum

# P22 Fiber Optic Magnetic Field Sensors Using Metallic-Glass-Coated Optical Fibers

Y. W. Bibby,<sup>a</sup> D. C. Larson,<sup>b</sup> S. Tyagi<sup>b</sup> and L. C. Bobb<sup>c</sup>

<sup>a</sup> Physics Department, Wilkes University, Wilkes-Barre, PA 18766

<sup>b</sup> Dept. of Physics and Atmospheric Science, Drexel University, Philadelphia, PA 19104

<sup>c</sup> Naval Air Development Center, Warminster, PA 18974

## 1. INTRODUCTION

The detection of a magnetic field by a magnetostrictive-type fiber optic magnetic field sensor (FOMS) essentially involves measuring the longitudinal strain produced in the optical fiber to which a magnetostrictive material has been bonded.<sup>1</sup> The performance of such a FOMS is critically dependent on the coupling efficiency between the magnetostrictive material and the optical fiber. The sensing elements are commonly (a) an unjacketed fiber bonded to a metallic glass ribbon or wire,<sup>2,5</sup> (b) an optical fiber wrapped around a metallic glass cylinder,<sup>2</sup> and (c) an optical fiber coated with a magnetostrictive film.<sup>6,7</sup> Configurations (a) and (b) require using an epoxy adhesive to bond the fiber to the magnetostrictive material, which introduces a substantial loading effect.<sup>4</sup> Configuration (c) eliminates the adhesive loading effect and couples the magnetostrictive strain more efficiently onto the optical fiber. Such a scheme was first proposed by Yariv and Winsor<sup>8</sup> and achieved experimentally by two groups. Dandridge et.al.<sup>6</sup> used electron beam evaporation to deposit 1.5  $\mu\text{m}$  films of nickel and 0.6  $\mu\text{m}$  films of metallic glass onto unjacketed fibers. Lenz et.al.<sup>7</sup> electroplated 20  $\mu\text{m}$  of Ni-Fe or Ni-Co onto an optical fiber that had been coated with a conducting layer. In our investigation, Metgals<sup>®</sup> 2605SC ( $\text{Fe}_{81}\text{B}_{13.5}\text{Si}_{3.5}\text{C}_2$ , Allied Signal Inc.) was chosen as the magnetostrictive material, and 5-15  $\mu\text{m}$  coatings of 2605SC were deposited directly onto optical fibers by using triode-magnetron sputtering. The theoretically predicted phase shift induced in such metallic glass coated fibers was discussed in our previous publication in the context of an elastic model of the coated fiber.<sup>9</sup> The experimental results of the FOMS using these coated fibers are the subject of this paper. A more complete characterization of the magnetostrictive coatings will be published elsewhere.

## 2. THEORY

The calculation of the magnetically induced strain in the fiber core is based on a model<sup>9</sup> of the sensing fiber as an elastic combination of core, cladding and metallic glass coating. Using cylindrical coordinates with the longitudinal direction of the fiber along the  $z$  direction, the strain in the fiber core, having components  $\epsilon_r$ ,  $\epsilon_\theta$  and  $\epsilon_z$ , can be expressed in terms of the magnetostrictive strain ( $\epsilon$ ) induced in the metallic glass coating as  $\epsilon_r = \epsilon_\theta = -C_T \epsilon$ , and  $\epsilon_z = C_L \epsilon$ , where  $C_T$  and  $C_L$  are the constants obtained through the calculations mentioned above. The total phase shift in the fiber core,  $\phi$ , then can be expressed as

$$\Delta\phi = \alpha L \epsilon, \quad (1)$$

where  $\alpha = (2\pi n/\lambda)[(1-n^2 P_{12}/2)C_L + (n^2/2)(P_{11} + P_{12})C_T]$  is the loading factor,  $L$  is the length of the coated fiber,  $\lambda$  is the vacuum wavelength of the light passing through the fiber, and  $n$ ,  $P_{11}$  and  $P_{12}$  are the refractive index and the Pockel's coefficients of the fiber core respectively.

The magnetostrictive strain can be calculated using Livingston's model<sup>10</sup> of coherent rotation of magnetization. In this model the strain at low field for amorphous magnetic materials is expressed as  $\epsilon = CH^2$ , where  $H$  is the total magnetic field,  $C$  is the magnetostrictive parameter which equals  $\lambda_s/H_A^2$  or  $3\lambda_s/2H_A^2$  depending on whether the initial magnetic domains are randomly oriented or transversely oriented to the magnetic field,  $\lambda_s$  is the bulk magnetostriction coefficient and  $H_A$  is the anisotropy field. The phase shift in the fiber is also affected by the boundary conditions, which influence the elastic resonances represented here by  $Q$ . Using Eq. (1), the phase shift may then be expressed as  $\Delta\phi = Q\alpha LCH^2$ . If the total field (applied along the longitudinal axis of the fiber) consists of both a slowly varying dc component and an ac dither component, then  $H = H_{dc} + H_{ac}\cos\omega t$ , and the resultant phase shift may then be expressed as

$$\Delta\phi = Q\alpha LC(H_{dc}^2 + 2H_{dc}H_{ac}\cos\omega t + (H_{ac}\cos\omega t)^2) \quad (2)$$

In this expression the resonance enhancement factor  $Q$  depends on the frequency of the ac dither field. At low fields, the phase shift amplitude at the dither frequency  $\omega$  can be written as

$$(\Delta\phi)_\omega = 2Q\alpha LCH_{ac}H_{dc} \quad (3)$$

which means that  $\Delta\phi$  is directly proportional to the magnitude of the dc field. The value of  $\alpha$  can be calculated from the model of coated fibers for a specific coating thickness, and the remaining parameters can be determined experimentally. The dither frequency was chosen high enough, specifically, above 100 Hz, so that low frequency phase noise did not appear in the output. In addition, the dither frequency was also chosen to coincide with one of the major resonance frequencies of the FOMS to provide a large amplitude signal.

### 3. EXPERIMENT

The metallic glass coatings on the unjacketed optical fibers were deposited using a triode magnetron sputtering technique. The sputtering target was made of Metglas® 2605SC cast alloy. The coating thickness was controlled by regulating the following parameters: filament current, plasma current and voltage, target bias current and voltage, argon pressure and sputtering time. These parameters were optimized for the best coating properties. The range of typical deposition rates was 65 to 96 nm/min. The coating thickness varied from 5 to 15  $\mu\text{m}$  with thickness variations of approximately 0.2  $\mu\text{m}$  for each deposition. On some samples a thin layer of chromium (20–100 nm) was evaporated onto the optical fibers before the Metglas coating. The chromium underlayer reduced the embrittlement of the fibers caused by the diffusion of the Metglas constituents into the optical fiber during deposition and further annealing. Results of x-ray diffraction measurements showed that the Metglas coatings were amorphous. Magnetic properties such as magnetic anisotropy and homogeneity, surface and bulk magnetization and coercivities were characterized using Ferromagnetic Resonance, Longitudinal Magneto-Optic Kerr Effect measurement and a Vibrating Sample Magnetometer. More detailed results on the coating characterizations will be published elsewhere.

The experimental apparatus for the FOMS is shown in Fig.1. The FOMS was constructed by incorporating a Metglas coated optical fiber into the sensing arm of a Mach-Zehnder interferometer. Light from a 1 mW single frequency, stabilized He-Ne laser ( $\lambda = 0.633 \mu\text{m}$ ) was coupled into the optical fiber by a 40x objective lens. A mode stripper was used to remove the light coupled into the fiber cladding. Fringe visibility was maximized using a polarization controller. The sensing arm was placed inside a set of Helmholtz coils. In the reference arm, a section of fiber was wound around a piezoelectric (PZT) cylinder. A feedback signal from the output of the sensor to the PZT cylinder was used to compensate for fluctuations in the phase due to low frequency drift caused by temperature fluctuations, noise, and low frequency magnetic fields. This feedback correction signal kept the sensor operating at quadrature for maximum sensitivity. A dc current applied to the Helmholtz coils generated the magnetic field signal to be detected. In addition, a small ac current at frequency  $\omega$  (100 to 6400 Hz) was also applied to the Helmholtz coils to provide the modulating dither field. The magnetostrictive response of the coating and the resulting phase shift in the optical fiber depend upon both of these fields. The output from the FOMS was detected by a pair of photodetectors and the signals were sent to an electronic signal processor. The high frequency signal ( $>100$  Hz) was separated from the output and was fed into a lock-in-amplifier that was tuned to the dither frequency to determine the value of the unknown magnetic field.

For calibration purposes the feedback control loop was disconnected and the PZT cylinder in the reference arm was driven directly by a triangular waveform. The interference fringes were obtained directly from the output of the FOMS with the feedback loop open. The output voltage from the FOMS was directly proportional to the phase shift produced between the two arms, and the constant of proportionality,  $k = (\Delta V / \Delta \phi)_\omega$ , was determined from the slope of the output at quadrature. A value of  $k = 1.08$  volt/rad was obtained for our system.

### 4. RESULTS

In Fig. 2 the phase change amplitude  $\Delta \phi_\omega$  is plotted versus  $H_{dc}$  at a dither frequency of 245 Hz. These hysteresis curves were obtained with slow cycling of the external field  $H_{dc}$ . The dc field was first increased quasi-statically from 0 to +5 Oe, decreased to -5 Oe and then increased to +5 Oe for a complete cycle. The results presented in Fig. 2 are for a 6  $\mu\text{m}$  thick Metglas-coated fiber with a 0.178m long coating length and a 0.1  $\mu\text{m}$  chromium undercoating. The coated fiber had been annealed for 10 min at 385  $^\circ\text{C}$  in an external 3000 Oe field applied transversely to the fiber. To control the initial magnetic state, the sample was demagnetized before each measurement. The traces in the plot shown in Fig. 2 were begun with the sample demagnetized, and the 0-field slope of the curve was measured to be  $d\Delta \phi_\omega / dH_{dc} = 0.91$  rad/Oe.

The output from the FOMS was very sensitive to the modulating dither frequency. The sensitivity at different dither frequencies can vary by more than 2 orders of magnitude, so the response of the FOMS can be enhanced considerably by choosing a high Q resonance frequency. The frequency dependence of the FOMS was obtained by applying a constant dc bias field and letting the frequency of the dither field sweep from 100 to 1800 Hz. Each complete sweep took about 15 minutes. The output from the Lock-in-amplifier as a function of dither frequency for the same specimen mentioned above at 0 bias field is shown in Fig.3. The major resonant frequencies were independent of the dc bias field as long as the fiber support arrangement was not changed. The amplitudes of the resonances, however, increased with increasing bias field. The 245 Hz frequency exhibited a resonance enhancement factor of  $Q = 96$  which was close to the maximum value obtained of  $Q = 106$  at 892 Hz.

## 5. DISCUSSION

The minimum detectable magnetic field at low fields can be calculated from  $H_{\min} = (\Delta\phi_{\omega})_{\min}/(d\Delta\phi_{\omega}/dH_{dc})$ . Assuming a signal-to-noise ratio of one, a value of  $(\Delta\phi_{\omega})_{\min} = 5.6 \times 10^{-4}$  rad/ $\sqrt{\text{Hz}}$  was obtained from a noise measurement at the 245 Hz dither frequency. The minimum detectable field is therefore  $H_{\min} = 6.2 \times 10^{-4}$  Oe/ $\sqrt{\text{Hz}}$ . (The dither field was 0.16 Oe; a lower dither field would have given a somewhat higher initial slope.) In order to compare diverse types of magnetostrictive sensors it is useful to calculate a figure-of-merit  $M = (V H_{\min})^{-1}$ , where  $V$  is the volume of the magnetostrictive material and  $H_{\min}$  is the minimum detectable field. In Table 1 the values of  $M$  are compared for amorphous metal cylinders, wires, and coatings. The value for  $M$  given for the optimized optical fiber is calculated by assuming (1) the interferometer noise can be reduced to the same level as that given in Ref. 5 ( $50 \times 10^{-6}$  rad/ $\sqrt{\text{Hz}}$ ), and (2) a lower dither field would be employed increasing  $d\Delta\phi_{\omega}/dH_{dc}$  by a factor of 3. This optimized sensor would have a minimum detectable magnetic field of  $2.6 \times 10^{-5}$  rad/ $\sqrt{\text{Hz}}$ , and would have a figure of merit comparable to the FOMS which utilize cylindrical or wire magnetostrictive elements. The coated-fiber FOMS requires the least volume of magnetostrictive material, and it may be well-suited to applications where small size is more important than maximum sensitivity.

Structure	$M$ ( $\text{Hz}^{1/2}/\text{Oem}^3$ )	Reference
Cylinder	$5.0 \times 10^{13}$	[Ref 5]
Wire	$1.9 \times 10^{14}$	[Ref 5]
Coated Fiber	$3.7 \times 10^{12}$	This Paper
Coated Fiber(Optimized)	$8.7 \times 10^{13}$	This Paper

Table 1. Figures of Merit for Several Types of FOMS

An experimental value of QC can be obtained from Eq.(3),  $(QC)_{\text{expt}} = (\Delta\phi)_{\omega}/2\alpha L H_{\omega} H_{dc} = 3.6 \times 10^{-6}/\text{Oe}^2$  for the 245 Hz dither frequency using  $\alpha = 4.4 \times 10^6$  rad/m.<sup>9</sup> Using the Q-factor value of 96, we obtain  $C_{\text{expt}} = 3.8 \times 10^{-8}/\text{Oe}^2$ . The value of  $C$  for Metglas 2605 SC ribbons is  $3.7 \times 10^{-5}/\text{Oe}^2$ .<sup>9</sup> Further improvement in the magnetostrictive response of the sensor could therefore be obtained through improvement of the magnetic properties of the sputtered films as well as enhancing the resonances.

## 6. REFERENCES

1. F. Bucholtz, K. P. Koo, A. D. Kersey, and A. Dandridge, "Fiber Optic Magnetic Sensor Development," SPIE Vol. 718, Fiber Optic and Laser Sensors IV, pp. 56-65, 1986.
2. K. P. Koo and G. H. Sigel, Jr., "Characteristics of fiber-optic magnetic-field sensors employing metallic glasses," Opt. Lett., Vol. 7, pp. 334-336, 1982.
3. A. D. Kersey, D. A. Jackson, and M. Corke, "Single-mode fiber-optic magnetometer with DC bias field stabilization," J. Lightwave Technol. Vol. LT-3, No. 4, pp. 836-840, 1985.
4. F. Bucholtz, K. P. Koo, G. H. Sigel, Jr., and A. Dandridge, "Optimization of the fiber/ metallic glass bond in fiber-optic magnetic sensors," J. Lightwave Technol. Vol. LT-3, No. 4, pp. 814-817, 1985.
5. K. P. Koo, F. Bucholtz, D. M. Dagenais, and A. Dandridge, "Amorphous metal wire transducers for fiber optic magnetometers," Proc. 6th Int. Conf., OFS '89, (Eds. H. J. Arditty, J. P. Dakin, and K. T. Kersten), Springer-Verlag, Springer Proc. in Phys., Vol. 44, pp. 366-372, 1989.
6. A. Dandridge, A. B. Tveten, G. H. Sigel, Jr., E. J. West, and T. G. Giallorenzi, "Optical fibre magnetic field sensors," Electron. Lett. Vol. 16, pp. 408-409, 1980.
7. J. E. Lenz, C. D. Anderson, and L. K. Strandjord, "Magnetic materials characterization using a fiber optic magnetometer," J. Appl. Phys., Vol. 57, pp. 3820-3822, 1985.
8. A. Yariv and H. V. Winsor, "Proposal for detection of magnetic fields through magnetostrictive perturbation of optical fibers," Opt. Lett., Vol. 5, pp. 87-89, 1980.
9. D. C. Larson, Y. W. Bibby and S. Tyagi, "Metallic-glass-coated optical fiber as magnetic field sensor," SPIE Proceedings, Vol. 1572, 1991.
10. J. D. Livingston, "Magnetomechanical properties of amorphous metals," Phys. Stat. Sol. (a) Vol. 70, pp. 591-596, (1982).

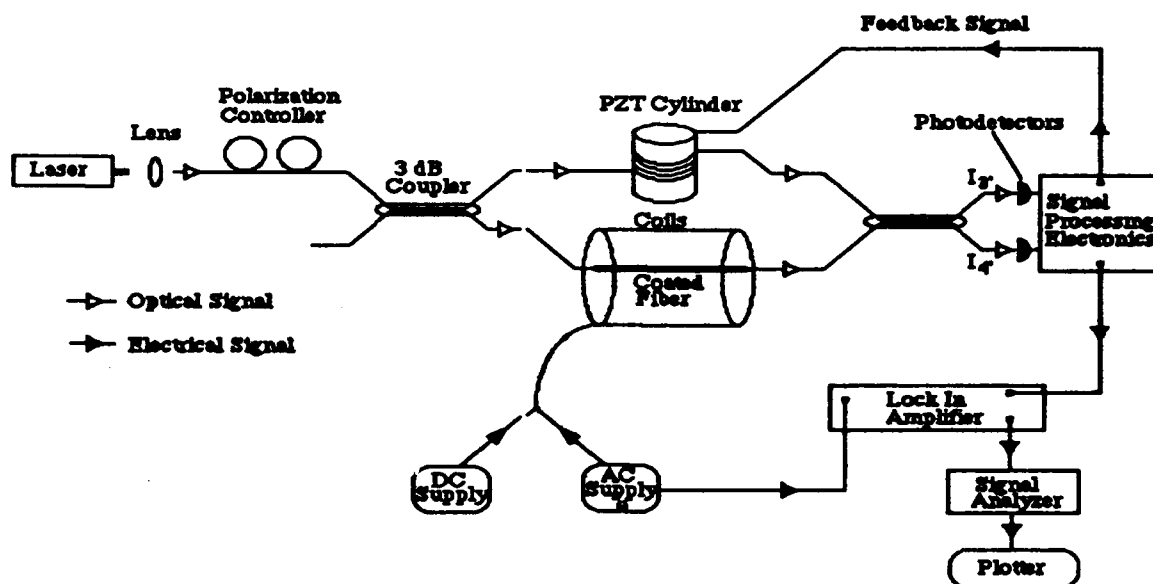


Fig. 1. Fiber optic magnetic field sensor experimental setup

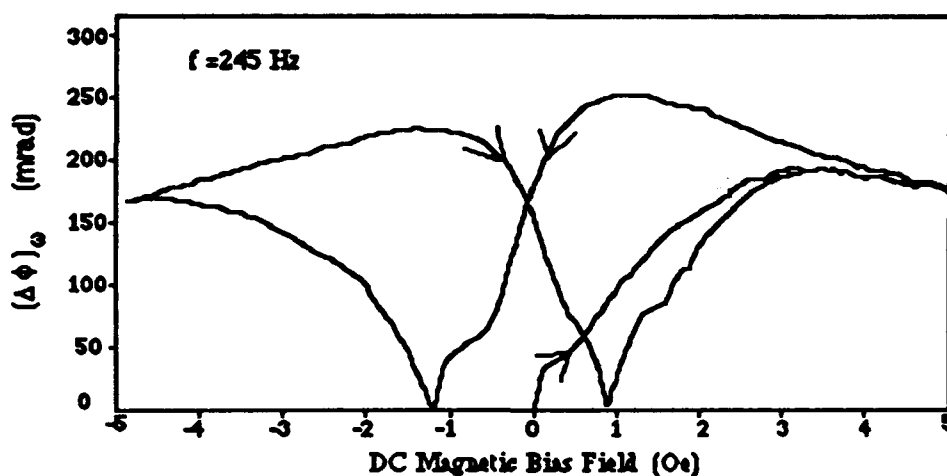


Fig. 2. Experimental phase shift vs. external field

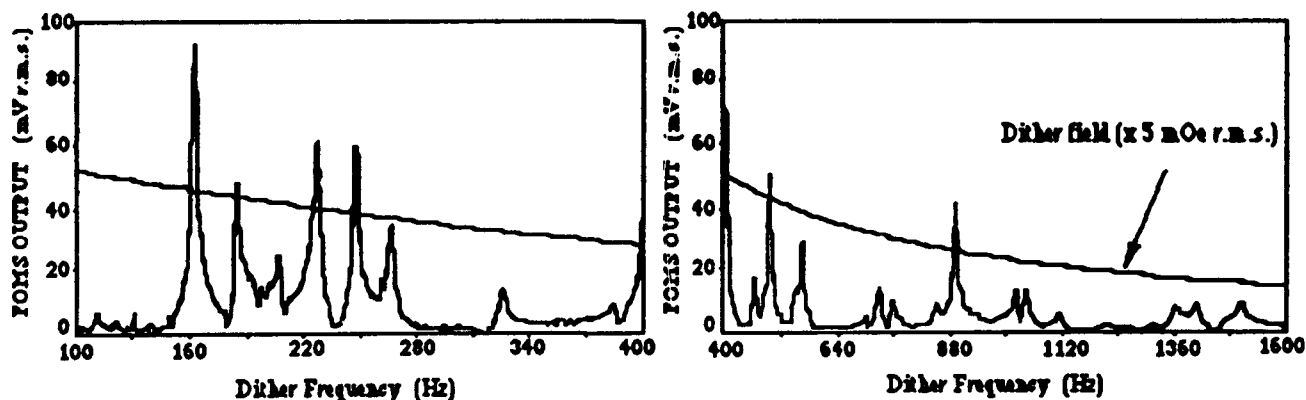


Fig. 3. Frequency response of the FOMS at 0 Oersted bias field



## P23 Interference Of The Faraday Coupled Signal With The Residual Mode Component In A Highly-Birefringent Optical-fibre Current Sensor

W. Chu D. Haldar D. McStay A.J. Rogers

Department of Electronic and Electrical Engineering  
King's College London  
Strand London WC2R 2LS U.K.

### Introduction

Highly linear-birefringent (HiBi) optical fibres have been widely used to transmit linearly polarised light in various applications because of their polarisation-holding properties [1]. Faraday coupling in linear-birefringent fibres have been reported previously [2,3]. Recently, an optical-fibre current sensor which makes use of the Faraday Effect to couple light resonantly from one mode to an originally-empty mode of a HiBi fibre, when the fibre is subjected to a periodic magnetic field, has been reported [4,5]. In this paper we report that the resonance of Faraday coupling is dependent on the relative axial position of the fibre and the magnetic field. This is caused by the interference of the Faraday coupled signal and the residual empty mode component, due to imperfect launching of purely linearly-polarised light into one eigenmode of a HiBi fibre. A good understanding of this dependence will be essential to the design of the HiBi fibre current sensor. The HiBi current sensor reported to date has used a periodic conductor array (PCA) to generate the required periodic magnetic field. In a practical environment, the required periodicity may be effected by periodically doping the fibre with materials which can either enhance or shield the magnetic field acting on the fibre. An initial result of Faraday coupling in a magnetically-shielded HiBi fibre using ferrites beads will be presented here.

### Faraday coupling in the presence of residual empty mode component

Consider a HiBi fibre with a front-end length of  $z_0$  before it enters a magnetic field. Orthogonally-polarised light components of amplitudes  $E_x$  and  $E_y$  (where  $E_x \gg E_y$ ) with phase difference  $\delta$  is launched into the fast and slow axes of the fibre. In the absence of Faraday rotation, the wave at distance  $l$  along the fibre is thus described by :

$$E_x(z_0 + l) = E_x(0) \cos(\omega t - \beta_x(z_0 + l) + \delta)$$

$$E_y(z_0 + l) = E_y(0) \cos(\omega t - \beta_y(z_0 + l))$$

where  $\beta_x$  and  $\beta_y$  are the phase constants of the fast and slow axes of the fibre.

Consider a sinusoidal magnetic field having a spatial phase constant  $\beta_H$  (where  $\beta_H = 2\pi / \text{the spatial period}$ ) acting over a total length,  $L$ , of fibre. Suppose that the peak value of the field is such as to induce a Faraday rotation of  $\rho$  per unit length. The component coupled from  $E_x$  to  $E_y$  at point  $z_0 + l$  is given by :

$$\begin{aligned} dE_y(z_0 + l) &= E_x(z_0 + l) \sin(\rho \cos(\beta_H l) dl) \\ &= E_x(0) \rho \cos(\beta_H l) \cos(\omega t - \beta_x(z_0 + l) + \delta) dl \end{aligned}$$

where we have assumed that the rotation over  $dl$  is very small..

Let  $\Delta\beta = \beta_y - \beta_x$ . The total  $E_y$  at the fibre end can be found by adding all the coupled components which reach  $L$  plus the residual empty-mode component, which arises from imperfect launch of linearly-polarised light and remains essentially constant throughout its propagation in the fibre; this can be calculated by integrating equation (1) along  $L$ , and then adding to the residual empty-mode component,  $E_y(0) \cos(\omega t - \beta_y(z_0 + L))$ . The total  $E_y$  at  $z_0 + L$  is therefore :

$$\begin{aligned} E_y(z_0 + L) &= 0.5 E_x(0) \rho L [\text{sinc}(A) \cos(\alpha + \delta + A) + \text{sinc}(B) \cos(\alpha + \delta + A)] + E_y(0) \cos(\alpha - \Delta\beta z_0) \\ \text{where } \alpha &= \omega t - \beta_x z_0 - \beta_y L \quad A = L(\beta_H - \Delta\beta)/2 \quad B = L(\beta_H + \Delta\beta)/2 \quad \text{sinc}(x) = \sin(x)/x \end{aligned}$$

The average power for the  $y$ -axis at the end of the fibre is given by :

$$\begin{aligned} P_y(z_0 + L) &= 0.5 E_y(0)^2 + (0.5 E_x(0) \rho L)^2 [0.5 \text{sinc}^2(A) + 0.5 \text{sinc}^2(B) + \text{sinc}(A) \text{sinc}(B) \cos(A - B)] + \\ &\quad 0.5 E_x(0) E_y(0) \rho L [\text{sinc}(A) \cos(A + \Delta\beta z_0 + \delta) + \text{sinc}(B) \cos(B + \Delta\beta z_0 + \delta)] \quad (1) \end{aligned}$$

the first term on the right hand side of (1) represents the original y-component while the second term represents the Faraday coupling at twice the signal frequency. It also shows that the coupled power is maximised when the fibre beat length equals the magnetic field period, as represented by the  $\text{sinc}(A)$  terms. The last term in (1) shows that the presence of the empty-mode component, due to imperfect launching of linearly-polarised light into the fibre, will cause interference with the Faraday coupled component. The cosine term indicates that the coupled signal will follow a sinusoidal variation with either an axial translation of the fibre with respect to the magnetic field, or a linear sweep in the x and y components' phase difference. For imperfect launching of light into the fibre, we have

$$\rho \ll E_y(0)$$

and therefore the interference term dominates the measured signal of  $P_y(z_0 + L)$ . A computer simulation of the interference term for different phase,  $\Delta\beta \cdot z_0 + \delta$ , of the cosine expression is shown in figure 1. The significance of figure 1 is that both of the size and position of the resonance peak can be altered by varying  $z_0$  or  $\delta$ . A series of experiments was then performed to verify the effect of the interference term in (1).

### Experimental

The periodic magnetic field required for the Faraday rotation was achieved by suspending an elliptically-cored HiBi fibre (Andrew's Corp. fibre, single mode at 633nm with 3.8mm beat length) just above a periodic conductor array (PCA) as shown in figure 2. The PCA consisted of 44 series-connected brass conductors which carried a current of 8 Amps. The PCA could be rotated and translated such that both the periodic field spacing, and the relative axial position of the magnetic field and the fibre could be varied independently. Linearly polarized light from a HeNe laser was launched into one eigenmode of the HiBi fibre, with an extinction ratio of 25dB. A Glan-Thompson analyser, whose acceptance axis was aligned with the empty mode, allowed light coupled into the other eigenmode to be detected by a silicon photodiode at the output end of the fibre. The output of the photodiode was connected to a lock-in amplifier, which took its reference from the current source.

In the first experiment, a PCA was slowly rotated at  $0.25^\circ$  interval while it was axially translated. The maximum and minimum values of the coupling signal were then recorded for every periodic spacing. This was done to verify the effect of  $\beta_H$  &  $z_0$  in (1) and the result is shown in figure 3. In order to test the effect of  $\delta$  in (1), a Pockel's cell (with half-wave voltage 230V at the laser wavelength) was placed at the input end of the HiBi fibre and was aligned with its birefringent axes parallel to those of the fibre. The PCA was initially rotated to produce a maximum coupling signal before the voltage across the Pockel's cell was varied. The resultant variation of the Faraday coupling signal with the Pockel's cell voltage is shown in figure 4. A sinusoidal variation of the coupling with a period of 460V is observed.

Finally, an experiment on the interference effect of Faraday coupling in a magnetically-shielded HiBi fibre using ferrites beads was performed. The magnetic field acting on the fibre is shown in figure 5. A HiBi fibre (Andrew's Corp. fibre, single mode at 633nm with 6.9mm beat length) was shielded with 17 ferrites beads (RS supplier, dimensions measures at 4mm outer diameter, 2mm inner diameter and 5mm thickness). The beads were placed periodically with a period equal to the fibre beat length. The shielded fibre was then placed in a solenoid whose magnetic flux at the center was independently measured at 7.6mT/Amp using a Hall Probe. To ensure that the fibre experienced maximum spatial variation of magnetic field, the solenoid carried a current of 4 Amps, which caused the ferrites beads to saturate. Under the action of the axial magnetic field, Faraday rotation took place in the region of the fibre where it was not magnetically shielded. A build-up of mode coupling in the HiBi fibre was therefore allowed to take place along the fibre. When the fibre was translated axially with respect to the ferrites beads a sinusoidal variation of the measured Faraday coupling signal was observed, as shown in figure 6. The period of the signal is consistent with the fibre beat length, as was predicted by (1).

### Discussion

In the derivation of the Faraday coupling equation (1), it has been assumed that the total coupling is small and the amount of light coupled back to the full mode is negligible. This causes  $P_y(z_0 + L)$  in equation (1) to increase monotonically. While this is true for small coupling, the same equation should not be applied in situation where both of the eigenmodes carry significant power, as in the case of an optical isolator [3]. In such cases, the well-established couple-mode equations, which deal with inter-modal coupling, should be used. The interference term in (1) is depicted in figure 1. It is composed of twelve different curves, each representing the Faraday coupling resonance for an increasing value of  $z_0$ . The same set of curves can be obtained if we vary the value of  $\delta$ , since both contribute to the phase term in (1). The set of twelve curves together completes the cycle of  $2\pi$  in the phase term.

This predicted interference term agrees well with the experimental results which are shown in figure 3&4. Figure 3 shows that the magnitude of the coupled signal follows a sinc function with periodic spacing while figure 4 shows that, at a given periodic spacing, the coupled signal varies with the phase difference of the orthogonally polarised electric vectors of the optical wave launched at the input. It is useful to compare this result with that reported by Simon and Ulrich [6]. In their experiment, the intensity of the output light from a Soleil-Babinet compensator and a polarising analyser was related to the ellipticity of the state of polarisation of light at the fibre where it interacts with the magnetic field. It is important to note that, in our experiment, although  $E_y(0)$  is 25dB less than the full-mode component it still contributes to the observed effect. In a practical application where temperature varies, the beat length will change and this will inevitably cause a subsequent change in the electric vectors' phase difference as the light propagates along the fibre. The combined effect can seriously affect the coupled signal and jeopardise the reliability of the sensor. Fortunately, the effect of the interference can be harnessed to advantage in using the HiBi current sensor. As we can see from figure 1 that the peak of the resonance, formed by the envelop of different phases, is effectively broadened. This broadening of resonance can accommodate a finite change in the fibre beat length (eg. due to temperature variation), or equally, larger tolerance on the design of the periodic current-carrying conductors which may be manufactured in the form of a periodically-grooved bus-bar structure [5], while preserving the measurand-selective nature of the current sensor. The phase term can be effected by sweeping the input light phase difference at a rate higher than the anticipated measurement bandwidth and employing peak detection of the coupled signal. It is envisaged that the need for the additional electronics can be replaced by using a wider-bandwidth light source. The source bandwidth needs to be small enough to be coherent within the length of the sensing region, so as to make constructive Faraday coupling possible, and wide enough to break the exact phase relationship of the eigenmodes before the light enters the measurand field. The use of periodic ferrites beads in shielding the fibre was demonstrated for the first time. The interference effect is evident from figure 6. The significance of the shielding technique is that it allows effective current measurement without the need for special design of busbars. Although ferrites beads are unlikely to be used in a practical environment, due to saturation and hysteresis, the shielding approach can be extended to a periodically-doped fibre with materials that can enhance or suppress Faraday coupling. The doping can be performed on the preform on it can be achieved using ion implantation on the fibre cladding.

### Conclusions

The interference of the Faraday coupled signal and the residual empty mode component due to imperfect launching of linearly-polarised light in one eigenmode of a HiBi fibre has been described and explained. Both the size and position of the resonance peak can be varied by either an axial translation of the HiBi fibre with respect to the periodic magnetic field or a sweep in the phase difference of the eigenmodes at the input. Since the coupling resonance can be altered in such a manner, it may provide the system engineer extra control on the sensor design, eg. in compensating the temperature effect of the sensor by broadening the resonance peak. The feasibility of magnetically shielding a HiBi fibre to achieve Faraday coupling was demonstrated for the first time. The coupling was also shown to exhibit the interference effect.

**Acknowledgements :** The research is supported by GEC Alsthom and the National Grid Company. D.Haldar is grateful to the British Council for the Commonwealth Scholarship.

### References

- 1) Dyott R.B., Cozens J.R., Morris D.G., *Elect.Letts*, Vol.15, pp380-382, 1979
- 2) Stolen R.H. and Turner E.H. , *Appl. Opt.*, Vol 19, No.6, pp842-845, 1980
- 3) Day G.W., Payne D.N., Barlow A.J., Ramskov-Hansen J.J., *Opt. Letts*, Vol 7, No.5, pp238-240, 1982
- 4) Chu W., McStay D. and Rogers A.J., *Elect Letts*, Vol 27, pp 207-208, 1991
- 5) Chu W., McStay D., Rogers A.J., 7th Optical Fibre Sensors Conference Proceedings, Australia, pp 93-96, Dec 1990
- 6) Simon A., Ulrich R., *Appl. Phy. Letts*, Vol 31, No.8, pp517-520, 1977

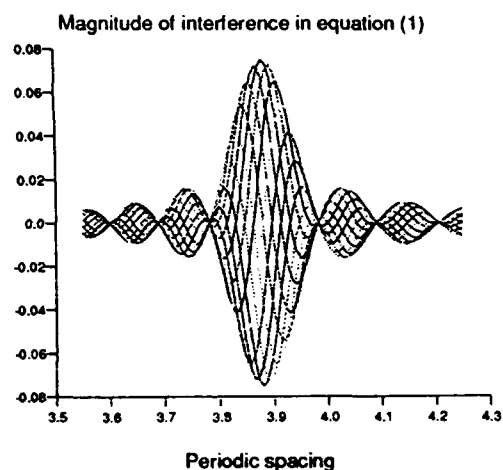


Figure 1

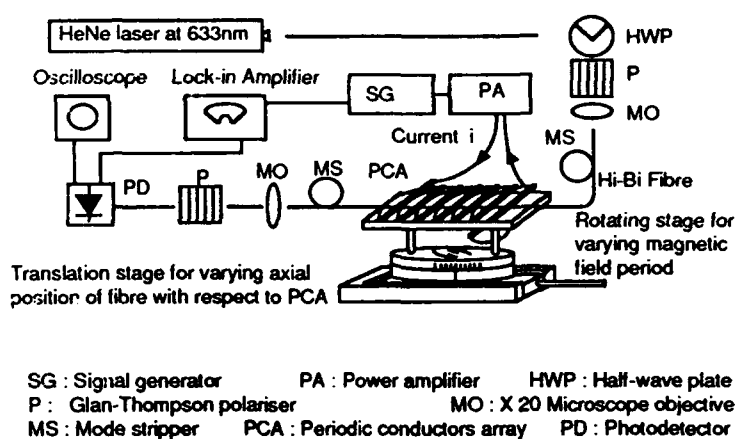


Figure 2

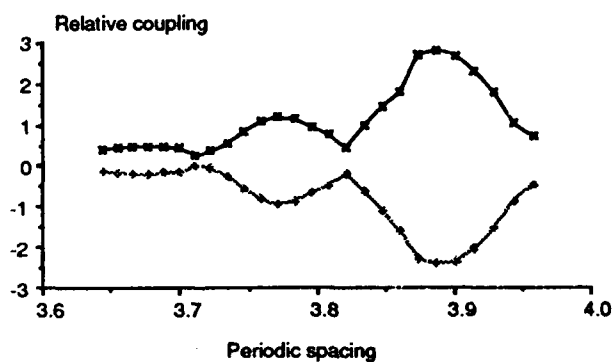


Figure 3

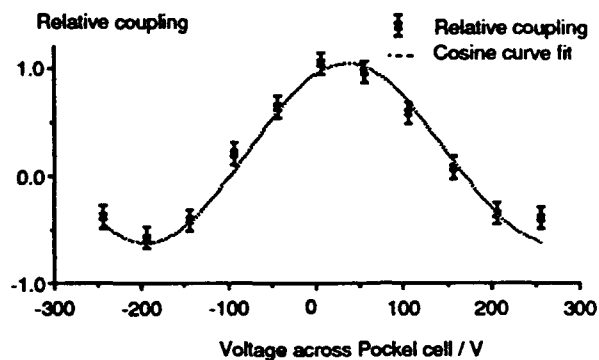


Figure 4

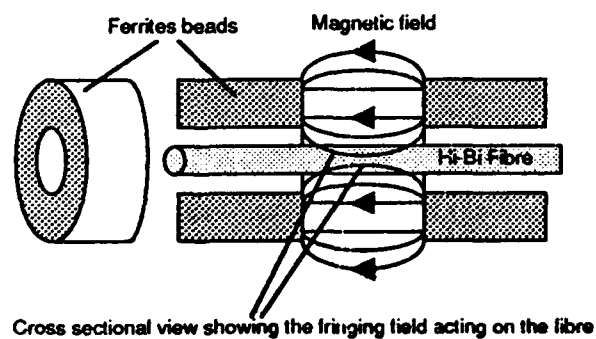


Figure 5

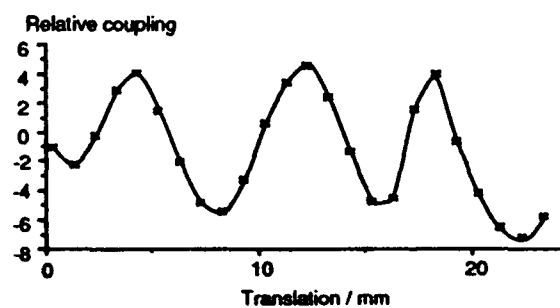


Figure 6

## A Novel Miniature Faraday Current Sensor Using a Bulk-optic-ring Sensing Element

Y.N. Ning, B.C.B. Chu and D.A. Jackson

Applied Optics Group, Physics Laboratory  
University of Kent, Canterbury, Kent. CT2 7NR, UK

### 1. Introduction

To date, most current sensors based on the Faraday effect have been in the form of a coil with a large number of turns of low birefringence monomode fibre wound around a current-carrying conductor [1-3]. In the Faraday effect, the change in azimuth,  $\Phi_F$ , of a linear polarised state propagating in a dielectric material subject to a magnetic field  $H$ , is given by

$$\Phi_F = \int_0^l V H \cdot dl \quad (1)$$

where  $V$  is the Verdet constant of the sensing material, and  $l$  is the distance traversed in the fibre. For the case of a solenoid of  $N_c$  turns with  $N_f$  fibre turns

$$\Phi_F = V N_c N_f I \quad (2)$$

where  $I$  is the current in the conductor.

Since the Verdet constant for an ordinary silica fibre is relatively small ( $4.68 \times 10^{-6}$  rad/A at 633 nm), particularly in comparison with other sources of birefringence within the fibre, high sensitivity fibre current sensors require a large number fibre turns. However, the increase in the number of turns results in an increase in both the intrinsic birefringence and the bend-induced linear birefringence [1,2], also, the light transit time through the fibre is increased, as a result, the sensitivity and the bandwidth of a fibre Faraday current sensor are severely limited [3].

High Verdet constant bulk glasses [4] are not subject to the problems associated with the presence of the intrinsic birefringence induced by core ellipticity and asymmetric stress or the extrinsic birefringence caused in deploying the fibre sensing element. Therefore, bulk glass based current sensor devices do not suffer the problems described above. However problems arise in designing closed loop bulk glass sensing elements, as additional phase shifts occur as a result of the reflections, the light beams must undergo to follow a closed path [5]

In this paper we introduce a new topology for a bulk glass Faraday current sensor. This novel sensor is in the form of a ring with an optically polished edge of high circularity. The current carrying wire passes through the central aperture. The light beam is coupled into the sensing element via a small 'roof top' prism. When the beam is injected at specific angles the light undergoes a large number of internal reflections at the critical angle, finally emerging at the other facet of the prism.

## 2. The configuration of the sensing element

Figure 1 shows a computer simulation of the optical path undertaken by the light inside the sensing element. The light enters the ring through the roof top prism at point E on the circumference and undergoes sequential internal reflections at the critical angle at positions (1), (2), (3), (4) etc., finally emerging through the prism after the 15th reflection. In passing through the ring the light will have effectively encircled the current 5 times thereby increasing the current sensitivity by the same factor.

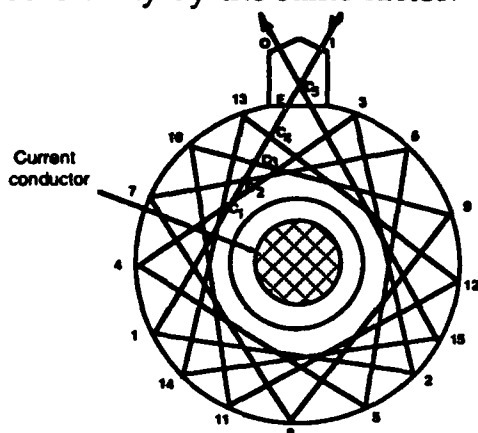


Figure 1. The configuration of the sensing element.

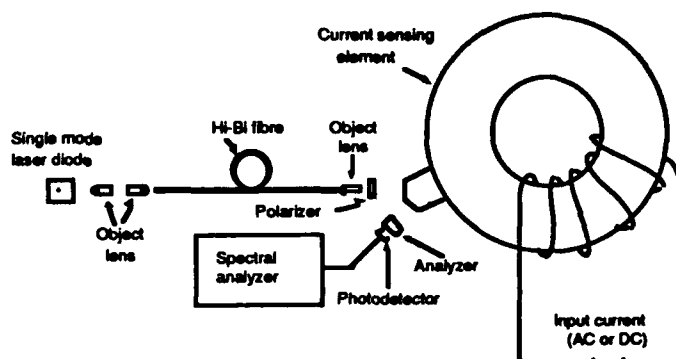


Figure 2. The experiment system.

When the Faraday effect is exploited for current measurement it is important that the light follows a closed loop in the dielectric material otherwise the line integral of the field will not be measured as required by equation (1). The path taken by the light on its first transverse around the central aperture is  $C_5 - E - C_1 - 1 - 2 - 3 - C_1$  and the first closed loop path is  $C_1 - 1 - 2 - 3 - C_1$  where  $C_1$  is the point where the loop closes. Hence the change in the azimuth of the light at  $C_1$  is given by

$$\int_0^1 \nabla H dl + \phi_c \quad (3)$$

where  $\phi_c$  is the additional rotation which occurs in the passage of the light from  $C_5$  to  $C_1$ .

For the second encirclement of the current the optical path is  $C_1 - 4 - 5 - 6 - C_2$  which is not a closed loop, however if the contribution from  $C_2$  to  $C_1$  is included then the correct line integral is effectively performed. This sequence of 'virtual closed' loop encirclement of the aperture is repeated five times in this figure and the error  $\phi_c$  which occurs in the first transverse of the light is sequentially reduced by subsequent traverses i.e.,  $\phi_1 \equiv (C_2 - C_1)$  for the second loop,  $\phi_2 \equiv (C_3 - C_2)$  for the third loop, etc.

Hence the azimuthal error  $\phi_c$  is effectively eliminated as the light exists the ring. This description is only valid if the ring exhibits no birefringence and the reflections all occur at the critical angle.

It can be shown that for certain combinations of ring diameters and incident angles of illumination that two output beams can be simultaneously generated. These beams are both spatially separated and have undergone a different number of closed loop paths. For the ring used in the experiments reported here outputs corresponding to 5 and 14 closed loop traverses of the ring were available corresponding to 15 and 44 total internal reflections at the critical angle respectively.

### 3. Experimental arrangement and the performance:

The optical system is shown in figure 2. Light from a low power ( $\sim 5\text{mw}$ ), single mode laser diode (ML 4102) with a wavelength of 780 nm is launched into a polarization maintaining fibre (PMF) via a 10 times objective lens. The emerging light from the fibre end is then collimated by a 40 times objective lens. The PMF employed serves not only as a channel to deliver the input polarised light to sensor, but also as a spatial filter, such that a well collimated beam is generated. This beam is then injected into the sensing element through a polariser P. The sensing element, made of SF6 Schott glass, had an outer diameter of 80 mm and a 35 mm central aperture. The light ejected from the sensor is detected by a photo detector after it has passed through an analyzer with its transmission direction at  $45^\circ$  to P. In applications where the current is at high potential, an optical fibre would be interposed between the analyzer and the detector.

Figure 3 shows the variations in the output signal as a function of applied AC current at a frequency of 50Hz (United Kingdom line frequency) when the light has made 5 traverses (channel 1) and 14 traverses (channel 2) of the ring. In both cases a linear relationship is obtained. The scale factor, determined from the slope of these curves, was 0.010 mVrms/Amp-turns for channel 1 and 0.032 mVrms/Amp-turns for channel 2 respectively. Figure 4 shows the results of a similar investigation for DC current. The scale factor for channel 1 was 0.008 mV/Amp-turns and for channel 2 was 0.033 mV/Amp-turns.

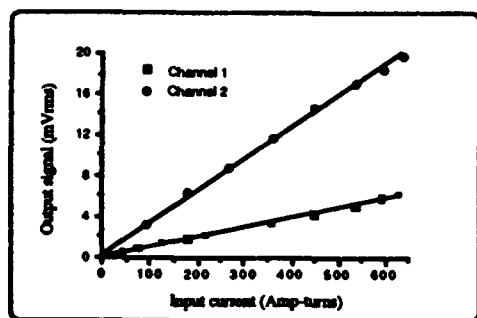


Figure 3. Variation of the output signal as a function of input AC current at 50Hz for channels 1 and 2.

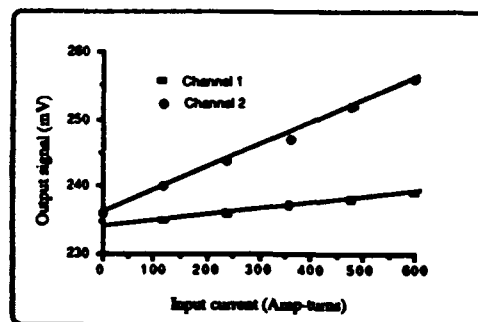


Figure 4. Variation of the output signal as a function of input DC current for channels 1 and 2.

In order to determine the sensitivity of the system, a measurement of the change in azimuthal angle as a function of the input DC current for channel 2

was made. The results of this measurement are shown in figure 5. The measured sensitivity of this channel, as defined by the slope of this line, is 0.022deg/Amp-turns.

The performance of the sensor was determined by measuring the minimum detectable AC current at a range of frequencies around the line frequency of 50Hz. As shown in figure 6, currents of ~ 1Amp-turns can be readily detected.

The frequency dependence of the system was measured with a variable frequency current source of 4.9 Amp-turns. The response was found to be constant  $\pm 1$  dB in the range 10 - 10<sup>4</sup> Hz.

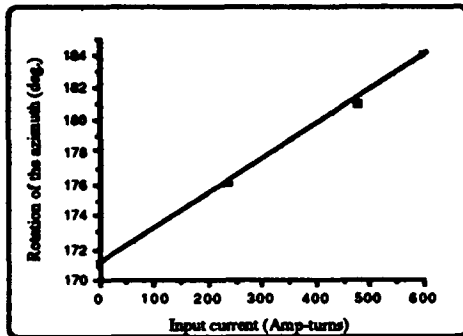


**Figure 5.** Variation in the azimuthal angle as a function of current for channel 2.

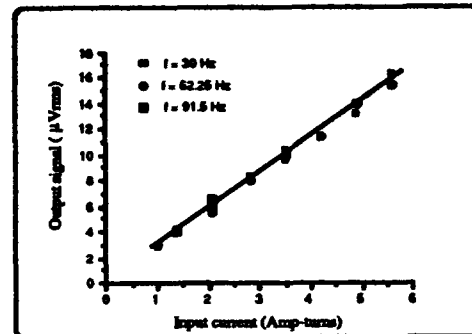


**Figure 6.** Variation in input signal as a function of frequency and current amplitude for channel 1.

#### 4. Conclusion:

In conclusion a novel high performance miniature optical current sensor based on the Faraday effect has been demonstrated. The bulk optical glass ring configuration overcomes many of the problems encountered with optical fibre current sensors and is much less complicated to fabricate than three dimensional bulk glass sensors.

This research was supported by the UK Science and Engineering Research Council and Sifam Ltd., Torquay under the Link-Joint Industrial Measurement Systems Programme.

#### References:

- [1] G. W. Day, Vol. 44 of Springer Proc. in Physics. Springer-Verlag, Berlin. 486, (1988).
- [2] A. J. Rogers, J. of Optoelectronics, 3, 391, (1988).
- [3] A Ben-Kish, N. Konforti, M. Tur, and E. Shafir, Proc. of the 7th opt. fibre sensors conf., 97, (1990).
- [4] C. L. Carter and J. C. Stites, In Tech. 34, 41 (1987).
- [5] S. P. Bush and D.A. Jackson, Opt. Lett., Vol. 16, 955, (1991).
- [6] S. Donati, V. Annovazzi-Lodi and T. Tambosso, IEE Proc. Vol. 135, 372, (1988).



## P25 The Performance Of A Fibre Optic Magnetic Field Sensor Utilizing A Magneto-Optical Garnet

*Hans Sohlström, Kjell Svantesson*

The Royal Institute of Technology, Instrumentation Laboratory,  
S-100 44 Stockholm, Sweden

### Introduction

Due to their intrinsically favourable behaviour with respect to electromagnetic interference and galvanic isolation, fibre optic sensors are good candidates for current and magnetic field measurements in high power electric transmission systems. Sensors utilizing the magneto-optic Faraday effect have been investigated for a number of years. When looking for a compact design, magneto-optical garnet materials such as YIG (Yttrium Iron Garnet,  $\text{Y}_3\text{Fe}_5\text{O}_{12}$ ) or preferably substituted YIG have shown promising properties.<sup>1,2,3,4</sup> One common advantage of these materials is their large Faraday rotation, up to  $2000^\circ/\text{cm}$  for Bi-substituted YIG.

The fabrication of pure YIG has a fairly long tradition due to its applications in microwave systems. However, samples resulting from the growth of bulk crystals are not suitable to prepare for optical applications, among other things they need to be carefully polished. More recently, the liquid phase epitaxy (LPE) technique for fabricating thick magneto-optical garnet layers, mainly for optical isolator applications in optical communication systems, has been developed to a stage where also several physical parameters could be handled at will. Furthermore the LPE technique can yield optical quality wafers of several inches in diameter. To prepare a sensor element from such a wafer only uncritical sawing is needed, which to a large extent facilitates the sensor fabrication.

The sensor reported in this paper utilizes an epitaxially grown (YbTbBi)IG ( $(\text{YbTbBi})_3\text{Fe}_5\text{O}_{12}$ ) layer on a GGG substrate, with a composition optimized for optical isolator applications, implying low temperature dependence.

### Sensing principle

To utilize the polarization rotation in an intensity based multimode fibre sensor, polarizers are placed before and after the sensing element. The intensity of the light transmitted through the second polarizer will then depend on the polarization rotation in the crystal. Thanks to the non-reciprocity of the Faraday effect it is possible to utilize a folded design according to fig 1. One then gets twice the polarization rotation for a given crystal thickness.

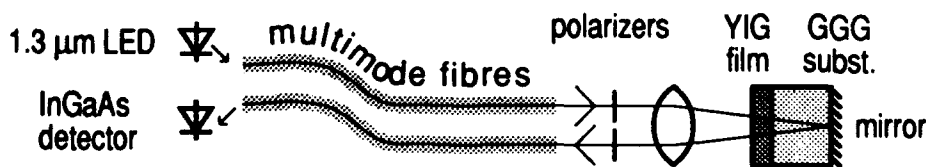


Fig. 1. Outline of the folded type magnetic field sensor.

Due to the ferrimagnetic properties of the garnet material, the picture of a homogeneous, magnetic field dependent, rotation of linearly polarized light is too simplified to be useful to predict the sensor behaviour.

The internal magnetization of the crystal leads to the presence of magnetic domains that will change their size and shape when an external magnetic field is applied. The resulting polarization state of a narrow ray of light will then depend on the actual domain distribution along its path. This will in general not yield reproducible conditions. However, by using a sufficiently wide beam of light the net rotation of a large number of individual domains will be measured, giving a useful sensor performance.<sup>5,6</sup>

In our case we assume that all domains reach through the entire thickness of the layer, with a magnetization direction which is either parallel or anti-parallel to the light propagation. In the absence of an external magnetic field, the two types of domains will occupy approximately equal volumes. However, when a magnetic field is applied, the domains of one kind will grow at the expense of those of the other kind.

In addition to the magnetic properties of the material, the optical conditions will affect the sensor performance. With a spatial coherence of the light, large enough to create interference between light having passed different domains, the sample will act as a phase grating. Sufficiently far behind the sample, the undiffracted light will then have a state of polarization and intensity that depends on the applied field, while the light in the first diffraction order will be polarized perpendicularly to the incident light.

The optical configuration used in our sensor, i. e. with the polarizer far from the sensing element, yields a sensor output that is given by the transmitted intensity of the undiffracted light after the second polarizer. The magnetic field dependence is in fact very similar to the one achieved with a material with a homogeneous magnetization.

Our sensor was realized with an epitaxially grown 0.13 mm thick (YbTbBi)IG layer on a GGG substrate. The domain magnetization was perpendicular to the plane of the layer. The thickness of the layer was chosen to give a single pass maximum rotation of  $22.5^\circ$  at  $1.3\mu\text{m}$ . The components of the sensor head, i. e. the sensing element, a gradient index lens and two polarizers, were mounted in a plastic enclosure of 6 mm length and 4 mm in diameter.  $100\mu\text{m}$  core fibres with a cladding diameter of  $140\mu\text{m}$  were used for the signal transmission.

### Measurement results

The DC magnetic field characteristics of the sensor is shown in fig 2. The saturation points fall at approximately  $\pm 100\text{ mT}$ .

The frequency spectra for different AC field levels were also studied to further investigate the central part of the characteristics. Fig 3 shows the output spectrum for a 1 kHz, 27 mT (peak) applied field. Even with this relatively large signal amplitude, the distortion was only about 1 %, The signal to noise ratio for a 1 Hz bandwidth was 90 dB. A 20 dB reduction of the signal to 2.7 mT further reduced the distortion to about 0.3 %, fig 4.

The signal was then reduced in steps of 20 dB down to 270 nT. At this signal level, the spectrum analyzer bandwidth was reduced to 88 mHz to separate the signal from the sensor amplifier noise, fig 5.

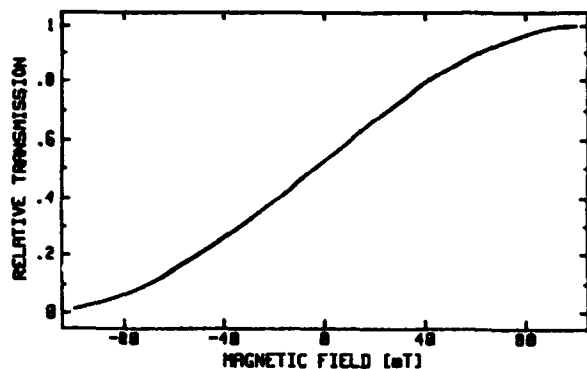


Fig 2. The magnetic field characteristics of the sensor.

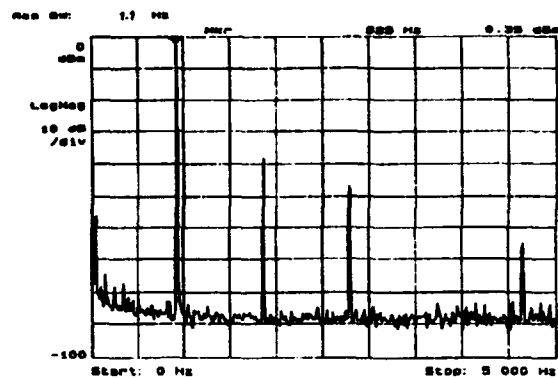


Fig 3. 0-5 kHz frequency spectrum of the sensor output for a 27 mT (peak) excitation at 1 kHz. (Sensor amplifier 3 dB bandwidth: 5 kHz; Analyzer bandwidth: 1.1 Hz)

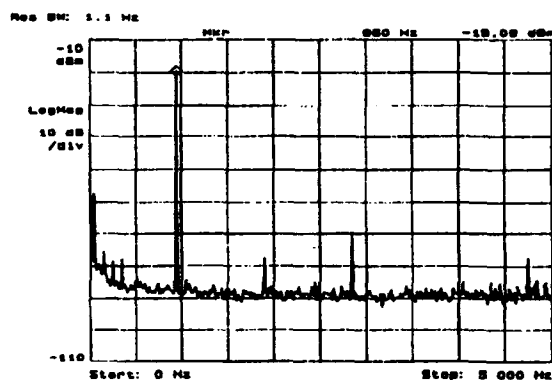


Fig 4. 0-5 kHz frequency spectrum of the sensor output for a 2.7 mT (peak) excitation at 1 kHz. (Sensor amplifier 3 dB bandwidth: 5 kHz; Analyzer bandwidth: 1.1 Hz)

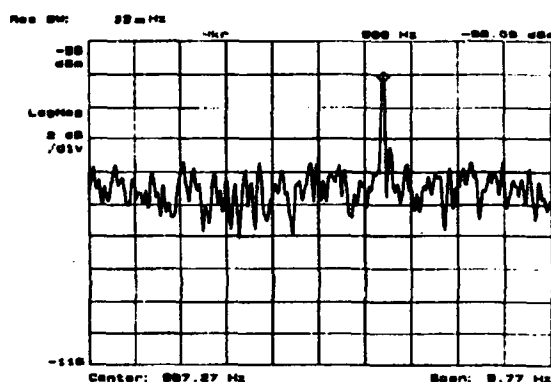


Fig 5. Narrow band frequency spectrum of the sensor output for a 270 nT (peak) excitation at 1 kHz. (Sensor amplifier 3 dB bandwidth: 5 kHz; Analyzer bandwidth: 88 mHz)

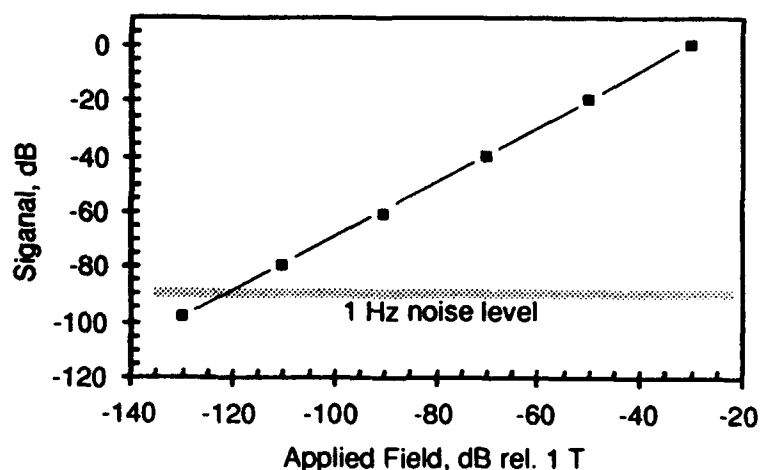


Fig 6. The signal amplitude (dB rel. signal at 27 mT) versus the applied field.

The measurement results are summarized in fig 5, where the signal amplitude is plotted versus the applied 1 kHz field amplitude. Apparently the sensor is, within the experimental accuracy, linear over a range of at least 100 dB. In the experimental data presented here, the lowest point is buried the 1 Hz noise. This noise, however, originates in the detector and its amplifier and is not an inherent property of the sensor itself. By decreasing the optical loss of the sensor and by improving the amplifier, a 20 dB increase in signal to noise ratio should be within reach.

### Conclusions

The multimode fibre optic magnetic field sensor that we have reported here is found to be linear over a range of more than 100 dB. The experimental data show a 1 Hz noise equivalent magnetic field of 1  $\mu$ T. The sensor is, however linear below this level. With an optimized design we consider it possible to reduce the noise equivalent field by a factor of 10.

### Acknowledgements

The garnet film sample used was provided by Sumitomo Metal Mining Co. Ltd, Tokyo, Japan. We would also like to thank Mr Bengt Molin for his skilful assistance in preparing the sensor prototype.

This work was supported by the National Swedish Board for Technical Development.

### References

1. G. Doriath, R. Gaudry, and P. Hartemann, "A sensitive and compact magnetometer using Faraday effect in YIG waveguide", *Journal of Applied Physics*, vol. 53, no. 11, p. 8263–8265, 1982.
2. K. Svantesson, H. Sohlström and U. Holm, "Magneto-optical garnet materials in fibre optic sensor systems for magnetic field sensing", *SPIE Proc*, vol. 1274: *Electro-Optic and Magneto-Optic Materials and Applications II*, H. Dammann, p. 260–269, 1990.
3. H. Sohlström, U. Holm and K. Svantesson, "A Polarization-Based Fibre Optical Sensor System Using a YIG Optical Waveguide for Magnetic Field Sensing", *Springer proceedings in Physics 44: Optical Fiber Sensors*, H. J. Arditty, J. P. Dakin, and R. Th. Kersten, p. 273–278, Springer-Verlag, Berlin, 1989.
4. H. Sohlström and K. Svantesson, "A waveguide based fibre optic magnetic field sensor with directional sensitivity", to be published in *SPIE Proc*, vol. 1511: *Fiber Optic Sensors: Engineering and Applications*, 1991.
5. U. Holm, H. Sohlström and T. Brogårdh, "YIG-sensor design for fibre optical magnetic field measurement", *OFS 84*, R. Th. Kersten and R. Kist, p. 333–336, VDE-Verlag, Berlin, 1984.
6. M. N. Deeter, A. H. Rose and G. W. Day, "Fast, Sensitive Magnetic-Field Sensors Based on the Faraday Effect in YIG", *Journal of Lightwave Technology*, vol. 8, no. 12, p. 1838–1842, 1990.

## **P26 Low-frequency Intensity Noise Reduction For Fiber-Optic Sensor Applications**

**D.M. Dagenais<sup>\*</sup>, K.P. Koo<sup>\*</sup>, A. Dandridge**

**Optical Sciences Division, Code 6570, Naval Research Laboratory**

**Washington, DC 20375**

**Permanent address: SFA Inc., Landover, MD 20785**

Fiber sensors have recently taken advantage of the 1.3 $\mu$ m diode-pumped laser technology, which offers high output power in a single frequency and orders of magnitude improvement in frequency stability over semiconductor devices [1]. The small frequency jitter [2] of Nd:YAG lasers enables one to attain submicron phase noise in interferometric sensors with as much as 10 meters of optical path difference. Because non-linear fiber sensors, such as magnetic fiber sensors, which make use of a carrier to upconvert low-frequency signals to be detected, are often limited by intensity noise upconverted around the carrier [3], we have measured the intensity stability of those devices. The intensity noise in fiber sensors originates from both the laser instabilities and the drifts in the fiber launch.

We report measurements of the low-frequency Relative Intensity Noise (RIN) of diode-pumped Nd:YAG ring lasers, before and after launching into a fiber sensor. We also demonstrate reduction of the RIN by an external remotely controlled modulator, to a value of  $<-100$  dB/ $\sqrt{\text{Hz}}$  at 1 Hz.

The schematics of the set-up are shown in figure 1. The laser is a series 120 or 122 Lightwave Electronics diode pumped Nd-YAG ring laser at 1.3  $\mu$ m. The optics module contains an electro-optic modulator and a beam splitter to sample light into a reference detector. Direct measurement of the RIN is obtained before launch, at the output of the

optics module. Light from the source is then launched into a single mode fiber through a 20X microscope, and split by a 10:1 fiber coupler into the input to a sensor and a sample detector.

The RIN obtained for the series 122 before and after closing its own intensity noise reduction loop [4] is shown in figure 2. The intensity noise obtained in an open loop configuration shows a  $1/F$  dependence, and the RIN,  $-70 \text{ dB}/\sqrt{\text{Hz}}$  at 1 Hz, is believed to be due to the modal fluctuations of the broad-area pump laser. Feedback into the pump laser improves the RIN by 40 dB, to  $-110 \text{ dB}/\sqrt{\text{Hz}}$  at 1 Hz. Unfortunately, such feedback affects phase as well as amplitude of the laser. As a comparison, figure 3 shows the series 120 laser RIN, before and after closing the loop on the external modulator, with a RIN reduced to  $-120 \text{ dB}/\sqrt{\text{Hz}}$  at 1 Hz.

After launching into a single mode fiber, the RIN below 10 Hz increases to about  $-70 \text{ dB}/\sqrt{\text{Hz}}$  at 1 Hz, due to drifts in the launch, which supersede any prior correction. Reduction of the intensity noise was then obtained by remotely controlling the modulator with a pigtailed detector, located after the launch fiber coupler. The output of the fiber coupler was checked, to ascertain correlation of the 2 output ports of the coupler down to subhertz regimes. The improvement in the RIN, shown in figure 4, (40 dB at 1 Hz), keeps the RIN below  $-80 \text{ dB}/\sqrt{\text{Hz}}$ , down to  $\approx 200 \text{ mHz}$ . The improved noise level obtained at frequencies larger than 1 Hz with the remote feedback, (RIN of  $-140 \text{ dB}/\sqrt{\text{Hz}}$  with remote feedback, vs  $-120 \text{ dB}/\sqrt{\text{Hz}}$  with external feedback ) is believed to be due to the advantages gained by selecting a small area low-noise detector (InGaAs) and a pigtailed configuration over a large area Germanium and bulk focusing configuration.

**Acknowledgments:** The authors wish to acknowledge the Office of Naval Technology for partial funding of this work and to thank C. A. Villarruel for valuable discussions.

## References

- 1- A. Dandridge and A.B. Tveten, "Phase noise of single-mode diode lasers in interferometric systems", Appl. Phys. Lett., Vol.39, p.530 (1981)
- 2- K.J. Williams, A. Dandridge, A.D. Kersey, J.F. Weller and A.B. Tveten,

"Interferometric measurement of low-frequency phase noise characteristics of a diode laser-pumped Nd:YAG ring laser", Electron. Lett., Vol.25, p.774 (1989)

3- D.M. Dagenais, F. Bucholtz, K.P. Koo, A. Dandridge, "Detection of low-frequency magnetic signals in a magnetostrictive fiber-optic sensor with suppressed residual signal", J. Lightwave Technol., Vol. LT-7, p.881 (1989)

4- T.J. Kane, "Intensity noise in diode-pumped single-frequency Nd:YAG lasers and its control by electronic feedback", IEEE Photonics Technol. Lett., Vol.2, No.4, P.244 (1990)

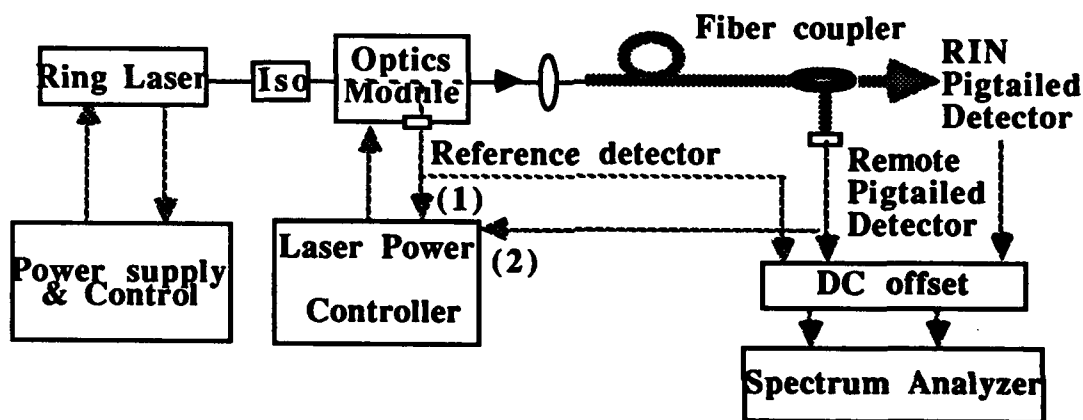


Figure 1- Schematic of the set-up for RIN measurement and compensation.

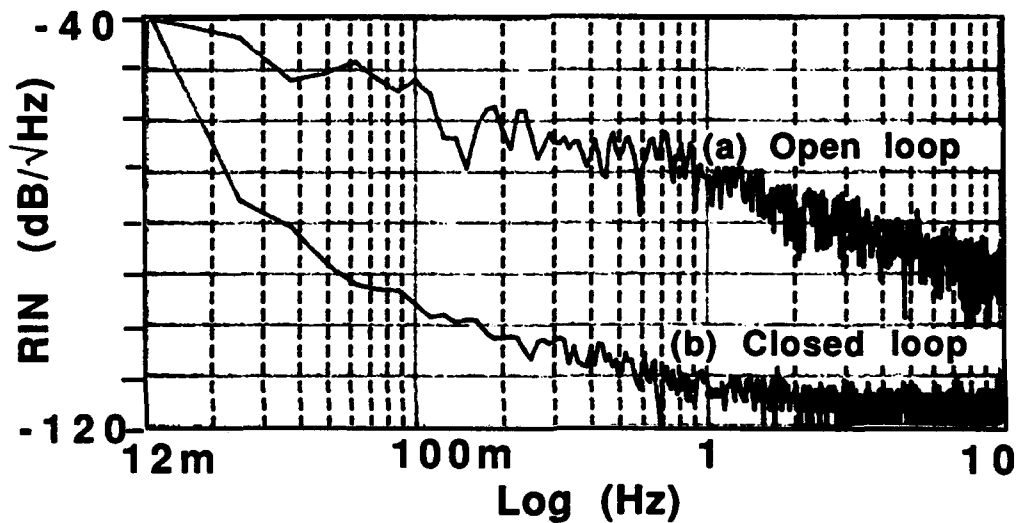


Figure 2- RIN of series 122 laser, with and without its own low-frequency correction.

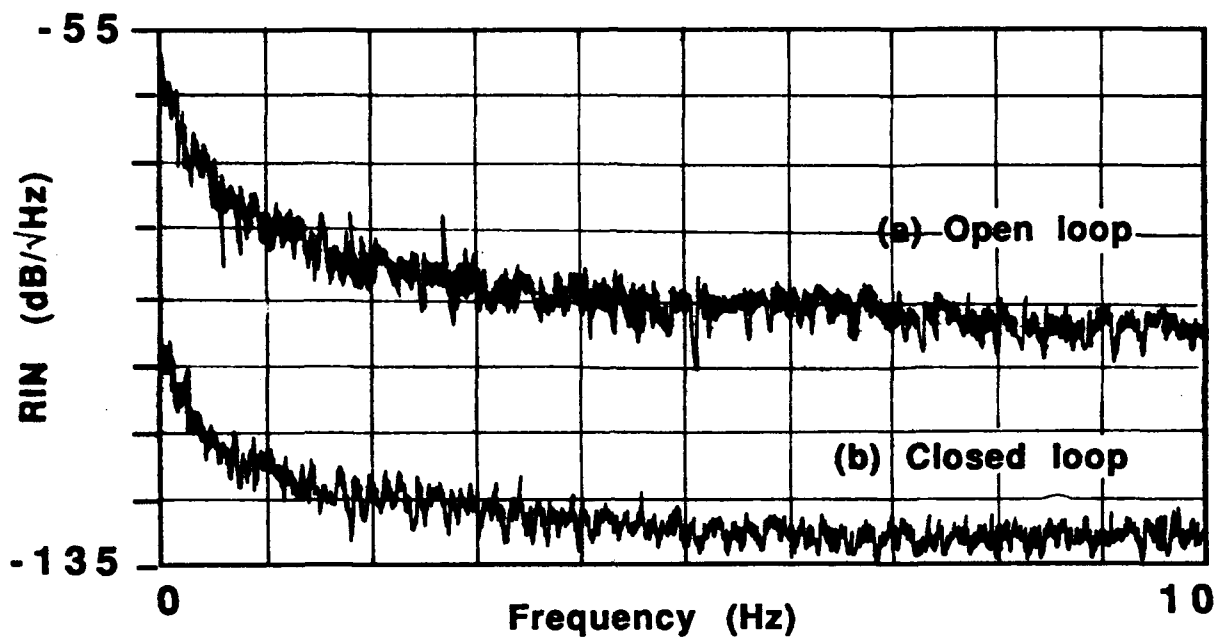


Figure 3- RIN of series 120 laser, with and without external control on the reference detector.

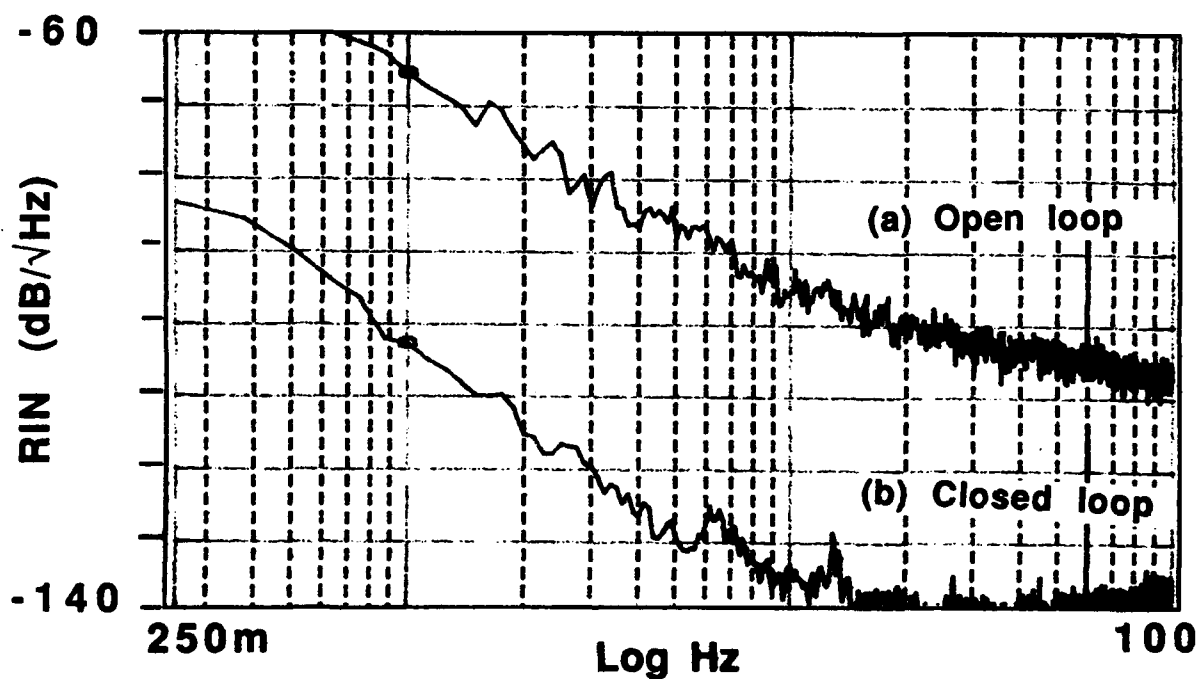


Figure 4- RIN of series 120 laser measured after injecting light into a fiber, with and without remote correction on the fiber pigtailed detector.



## **P27     A Fibre Optic Frequency Shifter Utilising Stimulated Brillouin Scattering In Birefringent Optical Fibre**

**R P Tatam**  
Optical Sensors Group  
School of Mechanical Engineering  
Cranfield Institute of Technology  
Cranfield, Milton Keynes  
United Kingdom  
MK43 0AL

**C J Duffy**  
Optics and Laser Technology Department  
Sowerby Research Centre  
British Aerospace plc  
FPC 267, PO Box 5  
Filton, Bristol  
United Kingdom  
BS12 7QW

Frequency shifting is a well established technique to produce a heterodyne carrier at a frequency suitable for subsequent electronic demodulation. An acousto-optic Bragg cell is traditionally utilised to produce 40 or 80 MHz carriers, for example. However, these devices are generally incompatible with fibre optic systems due to the losses incurred in coupling into and out of monomode optical fibre.

In-fibre components have been developed which operate by coupling light between polarisation or spatial modes of an optical fibre using externally generated travelling acoustic waves coupled onto the optical fibre. In general, such devices are difficult to fabricate, require several watts of electrical input power and are not mechanically rugged.

In this paper, an in-fibre technique for producing a heterodyne carrier frequency using Stimulated Brillouin Scattering (SBS) is reported. SBS is a non-linear effect associated with the interaction of a pump signal, optically induced acoustic phonons, and a frequency downshifted backscattered signal. By mixing the SBS signals produced independently from the two eigenaxes of birefringent fibre, carrier frequencies in the 1-20MHz region can be generated. This frequency is compatible with established electronic demodulation systems. This paper describes the background theory to the approach and its experimental validation, and then discusses the implications of the results for SBS based sensing systems.

**Theory:** SBS can be described as a three-wave interaction, between an optical pump, an acoustic phonon and the scattered signal. The pump beam is scattered by an acoustic phonon; the pump and scattered wave then interfere to induce more phonons in the fibre via electrostriction and the process builds up. The backscattered Stokes signal is frequency downshifted with respect to the pump and is given by:

$$\nu_p = \frac{2nV}{\lambda_p} \quad (1)$$

where  $\lambda_p$  is the pump wavelength,  $V$  is the acoustic phonon velocity and  $n$  the

core refractive index. For a 514.5nm pump in monomode fibre,  $\nu$  is approximately 34 GHz. This is generally too high for use in electronic demodulation schemes but may be reduced by at least three orders of magnitude by beating together the SBS signals produced from the fast and slow axes of the birefringent optical fibre. From eqn 1, this frequency,  $\delta\nu$ , is given by

$$\delta\nu = \frac{2V}{\lambda_p}(n_s - n_f) = \frac{2V}{L_b} \quad (2)$$

where  $n_s$  and  $n_f$  are the refractive indices of the slow and fast axes respectively and  $L_b$  is the beat length of the fibre. For high birefringent fibre, with  $L_b$  equal to 1mm, a beat frequency of 11.9 MHz is predicted. Note that no externally applied power is required to generate the optical carrier.

**Experiment and results:** The experimental arrangement used to demonstrate the SBS frequency shifting concept is illustrated in Fig 1. A Lexel 3000 Ar laser operating in a single longitudinal mode at 514.5nm was used as the pump. The light was coupled into an 800m sample of 3M/Eotec birefringent fibre via an optical isolator and half wave plate. The fibre was single mode at 633nm, with a 1.6mm beat length and losses of 14.3 dB/km at 630nm. The fibre demonstrated an SBS onset threshold of 24mW and produced 55% conversion efficiency for 110mW launch powers. The fibre was capable of supporting both  $LP_{0,1}$  and  $LP_{1,1}$  modes when operated at 514.5nm but the output spatial profiles of the SBS from each eigenaxis indicated that only the fundamental mode ( $LP_{0,1}$ ) was undergoing SBS. The backscattered flux was simultaneously monitored by both a scanning Fabry-Perot interferometer and a high speed detector, the latter being connected to an electronic spectrum analyzer.

The half wave plate was rotated to align the input polarisation plane of the pump at 45° to the fast and slow eigenaxes of the fibre. The SBS signals from each eigenaxis, when monitored independently, demonstrated some interesting features. The signals consisted of randomly occurring pulsed modes (life-times  $\ll 1$ sec.) superimposed on a broad spectrum, ranging from d.c. to 15MHz (3dB point). These observations are consistent with recent research investigating the chaotic properties of SBS in fibres. Chaotic behaviour results from feedback mechanisms arising both within, and at the air-core interfaces of the fibre and produces large intensity instabilities in the d.c. to MHz frequency region of the propagating light.

Typical results for the system are illustrated in Fig 2. Fig 2(a) shows the output of the system with both eigenaxes populated below SBS threshold. Fig 2(b) shows the system output when one eigenaxis was producing SBS. The broadband chaotic phenomenon associated with the SBS is displayed, though no pulsed modes were present when the frame was sampled. Fig 2(c) is a representative output for simultaneous SBS occurring along both axes. The mean upshift was 10.6 MHz, sampled from approximately 60 readings. Unlike the randomly occurring pulsed modes, the carrier was present at all times, though it was modulated about its mean value by  $\pm 8$  MHz (standard deviation), characteristic again of the chaos induced instabilities in the system. On insertion of the fibre parameters into eqn 2, a 9.2MHz carrier signal is predicted.

**Discussion:** Experiments indicate that a frequency shifter is attainable in principle. The frequency instabilities associated with the chaos, however, have repercussions for the whole concept of utilising SBS<sub>97</sub> for sensors and signal processing elements. Proposed SBS sensing systems<sup>97</sup>, in which the frequency of the SBS is modulated by an external measurand, have not indicated the presence of significant instabilities, suggesting that the choice of an alternative pump and/or fibre may minimise the effect.

Clearly, the frequency stability of the SBS signal is an essential factor in obtaining high resolution sensing systems.

The relatively high power requirements of the system described here can be relaxed by using infra-red laser diodes in conjunction with fibre ring resonator systems. Sub-milliwatt SBS threshold levels have been reported for such configurations, demonstrating the potential of developing a miniaturised, fibre compatible component.

## ACKNOWLEDGMENTS

The authors thank Professor R Harrison of Heriot Watt University for his helpful discussions and Lambda Photometric for the loan of equipment. CJD acknowledges an SERC/British Aerospace industrial studentship and Drs R Clarke and L Cooke at BAe.

## REFERENCES

1. Jones, J D C and Jackson, D A 'Fibre optic sensors', Optica Acta, 1986, 33, (12), pp. 1469-1503.
2. Pannell, C N, Tatam, R P, Jones, J D C and Jackson, D A 'A fibre optic frequency shifter utilising flexure waves in birefringent fibre', J. Inst. Electron. Radio Eng., 1988, 58, (5), pp. 592-598.
3. Kim, B Y, Blake, J N, Engen, H E and Shaw, H J 'All fibre acousto-optic frequency shifter', Opt. Lett., 1986, 11, (6), pp. 389-391.
4. Cotter, D 'Stimulated Brillouin scattering in monomode optical fibre', J. Opt. Commun., 1983, 4, (1), pp. 10-19.
5. Smith, R G 'Optical power handling capacity of low loss optical fibres as determined by stimulated Raman and Brillouin scattering', Appl. Opt., 1972, 11, (11), pp. 2489-2494.
6. Harrison, R G, Uppal, J S, Johnstone, A and Moloney, J V 'Evidence of chaotic stimulated Brillouin scattering in optical fibres', Phys. Rev. Lett., 1990, 69, (2), pp. 167-170.
7. Culverhouse, D, Farahi, F, Pannell, C and Jackson, D A 'Potential of stimulated Brillouin scattering as a sensing mechanism for distributed temperature sensors', Electron. Lett., 1989, 25, (14), pp. 913-915.
8. Bayvel, P and Giles, I P 'Linewidth narrowing in semi-conductor laser pumped all-fibre Brillouin ring laser', Electron. Lett., 1989, 25, (4), pp.260-262.

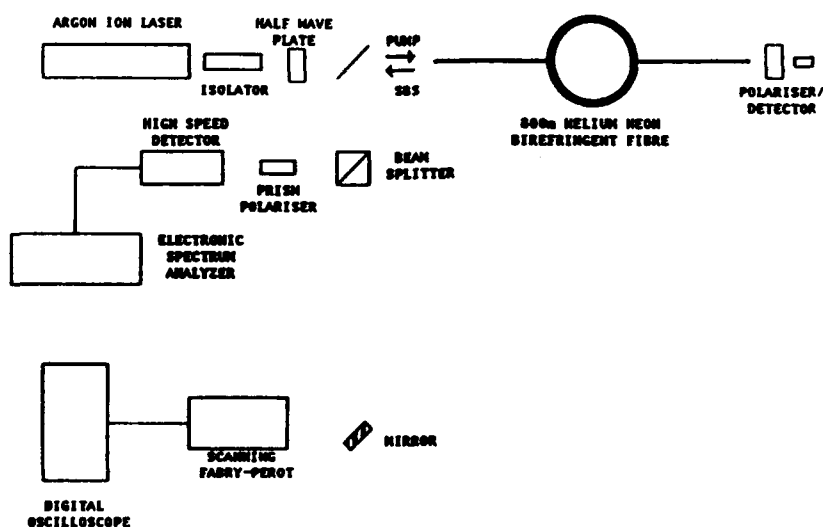
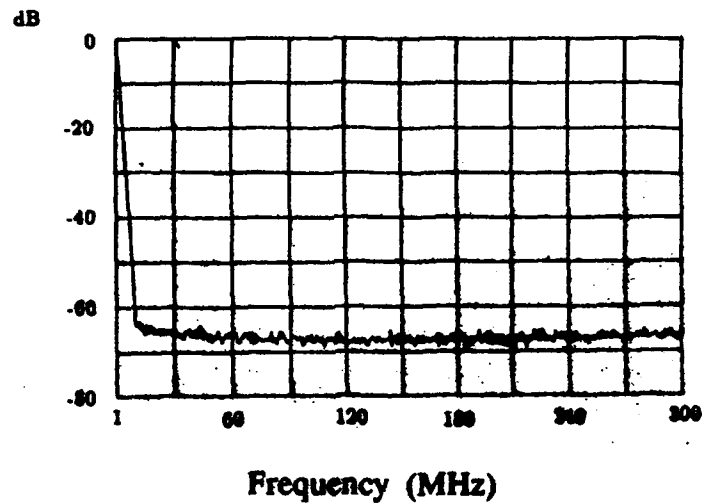
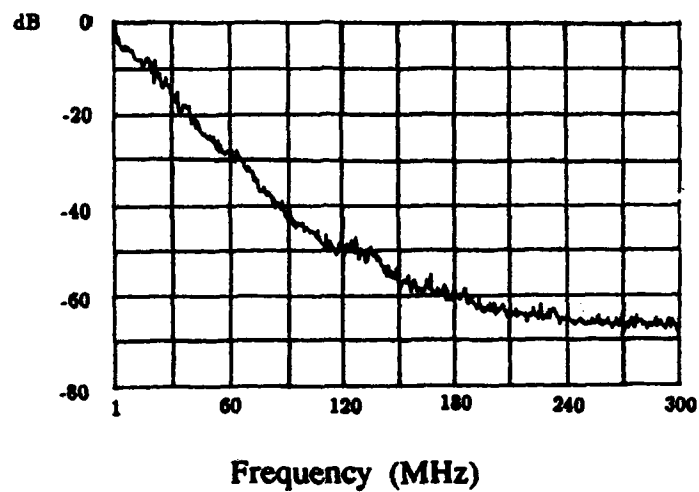


Fig. 10 Optical Frequency Shifter Experimental Arrangement



**Fig. 2(a) System Output Spectrum (1-3000MHz): No SBS**



**Fig. 2(b) System Output Spectrum (1-3000MHz): SBS Along one Eigenaxis**

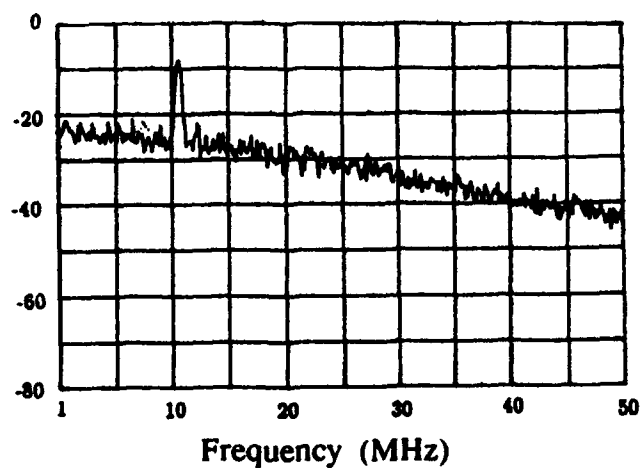


**Fig. 2(c) System Output Spectrum (1-50MHz): Simultaneous SBS Along Fast and Slow Eigenaxes Showing 10.6MHz Carrier**

## P28 Fibre Frequency Shifter Based Upon Stimulated Brillouin Scattering Generation In High Finesse Ring Resonators

K.Kalli, D.O.Culverhouse and D.A.Jackson\*  
Applied Optics Group, University of Kent, CANTERBURY, Kent.CT2 7NR.

The development of fibre optic based sensor systems<sup>(1)</sup> has created a need for an all fibre tunable frequency shifter in order that efficient heterodyne signal processing can be effected. Several methods have been reported in which an acoustic wave of wavelength equal to the beat length of the fibre is used to couple a guided optical beam from one mode to another for example  $L_{p01}$  to  $L_{p11}$  or between the non degenerate  $L_{p01}$  modes of highly birefringent fibre<sup>(2,3)</sup>. The acoustic wave being generated either by acoustic horns, acoustic torsional generators or surface acoustic waves<sup>(2,4,5)</sup>. Although all these devices show promise the fact that they must operate at fixed frequencies will tend to limit their applicability.

In this paper we report the use of Stimulated Brillouin Scattering (SBS) generated in two high finesse ring resonators to realize a tunable fibre frequency shifter in the range 10 - 60 MHz. The frequency shifted signal is line-narrowed with respect to the pump<sup>(6)</sup> and additionally the configuration provides complete suppression of any unshifted light.

SBS can be described as a 3 wave interaction involving the incident pump, a generated acoustic wave and the scattered Stokes signal. Classically, the pump creates a propagating pressure wave in the medium caused by electrostriction and the resultant variation in the density changes the optical susceptibility. Thus the incident wave pumps the acoustic wave which scatters it, and the scattering generates the Stokes signal. The Stokes wave is downshifted in frequency by an amount equal to the frequency  $\nu_a$ :

$$\nu_a = \frac{2 n V_a}{\lambda} \sin \theta/2 \quad (1)$$

where  $n$  is the refractive index,  $V_a$  the hypersonic velocity,  $\lambda$  the wavelength of the pump and  $\theta$  the scattering angle. For a typical single mode fibre at 633 nm the SBS frequency shift is ~27GHz, a frequency which is too high for general purpose signal processing. However, an equivalent optical shift in the region of 10 - 60 MHz should be achievable by mixing the outputs from two SBS ring resonator lasers.

For SBS signals generated in long lengths of fibre, the beat frequency  $\Delta\nu_B$  is given by:

$$\Delta\nu_B = \frac{2(n_1 V_{a1} - n_2 V_{a2}) \sin \theta/2}{\lambda} \quad (2)$$

and  $\Delta\nu_B$  is continuously tunable by varying the temperature of one fibre with respect to the other<sup>(7)</sup>. The situation is more complex in the case of mixing the outputs of two SBS lasers, as they can only oscillate at frequencies  $\nu_{Ln}$  where the SBS gain curve coincides with the resonant frequencies of the ring laser cavity<sup>(6)</sup>. Hence a discretely tunable, variable frequency, all fibre optic frequency shifter should be realizable by simply varying the temperature of one ring resonator laser with respect to the other. The advantage of this approach is that much lower optical powers, typically  $< 100\mu\text{W}$ <sup>(8)</sup> are required to generate SBS in ring resonators in comparison with the tens of mW required for generation in long fibre lengths.

The experimental configuration is shown in figure 1. The output beam from the single mode He-Ne pump laser of output power  $800\mu\text{W}$  was initially injected into a monomode fibre with a cut off wavelength of 600nm. This beam was launched into the two ring resonators

fabricated 'in-house' through a tunable polished coupler. Ring resonator (1), 2.4m in length (Free spectral range (FSR) 85.5 MHz) was fabricated from Lightwave Technology fibre whilst ring resonator (2) 2.36 m length (FSR of 87 MHz) was fabricated from York fibre. The finesse of both resonators was in excess of 400. Servo controlled piezo-electric stretchers were incorporated into each ring resonator such that they could be independently locked at the resonance peak corresponding to the pump frequency. Polarisation controllers were included in each resonator to ensure the SBS laser would only oscillate in one polarisation state. This ensures that the power circulating in the ring is at a maximum and hence the SBS threshold is at a minimum. Both rings were placed in thermal enclosures to maximise their frequency stability. For the data shown in figure 2, 210 and 280  $\mu\text{W}$  of input power was injected into rings (1) and (2) respectively. The overall optical efficiency of the fibre network was  $\sim 68\%$  and SBS thresholds were experimentally observed as 140 $\mu\text{W}$  and 110 $\mu\text{W}$  for rings (1) and (2) respectively.

The backward propagating SBS signals were then transferred by the tunable coupler and subsequently analyzed in two ways. Firstly with a photo-diode, the resulting beatnote,  $\Delta\nu_B$ , generated at the photo diode being detected with a high frequency spectrum analyzer. Secondly, via a third ring resonator (finesse 530, linewidth 260kHz) which resolved the generated SBS signal directly in the optical domain.

From the manufacturers data the values of the refractive indices of the fibre cores were 1.4619 and 1.460, hence the predicted beat frequency from equation (2) was  $\sim 35.8\text{MHz}$  at  $20^\circ\text{C}$ . The observed beat frequency was in fact 20MHz, indicating that the resonator's frequencies did not coincide with the peak of the SBS gain curve. The beat signal power was  $\sim 45\mu\text{W}$ , giving an overall frequency conversion efficiency of  $\sim 10\%$ .

Direct observation of the SBS signal in the optical domain gave an upper bound value for the linewidth of 260kHz (equivalent to the linewidth of resonator 3).

In order to achieve a different beat frequency the temperature of ring (1) was continuously varied relative to ring (2) which was held at room temperature. The variation of the beat frequency as a function of the differential temperature of the rings is shown in figure 2. The observed behaviour is predictable from the known value of  $3\text{MHz}/^\circ\text{C}^{(9,10)}$ ; the variation of the SBS gain peak with temperature ( $d\nu_g/dT$ ). A temperature change of  $\sim 10^\circ\text{C}$  will cause a significant change in the absolute frequency of the SBS gain peak causing the ring fibre laser to mode hop and oscillate at  $\nu_{Ln} \pm \text{FSR}$ . As anticipated  $\Delta\nu_B$  is virtually independent of temperature undergoing a discrete frequency jump at a finite differential temperature. The slight variation in  $\nu_B$  with temperature before and after the mode hop can be attributed to the servo in the heated ring locking to slightly different points on the resonance peak as, due to its limited range, it had to be reset several times during the experiment.

A priori it is not possible to predict the value of the new beat frequency as one of the rings is heated, because the absolute value of the SBS gain peak will decrease with temperature hence the new beat note will be either

$$\nu_B = (\nu_{Ln1} + \text{FSR}) - \nu_{Ln2} \text{ or } \nu'_B = (\text{FSR} - \nu_{Ln1}) - \nu_{Ln2}.$$

Assuming the temperature of the ring increases in the same sense all subsequent frequency changes will be equal to the FSR. The data shown in figure 2 where the frequency jump is 33MHz, corresponds to  $\nu'_B$ . The spectra observed in the optical domain confirm these results. Figure 3 shows the SBS generated in ring resonator 1. Upon heating, the Stokes line is clearly seen to shift by  $\sim 84.7\text{MHz}$  i.e. the FSR of ring resonator 1.

In conclusion we have for the first time demonstrated an entirely new topology for an all fibre frequency shifter. Although the frequency conversion efficiency was only  $\sim 10\%$  increased efficiencies can be anticipated if higher power single frequency lasers are used to generate the SBS signals<sup>(11)</sup>.

## REFERENCES

1. D.A.Jackson  
J.Phys.E.Sci.Instrum, Vol.18, 981, (1985)
2. B.Y.Kim, J.N.Blake, H.E.Engan, and H.J.Shaw  
Opt.Lett.11, 389 (1986)
3. M.Berwick, C.N.Pannell, P.St.J.Russell, and D.A.Jackson  
Electron Letts. 27, 713 (1991)
4. W.P.Risk, and G.S.Kino  
Opt.Lett 11, 336 (1986)
5. P.A.Greenhalgh, A.P.Foord, and P.A.Davies  
Electron Lett. 25, 1206 (1989)
6. S.P.Smith, F.Zarinetchi, and S.Ezekiel  
Opt.Lett. 16, 393 (1991)
7. D.O.Culverhouse, F.Farahi, C.N.Pannell, and D.A.Jackson  
Electron Lett. 25, 913 (1989)
8. R.Kadiwar, and I.P.Giles  
Opt.Lett. 14, No.6, 332 (1989)
9. T.Kurashima, T.Horiguchi, M.Tateda  
Applied Optics, Vol.29, No.15, 2219 (1990)
10. A.S.Pine  
Physical Review, Vol.185, No.3, 1187 (1969)
11. P.Bayvel, and I.P.Giles  
Opt.Lett. 14, No.11, 581 (1989)

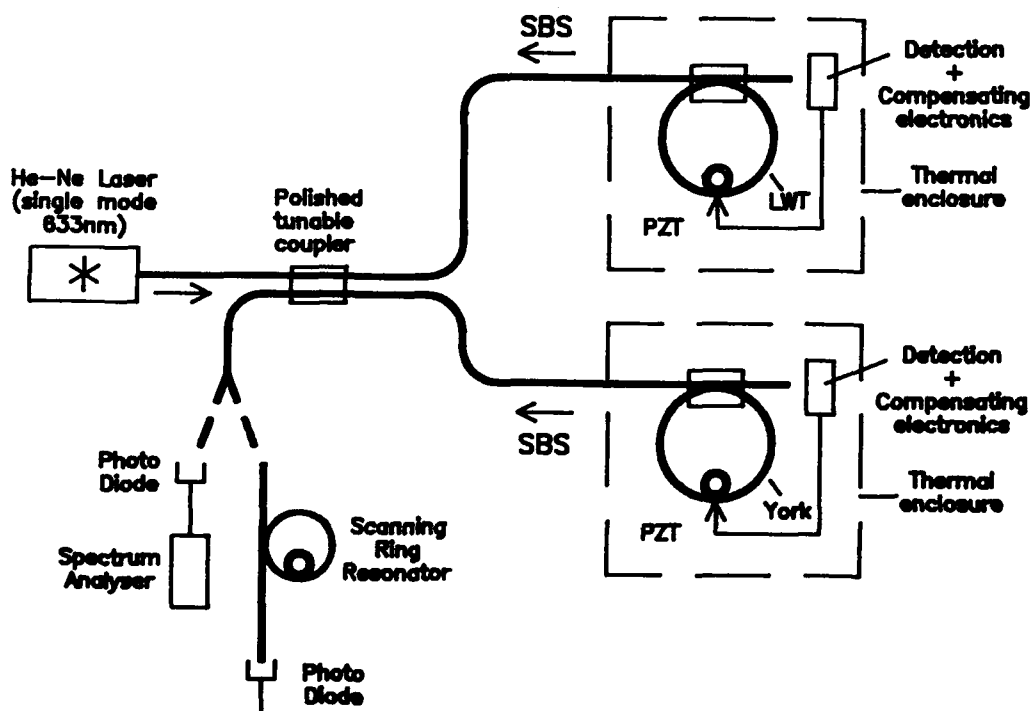


Fig.1 Experimental configuration for the all-fibre frequency shifter.

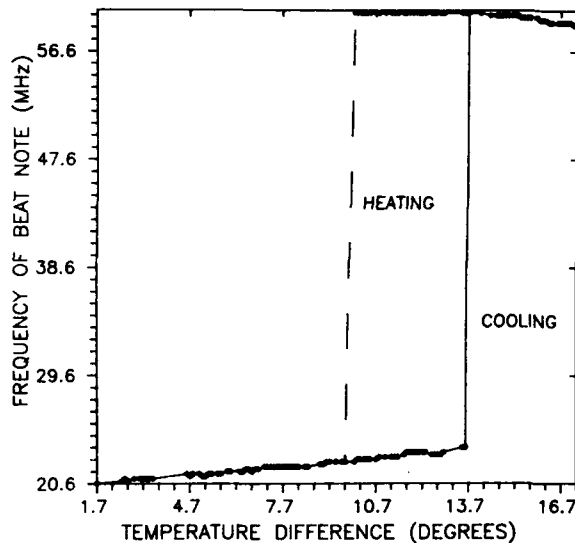


Fig.2 Variation of the beat frequency as a function of temperature on the cooling and heating cycles. The frequency jump of 33MHz is the same whether the ring was heated or cooled; the transition temperatures were different being 13.7°C (cooling) and 9.7°C (heating).

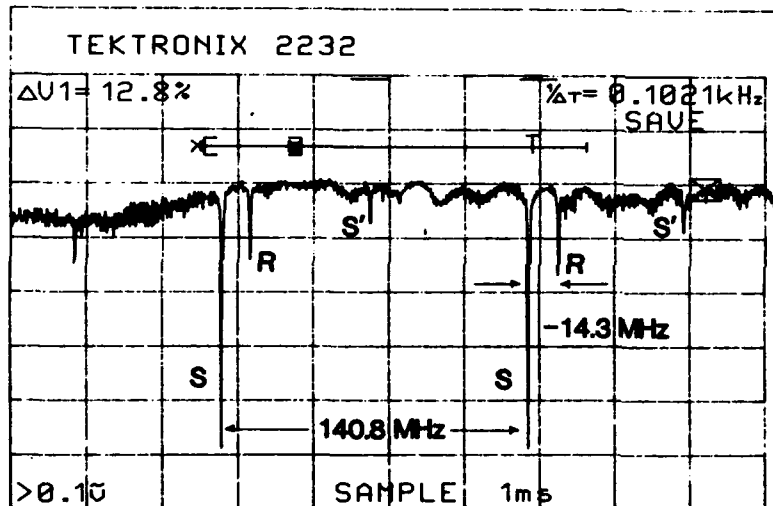
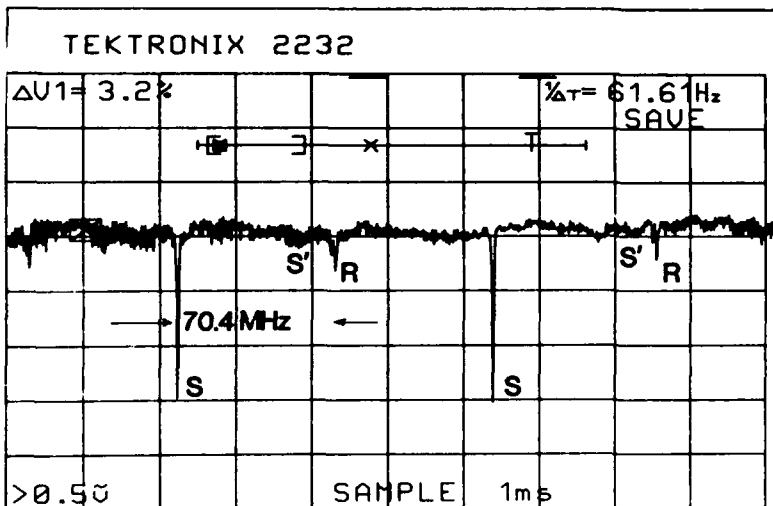


Fig.3

i) Before heating when the relative shift of S to R is -14.3MHz.



ii) After heating the relative shift from S to R is 70.4MHz. Hence corresponding to a frequency jump of 84.7MHz i.e. the FSR of resonator (1).

Optical spectrum of the SBS signal generated in ring resonator (1) analyzed with resonator (3). FSR equal to 140.8MHz: R indicates the Rayleigh line, S and S' the SBS signals corresponding to the polarization modes of the fibre.



## P29 Acoustically Scanned Delay For White-Light Interferometry

Erling Kolltveit and Kjell Bløtekjær  
Norwegian Institute of Technology  
Division of Physical Electronics  
N 7034 Trondheim, NORWAY

### INTRODUCTION:

In white-light interferometry, two unbalanced interferometers are coupled in tandem. Typically, two Michelson interferometers are used. The optical pathlength difference between the two arms in each interferometer is large compared to the source coherence length. The measurand acts on one arm of the sensing interferometer, determining its optical pathlength. The length of one arm of the second interferometer, which is called the reference or receiving interferometer, is scanned, and a visibility maximum is observed when the pathlength mismatch is the same for the two interferometers [1]. The technique is closely related to a multiplexing technique called coherence multiplexing, in which fiber-optic Mach-Zehnder interferometers [2,3] or polarimeters [4] are often used.

A drawback of the most common realization is that mechanical scanning of the reference interferometer is required. Recently, however, methods for electronic scanning have been developed. These employ spatial modulation and CCD arrays [5,6].

In this paper we demonstrate a novel method for scanning optical time delay without mechanical motion. The method is based on the difference in group delay between two modes in an optical fiber. The scanning is performed by an acoustic pulse propagating along the fiber, performing the coupling between the two modes.

In the present realization, we use two spatial modes in an elliptic-core fiber. An alternative would be to use two polarization modes. However, the difference in group velocity is less for polarization modes, and furthermore, acoustic coupling between spatial modes is much more efficient [7].

### PRINCIPLE AND EXPERIMENT:

The optical part of the experimental set-up is shown schematically in Figure 1. The source is a multimode diode laser of 670 nm wavelength, TOLD 9200 from Toshiba. Its coherence function consists of a series of peaks, spaced 2.5 mm apart. Each has a width of approximately 280  $\mu\text{m}$ . The delays involved in our experiment are so small that there is no interference between the peaks. For our purpose, therefore, the coherence function may be considered as having a single peak of 280  $\mu\text{m}$  width.

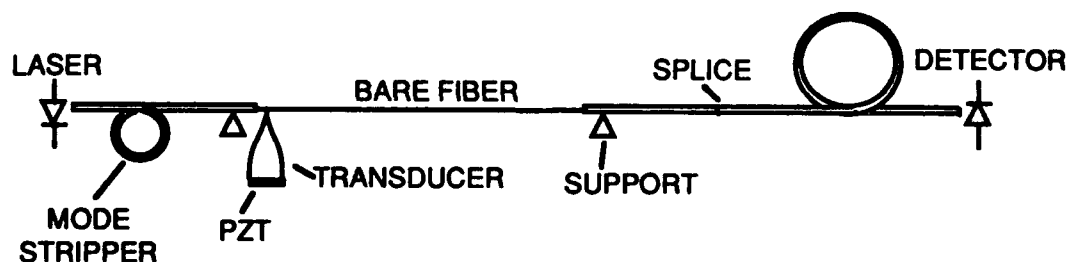


Figure 1: Schematic drawing of optical part of experimental set-up.

The light is launched into a piece of elliptical core fiber, PMF 820 from Lightwave Technology Inc.. This fiber is single mode at 820 nm. At the operating wavelength of 670 nm, two spatial modes can propagate, the fundamental  $LP_{01}$  mode, and the next higher mode,  $LP_{11}^{\text{even}}$ . The latter has two near-field intensity lobes in the direction of the long axis of the core. In the

following, we shall refer to it simply as the  $LP_{11}$  mode. The two modes can be coupled by an acoustic flexural wave with motion along the long axis of the elliptic core. The coupling is maximum if the acoustic wavelength equals the beatlength between the two optical modes, which is 0.775 mm for the present fiber. The flexural wave velocity at this wavelength is 3100 m/s, and the corresponding acoustic frequency is approximately 4 MHz.

The mode stripper shown in Figure 1 consists of a piece of fiber wrapped around a mandrel of 1 cm diameter. This arrangement effectively removes the  $LP_{11}$  mode. Thus, the input to the active part of the fiber is a pure  $LP_{01}$  mode.

The fiber coating is removed over a length of 59 cm. This part of the fiber is supported at both ends, and a flexural wave transducer, in the form of a tapered quartz rod excited by a PZT, is attached to the fiber by a low melting-point glass [7].

The transducer excites a 15  $\mu$ s long flexural wave pulse, corresponding to 4.65 cm on the fiber. At the position of the pulse, part of the  $LP_{01}$  mode power is converted to an  $LP_{11}$  mode with a downshift in frequency of 4 MHz relative to the  $LP_{01}$  mode. The fiber length from the transducer to the end is 102 cm. Thus the length of fiber where both modes propagate is scanned from 102 to 102 - 59 = 43 cm during the 190  $\mu$ s it takes for the flexural wave pulse to propagate down the bare part of the fiber. Since the group velocities of the two modes are different, a variable delay is introduced. The difference is not known exactly, but from the difference in phase velocity we calculate a delay of  $3 \times 10^{-12}$  s per meter fiber. With this value, the delay is scanned from 0.92 to 0.39 mm free space propagation. In reality, the group velocities differ less than the phase velocities, and hence, the real delays are smaller than these values [8].

In this proof-of-principle experiment, the variable delay interferometer is coupled to a second fiber interferometer of the same type, consisting of a piece of the same two-mode fiber. Cross coupling between the modes takes place at the non-ideal splice between the two fibers.

## RESULTS:

The results are shown in Figure 2. In Figure 2a the second fiber has a length of 85 cm. The upper trace shows the 15  $\mu$ s pulse of 4 MHz input to the PZT. The lower trace shows the 4 MHz beat frequency at the photodetector. A pulse appears when the flexural wave pulse is at a position which makes the two interferometers equal in length.

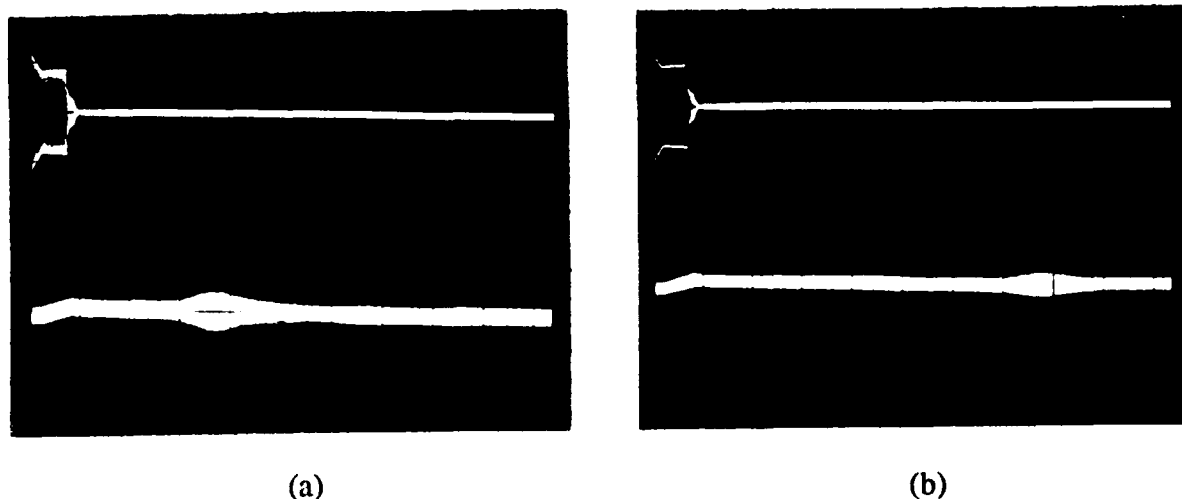


Figure 2: Input to PZT (upper trace) and output from photodetector (lower trace). a): Second fiber 85 cm. b): Second fiber 59 cm.

In Figure 2b the length of the second fiber is reduced to 59 cm, and the output pulse is moved correspondingly. The positions of the pulses in Figure 2a and 2b agree with expectations to within the measurement accuracy.

#### ALTERNATIVE DESIGNS:

Figure 3 shows some alternative realizations of the variable delay. Figure 3a shows the method reported here. In Figure 3b, flexural wave pulses propagate in both directions. In the first pulse, the input  $LP_{01}$  mode excites an  $LP_{11}$  mode with a frequency upshift. In the second pulse, the  $LP_{11}$  mode excites an  $LP_{01}$  mode again, with the same frequency upshift. At the output, two  $LP_{01}$  modes exist, with a relative delay, and a frequency difference of twice the flexural wave frequency [9].

In Figure 3c, two pulses are excited. They can be delayed relative to each other. The delay between the  $LP_{01}$  and the  $LP_{11}$  mode is constant during one sweep, but it can be varied from one sweep to the next by varying the delay between the two acoustic pulses. In this case, the two frequency shifts are in opposite directions, and the two output  $LP_{01}$  modes have the same frequency.

In both b) and c), separate transducers can be used if a longer delay is required. This will not influence the range over which the delay is scanned, however.

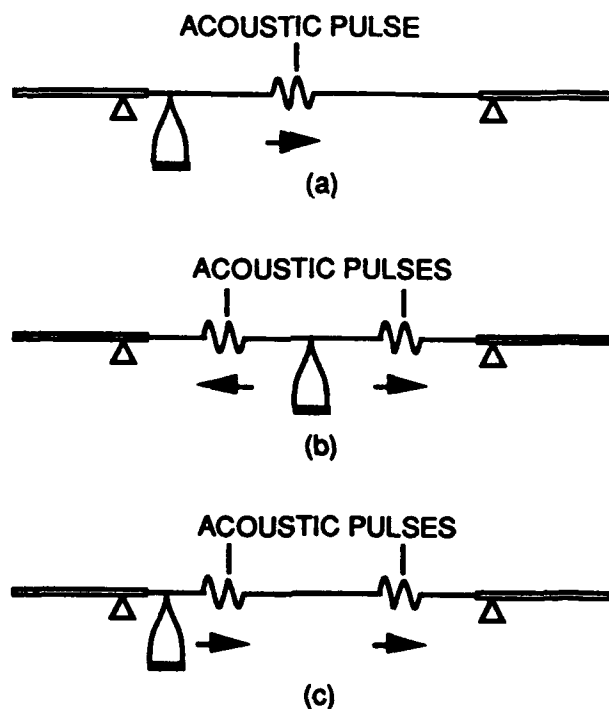


*Figure 3: Alternative designs.*

In many applications, a scan range larger than that obtained here is required. Larger scan ranges can be obtained by using specially designed fibers, to increase the group velocity difference. Using composite glasses, a fiber can be made with a central part of the core consisting of low group velocity glass, surrounded by a glass with high group velocity. Since the  $LP_{11}$  mode propagates farther away from the fiber axis than the  $LP_{01}$  mode, its group velocity will be determined primarily by the glass in the outer part of the core, whereas the group velocity of the  $LP_{01}$  mode is determined primarily by the glass in the central part of the core.

## REFERENCES:

1. Th. Bosselmann and R. Ulrich, "High-accuracy position-sensing with fiber-coupled white-light interferometers", Proc. 2nd Int. Conf. Optical Fiber Sensors, Stuttgart, 1984, pp. 361-364.
2. S. A. Al-Chalabi, B. Culshaw, and D. E. N. Davies, "Partially coherent sources in interferometric sensors", Proc. 1st Int. Conf. Optical Fiber Sensors, London, 1983, pp. 132-135.
3. J. L. Brooks, R. C. Youngquist, M. Tur, B. Y. Kim, and H. J. Shaw, "Coherence multiplexing of fiber-optic interferometric sensors", J. Lightwave Technol., Vol. LT-3, pp. 1062-1072, Oct. 1985.
4. V. Gusmeroli, M. Martinelli, and P. Vavassori, "Quasi-distributed single-length polarimetric sensor", Opt. Lett., Vol. 14, pp. 1330, December 1989.
5. A. Koch and R. Ulrich, "Displacement sensor with electronically scanned white-light interferometer", International Congress of Optical Sciences & Engineering, The Hague, March 1990, pp. 126-133.
6. S. Chen, A. J. Rogers, and B. T. Meggitt, "A novel long range opto-electronic scanner for coherence-multiplexed optical-fibre quasi-distributed sensors", Proc. 7th Int. Conf. Optical Fiber Sensors, Sidney, Dec. 1990, pp. 365-367.
7. B. Y. Kim, J. N. Blake, H. E. Engan, and H. J. Shaw, "All-fiber acousto-optic frequency shifter", Opt. Lett., Vol. 11, pp. 389-391, June 1986.
8. A. Kumar and R. K. Varshney, "Propagation characteristics of dual-mode elliptical-core optical fibers", Opt. Lett., Vol. 14, pp. 817-819, Aug. 1989.
9. J. O. Askautrud and H. E. Engan: "Fiberoptic frequency shifter with no mode change using cascaded acousto-optic interaction regions", Opt. Lett., Vol. 15, pp. 649-651, June 1990.

**Kent A. Murphy, Michael F. Gunther, Anbo Wang and Richard O. Claus**

Fiber & Electro-Optics Research Center, Bradley Department of Electrical Engineering  
Virginia Polytechnic Institute and State University, Blacksburg, Virginia 24061-0111

**Ashish M. Vengsarkar**

AT&T Bell Laboratories, Rm. 6D - 313, 600 Mountain Avenue, Murray Hill, NJ 07974

### Summary

Phase-modulated fiber optic sensors have been shown to possess high sensitivities for the measurement of strain, temperature, vibration, pressure and other parameters.<sup>1</sup> Fabry-Perot (FP) sensors that are based on multiple beam interference eliminate the need for a reference arm and do not require sophisticated stabilization techniques as in the case of Mach-Zehnder and Michelson interferometers.<sup>2</sup> Several techniques to create intrinsic optical fiber Fabry-Perot interferometers have been described in the past.<sup>3-5</sup> In a recent paper, we described an optical fiber extrinsic FP interferometer and used it as a sensor of microdisplacements and thermally-induced strain.<sup>6</sup> The fiber interferometer was classified as extrinsic because the FP cavity was an air-gap between two fiber ends and the sensor output was immune to perturbations in the input/output fiber.

We describe the construction of the extrinsic FP interferometer with reference to Figure 1. A single mode fiber ( $\lambda_0 = 1300$  nm), used as the input/output fiber and a multimode fiber, used purely as a reflector, form an air gap that acts as a low-finesse FP cavity. The far end of the multimode fiber is shattered so the reflections from the far end do not add to the detector noise. The Fresnel reflection from the glass/air interface at the front of the air gap (reference reflection) and the reflection from the air/glass interface at the far end of the air gap (sensing reflection) interfere in the input/output fiber. Although multiple reflections occur within the air gap, the effect of reflections subsequent to the ones mentioned above can be shown to be negligible. The two fibers in the silica tube are allowed to move longitudinally which results in changes in the air gap length thus changing the phase difference between the reference reflection and the sensing reflection. The phase difference can be monitored as intensity modulations at the output of a fused biconical tapered coupler.

The interference of the two-wave interferometer can be evaluated in terms of a plane-wave approximation. The observed intensity at the detector is a superposition of the two reflections and can be shown to be <sup>2</sup>

$$I_{\text{det}} = |U_1 + U_2|^2 = A_1^2 + A_2^2 + 2 A_1 A_2 \cos (\phi_1 - \phi_2), \quad (1)$$

which can be rewritten as

$$I_{\text{det}} = A^2 \left[ 1 + \frac{2ta}{a + 2s \tan [\sin^{-1}(\text{NA})]} \cos \left( \frac{4\pi s}{\lambda} \right) + \left( \frac{ta}{a + 2s \tan [\sin^{-1}(\text{NA})]} \right)^2 \right], \quad (2)$$

where we have assumed that  $\phi_1 = 0$  and  $\phi_2 = 2s (2\pi/\lambda)$ , and  $\lambda$  is the wavelength of operation in free space. In Equations (1) and (2),  $U_i(x, z, t)$  represents the complex amplitude of the interfering electromagnetic waves,  $a$  is the fiber core radius,  $t$  is the transmission coefficient of the air-glass interface ( $\approx 0.98$ ),  $s$  is the end separation and NA is the numerical aperture of the single-mode fiber, given by  $\text{NA} = (n_1^2 - n_2^2)^{1/2}$ . The terms  $n_1$  and  $n_2$  are the refractive indices of the core and the cladding, respectively. For a strain sensor, it is useful to plot the detected intensity versus gap-separation  $s$ , as shown in Figure 2. We see that the fringe contrast drops as the displacement increases; this is to be expected since the relative intensity of the sensing reflection recoupled into the input/output fiber starts dropping with respect to the reference reflection.

The extrinsic FP interferometer has been tested as a displacement sensor by attaching one fiber to a stationary block and the second fiber to a micropositioner which produces a known displacement between the fiber ends. For comparison with the theoretical results, we show in Figure 3 an oscilloscope trace of the continuously monitored output intensity of the sensor for  $s = 0$  to  $s = 203 \mu\text{m}$ . The experimentally counted number of fringes for the displacement was 310.5 which corresponds to a displacement of 202 micrometers.

The reduction in fringe contrast as a function of displacement has been improved by splicing a multimode optical fiber onto the end of the input/output fiber and then polishing the multimode fiber until the output light is somewhat collimated. The length of multimode fiber is on the order of a few millimeters and serves as a quarter-pitch GRIN lens. The experiment described in Figure 3 was repeated with the lensed fiber and the results are presented in Figure 4.

The principle of operation of a quadrature phase-shifted Fabry-Perot (QPS-FP) sensor has been described in detail.<sup>6</sup> A method of obtaining two signals  $90^\circ$  out of phase with respect to one another are shown in Figures 5. To test the validity of the quadrature phase-shifted sensors, a sensor (using the scheme shown in Figure 5) was attached to a cantilever titanium beam with an epoxy. The fiber sensor was attached parallel to the length of the beam and beam vibrations were monitored. A typical oscilloscope trace is shown in Figure 6. The figure clearly shows the shift in the lead/lag properties of the two signals as the relative direction of the strain in the beam changes from increasing to decreasing.

A QPS-FP sensor was tested as a thermally-induced strain gauge on a ceramic cross-flow (CXF) filter at Westinghouse Science and Technology Center, in Pittsburgh. CXF filters are used for hot gas clean-up of coal-fired power generation systems, such as pressurized fluidized-bed combustors and integrated gasifier-combined cycles. Figure 7 shows the QPS-FP sensor output as a function of time during the heat-up portion of the test compared to the filter temperature measured using a conventional thermocouple. The sensor performed equally well during the cool-down cycle.

A one centimeter gauge length QPS-FP sensor was attached to a cantilever beam and then

submerged in a liquid nitrogen ( $-273^{\circ}\text{C}$ ) bath. The tip of the cantilever beam was displaced and then released several times. a typical oscilloscope trace can be seen in Figure 8. The fringes correspond to 276 microstrain which is within 10% of the calculated value of strain. The minimum detectable phase shift was  $0.0996^{\circ}$  which corresponds to a minimum detectable strain of  $0.01\text{ }\mu\text{strain}$  for a gauge length of 19.03 mm. Static and dynamic loading data obtained from the sensors show a high degree of accuracy and a strain resolution of  $0.01\text{ }\mu\text{m/m}$ . The sensor was successfully demonstrated as a thermally induced strain monitor in an industrial environment up to  $450^{\circ}\text{C}$  (the limitation of the fiber coating not the sensor itself). The sensor has been used successfully in a laboratory up to  $975^{\circ}\text{C}$  with no coating. The sensor has also been demonstrated as a strain gauge at  $-273^{\circ}\text{C}$  attached to a cantilever beam.

### ACKNOWLEDGMENT

Research on this project was sponsored in part by the United States Department of Energy, Morgantown Energy Technology Center, under contract number DE-AC21-89MC25159.

### REFERENCES

1. J. Dakin and B. Culshaw, Optical Fiber Sensors: Principles and Components, Artech House, Boston, MA 1988.
2. T. Yoshino, K. Kurosawa, K. Itoh, and T. Ose, "Fiber-optic Fabry-Perot interferometer and its sensor applications," *IEEE J. Quantum Electron.*, vol. QE-18, pp. 1624-1632, 1982
3. K. L. Belsley, J. B. Carroll, L. A. Hess, D. R. Huber, and D. Schmadel, "Optically multiplexed interferometric fiber optic sensor system," *Proc. - SPIE Int. Soc. Opt. Eng.*, vol. 566, pp. 257-264, 1985.
4. A. D. Kersey, D. A. Jackson, and M. Corke, "A simple fibre Fabry-Perot sensor," *Opt. Comm.*, vol. 45, pp. 71-74, 1983.
5. C. E. Lee and H. F. Taylor, "Interferometric optical fibre sensors using internal mirrors," *Electron. Lett.*, vol. 24, pp. 193-194, 1988.
6. K. A. Murphy, M. F. Gunther, A. M. Vengsarkar, and R. O. Claus, "Quadrature phase shifted extrinsic Fabry-Perot fiber optic sensors," *Opt. Lett.*, vol. 16, pp. 273-275, 1991.

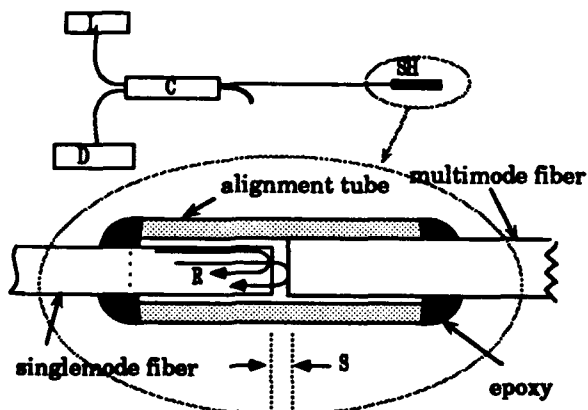


Fig. 1. Sensor system and sensor detail. L-laser, D-detector, C-coupler, SH-sensor head, R-reflections, S-gap separation.

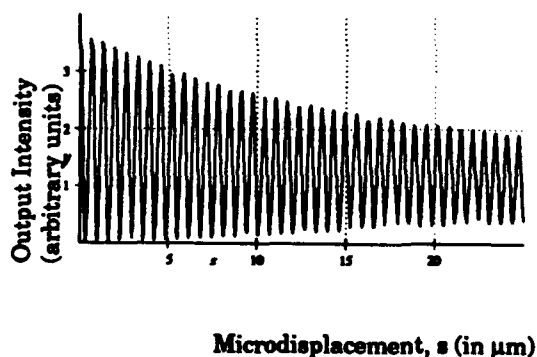


Fig. 2. Therotical output vs. gap separation.

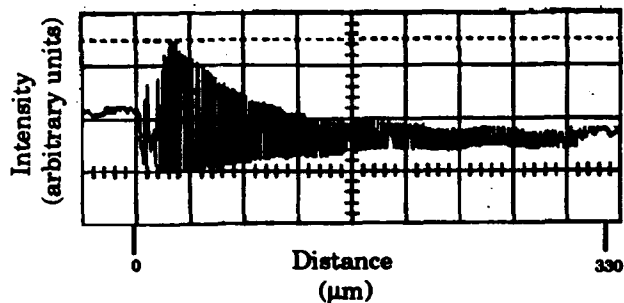


Fig. 3. Fringe contrast without lensed sensor.

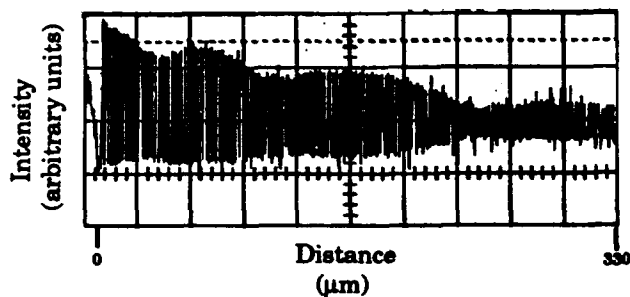


Fig. 4. Fringe contrast with lensed tip.

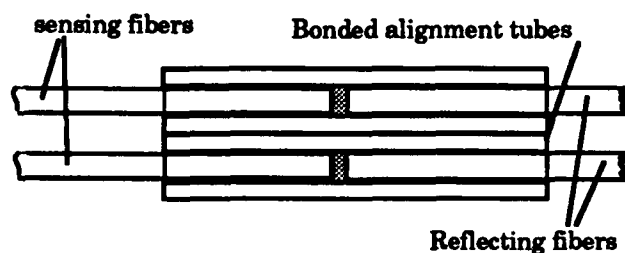


Fig 5. Detail of quadrature phase-shifted sensor.

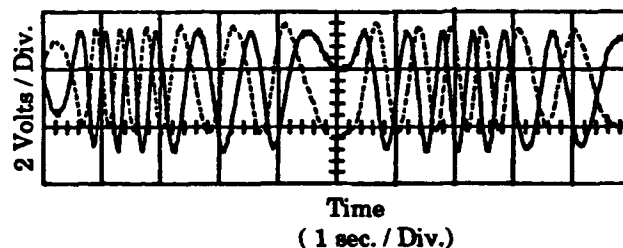


Fig. 6. Quadrature phase-shifted sensor trace showing lead-lag phenomenon.

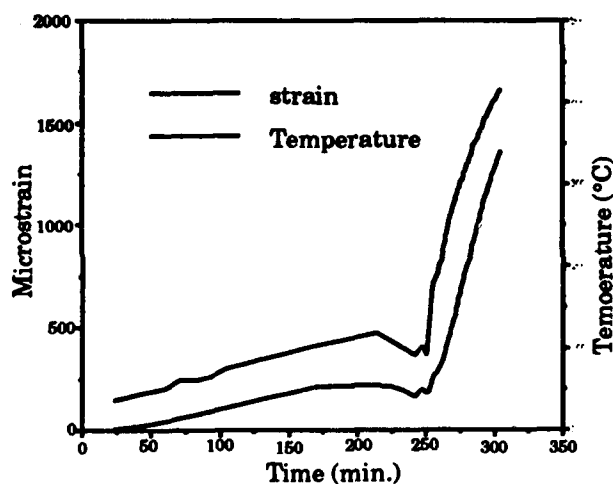


Fig. 7. Results of F-P sensor during high temperature testing.

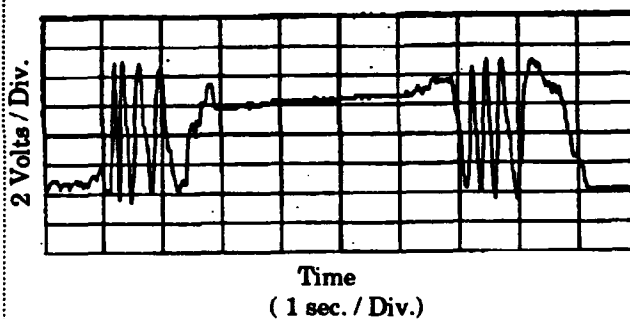


Fig. 8. Oscillograph of F-P sensor at temperatures of  $-273^{\circ}\text{C}$ .



## A Novel Fibre Refractive Index Sensor Using Resonance Shift Phenomena

G.Thursby, W.Johnstone, K.McCallion, D.Moodie and B.Culshaw.  
University of Strathclyde, Dept. of Electrical and Electronic Eng,  
204 George St. Glasgow G1 1XW.

### ABSTRACT

A fibre based refractive index sensor is described which is capable of detecting changes in refractive index of  $< 4 \times 10^{-5}$ . If an electro-optic overlay is used, there exists the potential for producing a closed loop device.

### INTRODUCTION

Refractive index sensors have many applications in the fields of biochemistry, chemical analysis and immuno-assaying. This paper describes a refractive index sensor which is an in-line, solid state, fibre based device, whose structure is similar to that previously described for producing modulators<sup>1,2</sup> and wavelength selective elements<sup>3</sup>. The device ( fig. 1 ) consists of a high index, (  $>$  fibre core index ), multimode, planar waveguide evanescently coupled to a side polished<sup>4</sup> single mode fibre. Light launched into the fibre will couple to the waveguide under resonance conditions, i.e. if the effective index of one of the modes of the waveguide matches that of the monomode fibre,  $n_{ef}$ .

Wavelength scanning such a device will give a transmission characteristic such as that shown in fig.2, where the sharp drops in throughput correspond to the light being coupled to the overlay. The wavelengths at which this occurs may be determined by considering the eigen value equation for an asymmetrically bound planar waveguide,

$$2\pi d/\lambda \cdot (n_2^2 - n_{\infty}^2)^{1/2} = m\pi + \phi_1 + \phi_3 \quad (1)$$

where  $d$  is the thickness of the waveguide,  $\lambda$  is the input wavelength,  $n_2$  the waveguide material index,  $n_{\infty}$  the mode effective index, and  $m$  the mode order.  $\phi_1, \phi_3$  are the phase changes at the  $n_1$  and  $n_3$  boundaries respectively, ( see fig. 1 ) and are given by  $\tan^{-1}\xi b_i$ , where  $\xi = 1$  for TE,  $n_2^2/n_1^2$  for TM and  $b_i = (n_{\infty}^2 - n_i^2)^{1/2} (n_2^2 - n_{\infty}^2)^{-1/2}$ ,  $i = 1, 3$

The wavelengths at which resonances occur can be derived from the above equation by putting  $n_{\infty} = n_{ef}$ . It can then be seen that the position of these resonances will shift in response to changes in the superstrate index, and it is this sensitivity which forms the basis of the sensor.

### DEVICE DEVELOPMENT

A piece of lithium niobate was bonded on to a side polished fibre block using a UV curing adhesive which had a refractive index just below that of silica. The niobate was then lapped and polished to the desired thickness, which was typically in the

range 10 - 25  $\mu\text{m}$ . The device was then scanned using a monochromator, with an in-line polarisation controller being used to establish either a TM or TE polarisation state at the device. This was necessary due to the birefringent nature of the niobate waveguide. Scans were repeated using a range of different refractive index liquids which were put on to the device to act as superstrates. The change in the position of the resonance point relative to that for air was determined as a function of superstrate refractive index. Fig. 3 shows a plot of these changes for both polarisation states for a device having a 10  $\mu\text{m}$  thick overlay. These experimental results are in good agreement with the theoretical curves derived using equation 1 by putting  $n_{\text{so}} = n_{\text{of}}$  ( fig.4). The polarisation dependence of the sensitivity of the device is as predicted, with TM being considerably more sensitive than TE.

The performance of the sensor at any point of its range is determined by both the sharpness of the resonance (  $\Delta I/\Delta\lambda$ , FWHM ) and the sensitivity of its position to a change in superstrate index (  $\Delta\lambda/\Delta n$  ). For any given device the maximum rate of change in intensity with wavelength is readily found from its wavelength scan. Typically this value is in the region of 20% I /nm ( fig. 2 ).  $\Delta\lambda/\Delta n$  varies with superstrate index,  $n_3$ , and is polarisation dependant. The same device shows a shift in resonance point of 1.4 nm for a change in superstrate index of 0.01 at  $n_3 = 1.44$  for the TM polarisation ( fig. 3 ). If the sensor is interrogated on the linear part of the resonance, the rate of change of intensity with superstrate index (  $\Delta I/\Delta n$  ) is simply the product of these parameters, i.e. for this case  $\Delta I/\Delta n = 28\% I / 0.01n$ . Given that a change in output intensity of 0.1% is readily detectable, these results indicate a minimum detectable index change of  $4 \times 10^{-5}$ . Preliminary work on structures having thinner overlays of lower refractive index has shown that there is the potential for producing sensors with a sensitivity of at least an order of magnitude better than this.

Although the sensor as described is dependent on measuring throughput intensity, if the waveguide material is active, as lithium niobate is, there exists the possibility of making a closed loop sensor. In this case the bulk index of the niobate could be electro-optically changed to maintain the position of the resonance point, and the voltage required to achieve this would then be related to the change in superstrate index. It should also be possible to produce sensors with different ranges of maximum sensitivity if a glass integrated optic channel waveguide were substituted for the fibre block. Further investigations are currently being carried out in these areas.

## CONCLUSIONS

A fibre based in-line sensor has been demonstrated with the ability to detect changes in refractive index of  $< 4 \times 10^{-5}$ . The range of the sensors optimum sensitivity could be changed if a glass integrated optic waveguide was substituted for the fibre, whilst the use of an electro-optically modulated overlay waveguide would give the possibility of producing a closed loop

device.

#### REFERENCES

1. W. Johnstone et al, Electronics Letters, 27, 11, 894, 1991
2. W. Johnstone et al, SPIE Proc, Vol 1580, Paper 26 ( to be published )
3. W. Johnstone et al, SPIE Proc, Vol 1580, Paper 21 ( to be published )
4. R. Bergh, G. Kotler, and H.J.Shaw, Electronics Letters, 16, 962, 1980

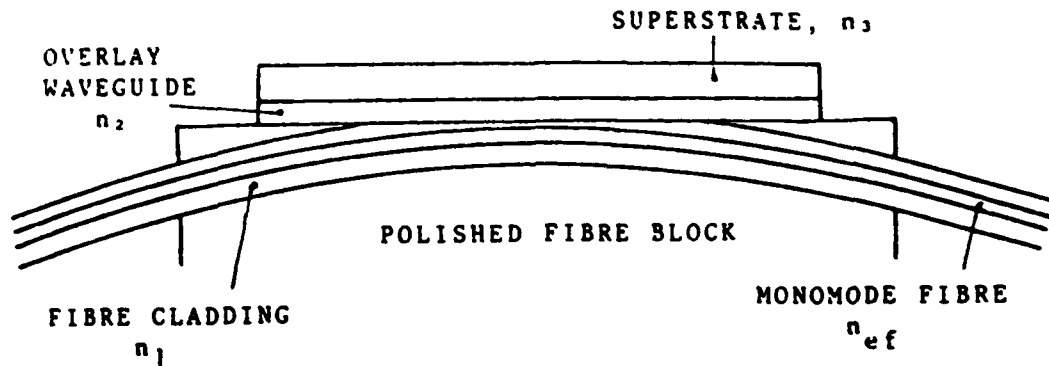
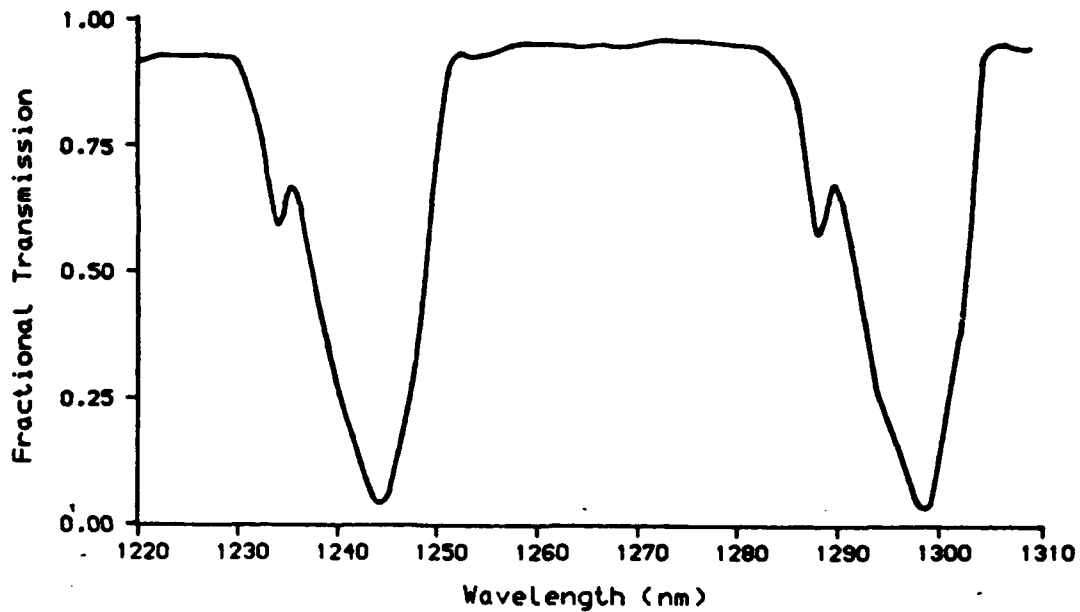


Fig. 1. DEVICE STRUCTURE



LiNbO<sub>3</sub>, 10 $\mu$ m, TM Polarisation, Air superstrate

Fig. 2. A DEVICE WAVELENGTH SCAN

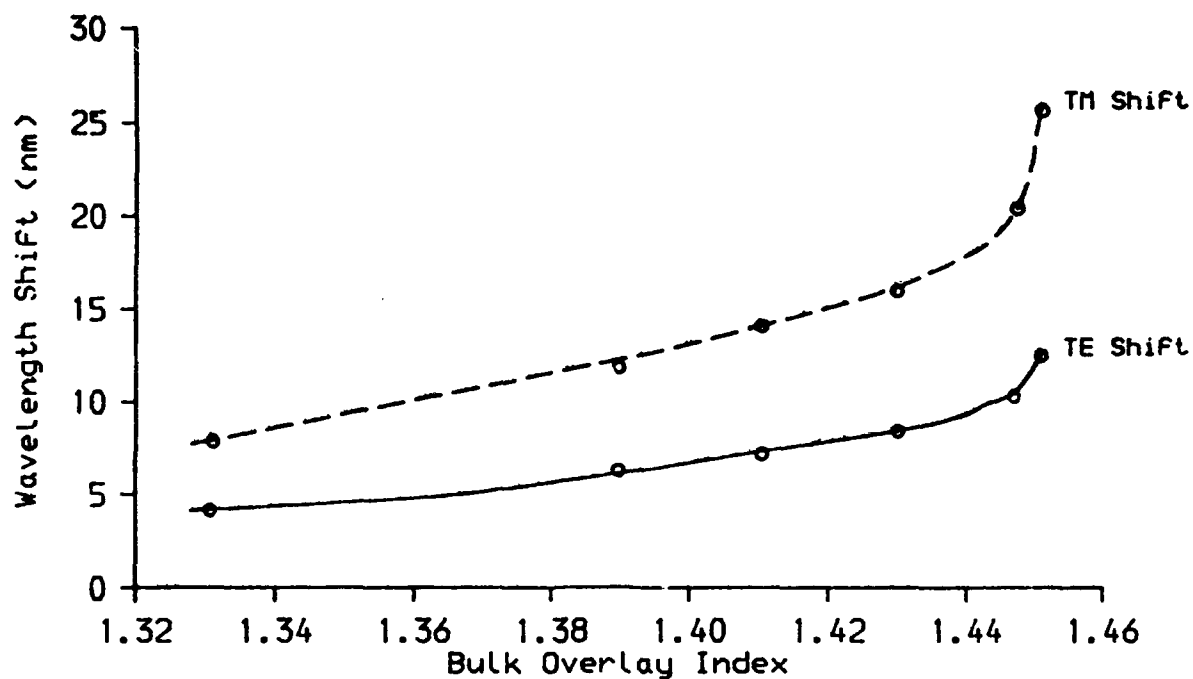


Fig. 3. SHIFT IN RESONANCE POINT WITH CHANGING SUPERSTRATE INDEX  
(  $10\mu\text{m}$  OVERLAY ), EXPERIMENTAL RESULTS

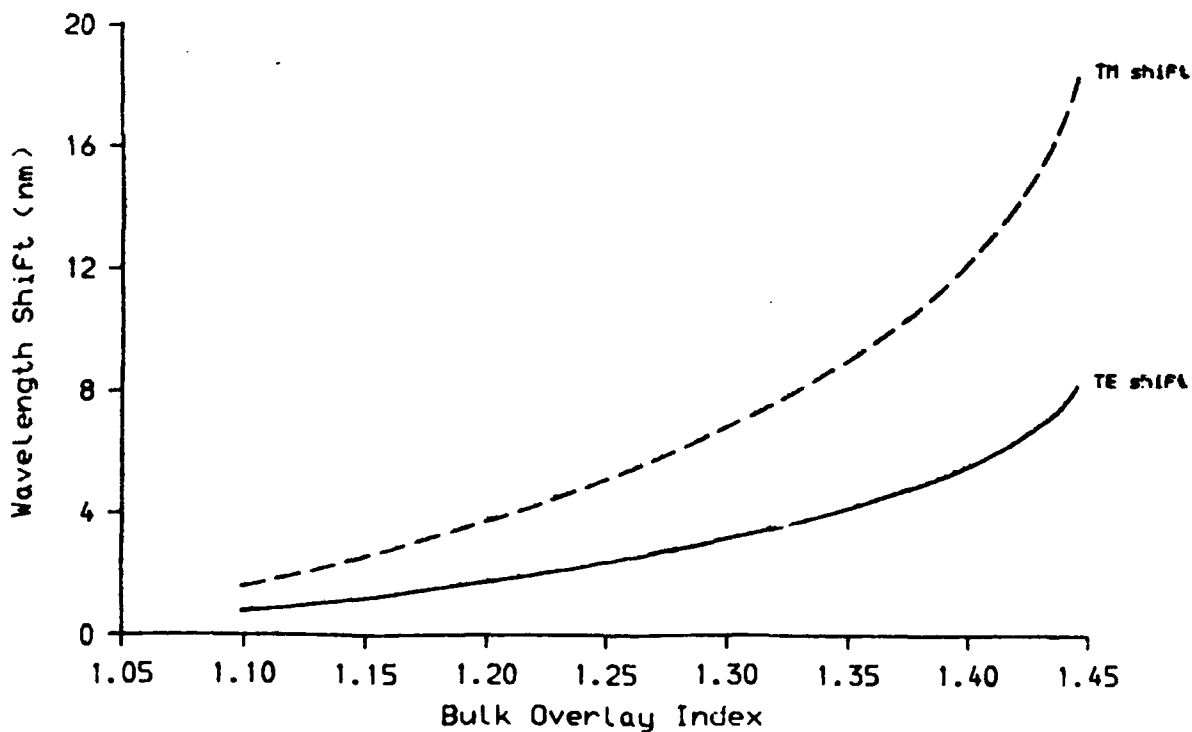


Fig. 4. SHIFT IN RESONANCE POINT WITH CHANGING SUPERSTRATE INDEX  
(  $10\mu\text{m}$  OVERLAY ), THEORETICAL CURVES

## P32 Quadrature Polarization-State Delivery Through Optical Fiber For Polarimetric Sensors

Mark Johnson and Chris Pannell

University of Southampton  
Optoelectronics Research Centre  
Highfield, Southampton SO9 5NH  
United Kingdom

### Abstract

Single-ended, active control of the output polarization state of a polarization-maintaining fiber is demonstrated. Normal eigenstate plus controlled quadrature outputs together allow stable phase demodulation and fringe counting in polarimetric fiber sensors.

### Introduction

Polarimetric optical fiber sensors measure the retardation of a birefringent optical element by injecting an optical signal of known state of polarization (SOP) and measuring the fraction of light  $I_t$  transmitted through an output polarizer. Many ingenious signal processing schemes have been proposed<sup>1</sup> to circumvent the fundamental problem of this class of sensors; the sensor transfer function is periodic, resulting in signal fading and directional ambiguity if the measurand drives the sensor over more than one fringe. To our knowledge, the signal recovery scheme described here is novel. It is of wide applicability and solves the above problems through the sequential generation of quadrature states.

Signal processing schemes previously proposed fall broadly into three categories: (a) heterodyne or pseudo-heterodyne, (b) active homodyne and (c) passive homodyne methods. The first category uses source frequency modulation to generate an output even in the absence of a change in the measurand<sup>2</sup>. Variations of the measurand then produce an instantaneous phase change which is recovered by standard FM demodulation techniques.

Active homodyne schemes rely on locking the phase to a particular point of the sensor transfer function using a low-frequency servo loop. High sensitivity operation is restricted to the linear portion of the sinusoidal transfer function and ambiguity results if phase changes occur which move the operating point more than one fringe.

In the passive homodyne technique the optical configuration itself produces two separate outputs which are in phase quadrature. The availability of two quadrature outputs allows the elimination of signal fading and the determination of direction in a fringe counting system. Such schemes are simple yet capable of excellent sensitivity<sup>3</sup>.

The remote polarization state control scheme proposed here is applicable to this third category of signal processing, and may be termed 'sequential passive homodyne'. It works by sequentially delivering two pairs of SOPs through polarization-maintaining (PM) optical fiber to a sensor head at a remote location. These are not only the orthogonal ( $\pi$  phase difference) states transmitted unchanged along the fiber eigen-axes, but additionally two states in phase quadrature ( $\pm \pi/2$  phase difference). The controlled state pair is locked using an active control loop modulating the fiber birefringence  $\Gamma_f$  by heating a small section of fiber.

In this work the actively-controlled states leaving the fiber are left- and right-circular states. Controlled and normal states may of course be transformed into any other pair of output quadrature states using a suitable retarder.

### Experiment

Figure 1 shows the experimental configuration. The SOP of light from a linearly polarized HeNe (633nm wavelength) laser was rotated using a bulk half-wave-plate and injected into the fiber (10m, PM, beat length  $\approx 1\text{mm}$ ) at  $-45^\circ$  to the H-axis (H,V designate the fiber axes). The fiber was cabled in plastic sleeving and both ends were polished at  $15^\circ$  to the axis to reduce disturbing reflections. At the output of the fiber the light was collimated and projected through a bulk quarter-wave-plate (QWP) at  $22.5^\circ$  and a normally oriented, 50% dielectric reflector. This *Primary Output* would be used as input to the polarimetric sensor.

Light reflected by the dielectric reflector travelled back through the QWP and fiber to be split off in a 50% pellicle beamsplitter oriented at  $< 10^\circ$  angle of incidence. This *Control Output* SOP was analyzed using a  $5^\circ$  deviation Wollaston prism and two photodetectors  $D_H$ ,  $D_V$ . The prism was oriented to resolve the H,V intensities.

In order to effect a SOP-control loop, the difference between the electrical outputs corresponding to the two detected intensities was amplified, normalized to the total intensity, integrated and used to drive a heater in contact with 150mm of bare fiber. This was close to the input end, but could be placed anywhere convenient. The fiber-heater was formed by dip-coating the fiber in conductive silver paint. The heater resistance was 40-200 $\Omega$  in different constructions. The heater allowed a fiber differential retardation ( $\Gamma_f$ ) of  $> 6\pi$  radians and a phase slew rate  $\approx 100$  rad/s.

In the absence of closed-loop control, the Primary Output state wandered randomly with stress and temperature variations in the cabled fiber, as is expected with non-eigenstate transmission. Closing the control loop forced the output state to a stable, linear state at  $-22.5^\circ$  to the fiber output eigenstates, independent of modest thermal perturbations to the fiber. Phase variations of less than  $2^\circ$  remained. With larger variations in fiber birefringence  $\Gamma_f$ , the range of the control loop would be exceeded, and lock lost.

### Theoretical Treatment

In order to describe the loop operation we use the Jones calculus<sup>4</sup>. For a linear input state at  $-45^\circ$  to the fiber axes the Jones vector is  $J_{\text{input}} = (E_H : E_V) = 1/\sqrt{2} \cdot (1 : -1)$ . The corresponding Control Output state is  $J_{\text{control}} = 1/2 \cdot (1 - e^{i\Gamma_f} : 1 + e^{-i\Gamma_f})$ . As the fiber retardation  $\Gamma_f$  varies from 0- $2\pi$  with environmental temperature variations both  $J_{\text{primary}}$  and  $J_{\text{control}}$  vary, with  $J_{\text{control}}$  being in the same SOP for only two values of  $\Gamma_f$  ( $\pi/2$ ,  $3\pi/2$ ). This is in stark contrast to the case if the retarder QWP is not present. Then the Control Output is of the form  $J_{\text{control}} = 1/\sqrt{2} \cdot (e^{2i\Gamma_f} : 1)$ , the  $2\Gamma_f$  term causing the SOP to repeat itself continuously for values  $\Gamma_f$  and  $\Gamma_f + n\pi$  where  $n$  is an integer. The double-angle characteristic would mean that while Control Output stabilization would function, the Primary Output would be ambiguous, taking on one of two possible orthogonal states.

We may better visualize the control scheme's operation using the well-known Poincaré sphere<sup>5</sup> representation of polarization states (Figure 2). On the sphere are shown two loci

of SOPs. With the QWP in place the Primary Output state varies with  $\Gamma_r=0-2\pi$  along a great circle through the points  $(-135^\circ, 45^\circ)$ ,  $(135^\circ, 0^\circ)$ ,  $(45^\circ, -45^\circ)$ ,  $(-45^\circ, 0^\circ)$ , where angles are sphere angles. The locus of states at the Control Output given above is wrapped into a figure-of-eight centred on P and touching the eigenstates H,V. The control loop forces the detected H and V intensities to be equal and the Control SOP to be P. To determine which of the two branches of the locus of states passing through P at  $\pm 45^\circ$  (corresponding to different primary output states at  $(135^\circ, 0^\circ)$  and  $(-45^\circ, 0^\circ)$ ) is stable we must also know the electronic phase of the control loop. On the figure-of-eight locus P is passed with increasing retardation  $\Gamma_r$  in the directions shown by the arrows. If we assume that an increase in the error control variable  $\epsilon=(I_H-I_V)/(I_H+I_V)$  increases  $\Gamma_r$ , then only the "North-West" branch is stable (Primary Output  $(-45^\circ, 0^\circ)$ ). Hence no state ambiguity exists. If the amplifier phase is reversed then the "North-East" branch is selected, with a flip of the Primary Output state to  $(135^\circ, 0^\circ)$ . Errors in angular placement of the QWP cause little change in the Control Output locus. The figure-of-eight lobes simply expand towards Q or contract to a smaller locus near P. Hence the loop is very insensitive to such errors.

Note further that any state on the PLQR great circle can be coupled in to the fiber. The control loop forces an identical output state  $(-45^\circ, 0^\circ)$  independent of the input state. It is not even necessary to change the position of the analyzing Wollaston prism. Of course, input H,V eigenstates can also be delivered, giving Primary Output states at  $(45^\circ, 45^\circ)$ ,  $(-135^\circ, -45^\circ)$  on the sphere. These are in quadrature ( $90^\circ$  on sphere) to the controlled states. Limited continuous control over most of the Primary Output locus can be achieved by offsetting  $\epsilon$  before passing to the servo amplifier.

### Application to Polarimetric Sensors

By way of example we apply the technique to the determination of the retardation of a birefringent element of known angular orientation. This is depicted in the 'Remote Sensing Head' of Figure 2. One possible configuration is as follows: An eighth-wave-plate oriented through SS' is used to rotate the Primary Output locus to the equatorial plane. Then the normal fiber eigenstates enter the sensing crystal as R,L-circular states. The sensing crystal is then oriented at  $45^\circ$  on the sphere. Variation of the unknown retardation  $\theta$  then causes rotation of the transmitted state along a great circle through RSLs'. A polarizer at S allows the sequential measurement of two intensities  $I_{11}=A \cdot \cos^2(\theta/2)$  and  $I_{12}=A \cdot \cos^2(\theta/2 + \pi/4)$ , where A is the unknown peak intensity and  $\theta$  the unknown phase. The state analysis and transmission to the sensor evaluation system can occur using a single- or multi-mode fiber.  $\theta$  may be determined from  $\theta=2 \cdot \tan^{-1}(1-\sqrt{2I_{12}/I_{11}})$  independent of A. Endless phase determination for  $\theta > 2\pi$  is simply effected by applying  $I_{11}$ ,  $I_{12}$  to in-phase and quadrature inputs of an electronic up/down counter.

### Summary

A technique for feedback-controlled delivery of non-eigenstates through polarization-maintaining fiber has been described. The output state is monitored in reflection through the same fiber, and controlled by a single fiber retardation variable. The ability to simply deliver two passive and two actively controlled states at  $90^\circ$  on the Poincaré sphere is sufficient for many applications in remote ellipsometry or requiring quadrature detection. Faster SOP control would be possible using semiconductor diode sources via current-induced wavelength shifts, fiber-stretchers or electro-optic devices.

## References

1. D.A. Jackson, 'Monomode optical fibre interferometers for precision measurement', J. Phys. E. 18, 981-1001 (1985).
2. H. Tsuchida, Y. Mitsuhashi, S. Ishihara, "Polarimetric optical fiber sensor using a frequency stabilized semiconductor laser", IEEE J. Lightwave Techn. 7, 799-803 (1989).
3. Z.B. Ren and Ph. Robert "Input polarization coding in fibre current sensors", Springer Proceedings in Physics 44, 261-266 (1989).
4. R.C Jones "A new calculus for the treatment of optical systems - Part V", J. Opt. Soc. Am., 37, 107-110 (1947).
5. G.N. Ramachandran and S. Ramaseshan in "Handbuch der Physik", S.Flügge, ed. (Springer, Berlin 1961), Vol. 25/1, p.1.

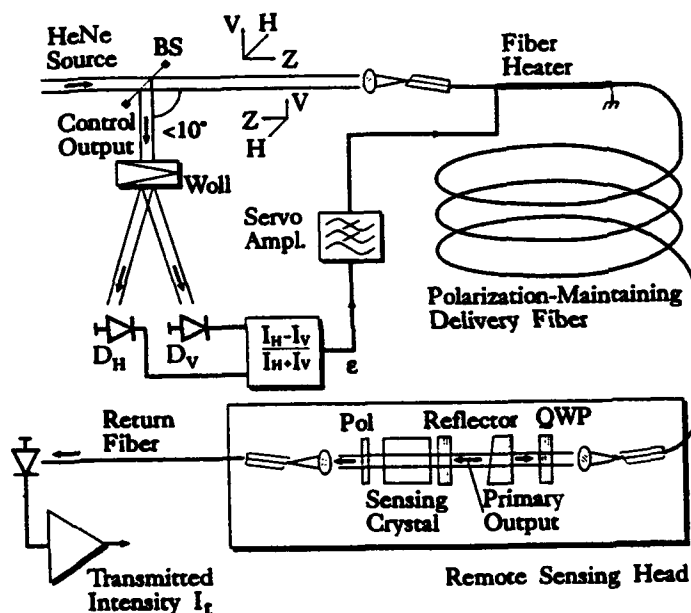


Figure 1: Active SOP control system. Light coupled into the delivery fiber at  $\pm 45^\circ$  to the fiber axes is analyzed after a double pass through fiber and QWP. Active control then locks the Control Output, and with it the Primary Output to a known state. Controlled and normal eigenstate outputs allow unambiguous determination of polarimetric phase of a remote sensing crystal.

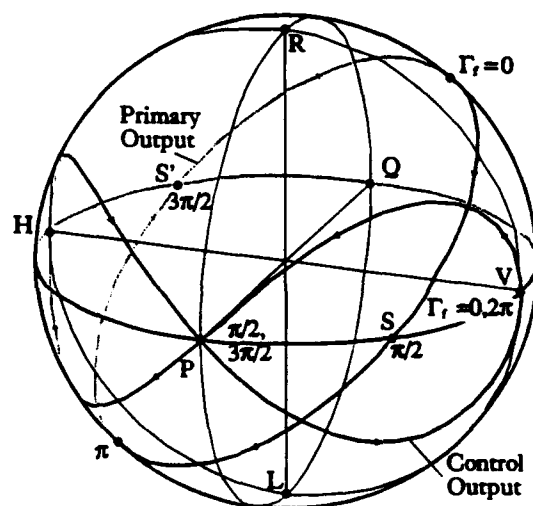


Figure 2: Poincaré sphere representation. As fiber retardation varies, the Primary Output state varies along a great circle, the Control Output in a figure-of-eight. Stabilized Primary Outputs are at S, S'.



## **P33            An Optical Fiber Network For Analog Temperature And Pressure Sensing Purposes**

M.R.H.Voet, GLÖTZL, Forlenweg 11, 7512 Rheinstetten, Germany;  
F.X.Desforages, PHOTONETICS, 52 Av.de l'Europe, 78160 Marly le Roi, France;  
A.R.F.Barel, VUB, Pleinlaan 2, 1050 Brussels, Belgium;

### **ABSTRACT**

The concept of a fibre optic pressure and temperature sensor network is presented. Time Domain Multiplexing (Continuous Wave or Pulse Wave method) is used to monitor up to 16 analog sensors (1% accuracy) for both, pressure and temperature measurements in a mixed configuration.

### **1) INTRODUCTION**

As there is an increasing interest to multiplex 10 to 20, medium accuracy (100 measuring points), passive optical sensors in a fiber network. The DEMOS project (Distributed Environmental Monitoring with Optical SENSORS: BRITE Research Program) aims at developing such a network together with the associated temperature and pressure sensors.

In our design, intensity modulated fiber sensors are used and in our setup both temperature- and a pressure sensor are monitored with Time Domain Multiplexing techniques. Two techniques are presented, nl., - the Continuous Wave technique  
- the Pulse Wave technique

Moreover, the reflected intensities are wavelength referenced in order to obtain a network which is independent from all environmental disturbances such as non-identical connector losses, source and detector aging, network fiber length and bent losses.

### **2. PULSE and CONTINUOUS WAVE METHOD**

#### **2.1 Description of the pulse method:**

This method has been extensively described previously ([1], 2)). The experimental set up is shown in fig. 1. A short time light pulse is launched into an optical star network through two 3 dB couplers. Analog intensity sensors are connected at the output ports of the optical star which are reflecting a variable amount of light related to the physical variable to be sensed (pressure or temperature).

In order to design a line-neutral network, a dual wavelength emission is used where emitted and reflected intensities are monitored with two opto-electronic receivers. The following quantity is measured:

$$S = \frac{I_1(901nm) * I_4(830nm)}{I_2(901nm) * I_3(830nm)}$$

The above described experimental set-up has been used to monitor the variations of the reflected light by a Schott glass color filter versus temperature. The sensing wavelength is 830 nm while the "reference wavelength" is 901 nm.

Fig. 2 shows the variation of the  $\log(S)$  quantity against temperature. The black squares act for the increasing temperature while the white squares act for the decreasing one. As it can be seen, the hysteresis is quite low and is inferior to the measurement accuracy ( $\pm 1.5\%$ ). This curve may be represented by a straight line whose equation is:  $\log(S) = at + b$  where  $a$  is the slope ( $5.9 \times 10^{-3} \text{ } ^\circ\text{C}^{-1}$ ),  $t$  is the temperature value in  $^\circ\text{C}$  and  $b$  is a constant. If we assume that the measurement accuracy is  $\pm 1.5\%$ , therefore the temperature accuracy may be written as:

$$\Delta t = \frac{(\pm 1.5\%)}{(5.9 \cdot 10^{-3} \cdot 2.3.)}$$

$$\Delta t = \pm 1.1^\circ\text{C}$$

These results are very promising and show that the goal of a 100 measurement point may be reached if we are able to extend the temperature sensor range up to  $200^\circ\text{C}$ .

At last, the optical budget calculations are showing that with this technique up to 16 of such sensors may be multiplexed on the same fibre network.

## 2.2 Description of the Continuous Wave method:

This method has already been presented in references [4] and [5]. The excitation signal is not purely CW but keeps all its system power budget advantages. The source, which is a simple LED, is powered by a superposition of an AC current at a modulation frequency ranging from 0.5 to 10 MHz and a DC bias current.

Each sensor of the network is characterized like in the pulse method by its own, unique and known transmission delay. The optical power is splitted by couplers into these different paths which behave as different phasors. The sensor modifies only the amplitude of its phasor. The demultiplex is then performed by measuring the I.Q. component of the sum of the detected phasors at several modulation frequencies with a synchronous detector followed by proper matrix inversion.

Line-neutrality is obtained by associating to each sensor, a dummy transmission path acting as a reference and this set up is compatible with a superposed wavelength multiplex method.

The pressure sensor used consists of a microbending sensitive inner part, connected into a pressurized housing. [4]

The sensor firstly was calibrated in a two wavelength 850 nm and 1300 nm transmissive set-up in order to obtain an exact knowledge of the attenuation-pressure relation, the linearity and the hysteresis. The sensor is then implemented in the above-mentioned test set-up and furthermore in the continuous wave set-up with a 3 dB loss simulation as can be seen from figure 3.

The results are in good agreement with the pulse wave method and shows similar accuracy values. See also reference [4] and [5].

### 3. CONCLUSION

This paper is reporting the results obtained during the DEMOS program. Up to 16 analog temperature or pressure sensors may be multiplexed with a 1% accuracy measurement and a good line neutrality in both the pulse- and the continuous wave method.

### 4. ACKNOWLEDGEMENT

The authors want to thank: the Commission of the European Communities and the French Ministry of Research and Technology which had partially funded this work.

### 5. REFERENCES

- (1) Nelson A.R., Mc Mahon D.H.; and Gravel R.L.: "Passive multiplexing system for fibre optic sensors" *Applied Optics*, 1980, 19, p. 2917.
- (2) Desforges F.X., Jeunhomme L.B., Graindorge Ph and Arditty H.J.: "On/Off fiber optic sensors network designed for an industrial use". *Proceedings of SPIE*, Vol 842, PP 121-131, 1987.
- (3) Johnson L.A. and Jensen S.C.: "Problems and approaches for Remote Fiber Optic Absolute Sensors" *Proceedings of SPIE*, Vol. 566, pp 45 - 53, 1985.
- [4] Voet, M.R.H., Barel, A.R.F. : " Performances of the Glötzl fibre optic pore water pressure transducer in a line neutral sensing system", *Proc. 7th Optical Fibre Sensors Conference*, OFS7, Sydney, New South Wales, 1990, 159-162.
- [5] Voet, M.R.H., Barel, A.R.F. : "Line-Neutral fibre optic sensing, combining time division- and frequency division multiplexing techniques", *Proc. ECO3*, The Hague, March 1990.

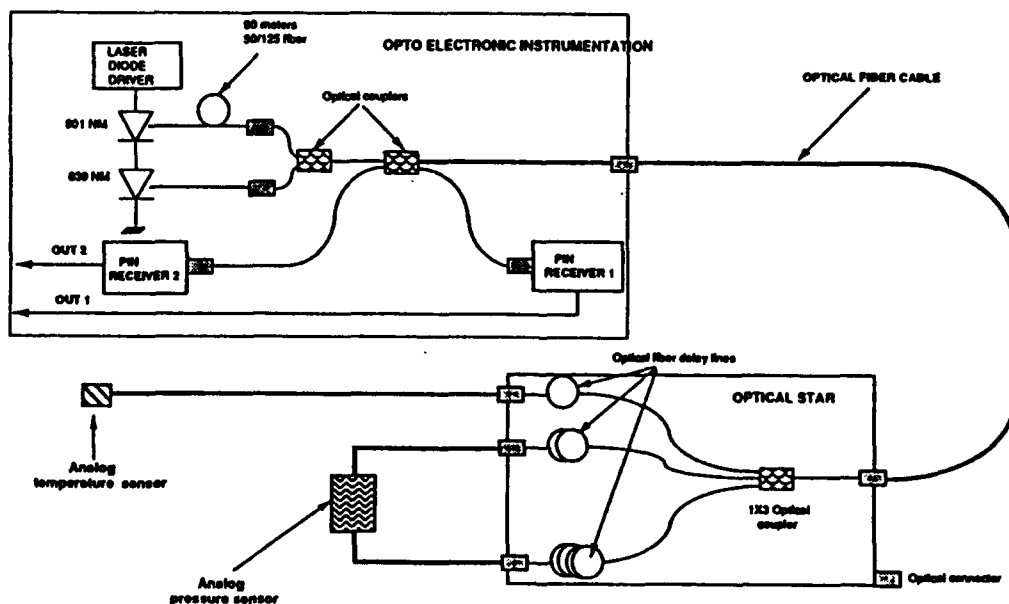


Figure 1: Experimental Set-Up of the Analog Fiber Optic Sensor Network

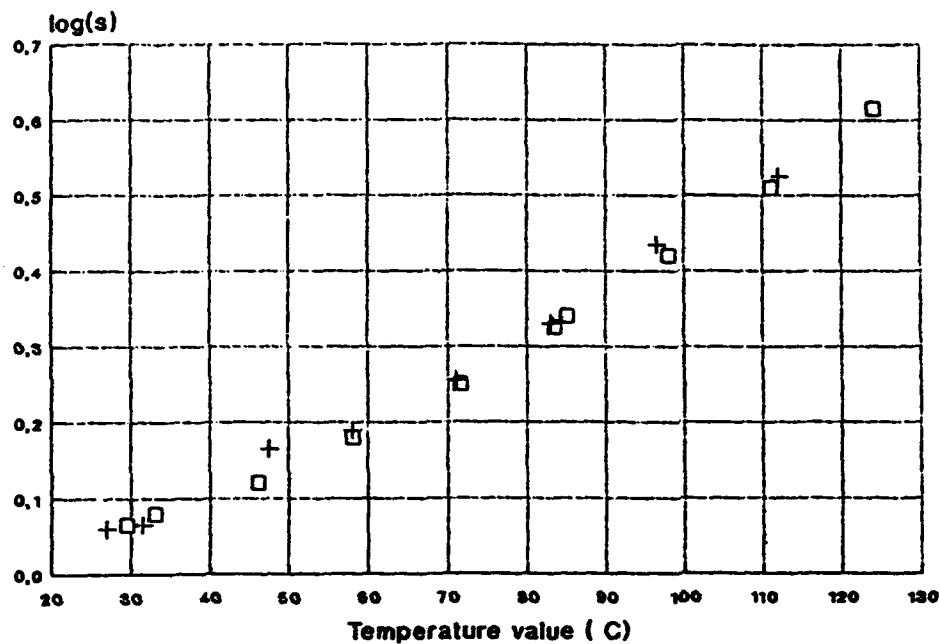


Figure 2: Variation of Log (S)

## Data from "LN46-1"

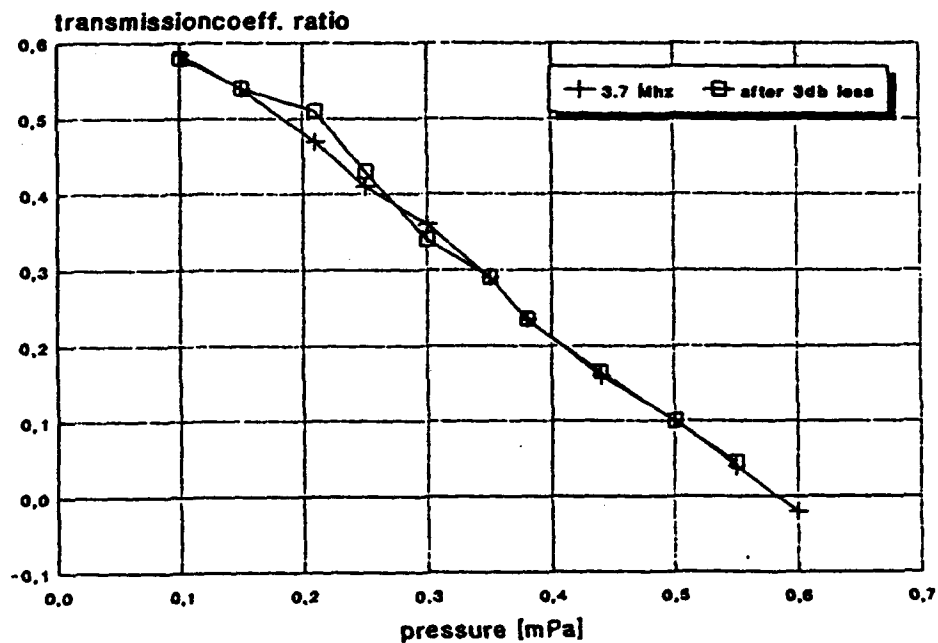


Figure 3: Continuous Wave Referencing

# **P34 A Multiplexing Scheme For Optical Fibre Interferometric Sensors Using An FMCW Generated Carrier**

S F Collins

Department of Applied Physics, Victoria University of Technology, PO Box 64, Footscray, Victoria 3011, Australia

B T Meggitt, A W Palmer and K T V Grattan

Department of Electrical, Electronic and Information Engineering, City University, Northampton Square, London EC1V OHB, U.K.

## **1. Introduction**

Numerous optical fibre sensors for a wide variety of physical measurands have been developed over the past decade. However industrial implementation of optical fibre sensors has been limited mainly to situations in which no suitable conventional electronic sensors were available. The advantages of fibre optic sensors over electronic sensors have long been recognized, including their immunity to electromagnetic interference and their intrinsic safety. Also the wide bandwidth of optical fibres allows a number of optical sensors to be multiplexed in a single scheme. Deployment of optical fibre sensors would be more economically attractive if they were part of a network of sensors, in which many sensors operated from the same instrumentation. Multiplexing schemes have been devised for various types of sensors, and require more complex instrumentation than that required for a single sensor.

Low coherence (or white light) interferometry [1], which potentially offers both high resolution and good stability, has become well-established in recent years. Light from a low coherence source is directed through two interferometers in sequence, known respectively as the "sensing" and "local" interferometer. The light source is pigtailed onto one arm of a  $2 \times 2$  port single mode fibre directional coupler, and the light is directed through it into the sensing interferometer. The two interferometric paths (all-fibre or partially fibre) are arranged to have unequal optical path lengths. The light is back-reflected through the coupler and into the free space local Michelson interferometer. The path imbalances of the two interferometers should be approximately equal (i.e. to within the source's coherence length), with the individual path imbalances being greater than the source's coherence length. Thus two temporally separated wave packets will be brought back into coincidence at the local interferometer's output. Any path length change in either interferometer will result in a phase change in the output signal. One of the local interferometer's mirrors is modulated over a distance of  $\lambda/2$  by a piezo-electric transducer with a serrrodyne ramp (frequency  $f_1$ ), and the resultant intensity has the form

$$I = I_0 (1 + \cos 2\pi f_1 t) \quad (1)$$

at time,  $t$ . Any change in the sensor's optical path difference will result in a phase change at the output.

Deployment of low coherence interferometers would be more attractive if they could be multiplexed. An optical time domain scheme has been demonstrated [2], but nanosecond pulses and complex signal processing were required. Therefore

simpler schemes, like the one proposed here, are of interest.

The scheme suggested here uses a variation of the FMCW (frequency modulated continuous wave) technique to provide each of the sensor outputs with a unique carrier frequency, in a manner similar to that used for identifying vibrating optical sensors [3]. Firstly the FMCW technique is summarized.

## 2. The FMCW Technique

The FMCW technique was first proposed for radar ranging applications [4]. A linear frequency sweep (i.e. sawtooth wave) is applied to the carrier. If the frequency chirped signal is reflected from a distant target at range,  $R$ , and superposed on the direct signal from the modulator a beat signal is produced whose frequency is

$$f_{\text{BEAT}} = \Delta f \cdot \frac{2R}{T_S} \cdot \frac{n}{c} \quad (2)$$

where  $\Delta f$  is the frequency deviation,  $T_S$  is the chirp period and  $c/n$  is the wave speed ( $n$  = refractive index). Detailed analyses reveal that the beat signal has a line spectrum with fundamental frequency  $1/T_S$ . The beat signal has a number of frequency components confined to a sinc envelope centred on  $f_{\text{BEAT}}$ . By choosing appropriate values of  $\Delta f$  and  $R$  in equation (2), the beat signal will be a single harmonic at  $f_{\text{BEAT}}$ , i.e.

$$f_{\text{BEAT}} = \frac{M}{T_S} \quad (3)$$

where  $M$  is the harmonic integer.

In the system being proposed an incoherent technique will be used in which the frequency sweep is applied to the light's intensity modulation. Indeed we have recently demonstrated this method for measuring distance [5], using a fibre Michelson arrangement. A typical beat pattern (which includes the RF carrier) is shown in figure 1(a), and the beat frequency is in agreement with equation (2). As expected, the observed time interval between adjacent beat maxima decreased with increasing range, as shown in figure 1(b), when aspects of the scheme discussed below were investigated experimentally.

## 3. The Proposed Scheme

The proposed multiplexing scheme is shown in figure 2. A low coherence source (SLED or multimode LD) is intensity modulated by a swept frequency from an RF oscillator. The light is launched into a single mode  $3 \times 3$  port directional coupler from where it is directed towards three interferometric fibre-based sensors, whose distances from the coupler are  $R_1$ ,  $R_2$  and  $R_3$ , which are in the ratio 1:3:5. As shown, each sensor has a path imbalance of  $L$ . Light from each sensor is reflected back towards the  $3 \times 3$  coupler and into the free space Michelson local interferometer, whose arm imbalance is  $nL$  (i.e. approximately the same optical path difference as the sensing interferometer) and where  $n$  is the fibre's refractive index. One of the mirrors in the local interferometer is modulated by a piezo-electric transducer over  $\lambda/2$  by a ramp (i.e. serrrodyne) whose frequency is  $f_1$ . The output of the photo-diode detector is mixed incoherently with the frequency-chirp signal being applied to the source. The resultant signal can be displayed on a spectrum analyser

or processed in an appropriate manner.

Incident on the detector will be 3 different time delayed versions of the source's frequency chirp. (The arm imbalances,  $L$ , of the interferometers are assumed to be much less than the sensor ranges,  $R_1$ ,  $R_2$  and  $R_3$ , so the time delay caused by the unequal paths in the interferometers can be neglected.) Therefore at the mixer, 3 distinct beat frequencies will be produced, corresponding to each sensor range, as given by equation (2). However each sensor return signal has, at the detector, superposed on it the cosine function (equation (1)) resulting from the coupling between the sensing and local interferometers, and the form of these signals is shown in figure 3. Consequently the electrical output from the mixer, for each sensor, will involve the product of these two effects, i.e.

$$E(t) = E_0 \cos(2\pi f_{\text{BEAT}}t) [1 + \cos(2\pi f_1 t)] \quad (4)$$

where  $E_0$  is the voltage amplitude. The frequency components of this waveform are  $f_{\text{BEAT}} - f_1$ ,  $f_{\text{BEAT}}$  and  $f_{\text{BEAT}} + f_1$ , i.e. the signal obtained from each sensor is a carrier with double side bands.

Since each sensor generates a unique carrier frequency, the mixer output for the scheme will have the frequency spectrum depicted in figure 4. The ratio of the sensor ranges was specified above to prevent any cross-mixing between the beat signals from occurring at one of the carrier frequencies. The state of each sensing interferometer is determined by monitoring the phase of the local interferometer output. This is achieved by band-pass filtering about the side bands and tracking their phase. The central beat frequency is a carrier only, and contains no useful information about the sensor.

#### 4. Conclusions

An incoherent FMCW technique for multiplexing low coherence fibre optic interferometric sensors has been proposed, and preliminary results are encouraging. Each sensor generates a unique carrier frequency, thereby enabling the individual sensor outputs to be distinguished from each other.

#### References:

1. A S Gerges et al, "Fibre optic interferometric sensors using a low coherence source", Int. J. Optoelectronics 3, 311-322, 1988.
2. J L Brooks et al, "Fibre optic interferometric sensor arrays with freedom from source induced phase noise", Opt. Lett. 11, 473-475, 1986.
3. K I Mallalieu, R Youngquist and D E N Davies, "FMCW of optical source envelope modulation for passive multiplexing of frequency-based fibre-optic sensors", Electron. Lett. 22, 809-810, 1986.
4. A J Hymans and J Lait, "Analysis of a frequency-modulated continuous-wave ranging system", Proc. IEE B 107, 365-372, 1960.
5. S F Collins, A W Palmer, B T Meggitt and K T V Grattan, "Intensity chirped laser diode modulation techniques for fibre optic based ranging applications", to be submitted to 16th ACOFT Conference (Adelaide, 1991).

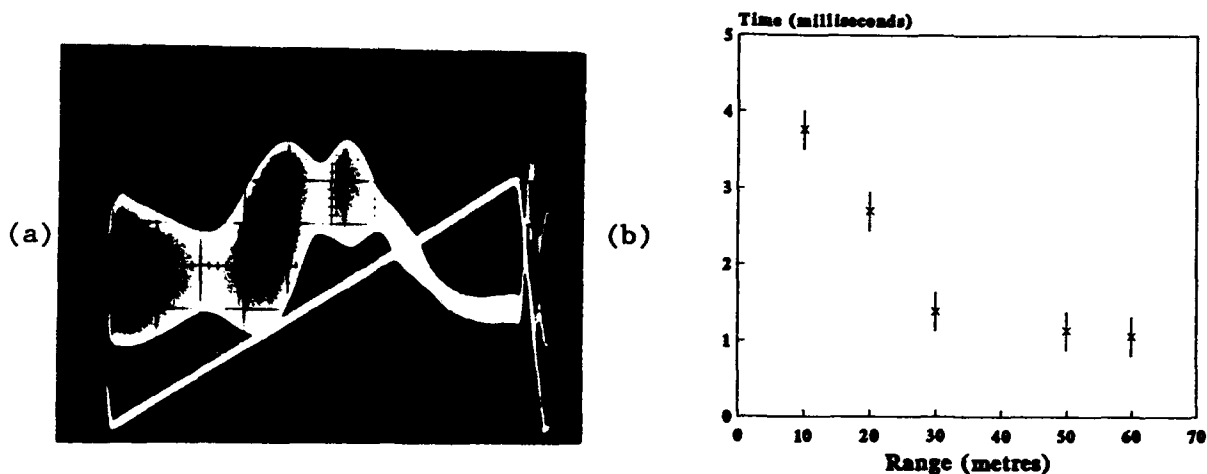


Fig 1. Determination of distance by incoherent FMCW. (a) Beat pattern obtained for  $R = 10$  m, using  $\Delta f = 40$  MHz and the depicted sawtooth wave ( $T_S = 10$  ms). (Preliminary result showing beating on the initial linear portion of the ramp, but degraded due to oscillator non-linearities). The beat frequency is about 4 times the sweep frequency. (b) Observed time interval between first and second beat maxima as a function of range.

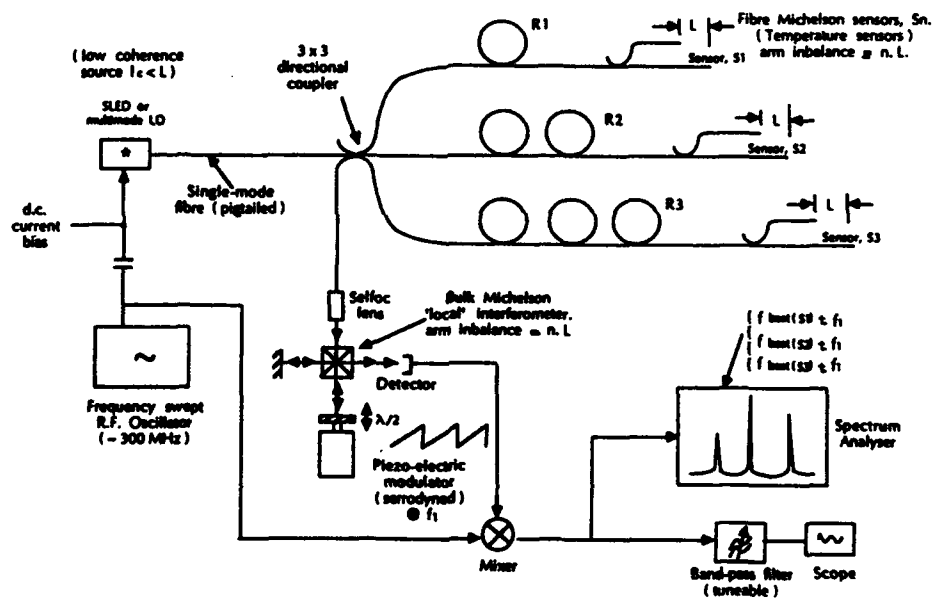


Fig 2. Proposed multiplexing scheme for low coherence interferometric sensors.

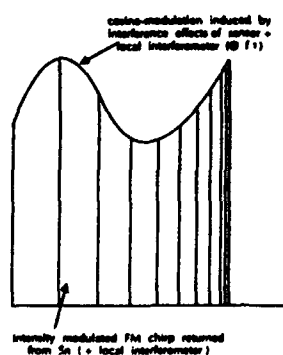


Fig 3. Photo-detector output (from  $S_n$ ) before electronic mixing.

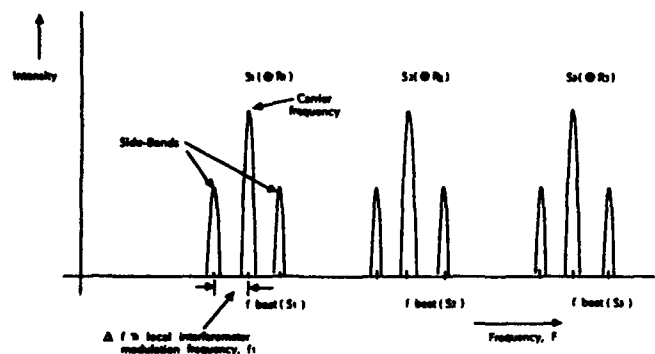


Fig 4. Expected spectrum analyser output (not showing cross-modulated components).



# P35 Visibility And Bias Phase Noise In Fiber-optic Interferometers With An Output Polarizer

M. Tur\* and H.J. Shaw

Ginzton Laboratory, Stanford University, Stanford, Ca. 94305

## Abstract

The presence of a polarizer at the output of a fiber-optic interferometer is shown to significantly increase the effect of fluctuations of the input polarization on the bias phase noise at the interferometer output.

**Introduction:** It is well known, [1]-[2], that the state of polarization (SOP) of the light at the input to a fiber-optic interferometer, such as schematically illustrated in Fig. 1a, may affect both the visibility ( $V$ ) and phase ( $\Phi$ ) of the measured output ( $I_{out} \propto [1 + V \cos(\Phi)]$ , [3]).

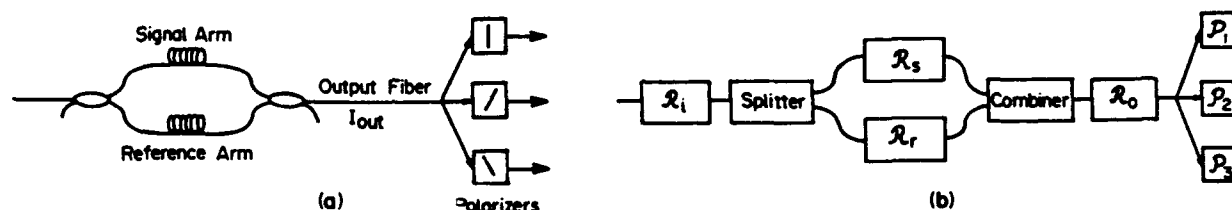


**Figure 1:** (a) Schematic of a fiber Mach-Zehnder interferometer with three output polarizers. (b) Equivalent birefringent network.

$V$  should be maximized to increase sensitivity and  $s/n$ . But even after a sufficiently long coherence source is used and the coupling ratios of both the splitter and combiner are appropriately optimized,  $V$  is still bounded by the scalar product  $|\mathbf{P}_{Sig.}(t) \cdot \mathbf{P}_{Ref.}(t)|$ , where  $\mathbf{P}_{Sig.}(t)$  and  $\mathbf{P}_{Ref.}(t)$  are the time-dependent unit-intensity polarization vectors of the output SOPs of the interferometer signal and reference arms, respectively [3]. In interferometers which use conventional low birefringence fibers and fiber components (and even in systems with polarization maintaining fibers but with non-ideal splices and couplers) environmental effects on the input fiber, as well as on the arms fibers, will change  $\mathbf{P}_{Sig.}(t)$  and  $\mathbf{P}_{Ref.}(t)$ , resulting in time-dependent polarization-induced fading of the visibility  $V$  [1]. One way to avoid complete fading (i.e.,  $V = 0$ ) and to increase the  $s/n$  is to use three polarizers, angularly spaced by  $120^\circ$ , at the interferometer output and to choose that channel with the highest  $V$  [4].

Ignoring source phase noise [3],  $\Phi = \Phi_{Signal} + \Phi_{Bias}$ , where  $\Phi_{Signal}$  is the optical phase induced by the physical measurand and  $\Phi_{Bias}$  denotes the optical phase difference between the two arms in the absence of the externally induced  $\Phi_{Signal}$ . Since  $\Phi_{Signal}$  must be extracted from  $\Phi$ , any random changes in  $\Phi_{Bias}$ , and in particular those related to fluctuations in the input SOP, should be considered noise [2]. Following Ref. [2], we denote this input-polarization-induced bias phase noise by  $\gamma$ . To

\* Permanent address: Faculty of Engineering, Tel-Aviv University, Tel-aviv, Israel 69978.

characterize the effect of small changes in the input SOP,  $\mathbf{P}_{in}(t)$ , on  $\gamma$ , it is sufficient to study the appropriate derivative  $\Delta\gamma/\Delta\mathbf{P}_{in}$  and its dependence on the input SOP and the other system parameters.

The purpose of this paper is to calculate the visibility and the input-polarization-induced phase derivative  $\Delta\gamma/\Delta\mathbf{P}_{in}$ , at the three polarized output channels of the interferometer of Fig. 1a, as a function of the SOP of the input light to the interferometer ( $\mathbf{P}_{in}(t)$ ). This work represents a generalization of the special case studied by Kersey *et al* [2], in which there is no polarizer at the output. In that case rather simple analytical expressions can be derived for the visibility and bias noise coefficient, which depend on only two parameters, one for the input SOP and one for the interferometer. However, in the present case, where an arbitrary linear polarizer is included, many more parameters are generally involved in the specification of the problem and computer simulation is an appropriate approach.

**Mathematical Formulation:** Following the method of Ref. [2], we model the interferometer of Fig. 1a by the equivalent birefringent network of Fig. 1b, with appropriate operator representations for the polarization transformations introduced by the input fiber ( $\mathcal{R}_i$ ), the signal and reference arms ( $\mathcal{R}_s, \mathcal{R}_r$ ), the output fiber ( $\mathcal{R}_o$ ), and the three output polarizers ( $\mathcal{P}_j, j = 1, \dots, 3$ ).  $\mathbf{P}_{in}$  is the input SOP. For simplicity we assume lossless arms and 1:1 splitting ratios in both splitter and combiner.

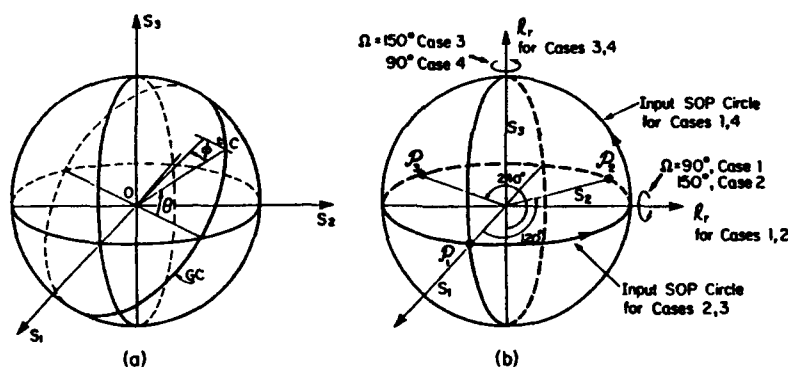


**Figure 2:** (a) The great circle  $GC$  on the Poincare sphere. (b) The Poincare sphere representations of the four cases.

On the Poincare sphere [3], Fig. 2a, we let the input polarization (denoted by  $C$  on the sphere) trace an arbitrary great circle,  $GC$ . For the given  $\mathcal{R}_i, \mathcal{R}_s, \mathcal{R}_r, \mathcal{R}_o$ , and  $\mathcal{P}_j, j = 1, \dots, 3$ , we use the Jones calculus [3] to numerically calculate the visibility  $V$  and  $\Delta\gamma/\Delta\mathbf{P}_{in}$ , as a function of  $\theta$ , which is the angle subtended by the radius vector  $OC$  and the radius of intersection between the great circle and the equatorial plane of the sphere (or with respect to  $S_1$  if the great circle  $GC$  coincides with the equator). To completely characterize  $\Delta\gamma/\Delta\mathbf{P}_{in}$  it is sufficient to study the two derivatives  $\partial\gamma/\partial\theta$  and  $\partial\gamma/\partial\phi$ , where  $\partial\theta$  and  $\partial\phi$  are orthogonal incremental angles around  $C$ , the first in the plane of  $GC$ , the second lying in the great circle perpendicular to  $GC$  at  $C$ , see Fig. 2a. Any other derivative can always be obtained as a weighted average of the above two derivatives.

In Ref. [2] only one great circle was studied, namely, the one which goes through  $C$  and the diameter whose tips represent the two input-polarizations which result in unit visibility (In fact, these tips are the eigen-polarizations of the operator  $\mathcal{R}_s^{-1}\mathcal{R}_r$ , [1]). In the absence of an output polarizer, the symmetry of the problem dictates that both the visibility and the input-polarization-induced bias phase noise are independent of the azimuthal angle of  $C$  around the above-mentioned diameter. In our notation,  $\partial\gamma/\partial\phi = 0$  and the great circle of Ref. [2] is, therefore, the natural choice. However, when an output polarizer is present,  $\partial\gamma/\partial\phi$  is generally non-zero and, as shown below, can even reach much larger values than  $\partial\gamma/\partial\theta$ .

**Results and Discussion:** Results were obtained for four special cases as examples illustrating the nature of the phenomena. For simplicity, the signal arm of the interferometer and the output fiber are taken to be non-transforming (i.e.,  $\mathcal{R}_s$  and  $\mathcal{R}_o$  are the identity transformation). The polarization transformation imposed by the reference arm can be represented on the Poincare sphere by a diameter and an angle of rotation ( $\Omega$ ) around it [1-3]. In cases 1 and 2 the diameter is parallel to the  $+S_2$  direction of the sphere and  $\Omega = 90^\circ$  and  $150^\circ$ , respectively, while in cases 3 and 4 the diameter is parallel to the  $+S_3$  direction of the sphere and  $\Omega = 150^\circ$  and  $90^\circ$ , respectively (Fig. 2b). For cases 1 and 4 the input SOP (after passing through the input fiber) is assumed to lie on the great circle containing the  $S_2$  and  $S_3$  axes, while for cases 2 and 3 it lies on the equator. Each case is run for each of three output linear polarizers, located at  $0^\circ$ ,  $120^\circ$  and  $240^\circ$  to the  $S_1$  axis on the equator of the sphere (Using the conventions of Ref. [3], one of the polarizers is parallel to the  $X$  axis ( $+S_1$  axis of the sphere) and the other two are rotated by  $60^\circ$  and  $120^\circ$  to the first one). Fig. 3 shows the results for the visibility, parallel bias phase noise coefficient ( $\partial\gamma/\partial\theta$ ) and perpendicular bias phase noise coefficient ( $\partial\gamma/\partial\phi$ ) as a function of the location of the input SOP on the great circle under test (see Fig. 2a for the definitions of  $\theta$  and  $\phi$ ).

All visibility curves show some nulls. For example: in case 1 that input SOP which forms an angle of  $270^\circ$  with the  $+S_2$  axis coincides with the south pole of the sphere, i.e., it is left-handed circularly polarized. According to our assumptions, the signal arm transmits its input left-handed SOP unchanged and each of the three polarizers will pass  $1/2$  of its power. But the reference arm will rotate, [1-3], the input SOP by  $90^\circ$  to the tip of the  $-S_1$  axis which represents a wave linearly polarized in the  $Y$  direction. Thus, the output of the reference arm will be completely blocked by  $\mathcal{P}_1$ , while the other two polarizers will transmit  $3/4$  of its power. It immediately follows that zero visibility will be observed at the output of  $\mathcal{P}_1$  and  $V = 0.98(= 2\sqrt{(1/2)(3/4)/[(1/2) + (3/4)]})$  at the outputs of both  $\mathcal{P}_2$  and  $\mathcal{P}_3$  (see the visibility curves at  $270^\circ$  for case 1, Fig. 3). Anyway, for any given  $\theta$  one can always choose a polarizer for which fairly high visibility values are obtained.

It is also clear from Fig. 3 that the perpendicular bias phase noise coefficients ( $\partial\gamma/\partial\phi$ ) are not only significant but most often exceed the corresponding parallel coefficients ( $\partial\gamma/\partial\theta$ ). Fortunately, high values of  $\partial\gamma/\partial\phi$  are usually observed near visibility nulls, which are not the recommended operating points for the interferometer.

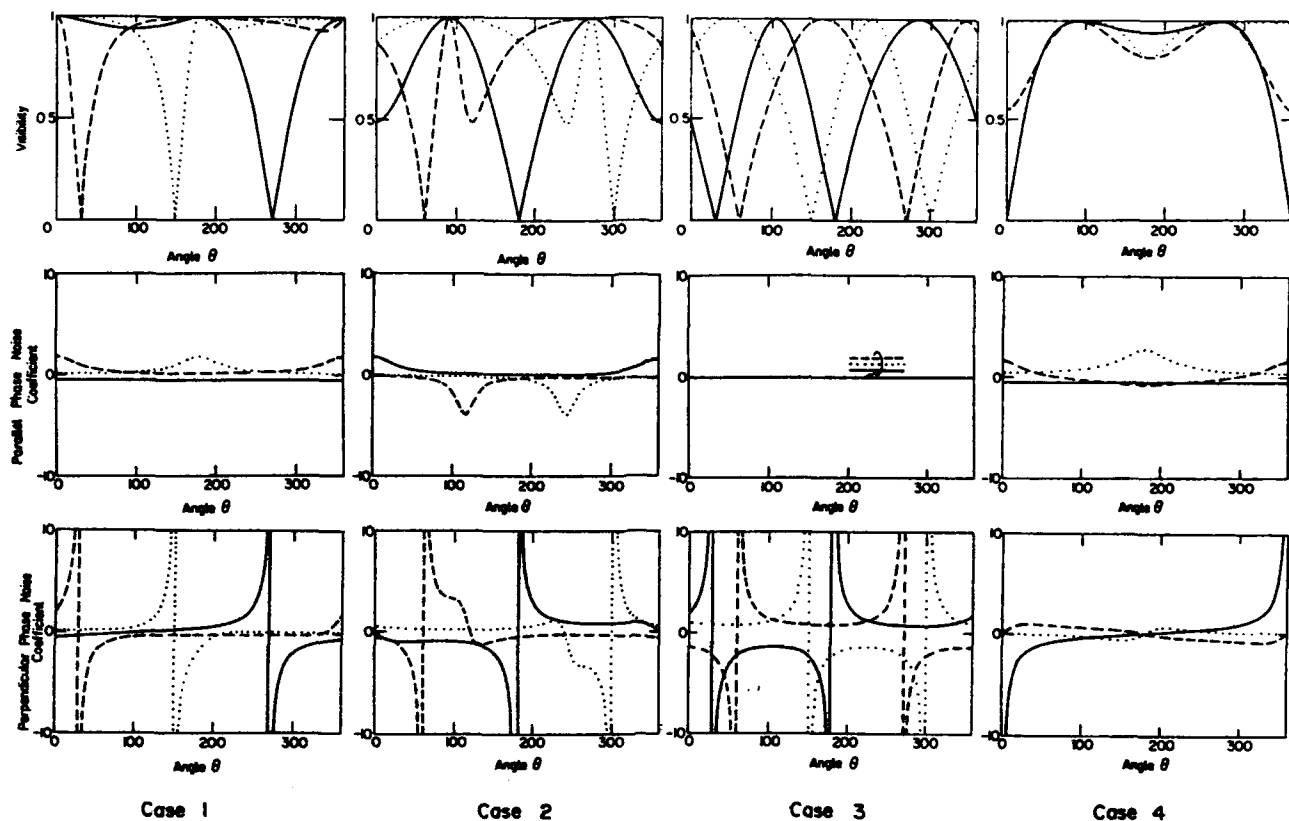


**Figure 3:** The visibility and bias phase noise coefficients,  $\partial\gamma/\partial\theta$  (parallel) and  $\partial\gamma/\partial\phi$  (perpendicular), as a function of  $\theta$  for linear polarizers at  $0^\circ$  (solid line),  $120^\circ$  (dashed line) and  $240^\circ$  (dotted line) to the  $S_1$  axis. Note: all three parallel phase noise coefficients are zero in case 3).

**Conclusions:** To properly evaluate the excess bias phase noise at the output of a fiber-optic interferometer containing output polarizers, due to fluctuations of the input polarization, it is necessary to calculate the effects of perturbing the input SOP in a direction on the Poincare sphere which is orthogonal to the direction involved in the no-polarizer case of Ref. [2]. Moreover, this orthogonal bias phase noise coefficient can be much larger than the parallel coefficient. Since output polarizers are important as means to overcome polarization-induced fading, this study should prove useful in the evaluation of proposed interferometers and in the design of experimental prototypes.

**Acknowledgement:** This work was sponsored by Litton Systems Inc.

## References

- 1) A.D. Kersey, A. Dandridge, and A.B. Tveten, Opt. Lett, Vol. 13, p. 288 (1988).
- 2) A.D. Kersey, M.J. Marrone, A. Dandridge, Opt. Lett., Vol. 13, p. 847 (1988).
- 3) *Optical Fiber Sensors: Principles and Components*, J. Dakin and B. Culshaw, Eds., Artech House, Boston, 1988.
- 4) N.J. Frigo, A. Dandridge, and A.B. Tveten, Electron. Lett., Vol. 20, p. 319 (1984).

## Applications Of Fibre Optic Electronic Speckle Pattern Interferometers Using Laser Diode Sources

H Atcha & R P Tatam  
Optical Sensors Group  
School of Mechanical Engineering  
Cranfield Institute of Technology  
Cranfield, Bedford. MK43 0AL, U.K.

Electronic speckle pattern interferometry (ESPI) has been used for a number of years for engineering applications, with conventional bulk optic technology, because of its advantages of pseudo-real time display of static and dynamic deformations of objects over an extended viewing area [1,2]. Recently, the incorporation of monomode optical fibre has considerably simplified the optical arrangement and combined with recent advances in image processing technology has led to powerful instruments that are readily employed in real engineering environments away from optical vibration isolation tables [3]. More recently the incorporation of solid state laser sources has demonstrated that further simplification in the optical system is possible in addition to increased versatility in the measurement capability, for example, the use of wavelength modulation of a diode laser to produce contour fringes and thus measurement of object shape [4,5].

In this paper we report the implementation of a solid state ESPI system using a laser diode as the source. Results of static and dynamic deformation measurements and shape measurement are presented. In addition the use of the diode laser in the signal processing to determine the amplitude and phase of vibration fringes, the distortion due to static loading and calculation of the shape of the object from contour fringes is presented.

The optical arrangement is shown schematically in figure 1. Light from a laser diode is coupled into monomode optical fibre using an optical 'pigtail'. This technique provides a robust stable coupling of the optical power into the optical fibre with no further adjustment necessary, which is particularly attractive in an engineering environment. Light is divided into an object and reference beam using a directional coupler. The object beam illuminates the object. The scattered light is collected by the receiving lens and imaged onto a CCD camera where it coherently mixes with the reference beam. The speckle pattern formed is stored in an image processing board housed in a PC. The piezoelectric phase modulator in the reference beam is used to facilitate data acquisition, discussed later. An example of the correlation fringes obtained is shown in figure 2 for a gas turbine compressor blade that has been loaded at the top left of the blade tip. For an harmonically vibrating object surface the intensity at each point on the detector may be written [6]

$$I(r_d) = I_o(r_o) J_0^2\left(\frac{4\pi}{\lambda} x_o\right) \quad (1)$$

where  $r_d$  and  $r_o$  are conjugate position vectors on the detector and object respectively.  $I_o(r_o)$  is the intensity distribution with the object stationary.  $\lambda$  is the free space wavelength of the source and  $x_o$  is the amplitude of vibration.  $J_0$  is the zeroth order Bessel function of the first kind. Equation 1 shows that for a periodic vibration of the object the recorded intensity is modulated by a  $J_0^2$  distribution and thus the visibility decreases for increasing vibration amplitude. The brightest or zero order fringe corresponds to nodal positions on the object surface. Subsequent fringe maxima correspond to positions of constant vibration amplitude on the object surface. An example of a time average vibration fringe pattern from a turbine

blade vibrating at 5.6kHz is shown in figure 3. The fringes provide information on the vibrational amplitude at any point on the object but not on the relative phase; both amplitude and phase are required to obtain complete information on the mode of vibration of the object. This information may be obtained by using heterodyne techniques [6,7]. In this technique the phase of the interferometer is modulated at the same frequency as the drive signal applied to the object, but the amplitude and phase are varied. Thus points on the object surface that are vibrating with the same amplitude and phase will appear stationary and give rise to the brightest fringes. The phase and amplitude can thus be mapped across the object surface. Heterodyning is usually accomplished by modulating the phase in the reference arm of the interferometer. For conventional bulk optic systems this is achieved by modulating a mirror mounted on a piezoelectric transducer or loudspeaker for example [6]. In fibre optic systems the phase is modulated by straining the fibre using a piezoelectric modulator [3-5,7]. This technique has the advantage that a uniform phase shift is achieved over the entire reference beam wavefront and no beam steering occurs during modulation as the light is guided by the fibre.

An alternative heterodyne technique is to modulate the laser diode wavelength by modulating the injection current. In an unbalanced interferometer this results in a change in the phase of the interferometer. The use of the diode laser has the advantages that an electro-mechanical component is not required in the interferometer, the frequency response is higher than a PZT and it does not exhibit the complex frequency characteristics of PZTs which also require moderate to high voltages. An example of heterodyning using a laser diode is shown in figure 4 with the blade vibrating at 5.6kHz. Note that the bright fringe has moved to a new position on the blade when compared to the unheterodyned case (figure 3).

The use of wavelength tuneable diode lasers enables the ESPI technique to be extended to the measurement of surface contours and thus surface shape. Contour or height profile fringes are obtained by storing an image of the object illuminated at wavelength  $\lambda_1$  and subtracting subsequent images obtained by illuminating at a second wavelength,  $\lambda_2$  [4,5]. The contour interval obtained is given by  $h = \frac{1}{2} \lambda_1 \lambda_2 / (\lambda_1 - \lambda_2)$  such that wider spaced wavelengths produce smaller scale fringes. Figure 5 shows 73 $\mu$ m contours on a U.K. tenpence coin (28mm diameter) obtained by illumination with two diode lasers separated in wavelength by ~10nm. The lasers were tuned by a combination of temperature and injection current variation.

Figure 6 shows 0.9mm contour fringes obtained on a turbine blade by modulating a single diode laser by 169GHz; in these experiments wavelength modulation was obtained by modulation of the injection current. The relative height across the object can be obtained using phase stepping and unwrapping techniques [1,8]. Figure 7 shows a 3D wire frame depicting the shape of the turbine blade obtained from three 3mm contour phase stepped images. The phase stepping was obtained by applying a voltage to the fibre wrapped piezoelectric modulator to produce a  $2\pi/3$  change in phase between each set of correlation fringes [1,8]; phase stepping using the diode laser for shape measurement will also be reported at the conference.

## ACKNOWLEDGEMENTS

The authors would like to thank C Buckberry and J Davies of Rover Group plc for their invaluable assistance with the image processing and J D C Jones of Heriot-Watt University, for many useful discussions.

## REFERENCES

1. R Jones and C Wykes 'Holographic and speckle interferometry', second edition, Cambridge University Press, 1989.
2. C Wykes, Opt. Eng. 21, 400, 1982.
3. J C Davies and C H Buckberry, VDI Berichte 617, 279, 1986.
4. R P Tatam, J C Davies, C H Buckberry and J D C Jones, Optics and Laser Technol 22, 317, 1990.
5. H Atcha, R P Tatam, C H Buckberry, J C Davies and J D C Jones 'SPIE' Proc 1504, paper 23, 1991.
6. O J Lokberg and K Høgmoe, Appl. Opt. 15, 2701, 1976.
7. J D Valera, D Harvey and J D C Jones, SPIE Proc. 1508, paper 24, 1991.
8. D W Robinson and D C Williams, Opt. Commun. 57, 26, 1986.

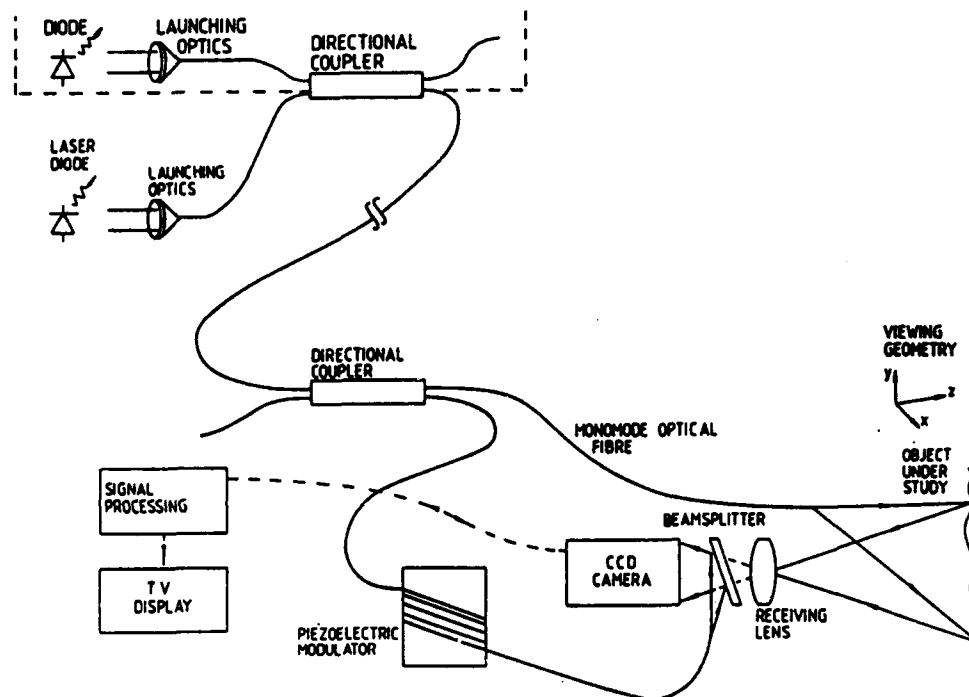


Figure 1. Fibre Optic ESPI System: The dashed line shows how a second laser is incorporated into the system.

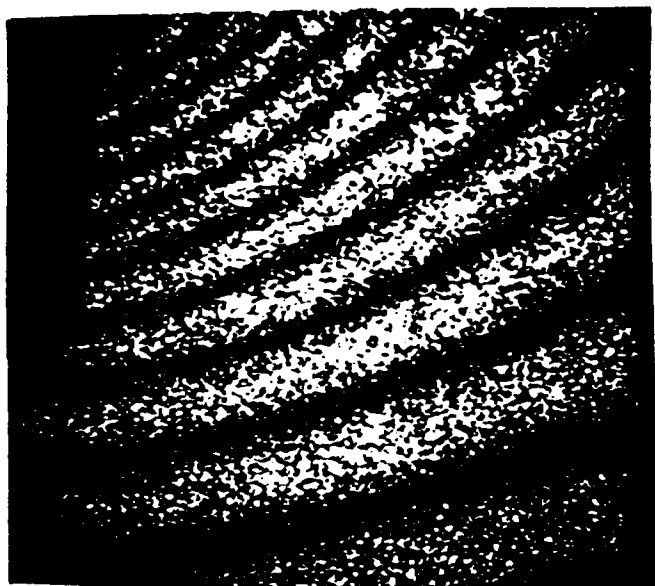


Figure 2. Static deformation fringes obtained by loading the turbine blade at the top left hand corner.



Figure 3. Time-average vibration fringes of the turbine blade at 5.4KHz



Figure 4. Time average vibration fringes of turbine blade at 5.4KHz with laser diode heterodyning

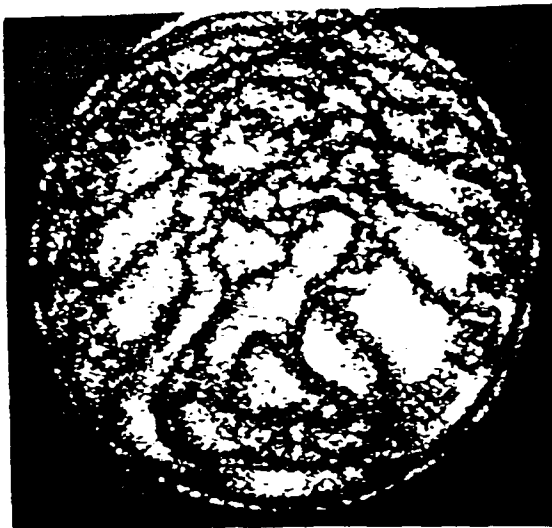


Figure 5. Two wavelength contour fringes of a ten pence coin:  
 $\Delta\lambda \approx 10\text{nm}$  (2 lasers) giving rise to  $73\mu\text{m}$  contour fringes



Figure 6. Two wavelength contour fringes of the turbine blade:  
 $\Delta\nu \approx 169\text{GHz}$  giving rise to  $0.9\text{mm}$  contour fringes

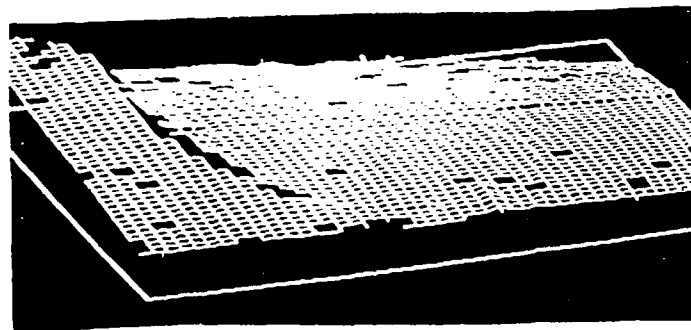


Figure 7. Wire frame of turbine blade obtained using phase stepping and unwrapping techniques.



# **P37      Novel Passive Compensation Technique Applied To A White Light Interferometric System**

D. Walsh and B. Culshaw  
Dept. of Electronic and Electrical Engineering  
University of Strathclyde  
204 George Street  
Glasgow G1 1XW  
Scotland

## **Introduction:**

White light interferometry provides a precise method of determining the path difference in a remote sensing interferometer when it is compared with a locally controlled reference interferometer. Interference fringes will be detected when the path length of each interferometer is greater than the coherence length of the optical source and the relative path difference between them is less than the source's coherence length [1,2]. White light interferometric sensing systems have previously been employed to monitor a variety of external measurands such as; displacement [3], pressure [4], temperature [5] and refractive index [6]. In all these cases the change in the measurand induces a change in the path length of the sensing interferometer. This variation in path length is monitored at the reference interferometer and can be directly related to the measurand change.

The high sensitivity of optical fibre interferometric sensing systems to very small phase changes is restricted by their  $\cos^2$  output transfer function. Thus complete signal fading can occur if the interferometer's operational point drifts to a zero sensitivity point (i.e at a maximum or minimum of the transfer function). Both active and passive homodyne processing schemes have been developed to alleviate this problem, though passive schemes are generally preferred as active compensation has a limited phase tracking range without the need for resetting the system and may also require the use of bulky active components in the interferometer arms. The use of passive techniques require that the interferometer is configured to produce two output signals which are ideally delayed by a constant phase difference of  $\pi/2$  radians. Therefore, since the two output transfer functions from the interferometer are of the form  $\sin\phi$  and  $\cos\phi$ , when one small signal output drifts to a zero sensitivity point the other small signal output will be maximised because its operational point will be biased at the quadrature position. Optical methods of producing this quarter wave phase shift have used the processed output signals from a 3x3 fibre coupler which was employed to combine the outputs from an interferometer[7] or a quarter waveplate to yield a  $\pi/2$  bias between the orthogonal polarisation states in a polarimeter [8].

This paper describes a new passive optical compensation technique using a white light interferometric detection scheme. In contrast to the general position sensing applications cited previously we detail the use of the white light interferometric

system to monitor the vibrations of a piezoelectrically driven mirror in the sensing interferometer.

#### Passively compensated interferometric system:

Fig.1 depicts the passively compensated white light interferometric detection system. Light from a LED source was fed via a multimode fibre coupler into a Fabry-Perot sensing interferometer. The Fabry-Perot cavity was formed between the end face of a collimating SELFOC lens coated with a quarter wave dielectric layer and a mirror mounted on a PZT. The light which was backreflected to the modified Michelson readout interferometer was encoded with a channeled spectrum related directly to the path length of the sensing interferometer. By matching the path lengths in both interferometers and applying a modulation to the sensing mirror interference fringes were observed.

The passive compensation scheme was realised in the readout interferometer using the combination of a retardation plate and a polarising beamsplitter (PBS). The incoming unpolarised light beam is amplitude divided at the polarisation insensitive beamsplitter yielding two equal amplitude unpolarised beams in the interferometer arms. Unpolarised light can be represented by two orthogonal, equal amplitude linearly polarised waves. Therefore the light which passes through the waveplate will experience a relative retardation of  $\phi_r - \phi_s$  between the orthogonal linearly polarised waves, where  $r$  and  $s$  refer to the fast and slow components passing through the birefringent waveplate. However, the two orthogonal linearly polarised waves which pass through the reference arm will both experience the same delay  $\phi_r$ . Now, although the two linearly polarised waves which represent each unpolarised beam are mutually incoherent and cannot interfere, each linear component in the delay arm will interfere with its respective component in the reference arm when the two beams recombine in the beamsplitter (provided that the path lengths in each arm are matched to within the coherence length of the source). When the resultant unpolarised beam is incident on the PBS it is split into its two orthogonal linearly polarised components which are emitted  $90^\circ$  apart with a delay of  $(\phi_r - \phi_s)$  between them. Thus the two output irradiances will be

$$I_1 \propto [1 + \cos(\phi_r - \phi_s)] \quad (1)$$

and

$$I_2 \propto [1 + \cos(\phi_r - \phi_s)]$$

When an eighth waveplate is used as the retardation plate the effective delay  $\phi_r - \phi_s$  is a quarter wavelength or  $\pi/2$  radians since there is a double pass through the waveplate. Thus

$$I_2 \propto [1 + \cos(\phi_r - \phi_s + \pi/2)]$$

or equivalently,

$$I_2 \propto [1 + \sin(\phi_r - \phi_s)] \quad (2)$$

Therefore as long as the delay between both interferometer arms  $(\phi_r - \phi_s)$  is less than the coherence length of the source interference will occur and the quadrature output signals listed in Eqs. (1) and (2) will be obtained. The quadrature output signals can then be suitably transformed using differentiate and cross-multiply electronics [9] allowing the relevant phase information to always be retrieved even if one of the small signal outputs fade.

## Results and discussion:

The operation of the quadrature output reference interferometer is demonstrated in Fig.2. The two periodic waveforms correspond to the output signals  $I_1$  and  $I_2$  when an  $8\pi$  peak to peak radian phase change is applied to the sensing mirror. The relative phase difference between the signals is clearly  $\pi/2$  radians i.e. they are in quadrature. The upper two traces in Fig.3 show the output signals when there is a  $2\pi$  peak to peak radian phase change at the sensing mirror. Here one output transfer function is biased at its quadrature position and the corresponding output signal is at the modulation frequency of the PZT drive for the mirror. However, as there is a quarter wavelength delay between the output transfer functions, the other output will be biased about a zero sensitivity point and hence, as is clear from the trace, the output is at twice the PZT driving frequency. The lower traces of Fig.3 depict the small signal outputs when each interferometric output is biased as above. Here we can see that the signal fades from the channel which is biased about a zero sensitivity point, while the output from the channel operating at its quadrature position is maximised.

This paper has demonstrated the feasibility of implementing a passively compensated white light interferometric system to detect the optical phase changes induced in a remote sensing interferometer by a vibrating mirror. However, this system could be applied more practically to monitor the resonant frequency changes in a microresonant transducer, such as a silicon microresonant pressure sensor [10]. Since the white light system will only give a periodic output when the path lengths are matched in both the sensing and the reference interferometers several such microresonant sensors could be multiplexed onto a single fibre bus with each forming a remote Fabry-Perot sensing interferometer but with each having a different path length. Then by tuning the local reference interferometer path length to that of each of the remote sensing interferometers the transducer signal from each could be monitored in turn, thereby combining some of the benefits of white light interferometry [2] with those of silicon microresonant sensors [11].

## Conclusions:

This paper has reported a simple passive compensation technique using a white light interferometric detection scheme, which is compatible with multimode fibre and cheap commercial optical sources.

## Acknowledgements:

The authors are grateful to the UK Optical Sensors Collaborative Association (OSCA) for financial support.

## References:

1. C.Delisle and P.Cielo, Can.J.Phys., 57, p.1047, (1975).
2. H.C.Lefevre, Proceedings of OFS 7 (Sydney), p.345-351, (1990).
3. Th.Bosselman and R.Ulrich, Proceedings of OFS 2 (Stuttgart), p.361-364, (1984).
4. M.T.Velluet, P.Graindorge and H.J.Arditty, SPIE Proceedings, Vol.838, p.78-83, (1987).

5. C.Marillier and M.Lequime, SPIE Proceedings, Vol.798, p.121-130, (1987).
6. R.Bohm and R.Ulrich, Proceedings of OFS 7 (Sydney), p.353-356, (1990).
7. K.P.Koo, A.B.Tveten and A.Dandridge, Appl.Phys.Lett., Vol.41, No.7, p.616-618, (1982).
8. A.D.Kersey, D.A.Jackson and M.Corke, Electron.Lett., Vol.18, No.9, p.392-393, (1982).
9. A.Dandridge, A.B.Tveten and T.G.Giallorenzi, IEEE J.Quant.Elect., QE18, p.1647, (1982).
10. K.E.B.Thornton, D.Uttamchandani and B.Culshaw, Electron.Lett., Vol.24, No.10, p.573-574, (1988).
11. B.Culshaw, Proceedings of OFS 7 (Sydney), (1990).

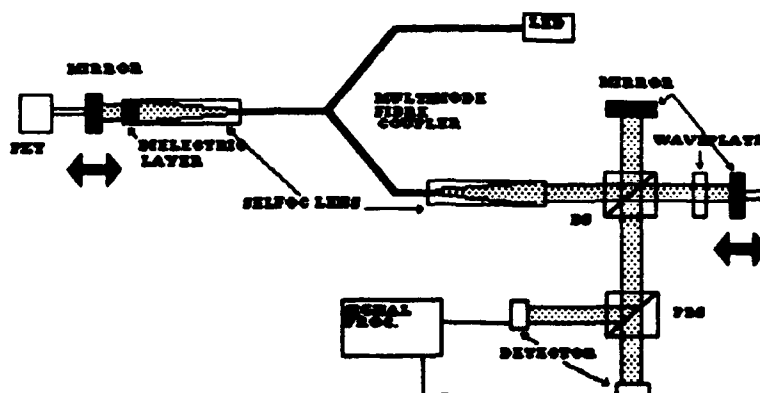


Figure 1: Passively compensated white light interferometric detection system.

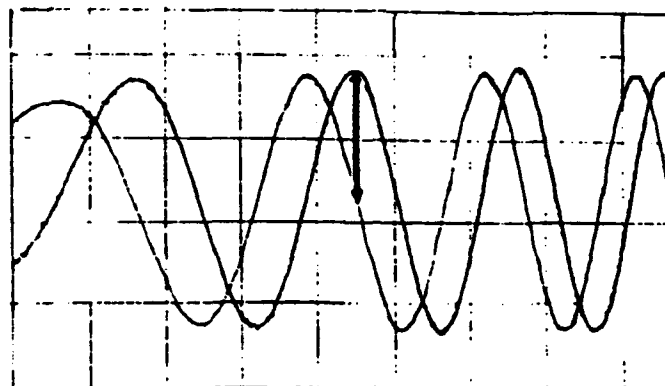


Figure 2: Quadrature outputs from the reference interferometer.

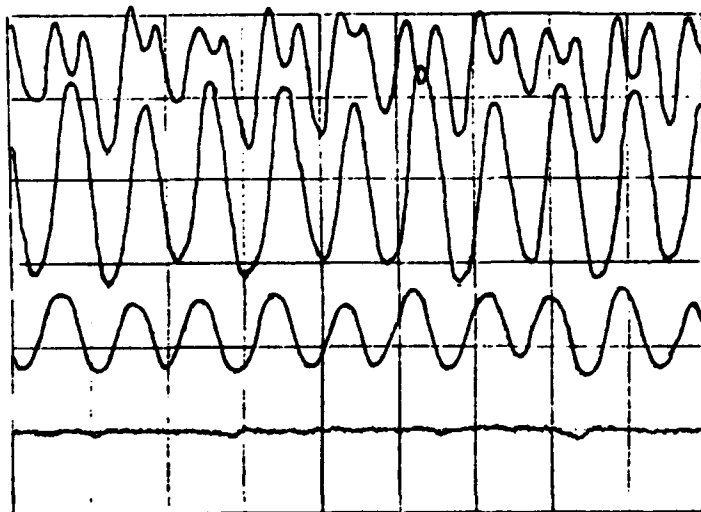


Figure 3:

Top two traces depict the interferometer outputs with a  $2\pi$  pk-pk radian signal applied to the sensing mirror. Lower traces show small signal outputs when one output transfer function is biased at its quadrature position.

## Spurious Sidebands Of Signal Carriers In Fiber-optic Interferometric Sensors

K.P. Koo\*, D. M. Dagenais\*, F. Bucholtz and A. Dandridge  
Naval Research Laboratory, Code 6570  
Washington, DC 20375

Baseband low-frequency signals up-converted to sidebands of signal carriers can mask out the detection of intended signals[1]. For example, laser source intensity noise up-converted to the sideband of the magnetic carrier can limit the detection of small low-frequency magnetic signals[2]. In this paper, we present experimental results which demonstrate the up-conversion of three types of baseband signals: 1) the interferometer optical input intensity fluctuation from laser intensity noise, 2) the frequency noise of the optical source or equivalent low-frequency interferometer phase noise, and 3) the input polarization fluctuation. Also, the dependence of the strength of these up-converted signals on the interferometer quadrature condition and on the frequency contents of these baseband signals are presented.

Figure 1 shows the set-up of our experiment. A Mach-Zehnder interferometer forms the core of a fiber-optic magnetic-field sensor. The optical input to the interferometer is designed to provide three types of modulation simulating the three types of baseband signals mentioned above. The optical source is a diode-pumped solid state laser (Lightwave Electronics, model 122) which provides a simultaneous laser modulation induced intensity modulated (LMIAM) and a laser modulation induced frequency modulated (LMIFM) signal. The laser output is intensity modulated by a light power controller (from Cambridge Research Corporation) providing a pure AM signal. The in-line fiber polarization modulator[3] provides a polarization modulation induced AM (PMIAM) and a polarization induced FM (PMIFM) to the interferometer optical input. An equivalent pure FM signal or an interferometer phase signal is provided by the piezoelectric (PZT) modulator which is also used for active stabilization. The two optical outputs are monitored by InGaAs detectors and the subsequent electrical signals are analyzed with a spectrum analyzer (HP3567A).

The interferometer output  $V$  is represented [4] by

$$V = (1/2) I_0 \{ 1 \pm \rho \cos(\phi - \gamma) \} \quad (1)$$

where + and - correspond to the two complimentary outputs of the interferometer,  $I_0 = [1 - m_a^2 \cos^2(\omega_f t)]$  is the modulated input power with modulation index  $m_a$ ,  $\rho = [1 - \sin^2(\theta) \sin^2(\Omega/2)]^{1/2}$  [ref.4] is the fringe visibility

modulated by the input polarization angle (reference to the eigenmode vector of the system according to ref..4)  $\theta = [B_0 - B_1 \cos(\omega_p t)]$  and  $\Omega$  is the differential birefringence of the interferometer,  $\phi = [\phi_0 + \phi_1 \cos(\omega_c t) + \phi_2 \cos(\omega_c \pm \omega_s)t + \phi_3 \cos(\omega_p t)]$  is the total interferometer phase consisting a static phase  $\phi_0$ , a phase carrier  $\phi_1 \cos(\omega_c t)$ , a low-frequency signal sideband  $\phi_2 \cos(\omega_c \pm \omega_s)t$  due to frequency mixing in a non-linear magnetostrictive transducer and a low-frequency phase signal  $\phi_3 \cos(\omega_p t)$ , and  $\gamma = \tan^{-1}\{\cos(\theta)\tan(\Omega/2)\}$  is the polarization induced phase modulation. It is clear from Eqn.1 that there will be frequency mixing among  $I_0$ ,  $\rho$  and  $\phi$ , resulting in frequency up-conversion of the modulation signals by the phase carrier. For  $B_0 = n\pi + \Delta$ ,  $\Delta \ll \pi$ , a measured  $\Omega \approx 160^\circ$ , one can assume  $\rho \approx 1 - m_p \cos(\omega_p t)$ .

The ambiguity of signal sideband vs. spurious sideband signals in a fiber-optic sensor is illustrated in a spectrum shown in Figure 2. The interferometer is stabilized at quadrature. A magnetic carrier of 0.03 rad. at 20 kHz up-converts a 11 mOe low-frequency magnetic signal at  $\omega_s = 1$  Hz to its sideband at the carrier offset frequency of  $\pm 1$  Hz. Similarly, an intensity modulated (AM) signal with  $m_a = 0.01$  at  $\omega_i = 4.3$  Hz, a polarization modulated (PM) signal with  $m_p \approx 0.01$  at  $\omega_p = 5.4$  Hz and a laser modulated (LM) signal at  $\omega_l = 3.2$  Hz are also up-converted. It should be noted that the sideband signal offset frequency is dependent on the interferometer quadrature condition. At quadrature, the 2nd harmonics of the FM (including LMIFM and PMIFM) signals or the low-frequency interferometer phase signal is strongly up-converted, while the fundamental frequency component of the AM (including LMIAM and PMIAM) signals are strongly up-converted. When the interferometer is 90 degree away from quadrature, the 2nd harmonics of AM and PM signals are strongly up-converted while the fundamental component of the FM is strongly up-converted. Our active stabilization circuit suppresses low-frequency FM signal with a cut-off frequency of 1 kHz and a roll-off of 20 dB/decade, resulting in low-frequency sideband signals dominated by up-converted AM, LMIA and PMIA signals. Therefore Figure 2 shows only the laser modulation induced intensity fluctuation (LMIAM) with an equivalent  $m_a \approx 2.8 \times 10^{-3}$ . The interferometer noise floor is equivalent to AM with  $m_a \approx 0.0001$  or  $m_p \approx 0.0001$ .

Suppression of the up-conversion of low-frequency FM signal is achieved by actively stabilizing the interferometer at quadrature. Figure 3 shows the PM, AM and LM sideband signals as a function of their modulation frequencies. To first order, AM and PMIAM sidebands at their respective fundamental modulation frequencies are frequency independent while all FM including PMIFM and LMIFM sidebands are suppressed for frequencies below 1 kHz with a roll-off of approximately 20 dB/decade. Note that the LM induced sideband for modulation frequencies above 1 kHz is FM dominated and at low-frequencies is AM dominated. At intermediate frequencies, the sideband signal is a superposition of AM and FM resulting in a frequency dependence as shown. Suppression of AM and PMIAM sideband signals by >30 dB has been achieved by a subtraction technique described in ref.[5].

The dependence of the up-converted signals normalized to the carrier signal on the quadrature state of the interferometer is shown in Fig. 4. All the modulation frequencies are above the cut-off frequency of the

interferometer stabilization circuit to reveal the intrinsic up-conversion process without suppression. The normalized sidebands due to pure AM (measured at  $\omega_c + \omega_i$ ) are relatively independent of the quadrature state because the sideband signal and the carrier signal change in unison. The normalized sidebands due to LM (measured at  $\omega_c + \omega_i$ ) and PM (measured at  $\omega_c + \omega_p$  with  $B_0 = n\pi + \Delta$ ) are dependent on the quadrature state. At quadrature ( $\phi_0 = \pi/2$ ), the sideband signals are dominated by LMIAM and PMIAM and as the interferometer is biased toward 90 degree away from the quadrature point, sidebands due to LMIFM and PMIFM become stronger than the AM effect.

In conclusion, up-conversion of low-frequency spurious signals such as source intensity and frequency modulation as well as input polarization modulation will obstruct the detection of intended signal such as the low-frequency magnetic signal. The up-converted signals depend on the carrier strength and the interferometer quadrature condition. Intensity and polarization modulation index of  $<0.0001$  is required to obtain sideband noise equivalent to an interferometer phase of a few micro-radian in the presence of a 0.3 radian phase carrier. AM and PM sideband can be suppressed by a subtraction technique[5] and FM sideband is suppressed by active interferometer stabilization.

We acknowledge valuable discussions with Carl Villarruel, and A.D. Kersey. This work is supported partly by the Office of Naval Technology.

\* Permanent address: SFA, Inc., 1401 McCormick Dr. Landover, MD 20785.

#### Reference

- [1] K.P. Koo, F. Bucholtz and A.Dandridge: Electron. Lett. 23, p.1062 (Sept. 24, 1987).
- [2] F. Bucholtz, K.P. Koo, M. Davis, M.J. Marone and A. Dandridge: Technical Digest of Optical Sensor Fiber Sensors Conf. 1988, Part 1, p.106.
- [3] A.D. Kersey, M.J. Marrone, A. Dandridge and A.B. Tveten: J. of Lightwave Techn., 6 p.1599 (Oct. 1988).
- [4] A.D. Kersey, M.J. Marrone and A. Dandridge: J. of Lightwave Techn., 8, p.838 (June 1990).
- [5] K.P. Koo, F. Bucholtz D.M. Dagenais and A. Dandridge: IEEE Photonics Techn. Lett., 1, p.464(Dec.1989)

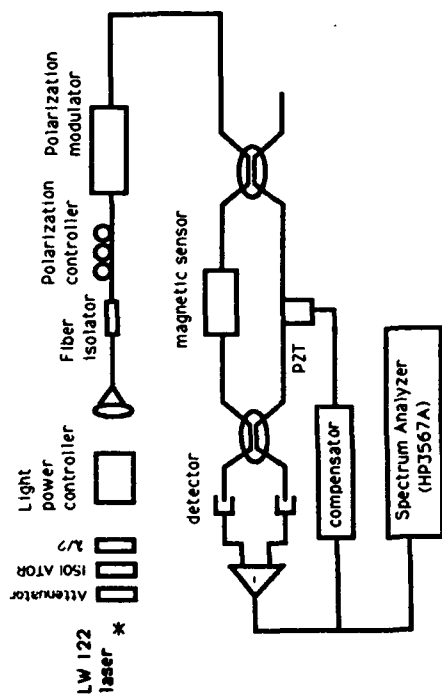


Fig.1. Experimental set-up

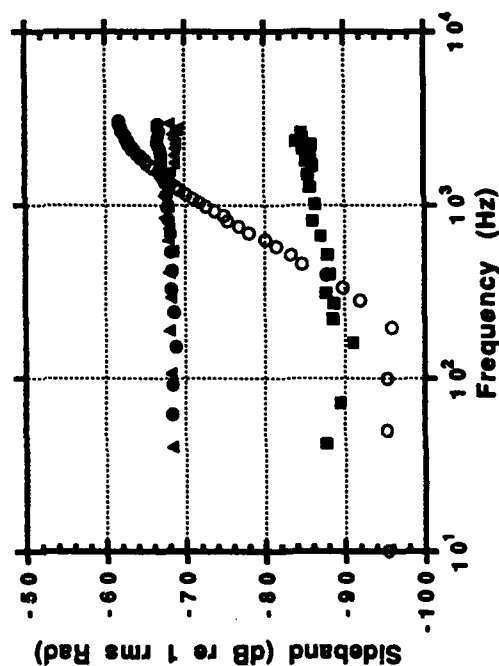


Fig.3. Sideband signal vs. baseband modulation frequency. AM(solid triangle), PM(solid circle), FM(open circle), LM(solid square).

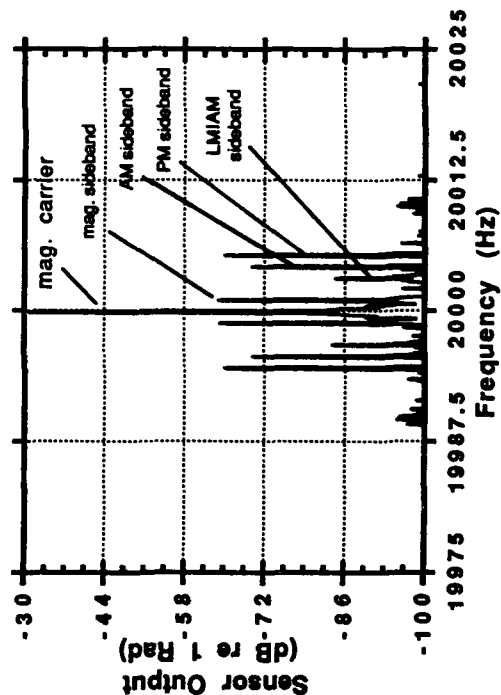


Fig.2. Frequency spectrum of sensor output

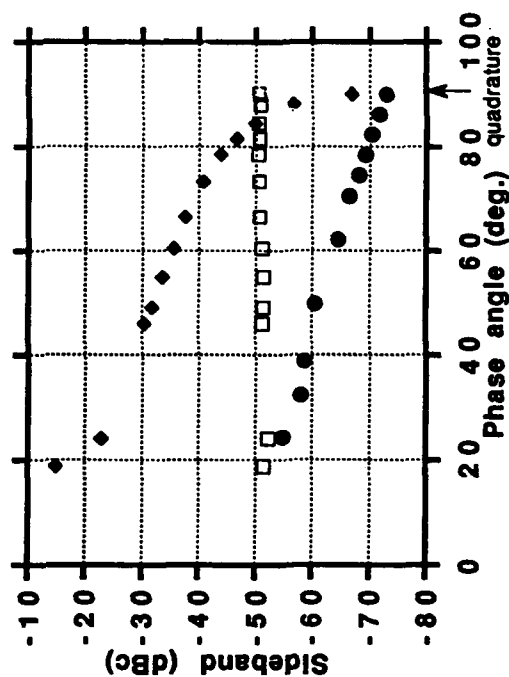


Fig.4. Normalized Sideband signal strength vs. interferometer phase. AM(open square), PM(solid circle), LM(diamond).



## **P39 Focus-sensing Characteristics Of A Monolithic 3-channel Laser Diode Array With Vertically Staggered Facets**

Yoshitada Katagiri, Yoshio Suzuki, and Hidenao Tanaka  
NTT Interdisciplinary Research Laboratories  
9-11, Midori-Cho 3-Chome Musashino-shi, Tokyo 180 Japan  
Telephone +81 422 59 2645 Facsimile +81 422 59 2593

### **1. Introduction**

Monolithically integrated optical devices on a laser wafer can be used to construct the optical microsensors that will be used in high-performance mechanical systems like future micromachines. The elements in these devices are precisely arranged by the use of lithography. In this paper, we propose a focus-sensing laser that has a monolithic 3-channel laser diode (LD) array with vertically displaced facets. This device operates with lenses and an external mirror, and we expect it to be used not only in vertical sensing systems but also in optical disk systems.

### **2. Device structure and principle**

The laser wafer has a separated confinement heterostructure with GaAs/AlGaAs triple quantum wells to reduce drive current. Liquid-phase epitaxy is used to fabricate three laser stripes with a buried heterostructure. The stripes are 130  $\mu\text{m}$  apart. Laser facets are fabricated by fast atomic-beam etching<sup>1</sup> and are coated with an anti-reflection (AR) coating by ion-beam sputtering.<sup>2</sup> The facets of each laser are vertically staggered by 12  $\mu\text{m}$  (Fig. 1). To individually monitor the output of each laser channel, the unstaggered end of each channel faces a photodiode (PD) across a 10- $\mu\text{m}$ -wide groove.

Focus sensing is based on the lasing characteristics of an external cavity laser consisting of the LD, lenses, and an external mirror. The optical system is schematically shown in Fig. 2. A collimator and objective lens pair is used to obtain a small spot.

The efficiency of light feedback from the external mirror decreases when the mirror is increasingly displaced from the focal plane. Light output is therefore a function of mirror displacement and is maximum at the focal plane. Due to the vertically staggered facets of the LD array, for each focal plane, the maximum points for each channel is at a different position. If the injection currents are adjusted until the maximum points for the outside channels have the same value, the difference between the light outputs of these channels indicates the vertical position of the mirror. This difference is an S-shaped function of mirror displacement, and it becomes zero when the mirror is just at the focal plane of the central channel.

### **3. Characteristics**

#### **Experimental set-up**

We measured the intensity and wavelength of this LD array's output in a static experimental system when the external mirror is vertically displaced by a piezoelectric transducer. The mirror was a glass substrate covered by an aluminium reflection layer with a reflectivity of 0.7. A Peltier device was used to

keep the LD drive temperature at 25°C.

#### Suppression of interferometric undulation

The light output of the external cavity laser was undulated at an interval of a half-wavelength of the emission light when the displacement of the mirror was varied. This was due to the interference between the feedback light and light reflected internally from the LD facet. This undulation generated many maximum points, thus offering many positions where the light output difference became zero, which made it impossible to obtain the focal plane by estimating the difference. Such undulation was suppressed by reducing the laser facet reflectivity, which weakened the interference. This suppression effect is demonstrated in Fig. 3. The undulation amplitude, defined as the light output difference between high and low points of the undulation, is considerable large for an non-coated LD (with a facet reflectivity of 0.32), while that is greatly reduced for an AR-coated LD (with a reflectivity of less than 0.001).

#### Focus sensing

For each channel of the LD array, Fig. 4 shows light output as a function of mirror displacement. The displacement of the neighboring maximum points was greater than 20  $\mu\text{m}$ , which is almost twice the facet displacement. The former displacement depends on the spacing between the laser facet and the lenses and could be optimized to obtain a spot as small as the diffraction limit. Other maximum points, completely different from those due to the interference, appeared around several micrometers. These were due to the aberration of the lenses. These additional points can be avoided by improving the lenses.

The maximum points for the outside channels were not always the same, so a focus-error signal was defined as the light output difference between the outside channels normalized by each maximum value. The focus-error signal is shown in Fig. 5 as a function of mirror displacement. It became almost all zero when the mirror displacement was zero.

#### 4. Application

The LD array can be used in an optical head by replacing the external mirror with an optical disk. Its central channel is used for detecting data signals, while the outside channels are used for detecting the focus-error signal for the central channel. The mechanism for detecting data signals is based on the switching characteristics of the external cavity laser for the central channel.<sup>3</sup> The optical disk consists of high- and low-reflectivity areas, and it gives two lasing thresholds to the external cavity laser. Under a bias current between these two thresholds, the laser produces stimulated and spontaneous emissions responding to the disk reflectivity (Fig. 6). Thus, a series of light outputs with dual values are obtained as data signals. This head has a very simple structure and operates with a simple optical system.

#### 5. Conclusion

We have demonstrated the sensing characteristics of a focus sensor that uses the 3-channel LD array, and we have shown its potential application in an optical head. Such LD arrays will be applied to a variety of systems that need micro sensors.

## References

1. F. Shimokawa, et al, J. Appl. Phys. 66 (1990) p.2613.
2. Y. Katagiri, et al, Appl. Opt. 29 (1990) p. 5074.
3. H. Ukita, et al, Appl. Opt. 28 (1989) p. 4360.

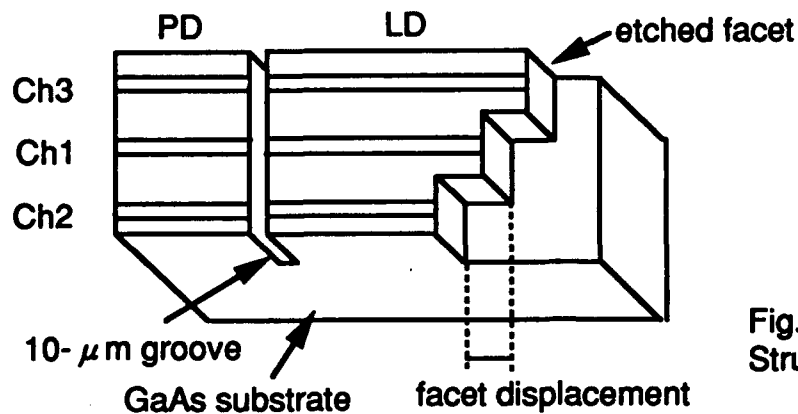


Fig. 1  
Structure of the LD array

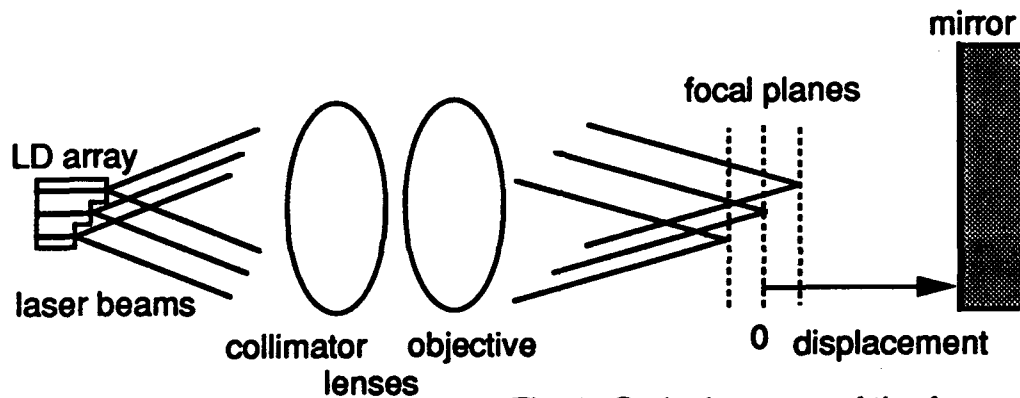


Fig. 2 Optical system of the focus sensor

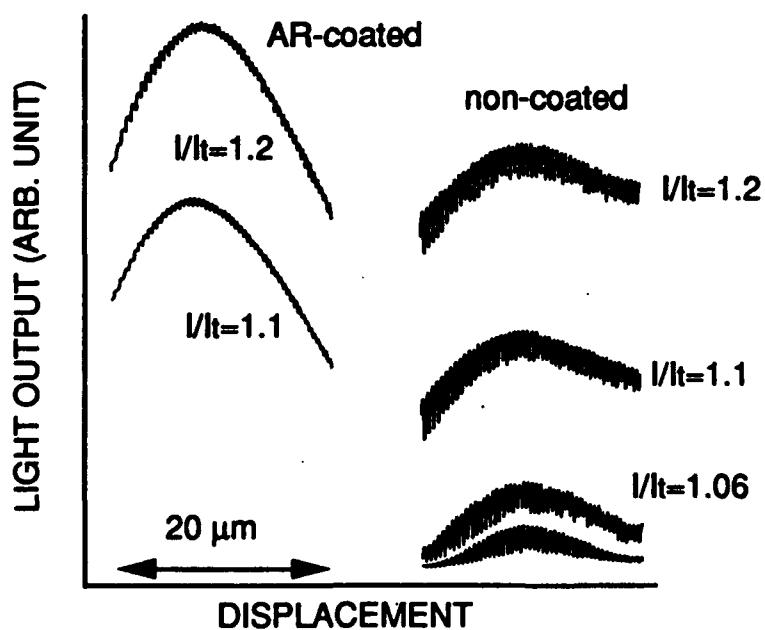


Fig. 3 Suppression of  
interferometric undulation  
( $I/I_t$  : normalized current)

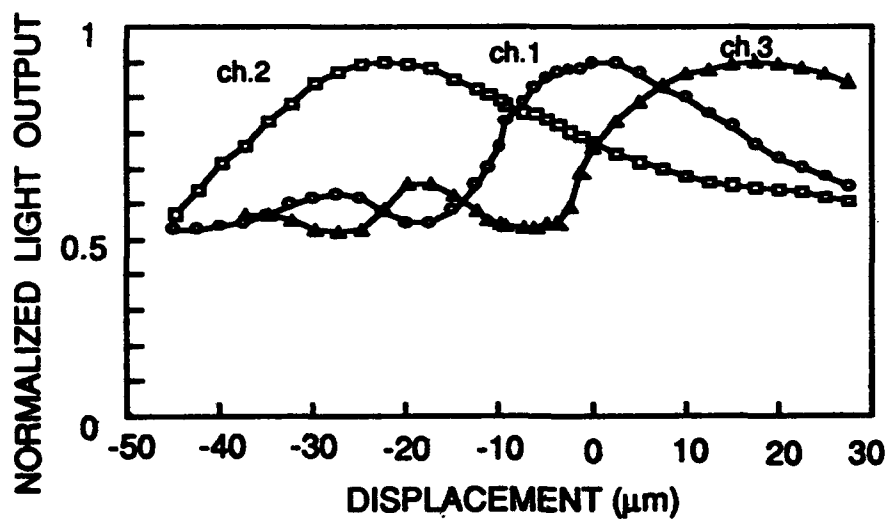


Fig. 4 Defocus characteristics of the LD array

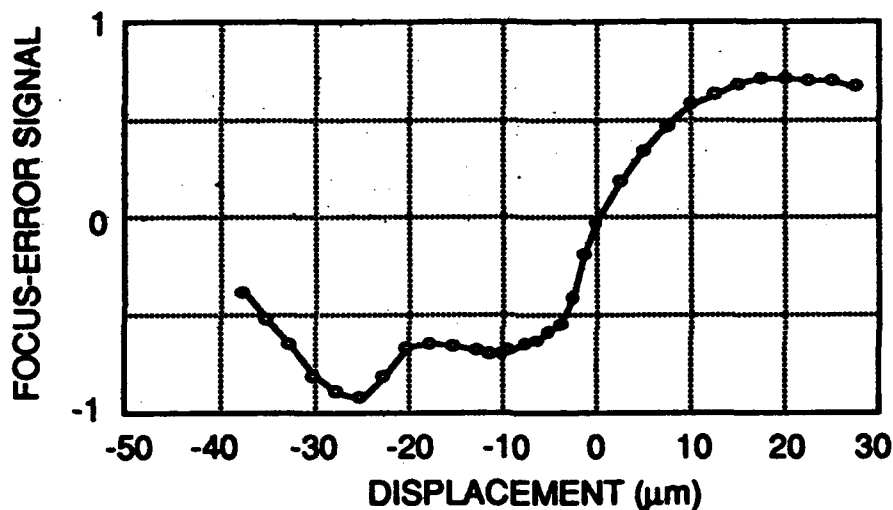


Fig. 5 Focus-error signal

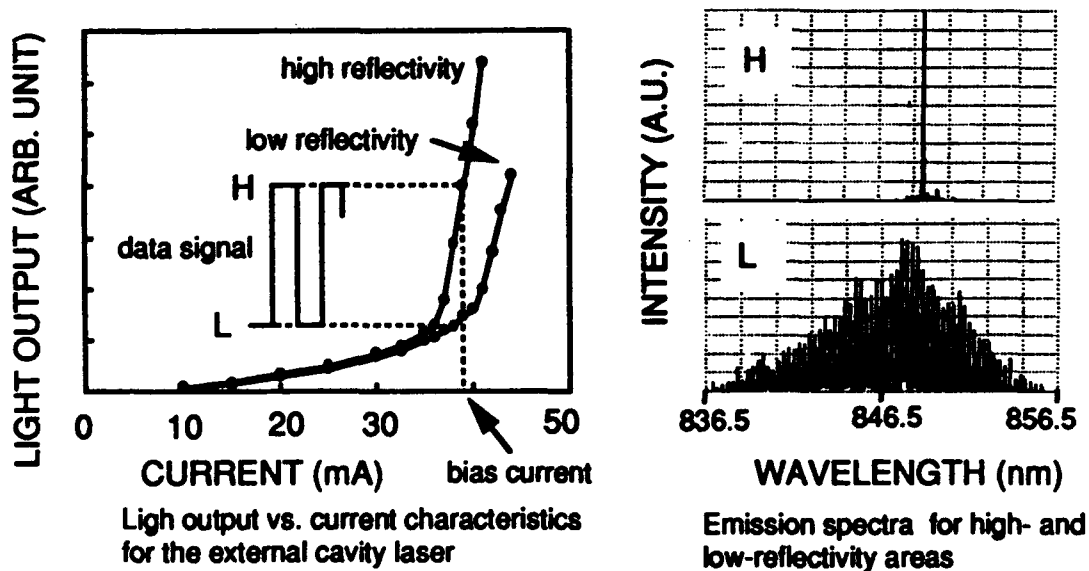


Fig. 6 The mechanism for detecting data signals

**Summary**

Sensing using silicon integrated optics exploits the advantages of both optics and integrated circuit technologies: the high bandwidth and electromagnetic noise immunity of optical sensing systems as well as the small size, durability, low cost and consistent reliability of established silicon technology. Sensor structures based on silicon integrated optics have, hitherto, been realized using low doped regions as waveguide cores, with either a combination of diffused and epitaxial regions of highly doped ( $N^+$ ) material as the cladding [1]. Rib structures for light confinement have also been realized using anisotropic etching techniques [1]. These types of structures have two drawbacks. Coupling of light to and from such devices is difficult because of the mismatch of refractive indices of the optical fiber and silicon. In addition, silicon is lossy at the standard wavelengths used with the fiber. The ARROW (Anti-Resonant Reflecting Optical Waveguide) [2] structure overcomes this problem. It supports the propagation of a leaky mode in a low index core despite a higher index cladding. By proper selection of layer thicknesses, the loss can be reduced to an acceptable level. The ARROW structure offers many advantages over previous silicon based integrated optical devices. It needs very little nonstandard IC process steps, provides a good match for fiber coupling, and allows integration of electronic devices, such as photodetectors, on the same chip. Furthermore, with the addition of simple post-processing steps, the ARROW structure offers the potential for sensing a wide variety of measurands (see [3]). In this paper, we present a micromechanical sensor based on an optical waveguide, for sensing mechanical signals. The waveguide core is the surface resonating layer of an ARROW structure. A pressure uniformly applied to the suspended sensing arm of an interferometer causes deflection. The resulting phase change at the end of the sensing arm causes a reduction of the light intensity at the sensor output due to destructive interference with light from the reference arm. There are two mechanisms for a change in phase of the light. The first is a change in effective length of the sensing arm due to pressure-induced beam deflection. The second is a change in effective index of refraction of the waveguide core, caused by pressure-induced beam stress. The phase change due to deflection is characterized in terms of the relative change in beam length ( $\Delta L/L$ ), the applied pressure, and the propagation constant of light in the ARROW. The stress induced phase change can be determined from a permittivity perturbation tensor, which is the product of a stress tensor and the stress-optical tensor for the core material. A change in propagation constant results from the permittivity change. These mechanisms are systematically discussed in what follows.

**Waveguide and Interferometer Structure: Mechanical and Optical Properties**

The overall structure of the sensor is an interferometer, including a reference arm and a sensing arm. The sensing arm is a beam suspended over an etched pit in the silicon substrate (Fig. 1). The ARROW structure has been fabricated using our in-house University of Waterloo bipolar IC process, using a  $\langle 100 \rangle$  Si substrate. The device cross section is shown in Fig. 2; SEM images are shown in figure 5. The sensing arm, viz., the suspended micromechanical ridge, was realized as a post processing step, using standard anisotropic etching techniques. These thicknesses are chosen to minimize loss in the waveguide, based on the guidance conditions of total internal reflection at the air/core interface and anti-resonant reflection at the core/cladding interface [1]. Under the second cladding is the substrate, except at the active sensing area; here the silicon is etched away leaving an air cavity. Because the waveguide is not single mode, there will be other modes which experience different propagation and phase changes in the sensing arm. It is possible to make the waveguide single mode by thinning the core and cladding layers appropriately.

**Beam Deflection as a function of Applied Pressure**

The deflection of a beam  $\Delta y$ , under uniform load conditions is (see derivation in Appendix A)

$$\Delta_y(z) = \frac{Pb}{24EI} \left( z^2 - \left(\frac{L}{2}\right)^2 \right) \left( z^2 + \left(\frac{L}{2}\right)^2 \right). \quad (1)$$

Here,  $P$  is the applied pressure,  $b$  is the width of the beam,  $L$  is the end to end length of the beam,  $z$  is the position along the beam (from the center),  $E$  is Young's modulus,  $I$  is the moment of inertia of the beam ( $\frac{1}{12}bh^3$  for rectangular cross-section), and  $h$  is the height of the beam.

**Change in Length of Beam**

The change in beam length as it is deflected can be found from the equation governing the shape of the loaded beam:

$$\Delta L = \int_{-L/2}^{L/2} \sqrt{1 + \left(\frac{d}{dz} \Delta y(z)\right)^2} - 1 \, dz. \quad (2)$$

For our application in question, equation (2) does not provide a convenient closed form solution for  $\Delta L$ . Instead, values of  $\Delta L$  were calculated for a range of pressures of interest, over a range of beam lengths of interest. The calculations were done using Maple (a symbolic math tool), and verified by numerical integration. The pressure range results were fitted for each length using fourth order polynomials. For a given length, the resulting curve fit coefficients are:

$$\Delta L(P) = A_2(L)P^2 + A_4(L)P^4. \quad (3)$$

Equation (3) is valid over the pressure range  $0 \leq P \leq 100$  atmospheres. The sets of coefficients for each pressure were then fit for the range of lengths of the beam, and the resulting functions for  $A_2(L)$  and  $A_4(L)$  are:

$$A_2(L) = 1.78 \times 10^{16} L^7 \left(\frac{m}{\text{atm}^2}\right) \text{ and } A_4(L) = -2.08 \times 10^{32} L^{12.986} \left(\frac{m}{\text{atm}^4}\right).$$

The final equation governing change in beam length over pressures up to 100 atm (101325 Pa) for beam lengths in the range 50  $\mu\text{m}$  to 200  $\mu\text{m}$  is:

$$\Delta L(L,P) = 1.78 \times 10^{16} L^7 P^2 (1 - 1.16 \times 10^{16} L^{5.986} P^2). \quad (4)$$

In (4), the pressure is in atmospheres,  $L$  and  $\Delta L$  are in meters.

#### *Phase Change due to Effective Length and Refractive Index*

The maximum phase change required in the sensing arm, with respect to the reference arm, is  $\pi$ . This determines the operating (pressure) range of the sensor in terms of beam length and layer thicknesses of the ARROW structure. A second source of phase change in the sensor arm of the interferometer is the stress induced in the beam by the applied pressure. Deflection of the beam causes stress, which causes a perturbation in the permittivity of the medium that the wave propagates through. This causes an effective change in the index of refraction; modifying the propagation constant of the wave in that medium. A stress tensor has been constructed for the beam. The resulting stress components (for a unit pressure) are,

$$\begin{bmatrix} \sigma_{zz} & \sigma_{zy} & \sigma_{zx} \\ \sigma_{yz} & \sigma_{yy} & \sigma_{yz} \\ \sigma_{xz} & \sigma_{xy} & \sigma_{xx} \end{bmatrix} = \frac{-Pb}{24I} \begin{bmatrix} y(12z^2 - L^2) & 3z(h^2 - 4y^2) & 0 \\ 3z(h^2 - 4y^2) & 0 & 0 \\ 0 & 0 & 0 \end{bmatrix}, \quad (5)$$

where  $y$  and  $z$  are measured from the center of the beam.

For the above stress tensor, the change in electric field of a propagating wave reduces to:

$$\begin{bmatrix} \delta\epsilon_{zz} \\ \delta\epsilon_{yy} \\ \delta\epsilon_{xx} \\ \delta\epsilon_{zy} \end{bmatrix} = \begin{bmatrix} C_1 & 0 \\ C_2 & 0 \\ C_2 & 0 \\ 0 & C_4 \end{bmatrix} \times \begin{bmatrix} \sigma_{zz} \\ \sigma_{zy} \end{bmatrix}, \quad (6)$$

where  $C_1 = -6.83 \times 10^{-13} [\text{Pa}^{-1}]$ ,  $C_2 = -4.19 \times 10^{-12} [\text{Pa}^{-1}]$ , and  $C_4 = 3.507 \times 10^{-12} [\text{Pa}^{-1}]$  are the stress-optical coefficients [4]. The change in refractive index is found from the relationship  $\delta n^2 = \delta\epsilon$ . The change in phase of the propagating light due to the stress-optical effect can subsequently be calculated as  $\Delta\theta = \int \Delta\beta \, dz$ . This will be evaluated as  $\int \Delta n_x k_z \, dz$  for TE modes and  $\int \Delta n_y k_z \, dz$  for TM modes.

### Simulation Results

Since the ARROW structure is based on precise layer thicknesses, the question of sensitivity to layer thickness arises. This sensitivity was tested for each layer, through simulation. It was found that for an optimized ARROW device, the sensitivity is low for variations up to 5%, which falls within fabrication tolerance. An important issue is the effect of the suspended beam on the interferometer output. If there are differences between the reference arm and the sensing arm caused by the etched pit, then the interferometer may not operate properly. For the device designed, it was found through simulation, that the propagation of light through the structure is relatively unaffected (for a TE<sub>0</sub> mode) by the change in layer material (from silicon to air) beneath the second cladding layer; both in terms of propagation constant and field pattern. The propagation constant in the core is 14.28596 rad/μm over the substrate and 14.28597 rad/μm over the etched pit (see Table 1). An effective index of refraction is calculated, which represents the equivalent core index seen by the propagating wave ( $n_{\text{eff}} = \beta/k_0$ ). An attenuation of 0.36 dB/cm occurs over the substrate. Over the etched pit, the light experiences total internal reflection (at the cladding/air interface), and virtually no attenuation occurs. For a 150 μm long sensing arm, the zero measurand relative phase error is less than 1.5 mrad. The power profiles for both waveguide cross-sections are shown (Fig. 4). For the same beam, an applied pressure of approximately 82 atm, produces a beam extension of 0.21 μm, yielding the desired maximum phase change. Figure 3 shows length and phase change for different beam lengths over the pressure range  $0 \leq P \leq 100$  atm. Characterization of this pressure-sensitive waveguide is currently in progress.

### Conclusion and Outlook

The device presented here requires a very long sensing arm to achieve small pressure resolutions. In view of the mechanical integrity of the structure, long suspended beam lengths may not be realizable. One disadvantage of the structure presented here is that it is only sensitive to a.c. pressures; a static pressure will cause no deflection. An alternative fabrication procedure is to etch the substrate from the backside of the wafer, thus providing SiO<sub>2</sub> (or heavily doped Si) diaphragms sensitive to static pressure. Despite the current technological limitations, devices of this form offer promising features: EMI immunity and high bandwidth.

### References

- [1] B. Culshaw, "Silicon in optical fiber sensors", in *Optical Fiber Sensors: Systems and Applications. Volume 2*, B. Culshaw, J. Dakin, eds., Norwood, MA: Artech House, 1988, pp. 504-507.
- [2] T. Baba, Y. Kokubun, T. Sakaki, and K. Iga, "Loss reduction of an ARROW waveguide in shorter wavelength and its stack configuration", *IEEE Journal of Lightwave Technology*, vol. 6, pp. 1440-1445, 1988.
- [3] A. Nathan, W.P. Huang, and A. Vadekar, "Micromechanical sensors based on integrated silicon guided wave optical structures", *Proceedings of the 4th International Forum on ASIC and Transducer Technology*, 1991, pp. 103-107.
- [4] W. Primak and D. Post, "Photoelastic constants of vitreous silica and its elastic coefficient of refractive index", *Journal of Applied Physics*, vol. 30, pp. 779-788, 1959.

Table 1: Propagation Constants for ARROW Waveguide (at 0.6238 μm)

Mode	Effective Substrate	Propagation Constant ( $\beta - j\alpha \mu\text{m}^{-1}$ )	$n_{\text{eff}}$
TE <sub>0</sub>	Silicon	14.28596 - $j4.24 \times 10^{-6}$	1.4387857
TE <sub>0</sub>	Air	14.28597 - $j1.82 \times 10^{-13}$	1.4387870
TM <sub>0</sub>	Silicon	14.28254 - $j9.24 \times 10^{-4}$	1.4384410
TM <sub>0</sub>	Air	14.28274 - $j1.80 \times 10^{-12}$	1.4384614

Figure 1: Sensing arm beam structure

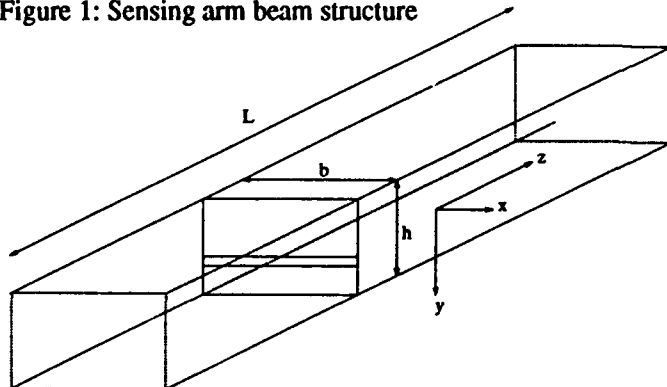


Figure 2: ARROW cross-section

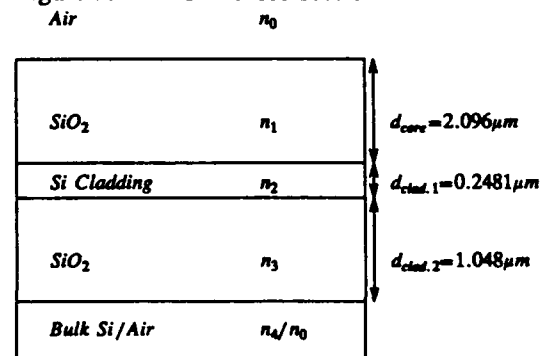


Figure 3: Change in length and phase versus pressure for different beam lengths

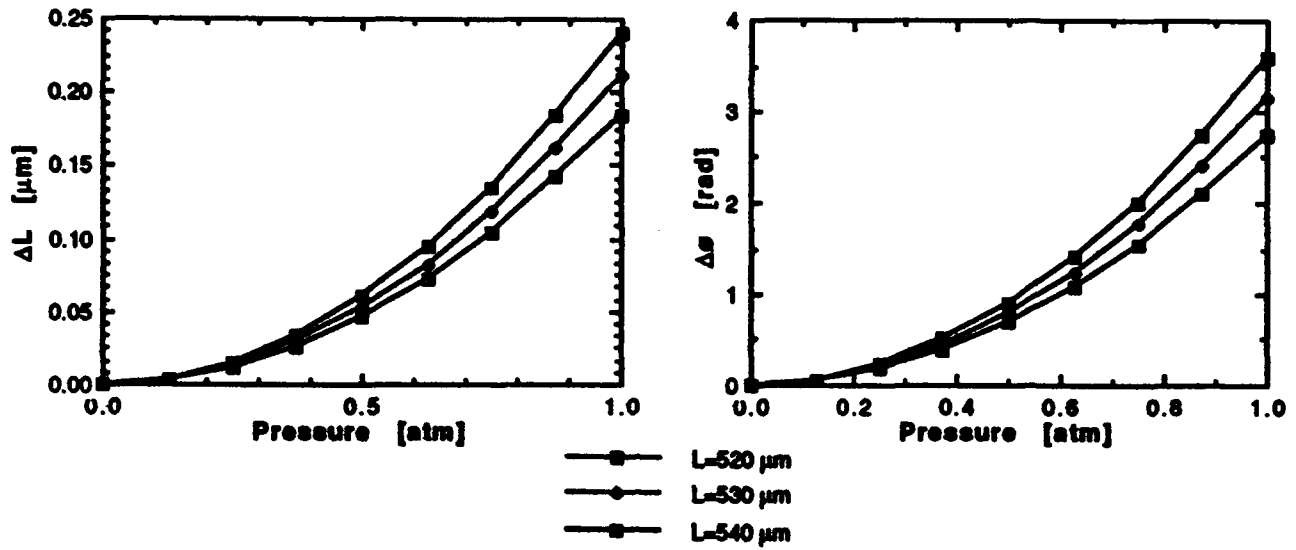


Figure 4: Simulated power in ARROW structure for TE and TM modes

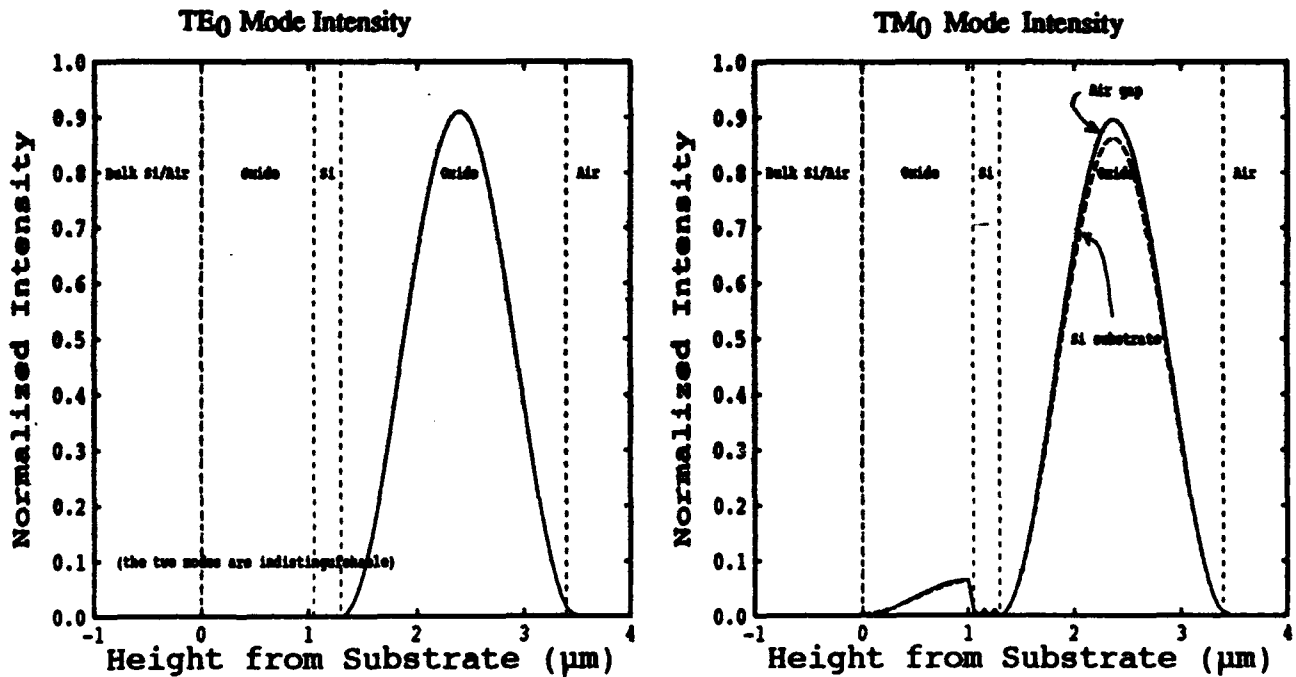
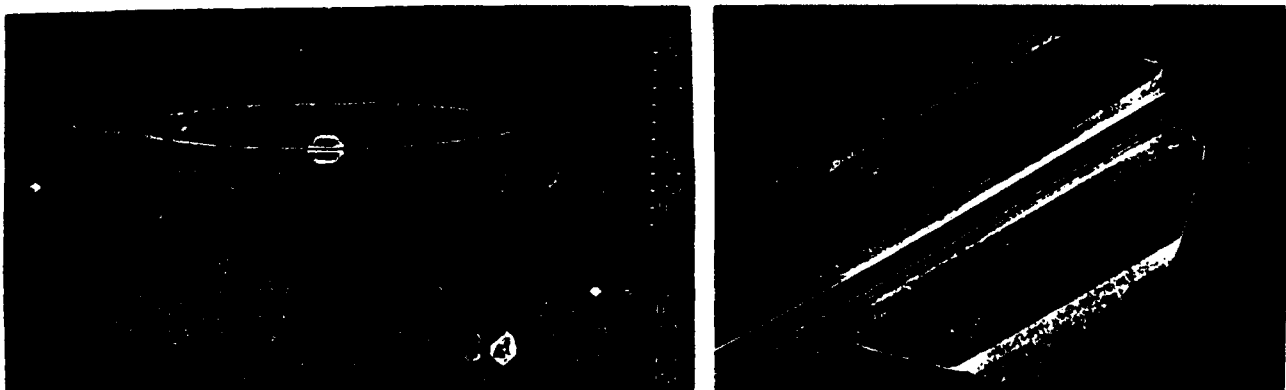


Figure 5: SEM photographs of fabricated ARROW device; complete interferometer and closeup of sensing arm





## **P41      A Fibre Optic, Low Coherence Laser Doppler Anemometer System For Determining Flow Velocity**

**K. WEIR, W.J.O. BOYLE, A.W. PALMER, K.T.V. GRATTAN & B.T. MEGGITT**

Measurement and Instrumentation Centre,  
Department of Electrical, Electronic and Information Engineering, City University,  
Northampton Square, London EC1V 0HB UK.

### **ABSTRACT**

A system comprising a fibre optic probe, low coherence light source and a modified recovery Michelson Interferometer is described and applied to the measurement of the flow velocity of scattering particles.

### **INTRODUCTION**

Fluid flow rate is often measured using optical Doppler anemometry techniques. Light scattered from the moving particles (seeds) in the flow is mixed interferometrically with light from a reference beam on a photo-detector (1). However, these measurements only determine the speed of the flow and not the actual direction. Complex optical systems utilising frequency shifting elements (2) (eg a Bragg cell) have been used to impose a carrier frequency onto the light beam and allow the flow velocity to be determined, but these are bulky and expensive optical arrangements. The use of optical fibres for measurement of fluid flow velocity is an obvious development of the technology. Their small physical dimensions and flexibility makes them an attractive proposition. However, the use of optical fibres does introduce problems. When used in interferometric arrangements the reflections from the fibre end faces can result in interference signals which give rise to erroneous information. Also, although the fibre probe is small, as the majority of the light scattered back down the fibre comes from a small region very close to the end of the fibre where the flow perturbation is greatest (the 'stagnation region'), there is an effect on the required signal.

The technique described here overcomes these problems by utilising a low coherence light source (3) to project the 'measurement region' ahead of the stagnation region. A modified recovery Michelson interferometer then provides two interferometric outputs. The relative phase of these two signals can be controlled independently. This phase difference is selected to be  $\pi/2$ , giving two outputs in quadrature. The signal processing discussed herein then allows the velocity rather than speed of the flow to be determined.

### **EXPERIMENTAL**

The light source used was a multi-mode laser diode. When operated in an interferometric arrangement, interference is only observed when the path difference between the two recombining beams is less than the characteristic coherence length,  $L_c$ , which is typically  $200\mu\text{m}$ . If the path difference is greater than the coherence length, interference can still be observed if a second, recovery, interferometer is used. This second interferometer is arranged to have a path difference equal to that of the first interferometer, thus bringing components of the light back into coherence (3).

In the present scheme, this second interferometer has a path difference of  $\sim 500\mu\text{m}$ . Thus, interference is only observed if the path difference of the measurement interferometer matches this value. For an optical fibre Doppler anemometer, the measurement interferometer is formed between the end of the fibre probe, which reflects light, and the particles which scatter light, back down the fibre core. Thus, the measurement region is projected ahead of the fibre probe and the stagnation region. This distance can be varied by adjusting the path difference

in the recovery interferometer, but is typically kept small (500-700 $\mu$  m) to maximise the return signal.

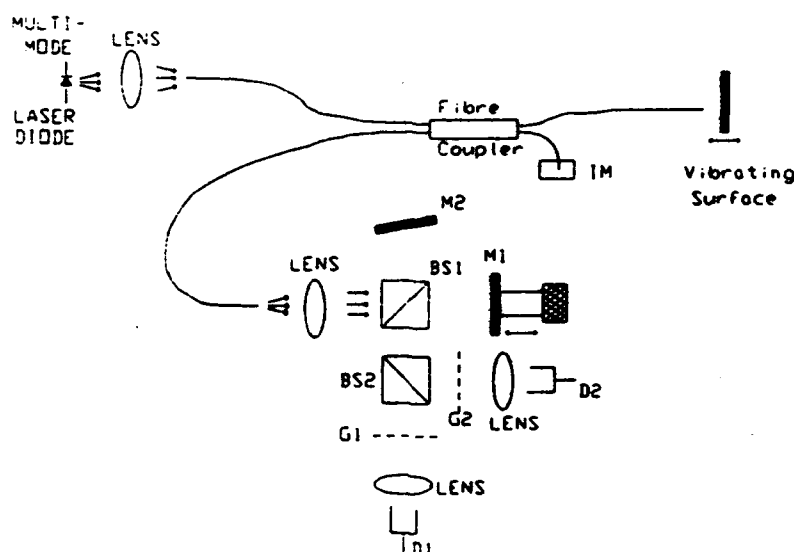


Figure 1: Experimental Arrangement

The experimental arrangement used is shown in figure 1. Light from the multi-mode laser diode (LD, Sharp LTO23,  $\lambda = 780\text{nm}$ ) is launched into a single-mode fibre optic coupler. One of the output ports of the coupler is terminated in index-matching gel (IM), and the other forms the fibre probe. Light reflected from the end face of the fibre and scattered from the flow is carried back down the fibre core. This light is then taken from the fibre coupler and collimated by a lens (L2) into a beam of 5-8mm diameter, which is then introduced into a Michelson interferometer. Adjustment of mirror M1, allows precise control of the path difference to match that of the probe.

Further processing of the returned light is provided in a novel arrangement of the Michelson interferometer by tilting the second mirror (M2) through a small angle about the vertical axis (4,5). This imposes a variation in path difference across the beam profile, and, if the two recombining beams are coherent, a series of bright and dark vertical fringes will be observed, across the beam profile. This pattern will move due to the Doppler signal imposed on one of the recombining beams. This output is further split by a beam splitter (BS2) to give two output beams. Each of these is then incident on a transmission grating (G1,G2) of period equal to the spatial period of the spatial fringe pattern. The transmitted light is then focussed onto photodetectors (D1,D2).

As the spatial fringe pattern moves across the beam profile over the grating, a time varying signal is detected. This signal is identical to the output from a conventional interferometer (apart from a reduction in visibility) (4) but the phase of the signal can be controlled by varying the spatial position of the transmission grating. By positioning each grating independently, the relative phase of the output signals can be controlled. Of practical importance is a relative phase difference of  $\pi/2$ , as the output signals  $I(1)$  and  $I(2)$  can then be written as (4):

$$I(1) = v \cos(Wd t) \quad I(2) = v \sin(Wd t) \quad (1)$$

where  $v$  is the visibility and  $Wd$  is the Doppler frequency shift, given by:

$$Wd = \frac{u \cos(\theta)}{\lambda} \quad (2)$$

where  $u \cos(\theta)$  is the component of the velocity resolved in the direction of the fibre probe, and  $\lambda$  is the wavelength of the source.  $W_d$  is positive for flow towards, and negative for flow away from, the fibre probe.

The signals are then digitised and transferred to a PC for analysis. The analysis consists of performing a fast Fourier transform (FFT) on the quantity:

$$X(t) = I(1) + i I(2) \quad (3)$$

where  $i$  is  $\sqrt{-1}$ . This will give a single side-band frequency at the Doppler frequency shift  $W_d$  from which the velocity of the scattering particles can be determined via equation 2.

## RESULTS

For the purposes of demonstration a simulated flow was used to impose the Doppler shift on the light beam. This consisted of a rotating disc with a highly scattering surface. Interrogation of a point at a fixed radius from the centre of the disc would then give a constant Doppler shift. The fibre probe was positioned at a distance of  $\sim 500\mu\text{m}$  from the rotating surface at an angle of 45 degrees to the surface normal. The path difference of the recovery interferometer was adjusted to match that of the probe cavity.

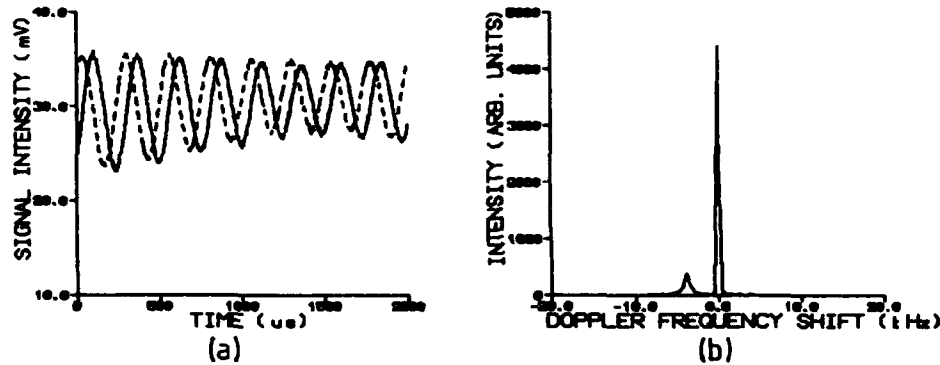


Figure 2: (a) Detected interference signals and (b) FFT Spectrum of signals for a velocity of  $-4.1\text{mm/s}$ .

The detected signals from the two photodetectors are shown in Figure 2(a). The quadrature nature of the two signals can clearly be seen. Figure 2(b) shows the FFT spectrum of the combination of these signals. The single side-band peak at a frequency of  $-3.7\text{kHz}$  can be seen corresponding to a speed of  $-4.0\text{mm/s}$  in the direction away from the fibre probe. The direction of rotation of the disc was then reversed. The output signals and the associated FFT are shown in figure 3. Here

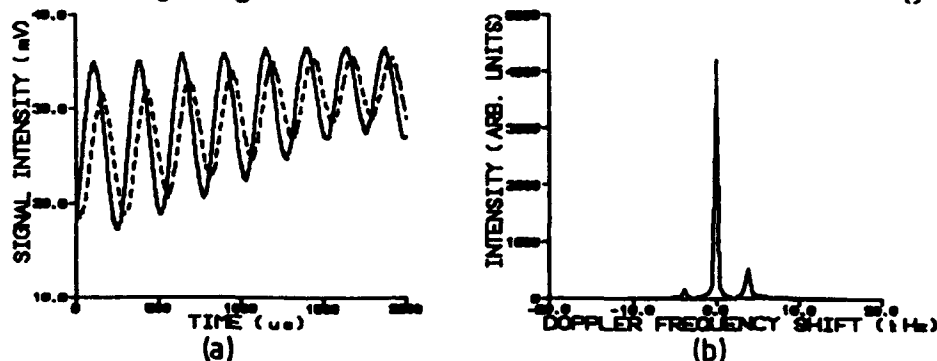


Figure 3: (a) Detected interference signals and (b) FFT Spectrum of signals for a velocity of  $+4.1\text{mm/s}$ .

the side-band is observed at +3.7kHz corresponding to the same speed but opposite direction.

The FFT spectra of figure 4(a) and 4(b) correspond to velocities of  $\pm 12.0$  mm/s respectively giving a measured Doppler frequency of  $\pm 11$ kHz. Here a true single side-band is not observed, as the phase difference was not maintained at precisely  $\pi/2$ , however, from the asymmetric nature of the spectra it is possible to extract directional information.

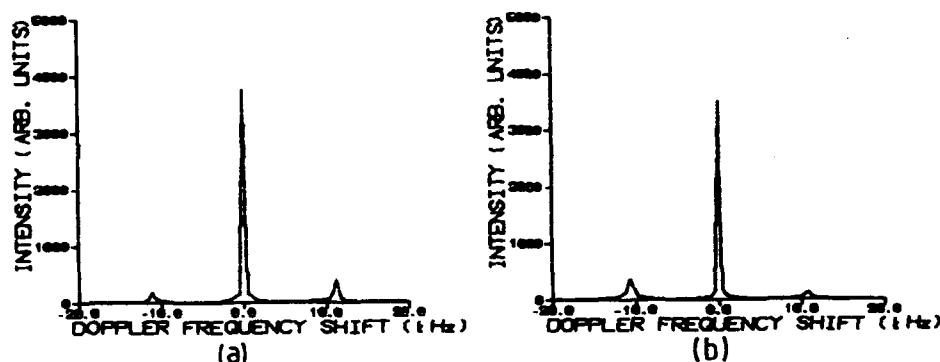


Figure 4: (a) FFT Spectrum of signals for velocity of +12.0 mm/s and (b) FFT Spectrum of signals for velocity of -12.0 mm/s.

## CONCLUSIONS

A system has been assembled for measuring the Doppler frequency shift of light scattered back down a fibre optic probe in order to determine velocity. The signal recovery scheme utilises a novel adaptation of a Michelson interferometer to give two output signals in quadrature. Simple signal processing of the output signals then allows determination of velocity rather than speed, in a system which uses simple inexpensive optical components. The system also utilises a low coherence light source. This suppresses unwanted signals and allows the measurement region to be projected ahead of the fibre probe. Current work is examining techniques to maintain the  $\pi/2$  phase change precisely, and testing the instrument in the measurement of fluid flow velocities.

## ACKNOWLEDGEMENTS

The authors are pleased to acknowledge the support of SERC for this work. One of us (KW) is currently supported by an SERC Fellowship.

## REFERENCES

- (1) Cochrane T., Earnshaw J.C., & Love A.G., Medical & Biological Engineering & computing (Sept 1981) 'Laser Doppler Measurement of Blood velocity in microvessels'
- (2) Oldengarm J., Van Krieken A.H. & Raterink H.J., Laser Technol. (1973) 'Laser Doppler Velocimeter with optical frequency shifting'
- (3) Ning Y.N., Grattan K.T.V., Boyle W.J.O. & Meggitt B.T., SPIE Proc. Vol 1267, (1989) 'The use of Multi-mode Laser Diodes in Low-coherence Coupled-cavity Interferometry'.
- (4) Weir K., Boyle W.J.O., Palmer A.W., Grattan K.T.V. & Meggitt B.T. J. Lightwave Technol., Inpress (1991) 'A novel adaptation of the Michelson Interferometer for the measurement of vibration'
- (5) Weir, K., Boyle, W.J.O., Palmer, A.W., Grattan, K.T.V. & Meggitt B.T. Electron. Letters, in press (1991). 'A low coherence interferometric fibre optic vibrometer using a novel optical signal processing scheme'

# Dual Aperture Single Mode Optical Fiber Laser Doppler Velocimeter

M. D. Mermelstein\* and J. A. Blodgett  
Naval Research Laboratory  
Washington, D.C. 20375

Single mode optical fibers and graded index microlenses have recently been utilized in laser light scattering experiments.<sup>1,2</sup> The utilization of single mode optical fiber technology offers many advantages over conventional bulk optic arrangements including: ease in alignment, unity heterodyne efficiency, polarization maintaining capability, high angular resolution and small size. A dual aperture single mode optical fiber heterodyne technique has recently been demonstrated which simultaneously measures the angular orientation, radial velocity and angular velocity of a target simulator.<sup>3</sup> This technique was demonstrated with an interferometer that utilized the exposed cores of the receiving fibers as the apertures. Presented in this report is a dual aperture heterodyne interferometer that employs pigtailed graded index microlenses as the detection apertures, thereby extending the range and angular resolution of the laser Doppler velocimeter (LDV). Although the velocimeter presented here utilizes microlenses, the results are applicable to lens systems of greater dimensions which are suitably coupled to the single mode fiber. This interferometer may be useful in a number of LDV applications including: particle flow measurements, atmospheric wind sensing, satellite tracking, laser radar and robotic positioning.

The experimental arrangement is shown below. A 40 mW cw, 1.06  $\mu\text{m}$ , diode pumped, single frequency Nd:YAG laser is used as the primary light source. Approximately 3.6 mW of the laser light at

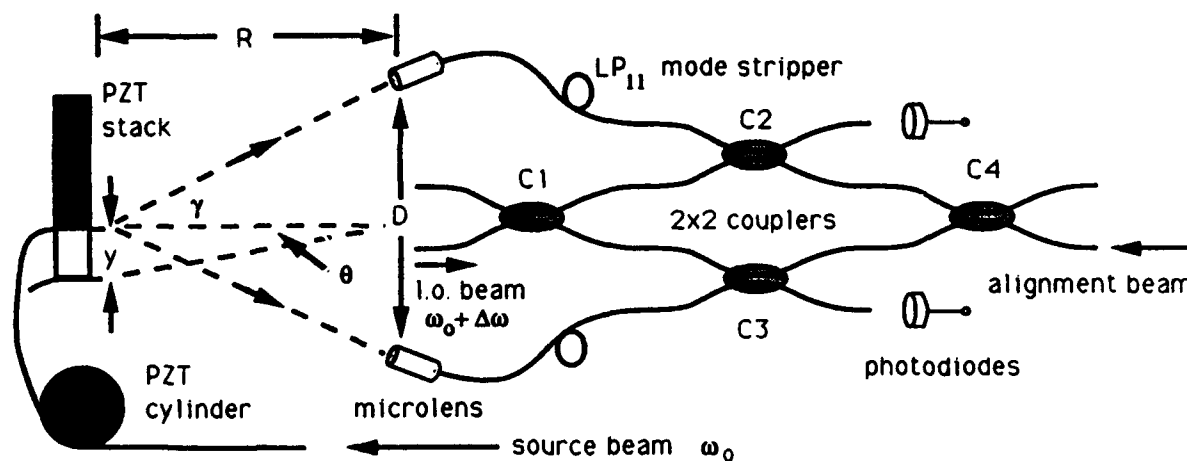


Figure 1. Experimental arrangement. Angular motion  $\theta$  is achieved by an extension of the piezoelectric stack. Dimensions are not drawn to scale.

\*University Research Foundation, Greenbelt, MD 20770

a frequency  $\omega_0$  is injected into the source fiber. Several turns of this fiber are wrapped around a piezoelectric cylinder and the end of the fiber is mounted on a piezoelectric stack. The cleaved endface of the fiber acts as a source or target simulator. An oscillating voltage at  $\Omega_r / 2\pi = 40$  Hz is applied to the piezoelectric cylinder which generates an oscillating phase shift in the radiated light, thereby simulating radial motion of amplitude  $\Delta R = 50$  nm. Also, an oscillating voltage at  $\Omega_t / 2\pi = 5$  Hz is applied to the piezoelectric stack which generates a transverse motion  $y = 0.25$  mm of the fiber source. Hence, this arrangement provides a simulation of light radiated from a source executing motion in two orthogonal directions. The radiated light is collected by two microlenses symmetrically located at a range  $R$  of 3.3 m and separated by a distance  $D$  of 2 cm. The microlenses focus the light onto the cores of the single mode fibers which carry the light to couplers C2 and C3. A local oscillator (l.o.) beam of approximately 100  $\mu$ W is split from the same laser. Its frequency is shifted by two successive Bragg cells to  $\omega_0 + \Delta\omega$  where  $\Delta\omega/2\pi = 280$  kHz. This l.o. beam is divided by coupler C1 and combined with the collected light at couplers C2 and C3.  $LP_{11}$  mode strippers, consisting of loops of fiber of about 1 cm in diameter, are utilized in each collection arm to insure that only the  $LP_{01}$  spatial mode is accepted by the collection optics. A second laser, at 1.06  $\mu$ m, provides an alignment beam which is injected into coupler C4 and renders the microlenses as collimated light sources, thereby facilitating optical alignment and verifying the spatial mode purity. The combined light beams are mixed at the photodiodes to generate carriers given by:

$$V_1(t) = V_{10}(\theta) \cos [\Delta\omega t + \Phi_1(t)] \quad (1a)$$

$$V_2(t) = V_{20}(\theta) \cos [\Delta\omega t + \Phi_2(t)] \quad (1b)$$

where  $V_{10,20}(\theta)$  are the angle dependent carrier amplitudes,  $\theta = y/R$  is the source angular orientation and  $\Phi_{1,2}$  are the phases of the two carriers associated with the source fiber motion. The phases  $\Phi_{1,2}$  are found from an elementary analysis and are given by:

$$\Phi_1(t) = k_0 \left[ R - \frac{D}{2} \sin \theta \right] \quad (2a)$$

$$\Phi_2(t) = k_0 \left[ R + \frac{D}{2} \sin \theta \right] \quad (2b)$$

where  $k_0 = 2\pi/\lambda_0$  and  $\lambda_0$  is the wavelength of light. Equations 2a and 2b may be added and subtracted to yield phases  $\Phi_{\pm} = \Phi_1 \pm \Phi_2$  that are solely dependent upon the range and angle respectively. The radial and angular velocities,  $\dot{R}$  and  $\dot{\theta}$ , are given by the phase rates:  $\dot{\Phi}_{\pm} = 2 k_0 \dot{R}$

and  $\dot{\Phi}_- = k_0 D \dot{\theta}$  in the limit  $\theta \ll 1$ . The heterodyne carriers are demodulated by Hewlett Packard 8901B modulation analyzers which utilize a phase-locked loop circuit to measure the frequency deviation or phase rate. Analog voltages from both modulation analyzers are either added or subtracted to yield voltages proportional to the radial and angular velocities:  $V_{\pm}(t) = (\eta/2\pi)\dot{\Phi}_{\pm}$  where  $\eta = 1.0$  mV/Hz is a frequency deviation to voltage conversion coefficient.

Shown in Figures 2a and 2b are the sum and difference voltage power spectra. The  $V_+$  power spectrum demonstrates the radial velocity peak of -35.9 dBV rms at 40 Hz while the angular velocity peak, at 5 Hz is suppressed at -59.5 dBV rms. The  $V_-$  power spectrum exhibits a prominent peak -39.3 dBV rms at 5 Hz, corresponding to the angular velocity, and a suppressed peak of -83.2 dBV rms at 40 Hz for the radial velocity. Hence the angular velocity

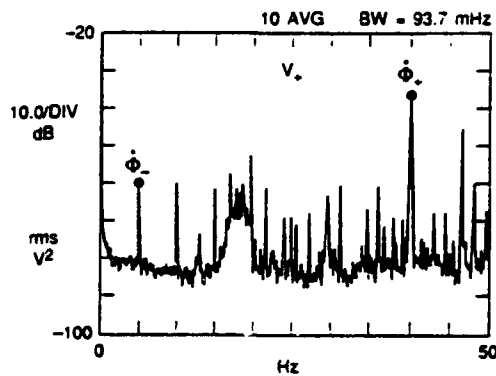


Fig. 2a

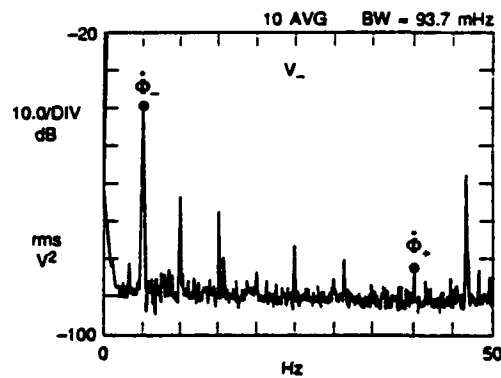


Fig. 2b

and radial velocities exhibit suppressions of 20.2 dB and 47.3 dB in the sum and difference voltage power spectra, respectively. These rms voltages are in good agreement with the expected voltages given by:  $[V_+]_{rms} = \eta \Delta R \Omega_r / \lambda_0 = -39$  dBV rms and  $[V_-]_{rms} = \eta D y \Omega_t / 2 \lambda_0 R = -33$  dBV rms. The discrepancy of 6 dB between the measured and calculated values for  $[V_-]_{rms}$  is attributed to the critical alignment required for the transverse measurement. Note that the  $V_-$  power spectrum suppresses noise common to both optical receivers.

The far field radiation pattern associated with the fundamental mode of the single mode fiber is Gaussian. This Gaussian beam is imaged onto the core of the pigtailed single mode fiber by the microlens. The analysis of the angle-dependent coupling efficiency  $T(\theta)$  of optical power into the fiber core is similar to that of the coupling efficiency between two parallel and displaced single mode fibers.<sup>4</sup> Adaptation of this latter analysis to the pigtailed microlens yields the following expression for the coupling efficiency:  $T(\gamma) = A \exp [-(\gamma / \psi)^2]$  where  $A$  is a constant,  $\gamma$  is the tilt angle between the optic axes of the launching fiber and the receiving optics

and  $\psi$  is the angular resolution of the pigtailed microlens found to be approximately 1.0 mrad. An error signal proportional to the source orientation angle may be generated by subtracting the two heterodyne carrier amplitudes. Since each carrier amplitude is proportional to  $\sqrt{T}$ , the error signal  $f(\theta)$  is given by:

$$f(\theta) = \sqrt{A} \{ \exp[-(\theta + \gamma)^2/2\psi^2] - \exp[-(\theta - \gamma)^2/2\psi^2] \} \quad (3)$$

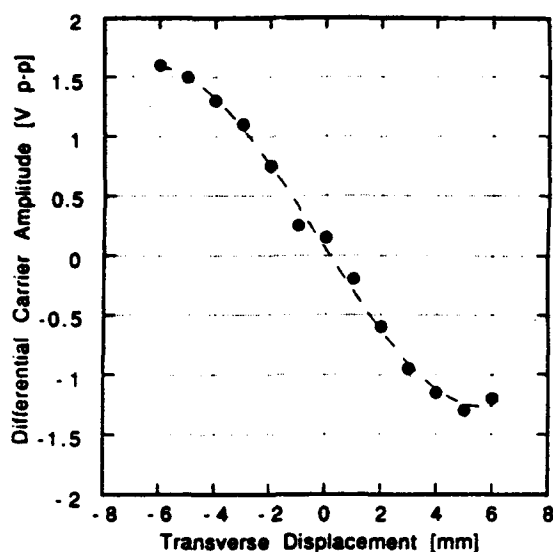


Figure 3. Angular orientation error signal.

where  $\gamma = D/2R$  is the offset angle determined by the range and receiver separation. A Taylor series expansion about  $\theta$  demonstrates the linear portion of the error signal given by:  $f(\theta) = \{2\sqrt{A}(\gamma/\psi^2) \exp[-\gamma^2/2\psi^2]\} \theta$ . Shown in Figure 3 is a plot of the differential carrier amplitude as a function of source transverse displacement. The broken line is a non-linear least squares fit of the data to a third order polynomial trial function. The fitting parameters indicate error signal sensitivities of 0.36 V/mm for the displacement and 1.2 V/mrad for the angular displacement.

In conclusion, a single mode optical fiber laser Doppler velocimeter has been presented which utilizes two graded index microlenses as the receiving apertures. This dual aperture heterodyne interferometer simultaneously measures the radial and angular velocities of a remote source and provides an error signal suitable for angular tracking.

## REFERENCES

1. R. G. W. Brown, "Dynamic light scattering using monomode optical fibers", *Appl. Opt.* 26, 4846 (1987).
2. H. S. Dhadwal and B. Chu, "A fiber-optic light-scattering spectrometer", *Rev. Sci. Instrum.* 60, 845 (1989).
3. M. D. Mermelstein and J. A. Blodgett, "1x2 Fiber optic heterodyne array for laser Doppler velocimetry and angular orientation measurements", to be published in *Optics Letters*, 1991.
4. D. Marcuse, "Loss analysis of single-mode fiber splices", *B.S.T.J.*, 56, 703 (1977).



**THURSDAY**  
**January 30, 1992**  
**MCC: Steinbeck Forum**

**TH1: MULTIPLEXED AND DISTRIBUTED SENSORS**

Chair: Kjell Bløtekjær, *Norwegian Institute of Technology, Trondheim, Norway*

**TH2: FIBER DEVICES**

Chair: Simon B. Poole, *University of Sydney, Sydney, Australia*

**TH3: PHOTONIC DEVICES**

Chair: Juichi Noda, *NTT Opto-Electronics Labs, Ibaraki-Ken, Japan*

**TH4: CHEMICAL AND ENVIRONMENTAL SENSORS**

Chair: Anna Maria Scheggi, *IROE-CNR, Firenze, Italy*

# **TH1.1 Recent Advances In Fiber Optic Distributed Sensing Systems**

**(Invited)**

**A. H. HARTOG**  
**York Sensors Ltd**  
**York House, School Lane**  
**Chandler's Ford, SO5 3DG UK**

**Abstract:** The development of the technology of distributed optical fiber sensors is reviewed, with particular emphasis on those sensors which have found implementation into usable devices. Applications and field trials are also discussed.

## **1. Introduction**

It is now ten years since the concept of a distributed fiber optic sensor was proposed. Apart from a few experiments, little progress was made in the following years until 1984-5, with the development of the Raman distributed temperature sensors. Although such sensor systems are now installed in a number of locations, the concept is still only beginning to be accepted amongst users and much is still to be learned as to how to apply the technology. There is considerable interest in using similar concepts for other measurands, but so far no instruments have become available. In this paper, the techniques of most interest are reviewed, followed by some examples of practical applications.

## **2. Distributed sensor technology**

The concept of distributed optical fiber sensors was based initially on optical time-domain reflectometry[1], the measurand-sensitivity being achieved either through alteration of the state of polarisation of the scatter return in a single-mode fiber[2,3], or through modulation of the backscatter intensity. In all cases, the information as to the location along the fiber was obtained from the time flight of the probe pulse.

The polarisation approach was explored initially, and the detection of bend-induced birefringence and of Faraday rotation were both demonstrated [3,4]. POTDR went into obscurity owing to the twin problems of the sensitivity of the state of polarisation (SOP) in standard single-mode fibers to almost any external influence and the very real measurement and computational difficulties involved in determining the evolution of the SOP in the first place. Moreover, once the SOP has been determined, the result must be differentiated to quantify the measurand, a procedure which demands a very high signal-to-noise ratio on the unprocessed data. Recently, however, Ferdinand [5] has reported progress in this technique, including automated measurement equipment and data reduction. Results on the measurement, for example, of side-pressure were reported. Another option is to use polarisation-maintaining fiber, which dramatically simplifies the data analysis, at the price of a modulation signal now in the microwave region.

As to approaches involving intensity modulation of the backscatter signal, they may broadly be divided between those involving changing the total attenuation of the fiber and modulating only the scatter coefficient.

The latter approach is clearly more efficient, since a high sensitivity does not necessarily involve inducing a high loss in the fiber[6]. The technique which, to date, has seen the greatest practical application is that of Raman thermometry, where the scatter return is optically filtered to select bands well separated from the incident wavelength and which are present owing to the phenomenon of the spontaneous Raman scattering [7,8]. This approach has the benefit of using standard telecommunications-grade optical fibers without modification. However, the signal is extremely weak which has resulted in the development of high-performance multi-channel averager (in order efficiently to improve the signal-to-noise ratio) and in the use of advanced laser sources (e.g. diode-pumped solid-state lasers).

When the first distributed temperature sensor was demonstrated [6] (in the laboratory and using Rayleigh scattering in liquid-core fibers), a performance of 1m spatial resolution over 100m of fiber was projected. Changing to the Raman scattering approach resulted in signal levels some 4 orders of magnitude weaker and it has taken almost ten years of technological development to recover the lost ground, with as added bonus, a range now covering 10km (i.e. a typical measurement capability of 10 000 points for each fiber connected to the instrument). This is the target at which much of the development effort has recently been directed. In addition, several research groups have focussed on achieving ultra-high spatial resolution with the aid of time-correlated single photon counting. In the latter approach, the level of the light is reduced until separate photons can be detected and the time of arrival of each is accurately determined [9].

Effects involving changes in the fiber attenuation with temperature, for example using rare-earth dopants, have been demonstrated [10], but these present significant performance disadvantages compared with the Raman approach and no real advantages. The technique may well come into its own, however for other types of measurand: for example as a means of performing distributed (or at least multipoint) gas detection using evanescent fields. Equally, micro-bending losses can be induced by a variety of external fields, and, if applied with adequate control, can provide access to a number of additional measurands.

One of the areas in distributed sensing where research is still at an early stage is concerned with non-linear interactions: for example between a CW beam and a counter-propagating probe pulse. The ranging is achieved in the same way as in standard backscattering, but the quantity now measured is the gain of the non-linear interaction. This approach has been applied to the measurement of strain using stimulated Brillouin

scattering [11]. In this case, the gain/frequency spectrum is explored as a function of distance along the fiber, by tuning the frequency difference between the two interacting lasers. The strain is then evaluated from a previous calibration of Brillouin gain spectrum vs fiber strain. Other proposals have explored stimulated Raman scattering and its polarisation dependence[12], or the optical Kerr effect[13].

Finally, distance resolution may also be achieved in the forward scattering regime, provided that the sensing process involves coupling power between at least two modes having sufficiently different propagation velocities. In this case[14], the measurement is one of power coupling coefficient vs distance. The requirement on time resolution is naturally orders of magnitude more stringent than in the case of a reflective method (a few ps vs tens of ns); however, coherent detection methods, by beating the coupled and not-coupled beams together, allow some of the resolution penalty to be recovered.

The methods now being explored will require new optical components -certainly sources with controlled spectra possibly combined with short pulse, high-power operation. There will also be a demand for special fibers, e.g. with special dopants, polarisation properties or or compositions especially suited to the type of interaction being used.

### 3. Applications.

Given the availability of instrumentation, it is not surprising that distributed temperature sensing has seen the largest range of applications. One of the driving forces behind the development of the technology was the requirement to monitor high-power transformers for hot-spots and a number of installations of this type are now underway. The power supply industry has also used the technology for the monitoring of power cables: again the small size, dielectric nature of the sensor, together with its ability to work amongst very high levels of electrical interference has made it a logical candidate.

In other areas where applications development is progressing well, it is simply the large number of points sensed by these systems which is attractive: very low (a few \$ per point) instrumentation and installation costs per sensed point may be achieved, provided there is a genuine requirement for a large number of sensors. Examples in this category include the monitoring of e.g. road tunnels as an early indication of fire, the monitoring of large process plant (e.g. drying ovens), of pipelines or of other large structures such as ships.

The requirement for other types of measurement is claimed to be just as great. For example, most large civil engineering structures require monitoring for strain over much of their area. In practice, the measurement of strain has only been shown on telecommunications cables to date. However, the present

considerable research activity in the "smart structures" field is likely to broaden the applications experience in the coming few years. A distributed isostatic pressure sensor is required for the monitoring of fluid distribution networks - e.g. in the gas industry. There is also a clear need for a distributed gas sensing technology -e.g. in the gas industry, but more generally in the field of environmental monitoring.

#### 4. Conclusions

In the first ten years of distributed fiber-optic sensing, one technique - the Raman temperature sensor - has reached an advanced stage of development and the beginning of commercial exploitation. Research into other measurement techniques and other measurands is active and it is expected that, in time, the measurement, inter alia, of strain, pressure and chemicals will be achievable routinely. Each new measurement, in addition to the development of the basic sensing technology requires significant applications expertise e.g.- in the fiber installation to ensure accurate measurement and in the use and interpretation of the results.

#### 5. References

1. M.K. Barnoski et al: Appl. Opt. Vol.15 pp2112-5, 1976.
2. A.J.Rogers. Electron. Lett. Vol 16, pp 489-490, 1980
3. A.H.Hartog et al: Proc 6th European Conf. Opt. Commun., York 1980, Post deadline session.
4. J.N.Ross: Electron. Lett.,Vol. 17, pp596-7, 1981.
5. P.Ferdinand: Doctoral Thesis, Nice University, 1990.
6. A.H.Hartog: J. Lightwave Technol., Vol.1,pp 498-505, 1983
7. J.P. Dakin et al: Electron.Lett., Vol 21, pp569-570, 1985
8. A.H.Hartog et al: ibid, Vol 21, pp 1061-3, 1985.
9. R. Stierlin et al: Appl Opt, Vol 26, pp1368-70, 1987.
10. M.C. Farries et al: Proc 6th International Conf. on Integrated Opt. and Opt. Fibre Commun. Reno, Nevada, 1987
11. M.Tateda et al: J.Lightwave Technol. Vol 8,pp1269-72,1990
12. M.C.Farries et al, Proc. OFS-2, Stuttgart, 1984,pp121-132
13. J.P.Dakin, Fibre-Opti Sensors II Conference, The Hague, The Netherlands, Proc SPIE, Vol 798, 149-155, 1987.
- 14 R.B.Franks et al: ibid, pp 36-41.

## **TH1.2 Detection Of Localised Polarization Mode Coupling Using The Optical Kerr Effect**

**V. A. Handerek, A. J. Rogers and I. Cokgor**

**Department of Electronic and Electrical Engineering, King's College London  
Strand, London WC2R 2LS, United Kingdom**

### **ABSTRACT**

The optical Kerr effect is used to determine the locations of discrete mode coupling points in a polarization maintaining fibre. Differentiation of the received signal is demonstrated to reduce confusion from interactions between coupling points.

### **INTRODUCTION**

The degree of mode coupling experienced by light propagating in an optical fibre can be influenced by the environment of the fibre. This offers the possibility of using mode conversion as a sensing mechanism. This approach to optical fibre sensing is attractive when distributed sensors are needed because the modal properties of the fibre are normally relatively independent of position along the fibre and provide a means of allowing the environment to affect the optical signal without going to the trouble of assembling many discrete transducers along the optical path.

One particularly appealing way to implement a mode conversion sensor is to use the orthogonally polarized eigenmodes of a polarization maintaining fibre. This is because the modes are easily excited and detected separately and many coupling mechanisms are relatively amenable to calculation. In particular, if the measurand is a vector quantity, (e.g. force/strain) then it will, if acting at an angle to the birefringence axes, rotate the axes to some extent and cause coupling of light from one linear eigenmode to the other.

The spatial variation of polarization mode coupling in a polarization maintaining fibre can be measured by various methods. Polarization optical time domain reflectometry (1,2) is one possible technique. Here, linearly polarized light is launched into one eigenmode of a polarization maintaining fibre and the returning backscattered signal is monitored for the orthogonal polarization. The signal will clearly be small unless mode coupling occurs, and changes in the level of this signal can be related to locations along the fibre through use of elapsed time after launching in the usual way. The drawback of this approach for sensing dynamic systems is that, in common with all optical fibre systems based on Rayleigh backscatter, the launched optical power is used very inefficiently, with only a very small fraction of the power ever contributing to the detected signal. Thus signal to noise ratios are normally low and integration times are long, leading to slow response to any changes in a measurand.

Alternative approaches which make more efficient use of the launched power have been demonstrated. These methods have been based on differential mode delay which occurs between the coupling point and the output end of the fibre. The differential delay increases linearly from zero as the coupling point is moved from the output end toward the launched end of the fibre. Early work (3,4) employed frequency swept sources and homodyne processing to produce beat frequencies dependent upon the mode coupling locations. These efforts suffered from signal beating problems in the case of strong coupling and multiple coupling points, and also from poor linearity of the source frequency sweep. More recently, the differential mode

delay has been measured much more accurately by coherence domain methods (5-7). In this case, crosstalk is reduced and delay measurements are more accurate, but the system response is still relatively slow.

In the present paper, we demonstrate a new method for determining the locations of discrete mode coupling points spaced along a polarization maintaining fibre using a pump-probe architecture based on the optical Kerr effect. The resulting system provides good spatial accuracy and fast response speed and may be valuable for use in applications such as intrusion sensing or real-time location of tracked vehicles.

### SYSTEM PRINCIPLES

The optical arrangement employs a length of polarization maintaining fibre carrying two counter-propagating beams. A CW probe beam is launched from one end of the fibre so as to equally excite the two eigenmodes and the polarization state of this beam is detected at the far end of the fibre by means of a beamsplitter and analyser oriented at forty-five degrees to the birefringence axes. An intense, pulsed, pump beam is also launched through the beamsplitter at this end of the fibre so as to propagate against the direction of the probe. This pump beam is launched on one of the birefringence axes. This arrangement is similar to the well-known Kerr-effect shutter system (Ref 8).

As in the Kerr shutter, the pump pulse causes a phase shift between the eigenmodes of the probe beam, leading to a change in the output polarization state of the probe. This is detected as a sharp change in the probe intensity passed by the analyser when the pump is initially launched into the fibre.

If, now, a force acts at an angle to the axes along a section of fibre, coupling of the pump light to the other axis will occur, and the Kerr effect on the probe will thus be modified. The probe light itself will also experience mode coupling, which will further modify the output polarization state. The actual change which occurs will depend, inter alia, on the states of polarization of the beams as they enter the perturbed region and thus, unless the birefringence perturbation is very small compared with the intrinsic birefringence, there will exist a mutual dependence of effects from different measurement locations, which only fairly complex signal processing would be able to resolve. However, it is clear that for any change in the direction of birefringence axes consequent upon the perturbation by a measurand, there will, in general, result a change in optical Kerr effect. A differentiated signal thus will, at least, indicate differential features of the measurand distribution, even though a fully quantified spatial distribution is more elusive.

### EXPERIMENT

The fibre used in the experiments was a mono-mode high-birefringence fibre manufactured by Andrew Corporation with a diameter of  $67\mu\text{m}$ , attenuation of 35dB/km at 633nm and core to cladding refractive index difference  $\Delta n = 0.032$ . The length of the fibre was about 100m. The arrangement of the experiment is shown in Fig 1. Pump pulses (617nm) of 8ns (FWHM) duration were generated in a dye laser with a repetition rate of 50 Hz. These pump pulses were launched onto one of the birefringence axes of the fibre with the help of a halfwave plate and with a peak power of 3W measured at the output end of the fibre. The linearly polarized probe beam of wavelength 633 nm, from a He-Ne laser, was launched into the fibre at  $45^\circ$  to the birefringence axes. On emergence, the probe beam was directed by a beam splitter to the detector via the polarization analyser. Its average power at the detector was about  $25\mu\text{W}$ . The

He-Ne laser and the detector were protected from the pump light by use of band-pass filters at 633 nm. Force was exerted by pressing metal rods on the fibre. The received signals were recorded, averaged and differentiated using the functions of the digital storage oscilloscope.

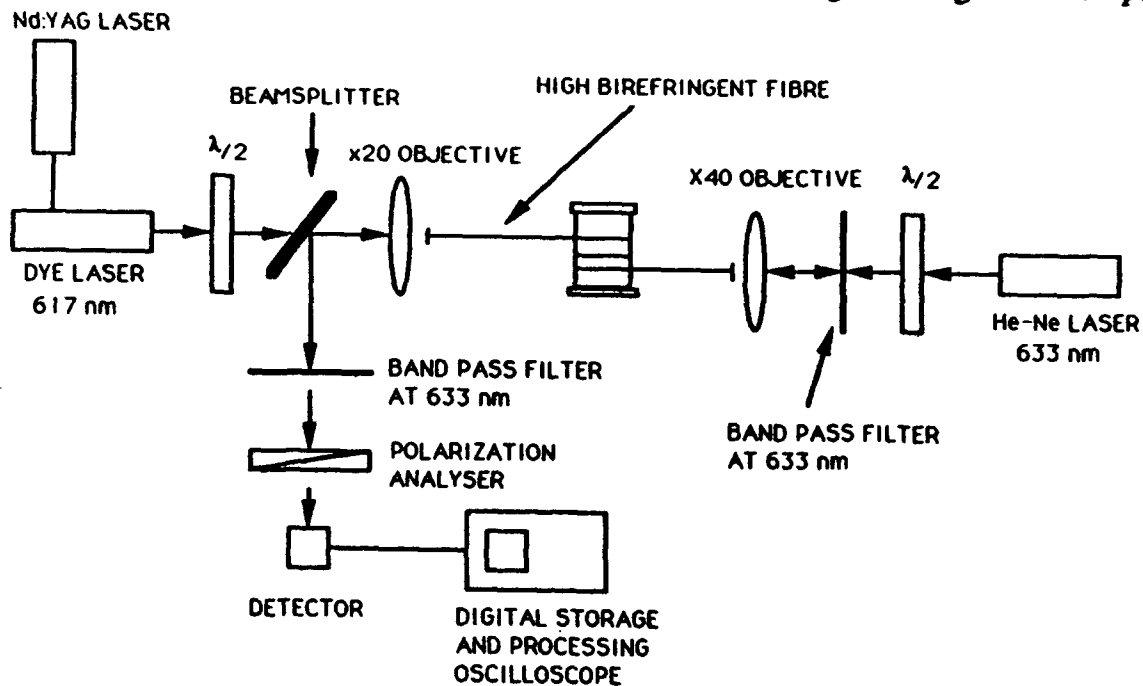


**Fig. 1:** Experimental arrangement

In the absence of any measurand-induced perturbation the Kerr effect of the pulse is to modify the local value of birefringence as it propagates, a modification which is sensed by the probe beam as a phase shift between the eigenaxes, and which is in principle constant for the duration of the pulse's passage through the fibre. The effect of this phase shift on the optical signal passing through the analyser is shown in fig (2a). In practice, the slow fall in the value of the phase shift is due to the attenuation of the pump pulse with distance along the fibre. Fig (2b) shows the effect of differentiating this signal with respect to distance.

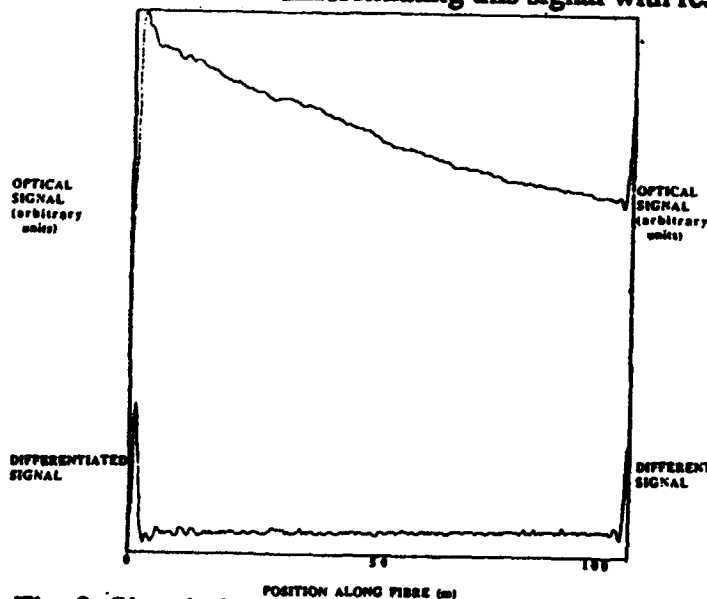


**Fig. 2:** Signals for undisturbed fibre

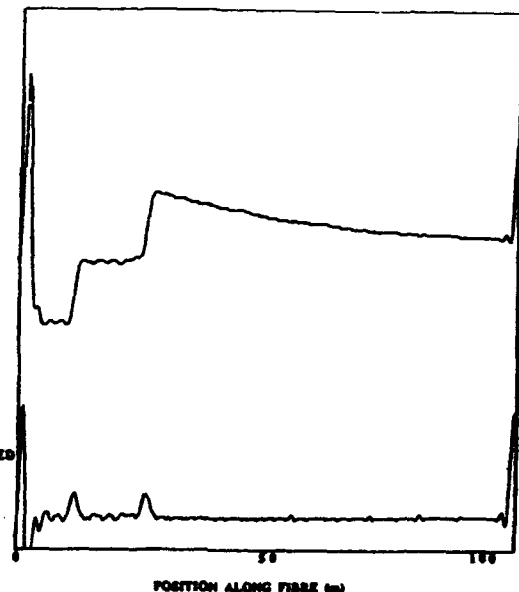


**Fig. 3:** Signals with two coupling locations



Figs (3a) and (3b) show, respectively, the fluctuating analyser signal when the fibre was perturbed at two points, and its differential with respect to distance. The points at which the weights were applied are clearly evident. Such a system, even as it stands, could be used as an intruder alarm or as an indication of anomalous disturbance of almost any kind.

### CONCLUSIONS

We have demonstrated the use of the optical Kerr effect to determine the locations of discrete mode coupling points spaced along a polarization maintaining fibre. Differentiation of the received signal with respect to time provides a simple way to reduce confusing interactions when multiple coupling points are present. Further work on this method is continuing with a view to developing practical real time processing and theoretical analysis of the potentialities of the technique.

### ACKNOWLEDGEMENTS

V Handerek thanks the UK SERC for research grant and advanced fellowship support.  
I. Cokgor is supported by the Turkpetrol Foundation.

### REFERENCES

1. NAKAZAWA M. TOKUDA M., and NEGISHI Y. 'Measurement of polarization mode coupling along a polarization-maintaining optical fibre using a backscattering technique.' Opt. Lett.. 8 (10) pp 546-8 (Oct 1983).
2. ROGERS A. J. 'Polarization-optical time domain reflectometry' Elect. Lett. 16 (1980) pp. 489-490.
3. FRANKS R. B. TORRUELAS W. and YOUNGQUIST R. C. 'Birefringent stress location sensor' Proc. SPIE Vol. 586 (1985) pp 84-9.
4. KUROSAWA K., HATTORI S. and YOSHINO T. 'Distributed fibre-optic sensor using forward travelling light in polarization maintaining fibre'. Proc. SPIE Vol.798 (1987) pp 36-41.
5. TAKADA K., NODA J. and SASAKI Y. 'Measurement of spatial distributions of mode coupling in polarization-maintaining fibres' Elect. Lett. 20(3) pp 119-121 (2nd Feb. 1984).
6. TSUBOKAWA M., HIGASHI T. and NEGISHI Y. 'Mode couplings due to external forces distributed along a polarization maintaining fibre: an evaluation' Appl. Opt.27(1) pp 166-173 (1st Jan 88).
7. CHEN S., MEGGITT B. T. and ROGERS A. J. 'Novel electronic scanner for coherence multiplexing in a quasi-distributed pressure sensor'. Elect. Lett. 26 (17) pp. 1367-9 (16th Aug 1990).
8. DZIEDZIC S. M., STOLEN R. and ASHKIN A. 'Optical Kerr effect in long fibres' Appl. Opt. Vol 20 pp 403-6 (1981).

## TH1.3      Structured Metal Coatings For Distributed Fiber Sensors

L. Falco, O. Parriaux

Swiss Center for Electronics and Microtechnology,  
Research and Development, CH-2000 Neuchâtel, Switzerland

### Abstract

A transducer continuum is integrated to the fiber coating by means of a sequence of on-line sputtering, electro-plating, photolithography and periodical etching processes. Applications to the distributed sensing of temperature, strain and pressure are reported.

### 1. INTRODUCTION

The present paper describes a technology whereby the organic coating of standard fibers is overcoated by a thin metal single- or multilayer. This non-organic overcoating can serve several purposes in the field of distributed sensors. First, it can be the stable and well defined interface between the sensing fiber and a monitored medium as in composite materials and skins (1) as well as in concrete structures. Second, this overcoating can be given the additional function of a continuum of transducers after it has been periodically patterned so as to induce microbending at a prescribed spatial frequency under the action of a selected measurand (2). Amongst the possible applications of this transducer configuration, temperature, pressure and elongation will be demonstrated.

### 2. THE TRANSDUCING MECHANISM

The continuous microbending transducer results from the periodical perturbation of the circular cylindrical symmetry of the metal overcoating. The field of any physical and chemical quantity along the fiber can be detected, provided it can translate into a stress field distributed within the bimorphous coated fiber line. The spatial frequency of the microbending depends on the mode coupling effect that one wants to use. Since it amounts to a flexion of the fiber rod, its spatial period  $\Lambda$  is down-limited to a few fiber ODs. This means that forward mode coupling only can be expected.

In the case of graded index multimode communication fiber, the coupling takes place between the groups of the almost degenerate fiber modes and ends up with a local or semi-local loss of power. The typical microbend period in this case is  $\Lambda \approx 1.3$  mm. OTDR is the preferred read-out technique allowing the spatially resolved monitoring of a measurand field. Similar coupling to radiation modes can also be achieved with single-mode fibers if  $\Lambda$  is adjusted so as to couple the guided mode to a leaky mode (3).

In the case of a dual-mode fiber (high birefringence fiber (4) or dual LP mode fiber (5)), the coupling takes place between two well guided modes. This scheme is therefore low loss. High dynamic range and short response time can be expected with a transit time spatial demultiplexing read-out technique (6). The spatial period in the  $LP_{11}$ - $LP_{01}$  case is of the order of 0.5 mm (5).

### 3. THE TRANSDUCER TECHNOLOGY

The transducer continuum is realized by on-line processes. The fiber is any coated fiber available on the market. A first contact layer is deposited by sputtering. It is a copper or aluminum film of 200 nm thickness. The sput-

tering machine performs an on-line coating. It is equipped with two feed-throughs which allow the processing of the fiber at the speed of 2 meters/min. Two opposite targets give the coating a good uniformity.

The fiber with its anchorage metal coating is then installed in a low traction force on-line electroplating machine where the metal thickness is augmented to a few microns. The final thickness is decided by the desired sensitivity. The type of metal(s) depends on the measurand (e.g. palladium for  $H_2$  detection) and also results from considerations on the built-in residual stress within the bimorphous line.

Finally, if required, the metallized fiber undergoes the on-line periodic structuring: photoresist dip-coating, prebaking, driving by a drum with a UV lamp inside and a periodic mask on its periphery, resist development, rinsing and final metal etching. The spatial frequency of the mask is slightly chirped so as to accommodate possible variations of the fiber characteristics.

#### **4. SENSOR APPLICATIONS**

The demonstrations hereafter have been achieved with 50/125 graded index fibers. A polyimide protective coating was chosen for possible medium temperature applications and also because it is thin enough to limit creeping effects.

##### **a) Temperature Sensing**

The temperature dependence of the losses of a 20 meter long fiber is represented in figure 2 for a 8  $\mu m$  thick copper coating. The sensitivity is very high; 0.08 dB per 10 meters per  $^{\circ}C$  at a value of 1 dB per 10 meters at an arbitrary 80 $^{\circ}C$  temperature threshold. The various curves of figure 2 represent a large number of thermal cycles. The reproducibility is remarkably good if one keeps in mind the existence of the organic coating. This means that such scheme could practically be used in a distributed fire alarm system provided the excess loss at ambient temperature can be made negligible. This is not the case in Fig. 2 but it is indeed what can be achieved by adjusting the metal growth conditions.

##### **b) Elongation Sensor**

The very same transducer configuration can be used as a strain sensor. When the fiber experiences an elongation, the neutral line tends to remain rectilinear which causes the perturbed bimorphous fiber line to undulate at the prescribed period. Figure 3 illustrates the results corresponding to a nickel coated fiber submitted to a traction force up to 3 Newton. Curves a and b are for a nickel thickness of 1 and 2  $\mu m$  respectively.

##### **c) Pressure Sensor**

The same structure with the etched notches of the metal coating filled by another material of different hardness can be made pressure sensitive. Such scheme can only be thought of for large pressure. Figure 4 illustrates the pressure dependence of the transmission of a 20 m long fiber coated with an etched nickel film of 4  $\mu m$  thickness which was in turn coated by a Dow Corning 184 resin. The fiber was submitted to a sequence of two pressure values, 4.5 bar and atmospheric pressure. From figure 4 one retrieves a typical sensitivity of -0.054 dB/m/bar, assuming a linear dependence.

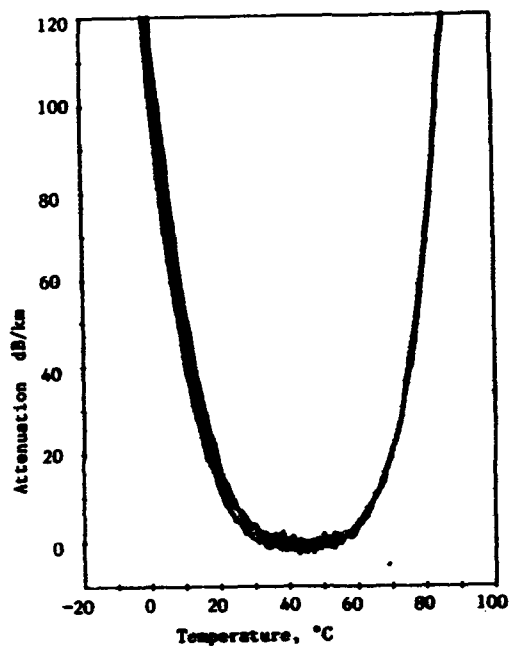
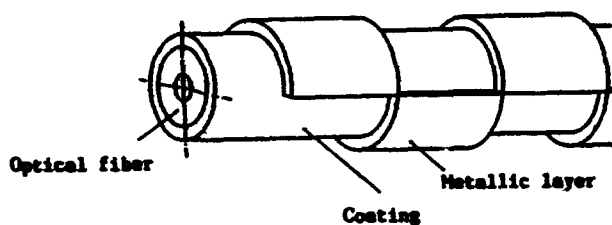


Fig. 1 Fiber with multimorph structure. Fig. 2 Attenuation in function of temperature for multiple cycles.

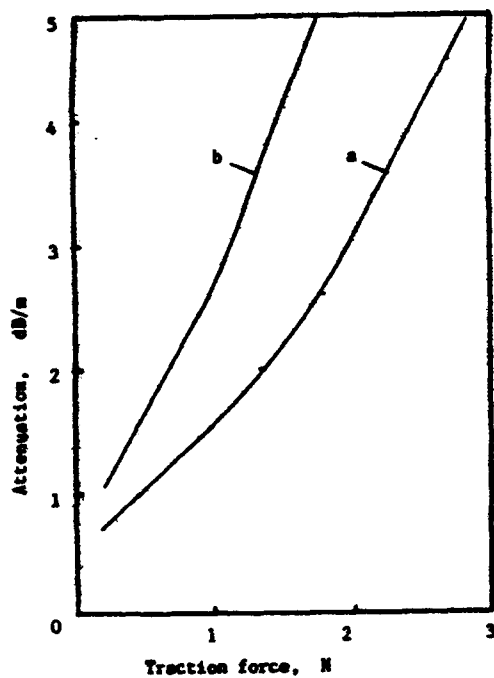


Fig. 3 Attenuation in function of elongation force for:  
a - Nickel thickness 1 micron  
b - Nickel thickness 2 microns.

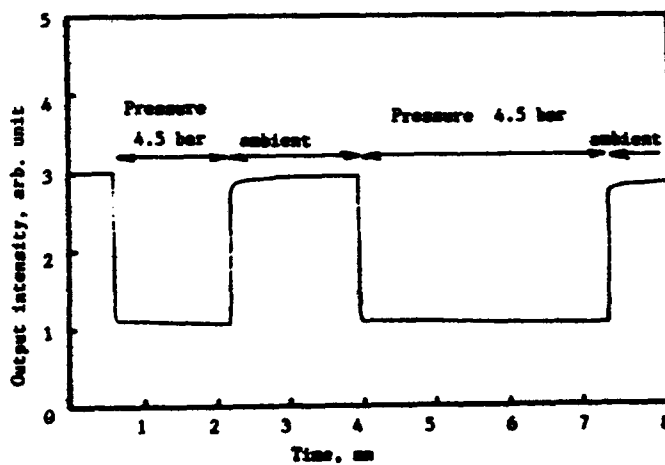


Fig. 4 Output signal for a sequence of two pressure values, ambient and 4.5 bar.

## 5. DISCUSSION

The general features of the described transducer technology can be summarized as follows:

1. This technology is basically cheap since on-line processes exist for all steps of the fabrication.
2. It uses standard fibers with their original protective coating.
3. The non-organic coating can be prepared as an interface having the desired properties with a host medium.
4. It can be best used in distributed ON-OFF and low accuracy sensors.
5. Its sensitivity can be easily adapted to a variety of sensor schemes: discrete and local, integrating semi-local and distributed sensors.
6. As compared with its hybrid counterpart in applications b) and c), the helical wired fiber (7), the present configuration shows non-zero sensitivity as from the lower values of the measurand range (figure 2).
7. Cross-sensitivity can be reduced by the selection of the metal (e.g. an etched Sn coating exhibits low temperature dependence).

## ACKNOWLEDGEMENT

The authors are grateful to the Swiss Foundation for Microtechnology Research (FSRM) and Securiton AG under a CERS project for their support of this work as well as to the companies VACOTEC SA and Flühmann AG for making the sputtering and galvanic growth resp.

## REFERENCES

1. J.S. Sirkis, A. Dasgupta, "Thermal plastic metal coating on optical fiber sensors", SPIE's Int. Symp. OE/FIBERS '91, Boston, 3-6 Sept. 91, Vol. 1588, Conf. 1588-09
2. L. Falco, P. Debergh, "Bimorphous distributed transducer for temperature threshold sensor", SPIE/Europtica, Hamburg, 19-23 Sept. 1998
3. A.W. Snyder, R.A. Sammut, "Radiation from optical waveguides: leaky-mode interpretation", Electron. Lett., Vol. 15, 1979, pp. 58-60
4. V. Gusmeroli, P. Vavassori, M. Martinelli, "A coherence-multiplexed quasi-distributed polarimetric sensor suitable for structural monitoring", OFS '89, Paris, Sept.18-20, 1989, pp. 513-18
5. G. Kotrotsios, O. Parriaux, F. Cochet, "Mode holding capability of dual-mode fibers", Opt. Lett., 15 (1990), p. 360
6. G. Kotrotsios, O. Parriaux, "White light interferometry for distributed sensing on dual-mode fibers". OFS '89, Sept.18-20, 1989, Paris, pp.568-574
7. A.L. Harmer, "Distributed microbending sensor", OFC/OFS '85, San Diego, p. 126

## TH1.4 An Ultra High Resolution Distributed Temperature Sensor

D.A.Thorncraft, M.G.Sceats, S.B.Poole

Optical Fibre Technology Centre  
University of Sydney, Australia

### Abstract

A high resolution optical fibre distributed temperature system using Raman backscatter and photon counting is presented. A spatial resolution of 10 cm with  $\pm 5^\circ\text{C}$  temperature resolution was obtained.

### Introduction

Over the past few years there has been an increasing interest in measuring the temperature over an entire length of optical fibre, creating the so-called distributed temperature system, or DTS. Many techniques have been proposed<sup>1-7</sup>, however all suffer from either limited spatial or temperature resolution. The most common form of DTS utilises the temperature dependence of the anti-Stokes component of the backscattered light. Such systems use either the Stokes - anti-Stokes ratio<sup>2</sup>, or double ended measurements<sup>3</sup> to obtain the required accuracy. The spatial resolution of such systems has been slowly improved from around 7.5 metres<sup>1</sup> to 1 metre (York DTS80). However there is a requirement for a DTS with an order of magnitude improvement in spatial resolution to around 10 cm over a fibre length of several hundred metres, with a temperature resolution of  $1^\circ\text{C}$ . Distributed temperature sensing systems developed in the past have had either high spatial or high temperature resolution, but not both in the one instrument. For example Stierlin et al in 1987 developed a DTS with a spatial resolution of 10cm and a temperature resolution of  $4^\circ\text{C}$ <sup>8</sup>, whilst most other systems compromise the spatial resolution to allow a  $1^\circ\text{C}$  temperature resolution.

As a first step towards this, we present here a DTS system based on the Stokes - anti-Stokes ratio with a spatial resolution of better than 10 cm and a measurement accuracy of  $\pm 5^\circ\text{C}$ . The system uses gated photon counting techniques and single mode fibre to obtain the required performance, and should be capable of  $1^\circ\text{C}$  resolution with further optimisation.

### Experiment

The experimental system is shown in Figure 1. The laser source was a mode locked Nd-YAG laser with a pulse width of 200ps FWHM at a repetition frequency of 100MHz. The output was frequency doubled to produce 532nm pulses with a width of 57ps FWHM to match the response of the detector and to increase the Raman scattering<sup>9</sup>. The Raman backscattered light from the single mode sense fibre was directed by the coupler to a monochromator filter system to separate the anti-Stokes component which was then incident onto a photomultiplier (PMT). The rise time of the PMT was approximately 300ps when operated in the photon counting mode.

The output from the PMT was time-correlated and stored in a 4096 channel multichannel analyser with each channel representing approximately 2.5ps. During a series of laser pulses the data collected formed an intensity distribution of the backscattered light (either anti-Stokes or Stokes) as a function of distance along the sense fibre. Once the data collection was completed it was downloaded to a personal computer for analysis and display of the computed temperature. To translate the very high spatial resolution in the experiment to the 5cm resolution envisaged in the prototype system, the experimental data was smoothed by performing a running average over 200 data points for the entire temperature trace. The resulting processed data now represents data taken at 5cm intervals.

The use of single mode fibre reduced the effect of dispersion on laser pulse broadening and backscattered photon arrival time spread. This was of particular importance due to the narrow laser pulse and desired timing/spatial resolution of the system.

The integration time required for a given temperature resolution is determined by the speed of the processing

electronics and the short term laser stability. The timing electronics was triggered from a PIN photodiode placed at the end of the 90cm long sense fibre. The processing electronics had a 10 microsecond timing overhead/reset time which limited the data throughput and consequently an integration time of 6 minutes was used, giving a calculated signal to noise ratio of 18dB and, hence, an expected temperature resolution of 6°C. Due to this high timing overhead, the Raman signal was collected from both output arms of the coupler, as shown in Figure 1. In a system with improved electronics only one sense fibre will be required, with the trigger signal being taken from the other output arm of the coupler.

### Results

The temperature and spatial resolution of the system was tested by constructing two wire wound heaters, each 10cm long by 10mm diameter. The sense fibres were placed axially through the silica heater tubes. Data was taken with the two heaters separated by 14cm with measured centre temperatures of 65°C in one and 85°C in the other. The time taken between data and normalisation traces was about 10 minutes, reducing the chances of laser or timing changes, and shows the measured temperature resolution was approximately  $\pm 5^\circ\text{C}$  for an integration time of 6 minutes. The resulting temperature trace is shown in Figure 2.

The spatial resolution is defined as the spatial separation of the 10% and 90% points on a given temperature step. A 20cm long wire wound heater heated the fibre to 80°C with a centre-line temperature profile measured by a type K thermocouple. The measured spatial resolution was less than 10 cm.

### Discussion

The results clearly show that a distributed temperature sensor spatial resolution of better than 10cm is possible. However, the reset time of the data acquisition system limits the temperature resolution attainable within a reasonable integration time. Calculations indicate that a resolution of 1°C with a measurement integration time of 1 minute should be attainable. However, the temperature resolution of 5°C compares favourably with the calculated resolution of 6°C for the present system.

It can be seen in Figure 2 that there are end effects in the ratio trace. Despite the short fibre lengths used, this effect does not influence the final temperature trace. These end effects are due to laser pulse amplitude and timing shifts between the time taken to obtain the temperature and normalisation traces and could, in any case, be removed by the simultaneous acquisition of both the Stokes and anti-Stokes signals. The effect of laser amplitude and phase variations are most apparent at the ends of the fibres where the Raman backscatter intensity has a high slope and small timing or amplitude variations result in a high error in the calculated temperature. A reduction in integration time and the collection of temperature and normalisation data simultaneously will therefore assist in reducing the effect of laser and timing variations.

The sense fibre length is currently limited by the repetition rate of the mode-locked Nd:YAG laser. However, either short-pulse semiconductor diode lasers or mode-locked fibre lasers<sup>10-12</sup> provide a route to reducing the laser repetition rate and hence increasing the sense fibre length. Calculations indicate that a 1°C temperature resolution should be achievable over 1km of fibre with an initial integration time of 5 minutes. This system will find immediate application in many areas including monitoring of power transformer hot spots, cure monitoring of composite structures and any applications in which both high temperature and spatial resolution are required.

### Conclusion

We have successfully demonstrated a high resolution distributed temperature sensor with 10 cm spatial resolution. A temperature resolution of 5°C was demonstrated, although 1°C should be achievable with faster integration electronics.

Whilst further experimental work is required to optimise the system, 10cm spatial resolution and 1°C temperature resolution should be readily achieved over up to 1km of sense fibre.

### Acknowledgements

This work was funded by the Department of Industry, Technology and Commerce under a Generic Industrial Research and Development grant 17011. The authors would like to thank Mr David Psaila for fabricating the fibre coupler used in this work.

### References

1. Hartog, A.H. et al., "Distributed Temperature Sensing in Solid Core Fibres". *El. Lett.*, 1985, 21, 23, pp. 1061-1062
2. Dakin, J.P., et al., "Distributed Optical Fibre Raman Temperature Sensor using a Semiconductor Light Source and Detector". *El. Lett.*, 1985, 21, 13, pp. 569-570
3. Hartog, A.H., "A Distributed Temperature Sensor Based on Liquid Core Fibres". *Jnl Lightwave Technology*, 1983, LT-1, 3, pp. 498-509
4. Rogers, A.J., "Polarisation optical time domain reflectometry". *El. Lett.*, 1980, 16, pp. 489-490
5. Marrone, M.J., et al., "Temperature Dependence of Stress Birefringence in an Elliptically Clad Fibre". *Opt. Lett.*, 1983, 8, 2, pp. 127-129
6. Farries, M.C., et al., "Distributed Temperature Sensor Using Nd<sup>3+</sup> Doped Optical Fibre". *El. Lett.*, 1986, 22, 8, pp. 418-419
7. Culverhouse, D., et al., "Potential of Stimulated Brillouin Scattering as a Sensing Mechanism for Distributed Temperature Sensing". *El. Lett.*, 1989, 25, 14, pp. 913-915
8. Stierlin, R. et al., "Distributed Fibre-Optic Temperature Sensor Using Single Photon Detection". *App. Optics*, 1987, 26, 8, pp. 1368-1370
9. Samson, P.J., *Electron. Lett.*, 1990, 26, 163
10. Duling, I.N., et al., "High-Power, Mode-Locked Nd:Fibre Laser Pumped by an Injection-Locked Diode Array", *El. Lett.*, 1988, 24, 21, pp. 1333-1335
11. Geister, G. and Ulrich, R., "Neodymium-Fibre Laser with Integrated-Optic Mode Locker." *Opt. Comm.*, 1988, 68, 3, pp. 187-189
12. Howell, M.D., et al., "Nd<sup>3+</sup> doped fibre laser with integrated acousto-optic mode-locking." *SPIE 1171 Fibre Laser Sources and Amplifiers* (1989), pp. 309-315



# Figures

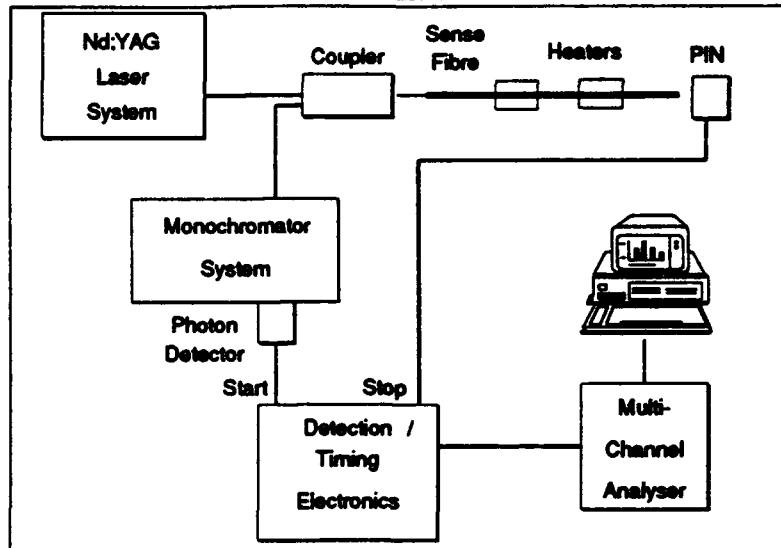


Figure 1 Proposed High Resolution Distributed Sensor System

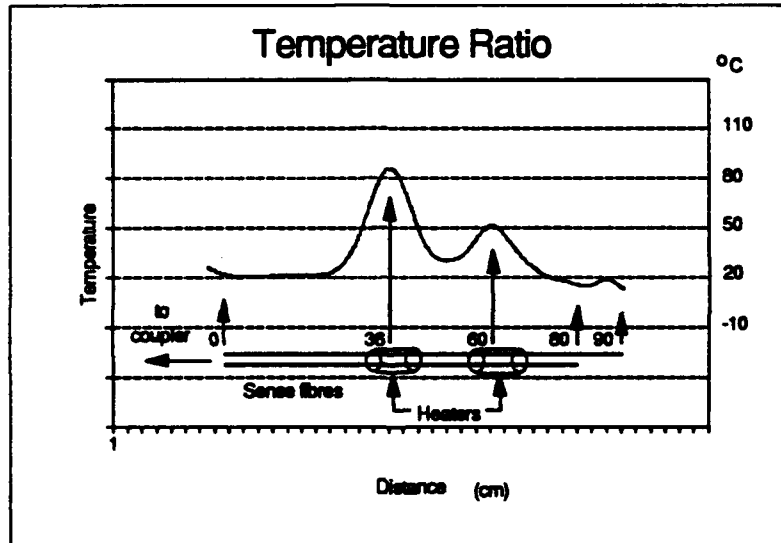


Figure 2 Temperature Trace.

## **TH1.5      A Temperature Optical Fiber Sensor Network: From Laboratory Feasibility To Field Trial**

H. FEVRIER \*, J. HERVO \*, S. ARTIGAUD \*, A. TARDY \*, M. JURCZYSZYN \*,  
A. DEROSSIS \*, D. BOULLERET \*\*, J.L. PIERRAT \*\*

\* Alcatel Alsthom Recherche, Route de Nozay, 91460 Marcoussis, France

\*\* GEC Alsthom, 3 Avenue des Trois Chênes, 90018 Belfort Cedex, France

### **INTRODUCTION**

In recent years there has been considerable interest shown in the optical sensor design and multiplexing concepts. Optical fiber sensors have been successfully demonstrated for a variety of physical fields. The aim of our study was to demonstrate a temperature optical fiber sensor network for electrical engineering applications and especially for AC generators. The need was to monitor individually the temperature of the water boxes of the stator bars, and therefore, optical fiber sensors were attractive candidates due to their immunity to the high electric fields encountered inside these generators. Moreover, as you can have up to 200 points to monitor, we needed a sensor concept compatible with a multiplexing technique.

### **PRINCIPLE OF OPERATION OF THE OPTICAL SENSOR NETWORK**

The basic principle of operation of the sensor (see Figure 1) is the variation of the reflection coefficient at the splice interface between a sensitive polymer whose index of refraction greatly varies with temperature and the optical fiber. Due to the very low insertion loss of such a sensor (typically 0.075 dB in transmission), we have the ability to achieve time-multiplexing of different sensors (10 to 20 sensors) located on the same optical fiber. To ensure time-multiplexing, we use a special OTDR we developed. The OTDR equipment characteristics are an operating wavelength of 904 nm, a pulse width of 12 ns, a pulse peak power of 3 W and a repetition rate of 16 kHz. We use a 100/140  $\mu$ m multimode fiber in order to get a high backscattering level. Inspecting the OTDR curve, we note the usual Rayleigh backscattering contribution with echoes surimposed on it corresponding to the mismatch of index of refraction of the different sensors. The amplitude of the sensor echo varies with temperature. In order to avoid any bias introduced for example by bending losses, we achieve a differential measurement by deriving the ratio of the echo amplitude relatively to the dark current baseline to the backscattering level. This ratio is then calibrated for the sensors as a function of temperature to give us a thermometric ratio. A typical calibration curve of such a sensor is presented on Figure 2. Figure 3 presents the OTDR trace of an optical line with 10 sensors. The minimal spacing between two sensors is 3 m due to the pulse width and the measurement method, and typical values in our experiments were 5 to 7 m. To achieve a 200 monitoring points system, we will for example use 10 optical lines of 20 sensors multiplexed via an opto-mechanical device (optical line switching). Finally, due to the power budget evaluation, the telemetring range of our system is up to one kilometer.

### **ENVIRONMENTAL BEHAVIOR**

To achieve most of the tests, we used a simple butt-splicing device for the optical fiber to realize the sensors. At first, we made thorough tests of different sensitive polymers in order to reach our targets which were : temperature accuracy of 1°C and temperature operating range from 20°C to 120°C. At this stage, we tested 21 polymers and five of them were selected. Then, we made a number of optical lines of sensors to survey as a function of time and temperature the ageing behavior of the polymers i.e. polymer stability in terms of accuracy, reproducibility, ... These tests could last up to six months. At this stage, two polymers were selected and we then focussed our attention over one polymer which fulfilled these basic specifications.

Due to the hydrogen atmosphere within the AC generators (2 to 5 bars), we checked during one month with one hydrogen atmosphere and an operating temperature of 90°C that hydrogen had no influence over the calibration curve of the thermometric ratio.

Some experiments showed us that humidity had some influence over the calibration curve. Therefore, at this step we had to use a specially designed packaging taking into account the need for humidity protection, use of an optical cable instead of an optical fiber, dimensions compatible with the application, ability to use this package to go through vibration and electrical field tests,...

The design of the packaging led us to outer dimensions of 50x10x7 mm and to the use of an aeronautic optical cable whose main characteristics are : tight structure, outer diameter of 1.5 mm and operating range up to 125°C. Seven resins were tested using this new packaging for the sensors in order to find the one enabling us to ensure a proper humidity barrier.

Vibrations is a main environment constraint in AC generators. Vibration tests were first conducted on 3 packaged sensors. Experimental conditions were : 100Hz frequency, 1 to 20 g acceleration i.e. 50 to 1000  $\mu\text{m pp}$ , 1 to 24 h test duration along one axis. Having passed this test, more severe conditions were applied on 3 other sensors : a combination of vibration and thermal cycling. Experimental conditions were : 100Hz, 20g,  $10^7$  vibration cycles, thermal cycling from 30 to 90°C, tests along 2 axes.

Finally, tests were conducted with 4 packaged sensors on a prototype of ends of two stator bars. The sensors were fixed on the water boxes. The aim of these experiments was to check that electrical conditions had no influence, and especially to choose the right package (nature of the metal parts used) in order to ensure a good thermal contact and to avoid any induced eddy field currents (amagnetic metal) which would bias the temperature measurements. Experimental conditions were : 40 to 85°C operating temperature, 5 kA current.

## FIELD TRIAL

Owing to these results, it was decided to realize a field trial in a 250 MW AC generator located in the suburbs of Paris. An optical line of ten sensors was implanted in September 1990 for a long term experiment. Figure 4 presents the schematic diagram of the experiment. Five sensors, coupled with five thermocouples, were located on the amagnetic shield which is not an electrical field sensitive part. Five other sensors were located on the active part of the machine (water boxes). This implantation allows us to monitor different possible calibration drifts of the sensors. To perform such an experiment, we had to develop a lot of accessories like optical cable feedthroughs. The sampling time cycle of the whole equipment has been slowed down to approximately 3 minutes due to the large amount of collected data.

Figure 5 shows a good correlation of the temperatures given by an optical sensor on the amagnetic shield and its coupled thermocouple. Interesting data processings can be performed to establish the relationship between different temperatures within the machine. Finally, a clear relationship is shown on Figure 6 between the temperature of a water box optically measured and the square root of the sum of the squared active and reactive powers.

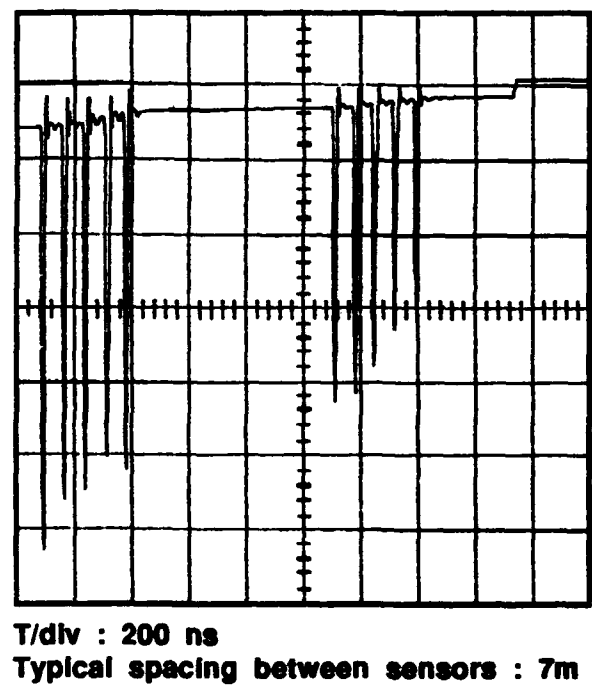
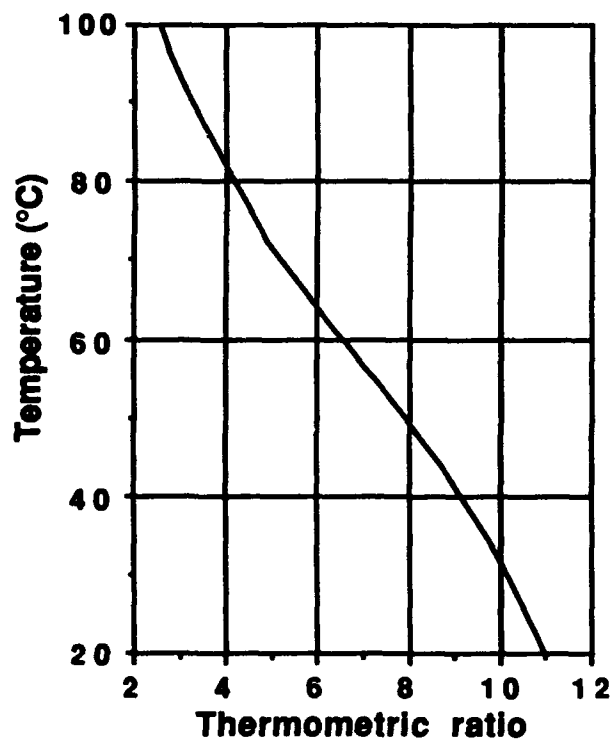
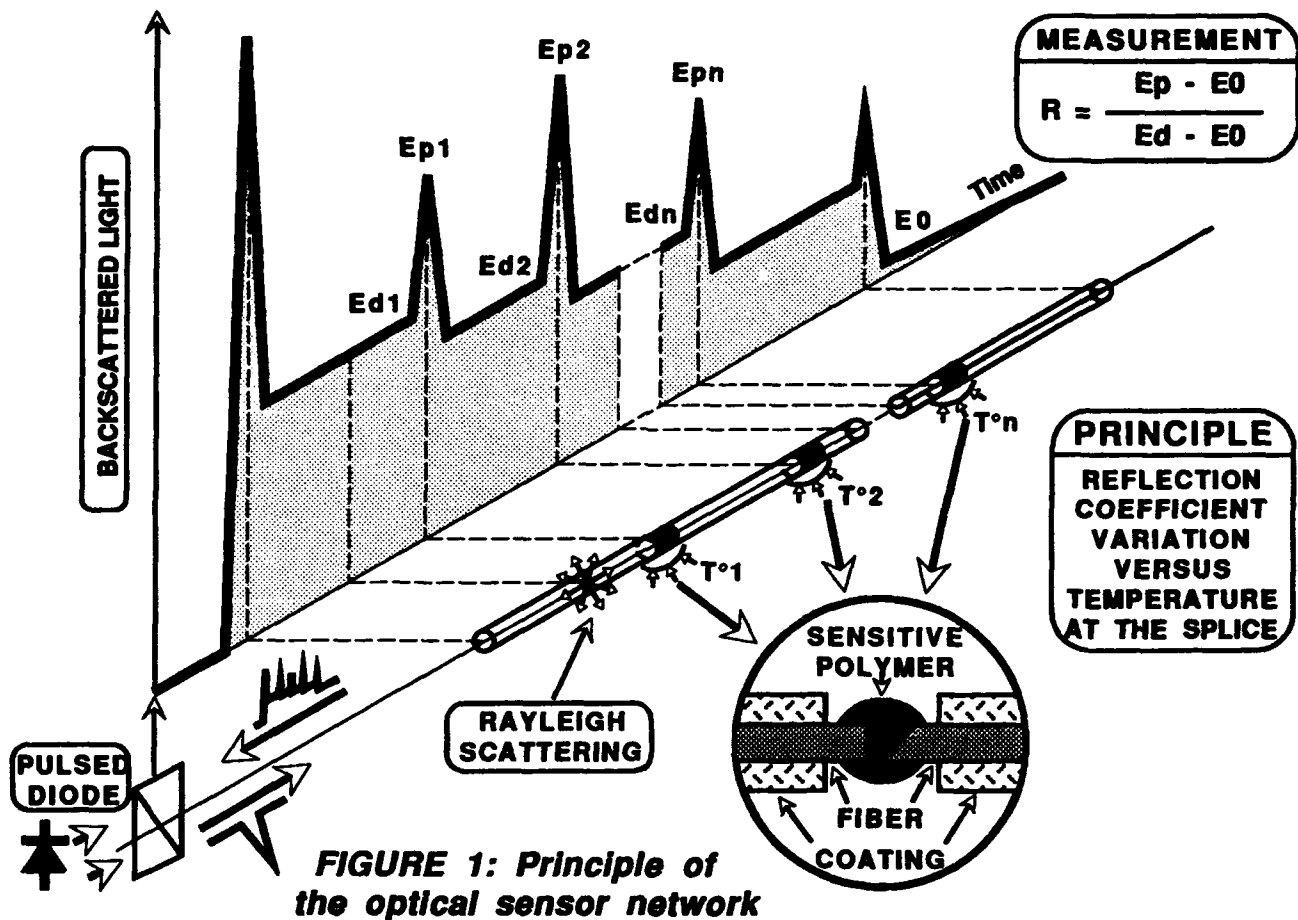
This experiment has been running for eleven months and the ten sensors and the different accessories had no damage during this period.

## CONCLUSION

As a conclusion, this study and this field trial experiment are a contribution to the demonstration of the maturing of the optical fiber sensor field in the recent years. This kind of sensor network can be used in the future to monitor large electrical engineering machines in order to optimize their running point, to prevent any accidental damage and to forecast their maintenance.

## ACKNOWLEDGMENTS

The authors are grateful to the staff of GEC Alsthom (Belfort) for technical assistance and fruitful discussions. This work was funded by EDF Etudes et Recherches and GEC Alsthom.



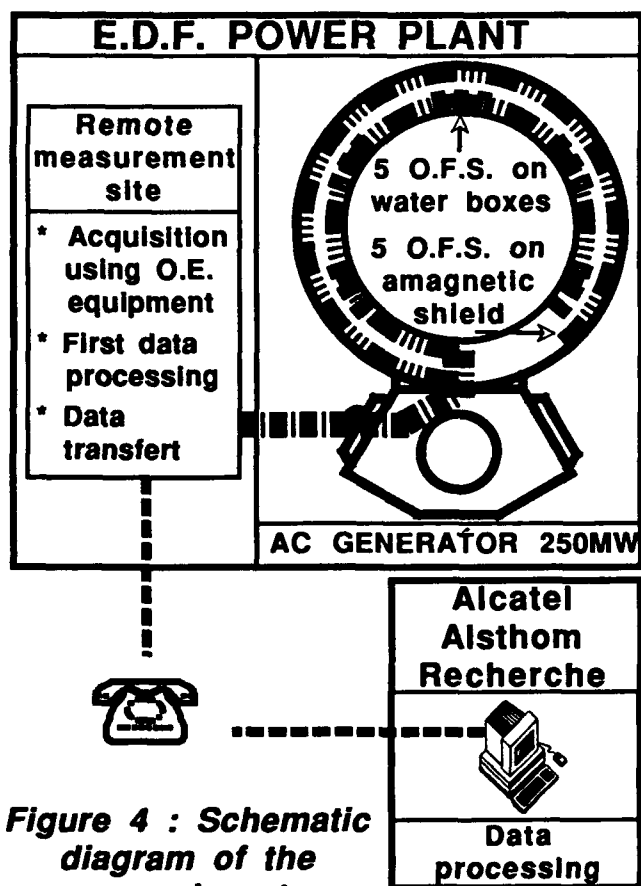


**Figure 4 : Schematic diagram of the experiment**

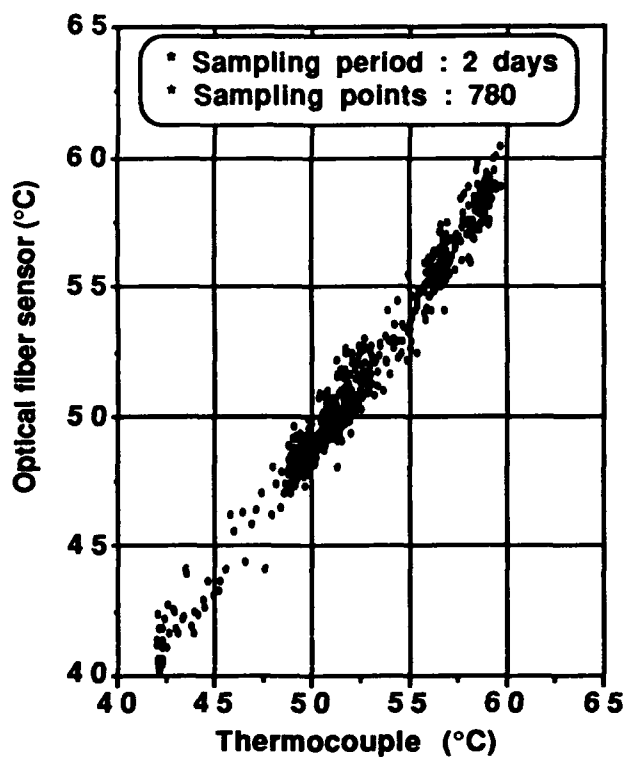


**Figure 5 : Correlation of the temperature given by an optical sensor and its coupled thermocouple**

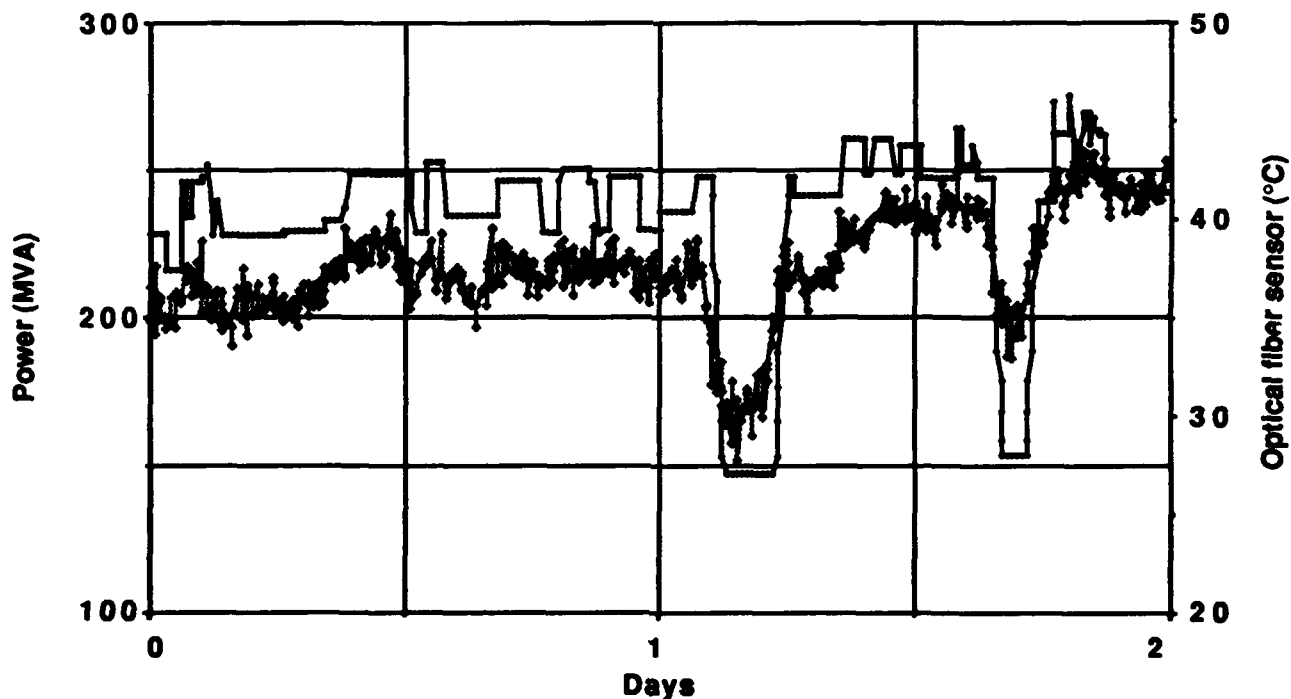


**Figure 6 : Relationship between the water box temperature and the square root of the sum of the squared active and reactive powers**

# TH1.6 Code-division Multiplexed Interferometric Array With Phase Noise Reduction And Low Crosstalk

A. D. Kersey, A. Dandridge and M. A. Davis

Optical Sciences Division  
Naval Research Laboratory  
Washington, DC, 20375-5000

## Abstract

The results obtained using code-division multiplexing with an array of eight sensors are reported. We demonstrate a phase noise sensitivity of 100  $\mu\text{rads}/\sqrt{\text{Hz}}$ , and show that crosstalk levels  $\sim 60$  dB can be achieved using this approach.

**Introduction:** Spread spectrum (SS) and code division multiplexed (CDM) techniques [1] have been applied to a variety of communications applications, including optical fiber systems [2]. This type of signal processing has also been previously investigated for optical time-domain reflectometry (OTDR) based sensing [3], and more recently, has been proposed and tested as a means for multiplexing interferometric sensors [4]. In this work, the interrogating laser source is modulated using a pseudo-random bit sequence (PRBS) of length  $2^m-1$  (maximal length sequence, or m-sequence), and correlation is used to provide synchronous detection to identify specific sensor positions. A delay equal to an integer multiple of the bit (or 'chip') period separate the sensors. The received signals from the array are then encoded by delayed versions of the PRBS, and correlation techniques can be used to extract the individual signals. Although this method may provide advantages in terms of power budget for time-division multiplexed systems, it would also seem to be limited by excess phase noise effects arising due to mixing of time co-incident pulses from different sensors, and relatively high crosstalk between sensors. In this paper we address these limitations of the technique, using a detection/signal processing approach which yields improved phase noise performance, and crosstalk levels lower than those expected from consideration of the code length.

**Principle:** Figure 1 diagrammatically represents the principle of operation of the CDM approach applied to an interferometric sensor array [4]. The PRBS input optical signal is fed to each of the  $N$  sensors, delayed by a multiple,  $n_j$ , of the bit period  $T$ , where  $j$  denotes a specific sensor ( $1 \leq j \leq N$ ). The total output signal comprises the intensity sum of the overlapping delayed PRBS sequences (each modified by the appropriate sensor transfer function). This results in a complex up-down staircase-like function at the optical detector which can be decoded using synchronous correlation-detection involving multiplication of the received signal with an appropriately delayed reference PRBS.

In spread-spectrum communications systems, this synchronous detection, or de-spreading process, decodes the information channel of interest whilst spreading any interfering signal occupying the same frequency spectrum. It can be shown that the amplitude suppression ratio of an interfering signal relative to a coded information signal is given by [1]

$$R = -20 \log_{10} [2^m-1]. \quad (\text{dB}) \quad (1)$$

In spread spectrum communications systems, this property is used to discriminate between the wanted coded signal and any uncoded 'interfering' signals. However, in the case of a sensor array, all signals received are coded but with different relative delays. Here we demonstrate that this allows the sensor signals to be demultiplexed with low crosstalk, provided the correct correlation signal processing is performed.

Normally, in investigating the correlation functions of noise-like codes, bipolar (+1, -1) digital states are of interest. The auto-correlation functions of m-sequence codes are characterized by peaks at  $\tau = 0, \pm kT[2^m - 1]$  (k- integer) of height  $= (2^m - 1)$  and width T on a baseline of -1. However, in the operation of the multiplexed sensor system, the optical power coupled to the array is switched on and off according to the m-sequence code, which represents a unipolar code,  $f(t) = 1, 1, 0, \dots$  sequence. If the detected optical signal is gated by a bipolar sequence;  $f'(t+\tau) = +1, +1, -1, \dots$ , the correlation function of interest is the modified auto-correlation:

$$\psi(\tau) = \int_{-\infty}^{\infty} f(t) * f'(t+\tau) dt. \quad (2)$$

This correlation function, for m-sequences, has peaks at  $\tau = 0, \pm kT[2^m - 1]$  (k- integer) of height  $= 2^{(m-1)}$  and width T on a zero baseline. Consequently, the correlation function is zero for any asynchronous alignment of the codes. This occurs because any m-sequence code contains  $2^{(m-1)}$  'ones' and  $(2^{(m-1)} - 1)$  'zeros' (corresponding to +1 and -1 digital states in the bipolar code  $f'(t)$ ). When the codes are synchronized, all the 'ones' in  $f(t)$  align with +1 states in the bipolar code  $f'(t)$ , whereas the zeros in  $f(t)$  align with the -1 states in  $f'(t)$ . This gives the correlation peak of height  $2^{(m-1)}$ . For any asynchronous alignment of the codes, half the 'ones' in  $f(t)$  align with +1 states in the bipolar code  $f'(t)$ , whereas the other half align with the -1 states in  $f'(t)$ ; This gives the correlation value of zero. This always holds for any asynchronous alignment of the codes, and thus ensures that delayed coded signals can be rejected with high isolation. In a multiplexed system, this property can be used to provide good isolation between sensors, providing the code length is greater than the number of sensors in the array., i.e.  $(2^m - 1) \geq N$ .

**Experimental:** The array system was of the basic ladder-type form shown in Figure 1, as previously used in our work on conventional time division multiplexing schemes [5]. The array comprised eight sensor elements coupled in the ladder topology, with delay coils of 30 m length separating the tap-couplers in the input fiber bus which feeds optical power to the sensors. Experiments were conducted with a variable number of sensors operating; this was accomplished using sharp bends in the output fiber of certain interferometers to attenuate the optical signal. This allowed the operation of the multiplexing scheme to be assessed for increasing numbers of sensor elements. The optical input to the array was derived from a 830 nm diode laser operating in a CW mode. An acousto-optic modulator (AOM) was used to encode the input to the sensor array with the PRBS which was generated using a linear shift register generator. The clock frequency was 6.8 MHz, corresponding to a single bit length of  $\sim 145$  nS, which matched the 30 m fiber delay between sensor elements. The electronic gating circuit used to perform the balanced-synchronous detection at the photo-detector output is shown in the inset box in Figure 1; this was the key element in obtaining low crosstalk performance with the array.

**Results:** Figure 2 shows the type of photodetected signals observed. The received signal with just one sensor signal coupled to the output (Figure 2.a) clearly shows the faithful reproduction of the PRBS code applied to the input. The complex form of the photodetector signal obtained with all 8 sensors coupled to the output (Figure 2.b) arises due to the multiple overlapping codes with varying delays. The code length used in these experiments corresponded to 31 bits ( $m=5$ ). One problem which is obviously apparent from Figure 2.b is the noise generated by the mixing of the optical components from the various sensors at the detector. To reduce this noise, we have utilized a suppression technique based on RF modulation of the laser [6], which effectively heterodynes the phase-noise to harmonics of the (RF) modulation frequency, thus improving baseband signal-to-noise. Figure 3 shows the measured phase noise of one sensor (at 1 kHz) for 1, 3 and 8 sensors coupled to the output, with and without phase noise reduction. A sensitivity of 100  $\mu\text{rads}/\sqrt{\text{Hz}}$  was achieved for a single demultiplexed sensor output with all 8 sensors operating (Figure 4).

The crosstalk between sensors was measured for the array configured with just three adjacent sensor outputs coupled to the output fiber. The sensors were driven with a phase shift signal of 300 mrad rms, each at a slightly different frequency (800 Hz, 1.0 kHz and 1.2 kHz). The reference PRBS delay was set to demultiplex the second sensor, and the crosstalk between sensors was evaluated using a spectrum analyzer. To ensure a reliable measurement of crosstalk was made, the bias phase of each sensor was adjusted so that all three sensors were simultaneously in quadrature. A crosstalk of -42 dB was obtained. Changing the code length to 7 or 15 bits ( $m=3, 4$  respectively) did not affect this result. We attributed this to the overlapping of the edges of the slightly non-rectangular pulses generated by the input modulator (AOM). To overcome this we modified the electronics to produce return-to-zero (RZ) type input pulses. The type of optical signals then produced at the detector is shown in Figure 5. The crosstalk of the system in this mode improved to  $\sim 60$  dB, as shown in Figure 6. Again, for the three-sensor experiment this result did not depend on the length of the code used, and was obtained for a 7, 15 and 31 bit codes<sup>†</sup>. For the 7-bit code, this represents a 43 dB improvement in expected crosstalk.

**Conclusions:** We have reported the operation of a code-division multiplexed interferometric sensor array with relatively low phase noise. We have demonstrated that the technique can be used to provide crosstalk levels as low as -60 dB between sensor elements in the array.

This work is supported by the Office of Naval Technology.

#### References:

1. R. C. Dixon, "Spread Spectrum Systems", Wiley, 1984.
2. P. R. Prucnal et al., J. Lightwave Technol., LT-4, p. 547, 1986.
3. J. K. A. Everard, Proc. Fiber Optic Sensors II, SPIE vol. 798, p. 42, The Hague, 1987.
4. H. S. Al-Raweshidy and D. Uttamchandani, Proc. Fiber Optics'90, SPIE vo. 1314, p. 342, London, 1990.
5. A. D. Kersey and A. Dandridge, Electron Lett., 25, p. 1298, 1989.
6. A. D. Kersey and A. Dandridge, Electron Lett., 22, p. 616, 1986.

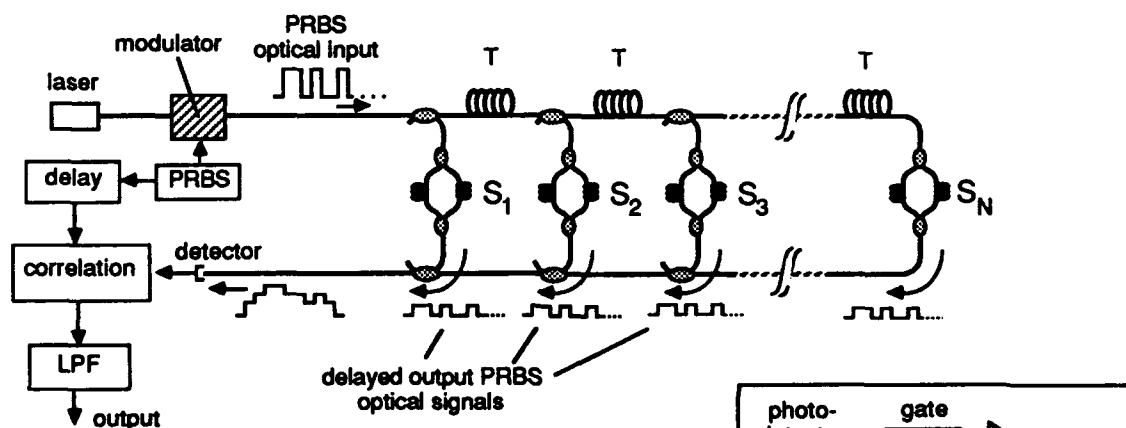
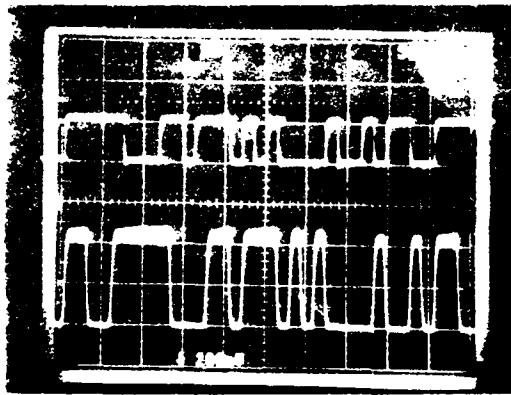


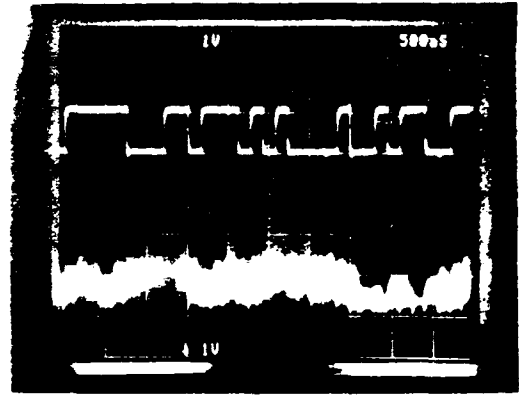
**Figure 1.** Basic schematic of the interferometric sensor array using code-division multiplexing. Inset to right shows balanced gating circuit used in signal processing.

<sup>†</sup> It is interesting to note that this result compares to rejection ratios between coded and uncoded signals of -17 dB, -24 dB and -30 dB for the same 7, 15 and 31 bit sequences.





(a)



(b)

**Figure 2.** Input PRBS code (upper traces) and detected optical output (lower traces) for: a) a single sensor coupled to the output fiber, and b) all eight sensors.

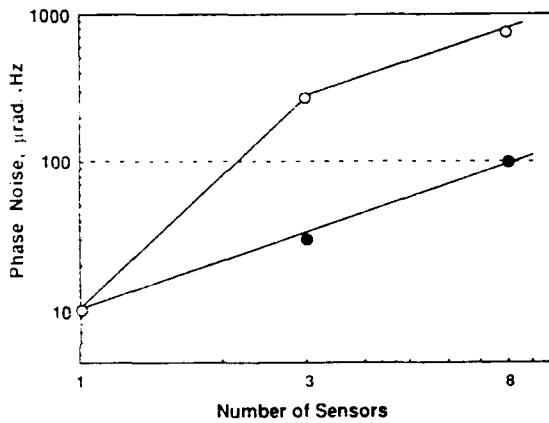


**Figure 3.** Variation in phase sensitivity for a single demultiplexed sensor vs. number of sensors multiplexed.

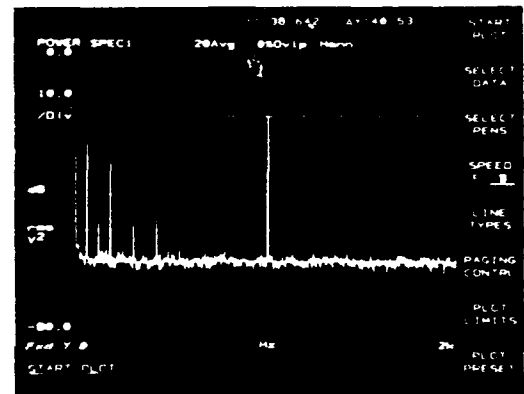


**Figure 4.** Phase noise sensitivity for a single demultiplexed sensor with eight sensors multiplexed: Test signal at 1 kHz corresponds to 20 millirads rms.

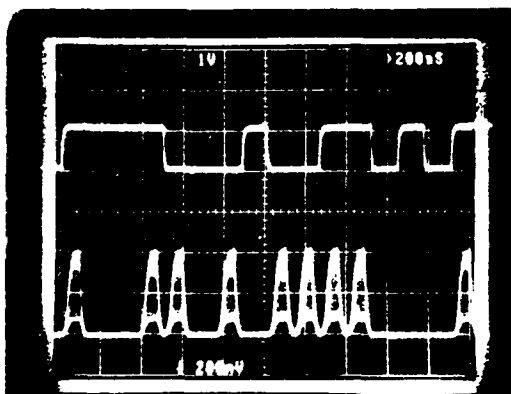


**Figure 5.** Pulse waveforms for a single sensor using return-to-zero input PRBS operation.

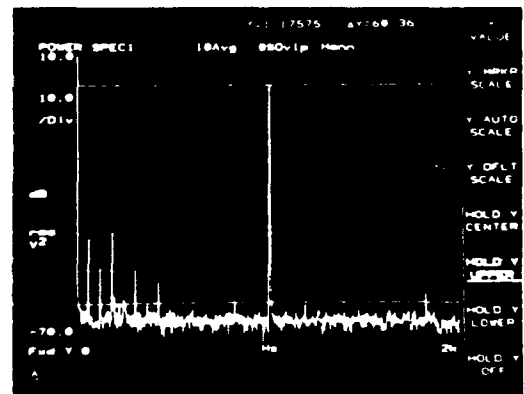


**Figure 6.** Measured crosstalk with three sensors operating: Note weak frequency components at 800 Hz and 1.2 kHz, 60 dB down on demultiplexed sensor signal at 1 kHz (central frequency component).

## TH1.7 An Improved TDM System Applied To The Multiplexing Of Silicon Microresonator Sensors Exhibiting Identical Characteristics

Y.J. Rao, B. Culshaw, and D. Uttamchandani,  
*University of Strathclyde, Glasgow, UK*

Division of Optoelectronics, Department of Electronic & Electrical  
Engineering, University of Strathclyde, Glasgow G1 1XW, United Kingdom

### Summary

**Introduction:** There has been much interest in the use of mechanically resonant structures as a means of measuring environmental parameters.<sup>1</sup> The greatest advantage of such resonator sensors is that the value of the measurand of interest is obtained by the measurement of resonant frequency of the sensor. This measurement for practical purposes is insensitive to light intensity transmission fluctuations, therefore free from corruption compared with conventional analog modulation. The measurement may also be made with extremely high accuracy. Additionally a frequency signal of the type obtained from the mechanical resonator may be transmitted along virtually any linear medium transmission line without distortion. In recent years much effort has been directed towards realizing a new class of silicon microresonator sensors for pressure, temperature, acceleration, vibration, mass flow.<sup>2-4</sup> These silicon microresonator sensors are usually fabricated using standard micromachining techniques, involving anisotropic chemical etching, and this promises the possibility of high volume, repeatable, and low cost production. The physically small dimensions of these microresonators (typically a few hundred micrometers long by tens of micrometers wide by a few micrometers thick) make them directly compatible with optical fibers for both optical excitation and interrogation, thereby enabling the realization of an all-fiber optically addressed silicon microresonator sensor which is compact, intrinsically safe, and electromagnetic interference free.<sup>5-6</sup> These characteristics may have special attractions in chemical, avionic, and in vivo medical applications. A multiplexing system which can automatically distinguish between responses of point silicon microresonator sensors exhibiting identical characteristics is very important for the practical applications of these sensors, because in practice point sensors in the multiplexing network must be interchangeable without any substantial recalibration to the system. However, there is little information on this topic to date.

Generally, the resonant frequency range of these sensors is between a few tens of kHz and a few hundred kHz and this is at least several times higher than the pulse repetition frequency (10kHz) of typical pulsed lasers used in prior TDM approaches.<sup>8-9</sup> Although the SAW pulse compression method using a multimode CW laser has been presented to improve average optical power, this method suffers from several drawbacks.<sup>10</sup> Firstly, the use of many high speed electrical components not only makes the system structure complicated, but has also the problem of matching these devices with each other. Secondly, the amplitude noise of the used multimode laser at high frequency (typically 60MHz) operation limits the system SNR. Finally, the improvement of crosstalk is limited by the performance of the SAW chirp filter. Furthermore, although a laser diode was utilised to improve the sampling frequency,<sup>11</sup> the technique for SMRS still has problems with both low optical power arriving at the detector, thereby resulting in low system SNR, and weak signal introduced by the very small light intensity modulation of SMRS.

In this letter, we report on the realization of an improved TDM system and its application to the multiplexing of silicon microresonator sensors. For the system developed, the SNR for shot-noise-limited case can be improved by at least 20 dB over that normally attained with a same laser

diode without any logic low intensity level adjustable. A sampling speed of up to 1MHz was used for the multiplexing of a four channel fiber optic network for use with four SMRS and simultaneously a more than 30dB system SNR were also obtained.

**System description:** The schematic of the multiplexing system is shown in Fig. 1. A Melles Griot 06DLL507 single mode quasi-CW GaAlAs diode laser head with thermoelectric cooling was used as the source, and operates at a wavelength of 830nm. Its output light intensity was modulated by a fast switching circuit (switching time  $\leq 8\text{ns}$ ) shown in Fig. 2. The advantage of this switching circuit is that it allows both logic high and logic low current levels to be adjusted independently such that the average optical power can be improved by increasing the logic low level. In our system, the modulation frequency and the width of the pulse train sent to the laser head were 1MHz and 40ns respectively, and the logic high level was adjusted to the maximum optical power output point (40mW). Compared with the ordinary TDM method, when the logic low level was adjusted to 57mA (giving an average optical power output of 10mW), the total average optical power output from the laser head was about 23.8dB greater than that from a same laser diode without any logic low intensity level adjustable. This means that the SNR for shot-noise-limited case can be improved by at least 20 dB due to the linear relationship between the average power and the SNR obtained from the eqn. 1 in Reference 8 and the Fig. 2 in Reference 10. The pulse train from the laser diode was launched into a 50 $\mu\text{m}$  core multimode fiber star network consisting of a 2x1 coupler and a 1x4 coupler. The forward excess loss and the excess reverse loss of the network were about 3.6dB and 6.4dB respectively. Four fiber delay line lengths differing by 10m were used to generate four pulse delay times from 100ns to 400ns with a time separation for the return pulses for each port of 100ns. An ANTEL ARX-SA ultra high-speed avalanche photodiode (APD) with a minimum detectable optical power of 50nW was utilized as the detector. Four electrical digital delay units D1-D4 were used to get the same pulse delay times with the optical delay times. The pulses P1 coming from the same pulse generator with two channel outputs were a little wider than that P2 sent to the laser driver. This reduced the demand for precise time-matching between the delayed electrical pulses and the delayed photoelectrical pulses. After amplification the return signals were sent to four WJ-S11 high speed electrical switches. The  $i$ th delayed electrical pulse opens the  $i$ th switch SW $_i$  and lets the  $i$ th delayed photoelectrical pulse pass through the SW $_i$ , and then closes the SW $_i$  before the  $(i+1)$ th photoelectrical pulse comes to the detector, where  $i \leq N-1$  and  $N$  is the number of the multiplexed sensors. Therefore, from the output end of the SW $_i$  we can obtain a pulse train amplitude-modulated by the vibration of the  $i$ th SMRS. By using an electrical low-pass filter we can remove the sampling pulses and obtain the envelope i.e. the resonant signal of the  $i$ th SMRS.

**Experiment:** The silicon microresonator sensor used in this work was a bridge structure which was 1.4mm long by 40 $\mu\text{m}$  wide by 2 $\mu\text{m}$  thick, clamped at both ends, with a 700nm thin aluminium coating evaporated on it. A periodic mechanical strain along the silicon bridge generated by the absorption of acoustic power produced by a piezoelectric transducer (PZT) resulted in a periodic expansion of the bridge. When the modulation frequency of the PZT matched the natural resonant frequency of the microresonator, maximum amplitude of vibration was obtained. The gap between the fiber end and the sensor surface was of the order of a few tens of micrometers. The detection scheme is similar to that described by Liu and Jones.<sup>12-13</sup>

For this system, the worst case optical power loss, including star coupler, couplings and sensor misalignment, was about 26dB per fiber

channel. About 11mW average optical power was coupled into the network and this was enough for the high SNR multiplexing of four SMRS. Fig. 3 displays (a) the gate signal coming from the delay unit D<sub>2</sub> for toggling the switch SW<sub>2</sub>, (b) the return photoelectric pulses when the second fiber delay line was addressed to the sensor, and (c) the sampling pulse output of the 'second' sensor. It can be seen clearly from Fig. 3(c) that only the required photoelectric pulse passes through the corresponding switch and other photoelectric pulses are rejected. By using a low-pass filter with a 3dB cutoff frequency of 100kHz at the switch output the resonator signal was achieved. The detected resonant frequency is 53.77kHz and the resonant peak, depending on the vibration amplitude of the sensor under the excitation of the PZT, is about 30dB above the noise level. The maximum measurable cross-talk in this system can only be -30dB due to the limit of the amplitude of the resonant signal although potentially the switch isolation is more than 70dB as quoted by the manufacturer.<sup>14</sup> By moving each of the four fiber delay lines to address the same SMRS respectively, and then measuring the corresponding channel output signals from the four switches, the passive multiplexing of four SMRS was realized successfully.

**Conclusion:** In conclusion, we have developed an improved TDM system using a logic low intensity level adjustable signal mode quasi-CW diode laser. A sampling frequency of up to 1MHz and a more than 30dB system SNR (for shot-noise-limited case) have been achieved simultaneously to realise the successful passive multiplexing of four fiber optic channels for use with silicon microresonator sensors exhibiting identical characteristics. The work of this paper can be easily extended to passive multiplexing for any fiber optic sensor that produces intensity modulation, especially for those requiring a high dynamic measurement range.

**Acknowledgement:** This work is a part of the LINK JIMS FOSMUX programme supported by the SERC/DTI. The authors wish to thank Dr. P. Steer of Sifam Ltd. for providing the multimode fiber star network, Miss Jane Briancon of Smiths Industries, and Dr. C. Michie of Strathclyde University for helpful discussions.

#### References

1. LANGDON, R. M.: 'Resonator sensors—a review, J. Phys. E: Sci. Instrum., 1985, 18, pp. 103-115
2. VENKATESH, S., and CULSHAW, B.: 'Optically excited vibrations in a micromachined silica structure', Electron. Lett., 1985, 21, pp. 315-317
3. THORNTON, K. E. B., UTTAMCHANDANI, D., and CULSHAW, B.: 'A sensitive optically excited resonator pressure sensor', Sensors & Actuators A, 1990, 24, pp. 15-19
4. HAUPTMANN, P.: 'Resonant sensors and applications', Sensors & Actuators A, 1991, 26, pp. 371-377
5. VENKATESH, S., and NOVAK, S.: 'Micromechanical resonators in fiber-optic systems', Optics Lett., 1987, 12, pp. 129-131
6. RAO, Y. J., WALSH, D., UTTAMCHANDANI, D., and CULSHAW, B.: 'Temperature dependence of resonant frequency in all-fiber optically addressed silicon microresonator sensors', Electron. Lett., 1991, 27, pp. 934-936
7. CULSHAW, B., and DAKIN, J.(Ed.): 'Optical fiber sensors: Systems and Applications'(Artech House, Norwood, MA, 1989)
8. NELSON, A. R., MCMAHON, D. H., and GRAVEL, R. L.: 'Passive multiplexing system for fiber optic sensors', Appl. Opt., 1980, 19, pp. 2917-2920
9. NELSON, A. R. and MCMAHON, D. H.: 'Passive multiplexing of digital fiber optic sensors', Appl. Opt., 1981, 20, pp. 915-916
10. NELSON, A. R., MCMAHON, D. H., and VAN DE VAART, H.: 'Multiplexing system for fiber optic sensors using pulse compression technique',

- Electron. Lett., 1981, 17, pp. 263-264
11. SANTOS, J. L., FARAH, F., NEWSON, T. P., and JACKSON, D. A.: 'Time division multiplexing of optical fiber sensors with sampled modulation of laser diode', Optics Comm., 1990, 78, pp. 143-148
  12. LIU, K.: 'Optical fiber displacement sensor using a diode transceiver', SPIE, 1987, 798, pp. 337-341
  13. JONES, B. E.: 'Optical fiber sensors and systems for industry', J. Phys. E: Sci. Instrum., 1985, 18, pp. 770-781
  14. WATKINS-JOHNSON Co.: 'RF and microwave components designer's handbook'(1990), pp. 780-781

**TH2.1**  
**(Invited)**

## **Application Specific Optical Fibres And Fibre Devices For Optical Fibre Sensors**

**Simon B. Poole**  
**Optical Fibre Technology Centre**  
**University of Sydney, Australia**

### **Abstract**

Recent developments in Application Specific Optical Fibres and Fibre Devices for Optical Fibre Sensors are outlined, with particular emphasis on fibre lasers, amplifiers and grating technology.

### **Introduction**

Optical fibres for telecommunications applications have, over the last decade, developed to the point where they are now virtually a commodity product. During that time, however, new applications for optical fibres have been developing, most noticeably the area of optical fibre sensors. One of the driving forces for this has been the development of Application Specific Optical Fibres (ASOF) whose properties are tailored, either through the fibre design or the use of novel glasses or dopants, to optimise their performance in a given application. This area has previously been extensively reviewed (see eg <sup>1,2,3</sup>) and this paper will therefore attempt to concentrate on recent developments whilst introducing any background information as necessary.

### **Birefringent Fibres**

This area was, perhaps, the first ASOF to reach commercial acceptance and efforts are now being directed less towards research and more towards the 'engineering' efforts of volume production and standardisation. The best example of this is the highly-birefringent fibre in its various forms (see eg ref 3) which is proving crucial in interferometric sensors, such as the optical fibre gyroscope <sup>4</sup> and hydrophone<sup>5</sup>. However, all highly-birefringent fibres (including quasi-circularly birefringent 'spun hi-bi' fibres<sup>6</sup>) suffer from large temperature dependence of the birefringence, which is a particular problem in single-fibre sensors such as polarimeters. Further research is therefore required to develop truly temperature insensitive fibres. A truly circularly-polarisation preserving fibre would also find instant application in optical fibre current monitors.

More recently, the two-mode elliptical-core fibre ("E-core" fibre) has come under intense investigation in the last few years <sup>7,8</sup> using the intermodal interference between the  $LP_{01}$  and  $LP_{11}$  modes. An elliptical-core fibre has the great advantage here that the  $LP_{11}$  mode is spatially stable, thus allowing simple, single-fibre interferometers to be constructed. The other major application of E-core fibres is in writing photorefractive gratings within the fibre core using a high-power Ar<sup>+</sup> laser (see below). The grating formed matches the modal interference pattern within the fibre and these have been proposed for optical switches and modulators, although their use on optical fibre sensors has not yet been demonstrated.

### **Non-silica fibres**

Whilst the low loss of silica makes it the ideal medium for optical communications, it should be noted that, in general, improvements in the performance of optical fibre sensors and other devices, where only a few metres of fibre may be required, can be obtained by abandoning silica altogether as a host material and employing non-silica glasses or even polymers. The increased loss inherent in this

approach is not normally a problem, since several orders of magnitude improvement in device sensitivity is obtainable and only a few metres of fibre are required.

Of the many 'soft' glasses which have been investigated over the past few years, those which have proven the most useful are fluoride and phosphate glasses for fibre laser and amplifier hosts. In particular, the low phonon energies of fluoride glasses make them attractive as laser hosts for upconversion laser systems (see below). However, there are many other known glasses with even lower phonon energies (eg chalcogenide, chalcohalide) which may give yet more efficient sources than those already demonstrated. These low phonon energy glasses also have increased transparency in the region beyond  $2\mu\text{m}$ , which makes them ideally suited for spectroscopic applications. Other non-silica glasses for fibres have been mainly developed for higher non-linear optical properties for optical switching, although lead-based fibres with a high Verdet constant have been fabricated for optical fibre current monitors<sup>9</sup>.

### Rare-earth doped fibres

The development of rare-earth doped fibres<sup>10,11,12</sup> has been one of the most significant developments in optical fibres in the last few years. The majority of work has been devoted to the development of Erbium-Doped Fibre Amplifiers (EDFAs) for communications applications<sup>13</sup>. However, although EDFAs are rapidly approaching commercialisation, they have yet to be incorporated in any sensor systems, where their broadband width and low excess noise may find many applications, particularly in improving power budgets for distributed and quasi-distributed sensors.

Early work on rare-earth doped fibres for sensors concentrated on passive devices, particularly filters<sup>14</sup> and temperature sensors<sup>15,16</sup>. More recently, the potential of fibre laser sources has become recognised, with communications applications again attracting much attention and in particular  $\text{Er}^{3+}$ -doped fibre lasers are now under intensive investigation as sources for soliton-based optical communications systems<sup>17</sup>. The field is developing rapidly, however, as evinced by the wavelengths which can be reached with fibre lasers (Fig 1.), and it is beyond the scope of this paper to cover all the developments in any detail. Nevertheless, four basic areas of interest can be identified, and these are outlined below:

**Superfluorescent sources** Of the fibre laser sources under development, greatest attention has been paid to the superfluorescent fibre laser<sup>18</sup> where the broad fluorescence linewidth of the rare-earth ions in a glass is utilised to produce highly temperature-stable, broad-spectrum sources. These have been demonstrated in both  $\text{Nd}^{3+}$  ( $1.06\mu\text{m}$ ) and  $\text{Er}^{3+}$  ( $1.55\mu\text{m}$ )<sup>19</sup> as a high power, broad-spectrum source for fibre gyroscopes. Such superfluorescent sources will also find application in low-coherence ('white-light') interferometry<sup>20</sup> where their high output powers, short coherence length and efficiency of coupling to single-mode fibres are also important. It is particularly worth noting that cladding-pumped devices<sup>21,22</sup> can be used to give extremely high coupling efficiency to GaAlAs phased array pump lasers, with a correspondingly high fibre laser output power (Fig 2). However, care must be taken in extrapolating results in this area, since it has been shown<sup>23</sup> that the excess noise in superluminescent fibre lasers also increases with increasing power.

**Pulsed Laser sources** Another important area for fibre lasers is as pulsed sources, in either Q-switched<sup>24</sup> or mode-locked<sup>25</sup> form. These can produce several 10s of watts of peak power when pumped by cheap semiconductor lasers and are particularly suited as sources for distributed sensor systems. Pulsed fibre lasers have developed rapidly over the past few years and commercial instruments based upon them are now available<sup>26</sup>. Most recently, the development of passively mode-locked short-pulse fibre lasers<sup>27</sup> offers a possibly cheap source of femto-second pulses for high resolution sensors, spectrally-encoded sensors (from the high spectral bandwidth of such lasers) and electro-optic sampling.

**Narrow-linewidth and tunable lasers** For interferometric and polarimetric sensors, a stable, narrow-linewidth source is required. Whilst the majority of sensors to date use either DFB semiconductor lasers or diode-pumped Nd:YAG lasers, fibre lasers provide a potentially low-cost alternative. Recent developments in both ring and linear cavities<sup>28</sup> have demonstrated stable, narrow-linewidth (~kHz) lasers in both Nd<sup>3+</sup> and Er<sup>3+</sup> doped fibres.

**Upconversion lasers** In the last year, up-conversion fibre lasers in fluoride glass fibres, where two photons at a longer wavelength than the lasing wavelength, usually in the infra-red, are absorbed to produce a photon of laser output at a shorter wavelength, have been demonstrated. This was first shown in fibre in a Ho<sup>3+</sup>-doped fluoride fibre<sup>29</sup>, but since then, many such systems have been demonstrated, particularly in Pr<sup>3+</sup>-doped fibres, where wavelengths from 491nm<sup>30</sup> to 910nm<sup>31</sup> have been reported. Such lasers may be important in the development of chemical and bio-medical sensors, where the majority of work to date in non-fibre systems has relied on visible light excitation of fluorophores by high-power argon or dye lasers operating. Their replacement with compact, tunable solid-state lasers will greatly increase the applications of such technology.

## Passive Fibre Devices

Recent developments in passive fibre devices have been concentrated in the area of in-line fibre gratings, particularly side-written photo-refractive gratings<sup>32</sup>. However, this year has also seen further commercial developments in fused-taper 3x3 and polarisation-preserving fibre couplers for interferometers. In another related development, we have developed a new technique for simplifying coupling into and out of twin and multi-core fibres. These developments are presented in more detail below.

**Twin core fibres** have long been known as an appropriate technology for optical fibre sensors for temperature and pressure<sup>33</sup>. However, a major disadvantage associated with their use is the difficulty in both exciting and detecting the signals in the two cores because of their small size and relatively close proximity. Since each core has typically a radius of only a few microns and their separation is of the order of a few times the core radius, it is impossible to either butt-couple or splice standard (125 or 80  $\mu\text{m}$ ) fibres directly to them. We have recently reported a novel design of connector to overcome this<sup>34</sup>, which is shown schematically in Fig 3. This comprises two tapered single-mode fibres located in a lower-index (eg boron-doped) glass capillary. The overall diameter of the fibres is then reduced by tapering whilst the mechanical stability and fibre separation are maintained so that they can be spliced to the twin-core fibre cores. This approach also enables the spot sizes of the tapered and twin-core fibres to be matched whilst crosstalk in the connector can be eliminated by the choice of suitable materials. The device should be easily fusion-spliced to twin-core fibre and may also be simply extended to multi-core fibres.

**Fibre Gratings** One of the most exciting developments of recent years has been the demonstration of in-fibre gratings, produced by etching a relief grating into the cladding of a polished fibre, close to the core<sup>35</sup> and more recently the in-fibre photorefractive grating<sup>36,37</sup> are the most well-developed. The latter are particularly important, since they can be made polarisation insensitive (or sensitive, if required) and are easily fabricated in many types of singlemode fibre. Whilst the fabrication technology for photorefractive gratings has developed considerably over the last few years, to the point where gratings several cm in length can be produced, the mechanism responsible for the formation of the grating remains obscure, limiting device optimisation for many applications.

To date, most authors have favoured the explanation based on index changes associated with absorption through the Kramers-Kronig relationship<sup>36</sup> although these are now generally understood to have severe limitations<sup>38</sup> and mechanisms based on compaction processes in silica<sup>38</sup> have been proposed. Recently, we have suggested an alternative mechanism based on



stress relief in the fibre <sup>40</sup> which should allow the optimisation of the fibre design to both improve the device performance and to simplify the fabrication of the devices.

Applications of these devices in optical fibre sensors are varied and include temperature and strain sensors<sup>41,42</sup>, laser linewidth selection elements<sup>43</sup> and, more recently chemical sensors<sup>44</sup>. However, availability of these devices is still limited and further rapid development of systems based on fibre gratings is expected as they become more widely available.

## Conclusions

Whilst some ASOF have now reached the stage of being mature commercial products, it is clear that a whole new range of ASOF are new under development. These new fibre will have an increasing influence on the design and operation of future optical fibre sensors, leading to more practical and environmentally robust systems.

## Acknowledgments

The author would like to thank his many colleagues, both within the OFTC and elsewhere, for their assistance in the preparation of this paper. OFTC Ltd is acknowledged as a Sponsor of the Optical Fibre Technology Centre.

## References

1. Payne, D.N., Proc OFS-7/ACOFT-15, Sydney, 1990
2. Poole, S.B., Payne, D.N. Proc SPIE, 734, pp.92-103, London, 1987.
3. Gambling, W.A., and Poole, S.B. in "Optical Fibre Sensors Vol 1: Principles and Components", eds J.Dakin & B.Culshaw, Artech House, 1989.
4. Proc 15th Anniversary Conference on Fiber Gyros, Proc SPIE, 1585, Boston, MA, 1991.
5. Dandridge, A., Kersey, A.D., Proc SPIE, 985, p.34, Boston, MA, 1988.
6. Laming, R.I., Payne, D.N., *J.Light. Tech.*, 7, pp.2084-2094, 1989.
7. Kim, B.Y., Blake, J.N., Huang, S.Y., Shaw, H.J., *Opt.Lett.*, 12, pp.729-731, 1987.
8. Murphy, K.A., Miller, M.S., Vengsarkar, A.M., Claus, R.O., *J.Light.Tech.*, 8, pp.1688-1696, 1990.
9. Edwards, H., Jedrzejewski, K.P., Laming, R.I., Payne, D.N., *Appl.Optics*, 28, pp.1977-1979, 1989.
10. Poole, S.B., Payne, D.N., Fermann, M.E., *Electron. Lett.*, 21, pp. 737-738, 1985.
11. Mears, R.J., Reekie, L., Poole, S., Payne, D.N., *Electron. Lett.*, 21, pp. 738-740, 1985.
12. Urquhart, P. *Proc IEE Part J*, 135, pp.385-4407, 1989 and references therein.
13. Proc 2nd Topical Meeting on Optical Amplifiers, Snowmass, USA, July 1991.
14. Farries, M.C., Townsend, J.E., Poole, S.B., *Electron.Lett.*, 22, pp.1126-1128, 1986.
15. Snitzer, E., Morey, W.W., Glenn, W.H., *Proc OFS 1*, pp.79-82, London, 1983.
16. Farries, M.C., Fermann, M.E., Poole, S.B., Townsend, J.E., *Proc OFC'87*, Paper W15, Reno, 1987.
17. Mollenauer, L.F., Evangelides, S.G., Haus, H.A., *J.Light.Tech.*, LT-9, pp.194-197, 1991.
18. Liu, K., Dignonnet, M., Shaw, H.J., Ainslie, B.J., Craig, S.P., *Electron.Lett.*, 23, pp.1320-1321, 1987.
19. Morkel, P., *Proc OFS'89*, pp.143-148, Paris, 1989.
20. Bosselman, Th., Ulrich, R., *Proc OFS-2*, pp.361-364, Stuttgart, 1984.
21. E.Snitzer *et al* in *Proc OFS-6*, 1988, paper PD5.
22. Po, H., *et al*, *Proc OFC'89*, Houston, USA, Paper PD7, 1989.
23. Morkel, P., Laming, R.I., Payne, D.N., *Electron.Lett.*, 26, p96, 1990.
24. Alcock, I.P., Tropper, A.C., Ferguson, A.I., Hanna, D.C., *Electron.Lett.*, 22, pp.84-85, 1986.
25. Alcock, I.P., Ferguson, A.I., Hanna, D.C., Tropper, A.C., *Electron.Lett.*, 22, pp.268-269, 1986.
26. York Sensors Ltd DTS 80
27. Fermann, M.E., Hofer, M., *Proc IOOC/ECOC'91*, paper TuB4.2, Paris, 1991 and references therein.

28. Payne, D.N., *Proc IOOC/ECOC*, Paris, 1991 and references therein.
29. Allain, J.Y., Monerie, M., Poignant, H., *Electron.Lett.*, 26, pp. 168-188, 1990.
30. Smart, R.G., Hanna, D.C., Tropper, A.C., Davey, S.T., Carter, S.F., Szebesta, D., *Electron.Lett.*, 27, pp.1307-1309, 1991.
31. Allain, J.Y., Monerie, M., Poignant, H., *Electron.Lett.*, 27, pp.189-190, 1991.
32. Meltz, G., Morey, W.W., Glenn, W.H., *Opt.Lett.*, 14, pp.823-825, 1989.
33. Dunphy, J.R., Meltz, G., Abou El Leil, M.M., Snitzer, E., *Proc OFC'84*, pp.58-60, New Orleans, 1984.
34. Poole, S.B. and Love, J.D., *Electron.Lett.*, 27, pp.1559-1560, 1991.
35. Bennion, I., Reid, D.C.J., Rowe, C.J., Stewart, W.J., *Electron.Lett.*, 22, pp.341-343, 1986.
36. Hill, K.O., Fujii, Y., Johnson, D.C., Kawasaki, B.S., *Appl.Phys.Lett.*, 32, p.647, 1978.
37. Meltz, G., Morey, W.W., Glenn, W.H., *Opt.Lett.*, 14, pp.823-825, 1989.
38. Russell, P.St.J., Poyntz-Wright, L.J., Hand, D.P., *Proc SPIE*, 1373, 126-139, 1990
39. Russell, P.St.J., Hand, D.P., Chow, Y.T., Poyntz-Wright, L.J., *Proc SPIE*, 1516, 1991.
40. Sceats, M.G., Poole, S.B. Topical Meeting on Non-linear Guided-Wave Phenomena, Cambridge, England, 1991, Paper PDP-5.
41. Morey, W.W., Meltz, G., Glenn, W.H., *Proc OFS 6*, pp.526 - 531, Paris, 1989
42. Melle, S., Davies, B., Measures, R.M., *Proc SPIE*, 1588, Boston, 1991.
43. Kashyap, R., Armitage, J.R., Wyatt, R., Davey, S.T., Williams, D.L., *Electron.Lett.*, 26, pp.730-731, 1990.
44. Meltz, G., Morey, W.W., Dunphy, J., et al, *Proc SPIE*, 1587, Boston, 1991.

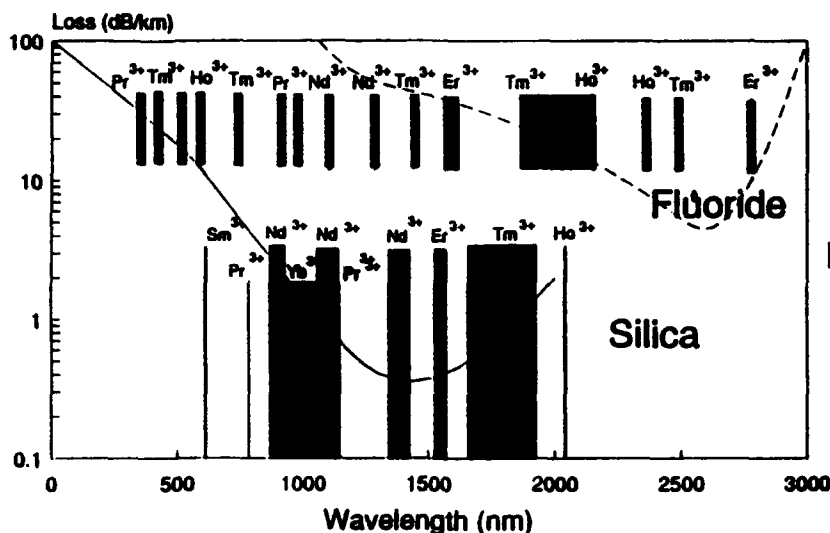


Figure 2. Cladding-pumped Fibre Laser

Figure 1. Demonstrated Fibre Laser Wavelengths

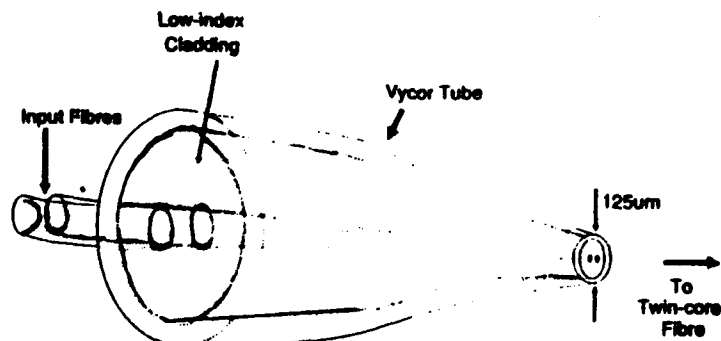
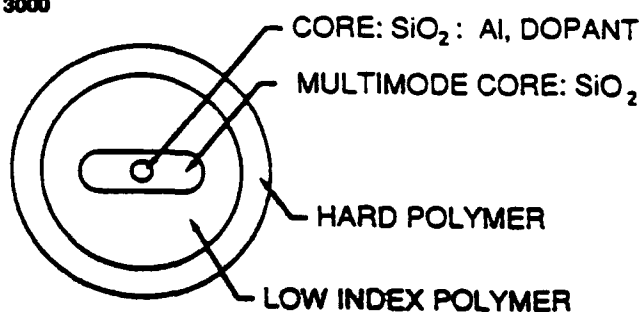


Figure 3 Single-mode to Twin-core Fibre Connector

## TH2.2      **Optical Fibers In Sensor Applications: Designing For Mechanical Reliability**

G. S. Glaesemann  
R. M. Hawk

Corning Incorporated

SPDV0108  
Corning Incorporated  
Corning, New York 14831

### Summary

Many sensor applications involving optical fiber have limited room for packaging the fiber. However, due to the statistical nature of fiber strength and the susceptibility of glass optical fiber to fatigue, it is advantageous to keep tensile- and bending-induced stresses as small as possible. Therefore, it is necessary to have a package design methodology that accounts for the mechanical reliability of optical fiber.

The design methodology must include the following components: first, one must have a model for fiber fatigue that is practical from an engineering point of view. Second, the statistical nature of fiber strength must be accounted for. Third, one must be able to scale the fiber strength distribution to the lengths representative of the application. The purpose of this development project is to propose a pragmatic mechanical design methodology for fiber sensors that incorporates the above components.

Recently, a design method for fiber fatigue was proposed, whereby, the allowable 40 year stress is determined to be  $1/3$  the strength measured in a fatigue environment for silica-clad fiber.<sup>1</sup> Thus, the allowable long-term stress is established via short-term dynamic fatigue testing.

Figure 1 is a strength distribution of 3.56 kilometers of 80  $\mu\text{m}$  diameter developmental polarization-maintaining single-mode fiber obtained under the following fatigue conditions. Testing was performed using 20 meter gauge lengths on a recently developed apparatus that loads all flaws to failure below a maximum stress level of 300 kpsi.<sup>2</sup> The strain rate was approximately 200%/min and the test environment was 50% relative humidity and 23°C. Using the above allowable stress to fatigue strength ratio of  $1/3$  along with published Weibull scaling laws,<sup>3</sup> one can create a design diagram for mechanical reliability of optical fiber. Figures 2 and 3 are design diagrams generated from the data in Figure 1 for tension and constant radius bending conditions, respectively. The curves in Figures 2 and 3 represent predictions of failure probability versus allowable stress for a range of application lengths. Note that in the case of bending, the allowable stress is expressed in terms of the maximum bend stress assuming a constant bend radius.

From curves depicting failure probability as a function of allowable stress, such as those in Figures 2 and 3, one determines the allowable bend radius or tensile load from application length and required failure probability information. For example, a 50 meter length of the fiber in Figure 1, placed in bending with a required failure probability of 1% has an allowable bend radius of approximately 0.50 in. Thus, dimensional requirements for packaging fiber can be estimated from fiber strength data. Given an estimate of the package design and preliminary strength distribution, one can determine the amount and type of strength testing required to make predictions in the failure probability range of interest.

Finally, in the case where fiber experiences multiple stress conditions in a single application, the overall reliability is governed by the stress and length combination determined to have the greatest failure probability. Such an approach leads the designer to the weakest reliability link in the package design.

#### References

1. G.S. Glaesemann and S.T. Gulati, "Design Methodology for the Mechanical Reliability of Optical Fiber," Opt. Eng., 30(6), 709-715 (1991).
2. G.S. Glaesemann and D.J. Walter, " Method for Obtaining Long-Length Strength Distributions for Reliability Prediction," Opt. Eng., 30(6) 746748 (1991).
3. G.S. Glaesemann, "Optical Fiber Failure Probability Predictions from Long-Length Strength Distributions," to be published in the proceedings of the 1991 International Wire and Cable Symposium, St.Louis Mo.

**Figure 1.**  
**Strength Distribution of 3.65 Kilometers**  
**of 80 Micron Sensor Fiber**

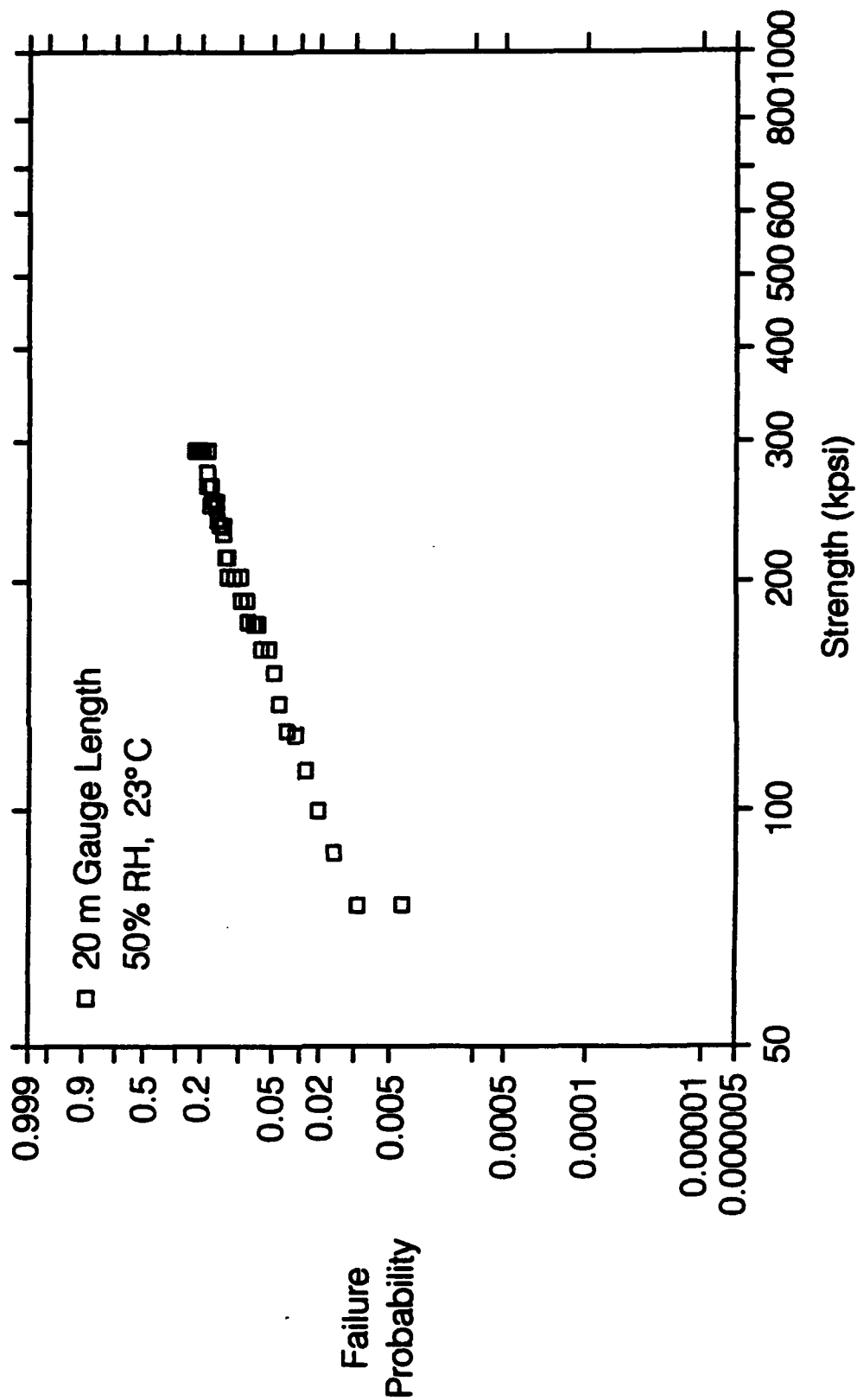


**Figure 2.**  
**Allowable Stress Predictions for 80 Micron**  
**Sensor Fiber in Tension**

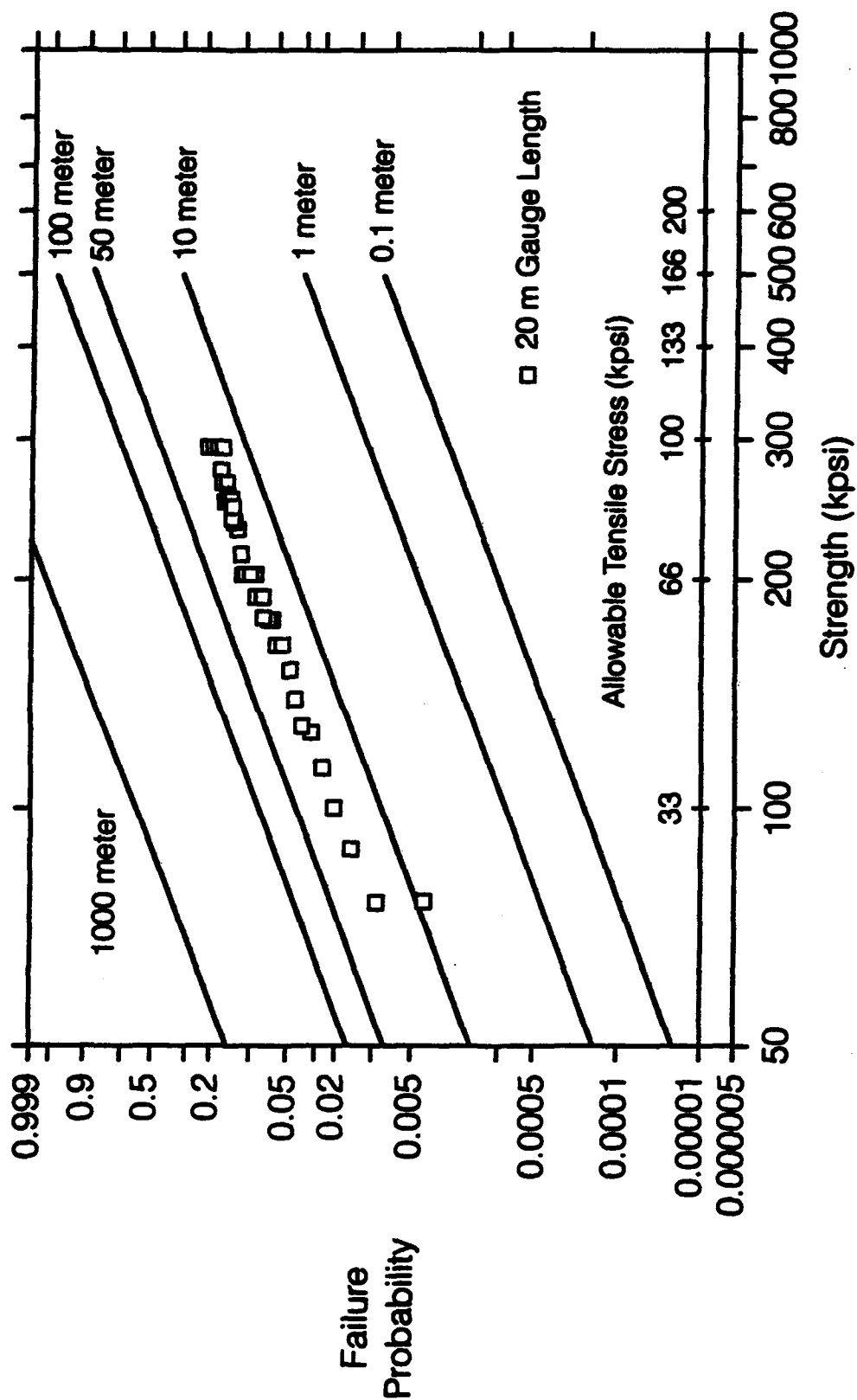
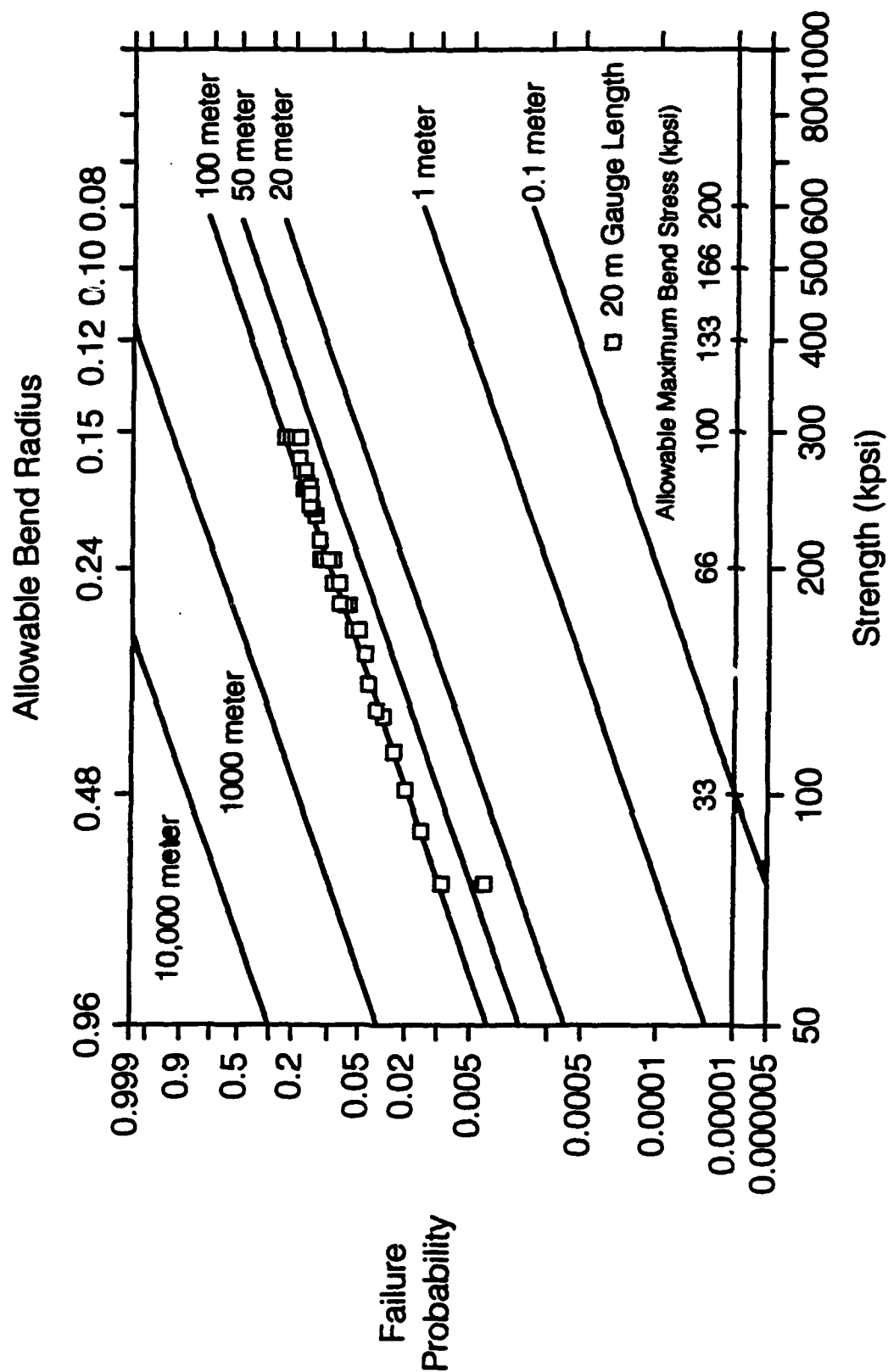


**Figure 3.**  
**Allowable Stress Predictions for 80 Micron**  
**Sensor Fiber in Bending**



Masahiro TAKAGI, Yuji KUBO, Eisuke SASAOKA, Hiroshi SUGANUMA

Sumitomo Electric Industries, Ltd.

1, Taya-cho, Sakae-ku, Yokohama, 244, JAPAN

### 1.Introduction

Several types of fiber polarizers have been proposed [1]-[4]. Most of them utilize the difference in bending loss between two orthogonally polarized modes [3][4]. However, the single polarization bandwidths of the conventional fiber polarizers are not wide enough to meet the operation wavelength specifications in practical use. Currently, we have developed the ultra-wide bandwidth fiber polarizer as an attractive component of fiber optic sensing systems. This paper describes characteristics of the fiber polarizer with the widest single polarization bandwidth over 320nm around 840nm wavelength, reported so far.

### 2.Design

In practical use for components in sensor systems, not only wide single polarization bandwidth but also compactness for fiber polarizer are required. With this in mind, a 30mm bending diameter and 10 turns for fiber coiling were selected. The bending characteristics of polarization maintaining fiber were theoretically investigated. It was revealed that birefringence ( $B$ ) could be the effective parameter to control the single polarization bandwidth ( $\Delta\lambda=\lambda_{cx}-\lambda_{cy}$ ), when the remaining parameters were adequately tuned. Figure 1 shows the calculated relationship between the  $B$  and the relative bandwidth, where the center wavelength in the single polarization band was 840nm. In the calculation,  $\lambda_{cx}$  and  $\lambda_{cy}$  were defined as the wavelengths where the excess loss of X-polarization (EL) became 0.5dB and that of Y-polarization became 30dB, respectively. It was clarified that  $\Delta\lambda$  could be widened by increasing  $B$ . On the other hand, the increase of  $B$  value resulted in the difficulties to prepare polarization maintaining fiber and finally was limited to  $12 \times 10^{-4}$ .



### 3. Polarizer characteristics

The fiber polarizers were fabricated by coiling polarization maintaining fibers with B of  $12 \times 10^{-4}$ . The used reel was 30mm in diameter and the turn number of fiber was 10. Figure 2 shows the typical loss spectra of each polarized mode. Characteristics of the fabricated polarizer are summarized in Table 1.  $\lambda_{cx}$  and  $\lambda_{cy}$  were 1070nm and 750nm, respectively.  $\Delta\lambda$  of 320nm, which is the widest reported so far, was actually achieved. Extinction ratio (ER) was 40dB and EL was less than 0.05dB, each measured with an LED at 840nm. The single polarization bandwidth is so wide that the tolerance of signal operation wavelength can be as large as 38%. It is large enough to cover variations of the center wavelengths of commercially available light sources. Conventionally, In order to meet the operation wavelength specifications, precise control for coiled conditions has also been required. Spectral dependence of bending loss on turn numbers was also investigated as shown in Figure 3. Because of its broad bandwidth, both ER and EL were very stable against coiled conditions. This is one of advantages for mass production of polarizers.

### 4. Reliability

The reliability of the polarizer on environmental changes are investigated. Figure 4 shows temperature dependence of ER and EL. The fabricated polarizer remained the initial characteristics over a wide temperature range, from -40 to +85°C. The performances of the polarizer under humid condition and high temperature have also been investigated. After keeping under +60°C and 95% humidity, and +85°C over 1000hr, there were no changes in its characteristics.

### 5. Conclusion

The fiber polarizer with the single polarization bandwidth of 320nm, the widest reported so far, was fabricated. The tolerance of the signal operation wavelength was enlarged to be as large as 38%, and an extinction ratio of over 40dB was demonstrated. The polarizer shows excellent stability against the harsh environments. The compact polarizer, as small as 30mm in diameter, with high performances is extremely advantageous for applications to optical fiber sensors, such as, fiber optical gyroscope.

## References

- [1] D.Gruchmann.,et al.,ECOC'83,Tech.Dig.,305-308,1983
- [2] R.A.Bergh.,et al.,Opt.Lett.,5,479-481,1980
- [3] M.P.Varnham.,et al.,Electron.Lett.,19,246-247,1983
- [4] K.Okamoto.,et al.,J.Lightwave.Tech.,LT-3,758-762,1985

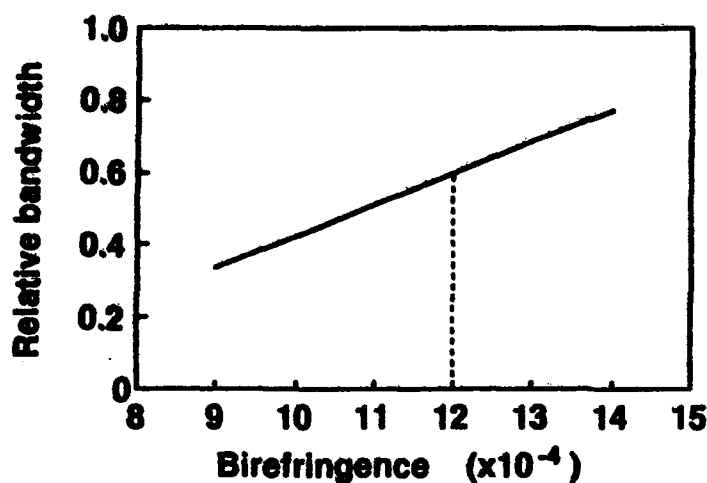


Figure 1 Calculated relationship between birefringence and relative bandwidth

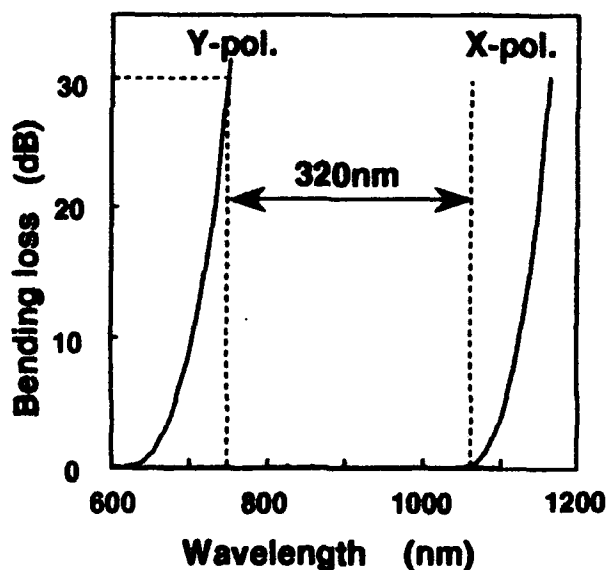
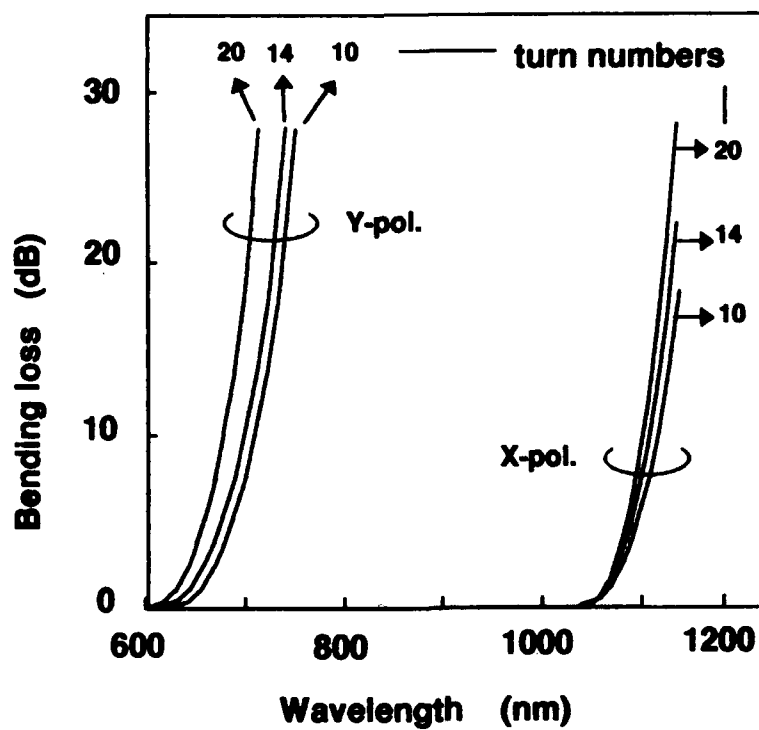


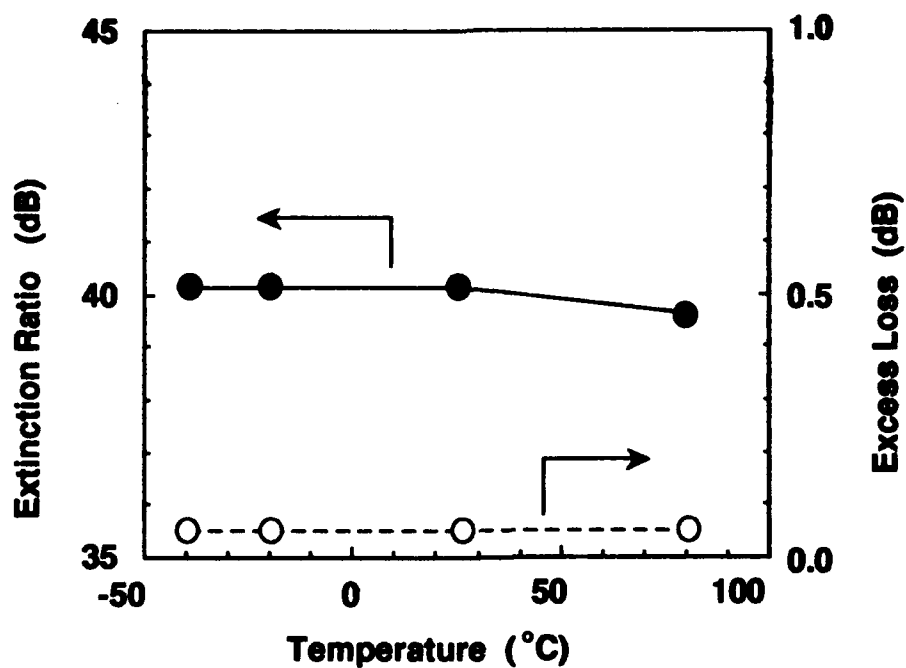
Figure 2 Typical loss spectra of fiber polarizer

Table 1 Characteristics of fabricated fiber polarizer

$\lambda_{cy}$ (nm)	750
$\lambda_{cx}$ (nm)	1070
$\Delta\lambda$ (nm)	320
ER (dB)	40
EL (dB)	0.05



**Figure 3 Loss dependence on turn numbers**



**Figure 4 Temperature dependence of ER and EL**

## TH2.4 Polarization Mode Couplers Made By Photoinduced Grating For White-light Quasi-distributed Polarimetric Sensors

J.J. GUERIN, J.M. MAILLARD, P. SANSONETTI  
BERTIN & CIE  
BP 22000  
13791 AIX EN PROVENCE CEDEX 3  
FRANCE

### SUMMARY

#### Introduction

Intrinsic optical fibre sensors, where the optical fibre is itself the transducer, offer low invasiveness and the potential capability for distributed measurement along a single fibre. Both properties are of high interest and find many applications, for instance, for the monitoring of structures.

A quasi-distributed technique, based on "white light" coherence multiplexing in two modes fibre, was recently reported<sup>1,2</sup>, which exhibits high accuracy and can offer real time measurement<sup>3</sup>. A polarimetric configuration uses the two polarization modes of a Highly-Birefringent (Hi-Bi) fibre<sup>4</sup>. Light from a short coherence length source is polarized and launched into only one polarization mode of a fibre possessing polarization mode couplers spaced along it. An analyzer, placed at the end of the sensing zone and axes of which are orientated at 45° from those of the fibre, then creates a set of polarimetric interference signals with various Optical Path length Differences (OPD). If the spacing between OPDs is greater than the source coherence length, e.g. the optical fibre length between polarization couplers is big enough, each signal can then be demultiplexed by white-light coherence technique. The measurement of the phase difference between successive signals then yields the polarimetric information between each couple of polarization couplers.

Polarization mode coupler is a keypoint of such a system. Ideally, it should not degrade the optical and mechanical properties of the optical fibre and should be easily and reproducibly implemented. It must have a wide spectral bandwidth because of the broad spectrum source and also provide with low power coupling ratio since the system crosstalk is proportional to it.

Implementation of such couplers with mechanical squeezers were reported<sup>2</sup>. However putting such squeezer on the fibre implies the presence of a mechanical piece on the fibre which could be detrimental to several applications. An equivalent technique was also reported for coupling two transverse modes<sup>5</sup>. Other work used chemical etching to locally suppress the fibre birefringence<sup>6</sup>. However the fibre becomes fragile at this point which again is detrimental. An alternative technique that would not degrade the fibre mechanical properties would be to use photoinduced grating. Photoinduced reflection Bragg gratings were first reported with internal illumination at 488 nm<sup>7</sup>. An equivalent technique was used to couple transverse modes<sup>8</sup> as well as polarization modes<sup>9</sup>. However such internal illumination suppose the grating is used at the same wavelength as the wavelength of exposure e.g. around 488 nm, which impedes the use of classical semiconductor sources. Experiments have been made<sup>10</sup> to overcome this point by using the beat length dispersion which allowed an operation at 720 nm. However, this is still not at the 800 nm band, and special and reproducible design of the fibre would be needed. Moreover such couplers can hardly be put at any desired location on the fibre.

However, it was shown that, with a higher efficiency band around 244 nm<sup>11,12</sup>, Bragg reflection grating could be realized through holographic external illumination, which potentially allows Bragg operation at any desired wavelength and any location on the fibre.

We here report the fabrication of polarization modes couplers made by an externally photoinduced grating, period of which is matched to the fibre beat length. The grating is simply created by the transverse illumination of the Ge-doped core, through a periodic transmission mask<sup>13</sup>, by the beam of a KrF laser emitting at 248 nm. This technique is simple, the coupler can be located wherever needed on the fibre and nothing has to be installed on the fibre. Furthermore, a low number of periods allows the obtention of wide spectral bandwidth and low coupling ratio, which are both favourable for white-light quasi-distributed systems.

### Grating fabrication

The scheme of the experiment, including the coherence monitoring of the obtained amplitude coupling, is represented in Figure 1:

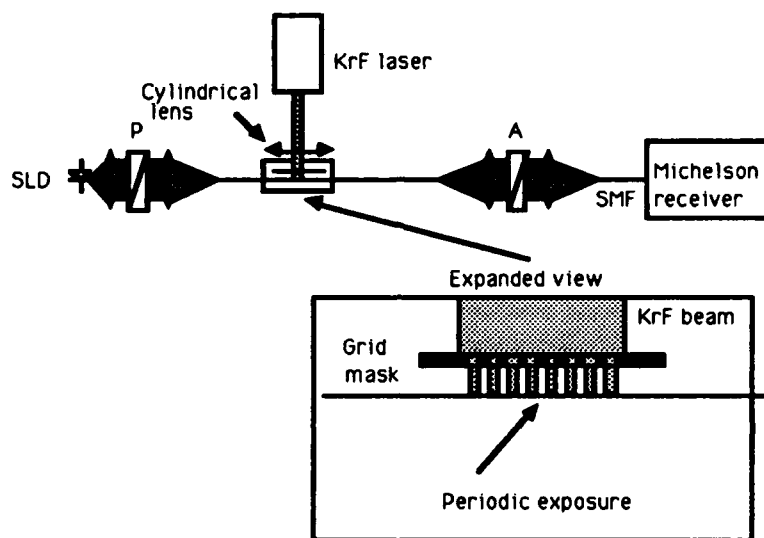


Figure 1 - Scheme of the grating fabrication and coherence monitoring of the coupling. P and A are the polarizer and analyzer; The lead out from A is through a Single Mode Fibre (SMF)

The measurement of the resulting coupling is based on the "white-light" quasi-distributed configuration. The optical fibre is of the Hi-Bi type and suited to work at this wavelength. The source is a Superluminescent diode emitting around 800 nm. The receiving interferometer is of the Michelson type. Its OPD is locked on the group OPD between the two polarization modes created by the propagation from the polarization coupler to the analyzer. The PZT ramping of one its mirror is then used to measure the index of modulation  $m$  of the resulting signal, which is given by:  $m = K m_0$ . Here,  $K$  is the amplitude coupling ratio of the polarization coupler and  $m_0$  is the index of modulation of the Michelson at zero OPD. The latter value was measured to be 95%. The measurement of  $m$  therefore yields the desired  $K$  value.

To realize the polarization coupler, a pulsed KrF laser emitting at 248 nm is used. Its output beam, of about  $20 \times 25 \text{ mm}^2$ , passes through a cylindrical lens that shapes the beam on the fibre. Before incoming on the fibre, the beam passes through a mask, transmission of which is periodic. The fibre core is therefore periodically illuminated. Here, a simple periodic grid was used. Such simple technique is possible due to the required period of the order of 1 mm (the fibre beat-length).

In order to have efficient coupling the grating period  $p$  must be equal to the fibre beat length at the source center wavelength  $\lambda_0$ , that is:  $p = \lambda_0 / \Delta n$  where  $\Delta n$  is the fibre birefringence e.g. the difference between the effective indices of both polarizations. In order to find the optimum  $p$  value, experiments were made with different grating periods.

We have represented in Figure 2a, the amplitude coupling coefficient  $K$  vs the value of  $p$  for a grating with twelve periods. Such low number of periods is taken to have wide spectral bandwidth and low power coupling ratio. A number of 400 pulses, each with a power density on the fibre of the order of  $0.2 \text{ J/cm}^2$ , was used in this experiment. It must be noted that a saturation of the coupling coefficient value begins to occur above 400 pulses. A maximum is found around  $1.56 \text{ mm}$  which therefore corresponds to the fibre beat length. The FWHM bandwidth of the grating period is about  $0.13 \text{ mm}$ . The beat length of  $1.56 \text{ mm}$  is to be compared to the group beat length e.g.  $\lambda_0/\Delta n_g$ , where  $\Delta n_g = \Delta n - \lambda \frac{d(\Delta n)}{d\lambda}$ . The latter is directly obtained in the coherence technique since the Michelson OPD must be equal to  $\Delta n_g l$ ,  $l$  being the distance between the polarization coupler and the analyzer. The group birefringence is measured to be  $1.47 \text{ mm}$ , which confirms that  $\Delta n$  has a lower value than  $\Delta n_g$ .

We have also represented, in Figure 2b, the amplitude coupling coefficient versus the number of periods in the grating, for instance for a period value of  $1.6 \text{ mm}$ . A linear behaviour is observed.

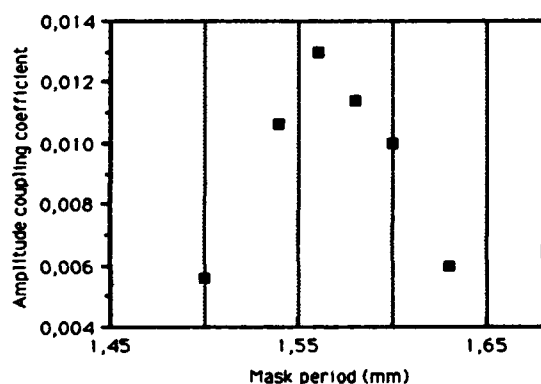


Figure 2 - Amplitude coupling coefficient vs the period value for 12 lines grating

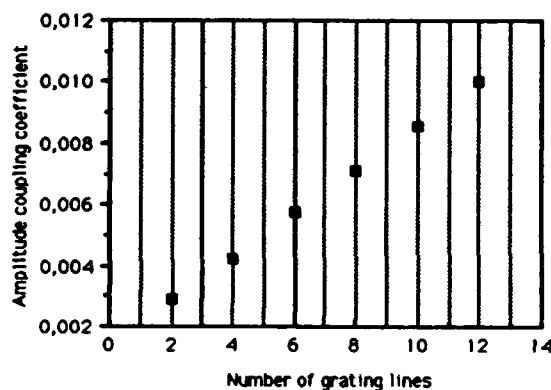


Figure 2b - Amplitude coupling coefficient vs the number of lines for a period of  $1.6 \text{ mm}$

#### Polarization couplers for white-light quasi-distributed polarimetric sensors

Such polarization couplers are very interesting for white-light quasi-distributed polarimetric sensors, because reproducible low coupling values are obtained. Such low coupling values lowers the level of crosstalk which is proportional to the power coupling ratio. This means that a 1% amplitude coupling value generates a crosstalk proportional to  $10^{-4}$  which allows to increase the number of sensing zones on the fibre. On the other hand an index of modulation of 1% still yields very precise measurements with such sensors (sensitivity to strain is for instance of the order of  $100 \text{ mrd}/\mu\text{m}$ ).

One keypoint is the filtering properties of such grating coupler w.r.t. the source spectrum and finally its influence on coherence multiplexing. Using a twelve periods photoinduced polarization coupler, we have represented, in figure 3, the oscilloscope trace of the AC part of the coherence demultiplexed signal detected at the output of the Michelson receiver, when the OPD of the latter is ramped with a PZT.

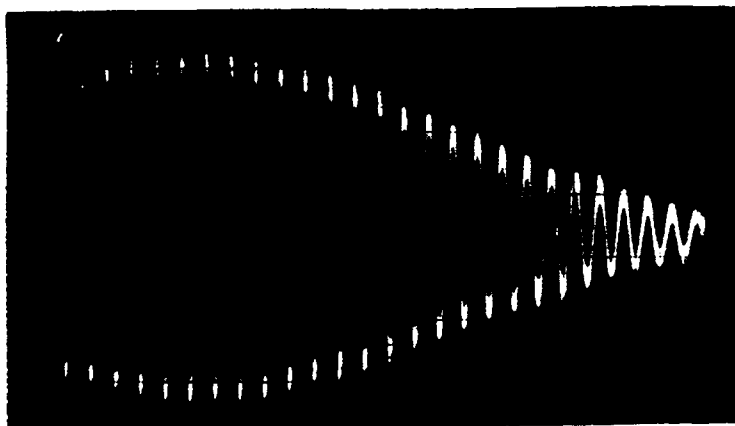


Figure 3-Coherence demultiplexed signal (one Michelson mirror is PZT ramped)

The OPD variation at  $1/e$  is  $12\ \mu\text{m}$ , unchanged from the value obtained at zero OPD of the Michelson. This means that, for such a number of periods, the source spectrum is not altered and coherence multiplexing with minimum spacing between polarization couplers is therefore feasible. This is not surprising since the grating period bandwidth of  $0.13\ \text{mm}$  should yield a spectral bandwidth of  $70\ \text{nm}$  which is to be compared to the source spectrum FW at  $1/e$  of around  $20\ \text{nm}$ . This means that a even higher number of lines could be used in order to increase the amplitude coupling coefficient if required.

Finally three such couplers, with reproducible coupling values, were spaced along one fibre and coherence demultiplexed using the Michelson receiver.

### Conclusion

Polarization mode couplers were implemented in Highly-Birefringent fibre with a grating realized by transverse illumination, through a periodic transmission mask, with a KrF laser emitting at  $248\ \text{nm}$ . Such polarization couplers with low amplitude coupling values of the order of  $1.3\%$  and wide spectral bandwidth were realized for white-light quasi-distributed polarimetric sensors. It was further shown that the coherence properties of the system were unaltered because of the coupler wide spectral bandwidth, and that even a higher number of lines could be used if required. Three such polarization couplers were spaced along the same fibre and coherence demultiplexed.

### Acknowledgments

This study was made under contract from the "Délégation Générale pour l'Armement-Direction des Recherches, Etudes et Techniques".

### References

1. M. Turpin, D. Rojas, C. Puech, Congrès MESUCORA, 1988, PARIS, pp 33-41.
2. V. Gusmeroli, P. Vavassori, M. Martinelli, OFS'89, PARIS, pp 513-518.
3. P. Sansonetti, JJ. Guerin, M. Lequime, SPIE "Smart Structures and Skins IV", 1991.
4. H.C. Lefevre, SPIE "Fiber Optic and Laser Sensors V", 1987, 838, pp 86-97.
5. G. Kotrotsios, O. Parriaux, OFS'89, PARIS, pp 568-574.
6. M.J. Marrone, C.A. Villarruel, Appl. Opt., 26(16), 1987, pp 3194-3195.
7. K.O. Hill, Y. Fujii, D. Johnson, B.S. Kawasaki, Appl. Phys. Lett., 32(10), 1978, pp 647-649.
8. H.G. Park, B.Y. Kim, Elect. Lett., 25(12), 1989, pp 797-799.
9. P. ST. J. Russell, D.P. Hand, Elect. Lett., 26(22), 1990, pp 1846-1848.
10. F. Ouellette, Electr. Lett., 25(23), 1989, pp 1590-1592.
11. G. Meltz, W.W. Morey, W.H. Glenn, Optics Letters, 14(15), pp 823-825.
12. R. Kashyap, J.R. Armitage, R. Wyatt, S. Davey, D. Williams, Elect. Lett., 26(11), pp 730-732.
13. P. Sansonetti, French Patent N° 90 01345, February 1990.

## TH2.5 Effect of Parasitic Birefringence Modulation In Interferometric Fiber Sensor Transducers

A. D. Kersey, K. H. Wanser<sup>‡</sup> and M. A. Davis

Optical Sciences Division, Naval Research Laboratory  
Washington, D.C. 20375-5000

<sup>‡</sup> Dept. of Physics, California State University, Fullerton, Ca 92634

### Abstract

The parasitic birefringence modulation which can occur in fiber transducers under normal phase modulation conditions is assessed and compared to a theoretical model. We also demonstrate that the effect is compensated for by using a polarization independent interferometer configuration.

**Introduction:** The state of polarization (SOP) of the light in interferometric sensor systems is important from two principal viewpoints; firstly, with regard to signal fading, which occurs when the mixed optical fields become orthogonal [1], and secondly with regard to induced phase noise, which can occur as a result of fluctuations in the SOP of light coupled to a fiber interferometer [2]. An issue which has been largely overlooked to-date is the parasitic SOP modulation effect of light in an interferometer due to the birefringence modulation which can occur in a fiber transducer under normal phase modulation. Generally, this weak effect is of minor importance, however, in systems where a large phase signal is nulled utilizing feedback, this parasitic birefringence modulation effect modifies the level of residual phase shift signal present in the output, leading to drift. Here we analyze this effect for the case of bending and tension-induced birefringence of fiber wound on a cylindrical transducer, and measure its magnitude for various fiber-coiling diameters. We also show that this effect is compensated for by utilizing a recently demonstrated polarization independent fiber optic Michelson interferometer configuration [3,4].

**Theory:** For a fiber wound under tension giving rise to an axial strain,  $\epsilon_z$ , on a cylindrical transducer of radius  $R$ , the induced birefringence  $\beta$  is given by

$$\beta = \frac{C_b}{R^2} + \frac{C_t}{R} \epsilon_z, \quad (1)$$

where  $C_b + C_t$  are the pure bending and tension-coiled birefringence coefficients [5,6]. The phase difference between two polarization modes is thus

$$\phi_{xy} = \phi_x - \phi_y = \beta L = 2\pi N \left\{ \frac{C_b}{R} + C_t \epsilon_z \right\} \quad (2)$$

where,  $L$  is the total length of fiber on the transducer, i.e.  $L = 2\pi NR$ , with  $N$  the number of fiber turns. Radial modulation of the transducer results in a modification of the birefringence in the fiber. The resultant change in the phase difference  $\phi_{xy}$  is given by

$$\frac{\delta\phi_{xy}}{\delta R} = 2\pi N \left\{ -\frac{C_b}{R^2} + C_t \frac{\delta\epsilon_z}{\delta R} \right\} \quad (3)$$

The factor  $(\delta\epsilon_z/\delta R)$  relates the change in axial tension to the change in radius. For an incremental increase in radius  $\Delta R$  ( $\Delta R \ll R$ ), the axial strain of the fiber increases by  $\Delta\epsilon = \Delta R/R$ , consequently equation 3 becomes:

$$\frac{\delta\phi_{xy}}{\delta R} = \frac{2\pi N}{R} \left\{ -\frac{C_b}{R} + C_t \right\} \quad (4)$$



The mean phase delay of the light passing through the transducer is

$$\bar{\phi} = \frac{2\pi n L}{\lambda} = \frac{4\pi^2 n R N}{\lambda} \quad (5)$$

The phase modulation due to a change in radius is given by:

$$\frac{\delta\bar{\phi}}{\delta R} = \frac{4\pi^2 n \zeta N}{\lambda} \quad (6)$$

where,  $\zeta = \{1 - n^2[(1-\sigma)P_{12} - \sigma P_{11}]/2\}$ , with  $n$  the index of the fiber,  $\sigma$  Poisson's ratio, and  $P_{ij}$  Pockels strain optic coefficients. The ratio of polarization-mode phase delay (retardance) modulation to the mean phase delay modulation for a finite change in radius  $\Delta R$  is thus

$$\frac{\Delta\phi_{xy}}{\Delta\bar{\phi}} = \frac{(\delta\phi_{xy}/\delta R) \Delta R}{(\delta\bar{\phi}/\delta R) \Delta R} = \frac{\lambda}{2\pi R N} \left\{ -\frac{C_b}{R} + C_t \right\}. \quad (7)$$

As an example of the magnitude of this effect, for a 80  $\mu\text{m}$  OD silica fiber wound on a transducer of diameter  $2R = 2.5$  cm, the ratio  $\{\Delta\phi_{xy}/\Delta\bar{\phi}\}$  has a magnitude of  $1.87 \cdot 10^{-3}$  (It is interesting to note that for this example the tension coiled birefringence is the dominant effect by a factor of  $\sim 1000:1$ ). As a result of this birefringence modulation, the phase modulation for one polarization component on passage through the transducer is 0.187 % higher than that for the other in the above example. In most systems, this simply represents a minor polarization-dependent variation in the effective scale factor or responsivity of the transducer. However, in situations where it is desirable to null a large phase shift using a piezoelectric cylinder for example, this variation in responsivity limits the ability to completely null the signal. For example, a signal of 1 rad. rms would give rise to a possible 1.87 millirad rms polarization-dependent residual phase term for the transducer dimensions given above. This limitation can be a problem in various sensor systems, particularly those employing non-linear phase transducers, such as magnetometers based on magnetostrictive elements [7] and sensors those based on the type of transduction scheme reported in ref. 8, where the suppression of residual phase components at both the fundamental and second harmonic of the ac dither signal is important for optimal performance of the sensor.

**Experimental system & results:** The degree of birefringence modulation induced in a cylindrical transducer was investigated using the set up shown in Figure 1. Light in one arm of a path-matched fiber interferometer is coupled through the transducer as shown. After the transducer, a fraction of the light was tapped off and coupled to a polarization analyzer comprising rotatable fiber waveplate elements ( $PC_3$ ) and a rotatable Glan prism. This allowed determination of the birefringence modulation induced in the fiber wound on the transducer. All experiments were conducted using nominally 80  $\mu\text{m}$  OD fiber with a soft acrylate coating ( $\sim 140$   $\mu\text{m}$  OD). Piezoelectric cylinder transducers were used ranging in diameter ( $2R$ ) from 12.7 mm to 65 mm (0.5 to 2.55 in.). Polarization controllers ( $PC_1$ ,  $PC_2$ ) located at the input fiber and immediately before the transducer allowed to SOP of the light at various points in the system to be manually adjusted. The interferometer output served to indicate the mean phase shift induced by the transducer, which was typically set at  $> 10\pi$  rads peak. Figure 2 shows a typical output observed with a 25.4 mm OD transducer for two conditions; a) with the light in the transducer in both polarization modes, and b) with the light in one mode only. The lower trace in Fig. 2.a. corresponds to a modulation in the phase delay difference  $\Delta\phi_{xy}$  of 0.165 rads pk-pk, compared to a direct interferometer output of  $\sim 163$  rad pk-pk. (i.e.  $26 \times 2\pi$  pk-pk). The manifestation of this birefringence modulation as a change in the visibility of the interferometer output is also clearly seen in this figure. Figure 3 shows the measured dependence of  $\{\Delta\phi_{xy}/\Delta\bar{\phi}\}$  on  $R$  for the three transducers investigated. Also shown here is the theoretically expected dependence according to Eqn. 7. As can be seen, the experimental data show a  $1/R$  dependence, as theoretically expected,

but fall short of the predicted magnitude by a factor  $\sim 0.6$ ; this may be due to the effect of fiber coating which is neglected in the derivation of Eqn. 7.

Figure 4 shows the set-up used to investigate the elimination of variation in the residual signal with polarization changes in an interferometric system. The configuration used is a recently demonstrated 'polarization-independent' Michelson interferometer [3,4] with 'ortho-conjugate reflectors' (OCR), which comprise  $45^\circ$  Faraday rotators placed immediately before the mirrors in each arm. With this set-up, the evolution in the state of polarization (SOP) one direction through the fiber is essentially undone in the reverse direction, thereby providing a stable and optimized output visibility. A further feature of this scheme is that the SOP of the returned light is always orthogonal to that of the input light, and consequently, the two birefringence axis of a transducer are automatically sampled equally on the double passage of the light. This leads to an averaging effect which eliminates the polarization-dependent fluctuation in the amplitude of the phase shift induced by the transducer.

To test this, a phase shift signal of  $\sim 63$  rads pk-pk ( $10 \times 2\pi$ ) at  $\sim 2$  kHz was applied to one piezoelectric transducer in one arm, while a compensating signal was applied to the other. The transducers used were 25.4 mm and 65 mm OD cylinders to provide differing  $\{\Delta\phi_{xy}/\Delta\phi\}$  ratios. Active homodyne stabilization of the interferometer was used to lock the system in quadrature, allowing the residual phase carrier amplitude to be observed at the photodetector outputs. Figure 5.a shows the variation in the residual phase shift signal observed without the Faraday rotators in the system. Here, the phase shift was initially nulled to a level  $\sim <1$  millirad, then monitored with variation of the input SOP; this resulted in a  $\sim \pm 20$  millirads variation in the residual phase amplitude (the elements of  $PC_2$  were set to ensure no variation in visibility occurred with input SOP adjustment). With the Faraday rotators in place, the same variation in input SOP gave rise to a reduced variation of the residual phase signal by a factor  $\sim 50$  (-36 dB).

**Conclusions:** We have investigated the birefringence modulation in fiber optic transducers which occurs during normal phase modulation. We have characterized the effect for various coiling diameters (R), and shown that the effect is characterized by a  $1/R$  dependence. We have also demonstrated that the effect can be compensated for by using a polarization independent Michelson interferometer configuration.

This work is supported in part by the Office of Naval Technology.

#### References:

1. D. W. Stowe et al., J. Quant. Electron., QE-18, p. 1644, 1982.
2. A. D. Kersey et al., J. Lightwave Technol., 8, p. 838, 1990.
3. A. D. Kersey et al., Electron. Lett., 26, p. 518, 1991.
4. K. Wanser, Proc. SPIE, 891, p. 204, 1988.
5. R. Ulrich et al., Optics Lett., 5, p. 273, 1980.
6. S. C. Rashleigh and R. Ulrich, Optics Lett., 5, p. 354, 1980.
7. Dagenais et al., J. Lightwave Technol., 7, p. 881, 1989.
8. Bucholtz et al., Electron. Lett., 22, p. 451, 1986.

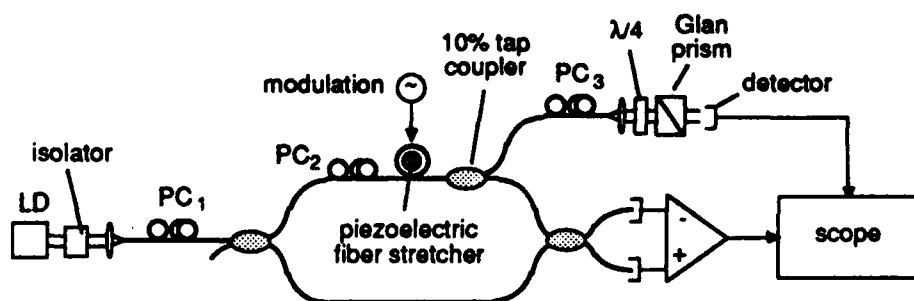


Figure 1. System used to characterize birefringence modulation in fiber transducers.

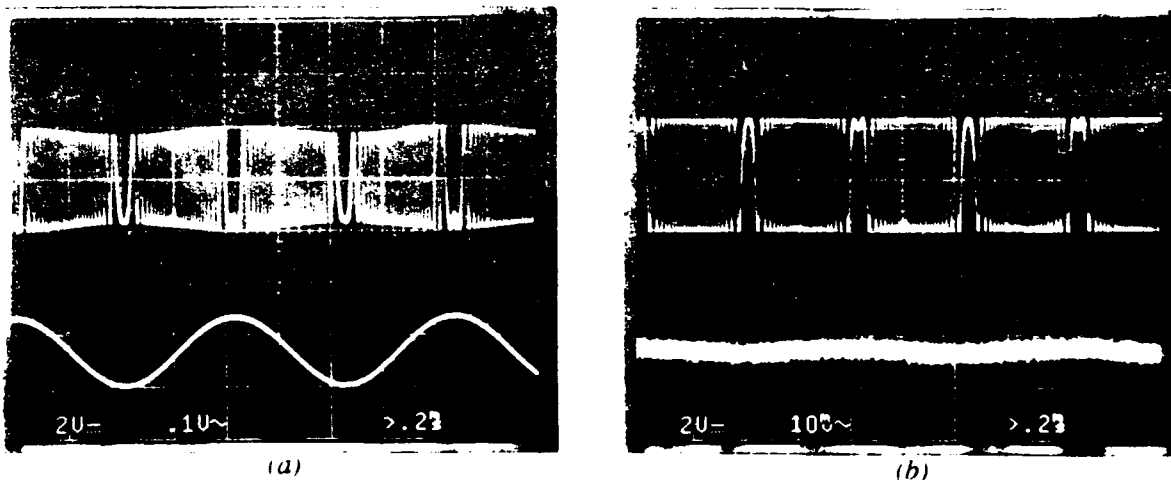


Figure 2. Interferometer output driven with multiple  $2\pi$ -deviation phase shift ( $26 \times 2\pi$  pk-pk) signal applied (upper trace), and polarization modulation detected at the output of the Glan prism (lower trace) with the SOP of the light in the transducer fiber exciting (a) both birefringence axes, and (b) predominately one birefringence axis of the of the transducer fiber.

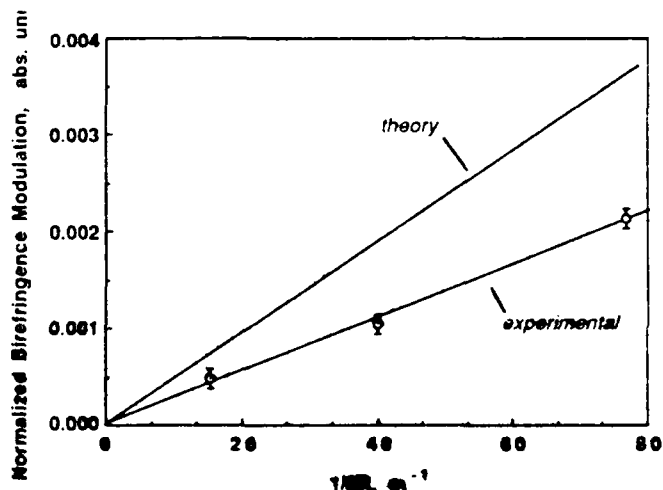


Figure 3. Measured dependence of the ratio  $\{\epsilon_{xy}/\epsilon_{xx}\}$  with coiling diameter  $2R$ . Solid line shows theoretical curve according to Eqn 7.

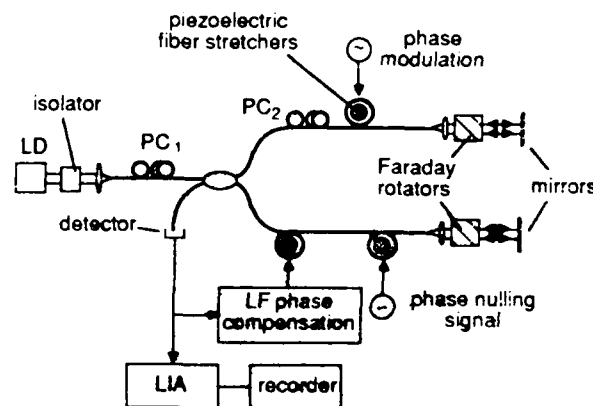


Figure 4. Experimental system used to demonstrate the effect of residual phase amplitude drift, and its compensation.

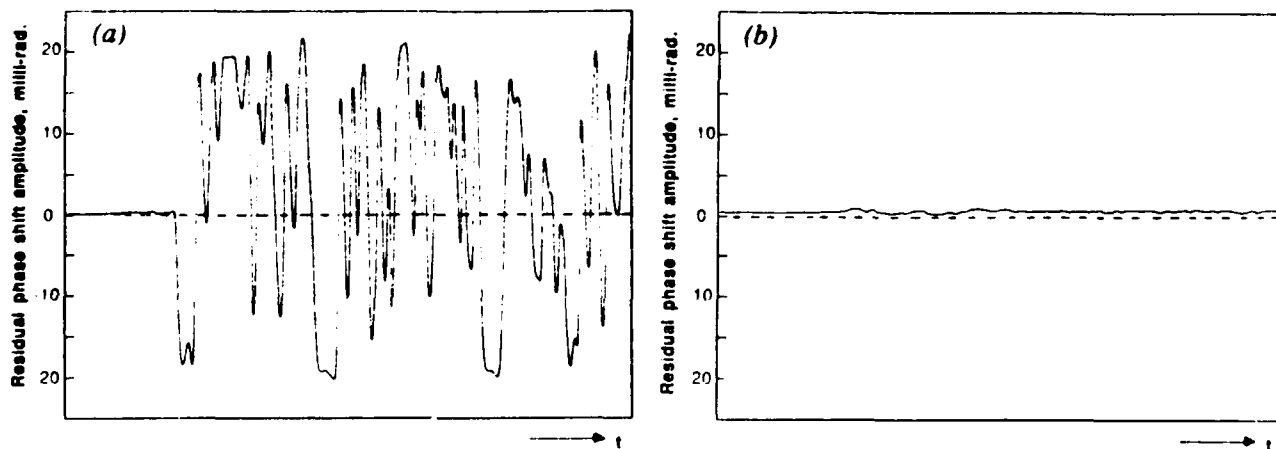


Figure 5. Measured variation in residual phase shift amplitude with input SOP: (a) without Faraday rotator elements, and (b) with Faraday rotators. (30 sec  $\rightarrow$ )

**TH3.1**  
*(Invited)*

**Integrated Optical Circuits For Fiber Optic Sensors**  
P.G. Suchoski, *United Technologies Photonics, East Hartford, CT*

P.G. Suchoski

United Technologies Photonics  
East Hartford, CT 06108

Over the last several years, there has been a growing interest in the use of integrated optic (IO) components and circuits in fiber optic sensor systems. Initial work on integrated optic sensors focused on the use of IO chips themselves as sensors for temperature and pressure. More recently, integrated optics has generally been employed to perform key optical signal processing functions in a fiber sensor or as a signal transduction mechanism for an electrooptic sensor system. This paper will focus on these latter applications. Emphasis will be on chips for fiber optic gyroscopes, laser vibration sensors, and electromagnetic field sensors. In many cases, recent advances in chip technology such as annealed-proton-exchange waveguides in  $\text{LiNbO}_3$  and  $\text{LiTaO}_3$ , has enhanced circuit performance and manufacturability, making IO technology a viable choice for the fiber sensor designer.

Keigo IIZUKA\* and Satoshi FUJII\*\*

\* Presently with the ATR on leave of absence from  
the University of Toronto, Toronto Canada, M5S 1A4

\*\* ATR Optical and Radio Communications Research Laboratories,  
Seika-cho Soraku-gun, Kyoto, 619-02, Japan

### Introduction

Power of resolution of a fault locator has been improving by leaps and bounds. The best values reported so far are of an order of millimeters and the locators are primarily used for finding faults in the bulk media such as breaks in an optical fiber.

This paper reports the achievement of improvement by 1,000 times over the current resolving power of the fault locators by widening the range of the frequency shift of the laser source. The power of resolution of an order of microns was achieved and it was demonstrated that such a fault locator can detect the faults in such an integrated optics devices as an optical guide. It was even possible to make a non-destructive measurement of the cross-section of an optical fiber. It was also made possible to quantitatively measure the anisotropy of a lithium niobate crystal. Moreover an IR laser beam being used, it was possible to see through such optically opaque media as Si or GaAs wafers.

### Principle of operation

The present fault locator uses the CW oscillation of the laser diode source. The carrier frequency of the source was stepwise shifted. The distance to the target was determined by knowing how the amplitude and phase of the received signal changes as the frequency of the source steps. Both FFT and Neural Network were tried to reduce the information about the distance and magnitude of the scatters in the targets.

When the frequency of the laser beam is at  $f = f_0 + n\Delta f$ , the received signal  $H_n$  is

$$H_n = \sum_{k=0}^{N-1} \frac{S_k E_0}{X_k} \exp(j4\pi \frac{f_0 + \Delta f}{v} X_k). \quad (1)$$

If the distance  $X_k$  is also quantized as  $X_k = X_0 + k\Delta X$ , and a condition,

$$\frac{2\Delta f \cdot \Delta Z \cdot N}{v} = 1, \quad (2)$$

is imposed, Eq.(1) can be rewritten as a form of DFT after some manipulation as

$$H'_n = \sum_{k=0}^{N-1} h_k \exp(j2\pi \frac{nk}{N}), \quad (3)$$

where  $h_k$  contains the parameters about the target[1][2][3]. Equation being a form of the inverse DFT, the simplest, if not the most sophisticated way, of obtaining the values of  $h_k$  is the use of the DFT. In this paper an attempt was also made to use the theory of Neural Network[4] to recover  $h_k$ .

Fig. 1 shows a layout of the fault locator. An external cavity controlled laser diode can change the wavelength of the output light as much as 100nm from 1.5 to 1.6 $\mu$ m. The laser beam is first split into the object and reference beams by an AOM (Acousto Optic Modulator). The AOM not only split the beam but also shifts the carrier frequency of the reference beam from that of the object beam by 40MHz which is later used as IF frequency.

The object beam is focussed into the target optical guide and the reflected object beam is mixed with the reference beam at an APD mixer. The 40MHz IF frequency from the mixer is fed into the network analyzer which provides the amplitude and phase of the reflected object beam with respect to the reference beam.

The output from the network analyzer is then put into either an FFT or Neural Network processor to obtain the final display signal. A HeNe laser beam was mixed with the object beam through an optical fiber coupler. The HeNe laser beam was useful for aligning the object beam to the target.

The resolution  $\Delta Z$  of the fault locator is increased with an increase in the total shift of the frequency  $N\Delta f$  as seen from Eq.(2). The value of  $N\Delta f$  obtained was 12.55THz which corresponds to the resolution  $\Delta Z$  of 12 $\mu$ m in free space or 5.4 $\mu$ m in a lithium niobate optical guide used as a target.

### **Experimental results**

Fig.2 shows the display of the fault locator. The target was a sheet of fused silica glass with an air void. The horizontal axis of the display is the distance and the vertical axis, the scattering amount. The over-all dimensions as well as 27 $\mu$ m thick void is accurately monitored by the fault locator.

The solid line is the display obtained by the DFT processing and the dotted line is that obtained by the Neural Network processing. The Neural Network processing not only reduces the background noise but also improves the sharpness of the peaks significantly.

Fig.3 shows the cross-section of a multimode optical fiber type EPF by Nippon Sheet Glass. The indices of refraction of the core and cladding regions are 1.59 and 1.52 respectively. The object beam was injected perpendicularly to the fiber axis. Such a fault locator may be useful as a monitor during the fabrication of an optical fiber because the cross-sectional information can be obtained with neither touching nor cutting the optical fiber.

Next, a thin lithium niobate wafer was used as a target so that the anisotropy of the crystal be determined. The optical axis of the lithium niobate was in the plane of the plate surface. The change in the apparent thickness of the crystal by the rotation is shown in Fig.4.

The top graph is for the case when the direction of the optical axis was parallel to that of the polarization of the incident beam. The two peaks represent the front and back surfaces of the crystal, and the distance between these represent the thickness in terms of the wavelength in the crystal.

The middle graph is for the case when the direction of the optical axis was rotated at 45° with respect to the direction of the polarization of the horizontally polarized incident beam. The *e* wave component whose direction of polarization is parallel to the crystal axis and the *o* wave component whose direction of polarization is perpendicular to the optical axis are simultaneously transmitted. The peak corresponding to the back surface is now split into two. This is because of the difference in the wavelengths of the two waves due to

the difference in the indices of refraction  $n_e$  and  $n_o$ .

The bottom graph is for the case when the direction of the optical axis was made perpendicular to the polarization of the incident beam. The back surface peak became a single peak again. The thickness of the crystal appears wider than that in the top graph.

Reported ratio between the two indices of refraction of the  $\text{LiNbO}_3$  in the two directions is  $2.286/2.200 = 1.039$ . Our measured ratio between the apparent thicknesses is 1.033 and good agreement was obtained.

Now that the achieved resolution was  $5.4\mu\text{m}$  (When the Neural Network processing is used, it is even better), it is feasible to use the device to find the faults inside an optical guide. A score of a predetermined dimension was made in a Ti diffused  $\text{LiNbO}_3$  optical guide at a predetermined distance. The display from the fault locator is shown in Fig.5. Insert of the graph at the upper left corner is the depth profile of the score measured by a profile meter. The middle graph is the display by the fault locator. The horizontal axis is the distance and the vertical axis, the scattering amount. The bottom is a microscope photograph of the optical guide. An array of the horizontal lines in the picture represents the array of optical guides one of which was used and the vertical lines, the score made on the wafer by a rotating diamond blade. The location of the score in the fault locator display and that in the photograph match well.

Advantages of such a fault locator are that the amount of scattering can be measured at the same wavelength as the guide is operated at and the faults can be located even when the optical guide is not straight because the object beam follows the path of the guide.

## **Conclusions**

A fault locator with  $5.4\mu\text{m}$  resolution was reported. Its usefulness as a device was demonstrated by the performances including

- (1) Fault location in optical guides,
- (2) Cross-sectional profile of an optical fiber,
- (3) Faults in Si and GaAs wafers,
- (4) Anisotropy of a crystal.

## **Acknowledgement**

The authors are grateful for Dr. I. Kitano of NSG, Professor T. Sueta, M. Izutsu, H. Nishihara of Osaka University, Dr. Y. Sakauchi of Sanyo Electric Co., and Dr. J. Minowa of Sumitomo Cement Co. all for providing us with various kinds of targets for us to try with our fault locator. They are also grateful for Professor Y. Imai for his suggestion of using the fault locator as a device to determine the anisotropy of a crystal. Mr. K. Kawashima of ATR was helpful in preparing the samples. Dr. H. Murata suggested a possible use as a monitor during the fabrication of the fiber.

## **References**

- [1] K. Iizuka, "Tera Hertz Coherent Radar," ATR Technical Report TR-O-0012, Oct. 1989.
- [2] K. Iizuka and S. Fujii, "Tera Hertz Imaging Radar," ATR Technical Report TR-O-0036, Dec. 1990.
- [3] K. Iizuka, Y. Imai, A. P. Freundorfer, R. James, R. Wong and S. Fujii, "Optical step frequency reflectometer," J. Appl. Phys., 68-3, pp. 932-936, 1990.
- [4] T. Manabe and S. Fujii, "Array processing with neural networks for multiple emitter bearing estimation," 1990 IEEE AP-S Symposium Digest, pp. 1458-1461, 1990.

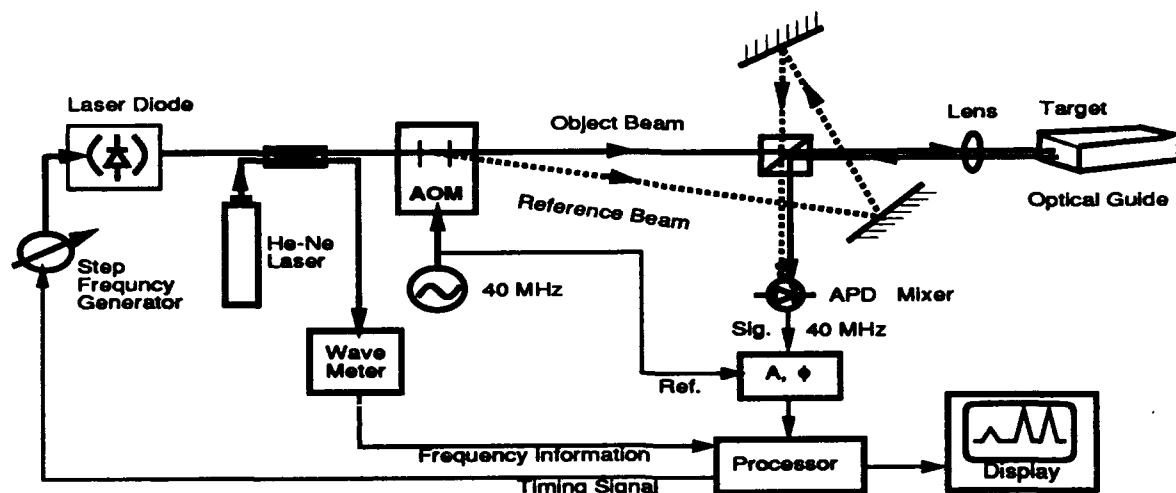


Fig. 1: Layout of the fault locator for integrated optics.

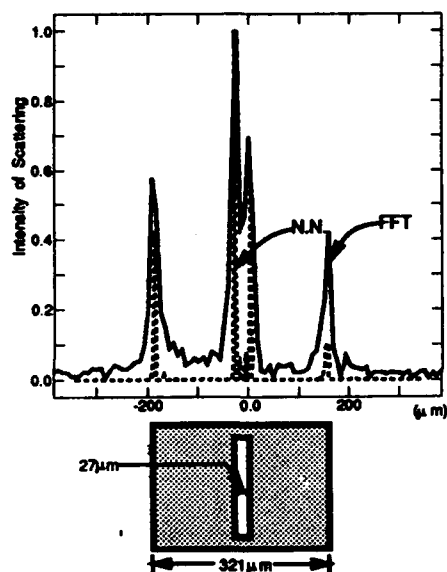


Fig. 2: Detection of a void in a fused silica glass.

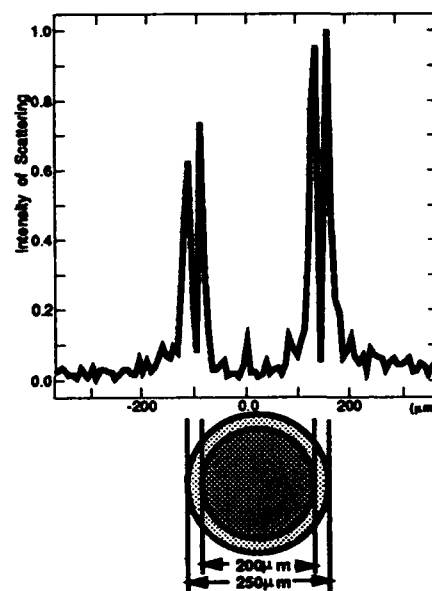


Fig. 3: Measured cross-section of a multi-mode fiber.

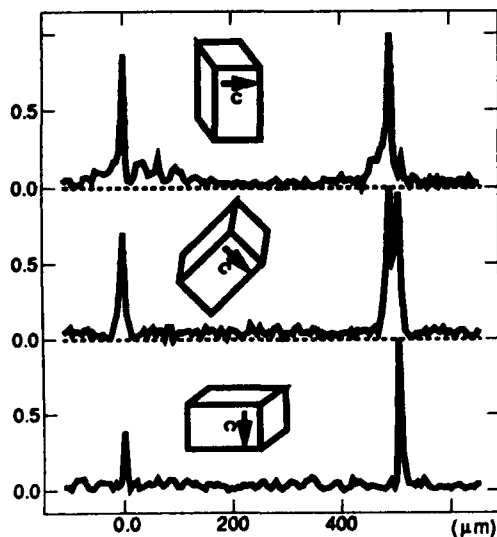


Fig. 4: Determination of birefringence of  $\text{LiNbO}_3$

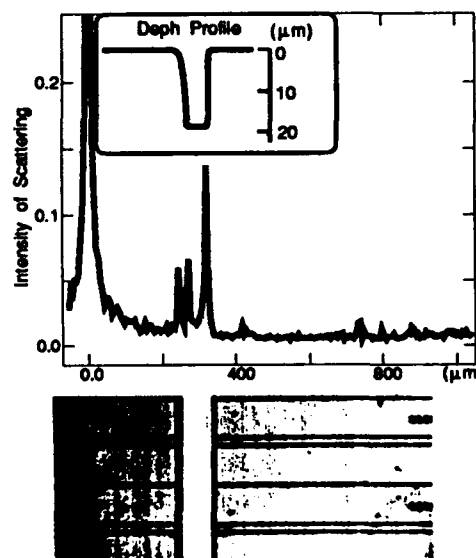


Fig. 5: Detection of faults in an optical guide.



**A Differential Measurement Technique For Optical  
Fibre Sensors Using Intensity Modulation**

by

**R.I.MacDonald and R.Nychka  
Telecommunications Research Laboratories(TRLabs)  
4245 97th St  
Edmonton, Alta.,  
Canada T6J 5Y7**

**1. Introduction**

Fibre sensors that modulate optical intensity can be very simple but are subject to interference from attenuation variation in the download. We present a method (Q-modulation) of compensating such interference by performing a differential measurement. The method requires neither the mechanical precision of spectral modulation sensors /1/, nor the bandwidth of time of flight techniques /2/. In Q-modulation sensing, the intensity modulation produced by a sensor occurs in a fibre resonator as shown in Fig.1. The transfer function of the resonator for the intensity modulation subcarrier is peaked at the resonance frequencies. The light launched into the fibre download is intensity- modulated near the fundamental resonance frequency. The influence of loss induced by the sensor is detected by its influence on the quality factor (Q) of the resonator. As the attenuation of the sensor increases, the loop Q- factor decreases, and the frequency response peak broadens. The ratio of the modulation factor at resonance to that off resonance decreases with increasing sensor attenuation in the loop.

The ratio of the subcarrier modulation index measured at the receiver off- resonance to that of at the resonance frequency provides an indication of the Q- factor of the loop, and is independent of the download attenuation. If variations in loop loss are known to be due to the sensor, the Q measurement provides a robust method of interrogating it. Since the method uses incoherent optical transmission, it can be used with multimode fibre and is not subject to mechanical tolerances on the optical scale. The wavelength at resonance is of the order of centimetres or metres. In comparison to spectral modulation the Q-modulation technique has the advantage that a wide optical bandwidth is not required of the transmitter, and in consequence considerably higher carrier power is obtainable by using laser diodes rather than light emitting diodes or other wideband optical sources. In comparison to the loop-TDM approach it has the advantage of requiring a much smaller loop length for electronics of a given bandwidth.

### 3. Experiment

An experiment was undertaken to confirm the principles of Q- modulation sensing. To explore systems for simple installation, easily handled plastic multimode optical fibre was employed in combination with visible light emitting diode sources (660nm). A 10.9m loop of fibre was coupled to a short download by means of a variable plastic fibre four- port coupler developed especially for this project (This coupler will be described elsewhere .) The excess loss of the coupler was approximately 1dB, and that of the fibre loop about 4dB at the wavelength used. The mode mixers shown in Fig 1 at the inputs to the coupler ensure a constant mode distribution to prevent mode selection effects on the coupling ratio. The mode mixer in the loop is formed by wrapping the fibre into a coil for packaging with the sensor. The resonance frequency was 18.7MHz, and the normalised measurement frequency was 0.786 (14.7 Mhz). A fairly small frequency shift was chosen to minimise the effects of nonlinearities in the frequency response of the receiver. Loss in the loop representing modulation from the sensor was induced by misaligning a fibre connector in the loop. Similarly, loss in the download was induced by misaligning the source or detector connector fibres. Frequency response measurements were made with a network analyser using a 10 kHz noise window, and the ratio between the resonance and measurement responses was read off the network analyser directly.

Calculated and measured sensor calibration curves are shown in Fig.2 The measurement, consisting of the ratio between the off resonance and the on- resonance modulation levels is plotted as a function of the loop loss for two different settings of the variable coupler. The power division ratio of the coupler depends slightly on the input port used: a ratio  $x_x$  is coupled from the download into the loop, while  $y_x$  is coupled from the loop into the return lead. The combined parasitic losses of the coupler and loop were measured to be 5 dB, and coupler ratios of  $x_x=0.725$  ,  $y_x=0.666$  and  $x_x=0.563$  ,  $y_x=0.474$  were determined for the two devices studied. The calibration of the device is in excellent agreement with elementary modelling using these parameters. While it is nonlinear, the calibration can be seen to be reliable over a range of loop loss exceeding 15dB. We anticipate that the use of high power optical sources such as diode lasers, and an optimum choice of normalised frequency will yield a considerably wider measurement dynamic range.

The system exhibited no detectable variation in the measurement of the sensor attenuation for fibre download attenuations up to 7dB, at which point the receiver noise became influential. We anticipate that with the use of higher power optical sources such as lasers, and glass fibres, very high isolation of the measurement from the download can be obtained.

### 4. Implementation issues

The Q-factor modulation technique can be used with any localised or distributed, single or multimode fibre sensor whose attenuation changes as a function of the measurement. The resonance at the subcarrier frequency may be induced by a fibre loop, or a fibre cavity subcarrier resonator analogous to a fibre Fabry- Perot resonator. With simple electronics designed for frequencies in the 10MHz range such resonators will

typically involve a few metres of fibre. The technique offers the possibility of using simple optical fibre sensors remotely with greatly enhanced accuracy as a result of the differential measurement. We anticipate that sensor multiplexing by Q- modulation may be possible on a single download if each sensor is provided with a resonant cavity at a different frequency.

#### Acknowledgement

This work is sponsored by the Telecommunications Research Laboratories.

#### References

1. E.W.Saaski, J.C.Hartl, G.L.Mitchell, "A fibre optic sensing system based on spectral modulation" Proceedings of the Instrument Society of America, 41, pp1177-1181,(1986)
2. G.Adamovsky, "All- fibre sensing loop using pulse modulated light emitting diode", Electron.Lett., 21, pp922-923, 1985

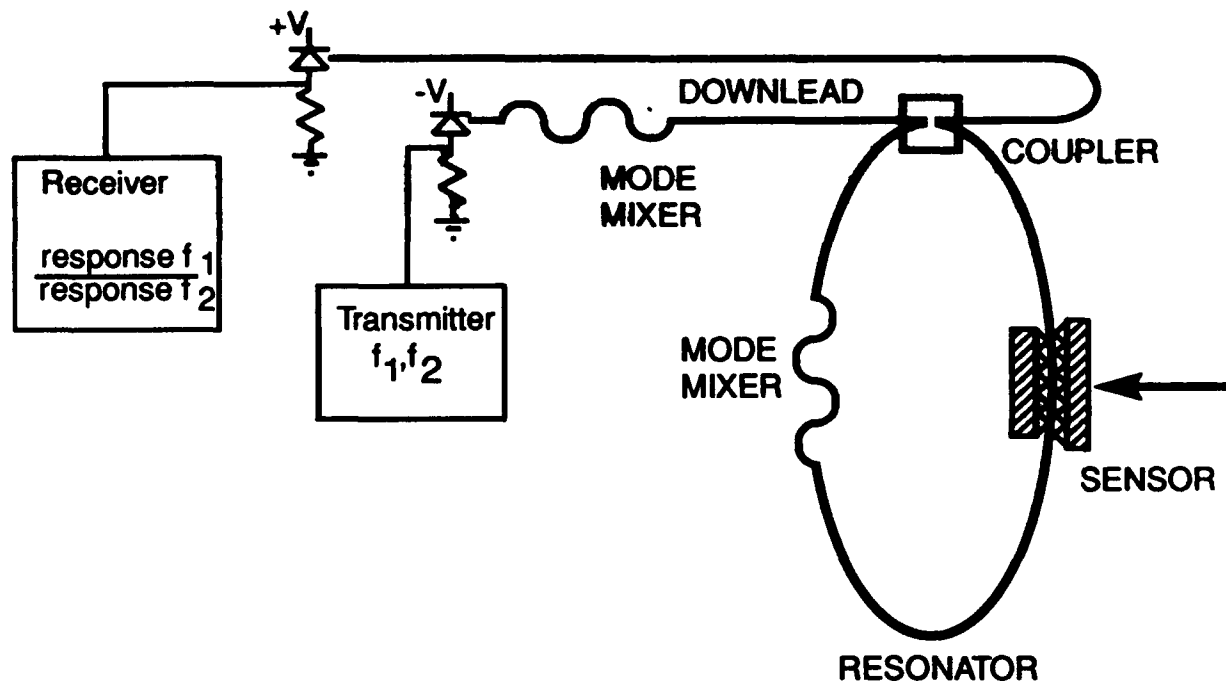


Fig.1 Concept of a Q- modulation sensing system using a loop resonator. In the experiments the intensity- modulation sensor operated by fibre misalignment and the transmitter and receiver were connected to a network analyser which measured the frequency response of the loop directly.

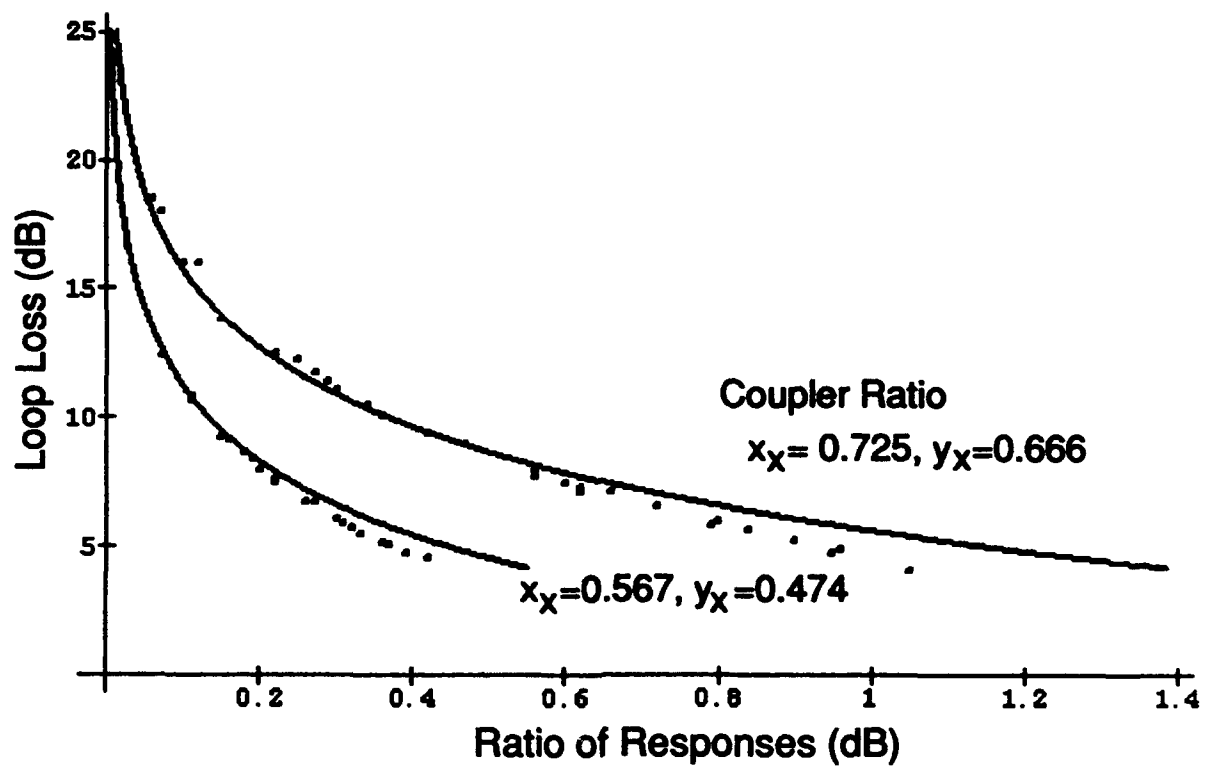


Fig.2. Calculated and measured calibration curves for the Q- modulation sensor system for coupler crossover ratios  $x_x = 0.725$ ,  $y_x = 0.666$ , and  $x_x = 0.563$ ,  $y_x = 0.474$ . The curves show the ratio between the responses measured on resonance and at a normalised frequency of 0.786 as a function of loss induced in the model sensor by fibre misalignment.

## TH3.4      Optical Displacement Sensor By Focus Error Detection

M.Shigehara,Y.Hattori

Sumitomo Electric Industries, LTD.

1, Taya-cho, Sakae-ku, Yokohama, 244 Japan

Tel.(045)-862-7167 Fax.(045)-851-1557

### I.Introduction

The non-contact measurement of three dimensional profiles or minute displacement is important in many fields, including the assembly of various optical components. We have developed a small optical displacement sensor by using polarization maintaining optical fiber as a laser beam guide within 0.1 $\mu$ m reproducibility using focus error detection techniques. We used the critical angle method<sup>1</sup> for focus error detection.

### II.Principle

We employed the critical angle method,because it has a higher sensitivity than other focus error detection techniques, such as, the astigmatic method<sup>2</sup> or the knife edge method.

Figure 1 shows the principle of the critical angle method. A prism is positioned at a critical angle to the optical axis( $P_1$  to  $P_2$ ). When a sample surface is in focus(Case B), reflected light, after passing through an objective lens, becomes parallel and all of the light is reflected by the prism. Thus the intensity of the light detected by the two photodiodes( $PD_1, PD_2$ ) is the same. If the sample surface is close to the lens(Case A), the reflected light which comes into the prism becomes divergent. A part of the light incident on the upper side of the prism passes through it, as the incident angle of light becomes smaller than the critical angle. This phenomena causes a difference between the light's intensity which is detected by the two photodiodes( $PD_1, PD_2$ ). If the sample surface is distant to the lens(Case C), the reflected light which comes into the prism becomes convergent. A part of light incident on the lower side of the prism passes through it, as the incident angle of light becomes smaller than the critical angle. This phenomena causes, opposite to that of Case A, difference between the light's intensity which is detected by the two photodiodes( $PD_1, PD_2$ ).

## 3. Design

Figure 2 shows the configuration of the optical head. To design for small optical head, we used a fiber collimator as a light source. It is composed of a polarization maintaining optical fiber and a graded index lens. The other side of the optical fiber is coupled to a laser diode of 780nm wavelength by a lens. The light collimated by the graded index lens is adjusted S-polarized light and is reflected by a polarization beam splitter. The light reflected by the sample surface is converted to P-polarized light by passing twice through a quarter wave plate. The light is then transmitted through the polarization beam splitter, reflected by the critical angle prisms, and finally goes into the photodiodes. Axial displacement ( $\Delta \mu\text{m}$ ) is calculated by the follow expression,

$$\Delta = kS \quad k:\text{constant} \quad (1)$$

where

$$S = \frac{(P_A - P_B) + (P_C - P_D)}{P_A + P_B + P_C + P_D} \quad (2)$$

Here,  $P_A$ ,  $P_B$ ,  $P_C$ , and  $P_D$  represent the output of detectors A, B, C, and D respectively.

The advantage of using the optical fiber collimator is not only the miniaturization of the light source. There are two other advantages. One is that it is possible to get a circular collimating beam. Generally, the pattern of the beam from a laser diode is elliptical. Therefore, the pattern of a collimated beam using a collimating lens and that of a focusing beam using an objective lens are elliptical. A beam rectification prism is usually used to convert an elliptical beam into a circular beam. A fiber collimator does not require a beam rectification prism at the optical head. Another advantage is that it is easy to replace the laser diode if it becomes damaged, because adjustment of the optical head is unnecessary when exchanging the laser diode.

On the basis of the above investigation, we have experimentally made an optical head as small as  $30\text{mm} \times 30\text{mm} \times 100\text{mm}$ .

#### IV. Experimental result

Figure 3 shows the characteristic curve of output dependence on displacement of the sensor. We used a reflecting mirror as a sample surface, and mounted it on an automatic stage which moves in the direction of the objective lens. The horizontal axis represents a displacement of the mirror measured by an HP Laser System(5528A), and the vertical axis represents an output of the sensor by equation(2). We obtained  $0.1\mu\text{m}$  reproducibility( $3\sigma$ ) using this sensor.

Figure 4 shows an example of the surface roughness measurement. Here, we used a turned ZnS(infrared optical part) as a sample.

#### V. Conclusions

In conclusion, a small size optical displacement sensor has been developed by using a fiber collimator. This makes it possible to use the sensor in narrow spaces. It is expected that sensors as small as  $25\text{mm} \times 25\text{mm} \times 40\text{mm}$  could be constructed by using an aspherical lens instead of a microscope objective lens.

We obtained  $0.1\mu\text{m}$  reproducibility( $3\sigma$ ) using the sensor.

#### References:

- 1) T. Kohno et.al, Appl. Opt., Vol.27, No.1, January 1988
- 2) K. Mitsui et.al, Opt. Eng., Vol.27, No.6, June 1988

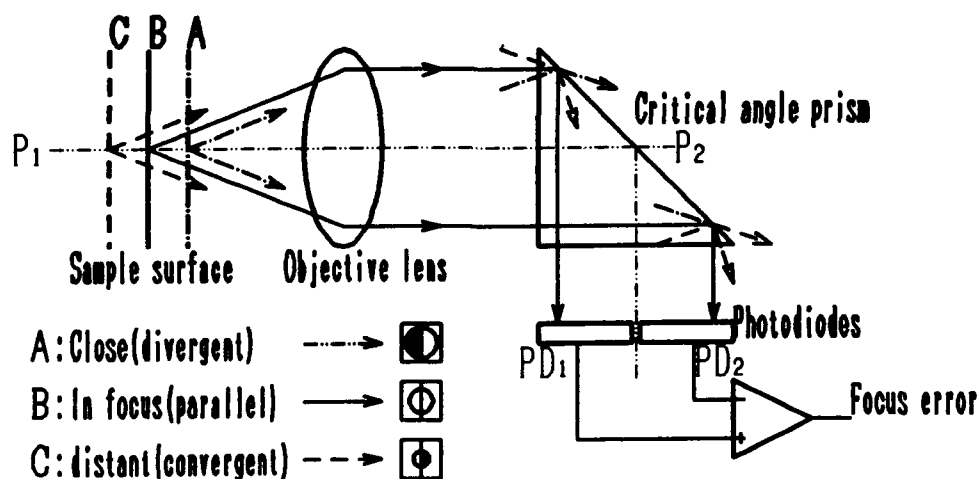


Fig.1 Principle of critical angle method.

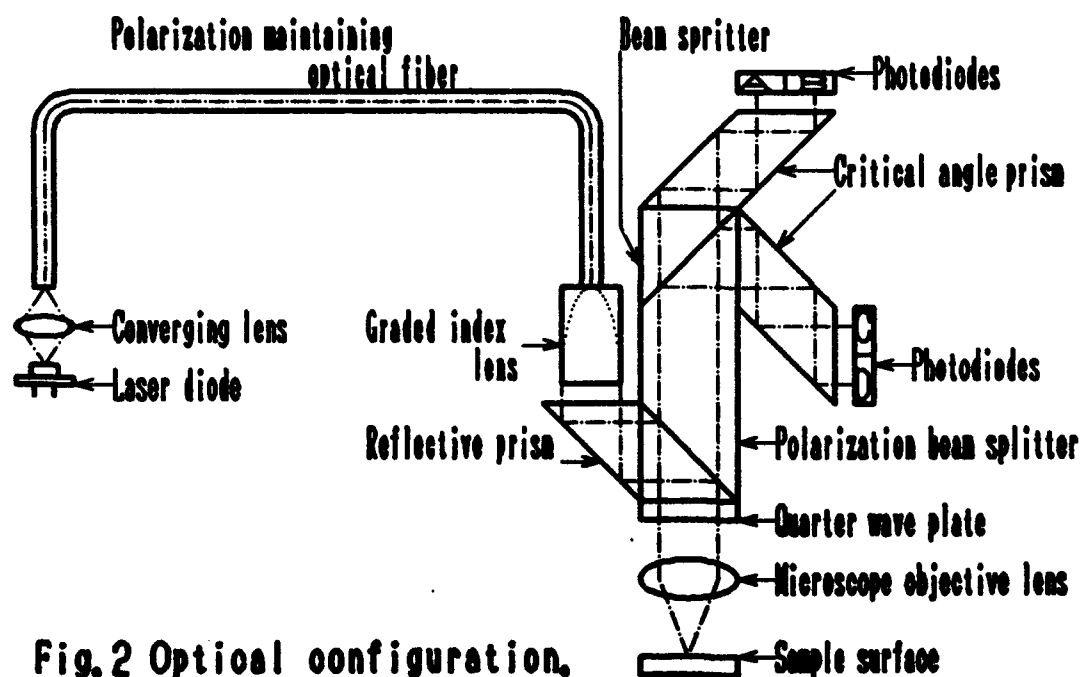


Fig.2 Optical configuration.

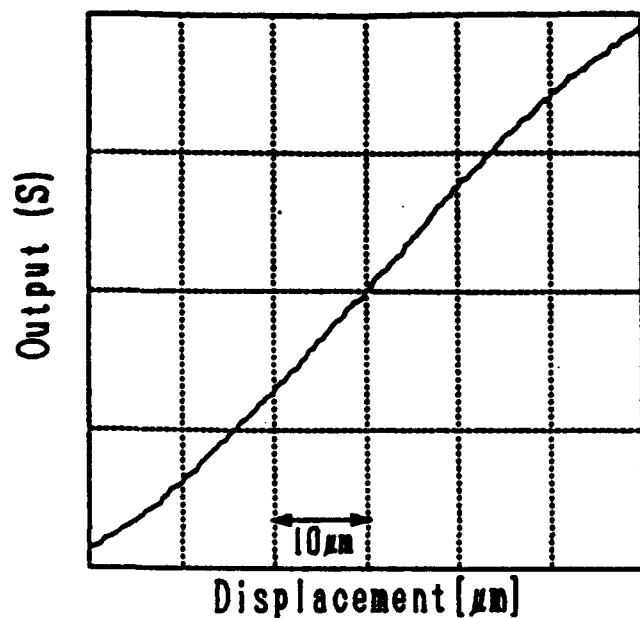


Fig.3 Experimental results.

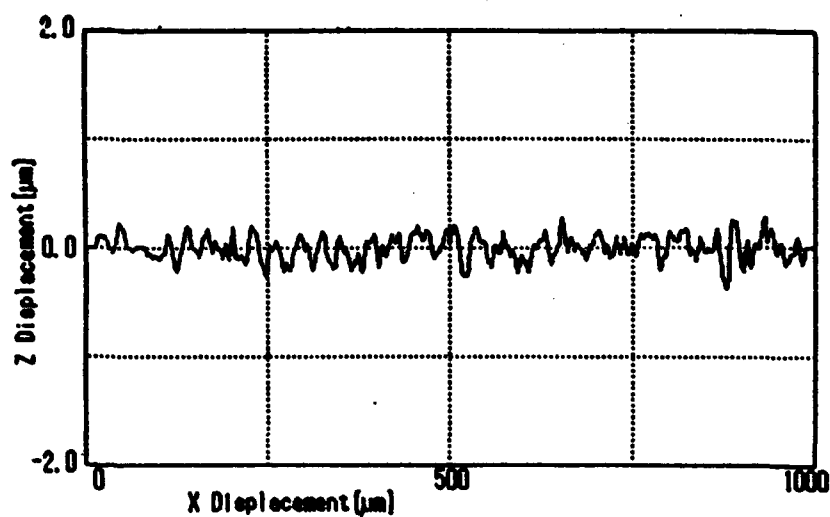


Fig.4 Example of surface roughness measurement of turned ZnS.



# TH3.5 Proposal Of Ultra-High Finesse, Bi-directional Vernier Based On Er-Doped Fiber Ring Resonator

Haruo Okamura and Katsumi Iwatsuki  
NTT Transmission Systems Laboratories  
1-2356, Take, Yokosuka-shi, Kanagawa, 238-03, Japan  
Tel +81 468 59 3219, Fax +81 468 59 3396

## 1. Introduction

An active fiber ring resonator has very recently been proposed<sup>(1)</sup> that uses an Er-doped fiber amplifier(EDFA) to compensate for round-trip optical loss, thereby enhancing the finesse. The prototype linked several commercially-available optical components including two fiber-couplers by fusion splicing, and yet attained a better-than-100-kHz spectrum resolution.

Testing such a high-resolution resonator, however, has been difficult because light sources narrower in linewidth than the resonator passband are not freely available. Moreover, the prototype resonator's length is ~24 m [free spectral range(FSR):~8.5 MHz] mainly because of the length requirement of the EDF. If the FSR were much wider, such resonators would be far more useful as wide-band spectrum analyzers and mode-selectors or filters. Reported vernier structures for FSR expansion<sup>(2)-(4)</sup>, however, consist of two or more concatenated but independent resonators. Thus they suffer from instability in addition to complexity.

This paper presents a narrow resonant-linewidth measurement technique which does not demand an even narrower-linewidth light. Also proposed is a simple bi-directional vernier configuration of the Er-doped fiber ring resonator that effectively realizes wide FSR.

## 2. Theory

**Finesse enhancement**<sup>(1)</sup> Fig. 1 shows a typical two-coupler-type active resonator. The finesse  $F$  in sharp resonance is approximated as  $F \approx \pi \sqrt{A} / (1 - A)$ , where  $A = e^{-\alpha L} \sqrt{G(1-\eta)(1-\gamma)(1-K)}$ ,  $G$  is optical amplifier gain, and  $\gamma$  and  $K$  are the fractional intensity loss and intensity coupling coefficient of the input coupler. Fibre attenuation, propagation constant and the fiber ring length are  $\alpha$ ,  $\beta$  and  $L$ , respectively. The fractional over-all loss in the ring is  $\eta$ . Therefore, the appropriate value of  $G$  makes "A" unity and the finesse infinity. Fig.2 shows calculated finesse as a function of  $G$ .

**Resonant linewidth measurement** The "mode-filtered heterodyne method" proposed here is outlined in Fig. 3. Highly resonant passbands are known to have a Lorentzian form. Therefore, if two resonator-passbands are simultaneously illuminated by two uncorrelated broad-band lights, the RF-beat-noise linewidth should be twice<sup>(5)</sup> the resonant linewidth.

**Bi-directional vernier resonator** The resonant light in one direction is fed into the same ring in the opposite direction. The EDFA operates bi-

directionally. Here, a selective double-path module is needed to develop different FSRs. Suppose each resonator has similar finesse  $F_{cw} \sim F_{ccw}$  but different length  $L_{ccw} > L_{cw}$ , then  $FSR_{cw+ccw} = \alpha FSR_{cw} = (\alpha + 1) FSR_{ccw}$  where  $\alpha(\text{integer}) = (L_{cw}/L_{ccw}) / (1 - L_{cw}/L_{ccw})$ . Here,  $L_{cw}$  and  $L_{ccw}$  have to be chosen such that the value of  $\alpha$  is as close to an integer as possible. Under the condition that the next-higher modes are to be reduced by 20 dB, the effective finesse is raised to  $0.32 F_{cw} F_{ccw}$ . The overlapped passband narrows to 64%(3).

### 3. Experiment and results

**Experimental set-up** Fig. 4 shows the fusion-spliced all-PANDA bi-directional ring resonator. The ring length is  $\sim 24$  m, a 15-meter-length of which is a 300-ppm-Er-doped PANDA fiber pumped with a 1.48- $\mu\text{m}$  Fabry-Perot LD. A circulator was used, in which the optical path difference was made adjustable by changing reflecting fiber lengths. Polarization cross-talk, return loss and insertion loss of the fabricated circulator were measured as -25 dB, 55 dB and 2.7 dB, respectively. A 1-nm bandpass filter tuned the resonator from 1549.3 nm to 1552.1 nm and prevented spurious lasing.

**linewidth measurement** To create two uncorrelated lights, a 340 kHz-linewidth laser light was fed to a Mach-Zehnder interferometer(M-Z). One arm had an intensity modulator sinusoidally driven at  $\sim 8.5$  MHz(=FSR) to generate sidebands. The other arm was 5-km of fiber to eliminate correlation. Detected beat-noise linewidth decreased with the LD pump power until the commencement of lasing. Fig. 5 shows the uni-directional finesse thus measured, in which the narrowest linewidth was 15~17 kHz (finesse:560~500).

**Vernier resonator** Fig. 6(1) shows the 35 MHz LD light spectrum used as the resonator input as observed with a scanning Fabry-Perot interferometer(FSR:6 GHz, finesse: $\sim 6000$ ). Fig. 6(2) is an observed uni-directional output spectra having a  $\sim 8.5$ -MHz spacing. Fig. 6(3) is an observed bi-directional output spectra with a  $\sim 2$  m path difference, in which only one dominant spectrum with negligibly small side-spectra was observed. This confirms the vernier effect. Here,  $FSR_{ccw} = 7.85$  MHz and  $FSR_{cw} = 8.5$  MHz. Therefore,  $FSR_{cw+ccw} = 102$  MHz. And,  $F_{cw+ccw} = 9375$  if  $F_{cw} = F_{ccw} = 500$ .

Fig. 6(4) is the bi-directional output spectra observed with a 0.25-m path difference. Though it was unstable, spectra similar to Fig. 6(3) was observed. Here,  $FSR_{ccw} = 8.41$  MHz,  $FSR_{cw} = 8.5$  MHz. Therefore,  $FSR_{cw+ccw} = 816$  MHz. And,  $F_{cw+ccw} = 75000$  if  $F_{cw} = F_{ccw} = 500$ .

### 4. Discussions.

Though the vernier effect was experimentally confirmed, several issues still exist to stably and effectively expand the FSR. They are:(1) EDFA gain stabilization (2)Resonator length locking to the optimum

vernier condition (3) Minimizing the effect of loss and gain dependence on signal propagation directions(6).

The all-optical feedback scheme(7) is applicable to automatically offset the loss fluctuation(8) thereby clamping the highest finesse. Also note that when using the bi-directional resonator as a spectrum analyzer, the ring-length scanning would degrade the frequency-overlap sharpness because common scanning results in a different scan ratio for each resonator. This problem is avoided by scanning the input signal frequencies.

## 5. Conclusion

The vernier effect of the proposed bi-directional Er-doped fiber ring resonator was experimentally confirmed. The "mode-filtered heterodyne method" measured a narrow resonant linewidth with conventional light sources. This method confirmed that the narrow uni-directional passband of 15-17 kHz (finesse:560~500) was achieved. Though several important issues still exist, experiments and a theoretical analysis revealed the possibility of extremely high finesse enhancement, even as high as 75000(effective FSR:816 MHz, linewidth:10.88 kHz).

**Acknowledgements** The authors acknowledge suggestions on the bi-directional use of fiber ring by R. Esman and on the circulator by M. Koga. They thank M. Saruwatari, S. Saito for helpful discussions and H. Ishio, T. Ito and K. Nakagawa for encouragement.

## References

- (1) H. Okamura and K. Iwatsuki, "Er-doped fiber ring resonator applied to optical spectrum analyzer with less than 100 kHz resolution", *Electron. Lett.*, Vol. 27, No. 12, pp.1047-1049, 1991
- (2) P. Urquhart, "Compound optical-fiber-based resonators", *J. Opt. Soc. Am. A*, Vol. 5, No. 6, pp.803-812, 1988
- (3) I. P. Kaminow, P. P. Iannone, J. Stone and L. W. Stulz, "A tunable vernier fiber Fabry-Perot filter for FDM demultiplexing and detection", *Photon. Technol. Lett.*, Vol. 1, No. 1, pp. 24-26, 1989
- (4) K. Oda, N. Takato and H. Toba, "A wide-FSR waveguide double-ring resonator for optical FDM transmission systems", *IEEE J. Lightwave Technol.*, Vol. 9, No. 6, pp. 728-736, 1991
- (5) T. Okoshi, K. Kikuchi and A. Nakayama, "Novel method for high resolution measurement of laser output spectrum", *Electron. Lett.*, Vol. 16, pp. 630-631, 1980
- (6) T. Kakinuma, T. Takeda, E. Nishimura and Y. Tamura, "Gain and Noise characteristics of Er-doped fiber amplifiers with different pumping directions", *Topical meeting on optical amplifiers and their applications*, TuB1, 1990
- (7) M. Zirngibl, 'Gain control in Erbium-doped fibre amplifiers by an all-optical feedback loop', *Electron. Lett.*, Vol. 27, No. 7, pp.560-561, 1991
- (8) H. Okamura, "Automatic loss compensation by using an Er-doped fibre amplifier", to be submitted to *Electron. Lett.*

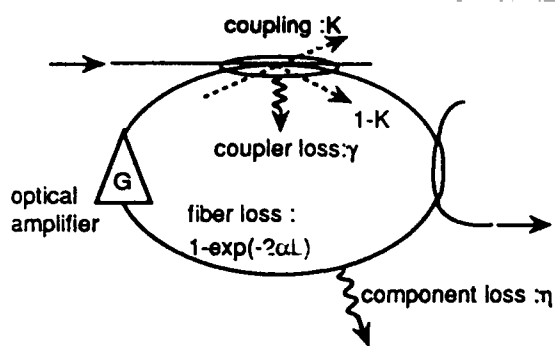


Fig. 1 Er-doped fiber ring resonator

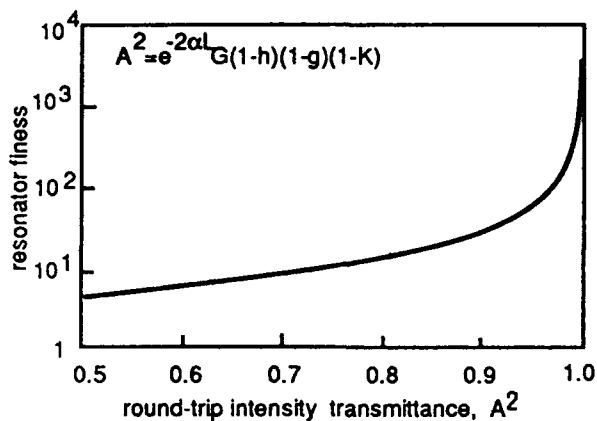


Fig. 2. Finesse enhancement(calculated)

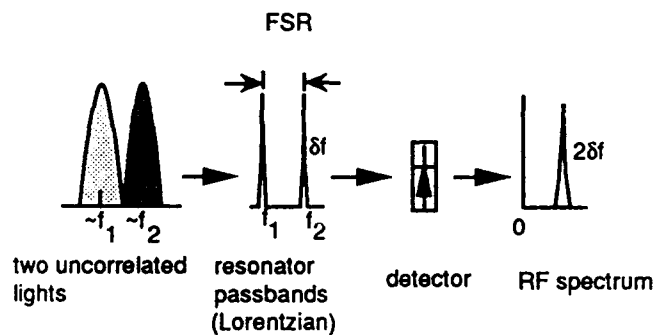


Fig. 3 Mode-filtered heterodyne method

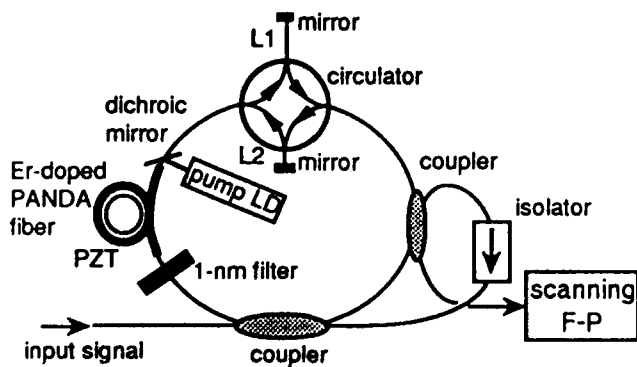


Fig. 4 Experimental configuration

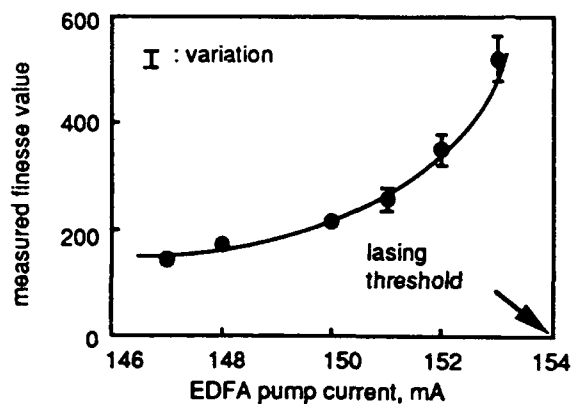


Fig. 5 Finesse enhancement by EDFA (uni-directional resonance)



(1) input LD light spectrum



(2) output spectrum from unidirectional resonance



(3) bi-directional resonance with 2 m path imbalance



(4) bi-directional resonance with 0.25 m path imbalance

Fig. 6 Spectral observation with a scanning F-P

M.Brenci, F.Baldini  
Istituto di Ricerca sulle Onde Elettromagnetiche  
Via Panciatichi 64, I 50127 Firenze (Italy)

## 1. INTRODUCTION

There has been a remarkable development of chemical fiberoptic sensors in recent years. The first chemical fiberoptic sensor, which was a sensor for detecting ammonia, was described in 1976<sup>1</sup>. Since then, investigations have been made of numerous parameters, from pH<sup>2</sup> to gases<sup>3</sup>; from antibodies<sup>4</sup> to metallic ions<sup>5</sup>. This particularly intense interest is completely justified, both because the detection of chemical parameters is extremely important in many industrial and chemical processes, in environmental control and in the biomedical field; and also because chemical fiberoptic sensors offer considerable advantages compared to traditional sensors.

In industry the possibility of perfecting remote-detection measurements in a hostile environment and of achieving continuous monitoring of the parameter under investigation is often essential. The monitoring of oxygen or gases in general in potentially hazardous or explosive environments<sup>3</sup>, the on-line definition of uranium in nuclear industries<sup>6</sup>, the in-situ analysis of metallic ions (copper, etc.) in galvanic baths<sup>7</sup> are only a few examples of situations in which chemical fiberoptic sensors have already been applied in industry.

In environmental analyses, the possibility of performing continuous in-situ controls without having to resort to drawing samples is of great importance, and is often a winning characteristic for fiberoptic sensors, as can be witnessed by the use - already underway - of sensors for the detection of gases (methane, propane, etc.)<sup>3</sup> and of cancerogenous or highly-toxic (e.g. formaldehyde)<sup>6</sup> pollutants for the detection of traces of organochlorides and other pollutants in aqueous water-drainage coming from industrial processes or in water wells<sup>8,9</sup>.

But it is perhaps in the biomedical field that the detection of chemical parameters by means of optical fibers has had its greatest development: their high degree of miniaturization, considerable geometrical versatility, and extreme manageability make it possible to perform a continuous monitoring of numerous parameters, thus enabling the performances of services which are often "unique"<sup>10</sup>: "in vivo" analyses of numerous parameters present in the blood (such as pH, oxygen partial pressure, carbon dioxide partial pressure, calcium, potassium, glucose); "in vivo" measurement of enterogastric reflux; analysis of enzymes and antibodies.

Besides the unquestionable advantages described above, however, several aspects should be kept in mind which, should they be overlooked, could compromise the functionality and performance of the sensor:

- there often exists a transfer of mass between the external environment and the sensor since the optically sensitive reagent and the investigated species can be in different phases, which fact is translated into a lengthening of the response time;
- since the optically-sensitive reagent is often an organic compound, particular attention must be paid to the long-term stability and to the photodecomposition;

It should be emphasized, however, that these problems can be overcome in part by using special expedients, for example by means of a careful advance spectrophotometric analysis that will make it possible to choose the best sensitive reagent.

## 2. OPERATING PRINCIPLE

Fiberoptic sensors are mostly amplitude-modulation sensors: that is, sensors in which the intensity of the light transported by the fiber is directly modulated by the parameter being investigated which itself has optical properties (spectrophotometric sensors); or by a special reagent connected to the fiber, whose optical properties vary with the variation in the concentration of the parameter being studied (transducer sensors). Only in a few special cases is the optical modulation a phase modulation, since the chemical species being investigated modifies the optical path of the light transported by the fiber.

Let us now examine the main physical phenomena which are exploited for the realization of chemical sensors. The most utilized phenomena are definitely fluorescence and absorption, even if chemical fiberoptic sensors have been realized by exploiting other physical phenomena, such as chemical luminescence, Raman scattering, evanescent-wave coupling, and plasmonic resonance.

**Absorption:** in addition to the substances having their own absorption bands<sup>11-13</sup>, substances can also be detected that, by interacting with an appropriate reagent, vary their absorption<sup>14-16</sup> (e.g. acid-base indicators vary their own absorption depending on the concentration of the hydrogen ions). If measurement of the sensor is made during transmission in a solution, the concentration of the parameter being investigated is proportional to the absorbance (Lambert-Beer law); if, instead, the measurement is made during reflectance (e.g. reflection by a solid

substrate), a special function (function of Kubelka-Munk) must be introduced which is proportional to the concentration of the substance under examination.

**Fluorescence:** also in this case, two cases can be distinguished: 1) the substance being investigated is itself fluorescent<sup>9</sup>; 2) the substance is not fluorescent: in this case, it can be labelled with a fluorophore<sup>17,18</sup> or else it can react chemically with a reagent, giving rise to a fluorescent product<sup>5</sup>, or even interact with a fluorophore, causing a variation of it in the emission of fluorescence<sup>19,20</sup>. In the latter case, of particular interest is the phenomenon known as fluorescence "quenching", in which the fluorescence intensity decreases, following interaction with the substance under examination, which can thus be detected<sup>21-24</sup>. In several cases, it can be convenient to measure the decay time of the fluorophore, and not the emission intensity<sup>25</sup>. One advantage of this technique is the possibility of eliminating the effects due to photodecomposition and to small losses, since the decay time is independent of the concentration of the fluorophore. Furthermore, in the case in which several species interact with the reagent, causing emission of fluorescence characterized by different decay times, these can be detected simultaneously, by using time-resolution devices<sup>5</sup>.

It is well to emphasize that the sensors functioning due to absorption - even if less sensitive than the ones functioning due to fluorescence (sometimes even of several orders of size) - are practically undamaged by interferences coming from other compounds. For this reason, while in the analyses on pure (or at least "controlled") samples, the use of fluorophores is preferable because it makes it possible to obtain greater sensitivities, in the case of analyses on highly-heterogeneous and "complex" samples, as for example biological liquids, if the fluorescence resolved in time cannot be utilized, the indicators functioning in absorption guarantee analogous performances with (if not ones superior to) those of the fluorophores.

**Chemiluminescence:** in this case, the emission of photons associated with the reaction between the parameter under investigation and the appropriate reagent is detected: one of the products of the reaction is found in an excited state, and degenerates into the basic state with the consequent emission of light<sup>26</sup>. Good levels of sensitivity can be reached by exploiting this principle. However, since luminous radiation is generated by the chemical reaction and clearly cannot be modulated, as in the case of an external source, interference with ambient light must be carefully avoided.

**Evanescent Wave Coupling:** by adsorbing a certain chemical species on the core or on the cladding of the fiber, a perturbation of the corresponding refraction index is obtained and, consequently, a different penetration of the evanescent wave, which gives rise to a modification in the intensity of the light transported by the fiber: the adsorbed species can thus be detected<sup>27</sup>. Even if very sensitive, this method has the problem of lacking selectivity since, whatever the substance adsorbed may be, there is a variation in the refraction index and, therefore, in the intensity of the light. This snag can be overcome by combining the coupling via evanescent wave with the analysis by absorption or by fluorescence, by setting on the fiber a selective chromophore for the species being investigated<sup>1,28,29</sup>. In this way, a diminishing of the transported light can be observed following absorption, or else the appearance of light emitted by fluorescence, which are function solely of the chemical parameter that interacts with the chromophore.

**Raman Scattering:** the Raman techniques offer considerable advantages over the methods based on absorption or fluorescence, since they make it possible to obtain important information of the structure of the species being investigated, analogous to information obtained by IR spectroscopy. These utilize wavelengths in the visible band and are therefore both useful for analyses in aqueous means, which are highly absorbent in the IR region, and also compatible with the use of fiber optics, which are transparent in the visible region. So far, the greatest limitation of the Raman scattering was its rather low sensitivity. On the other hand, in the case of molecules adsorbed on corrugated metallic surfaces, an increase in the Raman signal of several orders of size ( $\approx 10^7 \div 10^8$ ) has been observed recently. This phenomenon, which is known as Surface-Enhanced Raman Scattering, is still the subject of investigation: it can be attributed to various chemical-physical mechanisms, such as the presence of extremely amplified local electro-magnetic fields on the metallic surface and the resonant charge-transfer excitation of the surface/adsorbate complexes. It is clear that in this case, the fiberoptic sensor must be connected to a spectroscopic apparatus, since the Raman spectrum of the sample under examination is obtained as a result of the detection<sup>30</sup>. On the other hand, the potentials of this technique - which is used with fiber optics and is therefore capable of making a chemical analysis on samples in a hostile or remote environment and, in any case, ones to which access is difficult when using the customary spectroscopic equipment - are extremely high.

**Plasmon Resonance:** this physical phenomenon, still very little exploited but potentially suitable for the detection of chemical species, is based on the variation in the light reflected by a fine metallic layer as a result of the surface-plasmon resonance<sup>31</sup>. Experimentally, this resonance is detected by observing the presence of a minimum in the light reflected in the variation of the angle of incidence on the metal/optical guide interface. This

value also depends on the refraction index of the external medium, so that with this method variations in this index can be detected. Hence, the presence of a chemical species can be detected following a variation in the refraction index.

### 3. PARAMETERS INVESTIGATED WITH FIBEROPTICS

It is evident that, in order to be able to perform a detection using fiberoptics, the working wavelengths must be included within the transmission windows that are characteristic of the fibers. Silica fibers with a low OH content (low OH silica fibers) guarantee low attenuations for wavelength values included between 500 nm and 1750 nm. For  $\lambda < 500$  nm, as the wavelength decreases, the attenuation increases up to values on the order of 3 dB/m for  $\lambda \approx 200$  nm, making the use of very short fiber lengths necessary; while for  $\lambda > 1759$  nm, special fibers (ZrF and chalcogenide glass fibers) must be used, also if, in the best of cases, these have attenuations on the order of tenths of dB/Km. In the case in which fiber lengths are used for the realization of sensors over long distances ( $\geq 1$  Km), only the wavelengths in which the attenuation of the fibers is particularly low: 1) 770 nm  $< \lambda < 900$  nm (attenuation  $\approx 3 \div 5$  dB/Km); 2) 1050 nm  $< \lambda < 1350$  nm (attenuation  $\approx 0.5 \div 2$  dB/Km); 3) 1450 nm  $< \lambda < 1750$  nm (attenuation  $\approx 0.2 \div 3$  dB/Km) can be considered useful. For detection of chemical parameters using fiberoptics, the working wavelengths differ in accordance as to whether they are considered electronic or vibrational transitions. In the former case, the region in question is the UV visible, which can then be exploited for detection using optical fibers (e.g. bilirubin  $\lambda_{\text{abs}} = 452$  nm, nitrogen dioxide  $\lambda_{\text{abs}} = 496$  nm; nitrates  $\lambda_{\text{abs}} \approx 210$  nm; phenols  $\lambda_{\text{exc}} = 266$  nm and  $\lambda_{\text{em}} = 270 \div 400$  nm). Instead, in the case of vibrational transitions, the wavelengths involved fall within the mid-IR (e.g. heavy water  $\lambda_{\text{abs}} = 4$   $\mu\text{m}$ ; propane  $\lambda_{\text{abs}} = 3.3$   $\mu\text{m}$ ), even if it is preferable at times to operate in the overtones or on combinations of the absorption bands, which fall within the near-IR in which attenuation of the fibers is less (e.g. methane  $\lambda_{\text{abs}} = 1.33$  and  $1.66$   $\mu\text{m}$ ; propane  $\lambda_{\text{abs}} = 1.68$   $\mu\text{m}$ ).

In the case of spectrophotometric sensors, the absorption band of the associated parameter or the possible emission of fluorescence is exploited. In the case of transducer-type sensors, use is made - as has been mentioned - of a special reagent whose optical properties vary in accordance with the variation in the concentration of the parameter under examination. In the simplest case, the reaction between reagent and parameter being investigated is direct. Typical examples are oxygen sensors in which the oxygen interacts directly with a fluorophore, causing in it a decrease in the emission of fluorescence, and pH sensors in which the hydrogen ions react with an acid-base indicator or a fluorophore, causing a variation in the absorption or fluorescence, respectively.

In other cases, the parameter under investigation does not directly modify the optical properties of the reagent connected to the fiber, but reacts chemically, giving rise to a detectable product. For example, the detection of carbon dioxide is based on the detection of the pH of a carbonated solution, since the acidity of this solution depends on the quantity of  $\text{CO}_2$  which is dissolved in it:



The detection of ammonia is generally based on the pH variation which it causes by being dissolved in an aqueous solution:



Of particular interest are the enzyme sensors which make it possible to detect numerous biological parameters and which, therefore, find important applications in biomedicine. Detection is based on a selective conversion, catalyzed by a special enzyme, of the parameter under examination in a product which can be optically detected. The concentration of the parameters being analyzed can be linked to the rate of formation of products or to the steady-state concentration of the products. It is evident that, in this case, in addition to the optical reagent, the special enzyme must be immobilized at the tip of the fiber.

### 4. THE PROBE

Spectrophotometric-type sensors are the simplest, and at most require the realization of an optimized photometric cell to be connected to the fiber. An example is given by the sensor for detection of the enterogastric reflux (bile reflux from the duodenum to the stomach)<sup>11</sup> in which the presence of bile in the stomach is registered by means of the detection of its main pigment, bilirubin, having its absorption peak centered at  $\lambda = 452$  nm. Fig.1 shows an outline of the "cell": it consists of a Teflon cylinder, connected with a bundle of optical fibers, the structure and dimensions of which have been chosen so as to permit "in vivo" measurements, avoiding problems connected to reflection from the stomach wall and to the possible pollution of the

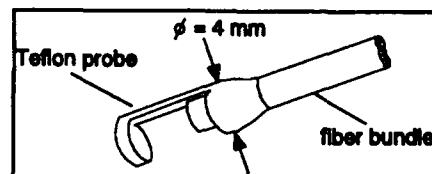


Figure 1 Sketch of the optical probe for bile detection.

probe by elements besides bile and gastric juice (e.g. particles of food, mucus, etc.).

In the case of transducer detectors, the reagent can be immobilized directly on the fiber or on a solid external support, which will constitute the probe, referred to as the optrode (from "optical electrode"). In the former case, we are talking about intrinsic-optrode sensors, while in the latter case we are talking about extrinsic-optrode sensors. With the intrinsic optrode, a compact, highly-miniaturized structure is attained, since the probe is practically the fiber itself. It is necessary, however, to distinguish the case in which the chromophore is immobilized at the fiber's extreme tip or along it on the core or on the clad. In the first case, the signal levels obtainable are generally weak, since the modulation of the optic signal comes from a thin layer of reagent connected to the fiber: the use is thus made necessary of sophisticated and costly electronic and optical components (laser sources, lock-in, photomultipliers, etc.). By specially treating the tip-end surface of the fiber, sufficiently to increase the sites available for attaching the chromophore<sup>32</sup> it is possible to obtain a partial improvement in the signal-to-noise ratio. Instead, in the case of the immobilized chromophore along the fiber, modulation of the luminous intensity, even if due to a thin layer of reagent, occurs on a section of fiber that is long enough to guarantee good signal levels.

In general, better results are obtained in the extrinsic-optrode sensors, since a larger surface is available for attaching the chromophore, even if the realization of a special "envelope" is made necessary for attaching the support to the tip-end of the fiber. Special care must therefore be given to the search for the most appropriate "envelope", since this can weigh heavily on the performance of the probe, and in particular on the response time. In fact, it must be kept in mind that a free exchange for the chemical species being investigated must be guaranteed between the inside of the optrode, where the chromophore is located, and the external environment.

It is evident that, in the case of optrode sensors, the chemical aspect takes on a relevant role in the realization of the entire sensor. Diverse techniques are utilized for the immobilization of the optically-sensitive reagent. Here as follows, let us briefly examine the main immobilization techniques followed:

**Adsorption:** the chromophore is adsorbed on special polymeric resins (e.g. XAD-2)<sup>33,34</sup>, or directly on fiber<sup>35</sup>. This technique consists simply of immersing the support in a solution of the chromophore in an appropriate solvent. This, however, presents the problem of a progressive - if at times slow - detachment from the support or from the fiber, which makes the use of probes realized in this manner unsuitable for many applications, in particular medical ones. Numerous optrodes have been realized by means of adsorption: an example of an optrode for detecting pH, realized with this technique, is shown in Fig. 2<sup>35</sup>. Phenol red, an indicator that functions by means of absorption, is adsorbed on XAD-2 microspheres inserted in

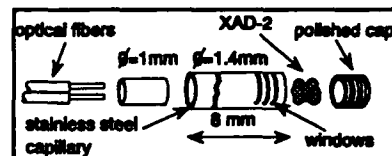


Figure 2. Probe for Ph detection.

a small stainless steel cylinder with lateral openings, the dimensions of which are such as to prevent the microspheres from coming out and, at the same time, to guarantee a good exchange with the outside environment. The interval of operation is 6.8÷7.9 pH units; the sensitivity is equal to 0.02 pH units; and the response time is less than one minute.

**Covalent bond:** at the moment, coupling of the optically-sensitive reagent by means of a covalent bond seems to be most promising, since it guarantees compactness for the probe and, at the same time, completely avoids losses of the chromophore. A much-followed method for the coupling of the chromophore exploits a silylation process, by means of which the reagent is coupled either to the fiber<sup>33</sup> or to a fixed support<sup>4</sup>. An example of a chemical

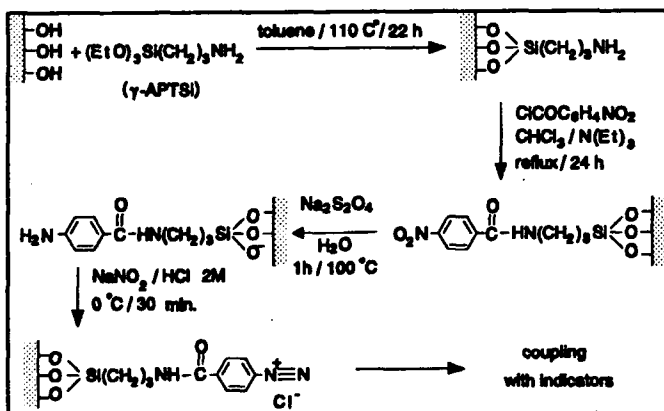


Figure 3. Sequence of silylation reactions to bind covalently pH indicators on glass supports.

sequence of silylation of a glass surface, making use of  $\gamma$ -aminopropyltriethoxysilane as a silylating agent, is shown in Fig.3. Various pH indicators have been coupled with this chemical sequence<sup>16</sup>, but the method can be considered valid for other types of chromophores.

**Entrapment in polymeric structures:** in this case, the chromophore is entrapped in a polymeric structure permeable to the parameter being investigated<sup>36,37</sup>. This technique, just like the covalent-bond technique, ensures good compactness and guarantees - with an appropriate choice of the entrapment technique - the almost complete loss of the chromophore. An example of an extrinsic optrode, in which covalent bond and entrapment



in a special matrix are utilized, is shown in Fig.4<sup>38</sup>. The said optrode makes possible the simultaneous detection of oxygen and of carbon dioxide. The two fluorophores utilized are tris(2,2'-bipyridyl)ruthenium(II) dichloride (RTDP) for oxygen, and 1-hydroxypyren-3,6,8-trisulfonate (HPTS) for carbon dioxide. The former is a fluorophore whose fluorescence is quenched in the presence of oxygen, while the latter is a pH indicator. The two chromophores are coupled in different ways: RTDP is adsorbed on Kieselgel particles incorporated on a layer of hydrophobic silicone rubber that is permeable to both O<sub>2</sub> and CO<sub>2</sub>, while HPTS is bonded covalently on granules of cellulose soaked in a solution of bicarbonate. The two sensitive layers are deposited on a solid support consisting of a transparent polyester membrane, attached to the tip of a bundle of optical fibers. A thick layer of opaque silicone permeable to gas supplies a type of optical isolation that avoids possible interferences due to fluorescent compounds present in the sample being examined. The two fluorophores have the same excitation length ( $\lambda_{exc}=460$  nm) but emission wavelengths that are sufficiently different ( $\lambda_{em}=520$  nm for HPTS, and  $\lambda_{em}=630$  nm for RTDP), so that a single source can be used, separating the two fluorescence signals by means of interferential filters. Also to be noted are the extremely reduced dimensions of the optrode. With this optrode, the partial pressure of oxygen and of carbon dioxide can be detected in the 0÷200 torr range with an accuracy of  $\pm 1$  torr, and in the 0÷150 torr range with an equal accuracy of  $\pm 1$  torr, respectively. The response times obtained are 40 seconds for the O<sub>2</sub> sensor and  $\approx 5$  minutes for the CO<sub>2</sub> sensor.

**Langmuir-Blodgett film:** until now, the realization of Langmuir-Blodgett films with an incorporated chromophore has been a very promising technique for the realization of fiberoptic detectors<sup>7,20</sup>, also because these films are, in principle, applicable to the outside surface of the fiber, thus realizing evanescent-wave sensors that are extremely compact and miniaturized.

An optrode for the detection of potassium<sup>20</sup> has been realized adsorbing lipid multi-layers, labelled with a fluorophore, on quartz supports made previously hydrophobic by means of silylation in such a way that its adhesion to the multi-layers is facilitated (Fig. 5). The lipid phase is formed either of arachidic acid or of octadecan-1-ol, of rhodamine B, specially modified so as to be soluble in lipids, and of valinomycin (which is electrically neutral) as bearer of ions. By spreading on the multi-layer and bonding itself with the valinomycin, potassium creates a variation in the electrical potential between lipid phase and aqueous phase that causes a decrease in the fluorescence of the fluorophore incorporated in the multi-layer.

As we have already said, this multi-layer has been realized on a quartz structure, and the preliminary optical measurements were taken without utilizing fiber-optics. On the other hand, it is important to emphasize that the entire chemical process can easily be applied to the nucleus of the fiber, so that an evanescent-wave fiberoptic sensor for the detection of potassium can potentially be realized.

**Sol-gel procedure:** a new technique for the realization of optrodes has recently been developed<sup>29</sup>, based on a sol-gel procedure. With this technique, a porous glassy-oxide network can be obtained by means of the hydrolysis of an organometallic precursor followed by condensative polymerization. The precursor can easily be doped with soluble chromophores which are thus entrapped in the glassy-oxide network. The main advantage of this technique is the possibility it offers for producing these glass structures, with the chromophore incorporated, shaped to the form of the fiber. In this way, a section of fiber is realized which is sensitive to a certain chemical species, and the problem of the optrode simply remains the connection between two fibers, with all the ensuing advantages of simplicity, compactness and miniaturization.

**Optrode in solution:** in order to eliminate any sort of problem connected with chemical bonding, in some cases the chromophore is in solution and the solution is blocked at the tip of the fibers by means of a highly-selective membrane. This prevents the chromophore from exiting, and makes possible the exchange with the external environment<sup>8,15</sup>. However, this particular solution involves both disadvantages - such as the difficulty in identifying the selective membrane and the long response time, related to the diffusion of the chemical species being analyzed throughout the membrane - and problems of mechanical nature, due to the resulting fragility and poor compactness of the optrode. This solution, therefore, is not always capable of offering the same advantages

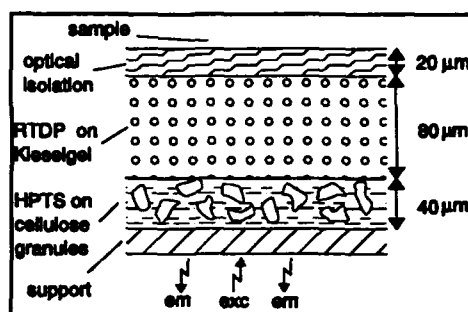


Figure 4. Optrode for the simultaneous detection of oxygen and carbon dioxide.

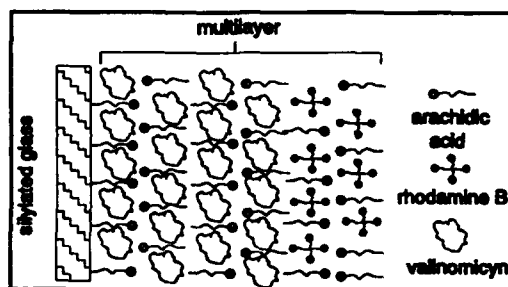


Figure 5. Optrode for the detection of potassium.

as those that are connected with other types of immobilization. On the other hand, it is the only solution to be followed when irreversible reactions are involved which would implicate rather complex problems in terms of the lifetime of the probe and of the calibration of the entire sensor, since a continuous flux of reagent to the inside of the optrode must be guaranteed, in order to maintain constant its concentration. An ammonia detector with a continuous flux for the chromophore has recently been realized<sup>15</sup>. The chromophore is bromothymol blue, a pH indicator that functions in absorption. In Fig.6 there is a diagram of the probe: a hollow fiber of semipermeable polypropylene ( $\varnothing=400\mu\text{m}$ ), hydrophobic and permeable to  $\text{NH}_3$ , is attached to a section of glass capillary ( $\varnothing=1\text{ mm}$ ). Three optical fibers are inserted inside the membrane; of these, one transports the radiation of the source (fiber a) while the other two (fiber b and fiber c) transport, respectively, the reference signal and the modulated signal from the optrode to the detector. Fibers a and b are immersed in a transparent epoxy glue which is impervious to hydrogen ions, so that the signal picked up by the reference fiber is not modulated by the chromophore. The tip-end is sealed with an epoxy glue enriched with silver, so that a reflecting surface is obtained. A glass capillary ( $\varnothing=100\mu\text{m}$ ) transports the reagent solution to the inside of the probe, while a second probe, made of teflon, performs the sample-taking. The functioning interval of this sensor is  $1.5\mu\text{M}\div 800\mu\text{M}$ , while the response time is  $\leq 40$  seconds. Even if the chemistry of this optrode is completely reversible and the consumption of reagent is minimal, this probe shows how it is possible to realize optrodes by making use of irreversible chemical reactions or by involving a consumption of the chromophore.

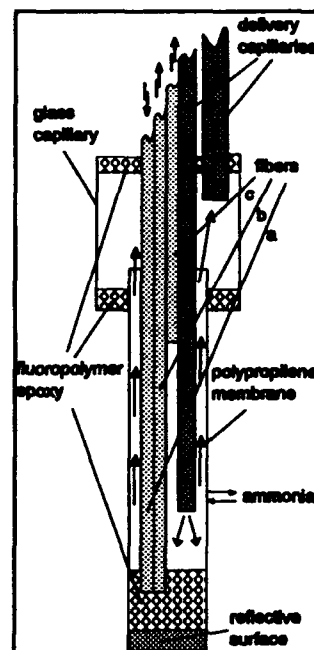


Figure 6. Optrode for the detection of ammonia

As of now, few chemical fiberoptic sensors have already been industrialized. One of these is the previous described enterogastric reflux sensor, an industrialized prototype of which already exists (Prodotec srl, Florence) that will soon be put on the market. An example of an industrialized prototype consists of a sensor for the simultaneous "in vivo" measurement in the blood of pH, oxygen and carbon-dioxide partial pressures, manufactured by the firm Cardiovascular Device (California, USA)<sup>20</sup>. Fig. 7 provides a diagram of the probe: it uses 3 optical fibers ( $\varnothing=125\mu\text{m}$ ), and its overall diameter ( $\varnothing=0.65\text{ mm}$ ) is such as to allow its insertion into an artery catheter. The three sensors are optically isolated by means of the individual encapsulation of each optrode, consisting of an opaque cellulose membrane. All three chromophores are fluorescence indicators. Since the measurement of  $\text{pCO}_2$  is based on a measurement of acidity, both the optrode for pH detection and the one for detection of the partial carbon-dioxide pressure use the same fluorophore: HPTS. In the

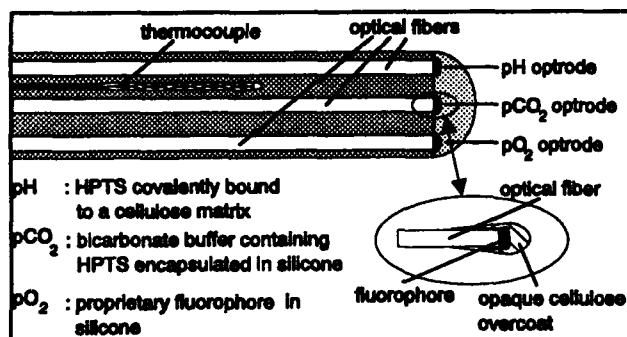


Figure 7. Sketch of the probe for the simultaneous detection of pH,  $\text{pO}_2$  and  $\text{pCO}_2$  in human blood.

former case, the fluorophore is covalently bonded to a matrix of cellulose attached to the tip of the fiber, while in the latter case it is dissolved in a buffer solution of bicarbonate encapsulated inside a hydrophobic siliconic membrane that is permeable to  $\text{CO}_2$  and is attached to the fiber tip. In both cases, the excitation band is used both of the acid form ( $\lambda_{\text{exc}}=410\text{ nm}$ ) and of the base form ( $\lambda_{\text{exc}}=460\text{ nm}$ ) of the fluorophore, that have the emission band centered on the same wavelength ( $\lambda_{\text{em}}=520\text{ nm}$ ). The ratio of the fluorescence intensity for the two different excitations appears to be relatively insensitive to optical fluctuations. For the detection of  $\text{pO}_2$ , a specially-synthesized fluorophore ( $\lambda_{\text{exc}}=385\text{ nm}$ ,  $\lambda_{\text{em}}=515\text{ nm}$ ) is utilized, connected to a second fluorophore that is insensitive to oxygen, as reference, incorporated in a hydrophobic siliconic membrane that is permeable to oxygen, attached to the tip of the fiber. The performance of this probe is illustrated in Table I.

parameter	measurement range	precision	response time
pH	7.05÷7.65 pH units	0.03 pH units	35 sec
$\text{pCO}_2$	10÷60 mm Hg	2 mm Hg	95 sec
$\text{pO}_2$	20÷200 mm Hg	4 mm Hg	60 sec

Table I. Performances of the probe for the simultaneous of pH  $\text{pO}_2$ ,  $\text{pCO}_2$ .

#### 4. CONCLUSIONS

The detection of chemical parameters by means of optical fibers has had a decisive boost in recent years, thanks to the advantages and which these sensors are capable of offering in comparison with traditional sensors. The greatest problem is definitely the realization of the optrode, as regards both the structural aspect (sturdiness, compactness, the guarantee of a rapid and efficient exchange with the outside environment), and the chemical aspect (search for the most suitable optically-sensitive reagent and its application to the fibers), to which considerable attention must be dedicated in order to obtain very high performance from the probe in terms of response time, reversibility and stability. The first industrialized models have already appeared, or are just on the verge of appearing, on the international market: it is conceivable, therefore, that we can expect in the years to come an industrial conversion of numerous prototypes that until now have been realized only on a research level.

#### 4. REFERENCES

- [1] D.J.David, M.C.Willson, D.S.Ruffin, 1976, *Anal.Lett*, 9, 389.
- [2] F.Baldini, 1991, *Proc. SPIE* 1368, pp.184-190.
- [3] J.P.Dakin, 1988, *Proc. SPIE* 1011, pp.173-182.
- [4] J.P.Alarie, M.J.Sepaniak, T.Vo-Dinh, 1990, *Anal.Chim.Acta*, 229, 169.
- [5] M.K.Carroll, F.V.Bright, G.M.Hieftje, 1989, *Anal.Chem.*, 61, 1768.
- [6] H.H.Miller, T.B.Hirschfeld, 1986, *Proc. SPIE* 718, pp. 39-44.
- [7] J.E.Freeman, G.A.Childers, A.W.Steele, G.M.Hieftje, 1985, *Anal.Chim.Acta*, 177, 121.
- [8] N.R.Herron, S.J.Simon, L.Eccles, 1989, *Anal.Instrum.*, 18 (2), 107.
- [9] W.A.Chudyk, M.M.Carabba, J.E.Kenny, 1985, *Anal.Chem.*, 57, 1237.
- [10] A.M.Scheggi, A.G.Mignani, *EFOC LAN'89*, EFOC Proceedings (IGI Europe), 329-334.
- [11] F.Baldini, R.Falciai, P.Bechi, F.Cosi, A.Bini, F.Milanesi, 1991, *Proc. SPIE* 1510, in press.
- [12] J.Bock, E.Gersing, F.Sundmacher, G.Hellige, 1988, *Proc. SPIE* 906, pp. 169-172.
- [13] J.P.Dakin, C.A.Wade, D.Pinchbeck, J.S.Wykes, *J.Opt.Sens.*, 1988, 2 (4), 261.
- [14] R.J.Berman, L.W.Burgess, 1990, *Proc. SPIE* 1172, pp. 206-214.
- [15] S.A.Momin, R.Narayanaswamy, 1989, *Anal.Proc.*, 26, 372.
- [16] F.Baldini, M.Bacci, S.Bracci, 1991, *Proc. SPIE* 1368, pp.210-217.
- [17] B.J.Tromberg, M.J.Sepaniak, T.Vo-Dinh, G.D.Griffin, 1988, *Anal.Chem.*, 60, 1901.
- [18] J.D.Andrade, R.Wanwagenen, D.Gregonis, K.Newby, J.Lin, 1985, *IEEE Trans.Elec.Dev.*, ED-32 (7), 1175.
- [19] J.L.Gehrich, D.W.Lubbers, N.Opitz, D.R.Hansmann, W.W.Miller, J.K.Tusa, M.Jafuso, 1986, *IEEE Trans.Biom.Eng.*, BME-33 (2), 117.
- [20] B.P.H.Schaffar, O.S.Wolfbeis, A.Leitner, 1988, *Analyst*, 113, 693.
- [21] W.G.Miller, F.P.Anderson, 1989, *Anal.Chim.Acta*, 227, 153.
- [22] B.A.A.Dremel, B.A.A. Schaffar, R.D.Schmid, 1989, *Anal.Chim.Acta*, 225, 293.
- [23] E.Posch, O.S.Wolfbeis, 1989, *Mikrochim.Acta*, I, 41.
- [24] J.I.Peterson, R.V.Fitzgerald, D.K.Buckhold, 1984, *Anal.Chem.*, 56, 62.
- [25] M.E.Lippitsch, J.Pusterhofer, M.J.P.Leiner, O.S.Wolfbeis, 1988, *Anal.Chim.Acta*, 205, 1.
- [26] S.M.Gautier, L.J.Blum, P.R.Coulet, 1990, *Anal.Chem.*, 62, 1977.
- [27] M.D.Degrandpre, L.W.Burgess, 1990, *Appl.Spectr.*, 44 (2), 273.
- [28] R.A.Lieberman, L.L.Blyer, L.G.Cohen, 1988, *Proc. Optical Fiber Sensors '88*, Vol.2, pp.346-348.
- [29] B.D.MacCraith, V.Ruddy, C.Potter, J.F.MaGilp, B.O'Kelly, 1991, *Proc. SPIE* 1510, in press.
- [30] J.M.Bello, T.Vo-Dinh, 1990, *Appl.Spectr.*, 44 (1), 63.
- [31] B.Liedberg, C.Nylander, I.Lundstrom, 1983, *Sensors and Actuators*, 4, 299.
- [32] C.Munkholm, D.R.Walt, F.P.Milanovich, S.M.Klainer, 1986, *Anal.Chem.*, 58, 1427.
- [33] D.A.Russell, R.Narayanaswamy, 1989, *Anal.Chim.Acta*, 220, 75.
- [34] M.Bacci, F.Baldini, F.Cosi, G.Conforti, A.M.Scheggi, 1989, *Proc. Optical Fiber Sensors '89*, pp.425-430.
- [35] G.Boisdè, B.Biatry, B.Magny, B.Dureault, F.Blanc, B.Seuille, 1990, *Proc. SPIE* 1172, pp. 239-250.
- [36] C.Munkholm, D.R.Walt, F.P.Milanovich, 1988, *Talanta*, 35 (2), 109.
- [37] Y.Kawabata, T.Kamichika, T.Imasaka, N.Ishibashi, 1989, *Anal.Chim.Acta*, 219, 223.
- [38] O.S.Wolfbeis, L.J.Weis, M.J.P.Leiner, W.E.Ziegler, 1988, *Anal.Chem.*, 60, 2028.

**TH4.2**  
**(Invited)**

## **Environmental Sensing**

Robert Lieberman, *Physical Optics Corp.*, Torrance, CA

Paper not available at time of print.

## TH4.3

# Porous Fiber Optical Sensor For pH Measurement

J. Y. Ding, M.R. Shahriari and G. H. Sigel, Jr.

Fiber Optic Materials Research Program

Rutgers - The State University of New Jersey

P.O.Box 909, Piscataway, New Jersey 08854

### Summary:

Numerous fiber optic pH sensors have been proposed in the past decade. Most of these sensors utilize polymers as a substrate to immobilize optically active organic indicators<sup>1,2</sup>. However, these devices often exhibit significant degradation in the presence of organic solvents and are less stable at high temperatures or pressures typically encountered in many industrial and practical applications. Recently, the use of inorganic materials as the substrates for the immobilization of indicators has obtained more attention<sup>3,4</sup>. This report describes the development of a new fiber optic pH sensor based on the use of a porous silica glass fiber immobilized with pH indicators by sol-gel coating technique.

Porous glass fibers have been used for the development of fiber optic chemical sensors.<sup>5,6</sup> The fiber is prepared by chemically leaching a small section of a phase-separated sodium borosilicate glass fiber. In this work, the porous section is coated by silica gel impregnated with pH indicators. The silica gel is chemically bonded to the surface of the porous glass fiber and holds the pH indicators in the "cage" formed by the silica ring structure. The silica gel is chemically compatible with the silica glass and covalent bonds are formed between the silica gel and the silica glass surface due to condensation reaction of the hydroxyl groups. The trapping of the indicators in the silica ring structure gives resistance to the attack from water and organic solvents but still keeps the pH sensitive sites of the indicators active. The sol-gel coating technique is suitable for any organic indicators having a molecular size larger than that of the glass former (silica in this case). Thus, sensors with a wide dynamic pH range can be prepared by co-immobilization of several different absorbing indicators for which the pH range and optical properties correlate. In this work, bromocresol purple and bromocresol green were selected as the pH indicators. The individual dynamic pH range of these indicators is 3.8-5.4 and 5.2-6.8, respectively.

A schematic diagram of the experimental set-up for this sensor is shown in Figure 1. A chopped HeNe laser was launched into a silica optical fiber which was spliced to a 2 cm section of porous glass fiber. A second silica fiber was utilized to deliver the light signal passing through the sensor to the Si photodetector. The pH measurement was performed by placing the activated porous fiber in a fluid reservoir containing a magnetic stirrer and a reference electronic probe of a pH meter (Orion EA-920). Optical signal levels were measured under a variety of pH conditions.

Figure 2 illustrates the dynamic response and the reversibility of the sensor when exposed to a number of step changes in pH. When an acid or base was introduced into the testing reservoir, the sensor responds rapidly and the output signal reaches a stable value within a few minutes. The response from the porous fiber optic sensor is depicted as the solid line and the response of the electronic pH probe is represented by the dashed line. After a rinsing in deionized water to remove any unbound indicators, the sensor is stable to 5% over repeated cycling. The response time is mainly determined by the diffusion of hydrogen and hydroxyl ions through the silica matrix. Reduction in the coating thickness results in faster response time.

Room temperature calibration curves for the device are shown in Figure 3 in which the changes in the optical transmittance at 633 nm are normalized and plotted as a function of the changes of pH. A wide dynamic range of pH from 4 to 8.5 can be achieved by employing the sample coated with the indicator concentration of 0.24 mg/ml (bromocresol green/bromocresol purple=1:1). As the concentration of indicator is increased, the dynamic range of pH shifts toward the low pH end. The use of a porous glass fiber significantly increases the resolution of the sensor because of its high surface area. However, the resolution is also dependent on the indicator selected as well as its concentration. A resolution of 0.05 pH interval is typical for a porous fiber of 2 cm in length used in this experiments.

Figure 4 shows the effects of ionic strength of the test solution on the sensor. A shift of the calibration curve from the high pH side to the low pH side was observed after the introduction of KBr of which the concentrations are 0.01N and 0.1N.

The porous fiber optic pH sensor prepared by the sol-gel coating technique has demonstrated several advantages for chemical detection:

- a) A high sensitivity can be obtained due to the high surface area porous glass structure.
- b) The indicators immobilized in the silica gel matrix which is directly bound on the glass fiber are stable and durable. The potential applications for the sensor include the pH measurement for aqueous solutions at high temperatures and those containing organic solvents.
- c) A wide dynamic pH range has been achieved due to the co-immobilization of different pH indicators.
- d) The sol-gel coating technique offers the flexibility in selecting the appropriate indicators and this advantage also makes the homogeneous co-immobilization possible.

An apparent disadvantage of the present device is its somewhat sluggish behavior. However, the response time observed in this work can be improved through selection of the appropriate coating thickness of the silica gel as well as a modest enlargement of the pore size. The end result is a device with both enhanced sensitivity and operational lifetime relative to present generation fiber optic pH sensors.

**Reference:**

1. Peterson, J. I., Goldstein, S. R., Fitzgerald, R. V., and Buckhold, D. K.: 'Fiber Optic pH Probe for Physiological Use,' *Anal. Chem.*, 1980, **52**, pp.864-869.
2. Serra, G., Schirone, A. and Boniforti, R.: 'Fiber optic pH Sensor for Sea-water Monitoring Using a Single Dye,' *Analytica Chimica Acta.*, 1990, **232**, pp.337-344.
3. Badini, G.E., Grattan, K.T.V., Palmer, A.W. and Tseung, A.C.C.: 'Development of pH Sensitive Substrates for Optical Sensor Applications,' *Proc. OFS '89, Paris, Springer-Verlag "Proceedings in Physics"*, 1989, **44**, pp. 436-442.
4. MacCraith, B.D., Ruddy, V., Potter, C., O'Kelly, B. and McGilp, J.F.: 'Optical Waveguide Sensor Using Evanescent Wave Excitation of Fluorescent Dye in Sol-gel Glass,' *Electron. Lett.* 1991, **27**, in press.
5. Ding, J. Y., Shahriari, M.R. and Sigel, Jr., G. H.: 'Development of Porous Fiber Optic Sensor for High Temperature Moisture Sensing,' *International J. Optoelectronics*, 1991, **6**, pp. 385-393.
6. Ding, J. Y., Shahriari, M.R. and Sigel, Jr., G. H.: 'Fiber Optic pH Sensors Prepared by a Sol-gel Immobilization Technique,' *Electron. Lett.* 1991, in press.

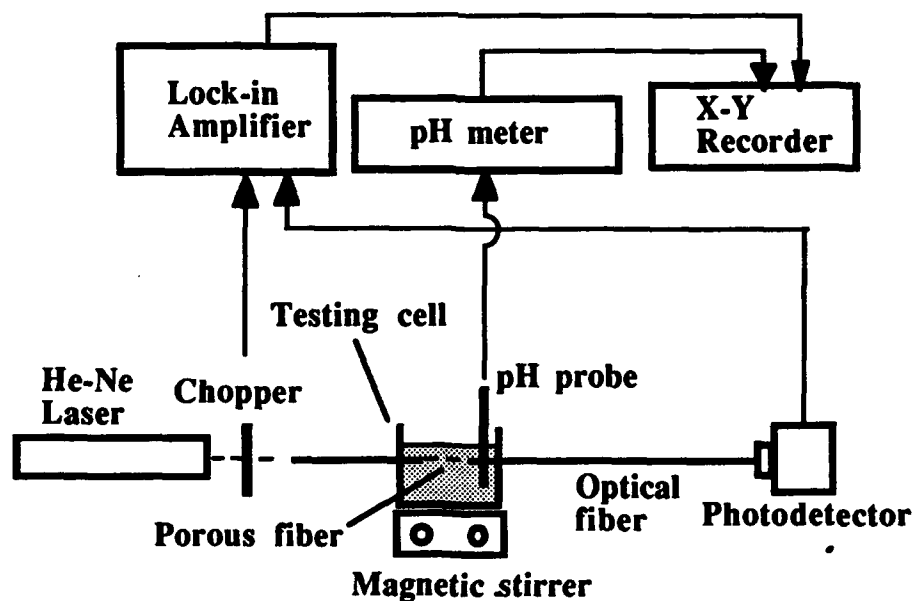


Figure 1 Schematic diagram of the experimental set-up for fiber optic pH sensor.

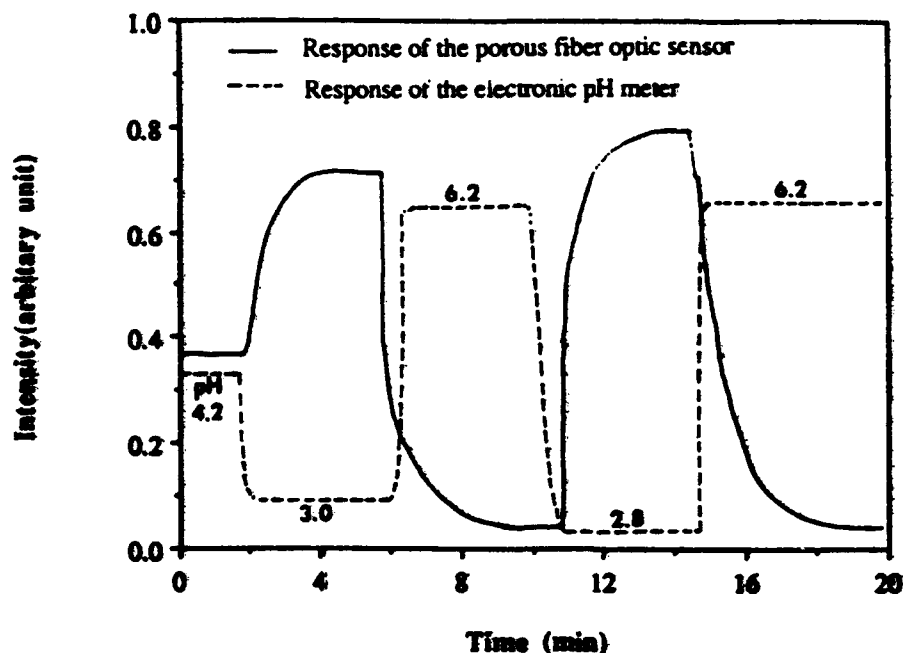


Figure 2 Dynamic response of the fiber optic pH sensor in step changes of pH. The solid line represents the response of the porous fiber sensor and the dashed line represents the response of the pH meter.

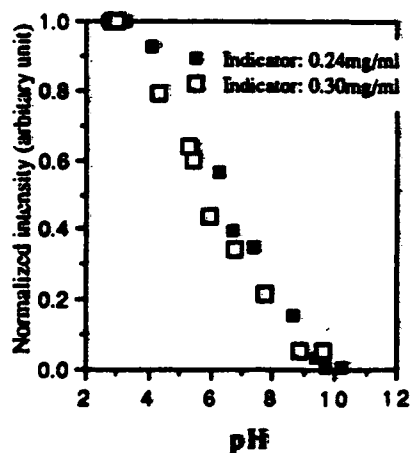


Figure 3 Calibration curves of the fiber optic pH sensor using a porous section of 2 cm in length. The sensing wavelength was 633 nm and the measurements were performed at 21 °C.

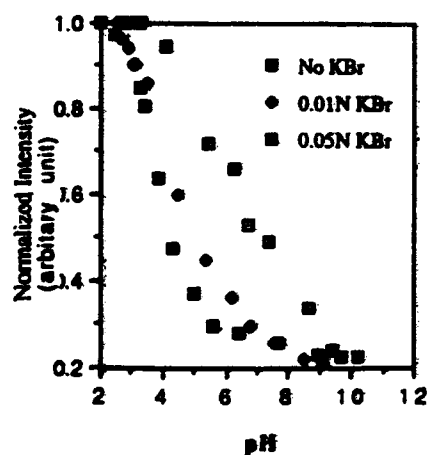


Figure 4 The effect of ionic strength on the fiber optic pH sensor. pH indicators of bromocresol purple and bromocresol green at 1:1 (weight) were used (1.5mg/ml for each indicator).



F.Baldini, M.Bacci, F.Cosi, A.Del Bianco, A.M.Scheggi

Istituto di Ricerca sulle Onde Elettromagnetiche del CNR  
Via Panciatichi 64, 50127 Firenze Italy

### ABSTRACT

An optical fiber sensor for the detection of oxygen is described, based on the absorption change of a bis(Histidinato)Cobalt(II) solution at  $\lambda=408$  nm as a function of the molecular oxygen concentration in the surrounding environment.

### 1. INTRODUCTION

Optical-fiber chemical sensors have undergone exceptional development in recent years. Such an evident interest is perfectly justified because optical-fiber sensors offer several advantages, in comparison with traditional sensors, for the measurement of chemical parameters, the detection of which is extremely important in many industrial and chemical processes, in environmental control and in the biomedical field.

Oxygen is surely one of the chemical parameters more investigated with optical fibers. So far, optical fiber sensors for the detection of oxygen exploit its capability of quenching the fluorescence of appropriate fluorophores<sup>1</sup>. On the other hand, this method, also if high sensitive, does not appear completely satisfactory, since other substances can compete with oxygen in the fluorescence quenching parameters, decreasing the accuracy of the sensor. For this reason an optical fiber oxygen sensor working on absorption would seem, in some cases, more convenient. The absorption change of haemoglobin in the presence of oxygen was utilized for the realization of an absorption-based optrode<sup>2</sup>, but the optical reagent does not seem appropriate for the realization of an optical sensor, due to its biological characteristics which prevent the construction of long-life probes.

Because our aim is the realization of an optical fiber sensor working on absorption, our attention has been devoted to the search of chemical compounds, the absorption of which undergoes changes in presence of oxygen. Since biological compounds are characterized by very poor stability, our research has been focused on synthetic substances. Some organo-metallic compounds are able to bind reversibly with molecular oxygen. These substances, known as oxygen carriers, are transition metal complexes<sup>3</sup>, the absorption spectrum of which may change during the oxygenation process, depending on the oxidation state of central atom.

The present work is concerned with the development of an oxygen optical fiber sensor, which exploits the optical properties of an appropriate transition metal complex.

### 2. SPECTROPHOTOMETRIC ANALYSIS

Four kinds of oxygen carriers showing a colour change during the oxygenation process were selected: the so-called Vaska's complex  $(\text{IrCl}(\text{CO})(\text{PPh}_3)_2)^4$ , bis(salicylaldehyde)ethylenediiminecobalt(II)  $(\text{Co}(\text{salen}))^5$ , bis(histidinato)cobalt(II)  $(\text{Co}(\text{His})_2)^6$ , and manganese complexes of the form  $\text{Mn}(\text{PR}_3)_x\text{Y}_2$  (where  $\text{PR}_3$  is a tertiary phosphine—except that triphenylphosphine  $(\text{PPh}_3)$ — $x$  may assume values 1 or 2 and  $\text{Y}$  is an halogen<sup>7</sup>). None of these was found on the market and, for this reason, synthesis was carried out<sup>8</sup> following, if possible, the methods already described, also if in some cases, particularly for manganese compounds, it resulted extremely difficult, both due to the complexity of

---

† This work has been supported and developed by CNR Finalized Program on Materials and Devices for Solid State Electronics

the operations to be followed and the lack of details reported in the literature. A thorough spectrophotometric study was carried in order to detect the most suitable one for optical oxygen detection: this step was necessary because no information on this point was available.

Spectrophotometric analysis was carried out using both a Perkin Elmer spectrophotometer (mod. 552) and a Guided Wave spectroanalyzer (mod. 200) equipped with optical fibers.

Absorption spectra in solution were recorded either by using anaerobic cuvettes (Hellma) coupled with the Perkin Elmer spectrophotometer or by using a 3-neck flask coupled with the probe of the Guided Wave spectrophotometer. Solid-state reflectance spectra were recorded by using an external integrating sphere connected with the Perkin Elmer spectrophotometer: the analyte was placed in an appropriately designed cell located over the hole of the integrating sphere. In each case, the percentage of oxygen contained in the atmosphere surrounding the oxygen carrier was rigorously controlled.

The results obtained may be synthesized in the following way:

**Vaska's complex:** Vaska's complex, dissolved in deoxygenated nitrobenzene (conc. =  $1 \times 10^{-3}$  M), shows a strong change in absorption at 420 nm, if exposed to an atmosphere containing oxygen. Notwithstanding the good sensitivity, this complex appears unsuitable for the realization of an optical sensor due to the very slow oxygenation process ( $\approx$  several hours).

**Co(salen):** although solid Co(salen) is characterized by different reflectance spectra when in the de-oxygenated and in the fully-oxygenated form showing a large change of reflectance for  $\lambda > 700$  nm, it appears unsuitable for a sensor, since it shows very good reversibility of the oxygenation process only at high temperatures and low pressures.

**Mn(PR<sub>3</sub>)<sub>2</sub>Y<sub>2</sub>:** different manganese complexes were tested, changing the ligand and the halogen of the compound. Best results were obtained by using triethylphosphine (Pet<sub>3</sub>) and iodine as phosphine and halogen, respectively. The resulting complex, Mn(Pet<sub>3</sub>)<sub>2</sub>I<sub>2</sub>, is characterized by a reflectance spectrum with several bands that are changed by the formation of the manganese-oxygen bond, due to the change of symmetry of the molecule from pseudo-tetrahedral to trigonal bipyramidal. Nevertheless its highly sensitivity to water makes difficult its use in an optical fiber sensor, since the least track of humidity oxidizes the phosphine groups, blocking the reactivity of this compound toward oxygen.

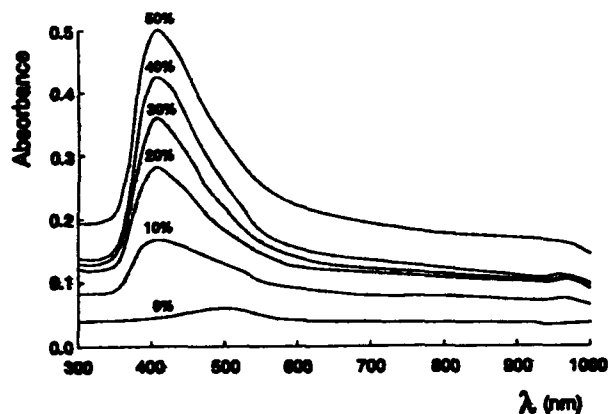


**Figure 1** Absorption spectra of Co(His)<sub>2</sub> in equilibrium with different oxygen concentrations in the surrounding atmosphere.

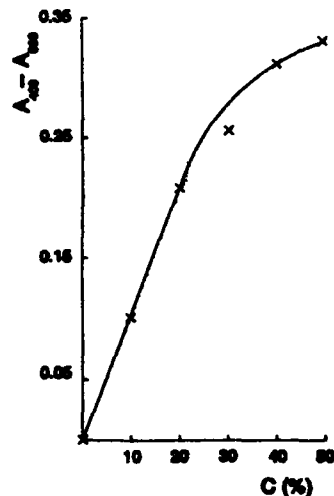


**Figure 2**  $A_{408} - A_{900}$  vs oxygen concentration in the surrounding atmosphere for Co(His)<sub>2</sub>.

**Co(His)<sub>2</sub>:** Figure 1 shows absorption spectra of Co(His)<sub>2</sub> in phosphate buffer at about pH 7.5 in equilibrium with different concentrations of molecular oxygen in the surrounding atmosphere. The formation of a band is apparent at  $\lambda = 408$  nm during the oxygenation process, due to a charge transfer between oxygen and metal levels. In Figure 2, the absorbance difference at  $\lambda = 408$  nm and at  $\lambda = 900$  nm versus oxygen concentration is reported. It is important to outline that Co(His)<sub>2</sub> shows a good reversibility at room temperature and atmospheric pressure.

On the basis of these results  $\text{Co}(\text{His})_2$  was selected as reagent for the oxygen optical fiber sensor.

## 5. OPTICAL FIBER SENSOR

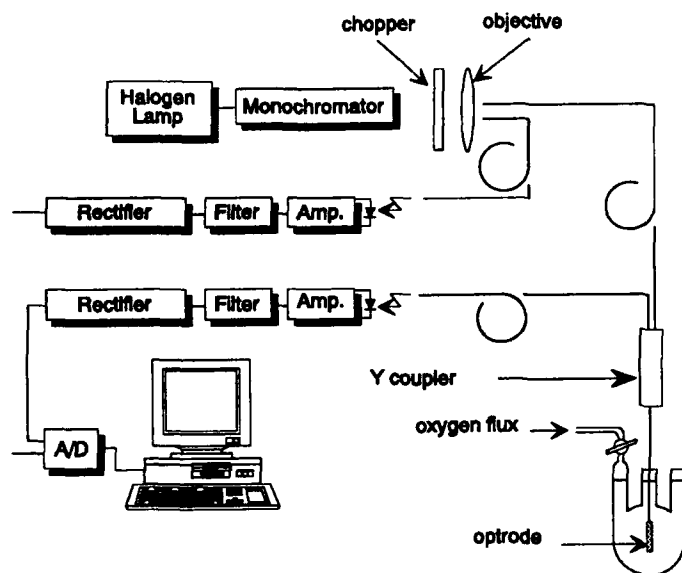


Figure 3 Block diagram of the oxygen sensor model.

totality of the modulated light, collected inside the probe, is sent to the photodetector. Two equal

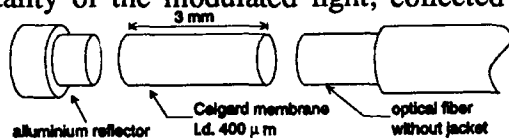


Figure 4 Sketch of the optrode for oxygen detection.

appropriate electronic circuits process the signals and the data are collected by using a personal computer. The optrode, shown in Figure 4, is made with a Celgard capillary (length=3 mm, internal diameter=400  $\mu\text{m}$ ), closed at one end with an aluminium cap as reflector. Celgard was chosen for the hydrophobic membrane because at the moment it seems to be one of the most efficient for guaranteeing a fast, complete diffusion of oxygen inside the probe. The membrane capillary is filled with the  $\text{Co}(\text{His})_2$  solution operating in dry-box in an inert atmosphere. Then the common branch of the Y-coupler is inserted into the capillary and the junction is sealed with black silicon in order to obtain a waterproof assembly and to avoid parasitic reflections. The probe obtained is inserted in a glass tube, sealed with a 1-cm-thick silicon layer, and inserted in a flow cell where it is possible to control the composition of the internal atmosphere.

A typical response curve of the sensor is showed in Figure 5 where the ratio  $I/I_0$  vs time is reported, where  $I$  is the intensity of the light coming from the optrode and  $I_0$  is the intensity of the light coming directly from the monochromator. The probe is in contact with pure argon atmosphere; in correspondence of the arrow pure oxygen begins to flow. The response time of such a sensor, defined as the time needed to have a signal variation from 10% to 90% of the final value, is about 2 minutes.

At this point it is important to outline that the measurement of oxygen concentration will not depend on the oxygen concentration inside the probe but on the response time because a fixed quantity of oxygen will block all the cobalt centers. This behaviour is due to the fact that the number of metal ions which are able to interact with oxygen inside the probe is well defined and in our case it can be calculated taking into account the dimension of the probe. The calculus is based upon the fact that oxygen bridges between

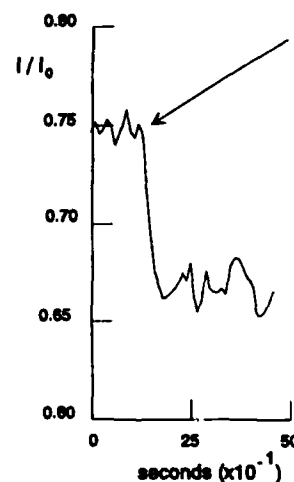


Figure 5 Response curve of the oxygen sensor for a step 0%  $\rightarrow$  100% in the oxygen concentration.

cobalt ions so that each mole of cobalt binds 2 moles of oxygen, hence the knowledge of the  $\text{Co}(\text{His})_2$  concentration is sufficient to know the maximum concentration of oxygen required, inside the probe, to obtain a full response. Quite obviously information of temperature and pressure are also necessary because the quantity of oxygen that diffuses inside the probe depends on these parameters. From these considerations, it is possible to estimate that a concentration of  $2 \times 10^{-2}$  ppm of oxygen in the atmosphere surrounding the probe at 25 °C and 760 torr of pressure is sufficient to obtain the maximum response of the sensor.

It is apparent that this sensor is potentially useful to detect the presence of oxygen everywhere its presence must be carefully avoided: explosive environments and all industrial processes in controlled atmosphere are only two examples.

## 7. CONCLUSIONS

The present study allowed to identify  $\text{Co}(\text{His})_2$  as optical reagent, working on absorption basis, for oxygen detection via optical fibers. In this way it was possible to avoid the interferences that very often characterize optical fiber sensors for the oxygen detection which exploited the quenching of the fluorescence emitted by organic fluorophores.

The optical fiber sensor here developed is characterized by a small optrode which allows the detections of very low concentrations of molecular oxygen, hence the sensor appears to be particularly suitable in industry where it is often important the detection of extremely low quantities of oxygen.

## REFERENCES

1. O.S.Wolfbeis, M.J.P.Leiner: "Recent Progresses in Optical Oxygen Sensing". "Optical Fibers in Medicine" III, Proc. SPIE **906** 42 (1988).
2. Z. Zhujun, W.R. Seitz: "Optical Sensor for Oxygen Based on Immobilized Hemoglobin". Anal. Chem. **58**, 220 (1986).
3. R.W. Erskine, B.O. Field: "Reversible Oxygenation". Structure and Bonding **28**, 684 (1976).
4. L. Vaska: "Oxygen Carrying Properties of a Simple Synthetic System". Science **140** (1963), 809.
5. M.Calvin, R.H.Bailes, W.K.Wilmarth: "The Oxygen-Carrying Synthetic Chelate Compounds I". J. Am. Chem. Soc. **68** (1946) 2254.
6. J. Simplicio, R.G. Wilkins: "The Kinetics of the Rapid Interaction of Bis(Histidinato)Cobalt(II) with Oxygen". J. Am. Chem. Soc. **89** (1967) 6092.
7. C.A. McAuliffe: "Manganese(II) Phosphine Complexes: Analogues of Transport Proteins". Oxygen and Life 2nd BOC Priesley Conference, Birmingham, 1980 p. 119.
8. F. Baldini, M. Bacci, F. Cosi, A. Del Bianco, A.M. Scheggi: "Transition Metal Complexes as Indicators for a Fiber-Optic Oxygen Sensor". Proc. SPIE OE/Fibers '91, in press.

## TH4.5 Sensitivity Enhancement Of Evanescent Wave Immunoassay

Masakazu Yoshida, Kazuhisa Shigemori, Mutsuyuki Sugimura,  
Masaharu Matano

Daikin Industries, Ltd., Electronic Engineering Laboratory  
1000-2 Ohtani, Okamoto-Cho, Kusatsu, Shiga, 525, Japan  
Phone 0775-65-9851 Facsimile 0775-65-5741

### Introduction

An evanescent wave immunoassay system has been developed to measure the amount of antibody or antigen present in a complex medium such as serum or whole blood quantitatively. The use of the evanescent wave enable much shorter measuring time than conventional immunoassay systems <sup>(1)</sup> <sup>(2)</sup> <sup>(3)</sup>.

The key technical devices are an optical waveguide and a fluorescent tag. The tag uses fluorescein isothiocyanate (FITC) excited at 490 nm.

In this paper we consider the effect of an exciting wavelength on the sensitivity of the system. Our experiments indicate that the combination of an exciting wavelength of  $\lambda = 650$  nm and allophycocyanin (APC) raises the sensitivity of the evanescent wave immunoassay by one order of magnitude higher than the sensitivity level found in conventional system.

### Background-noise

Characteristic fluorescence spectra of a plastic (PMMA) optical waveguide excited at 650 nm and at 490 nm are presented in Fig.1 (a), (b), respectively. Optical waveguide excited at 650 nm has broad characteristic fluorescence spectra, and its fluorescence intensity is approximately 1/20 of the intensity exhibited by an optical waveguide excited at 490 nm. Since it gives off less background-noise, a higher sensitivity can be expected.

## Experiment

The internal view and block diagram of the photometer are shown in Fig.2 and Fig.3, respectively. The major components are a laser diode, a flow cell with an optical waveguide, and electronics for data-acquisition. A laser diode (Toshiba,TOLD9410) is modulated by square waves at 220 Hz. The wavelength is stabilized by a thermo-control unit at a thermal fluctuation of  $\pm 0.01^{\circ}\text{C}$ . The laser beam is focused onto the front surface of the waveguide. A photomultiplier tube (PMT) (Hamamatu Photonics,R2371-02) is placed in front of the waveguide to monitor the change in light intensity. Two kinds of filter between the waveguide and the PMT are placed in order to block excitation light. The output signal is fed through a lock-in amplifier to a computer.

In the system, APC is used as the detectable reagent for reactant i.e. beta-2 microglobulin. The optical absorption peak of APC is around 630 nm, which is suitable for emitting wavelength of the laser diode used<sup>(4)(5)(6)</sup>. The fluorescence of APC is detected at a longer wavelength than 695 nm, the point beyond which blocking of excitation light occurs.

The dose response curves for beta-2 microglobulin measured by the system using APC-labeled antibody excited at 652.2 nm and by the system using FITC-labeled antibody excited at 490 nm are shown in Fig.4(a) and Fig.4(b), respectively. Sensitivity for APC is  $10^{-11}$  M and for FITC is  $10^{-10}$  M.

## Conclusion

The effect of an exciting wavelength on the sensitivity of the evanescent wave immunoassay system has been considered experimentally. Our results indicate the importance of an exciting light at 650 nm to sensitivity. Additionally, a compact apparatus can be realized by using a laser diode.

## Acknowledgments

The authors would like to thank R.Akiyama and K.Yamashita for their experimental effort and discussions.

## References

- (1) R.M. Sutherland, et al., Clin. Chem. 30/9, 1533-1538 (1984)
- (2) J.W. Attridge, et al., Biosensors & Bioelectronics 6, 201-214 (1991)
- (3) W.F. Love, et al., OFS'86 143-146 (1986)
- (4) H.M. Shapiro, et al., Cytometry 4, 276-279 (1983)
- (5) J.K. Deacon, et al., Biosensors & Bioelectronics 6, 193-199 (1991)
- (6) M. Ohhira, et al., Haikangaku 30, 12, 1333-1337 (1990)

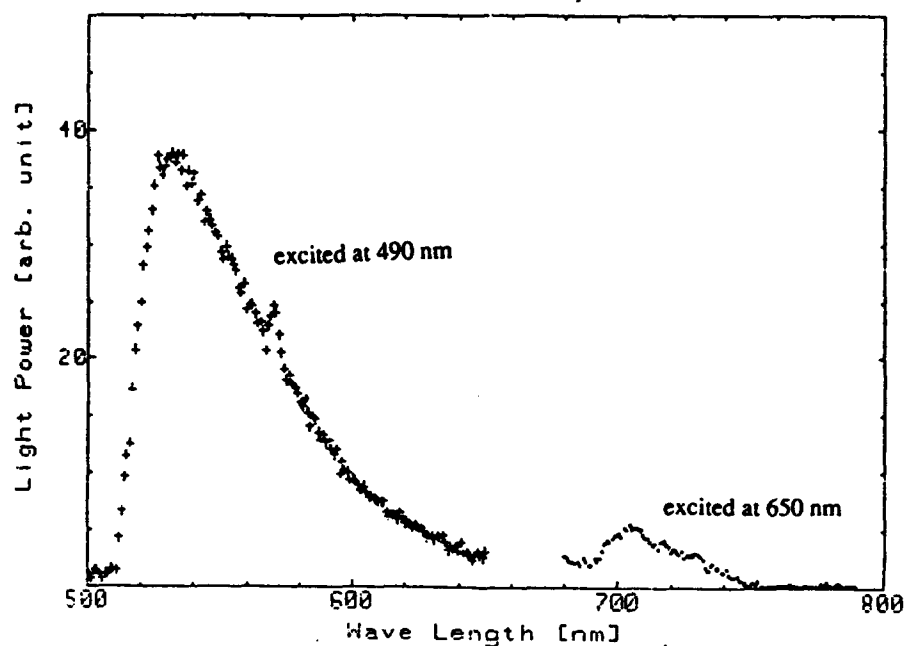


Fig 1. Characteristic fluorescence spectra of a plastic(PMMA) optical waveguide

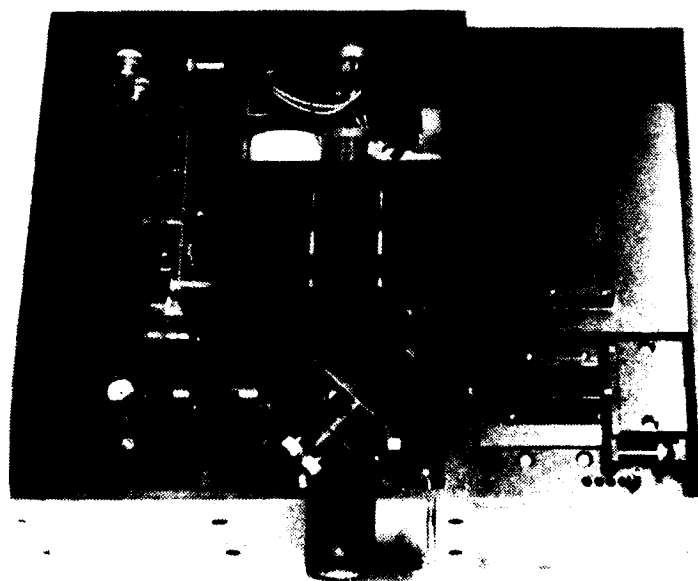


Fig 2. The internal view of the photometer

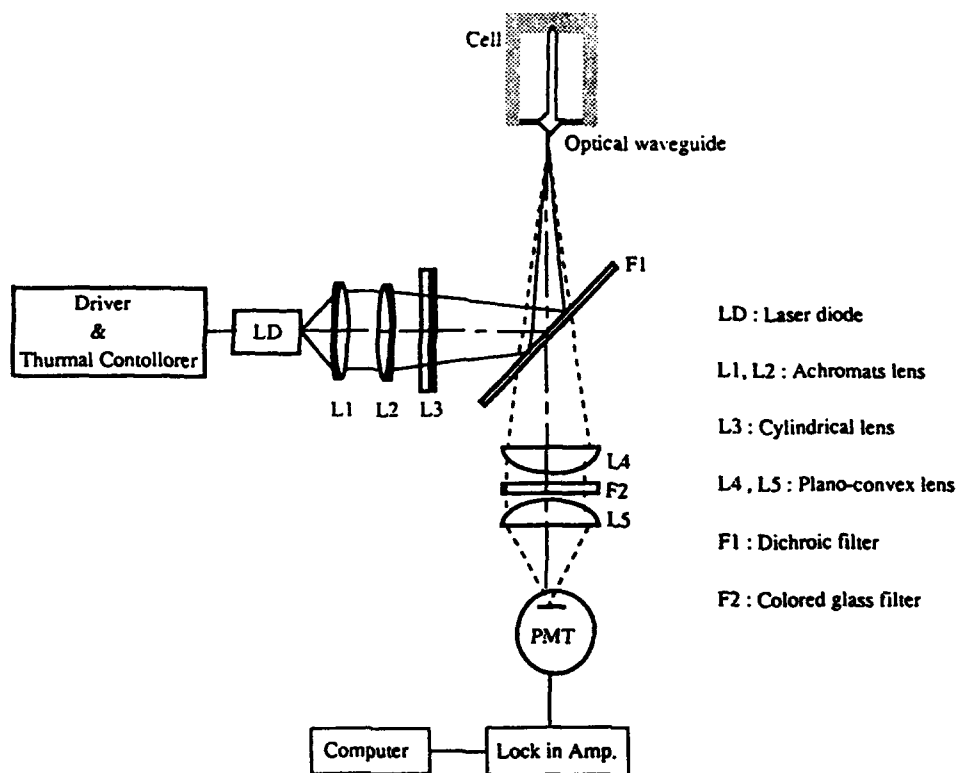


Fig. 3 Block diagram of the photometer

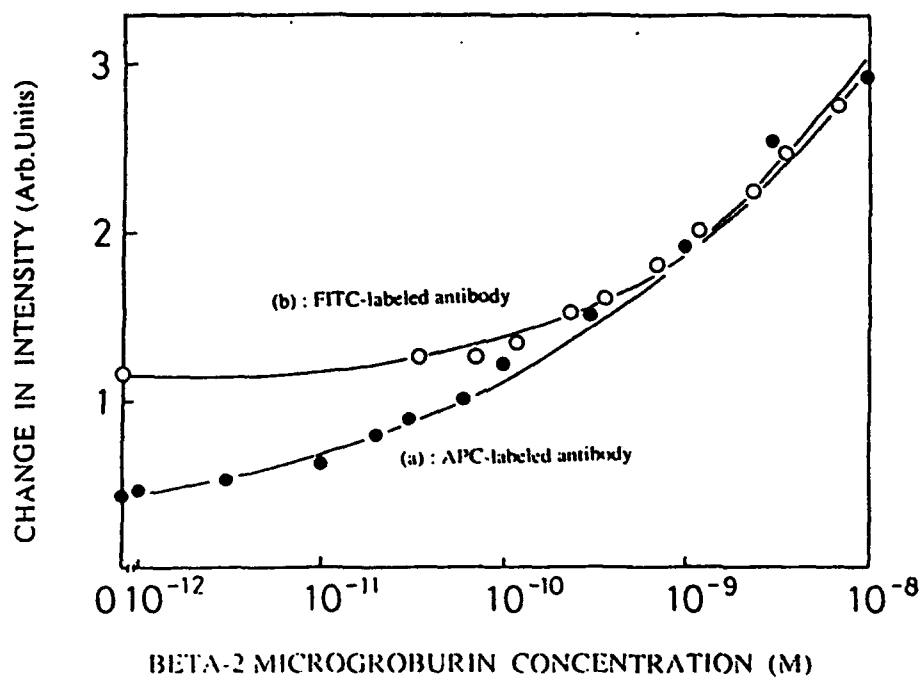


Fig. 4 The response curves for beta-2 microglobulin



## **TH4.6 Long-distance Simultaneous Detection Of Methane And Acetylene By Using Diode Lasers In Combination With Optical Fibers**

**Kazushige YAMAMOTO and Hideo TAI**

**Tokyo Gas Co., Ltd.**

**1-16-25 Shibaura, Minato-ku, Tokyo 105, Japan**

**Masahiko UCHIDA and Susumu OSAWA**

**Hitachi Cable, Ltd.**

**5-1-1 Hitaka-cho, Hitachi, Ibaraki 319-14, Japan**

**Kiyoji UEHARA**

**Keio University**

**3-14-1 Hiyoshi, Kohoku-ku, Yokohama, Kanagawa 223, Japan**

Remote detection of inflammable or poisonous gases leaked into the air is important for safety in chemical plants and facilities. Recently, a real-time methane detection system with a ppb sensitivity using a 1.66- $\mu\text{m}$  InGaAsP distributed feedback (DFB) laser has been developed by some of the authors [1], [2]. This system was then combined with optical fibers to achieve long-distance detection of methane with a 2-ppm-m sensitivity [3], which was approximately three orders of magnitude improved over the earlier fiber-coupled detection systems [4], [5]. A detection system which is capable of simultaneous monitoring of two or more chemical species will be of great use.

In this paper we report laboratory simulations of long-distance simultaneous detection of methane and acetylene with DFB lasers emitting at 1.66  $\mu\text{m}$  and 1.53  $\mu\text{m}$ , respectively. The two lasers are modulated by current modulation at different frequencies near 50 kHz and the wavelength of each laser is locked onto the center of an absorption line of methane or acetylene, respectively, by using a reference gas cell. The modulated lightwaves are sent to and from a 10-cm-long absorption cell in the probed area through common 4-km single-mode fibers and are received by a photodiode. Real-time detection of absorption of the two gases without interferences is accomplished by phase-sensitive detection with reference to each modulation frequency. Furthermore, the ratio of the phase-sensitive-detected fundamental and second-harmonic signals permits quantitative detection of gases even under the circumstances where the received laser power may change owing to various disturbances.

The strongest bands of methane and acetylene in the wavelength region below 2  $\mu\text{m}$  are located at 1.66  $\mu\text{m}$  ( $2\nu_3$  band) and 1.53  $\mu\text{m}$  ( $\nu_1+\nu_3$  band), respectively. DFB lasers at these wavelengths have been developed recently for use in gas detection [6].

Figure 1 shows the absorption signals of the P(13) line of the  $\nu_1+\nu_3$  band of acetylene in nitrogen at atmospheric pressure observed by a 1.53- $\mu\text{m}$  DFB laser. The laser injection current was modulated sinusoidally at a frequency  $f$  of  $\sim 50$  kHz for frequency modulation while the laser-center frequency was scanned by temperature tuning. Trace (a) shows the transmitted power while traces (b) and (c) show the phase-sensitive-detected  $f$  (fundamental) and  $2f$  (second harmonic) signals, respectively. The three traces were recorded simultaneously as functions of the laser junction voltage that proved to be a good monitor of the oscillation frequency [7], [8]. The Q branch of the  $2\nu_3$  band of methane, on the other hand, consists of dense but distinct lines [2], [3]. The P(13) line of acetylene and the Q(6) line of methane are both one of the strongest lines in respective absorption bands. The peak absorption coefficients

of the P(13) line of acetylene and the Q(6) line of methane at atmospheric pressure are calculated to be  $0.8 \text{ cm}^{-1} \cdot \text{atm}^{-1}$  and  $0.4 \text{ cm}^{-1} \cdot \text{atm}^{-1}$ , respectively, which are 12 and 25 times smaller than that of the typical strong absorption line of methane at  $3.4 \mu\text{m}$  [9].

As shown in Fig. 1(b), the  $f$  signal suffers a large offset. (Note that zero level is common to the three traces.) This is due to the fact that the modulation of the injection current results in intensity modulation as well as frequency modulation. On the other hand, the offset in the  $2f$  signal is much smaller as shown in Fig. 1(c), indicating that the  $2f$  signal is more advantageous for absorption detection. If the frequency of the laser is stabilized at the center of an absorption line, one can measure in real time the amount of gas from the  $2f$  signal once the signal intensity is calibrated. The  $f$ -signal intensity, on the other hand, is directly proportional to the laser power received by the detector. Therefore the  $2f$ -signal intensity normalized by the  $f$ -signal intensity indicates the amount of gas independently of the received laser power, as investigated in earlier studies [2], [10]. This ratioing technique for quantitative detection of gases will be useful when the received laser power may change owing to fiber deformation, changes in optical alignment, attenuation by dust in the probed region, etc.

Figure 2 depicts the block diagram of a set of the laser transmitter and modulator-controller. The diode laser is mounted on a thermoelectric element which controls the laser operating temperature to stabilize the oscillation frequency. The laser is modulated by a sinusoidal current of  $f = 49.5 \text{ kHz}$  for acetylene (or  $46.5 \text{ kHz}$  for methane), which is superposed upon a constant dc injection current. The laser light is emitted from both the front and the back facets of the laser chip. The light emitted forward is used as the probe beam. The power of the probe beam is about  $1 \text{ mW}$ . The backward light passes through a 3-cm-long reference cell containing 1 % acetylene (or 7 % methane) mixed with nitrogen at 1 atm and is received

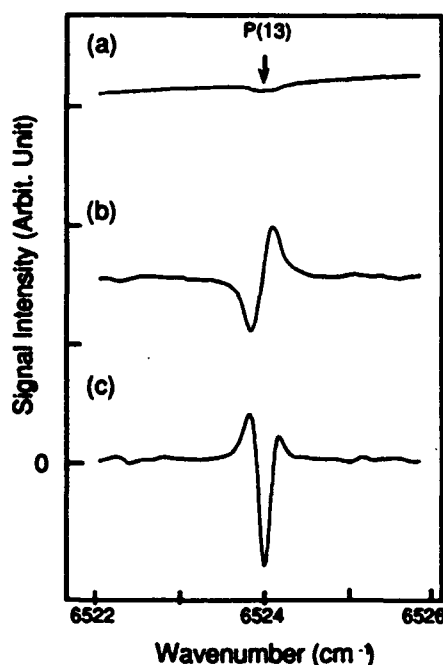


Fig. 1. Absorption signals of the P(13) line of the  $\nu_1 + \nu_3$  band of acetylene at atmospheric pressure observed by a  $1.53\text{-}\mu\text{m}$  DFB laser. (a) The transmitted power, and (b) the fundamental and (c) the second-harmonic phase-sensitive-detected signals. The zero level is common to the three traces. Acetylene concentration: 1 %; cell length: 3 cm.

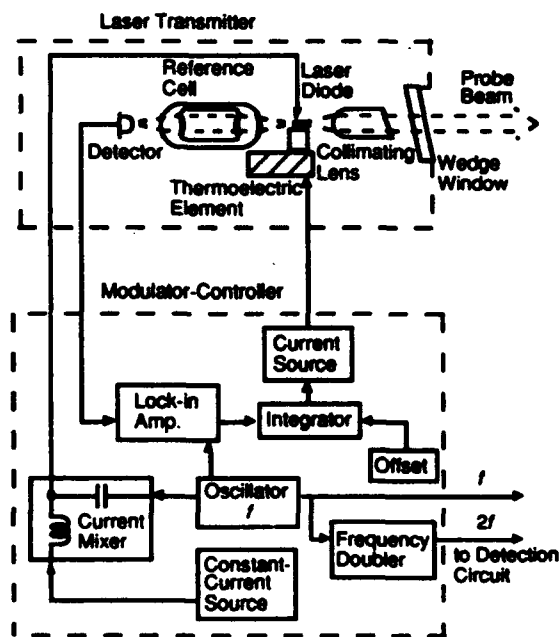


Fig. 2. Schematic diagram of the laser transmitter and the modulator-controller.

by a photodiode. The output of the detector is phase-sensitive detected at  $f$  by a lock-in amplifier. The signal from the lock-in amplifier is integrated after appropriate offset compensation and is fed into the current source of the thermoelectric element. The fluctuation of the laser frequency thus stabilized at the center of the P(13) line of acetylene (or Q(6) line of methane) is less than  $\pm 10$  MHz.

Figure 3 shows the setup for laboratory simulations of simultaneous detection of methane and acetylene. The two laser lightwaves thus modulated and stabilized are combined by a fiber coupler and are transmitted through a 4-km-long single-mode fiber. The combined laser beam then passes through a 10-cm-long absorption cell where the gas is probed. Methane-nitrogen and acetylene-nitrogen mixtures of calibrated concentrations are supplied from a gas handling system. The laser beam transmitted through the absorption cell is focused into another 4-km single-mode fiber and is finally received by an InGaAs p-i-n photodiode. The output signal of the detector is sent to four lock-in amplifiers, which detect the  $f$  and  $2f$  components of the two modulation frequencies. Analogue dividers are used to normalize the  $2f$  signal by the  $f$  signal for both modulation frequencies. The outputs of the dividers are recorded simultaneously on a chart recorder.

Figure 4 shows the  $2f$  signal normalized by the  $f$  signal for  $f = 49.5$  kHz obtained when a 1000-ppm acetylene gas at atmospheric pressure was introduced into the absorption cell and then purged by pure nitrogen. The signal averaging time was 1 s. Since the signal-to-noise ratio (S/N) in Fig. 4 is about 300, the minimum detectable concentration of acetylene in air in a 10-cm absorption pathlength is calculated to be 3 ppm assuming that  $S/N=1$  gives the detection limit. A similar measurement for methane gave a detection sensitivity of 5 ppm. The difference in detection sensitivity between the two gases can be attributed to the difference in absorption coefficient mentioned above.

Figure 5 shows the result of simultaneous detection of methane and

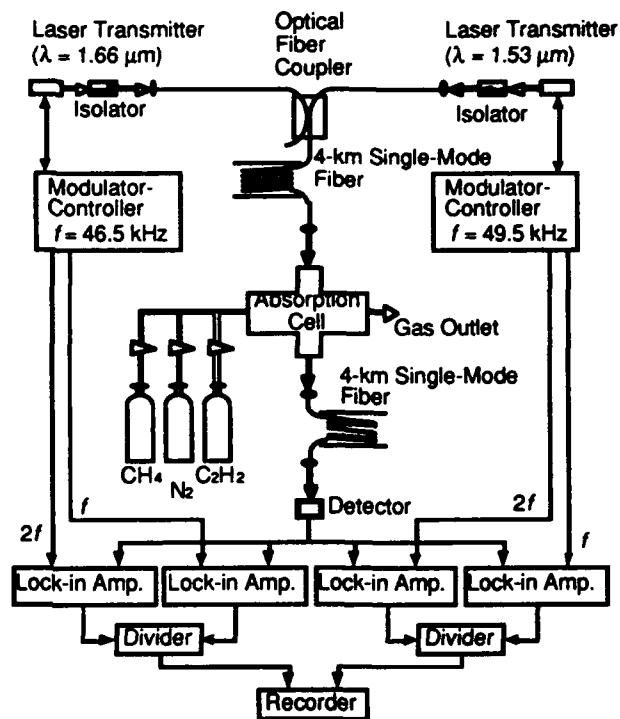


Fig. 3 Experimental setup for simultaneous detection of methane and acetylene.

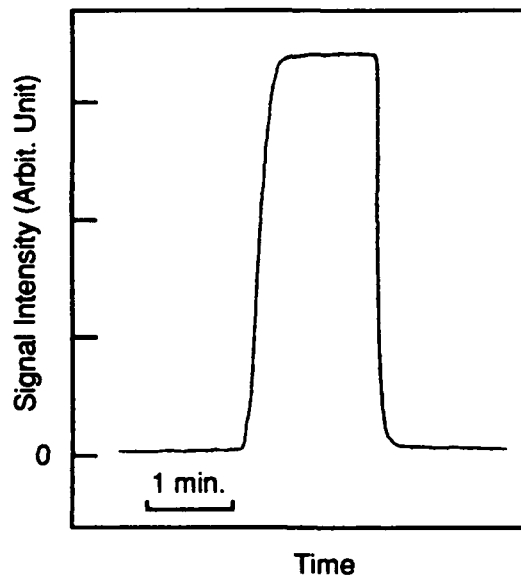


Fig. 4. The normalized detection signal of 1000-ppm acetylene in a 10-cm-long absorption cell. Signal averaging time: 1 s.

acetylene. Traces (a) and (b) are the normalized signals obtained with reference to 49.5 kHz and 46.5 kHz, respectively, when 1000-ppm acetylene and 5000-ppm methane were introduced successively into the absorption cell. This result indicates that there is no appreciable interference between the two signals.

In summary, long-distance real-time simultaneous detection of methane and acetylene by using DFB lasers in combination with 4-km optical fibers has been demonstrated by laboratory simulations. Detection sensitivities of 5 ppm and 3 ppm for methane and acetylene, respectively, have been obtained with a 10-cm-long absorption cell. The present method can be extended to multi-gas detection if diode lasers of appropriate wavelengths are available.

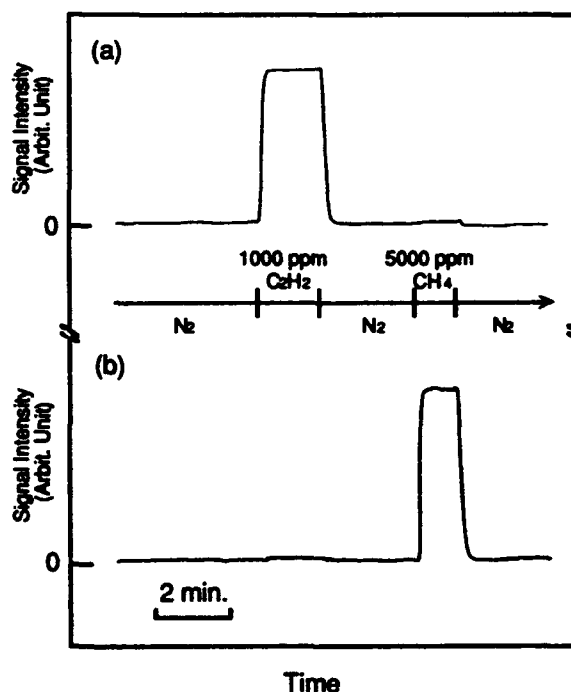


Fig. 5. The result of simultaneous detection of methane and acetylene. Traces (a) and (b) are the normalized signals obtained with reference to 49.5 kHz and 46.5 kHz, respectively, for 1000-ppm acetylene and 5000-ppm methane in a 10-cm-long absorption cell.

## References

- [1] H. Tai, H. Tanaka, and K. Uehara, "Remote detection of methane with a 1.66- $\mu$ m diode laser," 1990 OSA Annual Meeting, Technical Digest, p. 93 (1990).
- [2] K. Uehara and H. Tai, "Remote detection of methane with a 1.66- $\mu$ m diode laser," *Appl. Opt.*, in press.
- [3] H. Tai, K. Yamamoto, S. Osawa, and K. Uehara, "Remote detection of methane using a 1.66- $\mu$ m diode laser in combination with optical fibers," 7th Optical Fiber Sensors Conference, Proceedings, pp. 51-54 (1990).
- [4] K. Chan, H. Ito, and H. Inaba, "10-km-long fiber-optic remote sensing of CH<sub>4</sub> gas by near infrared absorption," *Appl. Phys. B*, **38**, 11 (1985).
- [5] A. Mohabati and T. A. King, "Remote detection of gases by diode laser spectroscopy," *J. Mod. Opt.*, **35**, 319 (1988).
- [6] Y. Shimose and T. Okamoto, private communication.
- [7] K. Uehara, "Signal recording and averaging in diode laser spectroscopy," *Opt. Lett.*, **12**, 81 (1987).
- [8] K. Uehara and K. Katakura, "New method of frequency stabilization of semiconductor lasers," *Jpn. J. Appl. Phys.*, **27**, L244 (1988).
- [9] V. A. Balakin, I. P. Kanovalov, A. I. Ocheretyanyi, A. I. Popov, and E. D. Protsenko, "Switching of the emission wavelength of a helium-neon laser in the 3.39  $\mu$ m region," *Sov. J. Quantum. Electron.*, **5**, 230 (1975).
- [10] D. T. Cassidy and J. Reid, "Atmospheric pressure monitoring of trace gases using tunable diode lasers," *Appl. Opt.*, **21**, 1185 (1982).

**FRIDAY**  
**January 31, 1992**  
**MCC: DeAnza Ballroom**

**F1: INTERFEROMETRY II**

**Chair:** Reinhard Ulrich, *Technische Universitat, Hamburg, Germany*

**F2: SMART STRUCTURES**

**Chair:** Eric Udd, *McDonnell Douglas Electronic Systems Co., Santa Ana, CA*

**F3: FARADAY EFFECT SENSORS**

**Chair:** Alan Rogers, *Kings College, London, UK*

**F4: ELECTROMAGNETIC SENSORS**

**Chair:** Gordon Day, *National Institute of Standards and Technology, Boulder, CO*

## **F1.1**

# **Status Of Fiber Optic Acoustic Sensing**

Aileen M. Yurek  
Naval Research Laboratory  
Optical Sciences Division  
Code 6574  
Washington, D. C. 20375-5000

### **Abstract**

In the past few years a great deal of development effort has gone into fiber optic hydrophones for a variety of Naval applications. Significant demonstrations of fiber optic hydrophone technology have taken place in fixed undersea, towed array, submarine and Arctic environments.

### **Introduction**

Fiber optic hydrophone technology is beginning to be considered a viable alternative to conventional hydrophones for several Navy applications. In the past few years there have been a variety of demonstrations in which fiber optic hydrophones have shown similar and sometimes superior performance to conventional hydrophones in side by side comparisons in realistic test environments. Among these demonstrations have been the deployment and testing of two fiber optic hydrophones in the Arctic by the Naval Research Laboratory (NRL)<sup>[1]</sup>, a 48-channel towed array built by Litton Guidance and Control Systems (LGCS)<sup>[2]</sup> under contract to NRL, a one-to-one comparison of a fiber optic and a conventional hydrophone in a submarine application by LGCS<sup>[3]</sup>, and a proof of concept test of a planar hydrophone for hull array applications by NRL<sup>[4]</sup>. A fixed underwater array built by Plessey Naval Systems has been in continuous operation since 1986<sup>[5]</sup>.

Research is also continuing in the areas of hydrophone and demodulation system development. Several laboratories have been looking at small diaphragm based hydrophone designs using Fabry-Perot interferometers and recently Lawrence Livermore National Laboratory has demonstrated a prototype hydrophone of this design<sup>[6]</sup>. Research is continuing at the Naval Postgraduate School on flexural disk hydrophones<sup>[7]</sup> as well as other novel designs. Several laboratories are looking into alternatives to the conventional analog processing of fiber optic hydrophone data.

Which type of hydrophone is chosen for a given application depends upon the required sensitivity and dynamic range as well as the operational environment. For most non-Arctic applications 10 dB below sea state zero is the required threshold detection with a dynamic range of  $\geq 95$  dB. For Arctic applications an additional 10 dB of sensitivity is required. With a minimum detectable phase shift of 3  $\mu$ rad at 1 kHz, these specifications postulate the hydrophone sensitivity to be  $\geq -145$  dB re rad/ $\mu$ Pa ( $\geq -135$  dB re

rad/ $\mu$ Pa for Arctic applications). Besides having the desired sensitivity in the lab, in most viable hydrophone designs the sensitivity does not change over the temperature and hydrostatic pressure ranges of interest. As an example, one could imagine an array of hydrophones located in a water column where the temperature at one end of the column is different than that at the other. Short of having a temperature sensor at each hydrophone, there would be no way to characterize the sensitivity of the individual devices. Also, in many applications the hydrophones are moving; in these applications it is difficult to characterize the hydrostatic pressure and ambient temperature of each hydrophone in real time. Furthermore, useful hydrophones must not have mechanical resonances in or near the frequency band of interest. While the non-constant sensitivity due to a resonance may be computationally removed, the rapidly varying phase that generally accompanies resonant behavior is not so easily dealt with and may introduce errors in a beamformed output.

At the present time, most of the hydrophones which have undergone field trials have been of mandrel design. There are several reasons why this is true. First, much of the initial effort in fiber optic acoustic sensing has been in the area of towed arrays. A mandrel design is an obvious choice for this application. Also, it is easy to increase the sensitivity of a mandrel design by increasing the amount of optical fiber wrapped on it. Sensitivity to longitudinal acceleration may be essentially eliminated by proper choice of materials or by proper mounting. Additionally, the experience of many of the researchers in the field to date has been that it is simpler to remove or damp undesirable resonances in mandrel structures than in many other structures.

Mandrel hydrophone sensitivity depends primarily upon two factors: the material of which the device is made and the amount of optical fiber which is wrapped on it. Additionally, one may incorporate air into the mandrel design to increase sensitivity. Generally the mandrel responds to the acoustic signal, stretching or compressing the optical fiber, the change in phase of the light in the optical fiber is proportional to the applied acoustic field. Additional sensitivity may be achieved by using a Michelson interferometer configuration rather than a Mach Zehnder or by using a push-pull design<sup>[8]</sup> where both arms of the interferometer are used for sensing. Either of these techniques will add 6 dB of sensitivity. Non-mandrel hydrophones such as flexural disks, prolate spheroids, and coated fiber designs also consist of optical fiber closely contacted to a compliant medium, thus the sensitivities of these devices depend upon the same factors as the mandrels. Only the Fabry-Perot diaphragm type hydrophone sensitivities depend entirely upon the characteristics of the materials of which they are constructed; there is no interaction length of optical fiber in these devices. Most of the fiber optic hydrophones which have been field tested have been mandrels constructed of either solid plastic or of air-backed plastic or metal.

It is clear that too little hydrophone sensitivity will not meet operational requirements. However, hydrophones which are far more sensitive than necessary to achieve the minimum detectable signal requirement may also introduce problems. Designs which are highly sensitive to acoustic signals usually are also sensitive to hydrostatic pressure; the optical fiber wrapped on a highly sensitive hydrophone may exceed its tensile limit be-

fore it ever reaches operating depth. Highly sensitive air backed hydrophones may reach their plastic deformation limit before they reach operating depth.

Many applications require that the hydrophones be operational in a changing temperature and hydrostatic pressure environment. While catastrophic failure (crushing the hydrophone or breaking the fiber) may not occur in these situations, care must be taken such that the acoustic signals are not contaminated by spurious information. Here again, too much hydrophone deformation, either due to temperature or hydrostatic pressure, can be a problem. One way to deal with large temperature gradients is to build the hydrophones in the push-pull configuration. Because both arms of the interferometer in this type of hydrophone respond in the same direction to a temperature change, the thermal effect would cancel. However, many field applications require that the hydrophones be booted in solid or fluid filled containers. These fill materials respond slowly to temperature change, hence effects due to thermal drift will occur at very low frequencies and will probably be outside the band of interest. Rapid hydrostatic pressure changes are far more of a problem. The change in hydrostatic pressure results in the hydrophone interferometer cycling through fringes; the more sensitive the hydrophone, the more rapid the cycling. With present demodulation techniques fringe cycling can introduce spurious signals in the processed output. If the frequencies of these spurious signals are high enough, they appear as tonals in the frequency band of interest; or, if the spurious signals are still higher in frequency, they may overload the demodulator. A push-pull hydrophone responds to hydrostatic pressure changes in the same way it responds to acoustic signals; this design does not provide any advantages in a fluctuating hydrostatic pressure environment.

In most fiber optic hydrophone systems, the fundamental limitation of the dynamic range is not the hydrophone itself, but the electro-optic system used to interrogate it. While state of the art electro-optic systems utilizing non-planar ring Nd:YAG lasers and phase generated carrier demodulators<sup>[9]</sup> have minimum detectable phase shifts of  $3\mu\text{rad}/\sqrt{\text{Hz}}$  at 1 kHz and dynamic ranges in excess of 120 dB<sup>[10]</sup>, this is much less than the ~250 dB dynamic range of the hydrophone elements themselves. However, the entire dynamic range of the hydrophone is present at the detector, so that if processing of the entire dynamic range is desired it may be done using multiple demodulators. These multiple demodulators could use different demodulation techniques depending upon the part of the frequency range and dynamic range they are covering. These could include fringe counting and phase generated carrier techniques as well as a variety of other analog and digital methods. In general the minimum detectable phase shift of the electro-optic system is set by the laser phase noise; however, with noise suppression techniques the laser phase noise can be brought very close to the electronic noise floor over much of the frequency range of interest. The dynamic range limitation is due primarily to nonlinearity in the analog demodulation scheme. Work is ongoing at many locations to make improved demodulators using alternate analog or digital techniques. At this time, for systems with all-optical interrogation, it appears that the phase generated carrier approach is still the technique that gives the largest dynamic range with the smallest minimum detectable phase shift.



Multiplexed hydrophone systems are also moving from the laboratory to the field. The LGCS towed array utilized frequency division multiplexing and the Plessey array is a time division multiplexed system. The performance of the LGCS 48-channel system was not degraded because of the use of multiplexing. Many future systems will depend upon multiplexing to reduce fiber count and overall cost.

More details of the various field trials of fiber optic hydrophone systems and some of the results will be discussed at the meeting.

### References

- [1] A. M. Yurek, A. B. Tveten and A. Dandridge, "High Performance Fiber Optic Hydrophones in the Arctic Environment," Proc. OFS'90, p. 321, 1990.
- [2] P. Davis et. al., "All Optical Towed Array (AOTA) December 1990 Sea Trial (90-17) Final Report (U)," NUSC Technical Memorandum TM 911131 (Classified), to be published.
- [3] A. Dandridge and G. B. Cogdell, "Fiber Optic Hydrophone for Submarine Noise Monitoring (U)," NRL Memorandum Report 6833 (Classified), June 1990.
- [4] A. M. Yurek, A. B. Tveten, and A. Dandridge, "The Design, Fabrication and Testing of a Fiber Optic Hydrophone for Planar Array Applications (U)," NRL Memorandum Report 6908 (Classified), June 1991.
- [5] M. L. Henning and C. Lamb, "At-Sea Deployment of a Multiplexed Fiber Optic Hydrophone Array," Proc. OFS'88, p. 84, 1988.
- [6] L. C. Ng and P. J. Kuzmenko, "Report on Lawrence Livermore National Laboratory (LLNL) Hydrophone Experiment at TRANSDEC," LLNL Memorandum ACE-91-13, dtd. March 20, 1991.
- [7] B. J. Flaskerud and J. B. Kreijger, "Fiber Optic Flexural Disk Hydrophone Design and system Evaluation," Thesis, Naval Postgraduate School, December 1990.
- [8] G. E. McDearmon, "Theoretical Analysis of a Push-Pull Fiber Optic Hydrophone," J. Lightwave Tech. **LT-5**, P. 56 (1987).
- [9] A. Dandridge, A. B. Tveten, and T. G. Giallorenzi, "Homodyne Demodulation Scheme for Fiber Optic Sensors using Phase Generated Carrier," IEEE J. Quantum Electron., **QE-18**, 1647 (1982).
- [10] A. Dandridge, A. B. Tveten, A. C. McGarry and A. M. Yurek, "Dynamic Range of a Differentiate/Crossmultiply Demodulator for Fiber Optic Sensors," NRL Memorandum Report 6641, dtd. May 17, 1990.

## F1.2 Parallel-Wrapped Optical Fiber Interferometric Ellipsoidal Shell Acoustic Sensors

David A. Brown (Physics Department, Code PH)  
Naval Postgraduate School, Monterey, CA 93943.

### Introduction

High sensitivity interferometric acoustic sensors have been demonstrated using optical fiber interferometry and ellipsoidal shells. A new push-pull winding scheme has been tested in which circular windings of optical fiber are bonded to the pole(s) and to the equator of an ellipsoidal shell. Previous push-pull ellipsoids incorporated one leg of the interferometer around the equator and the second around the meridional circumference. In the new scheme the polar leg replaces the equatorial leg while maintaining the desired push-pull performance.

A thin oblate ellipsoidal shell produces surface strains of opposite sign when subject to a uniform pressure loading. Generally, if the aspect ratio,  $a/b$ , exceeds the quantity,  $(2 - \nu)^{1/2}$ , where  $\nu$  is Poisson's ratio, the meridional circumferential strain will be compressive, while the equatorial circumferential strain will be tensile [Ref. 1-3]. If one winds optical fiber around these two principle circumferences, the differential strains can be detected in a push-pull fashion in the legs of an optical fiber interferometer. In this meridional / equatorial winding configuration, the two optical fibers comprising the legs of the interferometer cross at both the equator and crown of the shell, hence, we refer to this transducer as a "cross-wrapped" ellipsoidal shell. An illustration of the "cross-wrapped" ellipsoidal shell is provided in Figure 1a.

A disadvantage in the orientation of the optical fibers in the "cross-wrapped" design is that when using "squat" shells (large aspect ratio) a problem exists in exceeding the maximum bend radius of the optical fiber in the meridional leg as it crosses the equator. This restriction has motivated the discovery of a new winding approach that maintains the desired push-pull detection and alleviates the bend radius limitation by using two "parallel" circular windings of optical fiber. A fiber optic oblate push-pull flextensional transducer can be obtained by using a parallel fiber wrapping technique in which one leg is wound on the equator of the ellipsoid and the second circular (parallel) fiber winding is wound or bonded to the poles of the oblate ellipsoid. An illustration of the "parallel-wrap" design is provided in Figure 1b.

### Theoretical sensitivity

The acoustic sensitivity of an interferometric transducer is the amount of relative phase induced between the legs of the interferometer per unit pressure applied to the transducer. The major contribution of phase change arises from the axial strain in the optical fiber(s). The axial strain also induces a change in the index of refraction of the optical fiber, resulting in a contribution to the total phase modulation that is approximately 20% of direct length change contribution and of opposite sign. If we make the assumption that all of the optical fiber in one leg is placed on the "true" equator of the ellipsoid and that all of the optical fiber in the second leg is placed near the pole at a radial distance  $x$  perpendicular to the axis of rotation of the ellipsoidal shell, then the acoustic sensitivity of the "parallel-wrapped" optical fiber ellipsoidal shell transducer can be shown to be [Ref. 3]

$$\frac{\Delta\phi}{p} = \Xi \xi \frac{2\pi n}{\lambda} \frac{a^2\pi}{Et} \left[ \frac{a^2}{b^2} + (1 - \nu) \frac{x}{b} - (2 - \nu) \right] \quad (1)$$

The multiplicative factor,  $\Xi$ , accounts for the reduction in sensitivity due to the photoelastic effect and is approximately equal to 0.80,  $\xi$  is the interferometer configuration parameter which accounts for the number of passes of light through the sensing fiber before it combines interferometrically,  $n$

is the index of refraction of the optical fiber core,  $\lambda$  is the vacuum wavelength of the light,  $a$  is the semi-major axes of the ellipse,  $b$  is the semi-minor axes (the axis of rotation for an oblate spheroid),  $E$  is the Young's modulus,  $\nu$  is Poisson's ratio, and  $x$  is the Cartesian coordinate equal to the radius of the circular wrap of optical fiber near the pole of the shell.

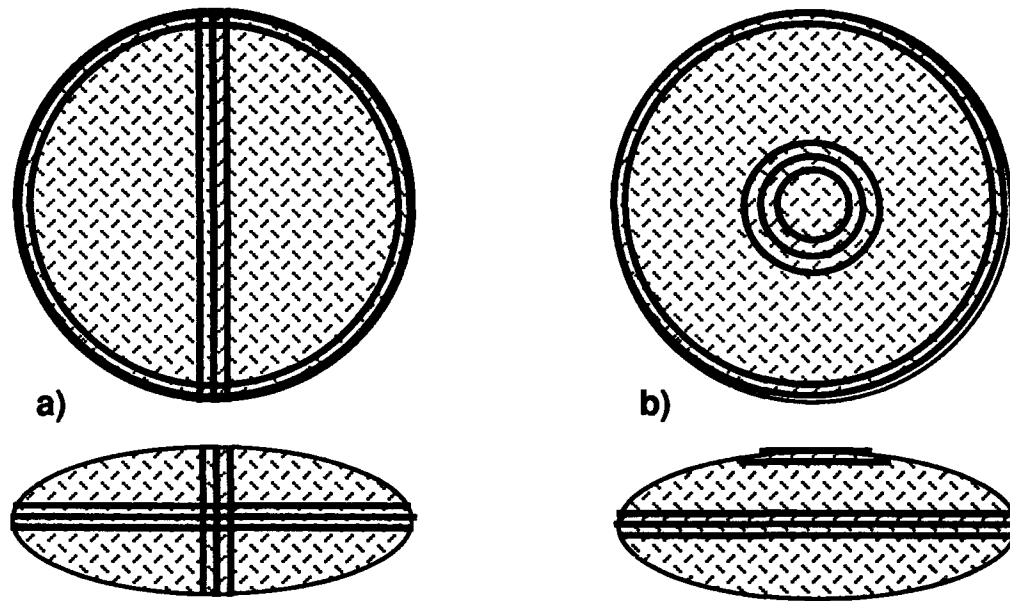


Figure 1. Illustration of a) "cross-wrapped" ellipsoid, b) "parallel-wrapped" ellipsoid.

#### Separation of regions of compressional and tensile strain: Nodal circles

It is of interest to determine the coordinate at which the circular strain changes sign. This "nodal circle" will set the practical limit to which optical fiber of a given interferometric leg could be wrapped while still exploiting the intrinsically differential nature of the interferometer. The location of the nodal circle in terms of the  $x$  coordinate of the ellipse can be shown to be [Ref. 3]

$$\frac{x_n}{a} = \sqrt{\frac{(1 - \nu)}{(2 - \nu)\left(1 - \frac{b^2}{a^2}\right)}} \quad (2)$$

The  $\theta$ -strain or circular strain (normalized by the factor  $\frac{-P}{2Et}$ ) is plotted versus  $\phi$  in Figure 2, where  $\phi$  is the angle between the radius of curvature (to a meridional segment) and the axis of revolution,  $b$ . The  $\theta$ -strain is plotted on the same graph as a function of the true azimuthal polar angle,  $\phi_{\text{polar}}$ . Note that the strain does indeed change sign reaching a relative maximum at the equator ( $\phi_{\text{polar}} = \phi = \pi/2$  radians). Also note that for a given strain,  $\phi \leq \phi_{\text{polar}}$ , and that the strain is relatively constant near the pole in the range  $\pm 0.5$  radians in  $\phi_{\text{polar}}$ . The relationship between  $\phi$  and  $\phi_{\text{polar}}$  is given below

$$\phi_{\text{polar}} = \tan^{-1} \left[ \frac{a^2}{b^2} \tan \phi \right] \quad (3)$$

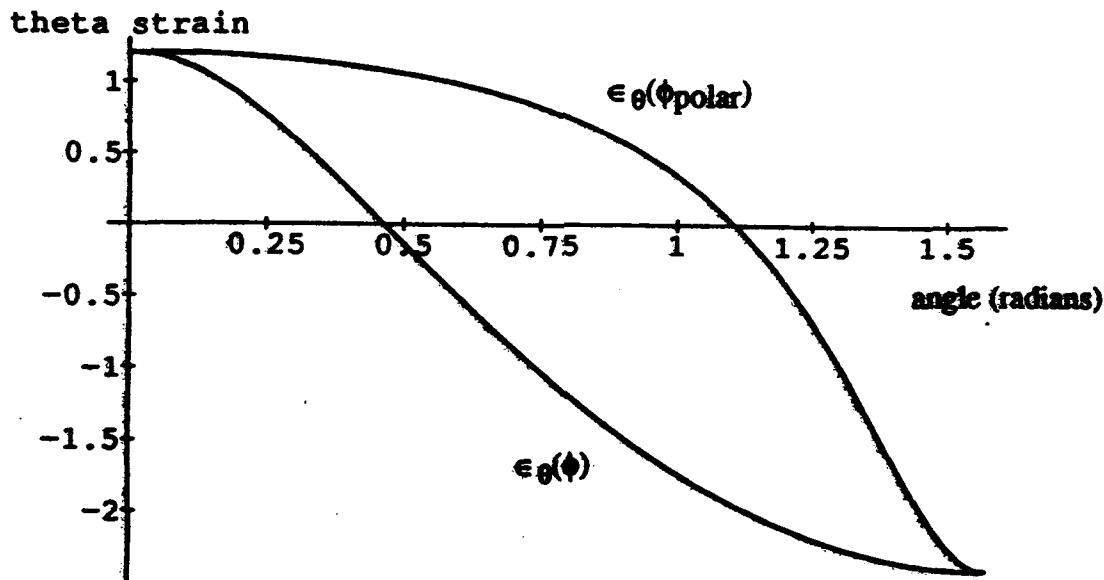


Figure 2. The normalized  $\theta$ -strain plotted versus  $\phi$  (the angle associated with the radius of curvature) and plotted as a function of the polar angle,  $\phi_{\text{polar}}$  for a Poisson's ratio = 0.4 and an aspect ratio,  $a/b = 2$ .

### Fabrication

An oblate spheroidal shell was constructed using Stycast<sup>TM</sup> 1266 castable epoxy to test the parallel wrap fiber optic detection scheme. The aspect ratio of the finished oblate spheroidal shell,  $a/b$ , was 1.96, with the major axis equal to 10.36 cm (outer diameter) and the minor axis equal to 5.28 cm (outer diameter). The actual shell thickness of the Stycast<sup>TM</sup> spheroid varied from a high of 0.91 mm (0.036 inches) at the both the equator and the poles to a low of 0.81 mm (0.032 inches) between the pole and the equator of the shell. In the azimuthal direction, the shell thickness was uniform with variations less than 0.001 inches. The finished polar coil of optical fiber had an inner radius of 1.6 cm and an outer radius of 3.9 cm and a total length of 4.00 meters of active fiber. The fiber on the equator consisted of 12 turns of optical fiber for a total active equatorial length of 3.83 m.

### Optical sensitivity measurements

The optical fiber was first wound around and then epoxied to the equator of the ellipsoid, keeping the second leg detached from the sensor, in order to obtain sensitivity measurements of the individual leg of the interferometer. The acoustic sensor (with temporary reference leg wrapped as a pancake coil to be later mounted on the pole of the ellipsoid) was inserted into a cylindrical coupler calibrator. Using a fringe counting calibration measurement technique, the measured acoustic sensitivity of the single interferometric leg was found to be  $0.99 \pm 0.02$  rad/Pa. Data was obtained in the frequency range from 30 to 100 Hz. Noting the radian path length of the 4.02 m equatorial leg, we arrive at a normalized sensitivity based on measurement of  $\Delta\phi/\phi\Delta p = 1.14 \times 10^{-8}$  Pa<sup>-1</sup> or -279.2 dB re  $\mu\text{Pa}^{-1}$ .

The second leg of the interferometer was then epoxied to the pole (one pole only) and the push-pull performance of the alternative winding scheme was fully tested. A photograph of the sensor placed in the calibrator is shown in Figure 3. The average overall sensitivity using both legs was determined to be 1.44 rad/Pa. The push pull performance was clearly demonstrated since the addition of the second leg increased the sensitivity from 0.99 to 1.44 rad/Pa for a net increase of 0.45 rad/Pa. The normalized sensitivity, obtained by dividing the radian path length by the average interferometer leg length, is -276 dB re  $\mu\text{Pa}^{-1}$ .



Figure 3. Photograph of the fiber optic oblate ellipsoidal acoustic sensor inside the calibrator with the polar and equatorial legs attached to the sensor.

## REFERENCES

1. D. A. Danielson and S. L. Garrett, "Fiber-optic ellipsoidal flextensional hydrophones", *J. Lightwave Tech.*, LT-7(12), pp. 1995-2002, (1989); S. L. Garrett and D. A. Danielson, "Flextensional hydrophone", U.S. Patent No. 4,951,271, (Aug. 21, 1990).
2. D. A. Brown, D. A. Danielson, and S. L. Garrett, "A fiber optic ellipsoidal shell hydrophone" in *Fiber Optic and Laser Sensors IX*, Proc. Soc. Photo-Optical Instrumentation Eng. (SPIE) 1369, (1990).
3. D. A. Brown, "Optical Fiber Interferometric Acoustic Sensors using Ellipsoidal Shell Transducers", Ph.D. Dissertation, Naval Postgraduate School, (June, 1991); D. A. Brown, "A parallel wrapped push-pull ellipsoidal shell acoustic transducer", U.S. Navy Case No. 73806, (Sept. 8, 1991).

## **F1.3                      Detection Of Acoustic Emission In Cutting Processes By Fibre Optic Interferometry**

**R. McBride            T. Carolan            J. S. Barton            W. K. D. Borthwick  
J. D. C. Jones**

**Department of Physics  
Heriot-Watt University, Riccarton  
EDINBURGH EH14 4AS  
United Kingdom  
Tel: (44) 31 451 3038  
Fax: (44) 31 451 3088**

### **1 Introduction**

Acoustic emission (AE) has been shown to be a useful technique in monitoring the state of wear in machine tools [1]. AE (or stress wave emission) produced by metal cutting processes generates various wave modes in the tool and workpiece, including out of plane vibrations of amplitude in the order of 1nm, in the frequency range 0.1–1MHz. Conventionally, contacting piezoelectric transducers have been used for AE detection. These are generally resonant devices with maximum sensitivities in the region 100kHz–500kHz and relatively narrow bandwidths. A non-contact technique of broader bandwidth would be preferred [2]. We have developed a technique based on a fibre optic homodyne Michelson interferometer [3] with a robust probe head which is capable of detection of AE waves during milling and other machining operations. AE was detected probing both the workpiece and the rotating tool holder.

### **2 Interferometer design**

A schematic diagram of the interferometer is shown in fig. 1. This consists of a Michelson interferometer generating antiphase outputs using some novel polarisation features. A fibre loop reflector was used in the reference arm using a birefringence controller so that the intensity of the return from this arm could be controlled. A piezoelectric cylinder fibre stretcher [4] was used as a phase modulator in the reference arm as part of a servo loop to maintain the interferometer at phase quadrature [5]. Polarisation control [6] was included before the phase modulator to maintain the beam in a polarisation eigenstate of the dynamic birefringence of the phase modulator. A polarisation controller was included in the signal arm to match the polarisation states of signal and reference returns and thus maximise fringe visibility. It may be shown that complete control of birefringence in the loop reflector allows independent control of both reflection coefficient and return polarisation state, thus this could be used to ensure that the return beam was always rejected by the polarising beamsplitter. Thus detectors D2 and D3 gave antiphase outputs and feedback to the HeNe laser was minimised. The output signal was obtained by subtracting antiphase outputs. For small signals around a quadrature bias point, this leads to an output intensity which varies linearly with optical phase and thus with surface displacement. Fibre arm lengths were balanced to within 1mm using an FM technique with a laser diode. D1 and D4 were used in setting up the interferometer.

The probe was designed for an N.A of 0.012, yielding a 30 $\mu$ m spot size and a 1mm depth of focus in an aberration-free system. The probe consisted of a 2mm dia ball lens bonded at a precisely controlled distance from the fibre end, which was held in a capillary tube. The region between fibre and lens was flooded with index matching adhesive. Prior analysis had shown that such a single element probe gave sufficiently low

coupling loss when the lens was sufficiently small. The probe fibre was enclosed in protective tubing to avoid damage in machine tests.

Vibrations in the milling machine lead to large fluctuations in the signal arm optical path length due to movement of the target surface and to vibration coupled into the fibre, via the strain optic effect. A type 2 second order servo was used [7] with the general transfer function

$$H(s) = \frac{K(s+a)}{s^2 + Ks + Ka}$$

and was adjusted for a bandwidth of around 3kHz. This gave a rejection of unwanted path length variations increasing by 40dB/decade as frequency is decreased below resonance. Path length changes of up to 200µm could be compensated.

With the interferometer locked in quadrature, any surface movement within the servo bandwidth may be detected by monitoring the error signal, ie the voltage applied to the phase modulator. (This signal will suffer some contamination due to vibrations of the probe lead.) Higher frequency surface displacements are allowed to modulate the phase and hence the output intensities of the interferometer. The AE signal was obtained using a 100kHz–1MHz bandpass filter. In the lab, noise levels in the filtered AE signal were typically 50pm peak to peak ( $1\mu\text{rad}/\sqrt{\text{Hz}}$  averaged over the bandwidth). This was chiefly due laser frequency noise via unwanted reflections and Rayleigh scattering.

### 3 Experiment

Tests were done milling mild steel blocks using 4 and 6 point tools in a Wadkins CNC milling machine.

In the first set of tests, the probe addressed the polished end face of the block (fig 7) as the block was milled using a 6-point cutter. The servo successfully tracked the surface during cutting, producing the periodic low frequency surface displacement signal shown in fig 2a. This signal is related to the force exerted by the tool on the workpiece via the stiffness of the workpiece mounting. The peaks thus correspond to tooth engagements. In this cutter, three raised teeth exert most force on the workpiece, whilst less prominent teeth contribute little to the cutting process. Bursts of acoustic emission were detected and found to coincide with tooth engagement, as expected (fig2b).

In order to verify that the detected signal was indeed caused by AE, a broadband piezo transducer was attached to the workpiece and the signals from interferometer and piezo recorded simultaneously (fig 3). There was a clear correlation between bursts from the interferometer and from the piezo, although the interferometer also suffered from some additional, shorter timescale, burst type noise. A section of these signals is shown on a shorter timescale in fig 4. They show similar, but not identical, periodic structure. This is not surprising as they were probing different parts of the workpiece and experienced different signal reflections etc. Power spectra of the two signals, obtained by 1024 point FFT, are shown in fig 5. These show the same broad peaks at roughly 100kHz intervals, with little distinct information above 500kHz.

In the second set of tests, the probe was used to address the rotating surface of a 4-point tool holder. The surface was polished to provide a sufficiently strong return signal. Again, AE was detected during the cutting of mild steel. Signals from the interferometer and a reference piezo transducer attached to the workpiece are shown in fig 6. This approach was more noise sensitive than probing the workpiece directly as imperfections in the tool holder surface appear as surface displacements as they traverse the probe.

### 4 Conclusion

A non-contacting interferometric sensor was developed which could detect small ultrasonic displacements in the presence of much larger mechanical vibrations. The interferometer operated successfully in a machine shop environment, detecting AE from both workpiece and tool holder during face milling. Results correlated very well with those from conventional contacting transducers. The sensor is capable of high resolution (50pm for a 1MHz bandwidth) and broad bandwidth (>1MHz).

**Acknowledgement:** The authors gratefully acknowledge the support of the European BRITE programme CEC DG XII, and receipt of an SERC studentship.

## References

- [1] Y. Kakino *J. Acoustic Emission* 5 (1986) 108
- [2] C. H. Palmer, R. E. Green, Jr. *Appl. Opt.* 16 (1977) 2333
- [3] D. A. Jackson and J. D. C. Jones *Opt. & Laser Tech.* 18 (1986) 243, 249
- [4] D. A. Jackson et al. *Appl. Opt.* 16 (1980) 2926
- [5] D. A. Jackson and J. D. C. Jones *Optics Acta* 33 (1986) 1469
- [6] H. C. Lefevre *Electron. Letts.* 16 (1980) 778
- [7] K. Fritsch and G. Adamovsky *Rev. Sci. Instrum.* 52 (1981) 996

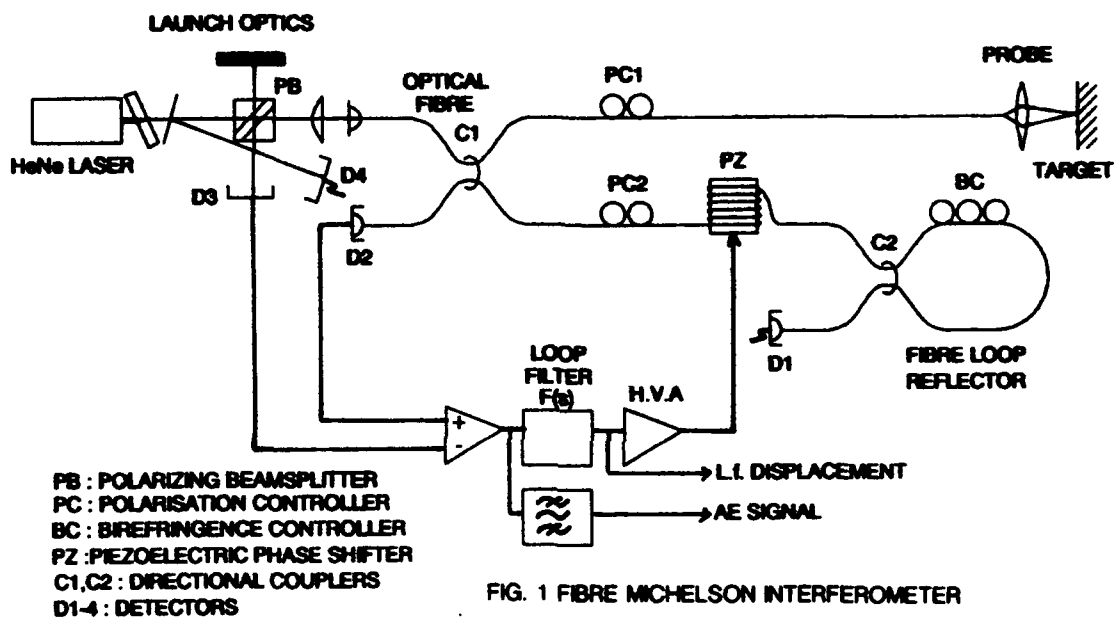


FIG. 1 FIBRE MICHELSON INTERFEROMETER

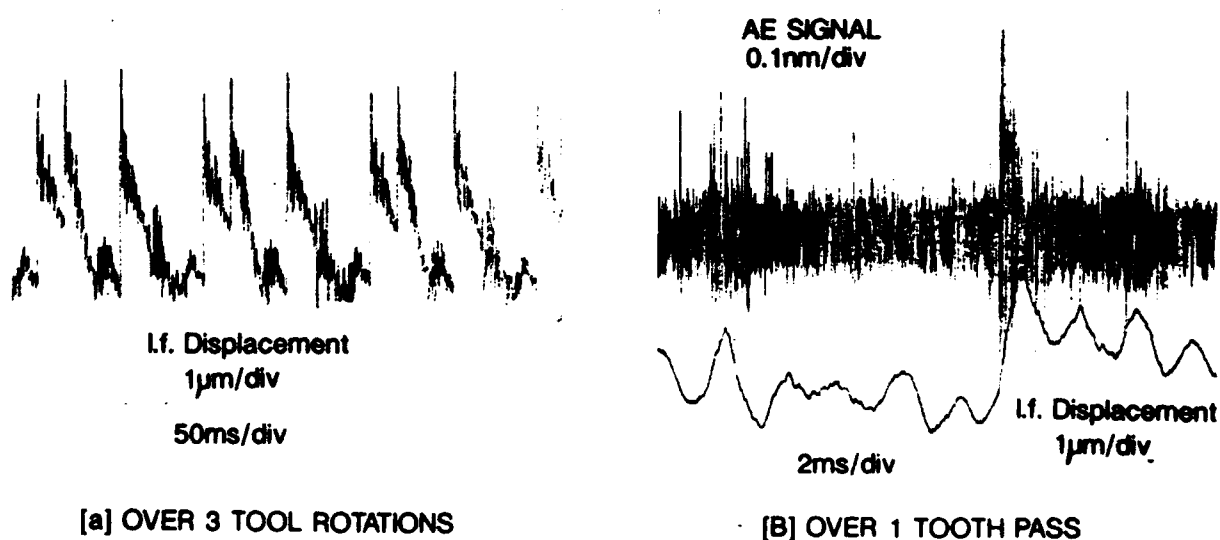


FIG. 2 LOW AND HIGH FREQ. DISPLACEMENT SIGNALS



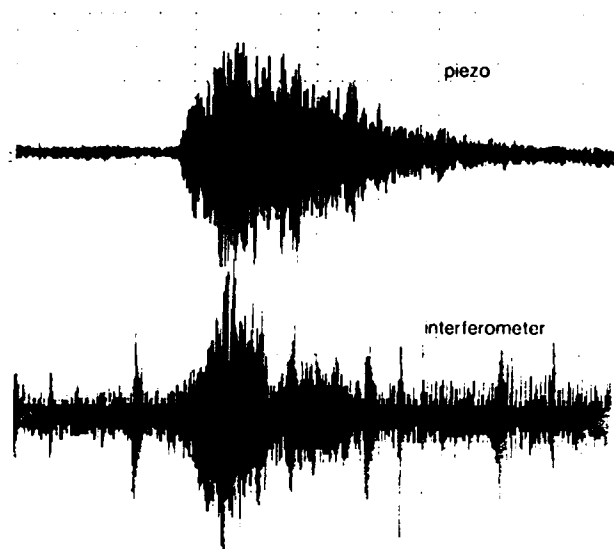


fig.3 AE BURST DURING MACHING [1ms/div]

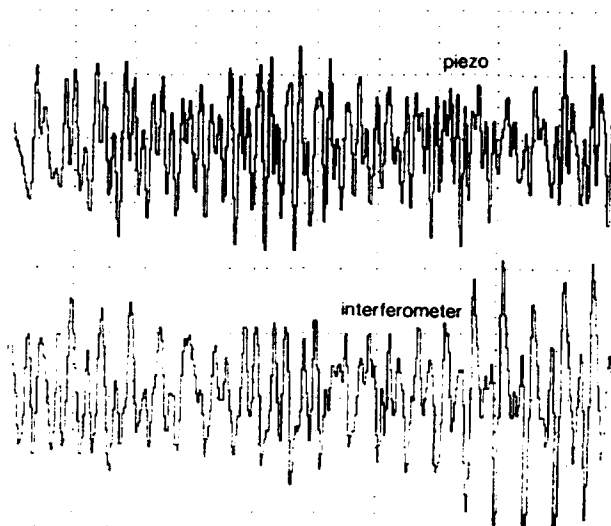


fig.4 PORTION OF FIG.3 ON EXPANDED TIMESCALE [20μs/div]

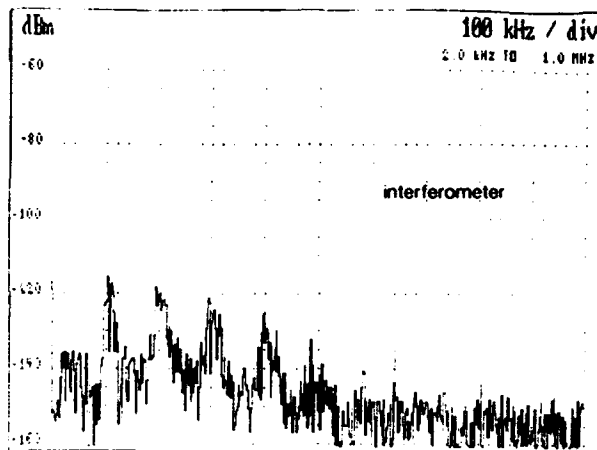
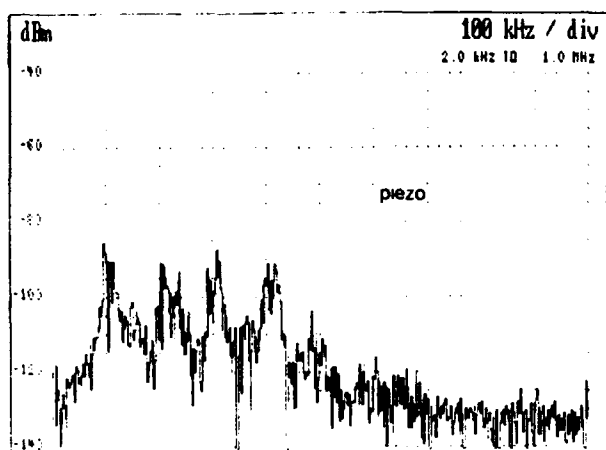


fig.5 POWER SPECTRA OF TRACES IN FIG.4

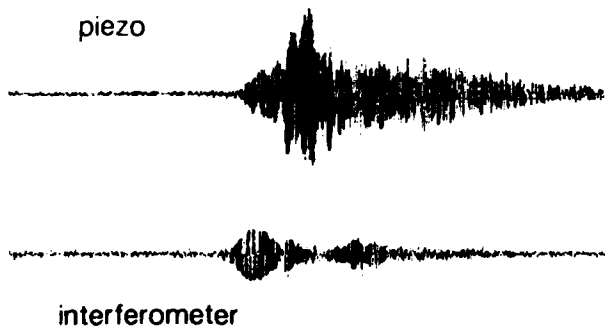


fig.6 AE BURST FROM ROTATING TOOL HOLDER [0.5ms/div]



fig.7 PROBE HEAD MOUNTED ON CNC MACHINE

## A High Frequency Fiber Optic Hydrophone

A. B. Tveten, A. M. Yurek, Y. Y. Chao<sup>1</sup>, and A. Dandridge

Naval Research Laboratory  
Optical Sensor Section  
Code 6574  
Washington, D. C. 20365-5000

### Abstract

Recently there has been interest in fiber optic hydrophones for high frequency applications. A fiber optic hydrophone with flat frequency response to 50 kHz has been designed and built at NRL and demonstrated at the USRD calibration facility.

### Introduction

In the last three years there has been a rapid advance in the performance of fiber optic acoustic transducers. In 1990 a number of important field demonstrations took place: two fiber optic hydrophone systems were demonstrated in the Arctic with 30 dB below sea state zero threshold detection<sup>[1]</sup>, a fiber optic hydrophone system was successfully tested on the USS Memphis (SSN 691)<sup>[2]</sup> and a 48-channel towed array system was also demonstrated at sea<sup>[3]</sup>. The advances in performance have been driven by improvements both in transducer design<sup>[4]</sup> and the opto-electronics interrogating the transducer. In general these demonstrations have concentrated on lower frequency ranges (below 10 kHz), however there is considerable interest in using fiber optic sensor technology for higher frequency applications. One significant factor in the design of a number of recent sensor systems has been the development of the long coherence length diode pumped Nd:YAG laser, which has not only allowed greater design flexibility, but has also reduced transducer complexity. This source has the added advantage that its frequency noise falls off as  $1/f$  (compared to the slower fall off of the semiconductor laser) which makes it ideal for higher frequency operation<sup>[5]</sup>. In this work we use these advantages of the Nd:YAG source to demonstrate a fiber optic hydrophone suitable for high frequency applications.

### Experimental Setup

The hydrophone consisted of an air-backed mandrel<sup>[6]</sup> 1.25 cm in outside diameter with 40 meters of optical fiber configured as a large path imbalance Michelson interferometer. A diagram of the hydrophone construction is shown in Figure 1. An air-backed mandrel was constructed of two pieces of brass tubing and the 40 m of optical fiber was wrapped on it. The fiber was Corning Payout fiber and was 80  $\mu\text{m}$  in diameter with a 25  $\mu\text{m}$  acrylate coating. The optical fiber coupler and the two mirrors were spliced to the fiber wound on the mandrel and then placed into the inside of the inner tube. Thick jacketed fiber (9 mm diameter) was fused to the input/output leads of the interferometer. The splices and the components were potted in place with a curable epoxy. The whole assembly was then dip coated in polyurethane to protect the device during subsequent handling.

The interrogation approach chosen for this hydrophone was a simple free running homodyne approach, the data being collected while the interferometer was in quadrature. This technique, which allows the measurement of the hydrophone sensitivity without requiring a demodulator, has a bandwidth determined by the frequency response of the photodetectors. The optical source was a Nd:YAG ring laser and the photodetectors had a frequency response of more than

1. University Research Foundation, 6411 Ivy Lane, Suite 110, Greenbelt, MD 20770.

200 kHz. A diagram of the experimental setup is shown in Figure 2. The hydrophone was then mounted in the free field sensitivity measurement test area at the Naval Research Laboratory Underwater Sound Reference Detachment (NRL USRD) and insonified by a high frequency acoustic projector. The output of the fiber optic hydrophone was compared with a conventional reference hydrophone to determine its sensitivity and frequency response.

## Results

The low frequency sensitivity of this fiber optic hydrophone was measured to be -142 dB re rad/ $\mu$ Pa, this response continues down in frequency to hydrostatic pressures. This sensitivity corresponds to a normalized sensitivity  $d\phi/dP$  of -317 dB re 1/ $\mu$ Pa, consequently the hydrophone should operate to depths of over 1000 m. The frequency response was flat to ~50 kHz, a plot of the response is shown in Figure 3, the acoustic excitation was broadside to the device. As can be seen in the Figure, there are no resonant peaks observed in the response of this hydrophone. This contrasts with the behavior of a number of designs of fiber optic hydrophones using plastic or air-backed plastic to form the compliant structure. Typically these devices have resonances between 2 and 15 kHz depending upon the specifics of the design.

The high frequency roll off of this device appears to be related simply to the diameter of the hydrophone. As the wavelength of the acoustic signal becomes smaller than twice the diameter of the hydrophone the hydrophone acts to cancel the acoustic wave. This phenomenon repeats as successive multiples of the acoustic half wavelength match the diameter of the hydrophone. A plot of the expected hydrophone frequency response with the hydrophone diameter as a parameter is shown in Figure 4. Curves are plotted for hydrophone diameters of 1.27 cm, 0.95 cm and 0.64 cm. The curves of the two smaller diameter hydrophone responses have been truncated for clarity. The response of smaller diameter hydrophones will be reported at the conference.

It should be noted that as the active length of these hydrophones was 10 cm this design of hydrophone would only be omnidirectional to 10 kHz. However, the active length of the hydrophone can simply be shortened; although, as the length of fiber would be reduced so would the hydrophone sensitivity be proportionally reduced.

The threshold detection of the hydrophone was limited by the laser frequency induced phase noise. The noise performance of a free running Nd:YAG ring laser source is shown in Figure 5. At 10 kHz this laser has a minimum detectable phase shift of 2  $\mu$ rad. This would give a minimum detectable pressure for the high frequency hydrophone of 28 dB re  $\mu$ Pa/ $\sqrt{\text{Hz}}$  at 10 kHz. The flattening of the threshold detection above 10 kHz is due to the frequency independent demodulator noise. The low frequency noise performance of these laser sources has been improved by a variety of feedback or common mode techniques<sup>[1]</sup>, thus threshold detections of ~ 30 dB re  $\mu$ Pa/ $\sqrt{\text{Hz}}$  should be possible over the frequency band shown.

## Conclusions

A hydrophone with a flat frequency response to 50 kHz has been built and tested. The high frequency hydrophone roll-off appears to be solely related to the diameter of the mandrel, no resonances of the structure are observed. Smaller mandrel designs should push this roll-off to above 100 kHz.

## References

- [1] A. M. Yurek, A. B. Tveten and A. Dandridge, "High Performance Hydrophones in the Arctic Environment", OFS'90, Sydney Aust., Dec 1990.

- [2] A. Dandridge and G. B Cogdell, "Fiber Optic Hydrophone for Submarine Self Noise Monitoring", NRL Memorandum Report #6833, 1991.
- [3] A. Dandridge, A. B. Tveten and A. M. Yurek, "Improved Phase and Coherence Data from the December 1990 AOTA Sea Trial", NRL Memorandum Report #6851, 1991.
- [4] A. B. Tveten, A. M. Yurek and A. Dandridge, "High Performance Fiber Optic Hydrophone", J. Underwater Acoustics, **40**, 295, 1990.
- [5] K. J. Williams et al, "Interferometric Measurement of Low-Frequency Phase Noise Characteristics of a Diode Laser-Pumped Nd:YAG Ring Laser", Electronics Lett., **25**, 774, 1989.
- [6] G. F. McDearmon, "Analysis of a Push-Pull Fiber Optic Hydrophone", J. Lightwave Technology, **LT-5**, 647, 1987.

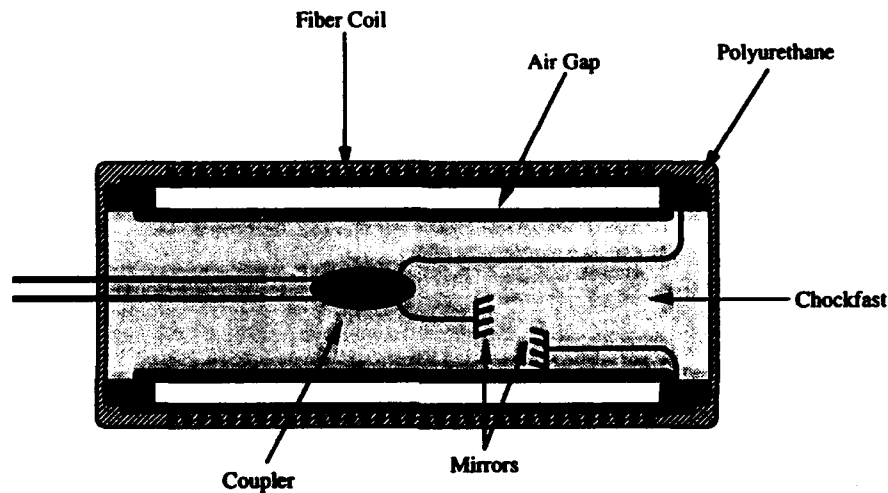


Figure 1 Diagram of the hydrophone construction.

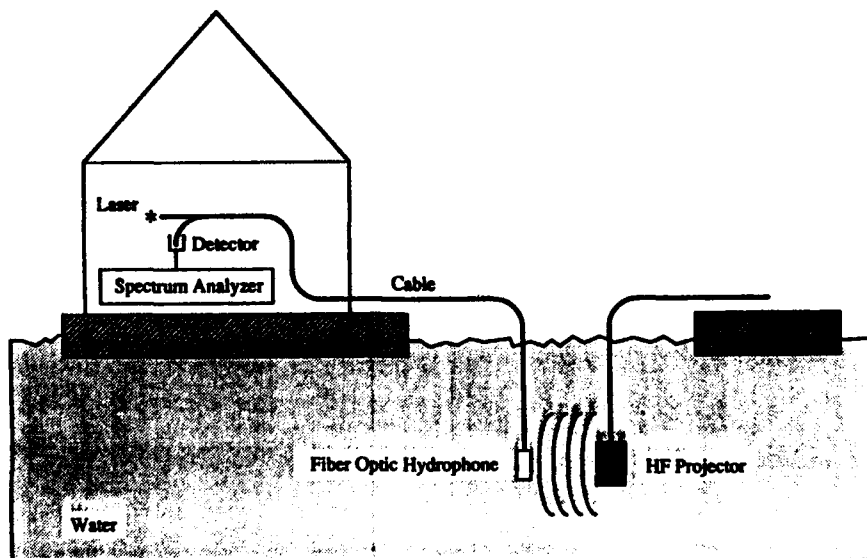


Figure 2 Diagram of the experimental setup.

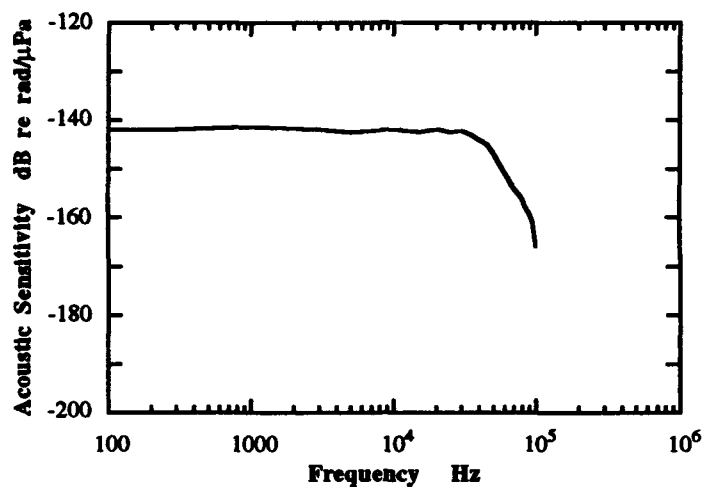


Figure 3 Hydrophone frequency response.

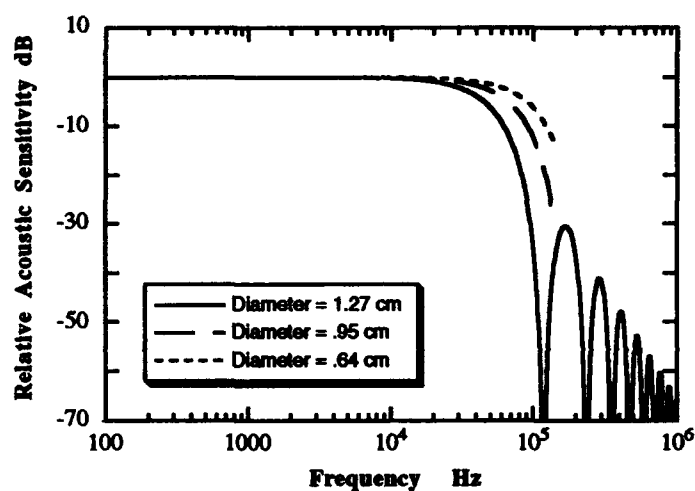


Figure 4 Theoretical hydrophone frequency response.

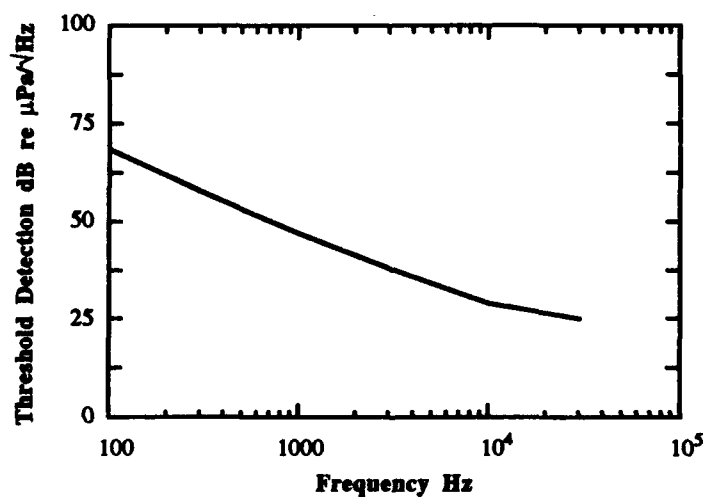


Figure 5 Noise performance of free running Nd:YAG ring laser source.

## **F1.5 Experimental Performance Of A Miniature Fabry-Perot Fiber Optic Hydrophone**

**Paul J. Kuzmenko  
Lawrence Livermore National Laboratory  
L-366, P.O. Box 808  
Livermore, CA 94551**

### **INTRODUCTION**

The advantages of fiber optic sensors in hydrophone applications are well known. They offer excellent sensitivity, resistance to electromagnetic interference, and all active electronics are kept out of the water. One aspect where they are not clearly superior to conventional piezoelectric transducers is their size. For some applications size is critical and existing designs are too large.

Some Japanese work described an acoustic sensor based on a Fabry-Perot interferometer [1,2]. Ohba and Uehira constructed an interferometer on the end of an optical fiber using the fiber tip as one mirror and a sound receiving diaphragm as the second mirror. The potential for making a very tiny sensor is clear. It seemed interesting to try to build a hydrophone based on this principle. This paper will describe the construction and testing of such a device.

### **SENSOR DESIGN AND OPERATING PRINCIPLES**

A functional sketch of the hydrophone is shown in Figure 1. The Fabry-Perot interferometer is formed between the cleaved end of the single mode optical fiber and the thin plastic membrane. A small vent hole is cut near the edge of the membrane to equalize static pressures. The air bladder, a rubber balloon over the front of the sensor, keeps water away from the interferometer while freely transmitting pressure fluctuations from the water to the air. Pressure variations in the air bladder cause the membrane to deflect, modulating the reflectivity of the interferometer. As depth increases, the balloon will slowly collapse on itself, keeping the internal and external pressures balanced.

The balloon can be modeled as a spherical bubble [3]. External acoustic waves incident on the air volume induce internal pressure variations. Theory tells us that at low frequencies the internal and external pressures have equal amplitudes, but at higher frequencies there is a sharp resonance around which the internal pressures are amplified. Above the resonance the internal pressure variations decrease as  $1/f^2$ . For a  $1 \text{ cm}^3$  bubble at a depth of 20 feet, the resonance occurs at about 670 Hz. Reducing the bubble size or increasing the depth increases the resonant frequency.

Although the balloon transmits low frequencies well, the sensitivity rolls off due to the pressure equalizing vent in the membrane. The rolloff frequency can be controlled by changing the diameter of the vent hole or the volume of the cavity behind the membrane. Since the compressibility of the air in this back cavity provides the restoring force for the membrane (the membrane tension is very low), adjusting the volume will alter the sensitivity of the hydrophone. One drawback of this situation is that the sensitivity of the hydrophone does vary with pressure. However, the overall sensitivity is very good and can be designed to meet desired values by controlling the back cavity volume.

A diagram of the controller box is shown in Figure 2. Light from the pigtailed laser diode (Seastar model PT-450) enters the fused optical coupler. Some is split off to a reference detector which monitors the power level injected into the fiber and the rest travels

to the sensor. Acoustic pressures in the water vary the mirror spacing in the Fabry-Perot interferometer, modulating the reflected power. On reentering the coupler a significant fraction of the return power is directed to the signal photodiode where it is detected, amplified and sent to the output of the box. In order to achieve the greatest sensitivity, the laser is mounted on a thermoelectric heater/cooler. This allows the operator to manually tune the wavelength of the laser to the best operating point by controlling the laser temperature.

### EXPERIMENTAL DETAILS AND RESULTS

To permit easier handling and fixturing, the interferometer was fastened with silicone inside a brass rod 0.5 inch in diameter and 1.5 inches long. The balloon is then pulled over the front and epoxied in place. The volume of the balloon is about  $1 \text{ cm}^3$  while the brass rod is about  $5 \text{ cm}^3$  making a total sensor volume of  $6 \text{ cm}^3$ . However, it could be easily reduced to  $>2 \text{ cm}^3$ .

We were invited to characterize the hydrophone in the TRANSDEC facility at the Naval Ocean Systems Center (NOSC) in San Diego. TRANSDEC, as shown in figure 3, is a large ellipsoidal pool instrumented for acoustic measurements. The hydrophone was lowered to a depth of 6 meters and positioned 0.5 meters from an NRL/USRD model J 11 sound projector. Adjacent to the fiber hydrophone was a model H52 reference hydrophone. The projector was excited at discrete frequencies and the output of the fiber optic hydrophone was averaged and measured with an electronic spectrum analyzer. One month later at LLNL the same hydrophone was characterized in an NRL/USRD model G19 calibrator at atmospheric pressure. Both sets of data are plotted in figure 4. The bubble resonance and the low frequency rolloff are readily apparent, as are the shifts in sensitivity and resonance due to the change in pressure.

We wanted to measure the self noise of the fiber optic hydrophone, but the TRANSDEC pool was not quiet enough. Both the reference hydrophone and the fiber optic hydrophone measured the same background level of +49 dB re  $1 \mu\text{Pa}$  at 1 kHz and +73 dB at 100 Hz.

Because of the sinusoidal nature of the interferometer, one would expect the hydrophone to saturate at a sufficiently high acoustic excitation. To verify this the electrical output of the controller was monitored on an oscilloscope while the sound level at 200 Hz was slowly increased. Clipping occurred at about +120 dB SPL, and at a voltage level below the electrical saturation level of the output amplifier.

### SUMMARY AND CONCLUSIONS

A new type of fiber optic hydrophone based on a Fabry-Perot interferometer has been demonstrated. Its volume of several cubic centimeters is much smaller than that of other reported sensors. The sensitivity of -122 dB re 1 Volt/ $\mu\text{Pa}$  also compares very favorably with existing devices. One drawback of this air-filled unit is that the sensitivity varies inversely with depth. However, the sea level sensitivity can be increased to compensate by enlarging the back cavity volume. More work needs to be done on the possibility of a fluid filled sensor whose sensitivity would be depth invariant.

### ACKNOWLEDGEMENT

Work performed under the auspices of the U. S. Department of Energy by the Lawrence Livermore National Laboratory under Contract W-7405-Eng-48.

## REFERENCES

- 1) M. Matsumoto et al., Tech.Digest OFS '86, p.43-6 (1986)
- 2) R. Ohba and I. Uehira, J. Phys E: Sci Instrum 20, 1380-2 (1987)
- 3) Physics of Sound in the Sea, Summary Technical Report NDRC Division 6 Vol.8, Chap.28 (1946)

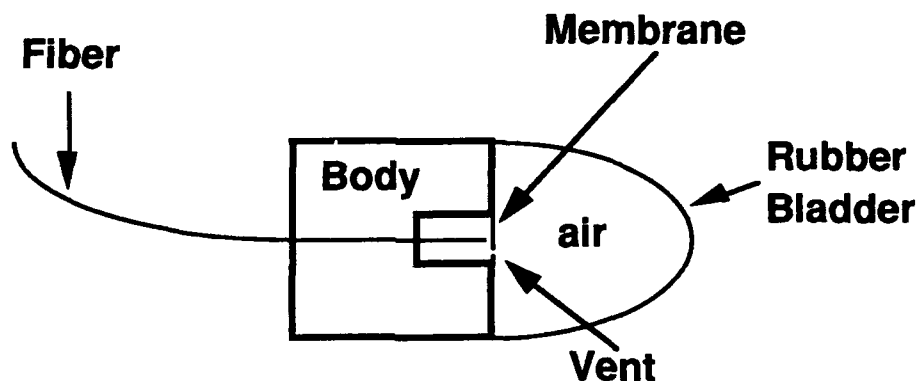


Figure 1 Internal details of hydrophone

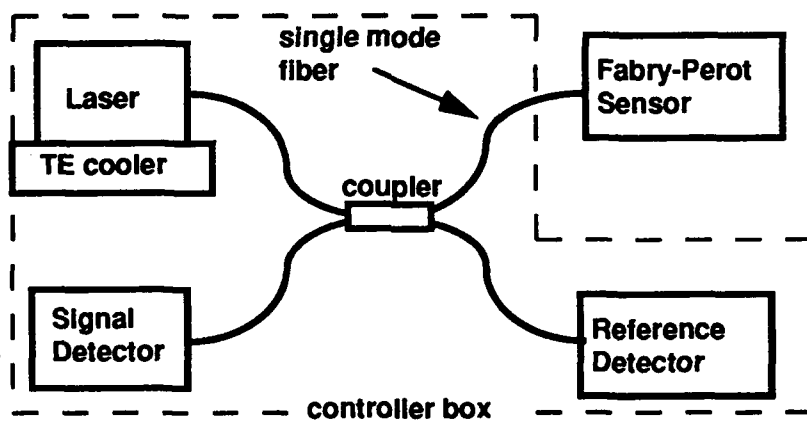
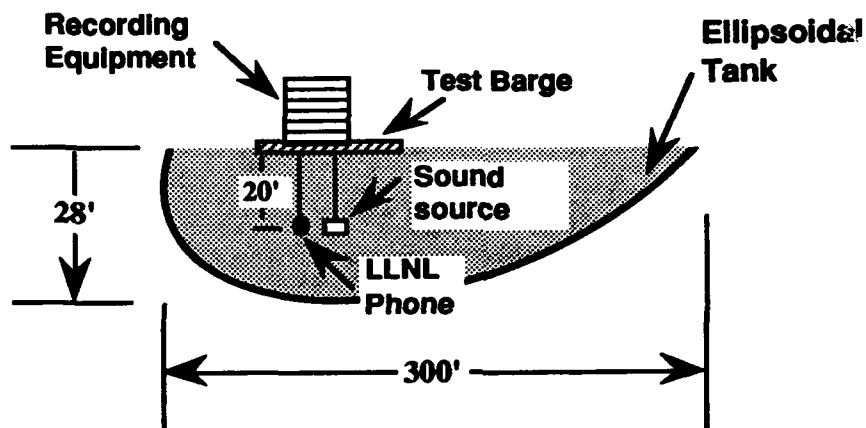


Figure 2 Details of hydrophone controller box



# Underwater Experiments at TRANSDEC/NOSC

(Conducted on January 29, 1991)



**Figure 3** Experimental setup at Naval Ocean Systems Center

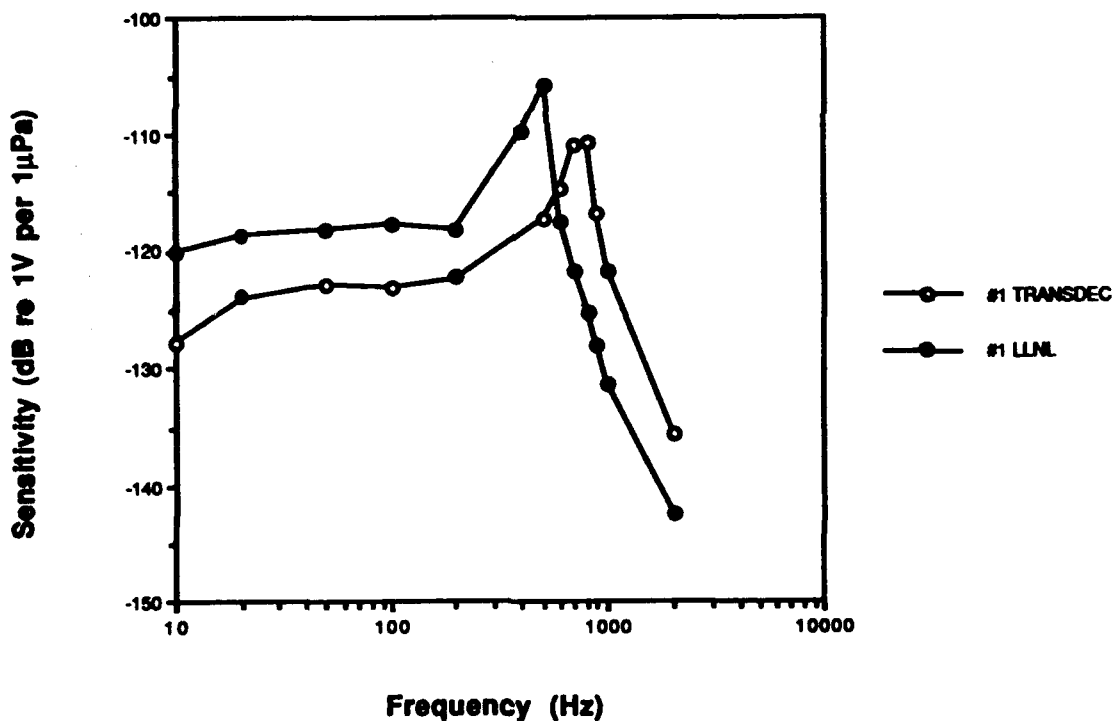


**Figure 4** Sensitivity of LLNL Fiber Optic Hydrophone #1  
Data from TRANSDEC pool (1/29/91) and from G19  
calibrator at LLNL (2/14/91)

## **F1.6 An Interferometer Incorporating Active Optical Feedback From A Diode Laser With Application To Vibrational Measurement**

**W.M.Wang, W.J.O.Boyle, K.T.V.Grattan and A.W.Palmer**

Measurement and Instrumentation Centre,  
Department of Electrical, Electronic and  
Information Engineering, City University,  
Northampton Square, London EC1V 0HB, England.

### **I. Introduction**

Optical self-mixing effects or backscattered intensity modulation in different lasers have been considerably exploited for various applications, such as Laser Doppler Velocimetry(LDV)[1-4], coherent ranging[5-6] and acoustic sensing[7]. The modulation mechanism inside a laser cavity caused by external optical feedback, however, is not well understood, which confines its applications to limited areas. A theory of the external optical feedback in a single-mode semiconductor laser has been developed and proposed by the authors, indicating that the intensity modulation by the external feedback results from the spectral linewidth variation of the laser used, which is due to a "phase interference" between the light from an external reflector and the light from one of the laser mirror facets. This study explains the various phenomena observed in our experiments.

In this work, a self-mixing interferometer incorporating a diode laser is proposed based on the effect of "self-mixing interference", where a portion of emitted light from the laser is reflected back into the laser cavity from a reflecting surface, and the resulting intensity modulation may be extracted to determine the parameter to be measured which is causing the phase change in the interferometer. A simple arrangement with different length multi-mode optical fibres is used for coherent ranging and vibration measurement. The experiments performed have demonstrated that self-mixing coherent ranging is not dependent on the

coherence length of the laser used, which provides the possibility of using coherent detection methods for range finding for much longer distances. In addition, for small vibrational measurements, the self-mixing interference method shows that the directional information of the vibration can be discriminated from the asymmetric nature of the resulting intensity output signal.

### **II. Self-mixing interferometer**

The experiments reported were carried out with a 780 nm VSIS-type AlGaAs diode laser(Sharp LT022MC) and different lengths of multi-mode optical fibres, all with a core diameter of 50  $\mu\text{m}$ , as shown in Figure 1. The light from the laser was collimated by a lens,  $L_1$ , and then focused by another lens,  $L_2$ , into a multi-mode fibre. This light travelled through the fibre and was reflected by an external mirror  $M$ . The reflected light was guided by the same fibre and re-entered the laser cavity, where the light from the laser front facet and from the target mirror,  $M$ , was mixed coherently inside the cavity, and the resultant laser intensity modulation was detected by a photodetector accommodated at the rear facet inside laser package. When the mirror  $M$  was vibrated periodically, an intensity modulation was observed from the laser photodiode, PD, which is very similar to conventional optical interference and termed "self-mixing interference". The light inside the laser cavity and the light from the mirror  $M$  constitutes two interfering beams of the self-mixing interferometer with self-aligning and self-detecting features and only one optical axis.

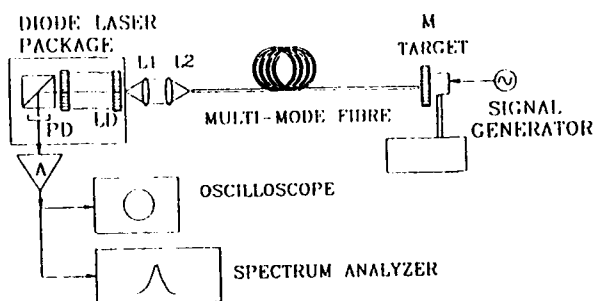


Fig.1 Experimental arrangement for self-mixing interferometer

A typical self-mixing interference signal is shown in Figure 2(upper trace) with a comparison to that of a Michelson interferometer(lower trace). The interference shows a  $2\pi$  periodicity, with respect to the phase change at the external mirror M, which is equal to a half of the wavelength of the laser. However, the upper signal shows two significant differences with that of the Michelson

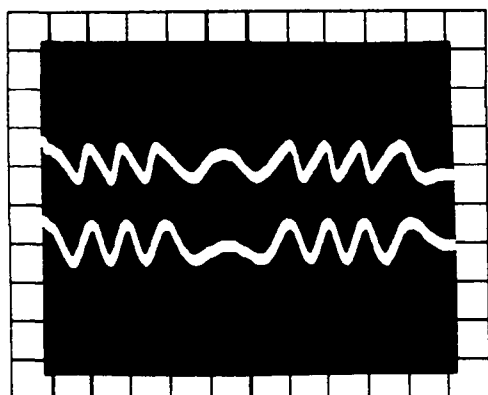


Fig.2 Self-mixing interference(upper trace) with comparison to conventional interference(lower trace).  
Time axis-0.2 ms/Div, Intensity-arb. units.

interferometer. First, it is sawtoothlike but not sinusoidal, and secondly it is asymmetric relative to the external vibrational direction, from which it is important to note that the inclination of the signal is dependent on the direction of the "target" movement, and when the target changes its movement direction, the signal changes its inclination. It is from such an asymmetry that the vibrational direction can be discriminated, which

shows a major advantage over conventional interferometric methods[8]. In experiments with different length optical fibres it was found that the interference pattern is not dependent on the coherence length of the laser used. These differences present some interesting features which could be utilised in various applications as discussed.

### III. Self-mixing coherent ranging

The intensity modulation in self-mixing interference, with weak external optical feedback, may be expressed approximately as:

$$I = I_0 [1 + m(\xi, \chi) \cos(2\pi \frac{1}{\lambda_0} \Delta L + \phi_0)] \quad (1)$$

where  $m(\xi, \chi)$  is defined as the modulation coefficient which is determined by the linewidth factor  $\chi$  of the source laser and the feedback factor  $\xi$  (the ratio of the external amplitude reflectivity to the laser facet reflectivity).  $\lambda_0$  is the central wavelength of the laser,  $\Delta L$  is the optical path difference(OPD) between the laser and the target, and  $\phi_0$  an initial phase condition. When a direct current modulation is applied to the diode laser, the resultant intensity modulation will include an FM modulation and an AM modulation[9]. If the amplitude and the frequency of the current modulation are very small, a beat frequency  $F_b$ , produced by the coherent mixing, can be easily observed and is given by:

$$F_b = (2\beta/\lambda_0^2)(dJ/dt)D \quad (2)$$

where  $\beta$  is the wavelength modulation coefficient (nm/mA),  $dJ/dt$  is the rate of the current change with time, and  $D$  is the target distance from the laser. If  $dJ/dt$  remains a constant, a fixed beat frequency  $F_b$  can be detected from the laser intensity modulation, and the distance  $D$ , then, can be calculated directly from Equation(2).

In the work herein, the laser was dc-biased, with an output power of 3 mW, and current-modulated by a triangular wave at 500 Hz with a peak-to-peak modulation current of 0.1 mA. The small current modulation provides two advantages, which are: (1) the feedback from the near end of the fibre is insufficient to produce a significant beat frequency due to the short OPD; and(2) the mode hopping produced by a large current modulation can be avoided. By substituting the experimental data

above, the required target distance may be expressed as:

$$D = 0.69 F_b \quad (3)$$

where  $\beta$  is given to be  $5.6 \times 10^{-3}$  nm/mA, and  $\lambda_0$  is 780 nm.

The intensity modulation of the laser was ac-coupled via an amplifier A(Figure 1) to an oscilloscope for waveform analysis and to a spectrum analyser for frequency measurement. Figure 3 shows the observed waveform in the experiment performed with a long multi-mode fibre of 3.48 m, where the upper trace was produced due to reflection from the far end of fibre without the mirror M, whilst the lower waveform was produced incorporating the reflection from the mirror M. It is clear that the two signals have the same beat frequency but different amplitudes of this higher frequency, which is due to the different reflectivities of the fibre end and the mirror. In the experiments carried out, three

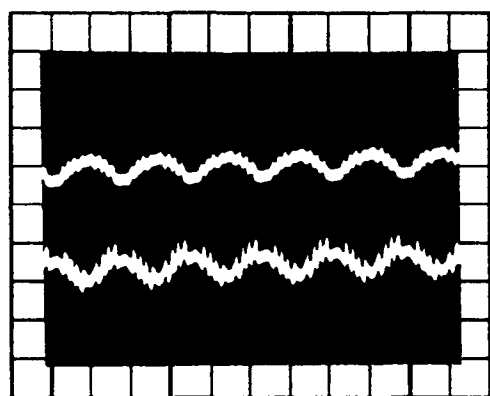


Fig.3 Waveform observed with 3.48 m multi-mode fibre, (a) reflection from fibre end(upper trace)  
(b) reflection from an external mirror(lower trace)  
Time axis-1.0 ms/Div, Intensity-arb. units

different length multi-mode optical fibres were used. Table 1 gives the measured fibre length,  $L_o$ , the calculated distance,  $D_o$ , using Equation(3), and the corresponding beat frequency,  $F_b$ . It is evident that the measured results are in good agreement with the theoretical calculations.

#### IV. Vibrational Measurement

To measure the nature of the vibration of an object under consideration, two factors must be determined, these being the amplitude and the

Table 1			
$F_b(\text{kHz})$	2.0	5.0	15.0
$L_o(\text{m})$	1.51	3.48	10.10
$D_o(\text{m})$	1.38	3.45	10.35

frequency of such a vibration. The amplitude can be determined by counting the fringe number of the interference in one direction. A linear relationship between the fringe number,  $N$ , and the vibrating amplitude,  $A$ , was obtained, as depicted in Figure 4. Thus the amplitude may be expressed as:

$$A = N \lambda_0 \quad (4)$$

where  $\lambda_0$  is the central wavelength of the laser used.

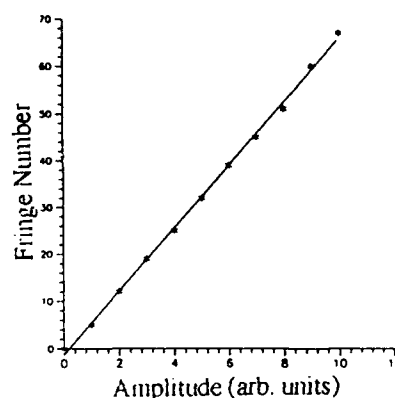


Fig.4 Fringe number dependence on vibration amplitude

Figure 5 shows the self-mixing interference for the vibration measurement, from which it can be seen

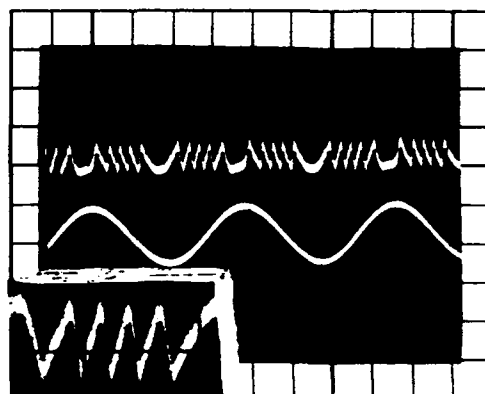


Fig.5 Self-mixing interference(upper trace) dependence on amplitude and frequency of vibration(lower trace)  
Time axis-0.1 ms/Div, intensity-arb. units

that the interference signal changes its inclination as the target changes its direction, which implies that the period can be determined by measuring the time of one directional change of the target. If the vibration is symmetrical, the vibration frequency may be given by:

$$f=1/2\tau \quad (5)$$

where  $\tau$  is the time for one direction change.

## V. Discussion

In the present study, a "self-mixing interferometer" incorporating a semiconductor laser is described and preliminary experimental results presented, which show some significant comparative advantages over the use of a conventional interferometer.

For coherent ranging, the laser diode used displayed a multi-mode nature with a low output power, the coherence characteristics of which were measured using a two beam Michelson interferometer at an output of 3 mW, as shown in Figure 6. In summary these features are: (1) the full width at half

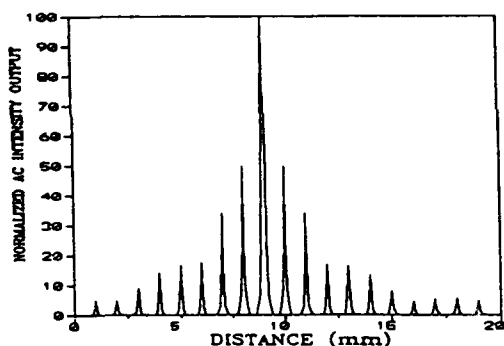


Fig.6 Visibility function of laser used for ranging experiments obtained from a two beam Michelson interferometer

maximum(FWHM) of each coherent region was 0.11 mm; (2) the separation between the adjacent coherent regions was 1.05 mm; (3) the FWHM of the envelope of all the coherent regions was 3.07 mm and the interference was not detectable when the OPD was greater than 11.65 mm. These data show that this type of laser cannot be used in a conventional coherent ranging system where the distance to be measured is greater than 11.65 mm. However, in a self-mixing ranging scheme, the measurable distance could reach as far as a distance

of 10 m, with the use of suitable circuitry. This represents a considerable improvement, using a cheap and readily available laser source.

For a vibration measurement, the self-mixing method combines simplicity of operation with the ability discriminating the vibration direction, as demonstrated.

## VI. Acknowledgements

The authors are pleased to acknowledge the support from SERC for this work, and WMW is pleased to acknowledge support from the British Council by way of a studentship.

## VII. References

- [1]. M. J. Rudd "A laser Doppler velocimeter employing the laser as a mixer-oscillator" *J. Phys.* **E1**, pp.723-726, 1968
- [2]. J. H. Churnside "Laser Doppler velocimetry by modulating a CO<sub>2</sub> laser with backscattered light" *Appl. Opt.* **23**, pp.61-65, 1984
- [3]. S. Shinohara, A. Mochizuki, H. Yoshida and M. Sumi "Laser Doppler velocimeter using the self-mixing effect of a semiconductor laser diode" *Appl. Opt.* **25**, pp.1417-1419, 1986
- [4]. H. W. Jentink, F. F. M. de Mul, H. E. Suichies, J. G. Aarnoudse and J. Greve "Small laser Doppler velocimeter based on the self-mixing effect in a diode Laser" *Appl. Opt.* **27**, pp.379-385, 1988
- [5]. P. J. de Groot, G. M. Gallatin and S. H. Macomber "Ranging and velocimetry signal generation in a backscatter-modulated laser diode" *Appl. Opt.* **27**, pp.4475-4480, 1988
- [6]. G. Beheim and K. Fritsch "Range finding using frequency-modulated laser diode" *Appl. Opt.* **25**, pp.1439-1441, 1986
- [7]. A. Dandrige, R. O. Miles and T. G. Giallorenzi "Diode laser sensor" *Electron. Lett.* **16**, pp.948-949, 1980
- [8]. E. T. Shimizu "Directional discrimination in the self-mixing type laser Doppler velocimeter" *Appl. Opt.* **26**, pp.4541-4544, 1987
- [9]. M. Imai and K. Kawakita "Measurement of direct frequency modulation characteristics of laser diode by Michelson interferometry" *Appl. Opt.* **29**, pp.348-353, 1990

## **F1.7 Interfero-Polarimetric Fiber Optic Sensor For Both Pressure And Temperature Measurement**

**M.TURPIN, M.BREVIGNON, J.P.LE PESANT (1)  
O.GAODITZ (2)**

- (1) Thomson-CSF LCR Domaine de Corbeville 91404 ORSAY Cedex FRANCE**
- (2) SEXTANT Avionique DIB Z.A. Les Boutries BP 207 78703 CONFLANS STE HONORINE Cedex FRANCE**

### **ABSTRACT**

A compact pressure sensor head with fiber optic temperature compensation has been built and tested which uses specific side-hole and "bow-tie" fibers respectively devoted to pressure and temperature measurements. The addressing scheme is based on the broad band interferometry technique. We describe the sensor arrangement and present the response curves for pressure and temperature in the ranges 0.1 to 1 MPa and 0 to 40 °C.

### **SUMMARY**

#### **Introduction**

The sensor concept is based on the interfero-polarimetric concept and uses the fundamental properties of the low coherence addressing and reading technique. In such a method, both eigen modes of a birefringent fiber are excited and the resulting differential light propagation induces a phase delay. The value of the phase delay is related to the variation of the measurand and can be measured by using an interferometric device. This method has been studied for several years and various authors have proposed sensors and multiplexed sensor networks (1,4).

For temperature measurements, the now well known high birefringent fibers are suitable devices because the internal stress (which causes the birefringence) of such fibers is directly related to the temperature gradient during the drawing of the fiber. Generally "bow-tie" and "panda" fibers are used in such a way, providing a temperature sensitivity reaching a typical value of about 6 rad/°C.m. Because of the silica elasticity properties this type of intrinsic sensor has a potentially good enough reliability in a restricted operating range due to the presence of a polymer coating. The typical practical range is limited to 40°C when classical epoxy-acrylate coatings are used. Extended ranges are investigated with other coatings (polyimide for example).

In comparison to that temperature sensitivity, the hydrostatic pressure sensitivity of such fibers is not very attractive and limited to a typical value of about 10 rad/MPa.m. In order to make an intrinsic fiber optic pressure sensor the concept of side-hole fiber has been proposed and some preliminary results have been published (5,6). In such a fiber, two holes are present on each side of the core of the fiber, and consequently an external isotropic pressure is transformed into an anisotropic stress in the core region. By this way intrinsic optical fiber

pressure sensors having a pressure sensitivity in the range of 30 to 120 rad/MPa.m have been obtained, depending on the fiber-diameter to hole-size ratio.

Unfortunately the temperature dependance of such a pressure sensor is non-zero and the typical sensitivity is in the range of 1 to 3 rad/°C.m. Obviously this temperature dependance has to be considered as a spurious effect and a practical solution for a temperature compensation (or control) is required for any operational sensor.

Taking into account this fact, we have developed a splicing technique to allow the fabrication of a sensor arrangement based on the association of both types of fibers, spliced together, in such a way that pressure and temperature can be simultaneously measured.

### **Addressing scheme and sensor arrangement**

The addressing scheme takes advantage of the properties of a low coherence light source providing interference fringe patterns which act as sensor signatures after the phase delays induced by each sensing part of the sensor are compensated by a remote interferometer. If coherence laws are respected, the relevant signatures are uncorrelated and the variations of the mesurands (i.e. pressure and temperature) can be deduced without any ambiguity.

The sensor is composed of a first length of side-hole fiber "FASE: Fibre A Structure Evidée" mainly devoted to the pressure measurement, spliced with a second length of High birefringent (HiBi) fiber devoted to the temperature control. At each end of these sensitive parts up and down leads are added in order to get a fully remote sensor. Figure n°1 shows the schematic arrangement.

The splices between fibers of different types have been made by using a fusion splice machine and the relative orientation of the fiber axis has been controlled in order to get coupling points of several per cent in energy between the two eigen modes.

A specific housing has been designed in order to get a sensor brassboard compatible with aeronautic requirements in terms of size, weight, standard pressure inlet... This housing is comprising two pressure-tight outlets for up and down leads which will be replaced by tight connectors in a future design.

The standard pressure inlet allows to connect the sensor head to a pressure generator for experiments and calibration. In order to perform experimental investigations a classical temperature probe has been added into the sensor head.

### **Experiment and results**

Figure n°2 shows the experimental set up. The light emitted by an SLD is polarized and launched in one of the eigen modes of the up lead HiBi fiber. A first fused splice acts a coupling point to split the light in the two polarization modes of the side-hole fiber yielding the polarimetric operation of the pressure sensor. A second splice is made between the side-hole fiber and the Hi Bi temperature sensor and a third splice connects the sensor to the down lead. The typical length of optical fibers are as follows:

Up and down leads: 5 meters

Side-hole fiber (pressure sensor): 10 meters

HiBi fiber (temperature sensor): 2 meters

The coil diameter is 40 mm and the sensor housing is typically 50 mm \* 30 mm (Figure n°3).

For decoding and reading, the down lead is connected to a Michelson interferometer used for the optical path delay (i.e. phase delay) compensation.

A pressure generator and an oven are used for pressure and temperature calibrations.

Measurements have been performed in order to verify the pressure sensitivity dependance with respect to temperature variation.

The specific side-hole fiber has a measured pressure sensitivity of about  $S_p = -34$  rad/MPa.m. The intrinsic birefringence value, expressed in terms of beat length, at room temperature and atmospheric pressure is about 10 mm.

Figure n°4 shows the experimental recorded path delay versus the hydrostatic pressure applied onto the sensor coil. For comparison the pressure sensitivity of the HiBi fiber (temperature sensor) is also recorded and equal to 11 rad/MPa.m.

The pressure sensitivity has been studied for different temperatures in the range 0 to 40 °C. The more significant curves reported in figures n°5 and 6 show the good linearity of the pressure response of the sensor for three temperatures (0°C, 21°C and 40 °C), for each temperature the slopes of the curves keep a constant value providing a simple calibration mean. The measured temperature sensitivities for side-hole and HiBi fibers are respectively -0.51 rad/°C.m and -4.9 rad /°C.m.

Because of the constant pressure-temperature cross sensitivity of both fibers, the response of the sensor is obtained by solving a set of two equations:

$$\Phi_1 = -0.51 T - 3.4 P$$

$$\Phi_2 = -4.90 T + 1.1 P$$

Where  $\Phi_1$  and  $\Phi_2$  are the phase delays induces by the side-hole and the HiBi fiber, and T and P are the temperature and the pressure expressed in °C and bars.

A very simple calculation gives the pressure value by elimination of T. Both pressure and temperature can obviously be determined.

## Conclusion

A compact, temperature compensated, polarimetric pressure sensor has been built and preliminary characterisations show the capability of such a sensor to measure an hydrostatic pressure without any drastic effect of the temperature changes which are considered as spurious effects in our application.

The preliminary results which are presented here are only a part of a more comprehensive work devoted to the realization of an experimental complete network of coherence multiplexed sensors developed in the frame of a BRITE/AERONAUTICS European contract ( NIOSCA: New Optical fiber Sensor Concept for Aeronautics). The consortium involved in this research is composed of Thomson-CSF and SEXTANT Avionique (F), SMITHS Industries (UK), INESC (P) and DTH (DK). More detailed informations on the complete network will be discussed at the conference.

## References

- (1) Brooks et al., 1985, J.Lighthwave Technol., 3, 1062-1072.
- (2) Kersey et al., 1986, Electron.Lett.,22(11),616-618.
- (3) Turpin et al., 1988, Proc. Congrès Mesucora, Paris, 116-117.
- (4) Guresmoli et al., 1989, OFS89 Springer Proceed.in Physics,44, 513-518
- (5) Xie et al., 1986, Opt.Lett.,11, 333.
- (6) Charasse et al., 1991, Opt.Lett.16,13,1043-1045.



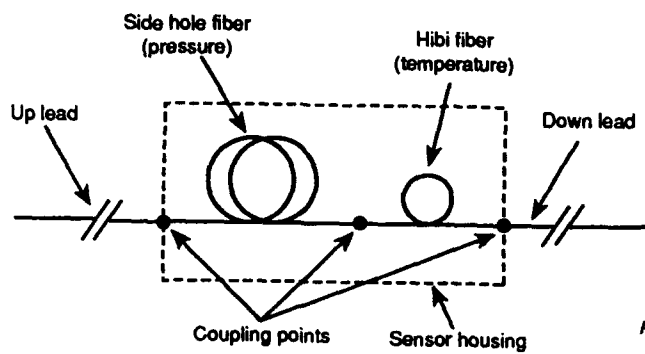


Fig. 1 : Schematic sensor arrangement

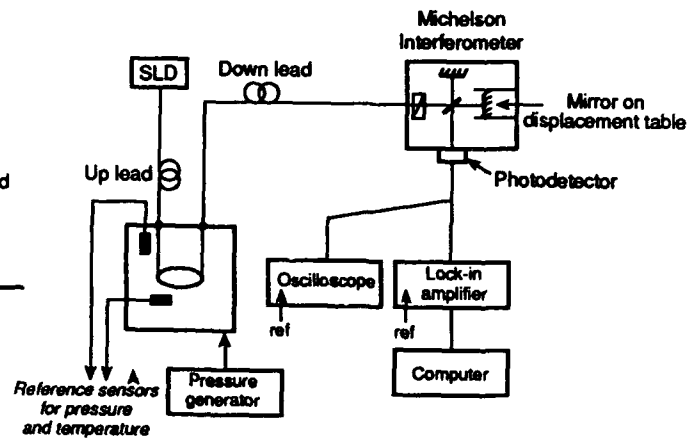


Fig. 2 : Experimental set up

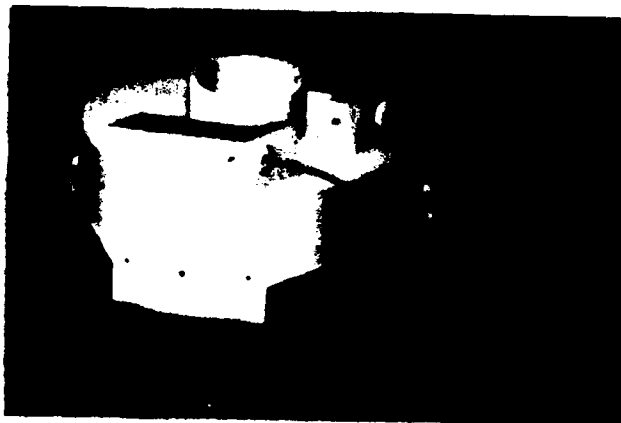


Fig. 3 : Sensor housing

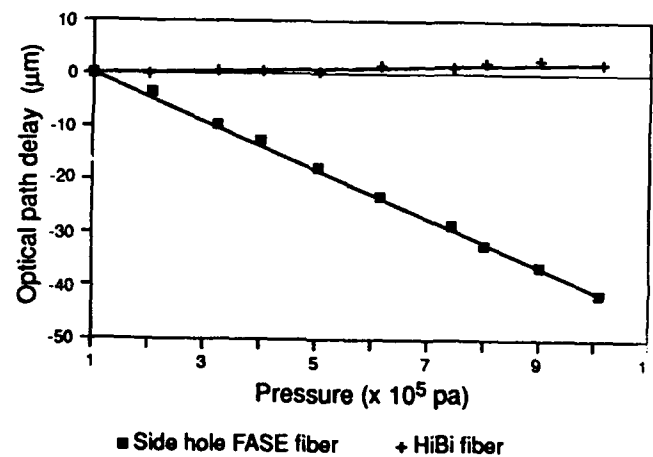


Fig. 4 : Pressure sensitivity

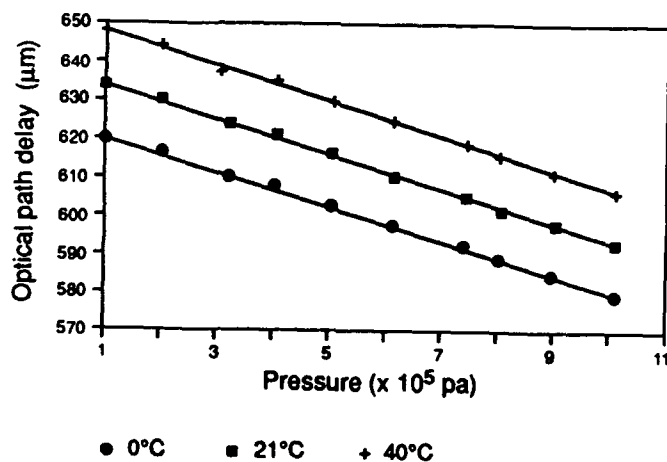


Fig. 5 : Side Hole fiber pressure sensitivity

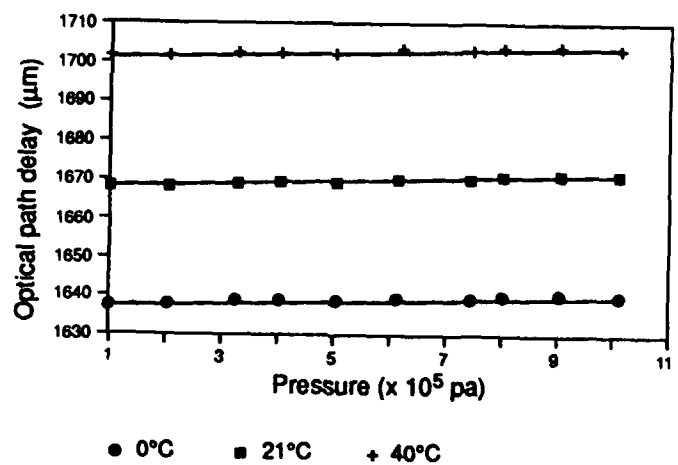


Fig. 6 : HiBi fiber pressure sensitivity

## F2.1

### **(Invited) Fiber Optic Sensing for Smart Materials and Structures**

Raymond M. Measures

University of Toronto Institute for Aerospace Studies  
4925 Dufferin St., Downsview, Ontario, M3H-5T6, Canada  
and

The Ontario Laser and Lightwave Research Centre

#### **Smart Materials and Structures.....The Promise**

The past five years has seen the emergence of a new field of engineering termed "Smart Materials and Structures." This multidisciplinary field will lead to a revolution in engineering principles and a radical change in structures as diverse as: Aircraft and Space Platforms, Marine Vehicles and Installations, Ground Transportation Systems and Terrestrial Structures.

The development of structurally integrated fiber optic sensing systems represents the first step in the evolution of Smart Materials and Structures. Sensing systems of this nature should be capable of undertaking a wide range of measurements. In the case of advanced composite materials it is possible that embedded fiber optic sensors could: monitor the cure state during fabrication then provide "in-service" health monitoring through tracking the internal strain field and undertaking "real-time" damage assessment. This field of engineering could lead to improvements in safety and economics and encourage greater use of composite materials for primary structures. Overdesign might also be avoided which could lead to weight savings, an important factor in Aerospace applications. Smart Adaptive Structures would use the information provided by their built-in sensing system to modify their shape or structural properties. In the 21st Century this could lead to aircraft with nonarticulated wings that change their shape in accordance with the flight conditions and large space structures that constantly adjust their shape and damp out unwanted vibration.

#### **Merits of Fiber Optic Sensors**

Fiber optic sensors should make ideal "nerves" for composite materials as they are: extremely small and light weight, immune to electrical interference, capable of large bandwidth, safe and practically incapable of initiating fires or explosions, and compatible with composites. They can serve both as sensors and conduits for the sensory signals and could integrate into the fly-by-light concept currently under active consideration for the next generation of aircraft. It is expected that the increasing use of optical fibers for communications will help reduce the cost of this technology.

#### **Technical Issues and Critical Developments**

In developing structurally integrated fiber optic strain sensing systems for use with Smart Materials and Structures a number of key issues will have to be addressed. These include:

- localization and spatial resolution,*
- strain resolution,*
- absolute measurement and interrupt immunity,*
- fast response and strain rate limitation,*
- large measurement range,*
- structural integration and sensor architecture,*
- multiplexing and multisensor demodulation,*
- thermal sensitivity and apparent strain,*
- optical/structural interconnections,*
- sensor/host interface and signal interpretation,*
- influence of embedded fiber optic sensing system, and*
- performance life of sensing system.*

This will narrow the choice of fiber optic sensing system suitable for use with Smart Materials and Structures, especially when low cost of fabrication, installation and operation is taken into consideration.

### **Current State of Sensor Development**

A review of the current state of development toward an ideal fiber optic strain sensing system for Smart Materials and Structures will be given. This will include our development of a Fabry-Perot sensor with a core localized internal mirror, work on its fast, high resolution demodulation and tests of its functionality when embedded within composite materials. The intracore fiber optic Bragg grating also has considerable potential to serve as one of the sensors of choice for this emerging field. However, its role has been impeded by the lack of a simple, passive and fast method of determining the wavelength of its narrow backreflected optical signal. We report on the development of a wavelength demodulation system that is inexpensive and easily implemented with a minimum of equipment. We shall also discuss our development of an optical strain rosette and its use within composite materials to evaluate the strain tensor.

### **Potential Sensing Applications**

The range of potential applications possible will be discussed, including the prospects for: *internal strain mapping, structural shape evaluation, vibration identification and structural integrity assessment*. The use of optoacoustics for cure state monitoring of thermoset composites during their fabrication will also be discussed. The economics of implementation would be most favoured if one type of sensor can be used for all of these measurements. We shall discuss the prospects of this achievement.

### **Future Sensing Systems for Smart Materials and Structures**

The nature of the structural interconnect problem hinges on whether the output from the structure is optical or electrical. Current thinking is predicated on optical signals flowing into and out of the structure via an optical interface. In general this interface must have minimal structural perturbation, be easy to fabricate and introduce into the production of the structure. If multiplexing is not used each sensor would have its own output and a ribbon or bundle of optical fibers would have to egress from the structure. This may be the case even with multiplexing since most schemes do not lend themselves to sufficient miniaturization to be embedded or included in the structural interface. Although, structural interconnects can be made to a broad surface or an edge, the former tends to be favored in many cases as edges are often trimmed or used for structural support. The development of a "reliable" and "convenient" structural interconnect is likely to represent one of the most critical steps in the implementation of Smart Structures for in many of the situations where this technology could be of significant benefit interconnection will have to be performed by unskilled personnel, possibly in hostile environments, such as an aircraft in a blizzard on a subzero runway.

The structural interconnect problem would be greatly simplified if a single electrical cable could be used, the interface would then serve as both a structural and electrical/optical interface. This is clearly only practical if a single optoelectronic chip can be developed that would generate the light signals used to interrogate the array of fiber optic sensors integrated into the structure and to convert the subsequent optical sensing signals back into electrical signals.

We shall show that the development of a Bragg grating based laser sensor may lend itself to sufficient miniaturization to consider the prospect of a structurally integrated optical/electrical interface. This approach might eventually lead to an optoelectronic chip that could process many fiber optic sensors, yet be small enough to be integrated within the structural interface and thereby offer the prospect of addressing simultaneously the: interconnect, multisensor demodulation, and multiplexing issues.

## F2.2

### Fiber Optic Fabry-Perot Sensors Embedded in Metal and in a Composite

C. E. Lee, W. N. Gibler, R. A. Atkins, J. J. Alcoz, H. F. Taylor  
Department of Electrical Engineering, Texas A&M University  
College Station, Texas 77843

K. S. Kim  
Department of Aeronautics and Astronautics  
Stanford University  
Stanford, California 94305

In recent years a strong interest has developed in embedded fiber optic sensors for the monitoring of strain, temperature, and other parameters in structural materials [1]. The fiber Fabry-Perot interferometer (FFPI) using internal mirrors [2-4] is a strong candidate for this application because it provides localized ("point") sensing capability and high sensitivity, and is amenable to time-division multiplexing. Here, new results on the embedding of FFPIs in metals and composites are reported.

Previously, metals in which fibers have been successfully embedded have had relatively low ( $< 200^{\circ}\text{C}$ ) melting temperatures [5]. In some early experiments in our laboratory on the casting of metal parts in aluminum (melting temperature =  $660^{\circ}\text{C}$ ), the fibers invariably broke at or near the air-metal interface upon cooling to room temperature. Here, a simple solution to this problem is described and the first results on fiber sensors embedded in aluminum are reported.

Dielectric mirrors for the FFPIs are formed in single mode Corning fiber by a fusion splicing technique described in detail elsewhere [3]. To embed the FFPI sensor, a graphite mold is machined to the desired shape. Stainless steel tubes (1.6 mm OD / 0.5 mm ID) are then positioned to extend about 1 cm into the mold at the bottom and top. The buffer on the fiber containing the interferometer is stripped back so that the total length of bare fiber in the direction of its axis is about 3 cm greater than the dimension of the part. The fiber is then positioned in the mold, passing through both of the tubes, with the interferometer located near the center. A tensile load of about 20 grams is applied to the fiber. The aluminum is heated in air in a crucible with an oxygen/acetylene torch and poured into the mold, as in Fig. 1. After the metal has cooled to near ambient temperature, the mold is removed. Several samples of various geometries containing embedded FFPIs have been produced without breaking the fiber. It is believed that passing the fiber through a tube to enter the metal greatly reduces the stress discontinuity at the air-metal interface, which otherwise causes the fiber to break. Data presented here are for a 1.0 cm long FFPI embedded in a 4 cm x 4 cm x 0.5 cm aluminum block.

The transmittance  $T$  and reflectance  $R$  of the embedded interferometers are evaluated using a single mode  $1.3\text{ }\mu\text{m}$  DFB laser with a Faraday isolator in series to suppress feedback, as in Fig. 2. In initial measurements on the embedded sensor near room temperature, the excess loss ( $= 1 - R - T$ ) was nearly independent of temperature at 10% (0.45 dB), as compared with 8% (0.36 dB) prior to embedding. Upon temperature cycling from room temperature to  $250^{\circ}\text{C}$  the excess loss was found to increase slightly, stabilizing at 13% (0.60 dB) after five

such cycles.

The interferometer round-trip phase shift  $\phi$  was close to a linear function of temperature over the range  $20^{\circ}\text{C}$  to  $300^{\circ}\text{C}$  for the metal-embedded sensor, with  $d\phi/dT = 2.4 \times 10^{-5}/^{\circ}\text{K}$ . This is a factor of 2.9 greater than the experimental value  $8.3 \times 10^{-6}/^{\circ}\text{K}$  for the same sensor in air. The difference is attributed primarily to the length change in the fiber due to the large thermal expansion coefficient of the aluminum ( $2.5 \times 10^{-5}/^{\circ}\text{K}$ , vs.  $5.5 \times 10^{-7}/^{\circ}\text{K}$  for fused silica).

The embedded FFPI has also been used to detect ultrasonic waves generated by a PZT transducer positioned on the surface of the aluminum directly above the sensor. A response was observed over the frequency range from 0.1 to 8.0 MHz. The maximum experimentally determined value for the phase modulation index was 1.45 rad at a frequency of 1.85 MHz. This indicates a much stronger response than in a previous experiment using a similar FFPI embedded in a graphite-epoxy composite, where the largest observed phase modulation index was 0.5 rad [6].

In another experiment, a FFPI and a thermocouple were positioned between the second and third layers of a 16-layer graphite/PEEK coupon. The coupon was then cured in a hot press using standard temperature and pressure profiles. Fig. 3 shows the dependence of round-trip optical phase shift in the interferometer on temperature (determined using the embedded thermocouple) during the curing process under a constant pressure of 250 PSI. An abrupt change in the slope of the curve is observed at around  $700^{\circ}\text{F}$  for heating and  $600^{\circ}\text{F}$  for cooling. This phenomenon is thought to be associated with the strain which results from decrystallization (for heating) or crystallization (for cooling) of the polymer in the coupon. This information is important in optimizing the curing process [7], since the crystallization or decrystallization temperature can be adjusted by changing the temperature and pressure profiles.

Another application for the fiber sensor is in strain monitoring [8]. For strain measurements, two electric strain gauges (ESGs) were bonded to opposite sides of the completed coupon, above and below the embedded FFPI. A strain was induced by applying a load to the center of the coupon, which was supported at opposite ends. The strain sensitivity of the FFPI, determined by comparing the optical phase shift with the ESG readings, was  $9.1 \times 10^6$  rad/m, about 14% greater than was measured for the same fiber in air.

Strain measurements were also made at elevated temperatures. Both the fiber optic and ESG sensors showed good linearity at  $200^{\circ}\text{F}$ . However, as indicated by the data of Fig. 4(a), the ESG response was unstable at  $300^{\circ}\text{F}$ . By contrast, the data of Fig. 4(b) shows the same linear load profiles at  $200^{\circ}\text{F}$  and  $300^{\circ}\text{F}$  for the FFPI sensor.

In conclusion, fiber optic Fabry-Perot interferometers embedded in cast aluminum parts have been used for sensing temperature and ultrasonic pressure. These are the first results on fiber sensors embedded in a metal widely used for structural purposes. Breakage of the fibers at the air-metal interface during the casting process is avoided through the use of stainless steel stress-relief tubes. A FFPI sensor was also used to monitor the curing of a graphite/PEEK composite coupon. Changes in the slope of the plot of interferometer phase shift vs. temperature were taken as evidence of phase transitions in the polymer matrix. Such data can be useful in

optimizing the composite fabrication process. Experiments on the finished composite sample indicate that an embedded fiber sensor can be used to measure strain over a much greater temperature range than conventional strain gauges.

This work was supported in part by DARPA through a subcontract with McDonnell Douglas Aircraft Company.

#### REFERENCES

1. E. Udd, "Fiber Optic Smart Structures," in *Fiber Optic Sensors*, E. Udd, ed. (Wiley, New York, 1991).
2. C. E. Lee and H. F. Taylor, *Electron. Lett.* 24, 193 (1988).
3. C. E. Lee, R. A. Atkins, and H. F. Taylor, *Opt. Lett.* 13, 1038 (1988).
4. T. Valis, D. Hogg, and R. M. Measures, *IEEE Photon. Technol. Lett.* 2, 227 (1990).
5. J. J. Kidwell and J. W. Berthold, *Proc. SPIE* 1367, 192 (1990).
6. J. J. Alcoz, C. E. Lee, and H. F. Taylor, *IEEE Trans. Ultrason., Ferroelec., Freq. Contr.* UFFC-37, 302 (1990).
7. P. R. Ciriscioli and G. S. Springer, *Autoclave Curing of Composites* (Technomic, Lancaster, PA, 1990).
8. T. Valis, D. Hogg, and R. M. Measures, *Proc. SPIE* 1370, 154 (1990).

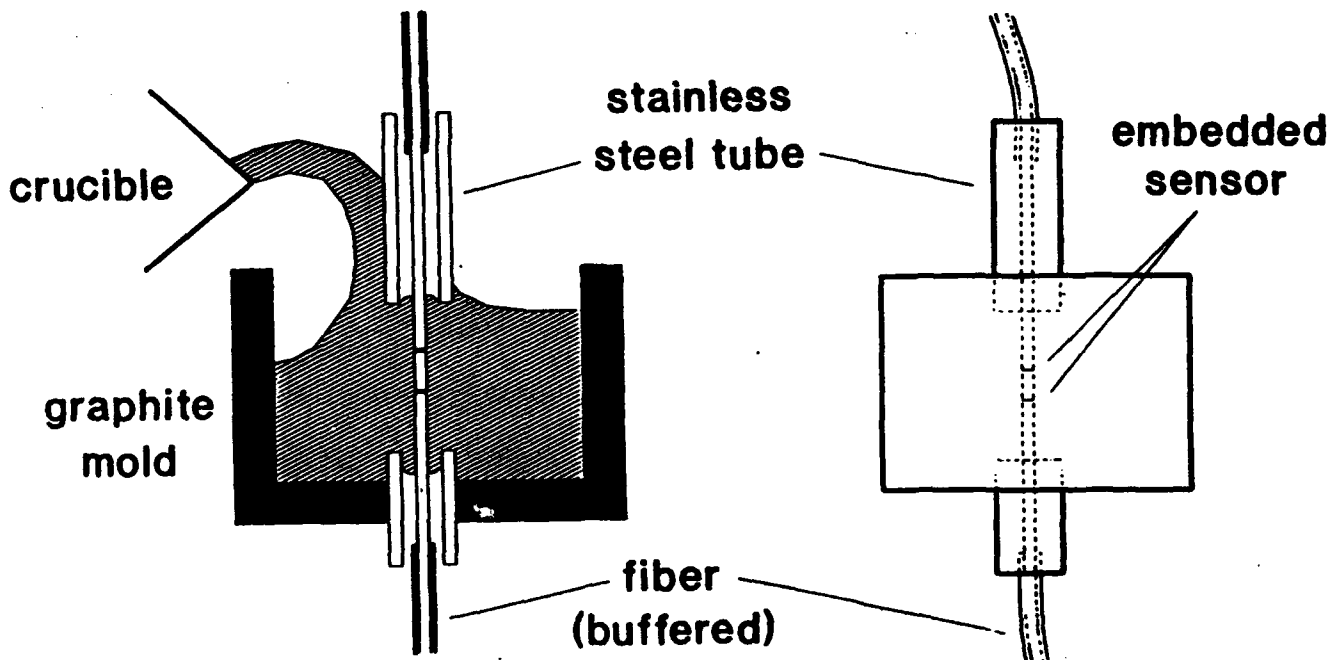


Fig. 1. Arrangement for casting metal part, and finished part with embedded fiber sensor.

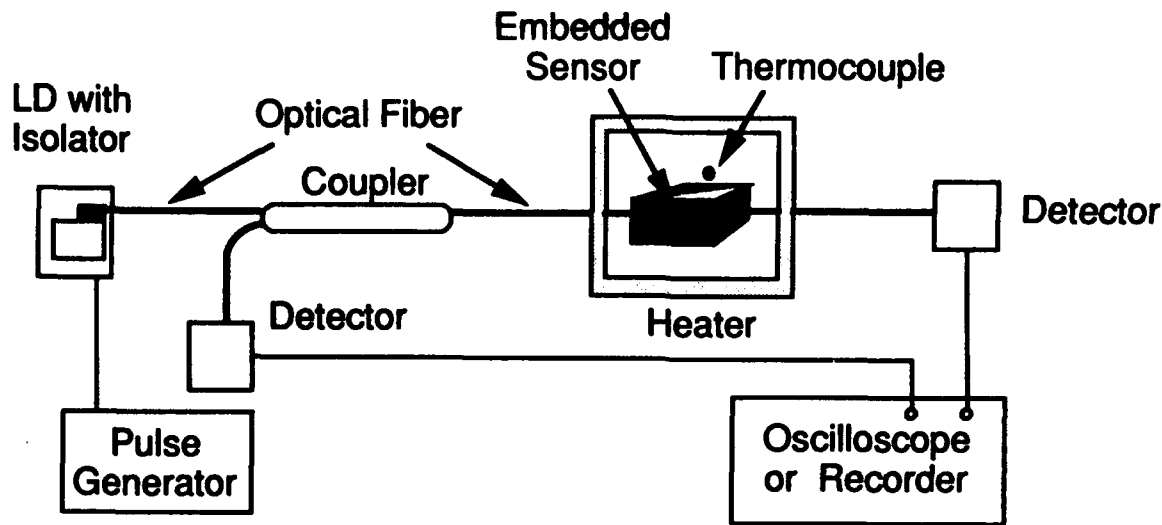


Fig. 2. Experimental setup for testing embedded sensor.

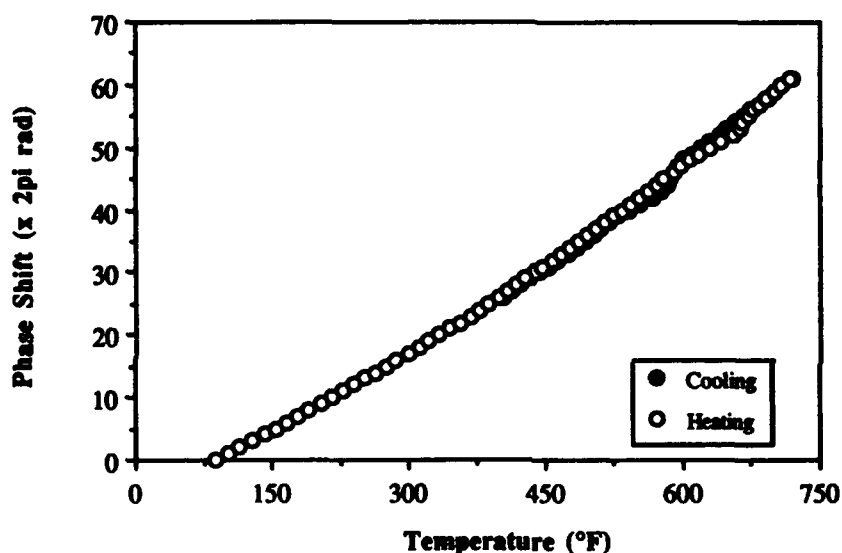


Fig. 3. Dependence of interferometer phase shift  $\phi$  on temperature during the curing process. Open and closed circles represent heating and cooling, respectively.

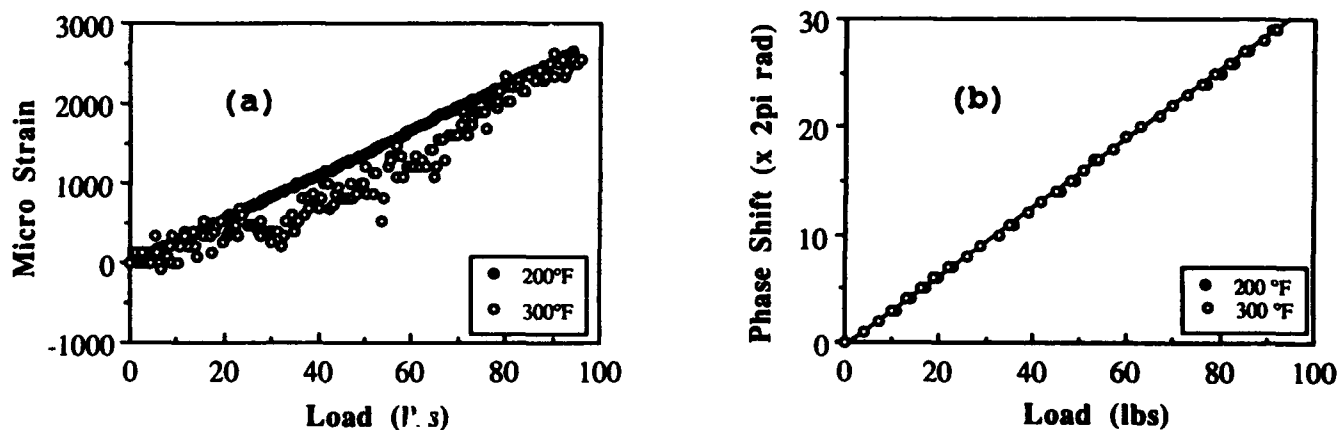


Fig. 4. Response of (a) ESG and (b) fiber sensor at 200°F and 300°F.

## F2.3      **Passive Interrogation Of A Lead-insensitive Two-Mode Elliptical Core Fiber Strain Sensor**

T. A. Berkoff\* and A. D. Kersey

Naval Research Laboratory, Optical Sciences Division, Code 6574,  
Washington, D.C. 20375 USA

\*Permanent address: SFA, Inc. 1401 McCormick Drive,  
Landover, MD 20785, USA

We report on a two-mode elliptical core fiber strain sensor system with a passive phase interrogation technique based on frequency modulation of the laser source. We demonstrate DC phase tracking capability and high resolution detectability of AC signals. A reflectometric configuration is also discussed.

**Introduction:** Few mode fiber sensors represent one of the earliest type of interferometric fiber devices proposed and tested [1]. Early work on these sensors utilized circular core fibers, however, more recently, significant attention has been directed towards the use of two-mode interferometry using elliptical core (e-core) fiber since the output interference orientation is spatially defined and stable [2]. Due to the 'single-fiber' nature of the configuration, these sensors have been widely proposed as suitable sensing elements for strain and vibration measurement in smart materials and structures [2,3]. However, the demonstration of passive remote, i.e. lead insensitive, interrogation schemes is necessary for practical applications of smart materials and structures to be further realized. Some methods have been described to recover phase shift information without signal fading by the generation of quadrature phase shift signals from the two-mode sensor output [4,5]. Several laser-frequency-modulation based interrogation techniques have been developed for single-mode interferometry [6,7] as well as for polarimetric devices [8] for the passive phase detection of signals, but few, if any, such techniques have been reported using two-mode e-core sensor systems. In the following, we demonstrate the use of such schemes with a two-mode e-core fiber sensor in a 'single fiber' configuration to measure strain. Furthermore, we demonstrate the potential of these methods in an experimental smart skin application where strain induced by 3-point bending and low-level vibrational excitation of a panel is recorded using this approach. A reflectometric version of the e-core sensor is also described, which has further advantages in terms of its suitability for embedded sensor applications due to the common input/output fiber used, which eases requirements for fiber ingress/egress in composite materials.

**Principle of Operation:** Light from a laser diode source is coupled to e-core fiber via a single mode fiber that serves as the sensor input lead as shown in Figure 1. The e-core fiber parameters allow for the propagation of the fundamental  $LP_{01}$  and the  $LP_{11}$  even modes, which results in an interferometric two-lobe intensity pattern at the output of the fiber. The optical power oscillates between the two lobes with phase changes between the two modes. By splicing to circular core single-mode fiber, the interference pattern can be spatially filtered to isolate the fringe intensity variation of a single lobe by misaligning the two different fibers [2]. The output intensity of the single-mode fiber then oscillates cosinusoidally with sensor phase shift. For a certain e-core fiber parameters, a suitable delay between the two modes can be achieved such that for a frequency change of the laser output  $\Delta\nu$ , there is a change in phase  $\Delta\phi = 2\pi k(\beta_{01} - \beta_{11}) \cdot \Delta\nu$  where the coefficient  $k(\beta_{01} - \beta_{11})$  is dependent on the difference in the propagation constants  $\beta_{01}$  and  $\beta_{11}$  of the  $LP_{01}$  and  $LP_{11}$  even modes respectively, which are determined by the e-core fiber parameters and source wavelength. The phase dependence on laser frequency allows for the application of many different FM methods of interrogation/demodulation including synthetic heterodyne [6] and phase generated carrier techniques [7] more commonly used with single-mode fiber interferometry. By frequency modulation of the laser source the photodetected intensity is of the form

$$I = 1 + V \cos(\phi_0 + \Delta\phi \sin\omega t)$$

where  $V$  is the fringe visibility and  $\phi_0$  is the static phase term of the interferometer. This phase modulated output contains a series of even and odd harmonics of  $\omega$  that vary as cosine and sine



respectively of the phase term  $\phi_0$ . By synchronous detection at the first and second harmonics of  $\omega$ , the following quadrature phase signals can be obtained  $S_1 = J_1(\Delta\phi)\sin\phi_0$  and  $S_2 = J_2(\Delta\phi)\cos\phi_0$  where  $J_1(\Delta\phi)$  and  $J_2(\Delta\phi)$  are Bessel functions. These two signals can be balanced by adjusting the depth of FM modulation to  $\Delta\phi = 2.6$  radians where  $J_1(\Delta\phi)$  is equal in magnitude to the  $J_2(\Delta\phi)$  Bessel function. With these quadrature phase signals available, a linear output corresponding to fiber strain can be readily obtained either by differentiate and cross multiply [7], directional sine/cosine fringe counting, or other [9] phase tracking schemes.

**Experimental Results:** Demonstration of phase-generated carrier demodulation with a two-mode fiber sensor was implemented using the configuration shown in Figure 1. Light from a 0.83  $\mu\text{m}$  laser diode source was coupled to single mode fiber which guides the light to the illuminate the sensing fiber consisting 10 meters of elliptical core fiber. This length of fiber was wound on a piezoelectric transducer so that test strain could be applied to the sensor. The output of the e-core fiber was spatially filtered using a single mode fiber in an offset splice to produce an interferometric signal at the detector. Figure 2 shows an example of the photodetected signal when sinusoidal modulation is applied to the laser diode supply current. To obtain sine/cosine quadrature phase signals a high frequency carrier of 40 kHz was used which was then synchronously detected at the photodetector output. Figure 3 shows the resultant x-y display for the phase quadrature output signals when a 50 Hz frequency  $2\pi$  radian test signal is applied the piezoelectric cylinder which clearly demonstrates the excellent phase quadrature relationship that can be obtained. Phase shift responsivity to fiber strain was determined by monitoring a phase carrier signal while applying voltage to the piezoelectric transducer. From this measurement, the strain responsivity of the fiber (fiber elongation for a  $2\pi$  phase shift) was calculated to be  $\sim 120 \mu\text{m}$ . To fully demodulate the sine/cosine signals, a differentiate and cross multiply circuit (DCM) was used to recover small AC phase shift information ( $< 1$  radian) the output of which is proportional to fiber strain. The noise floor of this arrangement was recorded at several different frequencies over the signal band and is shown in Figure 4; as can be seen, a phase sensitivity of 50  $\mu\text{rad}/\sqrt{\text{Hz}}$  or better was achieved from 20 to 1000 Hz which corresponds to a e-core fiber length change smaller than 1 nanometer, or a strain resolution of  $10^{-10}$  for the 10 m length used. The dependance of the phase noise on frequency shows the expected  $1/\sqrt{f}$  dependence due to the frequency jitter of the laser diode source.

The potential of this method for use in a smart structures applications was demonstrated by attaching 10 meters of e-core fiber in multi-pass fashion to the bottom surface of a plastic panel 52 cm X 34 cm. The panel was then subject to 3-point bending using a motorized translation stage to load the top surface of the panel. Figure 5 shows the resultant phase shift of the output carrier signal for a deflection range of 3 mm. For this particular measurement a carrier signal was synthesized by applying a sawtooth ramp to the laser supply current. DC changes in fiber strain were then monitored with a lock-in-amplifier (LIA) and configured as a phase analyzer. Figure 6 shows the output of the LIA for several 200  $\mu\text{m}$  step changes in beam deflection during a 100 second time period. As can be seen, 10  $\mu\text{m}$  changes in deflection can be resolved with this approach. The phase generated carrier approach with DCM demodulation of sine/cosine signals was used to recover weak time-varying phase changes. Vibration of the panel was induced by a low frequency acoustic signal generated by a speaker suspended above the surface of the panel. Figures 7a and 7b show the demodulated output spectrum of the sensor with and without a 5 Hz tone generated by the speaker. The noise floor at 10 Hz corresponds to a panel vibrational amplitude of 10 nm/ $\sqrt{\text{Hz}}$  rms.

A reflectometric sensor configuration has also been constructed as shown in Figure 8. Light is launched into the e-core fiber via single mode fiber lead from a 2X2 coupler near the source. The single mode to e-core offset splice in this arrangement serves the dual purpose of illuminating the two modes of the fiber and spatially filtering the return light. The  $LP_{01}$  and  $LP_{11}$  modes are reflected by a mirror chemically deposited on the cleaved end of the 10 meter length of e-core fiber wound on a piezo-electric transducer. Operation using the same FM interrogation scheme described earlier allowed for the passive demodulation of sensor signals over a common input/output lead. Figure 9 shows the responsivity to fiber strain as compared to the transmissive configuration demonstrating the increased responsivity as expected with the dual path of the reflectometric sensor.

**Conclusions:** A method for remote interrogation and demodulation of a two-mode elliptical core fiber strain sensor over lead-insensitive single-mode fiber has been demonstrated using a frequency modulated laser source. High resolution signal detection has been demonstrated and employed in an experimental smart skin application. A reflectometric version using a common input/output lead with remote laser interrogation was also reported.

#### References:

1. M.R. Layton and J.A. Bucaro, *Applied Optics*, Vol. 18, No. 5, 666 (1979).
2. B.Y. Kim, et. al., *Optics Letters*, Vol. 12, No.9, 729 (1987).
3. K. A. Murphy et. al., *Journal of Lightwave Tech.*, Vol. 8, No. 11, 1688 (1990).
4. S.Y. Huang, H.G. Park, and B.Y. Kim, *Optics Letters*, Vol. 14, No. 24, 1380 (1989).
5. A.B. Wang, et. al., *Electronics Letters*, Vol. 27, No. 16, 1454 (1991).
6. D.A. Jackson, et al., *Electronics Letters*, 18, 1081(1981).
7. A. Dandridge, A.B. Tveten, and T.G. Giallorenzi, *IEEE Journal of Quantum Electronics*, Vol. QE-18, No. 10, 1982.
8. A.D. Kersey, M. Corke, and D.A. Jackson, *Proc. 2nd Int. Conf. on Optical Fiber Sensors*, p. 247 (1984).
9. T.A. Berkoff, A.D. Kersey, and R.P. Moeller, *Fiber Optic and Laser Sensors VIII*, SPIE proceedings, Vol. 1376, 53 (1990).

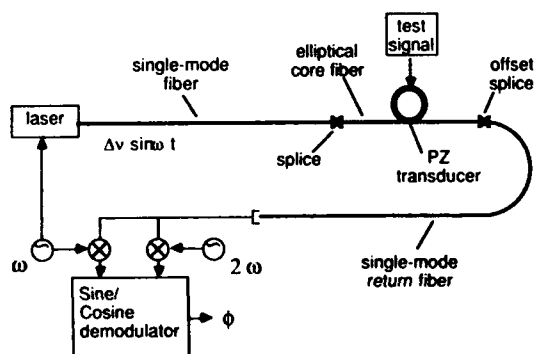


Figure 1: Experimental arrangement used to demonstrate remote demodulation of a two-mode elliptical core sensor.



Figure 2: Top: Sinusoidal modulation applied to laser supply current. Bottom: Resultant phase carrier signal at photodetected output.

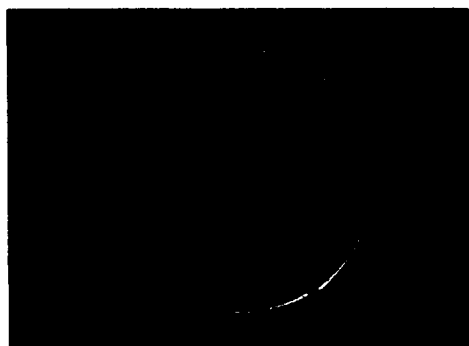


Figure 3: X-Y display of recovered sine/cosine quadrature signals with a 50 Hz  $2\pi$  radian test signal applied to the PZ element.

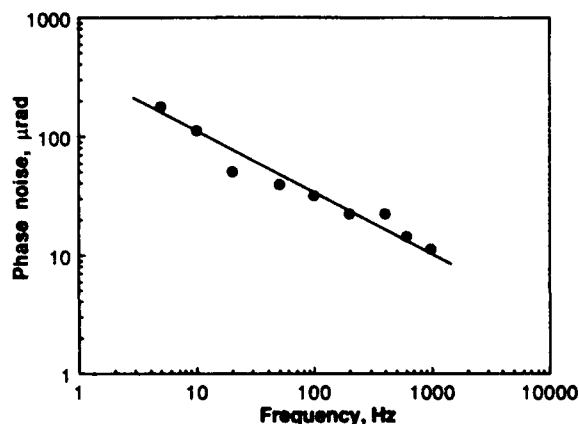


Figure 4: Demodulated output noise floor using differentiate and cross multiply circuit to process the sine/cosine quadrature signals.

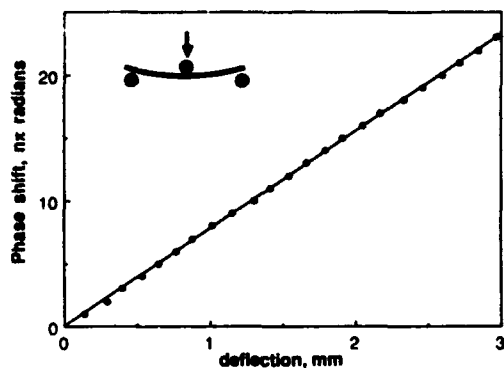


Figure 5: Recorded sensor phase shift response for 3-point deflection of a plastic panel.

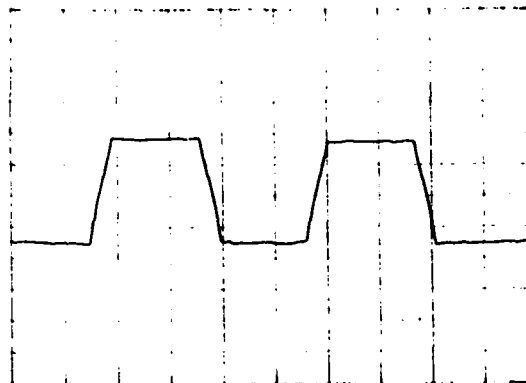
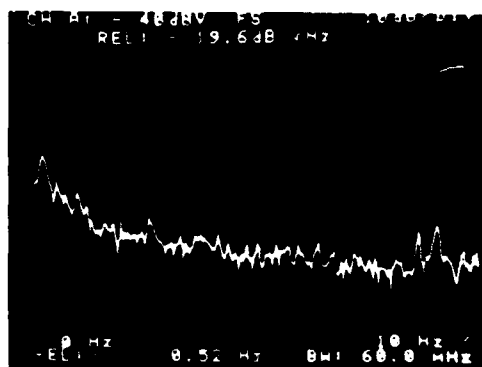
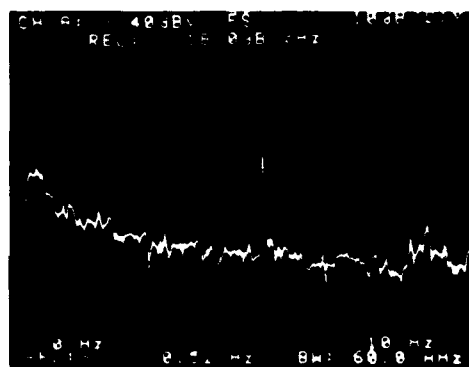


Figure 6: Lock-in-amplifier output for several 200 $\mu$ m step changes in panel deflection during a 100 second time interval.



(a)



(b)

Figure 7: Demodulated output signal spectrum of the two-mode sensor before panel insonification (a) and after insonification (b) with a 5 Hz acoustic signal the amplitude of which corresponds to a 2 mrad phase shift (equivalent to a panel vibrational amplitude of  $\sim 0.1 \mu$ m rms).

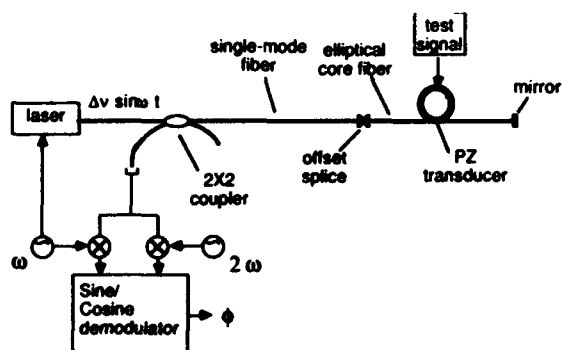


Figure 8: Experimental arrangement showing two-mode e-core reflectometric configuration.

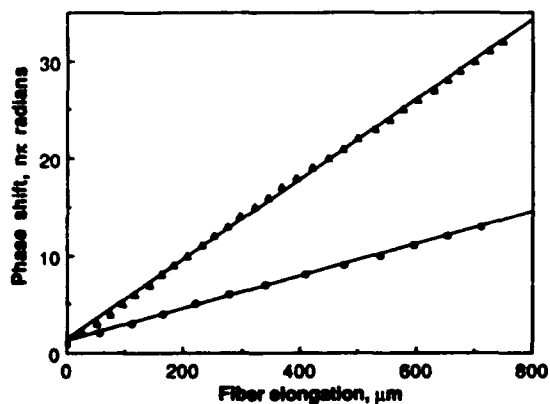


Figure 9: Phase shift responsivity to fiber strain for transmissive (—○—) and reflectometric (—●—) arrangements.

## F2.4 Grating-based, Two-mode Elliptical-core Optical Fiber Sensors

Ashish M. Vengsarkar

AT&T Bell Laboratories, Rm. 6D - 313, 600 Mountain Avenue, Murray Hill, NJ 07974

Jonathan A. Greene, Brian R. Fogg, Kent A. Murphy, and Richard O. Claus

Fiber & Electro-Optics Research Center, Bradley Department of Electrical Engineering

Virginia Polytechnic Institute and State University, Blacksburg, Virginia 24061-0111

Since the discovery of photo-induced gratings in germania-doped, single-mode fibers by Hill and coworkers in 1978, several extensions and applications of this phenomenon have been presented.<sup>1-3</sup> Permanent index gratings in two-mode, elliptical-core (e-core) optical fibers have been demonstrated, and their use in intermodal switching and chirped filters for dispersion compensation have been proposed.<sup>4-6</sup> We present here the effects of writing two-mode gratings in fibers and discuss their sensing implications. The effect of permanent-index gratings on the differential-phase modulation between the  $LP_{01}$  and  $LP_{11}^{\text{even}}$  modes in two-mode fibers is analyzed in detail and the use of these grating-based sensors for weighted-sensing applications is proposed. Our results show that strained fibers exposed to high-power writing beams from an argon-ion laser could be used as sensing elements with varying beat-lengths and hence, varying sensitivities.

Two-mode, e-core fiber sensors operate on the principle of differential phase modulation between the  $LP_{01}$  and  $LP_{11}^{\text{even}}$  modes.<sup>7, 8</sup> As the two modes propagate through the length of the fiber, an interaction between the symmetrical  $LP_{01}$  mode and the asymmetrical  $LP_{11}$  mode leads to a spatially alternating two-lobe pattern that evolves along the longitudinal direction with a period equal to the beat-length,  $L_B$ , of the fiber. When a high-power argon-ion laser beam is launched into a germanium-doped core, a two-mode fiber grating is formed after sustained exposure; the photoinduced refractive-index variation is an exact replica of the intensity profile within the fiber core and is shown schematically in Figure 1.

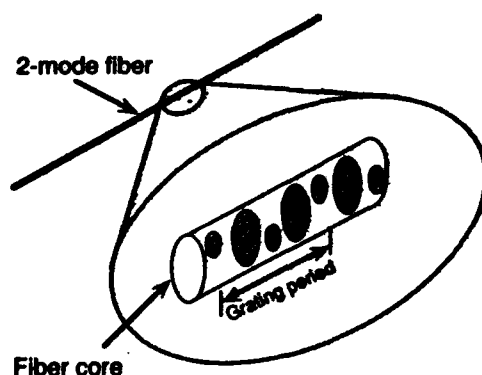


Fig. 1. Photo-induced refractive-index changes in a two-mode fiber.

We first analyze the effect of the grating on the beat-length of the sensor and find that we have a varying beat-length dependent on the induced strain. For example, a grating written in a fiber kept unstrained during the writing process shows a variation in beat-length as depicted in Figure 2. This result illustrates the principle of varying-sensitivity sensors and also lays the foundation for weighted-vibration sensing schemes. We show in an accompanying paper<sup>9</sup> that to obtain enhanced detection of a particular mode of vibration one needs to tailor the  $\Delta\beta''$  profile (where  $\Delta\beta$  is the difference in propagation constants of the  $LP_{01}$  and  $LP_{11}^{even}$  modes and the primes indicate derivatives with respect to the spatial variable  $x$ ) as a function of  $x$ . The parameter  $\Delta\beta''$  can be made to vary along the length of the fiber by inducing an  $x$ -dependent strain in a grating-based, two-mode, e-core fiber. The method we propose here consists of attaching a fiber to a one-dimensional beam and exposing the germanium-doped core to a high-intensity Argon-ion laser beam. During exposure, the beam is placed under static strain in a shape that is determined by the beam dynamics and the desired variation of the equivalent differential propagation constant.

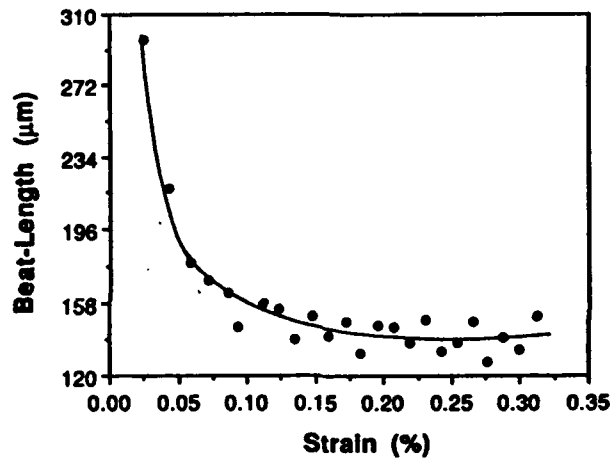


Fig. 2. Experimental result showing variation of beat-lengths with strain induced on a fiber with in-line grating. Filled circles are experimental data points, solid lines are best fits. Experimental error is  $\pm 5 \mu\text{m}$ .

From Fig. 2, we see that the beat-length varies almost inversely with strain. This variation, along with an analysis of the beam dynamics, leads us to the shape  $\psi_{\text{induced}}$ , the beam should be placed in during high-power writing and is given by

$$\psi_{\text{induced}} \propto \iiint \psi_n(x) dx, \quad (7)$$

where  $\psi_n(x)$  is the specific mode-shape of vibration one wishes to selectively enhance. We report results for a specific example, namely, a clamped-free beam for which the mode shapes  $\psi_n$ 's are expressed in terms of a linear combination of sine, cosine, hyperbolic-sine and hyperbolic-cosine functions. From the mathematical properties of these functions, one can see that a quadruple integral restores the original functions, except for a scaling factor. As a consequence, the beam needs to be positioned in exactly the same shape as that of the specific vibration-mode one wishes

to selectively enhance. Prior to writing a grating in the fiber, low-power (1 mW,  $\lambda = 514.5$  nm) probing of a two-mode, e-core fiber sensor provided the vibration-mode information of the cantilever beam under investigation. Fast Fourier transforms (FFT's) of the fiber sensor signal and an adjacent piezo-electric sensor signal attached to the beam are shown in Figure 3.

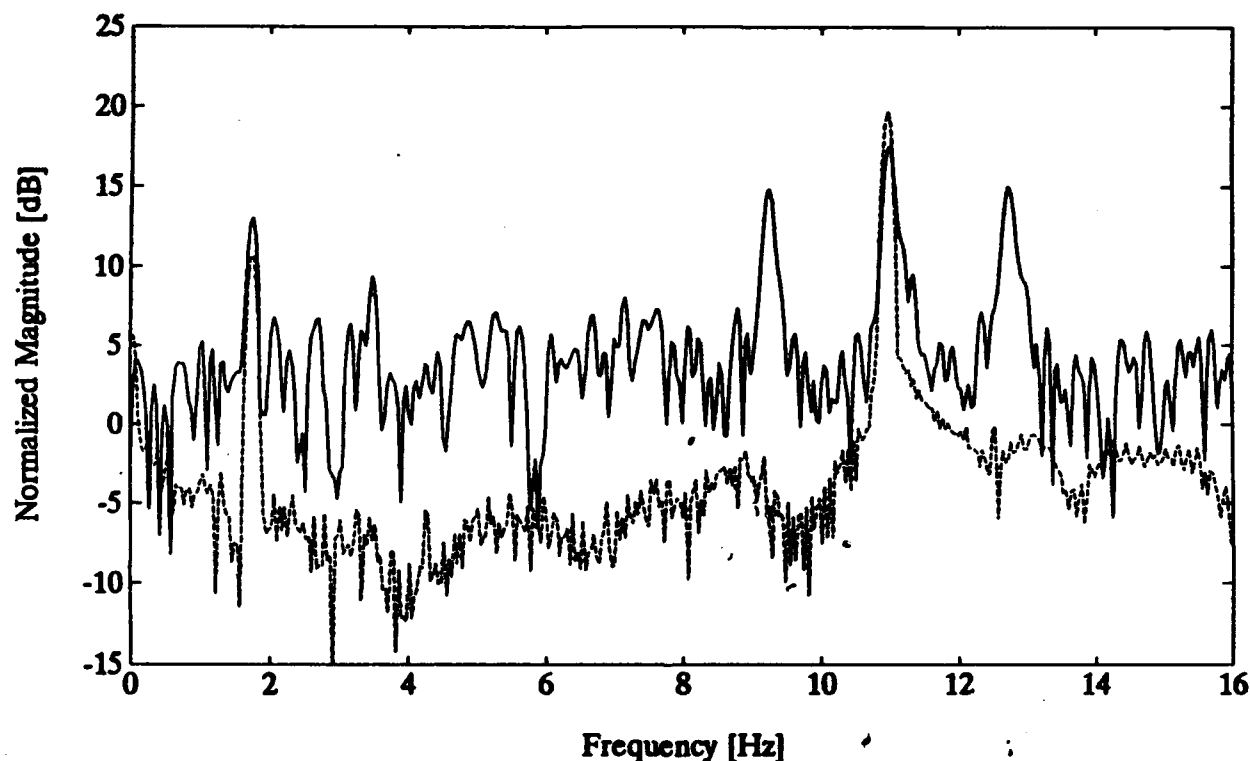


Fig. 3. Fast Fourier transform of output signals from a conventional e-core, two-mode fiber sensor and a piezo-electric sensor attached to the beam. First vibration-mode frequency is 1.78 Hz and second vibration-mode is seen at 11.2 Hz. Solid line: Fiber sensor output. Dashed line: Piezo-electric output.

A high-intensity Argon-ion laser beam (40 mW,  $\lambda = 514.5$  nm) was launched into the germanosilicate, e-core, two-mode fiber attached to a cantilever beam. The beam was held in its first vibration-mode shape during the high-power exposure of the fiber core. Post-exposure analysis of the fiber sensor with a low-power beam at 514.5 nm resulted in the output signal shown in Figure 4. A comparison of Figs. 3 and 4 indicates that the fiber sensor has suppressed the second mode of vibration by 10 dB. We have also managed to erase this filtering effect by overwriting another grating in the same fiber by placing the beam (with the fiber attached) in its equilibrium position [ $\psi(x) \equiv 0$ ] during exposure. Similar experiments have been performed with the beam placed in a shape corresponding to the second mode of vibration during grating formation and first mode suppressions on the order of 10 - 15 dB have been obtained.

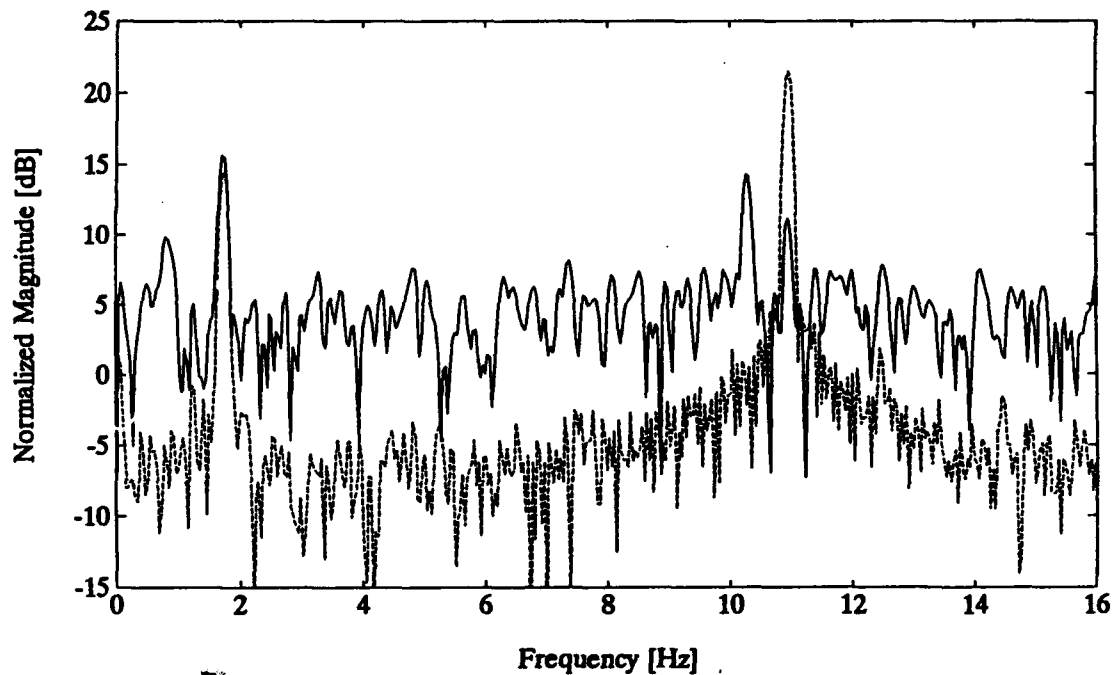


Fig. 4. Fast Fourier transform of output signals from a grating-induced, first-mode enhanced, e-core, two-mode fiber sensor and a piezo-electric sensor attached to the beam. The second mode is suppressed by the fiber sensor by 10 dB when compared to the relative signal levels in Figure 1. Solid line: Fiber sensor output. Dashed line: Piezo-electric output.

In summary, we present a detailed study of the effect of gratings in a two-mode, elliptical-core fiber on the sensing characteristics, analyze the behavior of a two-mode, elliptical-core fiber with a chirped grating, and demonstrate its use as a selective vibration-mode sensor.

## References

1. K. O. Hill, Y. Fujii, D. C. Johnson, and B. S. Kawasaki, *Appl. Phys. Lett.* **32**, 647 (1978).
2. B. S. Kawasaki, K. O. Hill, D. C. Johnson, and Y. Fujii, *Opt. Lett.* **3**, 66 (1978).
3. G. Meltz, W. W. Morey, and W. H. Glenn, *Opt. Lett.* **14**, 823 (1989).
4. H. G. Park and B. Y. Kim, *Electron. Lett.* **25**, 797 (1989).
5. H. G. Park, S. Y. Huang, and B. Y. Kim, *Opt. Lett.* **14**, 877 (1989).
6. F. Oulette, *Opt. Lett.* **16**, 303 (1991).
7. C. -K. Lee and F. C. Moon, *J. Appl. Mechanics* **57**, 434 (1990).
8. J. N. Blake, S. Y. Huang, B. Y. Kim, and H. J. Shaw, *Opt. Lett.* **12**, 732 (1987).
9. K. A. Murphy, M. S. Miller, A. M. Vengsarkar, and R. O. Claus, *IEEE J. Lightwave Technol.* **8**, 1688 (1990).

## **F2.5 Fiber Optic Sensors For Guy Wire Vibration Measurements**

*Peter L. Fuhr*  
*Dryver R. Huston*  
University of Vermont  
College of Engineering  
Burlington, VT 05405

*William B. Spillman, Jr.*  
Catamount Scientific Inc.  
P.O. Box 158  
Vergennes, VT 05491

### **ABSTRACT**

Wind induced motion in guy wires has proven to be of considerable importance when ascertaining the overall response of structures supported by such wires. We have investigated the use of fiber optic sensors to determine the guy wire's vibration field. The vibrational measurements have been correlated with locally measured meteorological data to provide a method of determining the wind parameters based on these values. A description of the fiber optic sensing technique, the fiber-guy wire physical arrangement, and the results of these studies are presented.

### **Introduction**

The study of guy wire motion has frequently relied on measuring the wire's tension then predicting parameters such as total maximum displacement or mode shape based on this value. Measurement of the wire's vibrating frequency could be made through the use of such devices as accelerometers, but the detectors add overall complexity to the wire while also slightly changing the wire's physical geometry. Regardless, the knowledge of how a guy wire is performing as it is being subjected to actual meteorological events is extremely important. We have investigated the use of fiber optic vibration sensing for in-service guy



wire vibration measurements. In a typical configuration, the fiber (which may be no larger than a single strand of hair thus causing minimal impact on the wire's integrity and/or physical shape) is wound around the guy wire and extends at least part-way up the wire. This type of sensor typically uses some mechanical perturbation of the multimode fiber, then analyzes the resulting speckle pattern variation to measure the perturbing force. In the case of vibration sensing, the recovered signal's frequency content is examined thereby revealing vibration frequency information which, in the case of large structures, may be used in a modal analysis of the structure.

## Fiber Sensor Theory

When coherent laser light is injected into a multimode optical fiber, the light travels down the fiber via many different paths resulting in a grainy interference pattern, composed of  $M$  individual speckles, being projected from the end of the fiber. For the system configuration used in this investigation, shown in Figure 1, a photodetector is illuminated by a few speckles. Therefore the photodetector output corresponds to an integration or summing of the speckle subpattern. Ignoring the steady state DC response, the output signal is proportional to the intensity variation within the summed speckle subpattern,  $DI$ , namely <sup>2,3</sup>

$$DI = \left[ \sum_{n=1}^m C_n \sin(d_n) \right] F(t) \quad \text{for } m \ll M \quad (2)$$

where  $C_n$  is the  $n_{th}$  speckle's total amplitude. It has been shown in previous work<sup>8</sup> that the bracketed term sums to a constant,  $K$ , which is dependent on experimental parameters. In the case of a vibrating perturbation force  $F(t) = F_0 \sin(Wt)$ , the summed speckle signal,  $DI$ , contains the vibration frequency component.

The implementation of the speckle pattern analysis is based on performing statistical analysis of a signal resulting from photodetection of a piece of the output pattern of the fiber. Subsequent electrical signal processing and filtering is then performed. As illustrated in Figure 1, statistical intensity processing is achieved optically by spatially filtering the speckle pattern (illuminating a transparency mask). The mask passes only a portion of the entire speckle pattern which illuminates a photodetector ( $m \ll M$  criteria of equation 2). By using a simple amplifier and high pass filter, which eliminates the d.c. portion of the optical field (those speckles which did not change under vibration), a stable and repeatable signal is found. The resultant electrical signal is therefore varying linearly with respect to the fiber's perturbation field (the vibration). (For a detailed theoretical description of the sensor's performance, see reference 3).

## **Experimental Arrangement and Procedures**

The basic experimental configuration is shown in Figure 2. A 20m long, 0.75 cm diameter wound cable was attached to a roof assembly on top of the Votey Engineering Building at the University of Vermont. The guy wire's maximum height was approximately 6m giving the guy wire an elevation angle of approximately  $20^{\circ}$ . A zipcord structured 100/140mm jacketed optical fiber was helically wound around the guy wire beginning at the base of the guy wire assembly traversing up then back down the wire thereby providing a common send/receive physical location with respect to the entire guy wire assembly. The fiber was then rigidly attached to the guy wire support structure, then run through PVC conduit across the remaining building roof, down the side of the building, and brought into the third story laboratory. The fiber's output pattern was spatially filtered for speckle subpattern isolation. Photodetection and speckle subpattern summing was performed by a PIN photodetector whose output was connected to a Hewlett-Packard Dynamic Signal Analyzer which was used to make frequency measurements. A small weather station capable of measuring the local temperature and wind speed and direction was installed adjacent to the guy wire's highest tie-down location. This meteorological information was hardwired into a Macintosh computer for time resolved data acquisition and recording. The data acquisition procedure thus amounted to executing a LabView Macintosh-based application which would acquire, briefly process, and record the time-tagged meteorological and fiber sensor vibration measurements. Repeated acquiring of this data occurred at user-specified time intervals. Actual event recording has since been improved to allow the computer to continuously monitor the data and only store the data when some particular event threshold (such as high winds) has been exceeded. Subsequent signal processing of the fiber sensor data has taken many paths, such as computing the RMS fiber sensor value then correlating that parameter with wind speed, as shown in Figure 3.

## **Results and Conclusion**

The use of a speckle based fiber optic vibration sensor for monitoring and measuring the perturbation of a roof-mounted guy wire has been investigated. Preliminary experiments have indicated that it may be possible to ascertain the local wind speed by monitoring the guy wire-fiber sensor output signal. Additionally, information regarding the guy wire's structural motion and vibrating mode shape may be obtained through an analysis of the vibration data.

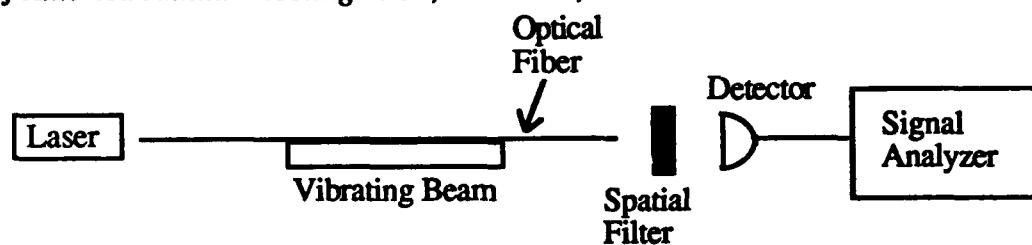
## **References**

1. B. D. Duncan, B. W. Brennan and R. O. Claus, "Intermodal pattern modulation in

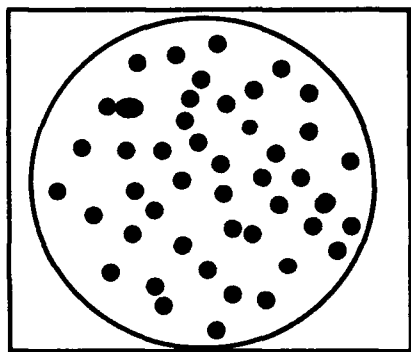
optical fiber modal domain sensor systems: experimental results," *Proc. SPIE - Int. Soc. Opt. Eng.*, Vol. 986, pp. 186-193, 1989.

2. W. B. Spillman, B. R. Kline, L. B. Maurice and P. L. Fuhr, "Statistical-mode sensor for fiber optic vibration sensing uses," *Appl. Opt.*, Vol. 28, No. 15, pp. 3166-3176, 1 Aug 1989.

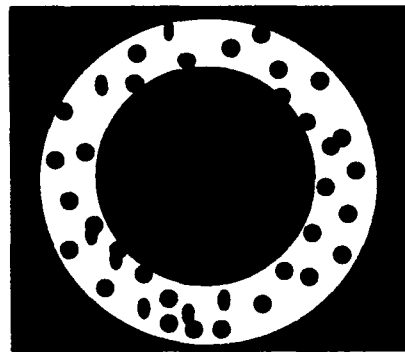
3. L. Maurice, P. L. Fuhr, and W. B. Spillman, Jr., "Theory and Simulation of Field Propagation within a Vibrating Few-Mode Optical Fiber", presented at the *Optical Society of America Annual Meeting 1989*, Oct. 1989, Orlando.



(a)



(b)



(c)

Figure 1. Fiber optic sensor: (a) configuration for measuring vibrations, (b) closeup of fiber's time varying speckle pattern, and (c) transmission of only a subsection of the total speckle pattern by annular filter.

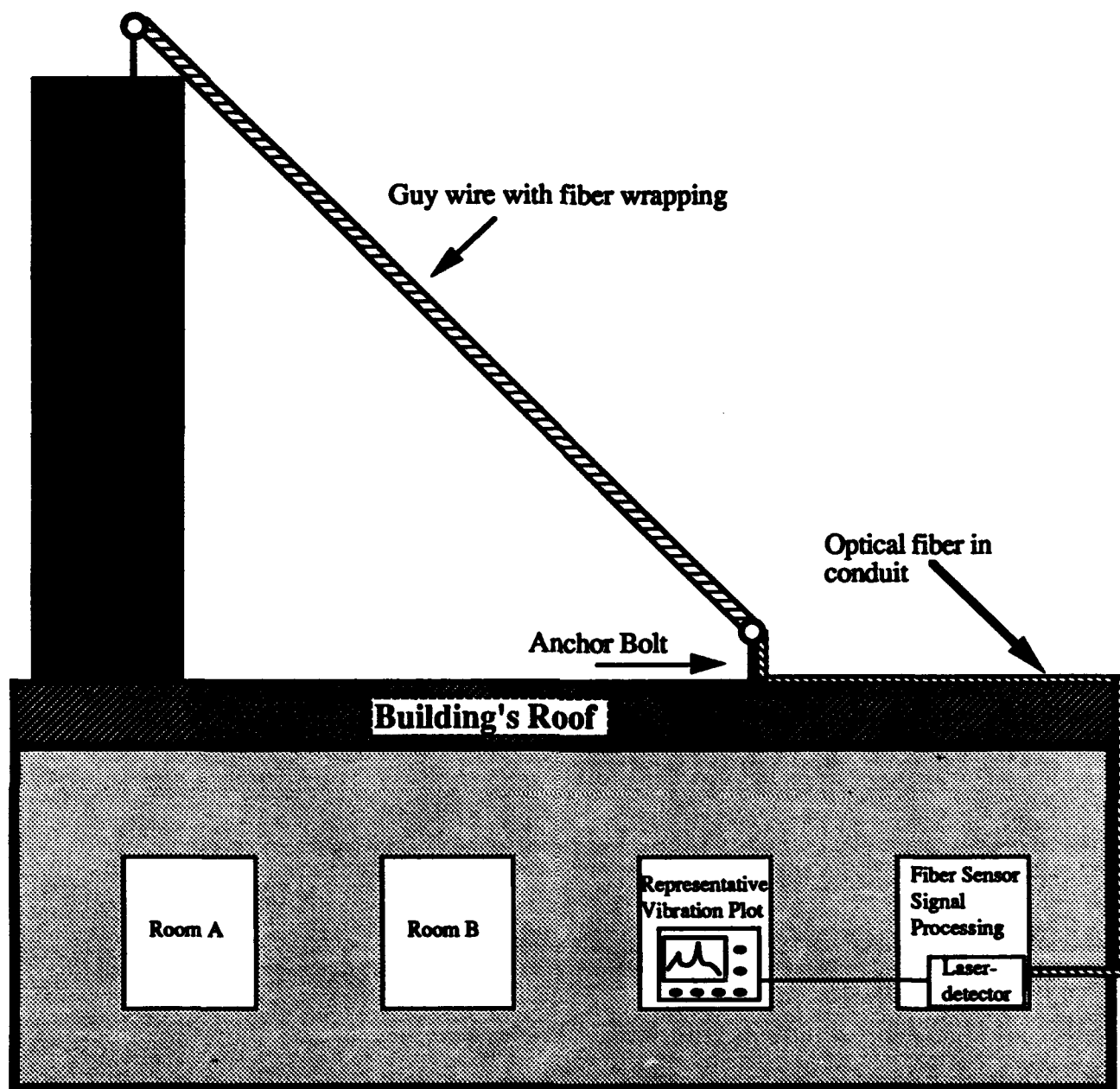


Figure 2. Basic experimental arrangement used in these guy wire vibration measurements.

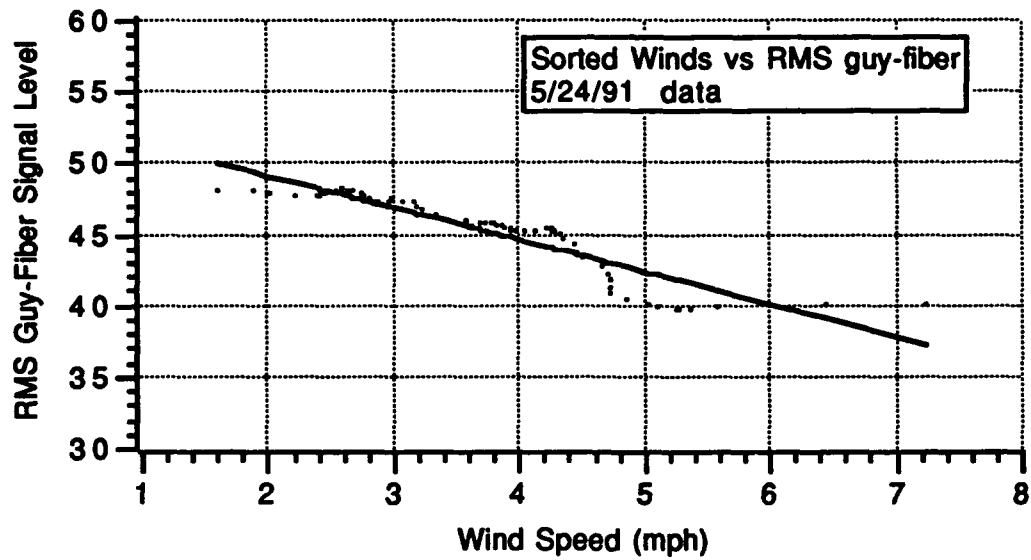


Figure 3. Representative data obtained from comparing the local measured wind speed with the RMS value of the fiber sensor's output.

## F3.1 Optical Magnetic Field Sensors Using Iron Garnet Crystals (Invited)

M. Imaeda  
Y. Kozuka  
Electronics & Optoelectronics Research Laboratory  
NGK Insulators, Ltd.  
2-56 Suda-cho, Mizuho-ku, Nagoya, 467, Japan

This paper describes the development of optical fiber sensors in NGK Insulators, Ltd., mainly optical magnetic field sensor using Yttrium Iron Garnet crystals and its application to ground fault current detector.

### 1. Introduction

Optical fiber sensors are now applying mainly to the equipment for electric power systems(1). Because they have advantages of compact size and light weight, high insulation performance and non electromagnetic interference under high voltage and high magnetic field.

In this paper, the development of optical fiber sensors performed in NGK Insulators Ltd., mainly optical magnetic field sensor using Yttrium Iron Garnet (YIG,  $Y_3Fe_5O_{12}$ ) crystals and Ground fault current detector, is described(2,3,4). These are the result by the collaboration with The Tokyo Electric Power Co. and other electric power company in Japan.

### 2. Optical fiber sensing system

We have investigated optical fiber sensing system for protection, control and fault detection in the transmission line, substation and distribution line. The key technologies, such as Faraday and Pockels crystals, new sensor structure for easy assembly and long durability, optical fiber containing insulators and electric circuit for calculation and indication, are produced in this investigation.

Table.1 shows the properties of our optical fiber sensors for voltage and magnetic field measurement. YIG and BSO ( $Bi_{12}SiO_{20}$ ) has Faraday effect and are used as magnetic field sensors, and BSO and LN ( $LiNbO_3$ ) has Pockels effect and are used as voltage sensors.

Table.1 Properties of optical fiber sensors

sensor	effect	material	detection range	temperature* coefficient
current (magnetic field)	Faraday	substituted YIG $Bi_{12}SiO_{20}$ (BSO)	0.003 ~ 500 Oe	$\pm 0.5 \sim 7 \%$
			0.5 ~ 5000 Oe	$\pm 1.5 \%$
voltage	Pockels	$Bi_{12}SiO_{20}$ (BSO) $LiNbO_3$ (LN)	0.1 ~ 100 V	$\pm 2.0 \%$
			0.1 ~ 100 V	$\pm 2.0 \%$

\* temperature range  $-20 \sim +60^\circ C$

### 3. Preparation of YIG and Bi-substituted YIG crystals

Concerning production method of these crystals, BSO and LN crystals are produced by Czochralski (CZ) method, and YIG crystal is produced generally by Floating Zone (FZ) method or Liquid Phase Epitaxial (LPE) method. CZ method, which is used to grow silicon single crystal, has mass-productivity, but FZ and LPE method have less productivity and grown crystals have inhomogeneity of optical properties.

So we have tried to adapt the solid-solid reaction method for producing single crystals of YIG(5). This is developed to produce manganese-zinc ferrite single crystal for magnetic recording head by NGK. This method was based on the idea to contact the polycrystalline with seed single crystal and heating the contacted body, and we can obtain single crystal through solid state. So it has the advantage, 1) homogenous composition and high purity, 2) low cost, 3) possibility to substitute of the elements.

Preparation process of YIG crystal is illustrated in Fig.1. Starting raw

powder is prepared by coprecipitated process, which is used to obtain fine and homogenous powder. According to ordinary ceramic processing, the powder is dried, calcined, milled, molded in stoichiometry and sintered. Stoichiometry control is the key process to obtain optical crystal. Sintered body is heated in hot isostatic pressing (HIP) furnace. The new process to produce YIG crystals with uniform optical magnetic properties at low cost was developed.

Next, substitution of the elements to improve magneto-optic properties, mainly Verdet constant and its temperature coefficient, was investigated. Table.2 shows the YIG crystals family we are developed in this research. Bi substituted YIG has larger Faraday rotation angle, so it has larger Verdet constant. Ga substituted YIG has smaller Saturated magnetic field, so it has also larger Verdet constant. And the temperature coefficient of the Verdet constant is improved by Tb or Gd substitution. By mixing these elements, various type of Faraday cell can be achieved.

Table.2 Magneto-optic constants of substituted YIG crystals

composition	Faraday * Rotation angle (deg/cm)	Saturated Magnetic field (Oe)	Verdet * constant (deg/cm Oe)	temperature** coefficient (%)	output stability (%)
$Y_3 Fe_5 O_{12}$	2 4 0	1 8 0 0	0. 1 8	$\pm 7. 0$	$\pm 0. 1$
$(Tb Y)_3 Fe_5 O_{12}$	3 2 0	1 8 0 0	0. 2 4	$\pm 0. 5$	$\pm 0. 0 4$
$Bi_{0.5} Y_{2.5} Fe_5 O_{12}$	8 0 0	2 0 0 0	0. 5	$\pm 2. 5$	$\pm 0. 0 2$
$Bi_1 Y_2 Fe_5 O_{12}$	2 2 0 0	2 0 0 0	1. 3	$\pm 2. 5$	$\pm 0. 0 1$
$Bi_1 (Gd Y)_2 Fe_5 O_{12}$	2 2 0 0	1 7 0 0	1. 4	$\pm 0. 5$	$\pm 0. 0 1$
$Bi_1 Y_2 (Fe Ga)_5 O_{12}$	1 4 5 0	5 0 0	4. 0	$\pm 5. 5$	$\pm 0. 0 3$
$Bi_1 (Gd Y)_2 (Fe Ga)_5 O_{12}$	1 6 5 0	3 0 0	4. 5	$\pm 1. 5$	$\pm 0. 0 3$
$Bi_{12} SiO_{20}$ (BSO)			0. 0 0 2	$\pm 1. 5$	$\pm 0. 2$

\* measured at 1.15  $\mu m$

\*\* temperature range  $-20 \sim +60^\circ C$

#### 4. Assembly of sensors

Fig.2 shows the principal of the optical magnetic field sensor and they are constructed by Faraday cell, polarizer, analyzer, focused lens and optical fiber. In this system multimode fiber is used, and the accuracy of the assembly of these elements is required within 2  $\mu m$ .

CTO ( $CaTiO_3$ ) ceramics is used as basis of these optical elements, because the thermal expansion coefficient of CTO is matching for them. CTO basis is precisely cutted, polished and grooved, so we can assemble these elements on the basis by adhesive without further adjustment.

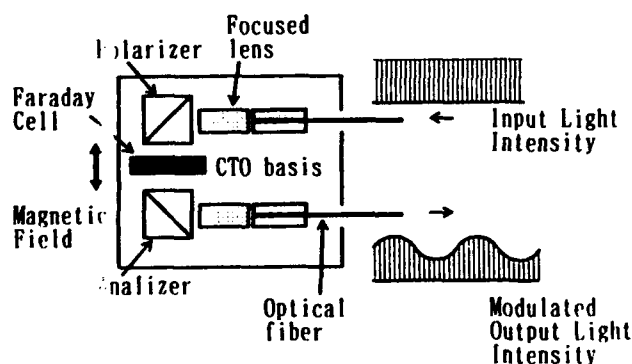


Fig.2 Principal and structure of optical magnetic field sensor

This method is good not only for easy assembly but also for long durability of the sensor. Optical fiber sensors for electric power systems are used under intense heat and cold atmosphere.

The thermal shock examination, which the sensor is soaked alternately in the  $+80^\circ C$  and  $-20^\circ C$  liquid, has exhibited that it functioned after 1700 cycles, which is converted over 25 years long durability. By using the ceramic basis and new adhesive method, the durability of the sensor is considerably

improved.

## 5. Application for ground fault current detector

Ground fault current detector is the devices for detecting and measuring zero-phase-sequence current of a three-phase power distribution line(Fig.3). The maximum load current of the line is 600A and the minimum zero-phase-sequence current by ground fault is 0.1A.

In the electric circuit for calculation and indication, we adopted the 3-phase current signal synthesizing circuit to detect such a small change of the current. Each system to calculate the load current is constructed by LED, PD and electric circuit. Three output of the current signal is synthesized in it, then load currents are diminished by interference and output signal is proportionate to zero-phase-sequence current.

By using Bi substituted YIG crystal with high sensitivity and high stability as Faraday cell, 0.1A zero-phase-sequence current by ground fault can be detected.

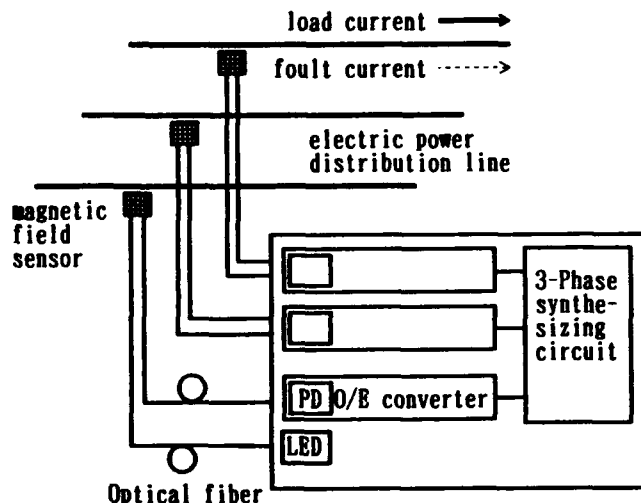


Fig.3 Ground fault current detector

## 6. Other applications

### 6-1 Fault location system for substation(6)

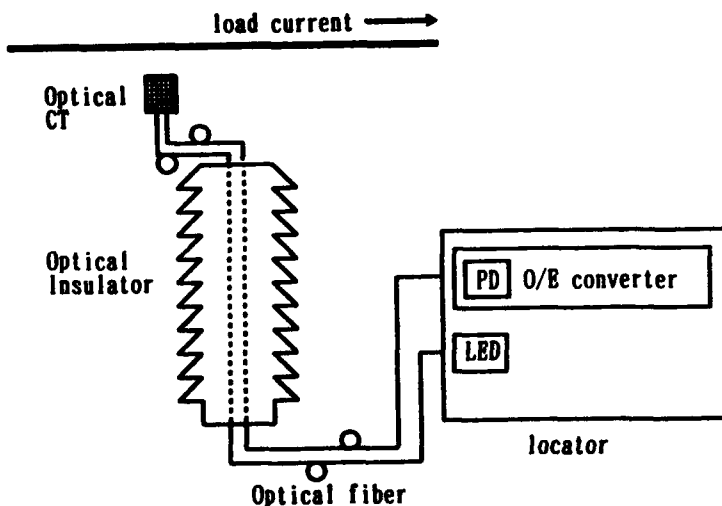


Fig.4 Fault location system for substation

This system is used for the detection of the fault current running through the bus within the station(Fig.4). Information concerning a fault current which will be detected by optical current transducer (optical CT) on the energized side will be transmitted to a locator via optical fiber containing insulators (optical insulators). BSO crystal is used in the optical CT, because the magnetic field by a fault current is very large.

### 6-2 Remote voltage sensor for transmission line

This system is used for the detection of the damaged insulators used in the transmission line. It is not the optical fiber sensor, but a optical remote sensing system. The sensor constructed by BSO crystal and corner cube mirror is set beside the insulators. The light beam from He-Ne laser is radiated to the sensor and reflected light is detected by PD. If damaged insulators are existed, the modulation by Pockels effect is detected in the reflected light. The minimum detection voltage is 10V, and they can be detected more easily than ordinary method.



## 7. Basic research

### 7-1 Voltage and current realtime measurement sensor(7)

BSO crystal has both of Faraday and Pockels effect, so it is possible to detect voltage and current at the same time. The sensor structure is almost the same we mentioned above except both of voltage and magnetic field is added to BSO, and the output from PD is separated according to its frequency by lock-in amplifier. When the frequency of objective electric power is  $\omega$ , intensity of the current is in proportion to  $\omega$  signal, and intensity of the voltage is in proportion to square root of  $2\omega$  signal.

### 7-2 Sensor with sensitivity independent of Verdet constant(8)

When the DC bias magnetic field is added to the Faraday cell, we can detect objective AC magnetic field with sensitivity independent of Verdet

constant(Fig.5). Using lock-in amplifier, the output from PD is separated two frequencies ( $1\omega$  and  $1_2\omega$ ). And the intensity of the current is in proportion to the value of  $1_2\omega/1\omega$ . So the temperature coefficient of the Verdet constant is canceled. Using Bi substituted YIG, the output of the signal is improved from  $\pm 2.5\%$  to  $\pm 0.3\%$ .

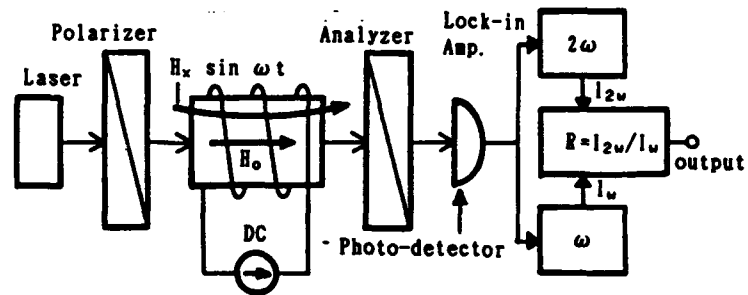


Fig.5 sensitivity independent sensor

## 8. Summary

Optical fiber sensing systems mainly for electric power systems are discussed. In the field of optical fiber sensors, we have developed from the materials such as YIG crystals with various properties to the systems for fault detecting and monitoring. And some of them are now produced commercially and some are tested in the field. And we are now trying to expand the application of optical fiber sensors.

## REFERENCE

- (1) K.Kurosawa: 7th Optical Fiber Sensors Conference, 67 (1990)
- (2) M.Morikawa, S.Waki, A.Okimoto, Y.Kamejima: 3rd meeting on Lightwave Sensing Technology, 119 (1989)
- (3) M.Morikawa, S.Waki, M.Imaeda, Y.Kozuka: 3rd meeting on Lightwave Sensing Technology, 127 (1989)
- (4) M.Morikawa, T.Matsumura, K.Tsuge, Y.Kamesima, M.Imaeda: IEE Japan 1990 National Conv. Rec., 1153
- (5) M.Imaeda, S.Matsuzawa: Proc. 1st Japan International SAMPE Symposium 419 (1989)
- (6) K.Goto, T.Oshi, T.Kawaguchi, H.Katsukawa, H.Abe: IEE Japan 1989 National Conv. Rec., 1245
- (7) Y.Kozuka, M.Asano, Y.Kakizaki, H.Abe, M.Abe: 5th meeting on Lightwave Sensing Technology, 91 (1990)
- (8) M.Abe, M.Shimosato, Y.Kozuka, M.Imaeda: J. Mag. Soc. Jpn., 13, 79 (1989)

## F3.2 High Frequency Magnetic Field Sensors Based On The Faraday Effect In Garnet Thick Films

*R. Wolfe, E. M. Gyorgy, R. A. Lieberman\*, V. J. Fratello, S. J. Licht*  
AT&T Bell Laboratories, Murray Hill, New Jersey 07974

*M. N. Deeter and G. W. Day*  
National Institute of Standards and Technology, Boulder, CO 80303

### INTRODUCTION

The Faraday effect in ferrimagnetic garnets can be used as the basis for fiber optic magnetic field sensors [1,2]. Single crystals of substituted yttrium iron garnet (YIG) can be in bulk form, or epitaxial thin films with planar anisotropy [3], or thick films with uniaxial anisotropy perpendicular to the surface [4]. The growth of magnetic domains parallel to the applied field at the expense of antiparallel domains results in changing Faraday rotation of the plane of polarization of transmitted infrared light. In this paper we report on the sensitivity and speed of sensors based on thick uniaxial garnet films, with the applied field and the light propagation direction perpendicular to the film. In zero field, these films have up and down magnetic domains of equal area, forming the familiar stripe pattern shown by their Faraday rotation in Figure 1. The changes in this pattern with magnetic field determine the sensitivity and limit the maximum operating speed of a magnetic field sensor.

### THEORY

For thick films, the magnetization increases linearly with field and it saturates (i.e. all of the stripe domains are wiped out) in a field which is approximately equal to the strength of the saturation magnetization,  $M_s$ . When linearly polarized light is used to probe a large number of stripe domains, with an analyzer set at  $45^\circ$  to the input polarization direction, the transmitted intensity also varies linearly with field for small rotation angles. The sensitivity is therefore inversely proportional to the magnetization and linearly proportional to the film thickness times the Faraday rotation constant [5]. The high frequency behavior of this field sensor depends on domain wall damping or domain wall resonance in the same way as the magnetic susceptibility. The standard theory of the susceptibility of thick uniaxial films [6,7] begins with the equation of motion for small displacements,  $x$ , of the domain walls (in SI units):

$$m\ddot{x} + \beta\dot{x} + \kappa x = 2\mu_0 H M_s \quad (1)$$

where  $m$  is the effective mass of the domain walls per unit area:

$$m = \frac{2}{\mu_0 \gamma^2} \left[ \frac{K}{A} \right]^{1/2} \quad (2)$$

$\beta$  is the viscous damping coefficient:

---

\* Present Address: Physical Optics Corp., Torrance, CA 90501.

$$\beta = \frac{2M_s}{\gamma} \left[ \frac{K}{A} \right]^{\frac{1}{2}} \alpha \quad (3)$$

and  $\kappa$  is the wall stiffness coefficient, related to the demagnetizing field.

$$\kappa = \left[ \frac{\mu_0}{4\pi} \right]^{3/2} \frac{(1.7)^{3/2} M_s^3}{[(AK)^{\frac{1}{2}} L]^{\frac{1}{2}}} \quad (4)$$

In these expressions,  $A$  is the exchange energy,  $K$  is the uniaxial anisotropy energy,  $\gamma$  is the gyromagnetic ratio,  $M_s$  is the saturation magnetization,  $H$  is the applied field perpendicular to the film,  $\alpha$  is the damping constant (proportional to the ferromagnetic resonance linewidth), and  $L$  is the film thickness.

Solving Equation 1 assuming a sinusoidally varying applied field with radial frequency  $\omega$  gives for the real part of the susceptibility  $\chi$  ( $= M/H$ ) divided by its low frequency value:

$$\chi/\chi_0 = \frac{\kappa(\kappa - m\omega^2)}{(\kappa - m\omega^2)^2 + \omega^2\beta^2} \quad (5)$$

If the damping is very small, the susceptibility at high frequencies shows a resonant behavior (domain wall resonance) at a frequency given by  $(\kappa - m\omega^2) = 0$ . If the damping is large, then  $\chi$  shows relaxation behavior: a constant value at low frequencies, falling to one half of this value at a frequency of  $\kappa/\beta$ , and then dropping off as  $1/\omega^2$  at high frequencies. (See Figure 4).

## EXPERIMENTS

In this study, three thick films grown for magneto-optic isolator experiments were studied. They all contained bismuth to enhance the Faraday rotation and were grown by standard liquid phase epitaxy (LPE) techniques on Ca-Mg-Zr substituted gadolinium gallium garnet (111)-oriented substrates. Films 1 and 2 are double films grown on both sides of the substrate. Film 3 is a free standing film with the substrate removed. The relevant properties of these films are listed in Table 1.

Table 1

	Film 1	Film 2	Film 3
Composition	(BiY) <sub>3</sub> Fe <sub>5</sub> O <sub>12</sub>	(BiTb) <sub>3</sub> (FeGa) <sub>5</sub> O <sub>12</sub>	(BiTb) <sub>3</sub> (FeGa) <sub>5</sub> O <sub>12</sub>
Film thickness (μm)	60 × 2	100 × 2	320
A (J/m)	3.7 × 10 <sup>-2</sup>	3.0 × 10 <sup>-2</sup>	2.5 × 10 <sup>-2</sup>
M <sub>s</sub> (kA/m)	143	56	28
K (J/m <sup>3</sup> )	1.4 × 10 <sup>4</sup>	4.5 × 10 <sup>3</sup>	4.7 × 10 <sup>3</sup>
Stripe width	7 μm	12 μm	50 μm
Damping	Low	High	High
Faraday rotation at 1.3μm	27°	27°	45°

The saturation magnetizations and uniaxial anisotropy energies were measured with a vibrating sample magnetometer. The exchange energies were estimated from the known values for the pure garnets, and the expected drop due to dilution of the iron with gallium [8]. The stripe widths were measured by observing the Faraday rotation of the domains at near infrared

wavelengths where the garnets are transparent and the TV camera still has some sensitivity. The stripes in Film 2 are shown in Figure 1. Film 1 appears similar. In Film 3 the domains are much wider and more complex, as shown in Figure 2. On one surface, the stripe domains have undulations with a period similar to the stripe width (Fig. 2a). As the focus is moved to the middle of the film, these undulations disappear. On the other surface they reappear, not correlated with the first surface, and small spike domains of reverse magnetization appear. This complex domain structure is associated with surface demagnetizing effects, and is typical of very thick films.



Fig. 1

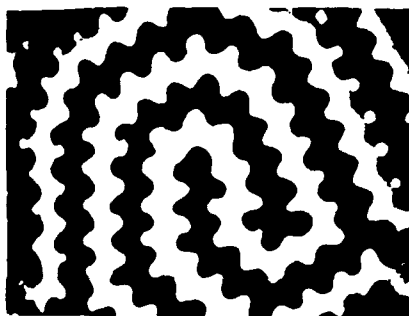


Fig. 2a

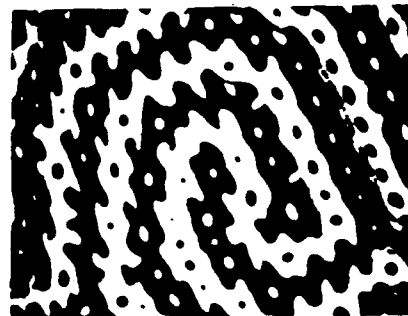


Fig. 2b

To measure the optical sensitivity,  $1.31\text{ }\mu\text{m}$  linearly polarized light was collimated into a  $0.5\text{ mm}$  beam, passed through the film and a  $45^\circ$  analyzer and was detected with a germanium detector. With  $50\text{ Hz}$  magnetic fields applied perpendicular to the film, the response was linear and the coercivity was less than  $10\text{ A/m}$  for fields up to at least half the saturation field in each case. The sensitivities of Films 1, 2 and 3 were in the ratio 1:2:7, close to the measured ratios of the Faraday rotation divided by the magnetization.

The high frequency response measurements were performed with a frequency synthesizer, an RF amplifier and a dielectric-filled coaxial transmission line that generated the RF magnetic fields. The coaxial structure contained a slot that held the sample in place near the center conductor, and transversely oriented holes that provided an unobstructed path to the sample for the collimated output of a  $1.32\text{ }\mu\text{m}$  solid state laser. The calculated amplitude of the RF magnetic field at the sample varied from  $5$  to  $15\text{ A/m}$ . As shown in Figure 3, the response for Film 1 rose to a resonant peak at  $6 \times 10^8\text{ Hz}$ . (Note: the apparent gentle rise at lower frequencies is believed to be an artifact related to the characteristics of the RF amplifier or the coaxial transmission line). Films 2 and 3 exhibit the relaxation behavior expected for these high loss films, as shown in Figure 4. The  $3\text{ dB}$  roll-off frequencies are  $8 \times 10^6\text{ Hz}$  and  $7 \times 10^5\text{ Hz}$ .

## DISCUSSION

For the low loss Film 1, the theoretical value for the resonant frequency, Equation 5, is  $1.6 \times 10^8\text{ Hz}$ . This is in reasonable agreement with the measured value. For the high loss materials, the excellent agreement between susceptibility theory and optical response experiments shown in Figure 4 was obtained by setting the one adjustable parameter,  $\alpha$ , to  $0.09$  for Film 2 and  $0.14$  for Film 3. These values are not unreasonable for films which contain sizable amounts of very lossy terbium ions.

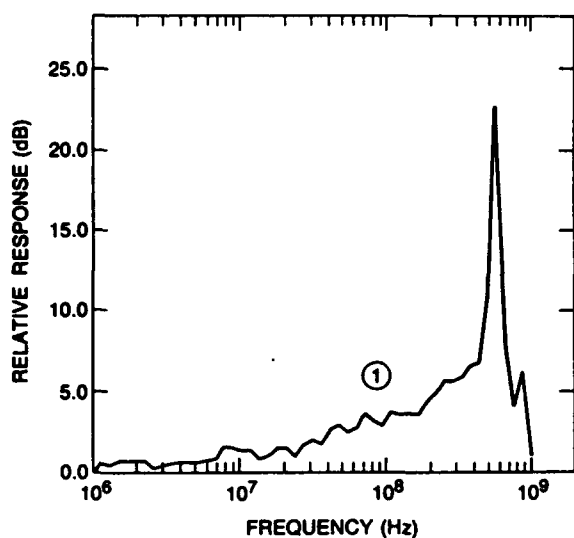


Fig. 3

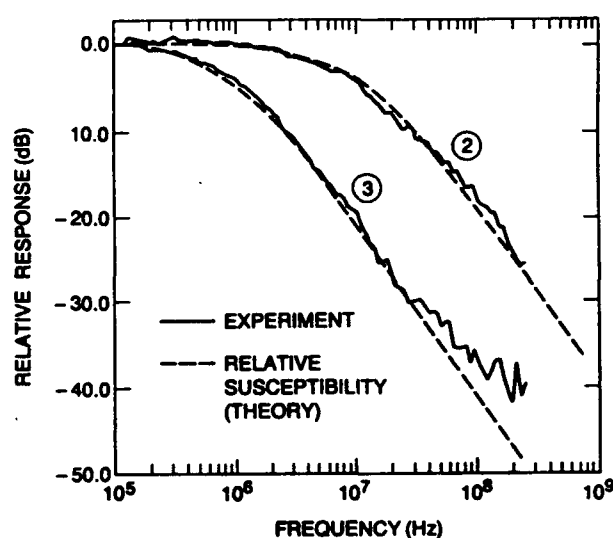


Fig. 4

In conclusion, the frequency response of magnetic field sensors based on uniaxial garnet thick films can be at least qualitatively understood in terms of the theory of magnetic susceptibility. In the presence of domain walls, higher wall resonance or relaxation roll-off frequencies can be obtained by maximizing the magnetization of the material and minimizing the film thickness, the uniaxial anisotropy and the damping. If rare earth ions are added to improve the temperature behavior of the material, terbium is the worst choice because it has the largest damping. The sensitivity of these field sensors can be optimized by decreasing the magnetization (as long as the corresponding coercivity and domain size are not too large) and increasing the thickness for greater Faraday rotation. Since these are conflicting requirements, a compromise must be reached for each potential application.

## REFERENCES

1. K. Svantesson, H. Sohlström and U. Holm, *SPIE Vol. 1274, Electro-Optic and Magneto-Optic Materials II* (1990), 260.
2. M. N. Deeter, A. H. Rose and G. W. Day, *J. Lightwave Tech.* 8, 1838 (1990).
3. R. Wolfe and R. A. Lieberman, *Appl. Phys. Lett.* 58, 1733 (1991).
4. K. Machida and Y. Asahara, *J. Magn. Soc. Jpn.* 11, *Supplement No. S1*, 347 (1987).
5. M. N. Deeter, A. H. Rose and G. W. Day, *Proc. 5th MMM-INTERMAG Conference*, Pittsburgh, PA, June 1991 (to be published).
6. E. M. Gyorgy, in *Treatise on Solid State Chemistry Vol. 2, Defects in Solids*, Editor: N. B. Hannay, (1975) 395.
7. C. Kittel and J. K. Galt, in *Solid State Physics, Vol. 3*, Editors: F. Seitz and D. Turnbull, (1956) 437.
8. A. H. Eschenfelder, *"Magnetic Bubble Technology"* Springer-Verlag, New York (1980). See p. 178.
9. S. Chikazumi, *Physics of Magnetism*, John Wiley, New York (1964). See p. 229 and p. 400.

### **F3.3: Submicroampere Per Root Hz, High Bandwidth Current Sensor Based On The Faraday Effect In Ga:YIG**

A. H. Rose, M. N. Deeter, and G. W. Day  
National Institute of Standards and Technology  
Boulder, CO 80303

#### **Abstract**

We demonstrate an optical fiber current sensor based on the Faraday effect in gallium-substituted yttrium iron garnet that has a measured sensitivity of approximately  $3.0^\circ/\text{A}$ , a noise-equivalent current of about  $500 \text{ nA}/\sqrt{\text{Hz}}$ , and a 3 dB bandwidth of approximately 10 MHz. The sensitivity-bandwidth product is about a factor of 40 greater than an all-fiber current sensor with the same diameter.

#### **Introduction**

EMI and EMP testing requires sensors with a bandwidth of at least 10 MHz and sometimes as great as 1 GHz, and noise-equivalent currents (NEI) as low as  $1 \mu\text{A}/\sqrt{\text{Hz}}$ . Conventional current sensors suffer from problems with interference and may lack the necessary bandwidth. Optical fiber current sensors using annealed coils may be able to provide the required bandwidth or NEI but, because of transit time limitations, probably not both.<sup>1-3</sup> For example, a fiber current sensor based on a 1 cm diameter annealed coil with 200 turns would have a transit-time-limited 3 dB bandwidth of about 15 MHz; such a sensor operated at 633 nm would have a sensitivity of about  $53^\circ/\text{kA}$ , a bandwidth-sensitivity product of  $0.8 \text{ MHz }^\circ/\text{A}$  and an NEI of about  $170 \mu\text{A}/\sqrt{\text{Hz}}$ .

Certain materials, not available in fiber form, exhibit Faraday effects that are thousands of times greater than that of silica. Using these materials in appropriate configurations it is possible to achieve substantially greater bandwidth-sensitivity products than with an all-fiber device. In this paper we describe a current sensor that is based on the Faraday effect in Ga:YIG, and has a bandwidth-sensitivity product a factor about 40 greater than has been achieved with an all-fiber current sensor with the same diameter. The bandwidth-sensitivity product of garnet sensors is limited by material properties, rather than transit-time, and can probably be improved.

#### **Sensor Design**

Gallium-substituted yttrium iron garnet, specifically  $\text{Y}_3\text{Fe}_{4.0}\text{Ga}_{1.0}\text{O}_{12}$ , was chosen as the material because its low-field Faraday effect was known from previous work to provide a rotation per unit field at  $1.3 \mu\text{m}$  that is as much as 24000 times greater than that of silica at 633 nm.<sup>4</sup> Ga:YIG also has a lower temperature dependence than other garnets.<sup>5</sup>

In ferrimagnetic materials, demagnetization effects generally lead one to choose samples that are rod shaped and several times longer than their diameter.<sup>5,6</sup> For these experiments, four samples approximately 1.5 mm in diameter by 5 mm long were selected; their geometrical demagnetization factor was approximately 0.083. Their low-field rotation varied from approximately  $22.5^\circ/\text{mT}$  to  $27.2^\circ/\text{mT}$  with a mean value of approximately  $24.9^\circ/\text{mT}$ . Their rotation was linear with applied field up to about 1 mT and saturated near 2 mT.

The current sensor configuration is depicted in Figure 1. The four Ga:YIG samples are arranged so that the optical path approximates a closed loop around the conductor. However, because the loop is not completely closed with the same material, the sensor will be somewhat sensitive to stray magnetic fields and currents on nearby wires. Two  $5 \times 5 \times 5$  mm right angle prisms were inserted between rods to achieve complementary total internal reflections and maintain linear polarization within the garnet samples.<sup>1</sup>

Using the measured rotation versus magnetic field of the four Ga:YIG samples, we predicted the sensitivity of the current sensor to be approximately  $3.6^\circ/\text{A}$ . The  $\pm 1\%$  linear current was expected to be about 3 A because of the sensor's sine response function. A saturation current of about 60 A was expected due to the magnetic saturation of the Ga:YIG.

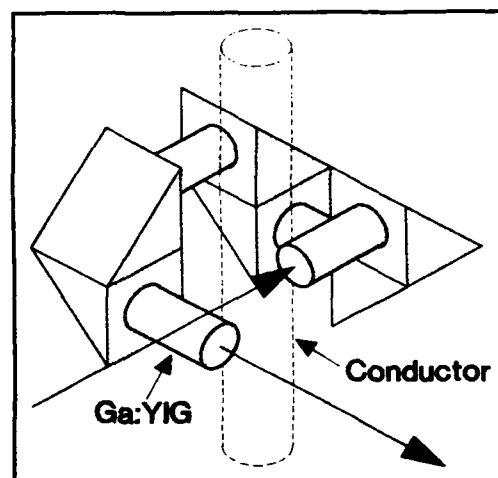


Figure 1 Ga:YIG current sensor optical design.

### Measurements

We have measured the sensitivity and NEI of the sensor using a low noise, solid state  $1.32 \mu\text{m}$  laser as the light source. The Faraday rotation was measured using standard differential polarimetric detection techniques.<sup>1</sup> Figure 2 shows the response of the two outputs (signal 1 and signal 2) from the polarizing beam splitter versus current. We suspect that depolarization and scattered light are the primary reasons the output signals do not extinguish fully. These effects and stress birefringence in the prisms and epoxy will reduce the sensitivity (slope of the response function near zero current). Using the period of the two sinusoidal output signals the ideal (maximum) sensitivity would be about  $4.4^\circ/\text{A}$ , but because of birefringence and depolarization effects the actual sensitivity is approximately  $3.0^\circ/\text{A}$ . There is some hysteresis in the response for values of current over 10 A which may be due to magnetic domain effects.

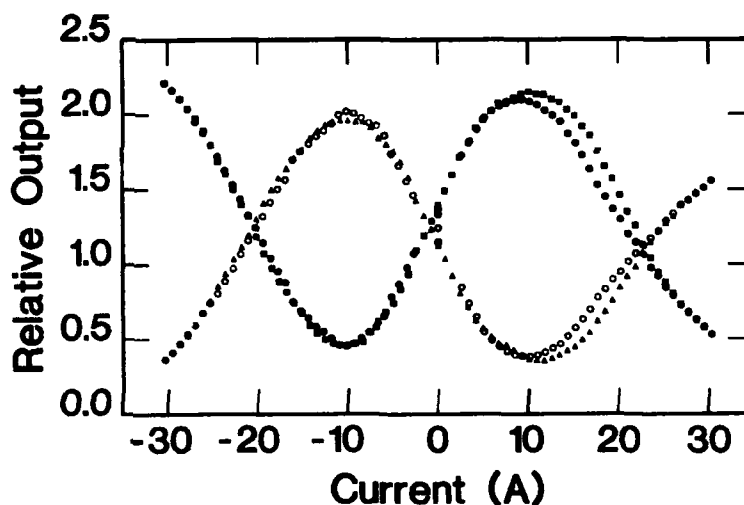


Figure 2 Response of the sensor versus direct current. The "•" and "○" are data taken from signal 1 and signal 2 for increasing current respectively. The "■" and "▲" are data taken from signal 1 and signal 2 for decreasing current respectively.

The output power spectrum of the sensor with a current of about 1 mA rms at 2 kHz applied is shown in Figure 3. The noise bandwidth is approximately 1 Hz. The NEI is 500 nA/ $\sqrt{\text{Hz}}$ . This spectrum was obtained using an analog circuit which produced a signal proportional to the quotient of the difference and sum of the two sensor outputs. It is about a factor of 3 greater than the shot noise limit for the parameters used. The sensor has a linear-response dynamic range of approximately 130 dB at this noise bandwidth. The signals at 2 kHz  $\pm$  60 Hz,  $\pm$  120 Hz, ... represent ripple on the applied signal. The other signals spaced at  $n \times 60$  Hz arise in the detector circuitry.

We have not yet measured the frequency response of the sensor, but have measured the frequency response of individual elements of the same material. A typical frequency response for a 1 mm diameter, 3 mm long specimen is shown in Figure 4. These data were taken by placing the Ga:YIG sample in a TEM cell with holes for the optical beam to pass through the cell perpendicular to the center conductor axis. Figure 4 shows that the 3 dB frequency for Ga:YIG is approximately 10 MHz. We presume the response of the complete sensor to be similar.

While Ga substitution in YIG increases its magneto-optic sensitivity, it also substantially reduces the frequency response. Pure YIG has a measured 3 dB bandwidth of 700 MHz.<sup>7</sup> Other data suggest that the frequency response of the Faraday effect in iron garnets is very dependent on composition,<sup>8,9</sup> so it may well be possible to choose a material with both a higher sensitivity and a higher frequency response than obtained here. These materials would allow the construction of a current sensor with a lower measured NEI and wider bandwidth.

This paper represents U.S. Government work and is not subject to copyright.

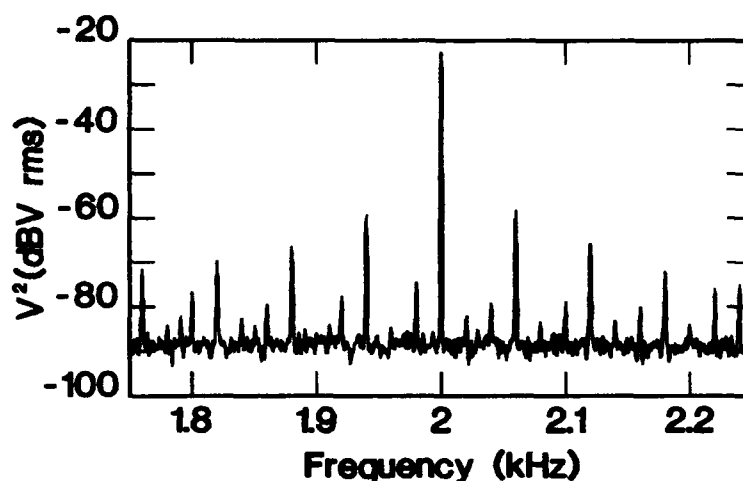


Figure 3 Output power spectrum when a 1 mA rms current at 2 kHz is applied.

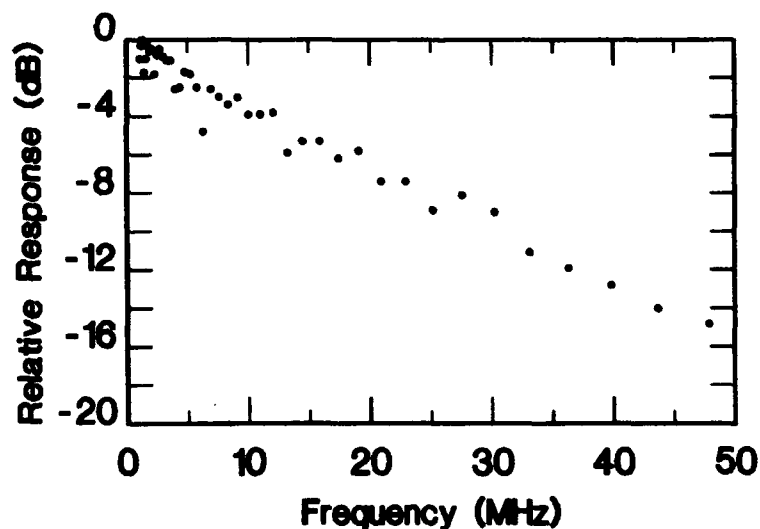


Figure 4 Relative rotation versus frequency in Ga:YIG.



## References

1. G. W. Day and A. H. Rose, "Faraday Effect Sensors: The State of the Art," *Fiber Optic and Laser Sensors VI*, SPIE Proceedings Vol. 985, pp. 138-150, 1988.
2. A. D. Kersey, F. Bucholtz, and A. Dandridge, "Sensitivity-Bandwidth limitations on optical-fibre Faraday-rotation current sensors," *International Journal of Optoelectronics*, Vol. 3, pp. 323-332, 1988.
3. R. W. Cernosek, "Traveling Wave Faraday Effect Fiber Current Sensors," *Proceedings of the 7th Optical Fibre Sensors Conference*, pp. 73-76, 1990.
4. M. N. Deeter, A. H. Rose, and G. W. Day, "Iron-Garnet Magnetic Field Sensors with 100 pT/ $\sqrt{\text{Hz}}$  Noise-Equivalent Field," *Proceedings of the 7th Optical Fibre Sensors Conference*, pp. 341-344, 1990.
5. M. N. Deeter, A. H. Rose, and G. W. Day, "Faraday-effect magnetic field sensors based on substituted iron garnets," *Fiber Optic and Laser Sensors VIII*, SPIE Proceedings Vol. 1367, pp. 243-248, 1990.
6. D. X. Chen, J. A. Brug, and R. B. Goldfarb, "Demagnetizing Factors for Cylinders," in press *IEEE Transactions on Magnetics*, July issue, 1991.
7. M. N. Deeter, A. H. Rose, and G. W. Day, "Fast, Sensitive, Magnetic-Field Sensors Based on the Faraday Effect in YIG," *Journal of Lightwave Technology*, Vol. 8, pp. 1838-1842, 1990.
8. R. Wolfe, E. M. Gyorgy, R. A. Lieberman, V. J. Fratello, S. J. Licht, M. N. Deeter, and G. W. Day, "High Frequency Magnetic Field Sensors Based on the Faraday Effect in Garnet Thick Films," submitted to the *Proceedings of the 8th Optical Fiber Sensors Conference*, 1992.
9. M. Ramesh, E. Jedryka, P. E. Wigen, and M. Shone, "Coupled oscillations of domain-domain wall system in garnet films," *Journal of Applied Physics*, Vol. 57, pp. 3701-3703, 1985.

# F3.4 High Frequency Response Of Fiber Current Sensors With Noncircular And Nonconcentrated Coils\*

R. W. Cernosek

Sandia National Laboratories  
Albuquerque, New Mexico 87185

## ABSTRACT

The frequency response of the Faraday rotation in fiber current sensors is computed and measured for sensor coils of noncircular cross section and with displaced coil and conductor axes. Resonances are observed at higher frequencies with magnitudes approaching that of the low frequency response. Narrowband current sensors at frequencies above 100 MHz are reported.

## I. INTRODUCTION

The general expression for the Faraday rotation of linearly polarized light in a single mode fiber is given by

$$\theta = V \int_0^L B \cdot dl, \quad (1)$$

where  $V$  is the fiber material Verdet constant,  $B$  is the magnetic flux density,  $dl$  is the incremental fiber length in the direction of light propagation and  $L$  is the total fiber length. At low frequencies the Faraday rotation reduces to  $\theta_0 = VBL$ , or in the case of a singlemode fiber current sensor formed of  $N$  turns of fiber around a current conductor,<sup>1</sup>  $\theta_0 = \mu VNi$ . At higher frequencies, the complex interaction of the magnetic field with the light propagating in the fiber must be considered. By transforming Eq. (1) to a time integral and accounting for the time variations in all system parameters, the frequency dependent Faraday rotation in a fiber current sensor becomes

$$\theta(\omega) = \theta_0 \frac{1}{2\pi N} \left( \frac{c}{n} \right) \int_0^{\tau} \frac{1}{r(t)} \cos[\gamma(t)] e^{-j\omega t} dt, \quad (2)$$

where  $r$  is the distance between the current conductor and the light element in the fiber,  $\gamma$  is the angle between  $B$  and  $dl$  (refer to Eq. (1)),  $\omega$  is the magnetic field angular modulation frequency,  $(c/n)$  is the speed of light in the fiber and  $\tau = (c/n)L$  is the transit time of the light in the fiber sensor. In the development of Eq. (2), it is assumed the magnetic field propagating along the current conductor is planar (TEM mode only). This simplifies both the analytical and experimental investigations at the high frequencies, although a real situation may be more complex. Further study would require a complete treatment of all field modes such as Sommerfeld's "waves on wires".<sup>2</sup>

The fiber current sensor coil can be constructed in almost any shape or geometry and Eq. (2) used to predict its high frequency Faraday response. For the simplest case, a coil will have a circular cross section and coincident coil and conductor axes. The relative magnitude of its frequency dependent Faraday rotation is

$$\left| \frac{\theta(\omega)}{\theta_0} \right| = \left| \frac{\sin(\omega\tau/2)}{(\omega\tau/2)} \right|, \quad (3)$$

and its 3 dB sensor bandwidth<sup>3</sup> is

$$\Delta B = \frac{c}{\sqrt{2} \pi^2 R n N}. \quad (4)$$

\* This work was performed at Sandia National Laboratories and supported by the U. S. Department of Energy under contract number DE-AC04-76P00789.

Other coils with noncircular cross section and/or displaced conductor and coil axes do not have such easily described frequency properties as expressed in Eqs. (3) and (4) but their response can be determined directly from Eq. (2). The investigation of these coil configurations is the subject of this brief paper. The relative magnitude of the Faraday rotation is computed and measured for several representative coils, and the responses are compared to Eq. (3). Some interesting high frequency resonances are observed in most sensors, and significant bandwidth changes occur in coils with only one or a few turns. All coils in these investigations are assumed to have fiber turns that are colocated in a single plane that is perpendicular to the current conductor. Nonplanar or helically distributed fiber coils are used in travelling wave sensor construction to enhance bandwidth<sup>4</sup> and are not discussed here.

## II. SENSOR COIL CONFIGURATIONS

The sensor coil geometries depicted in Fig. 1 represent configurations that may be encountered in fiber current sensor systems. In Fig. 1a the coil axis is displaced from the conductor axis, while in Figs. 1b and 1c the coil is elongated with only a difference in location of the conductor inside the coil. With all three configurations the high frequency response is changed significantly from that of Eq. (3). The change occurs because some points on the fiber are closer to the current conductor than others. Light propagating in the fiber will experience larger Faraday interactions at these points creating resonances in the frequency response. The magnitude of these resonances is dependent on coil geometry and conductor location, but their central frequency depends only on the light propagation time between points of closest approach in each fiber turn. This behavior is similar to that of the tapped fiber delay lines used for filtering and signal processing.<sup>5</sup>

### Circular Cross Section, Displaced Conductor

Equation (2) is solved for the coil geometry shown in Fig. 1a and the results are displayed in Fig. 2. The relative magnitude of the Faraday rotation is plotted as a function of the normalized frequency,  $\omega\tau/2$  (the function argument of Eq. (3)), which removes the response dependency on coil size. Frequency responses shown in Fig. 2 are dependent on the number of coil turns and the relative displacement,  $X_1/R$ . The resonances occur when  $\omega\tau/2$  is an integer multiple of  $N\pi$ , which corresponds to the light propagation delay through a single turn of fiber. For maximum displacement,  $X_1/R = 1$ , the relative magnitudes of the resonance peaks are  $\sim 0.5$ . The 3 dB bandwidth for the main low frequency lobe is significantly reduced for a single turn sensor coil (see Fig. 2a), but for the five turn coil (Fig. 2b), this bandwidth loss is not observed. Thus, for multiple turn current sensor coils, Eq. (4) can be used to estimate bandwidth regardless of axial displacement. At the higher frequencies, Faraday rotations will also occur in the fiber even if the coil is entirely outside the current conductor,  $X_1/R > 1$ . The sensor frequency response has resonant characteristics that resemble those in Fig. 2 only with the low frequency lobe missing (no d.c. response).

### Noncircular Cross Section

If the coil cross section is flattened to resemble that depicted in Figs. 1b and 1c, a different high frequency resonant response results. In the extreme case of a highly elongated coil with a fully displaced conductor (Fig. 1b), a 'delta function' type behavior results as the region of magnetic field interaction in the fiber is reduced to an extremely small distance. Frequency responses exhibit resonances with relative peak magnitudes approaching 1.0 and with symmetry about each peak. Center frequencies of the resonances are again only dependent on the single turn light transit time.

The bandwidth of this type of sensor coil does show some increase over that of Eq. (4). In theory, if the fiber only makes a single pass near the conductor and the interaction length is short, a nearly infinite bandwidth is approached. With two turns, or passes by the conductor, a 13% bandwidth increase is theoretically possible. For larger numbers of coil turns, the bandwidth quickly returns to that described by Eq. (4).

The elongated coil in Fig. 1c has the conductor symmetrically placed in the coil cross section. High frequency response is characteristic of a double 'delta function' interaction since two close approaches are made between the fiber and conductor during each coil turn. Corresponding resonances are shifted in frequency.

### III. EXPERIMENTAL VERIFICATIONS

A basic polarimetric test system was assembled to measure the high frequency Faraday rotation in noncentered and elongated sensor coils. The system used a 50 $\Omega$  expanded airline transmission cell<sup>6</sup> to contain the coils and provide for a TEM field exposure. The generation of high frequency currents was greatly simplified using the cell. Maximum test currents were  $\sim 0.45$  A<sub>rms</sub> which produced rotations of  $\leq 100$   $\mu$ rad in the singlemode fiber.

A 10 turn, 9.6 cm diameter sensor coil was wound from twisted and rejacketed low birefringence singlemode fiber.<sup>7</sup> It was placed in the coaxial test cell volume with a maximum available displacement,  $X_1/R = 0.38$ . The frequency response is plotted in Fig. 3. A first high frequency resonance occurs near 675 MHz; this is predicted theoretically using Eq. (2) and verified experimentally. The measured magnitudes shown in Fig. 3 agree well with the theory except for some discrepancy near the peak of the resonance.

The elongated sensor coil concept was tested using a 10 turn coil of the same twisted fiber with each turn being two meters in length. Only a small portion of each fiber loop was inside the cell; the remainder was left outside where no Faraday interaction could occur. In predicting the response of this sensor system, the integral in Eq. (2) is evaluated over the short fiber section inside the cell and the total rotation is found by summing over the 10 loops. The results of this test are plotted in Fig. 4 for frequencies below 500 MHz. Resonances occur at intervals of 101 MHz, each with a bandwidth of  $\sim 4.5$  MHz. Excellent agreement between theoretical and measured values is observed for these resonances. Although additional points are not plotted, measured magnitudes below 100 MHz follow all the intermediate lobes and nulls as predicted.

### IV. DISCUSSION AND CONCLUSIONS

From computations and measurements on these fiber current sensors, it is determined that coil cross section and conductor placement in the coil has essentially no effect on the sensor bandwidth if multiple turn coils ( $N \geq 5$ ) are used. These coil configuration changes, however, do produce resonances at higher frequencies where the response sensitivity is now adequate for good current detection. Sensitivity is determined by several coil properties: the number of fiber turns, coil-conductor axes displacement, and the eccentricity of the coil cross section. The center frequency of the resonances is a function of only the fiber length in a single turn, while the resonance bandwidth is determined by total fiber length.

The resonances observed in Fig. 4 do not continue indefinitely in frequency but roll off predictably. An enveloping function with a bandwidth determined by the short, but finite, fiber interaction length limits response at high frequencies. This envelope function is approximated by Eq. (3) with appropriate choice of  $\tau$ . Thus, the advantages of higher frequency sensing using this technique are not unlimited.

In summary, theoretical and experimental efforts have examined several aspects of the high frequency response in Faraday effect fiber current sensors. Coil cross section and conductor placement have been shown to affect response magnitude. Resonances at selected higher frequency bands can be produced by manipulating sensor coil geometry and then exploited for current sensing applications.

### REFERENCES

1. S. C. Rashleigh and R. Ulrich, "Magneto-optic current sensing with birefringent fibers," *Appl. Phys. Lett.*, **34**, pp. 768-770 (1979).
2. A. Sommerfeld, *Electrodynamics*, pp. 177-193 (Academic Press, N. Y., 1952).
3. A. D. Kersey, F. Bucholtz and A. Dandridge, "Sensitivity-bandwidth limitations in optical-fiber Faraday-rotation current sensors," *Int'l. J. Optoelectronics*, **3**, pp. 323-332 (1988).
4. R. W. Cernosek, "Travelling wave Faraday effect fiber current sensors," *Proc. 7th Optical Fibre Sensors Conference*, pp 72-76 (1990).
5. K. P. Jackson, S. A. Newton, B. Moleshi, M. Tur, C. C. Cutler, J. W. Goodman and H. J. Shaw, "Optical fiber delay-line signal processing," *IEEE Trans. Microwave Theory Tech.*, MTT-33, pp. 193-209 (1985).
6. R. W. Cernosek, "Expanded coaxial transmission cells for electromagnetic testing," *Sandia National Laboratories Technical Report*, SAND91-0768 (1991).

7. M. S. Maklad, P. E. Sanders, E. Dowd, A. Kuczma, "Single mode fibers for sensing applications," *Proc. SPIE*, 718, pp. 97-109 (1986).

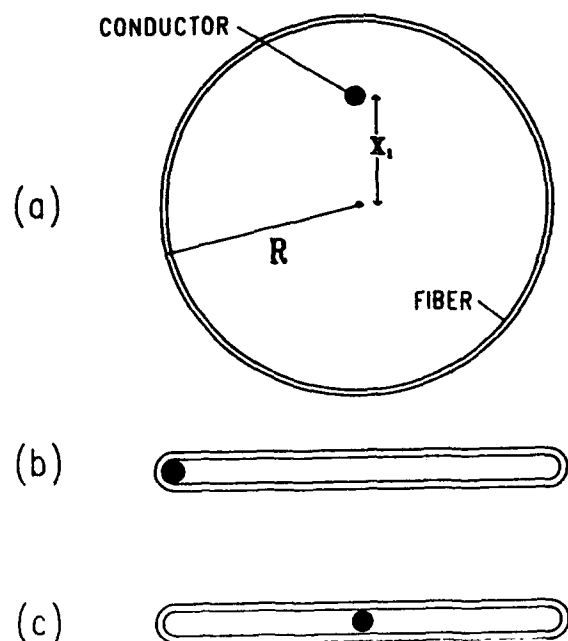


**Fig. 1** Three coil configurations for fiber current sensors.

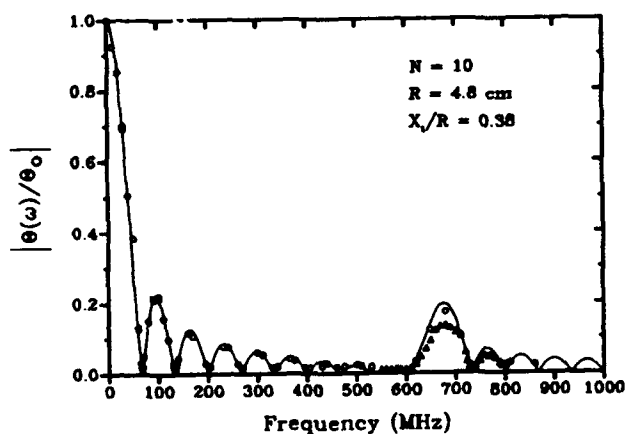


**Fig. 3** Theoretical (solid curve) and measured (two sets of points) Faraday rotation frequency response for a noncentered current sensor coil.

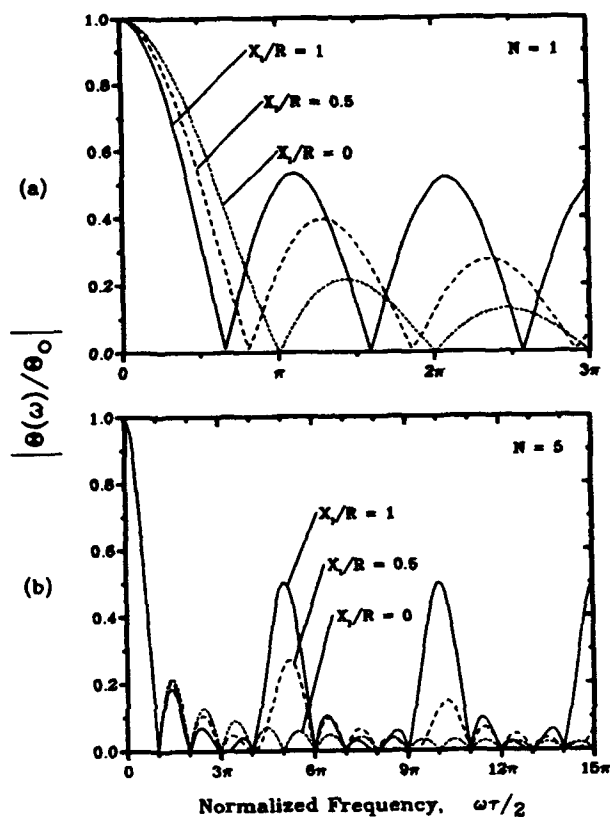


**Fig. 2** Computed relative Faraday rotation frequency response for a current sensor with displaced coil and conductor axes.

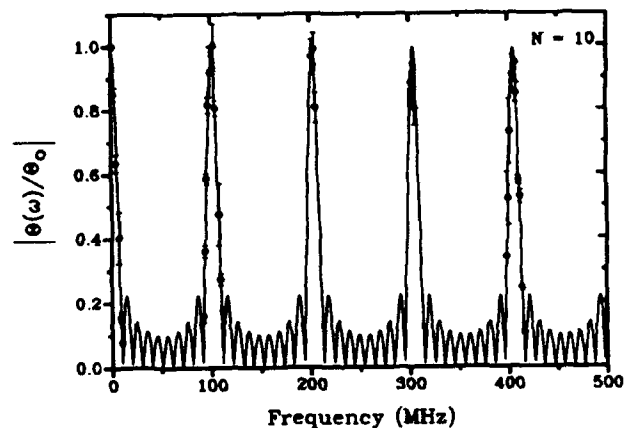


**Fig. 4** Theoretical (solid curve) and measured (points) Faraday rotation frequency response for an elongated coil with two meters of fiber in each turn.

## F3.5 Stabilized Sagnac Optical Fiber Current Sensor Using One Phase And Two Amplitude Modulations

P.-A. Nicati and Ph. Robert  
Laboratoire de Métrologie  
Swiss Federal Institute of Technology of Lausanne  
CH-1015 LAUSANNE (Switzerland)

### **Abstract :**

Novel design of a Sagnac optical fiber current sensor using a LiNbO<sub>3</sub> phase modulator and a special signal processing allowing both measurement and compensation of the linear birefringence in the fiber.

### **Introduction :**

The Sagnac interferometer has received a great deal of interest with the development of fiber optic gyroscopes. Its use as a current sensor is less known but nevertheless very attractive [1], [2], [3]. In addition to the well known interesting characteristics displayed by the optical fiber sensors (large bandwidth, high sensitivity, compact size, remote sensing ability and high galvanic isolation) this structure exhibits high sensitivity due to the interferometric techniques together with an absolute measurement ability as a result of its reciprocity properties.

The main factor which limits the performances of the Faraday optical fiber current sensors is the impossibility to manufacture a fiber coil free from linear birefringence. With ultra low-bi fiber the intrinsic linear birefringence is almost reduced to zero but the bending of this fiber to form the sensing coil can induce a non acceptable linear birefringence [4]. The most successful method of annealing the bend-induced birefringence is presented in ref. [5]. It allows to realize small multiturn fiber coils. However a residual linear birefringence of about 30-50 deg remains. The use of spun elliptically-birefringent fibers as circular-polarization-preserving fiber is no longer the ideal solution because of its temperature dependence [6].

In this paper a modified Sagnac current sensor allowing a compensation of the linear birefringence effects in the optical fiber is presented. The compensation is based on the measurement of the contrapropagating signals amplitudes before the interference occurs. This procedure relies on the fact that these signals contain information on the effects of the linear birefringence on the measured Faraday phase shift.

The output signal is biased using a classical phase modulation [7] performed by a LiNbO<sub>3</sub> guided-wave phase modulator working at about 2,5 MHz corresponding to the relatively short length of fiber used (about 40 m). A double amplitude modulation is also performed to avoid errors in the compensation procedure given by high Fresnel reflections at the surface of LiNbO<sub>3</sub> phase modulator ( $10\log(P_{in}/P_{refl.}) \approx 11\text{dB}$ ).

### **Theory :**

The principle of the stabilized Sagnac current sensor has been set out in a previous publication [8] (without phase and amplitude modulation), it corresponds to the set-up shown in fig. 1. The interference intensity  $I_3$  measured in the reciprocal output port is a function of the non-reciprocal phase shift induced by the Faraday effect in the Sagnac loop. Unfortunately  $I_3$  depends also on the linear birefringence in the fiber because the resultant of these two effects depends on their local vectorial addition and on the integration effect occurring along the fiber. The combination of the Faraday phase-shift and the linear birefringence is then non-linear. Physically the linear birefringence effect acts like a coupling of power between the two orthogonal circularly polarized modes. Thus by measuring the power remaining in the useful modes before the light beams interfere ( $I_1$  and  $I_2$  on the fig. 1) it is possible to compensate the output interference intensity  $I_3$  (see eq. (2)) against this effect.

When a non reciprocal time dependant phase shift  $\varphi_m(t) = \varphi_0 \sin(2\pi f_m t)$  is applied in an asymmetric manner in the Sagnac loop, the interference intensity  $I_3$  at the reciprocal output port is given by :

$$I_3 = a_1 I_1 + a_2 I_2 + 2a_3 \sqrt{I_1 I_2} \cos \left( 2\varphi_0 \sin \left( 2\pi f_m \left( \frac{\Delta\tau}{2} \right) \right) \cos \left( 2\pi f_m \left( t - \frac{\tau_1 - \tau_2}{2} \right) \right) + \Delta\varphi_{nr} \right) \quad (1)$$

$a_i$  = factors which depend on reflection and transmission coefficients of the optical elements as well as on the electric amplification

$I_1, I_2$  = light intensities before the interference occurs

$\tau_1, \tau_2$  transit times between the coupler and the modulator for the two contra-propagating waves,  $\Delta\tau = \tau_1 - \tau_2$

$\Delta\varphi_{nr}$  = non reciprocal phase shift induced by the Faraday effect in the presence of linear birefringence

Let  $\tilde{I}_3$  be the first harmonic of  $I_3$  obtained by electric filtering :

$$\tilde{I}_3 = \text{const} \cdot \sqrt{I_1 I_2} \cdot J_1(\varphi_m(\Delta\tau)) \sin(\Delta\varphi_{nr}) \quad (2)$$

$$\text{with } \varphi_m(\Delta\tau) = 2\varphi_0 \sin(\pi f_m \Delta\tau) \quad (3)$$

$J_1(\varphi_m(\Delta\tau))$  is the Bessel function of the first kind of order one which reaches its maximum for  $\varphi_m(\Delta\tau) = 1.84$  rad. The maximum efficiency of the modulation is reached for  $\sin(\pi f_m \Delta\tau) = 1$  which corresponds to  $f_m = 1/(2\Delta\tau)$ . In this case the two contrapropagating waves are in opposite phase conditions when they interfere.

The light intensities  $I_1$  and  $I_2$  depend on the Faraday phase shift  $F$ , the reciprocal circular birefringence  $T$  and the linear birefringence  $\delta$ . The basic idea of the compensation scheme lies in the fact that the expression  $\tilde{I}_3 / \sqrt{I_1 I_2}$  depends only on the non reciprocal phase shift  $\Delta\varphi_{nr}$ .

### Experimental set-up

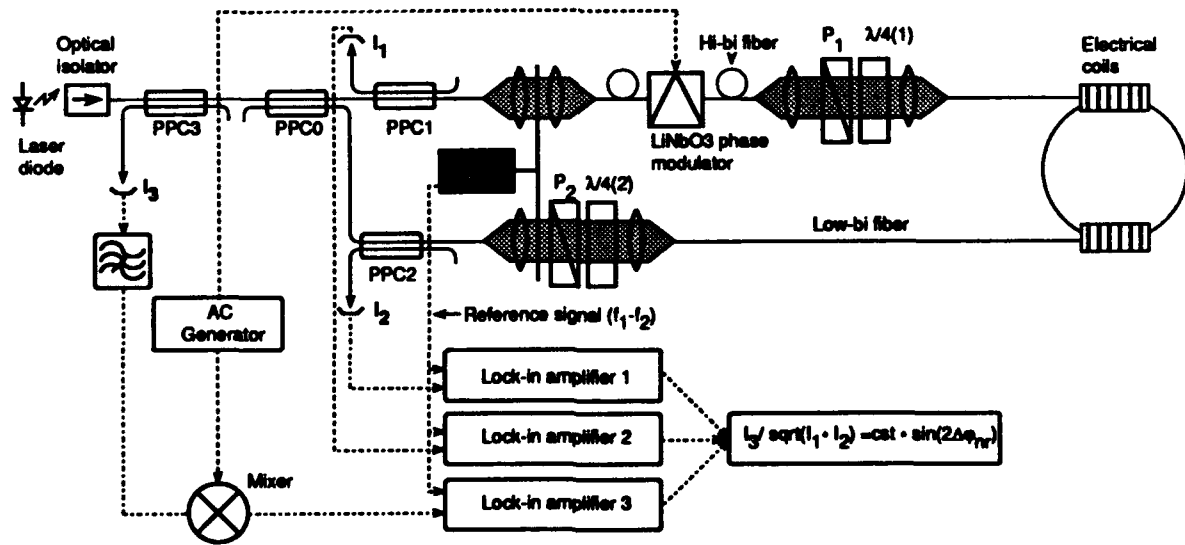


Fig. 1

The system is designed in order to keep the light linearly polarized in the whole system except in the sensing fiber. There are three main reasons for that :

- the effect of external perturbations is minimum;
- no polarization change occurs when light beams are split or recombined by the polarization preserving coupler (PPC);
- LiNbO<sub>3</sub> "x-cut" guided-wave phase devices are highly birefringent.

Polarization maintaining components (coupler, fiber) are used to keep the light beams linearly polarized. In order to remain in a strictly single mode configuration, the polarizers axis has to match one of the axes of the polarization preserving fiber.

The source is a 830 nm AlGaAs laser diode isolated against returned light by an optical Faraday isolator. The sensing optical fiber is made with 11 turns of low-bi fiber and a 45 kA electrical current is simulated using four coils with a total of 2287 spires. The modulation frequency is then fixed at 2.5 MHz by the condition  $f_m = C_0/2nl$  where  $C_0$  is the velocity of light in vacuum,  $n = 1,463$  is the refractive index of the fiber core and  $l = 41$  m is the fiber length in the Sagnac loop.

The problems encountered by using a LiNbO<sub>3</sub> phase modulator are the high insertion loss (~ 6 dB) and the high Fresnel retro-reflections due to the refractive index difference between silica fibers and LiNbO<sub>3</sub>. If the high insertion loss is not very critical, in contrast the retro-reflections worsen the compensation procedure in an unacceptable manner because they lead to measure the sum of the signal going to interfere plus the retro-reflected light. A double amplitude modulation at  $f_1$  and  $f_2$  obtained by the chopper shown in fig. 1 is applied to overcome these problems and to get a "quasi-reciprocity" in the compensation procedure. To achieve this double modulation the optical beam is chopped twice by both passing through the outer row of slots on the wheel and through the inner row and vice versa for the beam which propagates in the opposite direction. The requirement of "quasi-reciprocity" is therefore fulfilled by performing a lock-in detection at the frequency  $(f_1 - f_2)$  for all the measured intensities.

## Results :

The measured intensities  $I_3$  and  $I_1$  are plotted versus the electric current  $I_{el}$  in fig. 2 and 3 for three values of  $\delta$  ( $\delta = 70, 100$  and  $130$  deg). In practice,  $\delta$  is varied by applying a transverse mechanical stress on the fiber.

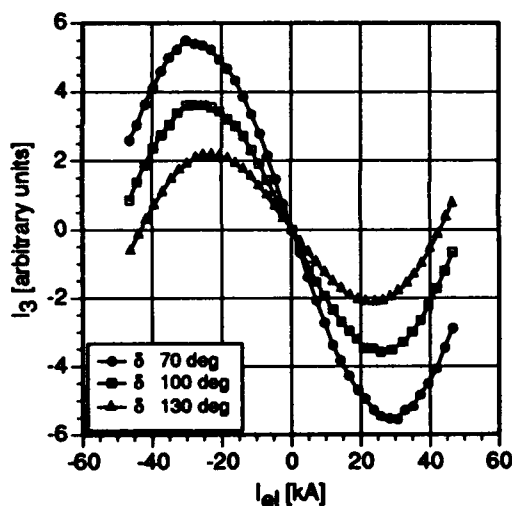


Fig. 2

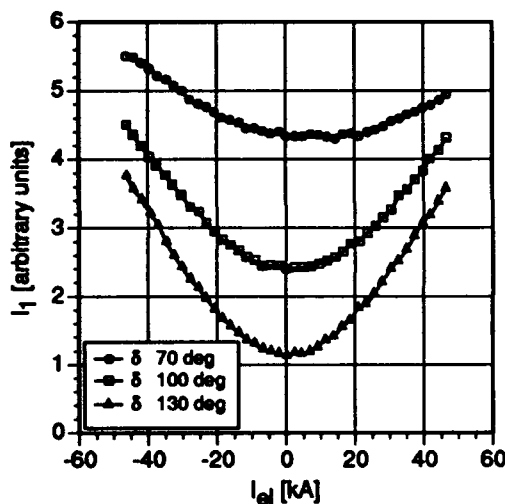


Fig. 3

On fig. 2 one can observe that both the amplitude and the period of the transfer function depend on  $\delta$ . The amplitude variations are due to a change in the intensity of the two modes going to interfere. This is illustrated in fig. 3 where the intensity  $I_1$  is plotted versus  $I_{el}$ . The corresponding graph for  $I_2$  is identical because the axes of the fibers have been oriented in order to obtain a reciprocal birefringence  $T$  equal to zero. If this is not the case, the curves are shifted to right or left for  $I_1$  and to left or right for  $I_2$  depending on the sign of  $T$ . In the presence of linear birefringence  $\delta$ , the reciprocal circular birefringence modifies also the interference intensity  $I_3$ . But this effect is automatically cancelled by the compensation procedure.

The corrected interference intensities  $I_3(\delta, \Delta\phi_{nr})/\sqrt{I_1 \cdot I_2}$  are plotted versus  $I_{el}$  in fig. 4 for the three values of  $\delta$ . These curves present a normalized amplitude which depends no more on the variations of :

- the intensity of the light source;
- the coupling coefficients of the light into the fiber
- the circular birefringence together with the linear birefringence
- the power coupling from the useful mode into the rejected mode due to the linear birefringence



In these measurements a large variation of  $\delta$  (60 deg) was applied in order to show how the non-reciprocal phase shift varies with  $\delta$ . In practice the sensor has to be designed in order to work in the linear part of the sine curve. In this case the effect of the linear birefringence is to change the slope of the transfer function (obtained by a linear fit). The most efficient compensation is obtained by deducing the mean value of  $\delta$  from the measurements of  $I_1$  and  $I_2$  and by making the suitable correction of the slope of the transfer function.

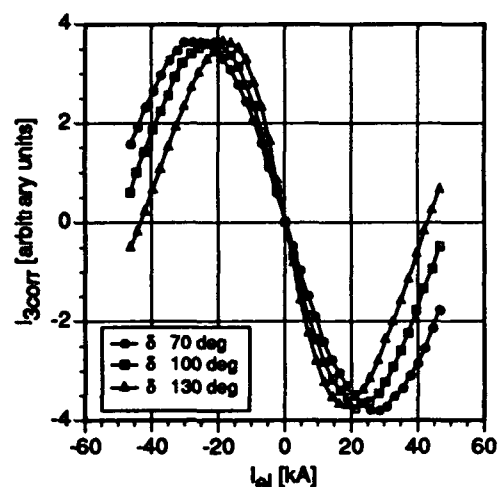


Fig.4

### Conclusion :

A new design of a stabilized optical fiber current sensor using a Sagnac interferometer has been built and tested with different values of linear birefringence in the sensing fiber. The main characteristics of this design are : First it compensates all the effects modifying the intensity of the interfering beams such as source variations, losses or mode coupling. Secondly the whole sensor except the sensing fiber is built in a polarization preserving technology in order to minimize the influence of external perturbations, to avoid polarization problems when the light is divided or recombined by the couplers and to be compatible with LiNbO<sub>3</sub> integrated optic technology. A particular attention is given to the signal processing. A phase modulation using a LiNbO<sub>3</sub> guided-wave modulator is performed in order to have the output signal at the quadrature point. A double amplitude modulation is also performed in order to solve the problem of high Fresnel retro-reflections at the interfaces between the silica fiber and the LiNbO<sub>3</sub> and to guarantee a quasi-reciprocity even in the compensation procedure.

### References :

- [1] H.J. Arditty, Y. Bourbin, M. Papuchon, and C. Puech, "Current sensor using the state-of-the-art fiber-optic interferometric techniques", Tech. Digest, Third Int. Conf. Int. Optics and Opt. Fiber Commun., San Francisco, 1981.
- [2] L. R. Veaser and G. W. Day, "Faraday Effect Current Sensing Using a Sagnac Interferometer with 3x3 Coupler", 7th Optical Fiber Sensor Conference, Sidney, Dec 2-6, 1990.
- [3] P. A. Leilabady, A. P. Wayte, M. Berwick, J. D. C. Jones and D. A. Jackson, "A pseudo-reciprocal fibre-optic Faraday rotation sensor: current measurement and data communication applications" Opt. Communications, vol. 59, pp 173-176, 1986.
- [4] R. Ulrich, S. C. Rasleigh and W. Eickhoff, "Bending-induced birefringence in single mode fiber", Opt. Lett., Vol. 5, pp 273-275, 1980.
- [5] G. W. Day and S. M. Etzel, "Annealing of Bend-Induced Birefringence in Fiber Current Sensors", 5th Int. Conf. Int. Opt. and Opt. Fiber Commun. and 11th ECOC, Venice, 1985.
- [6] R. I. Lamming and D. N. Payne, "Electric current sensors employing spun highly birefringent optical fibers", Journal of Lightwave Technology, vol. 7, no 12, pp 2084-2094, 1989.
- [7] H. J. Arditty, Ph. Graindorge et H. C. Lefevre, "Gyromètre à fibre optique : principes et technologie", Revue tech. Thomson CSF, Vol. 15, no 3, 1983.
- [8] P.-A. Nicati and Ph. Robert, "Stabilized current sensor using Sagnac interferometer", J. Phys. E, Sci. Instrum. Vol 21, pp 791-796, 1988.

## **F4.1**

# **A High Resolution Three-Axis Fiber Magnetometer**

**D.M.Dagenais<sup>\*</sup>, K.P.Koo<sup>\*</sup>, F.Bucholtz**

Optical Sciences Division, Code 6570, Naval Research Laboratory,

Washington, DC 20375

<sup>\*</sup> Permanent address: SFA Inc., Landover, MD 20785

A vector magnetometer is typically configured as a three-axis device to measure the field along three orthogonal directions. Magnetostrictive fiber optic magnetometers [1] operate as a vector device, sensing the component of magnetic field along a particular direction. Previously we demonstrated a low resolution ( $10^{-2}$  Gauss/ $\sqrt{\text{Hz}}$ ) three-axis magnetometer for heading sensor applications [2]. In this work, we designed and tested a three-axis fiber-optic magnetic sensor with a resolution of  $10^{-5}$  Gauss/ $\sqrt{\text{Hz}}$  below 1 Hz. An important application of this device is the remote sensing of ambient low-frequency magnetic noise. We present the low-frequency resolution and demonstrate the low cross-talk and high directionality of such a device, as well as its temperature stability between  $0^{\circ}$  and  $55^{\circ}$  C.

The device consists of three magnetostrictive transducers bonded onto a single fiber Mach-Zehnder interferometer operating singlemode at 1.3  $\mu\text{m}$ , as seen in figure 1. Each compact transducer comprises two transversely annealed strips (5 cm x 5 mm x 25  $\mu\text{m}$ ) of Metglas 2605 S2, each bonded to 20 passes (1m) of fiber and mounted on a beam with fixed boundaries. The transducers are each inserted into a solenoid (to provide the dither magnetic field  $h \cos \alpha$ ), and finally positioned in three orthogonal, planar slots (x,y,z) in a Delrin block.

The frequency response of the transducers normalized to the magnetic dither field  $h$  shows a broad resonance with peaks near 32 kHz and 48 kHz. The magnetostriction coupling parameter at resonance (48 kHz) for the three transducers varies between 2 and  $4 \times 10^{-6}$  Gauss $^{-2}$  (see figure 5 and discussion below).

The cross-talk between transducers was measured by splicing only the center (y) transducer into the fiber interferometer and measuring the strain while all transducers were dithered at their respective frequencies with magnetic fields of same amplitude. The dither frequencies were chosen to lie off resonance, offering higher stability at the expense of somewhat decreased responsivity. The cross-talk, defined as the ratio of the strain at the orthogonal frequency (x or z) to the strain at the center frequency (y), is less than -80 dB, as calculated from figure 2. This value is acceptable for high resolution vector magnetometers. Sidebands of the y carrier correspond to power lines and harmonics.

The directionality of the transducers was obtained by splicing all three transducers into the single interferometer and placing the sensor at the center of a three-axis test coil. Low frequency test signals were applied on each test coil axis. The antenna pattern of transducer y, obtained by rotating the sensor inside the test coil, is shown in figure 3, where the dashed line shows the expected cosine/sine response to a longitudinal / transverse field. The directionality, defined as the ratio of the transverse to the longitudinal field response, for equal strength fields, is in the range -90 to -100 dB as calculated from figure 4, indicating the excellent intrinsic directionality of the transducers.

The resolution was measured by phase sensitive detection with the sensor inside a mumetal shield and operating in a magnetic closed loop. We obtained a minimum detectable field of  $\approx 3 \times 10^{-6}$  Gauss/ $\sqrt{\text{Hz}}$  at 0.5 Hz, corresponding to a phase shift  $\approx 1$   $\mu\text{rad}/\sqrt{\text{Hz}}$ . The phase resolution of the interferometer was  $\approx 0.3$   $\mu\text{rad}/\sqrt{\text{Hz}}$  in the range of dither frequencies. The limiting "1/f" noise results from a combination of upconverted low-frequency intensity noise and current drift in the feedback coil drivers.

Preliminary tests of the temperature dependence of the magnetometer were performed. The sensor was inserted into an environmental chamber [3] and cycled between 55 $^{\circ}$  C, and 0 $^{\circ}$  C. The normalized frequency response of the y transducer shown at 0 $^{\circ}$ , 25 $^{\circ}$ , and 55 $^{\circ}$  C in figure 5, exhibits no significant change with temperature.

In conclusion, we have described the design of a three-axis fiber magnetometer demonstrating low cross-talk (< - 80 dB), high directionality (< - 90 dB), and resolution of  $3 \times 10^{-6}$  Gauss/ $\sqrt{\text{Hz}}$  at 0.5 Hz.

**Acknowledgments:** The authors wish to acknowledge OCNR for partial funding of this work and to thank J.A. Mc Vicker for field-annealing the magnetostrictive strips.

## References:

- [1] F. Bucholtz, D.M. Dagenais, K.P. Koo, and S.T. Vohra, "Recent developments in fiber optic magnetostrictive sensors", SPIE Vol. 1367, *Fiber Optic and Laser Sensors VIII*, 226-235 (1990)
- [2] F. Bucholtz, J.A. McVicker, D.M. Dagenais, K.P. Koo and A. Dandridge, "Three-axis, optically-powered fiber optic magnetometer", 1988 LEOS Conference Proceedings, 279-280 (1988)
- [3] Temperature tests performed at the laboratory of Optical Technologies, Inc., Herndon, VA.

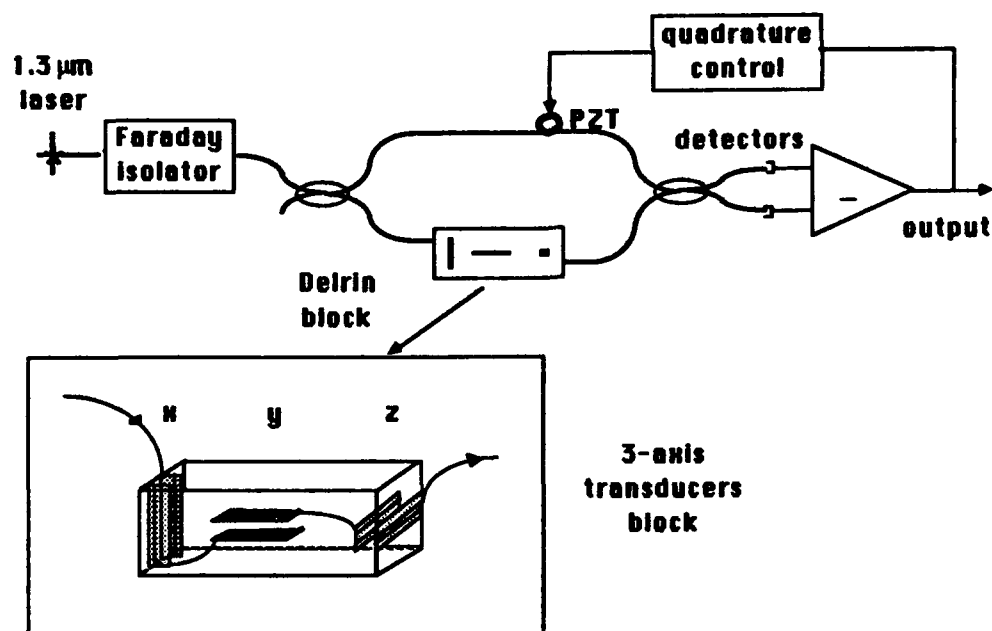


**Figure 1-** Schematic of the dual-strip transducer configuration and the magnetometer system.

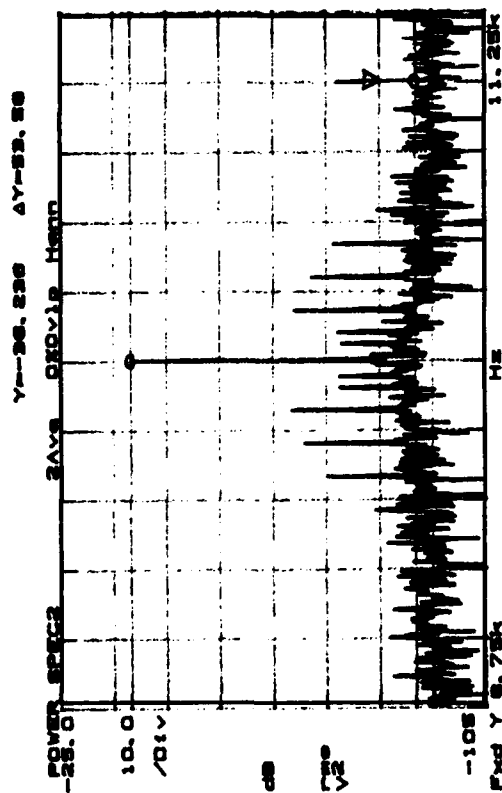


Figure 2-Cross-talk measurement.  $h_y = 88$  mG rms @ 10 kHz,  $h_x$  or  $h_z = 2$  G rms @ 11 kHz

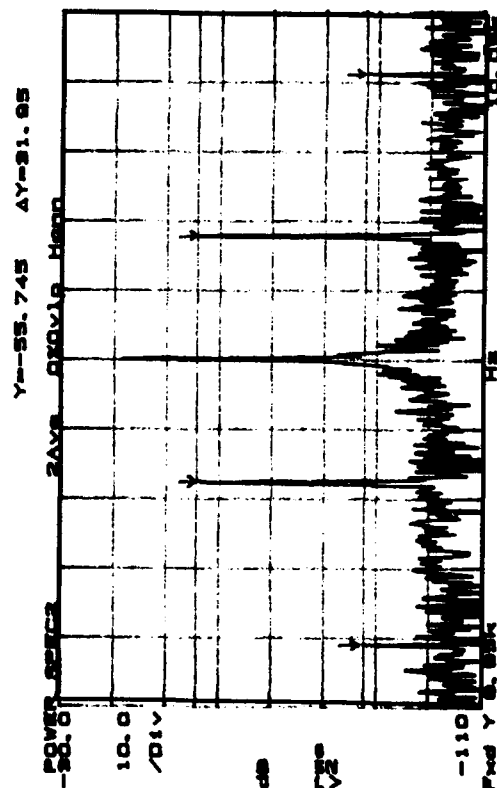


Figure 4- Directionality of the y transducer. Carrier is 80 mG rms @ 10 kHz, test fields are 1 mG rms @ 18 Hz (longitudinal), and 2.3 G rms @ 41 Hz (transverse).

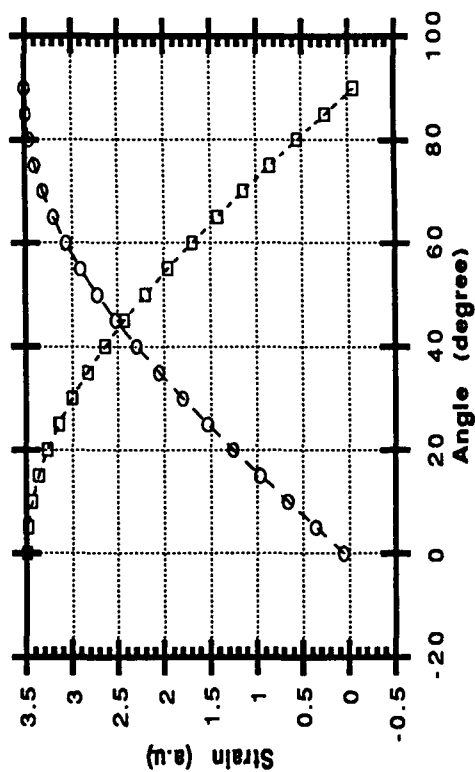


Figure 3- Antenna pattern of y transducer ( $h = 80$  mG rms @ 15 kHz).  $\square$  = longitudinal field (10 mG rms @ 10 Hz)  $\circ$  = transverse field (10 mG rms at 6.5 Hz) and dashed line is the cosine fit.

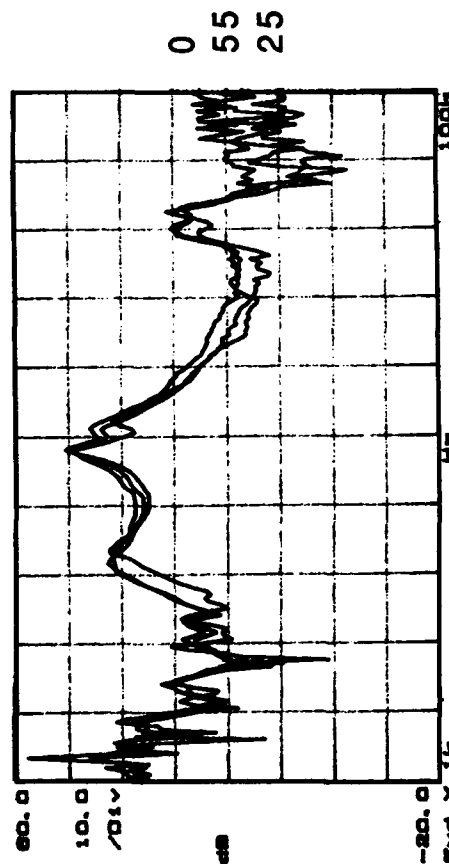


Figure 5- Normalized frequency response of y transducer at  $0^\circ\text{C}$ ,  $25^\circ\text{C}$ ,  $55^\circ\text{C}$ .

## An Optical Fiber Alternating-Gradient Magnetometer

L. C. Bobb and H. D. Krumboltz  
Naval Air Development Center  
Warminster, PA 18974

and

P. M. Shankar  
Department of Electrical & Computer Engineering  
Drexel University  
Philadelphia, PA 19104

Biconically tapered single-mode fibers have been used for a number of applications that involve sensors. These applications have been based on the sensitivity of the optical throughput of the stretched fiber to any change in the stretched (tapered) region. Most of the applications arise from having the stretched region surrounded by a material whose characteristics can be altered by an external disturbance. Recently, the authors have shown that the optical throughput of the stretched region (the waist) is extremely sensitive to bending.<sup>1,2</sup>

The fibers used in these experiments were made by Lightwave Technologies, Inc. These single-mode fibers (F1506-C) have a 4.2- $\mu\text{m}$ -diameter core, a 125- $\mu\text{m}$  outer diameter, a core index of 1.462, and a cladding index of 1.458. The fibers in our studies were heated by gas flame, electrical discharge, and by a resistively heated furnace. The single-mode fiber used in this study was stretched by heating in a 1-cm-wide U-shaped platinum ribbon furnace that was closely coupled to the fiber. A tension of 5-10 g was applied to one end of the fiber while the other end was fixed. Elongation occurred when the fiber softened. The amount of elongation was monitored, and, when the overall length of the fiber had increased by 1.5 cm, the temperature was reduced and the stretching process was halted. During this procedure the fiber was excited by a He-Ne laser source (0.6328  $\mu\text{m}$ ). The optical throughput was monitored during the stretching process. The power received varied by ~ 20% over 5 or 6 cycles as the fiber was elongated. Such oscillatory behavior of the optical power as a function of the taper length has been reported previously and is consistent with our theoretical results.

The above stretching process yields a biconically tapered region with a waist diameter of 20  $\mu\text{m}$  and a length of approximately 2.5 mm. Some asymmetry in the increasing and decreasing tapers was noted. This is a result of the stretching procedure employed, in which the fiber was kept fixed at one end while the other end was being subjected to tension. Several experiments were performed in which tension was applied to both ends of the optical fiber, and symmetrical tapers were fabricated. However, the behavior of these fibers subjected to the bending was nearly the same as that of the asymmetrically

tapered fiber. Once the desired taper was realized, the fiber was removed from the U-shaped platinum ribbon furnace and placed into a bending fixture in which the tapered fiber was brought into contact with two fixed glass rods and the fiber waist was centered at a micrometer driven capillary tube. A piezoelectric element (PZT) was used for inducing very small displacements in the fiber waist. Large displacements were provided by the micrometer driven capillary tube. The bending angle was calculated by measuring the displacement. The optical power transmitted through the core of the fiber was measured. The relative optical power in the cladding was measured at a mode stripper. The results of this measurement are shown in Fig. 1 along with the theoretical results. The optical throughput (theoretical) was calculated for the tapered fiber profile used in this experiment. In the model, the lengths of the contracting and expanding tapers were assumed to be different; and, the tapers were considered to be linear. The tapered region was modeled using a stepwise linear approximation. The total number of steps used in the calculation was 80, with 40 steps each in the contracting and expanding region of the taper, described by  $V_{\text{core}}(z) < 1$ . The number of minibends used was 20 and the minibends were distributed in the region within  $V_{\text{core}}(z) < 1$ . There were eight minibends in the waist region and six each on the expanding and contracting regions of the tapers. Seven modes,  $HE_{11}$ ,  $HE_{12}$ ,  $EH_{11}$ ,  $HE_{21}$ ,  $EH_{21}$ ,  $TM_{01}$ , and  $TM_{02}$ , were used in the calculation. The optical power in the core goes through a series of maxima showing strong oscillations. When the power in the core is a minimum, the power in the cladding is a maximum. This shows that most of the power is exchanged and not radiated. For small angles, there is good correlation between theory and experiment.

From Fig. 1 it can be observed that the maximum sensitivity to displacement (bend) occurs near  $2^\circ$ . For measurements taken near the mechanical resonance of the fiber, displacements as small as 0.015 nm were detectable. For the magnetometer measurements, the fiber was bent to the maximum sensitivity position after the Metglas sphere was fixed to the waist.

The experimental arrangement for measuring magnetization is shown schematically in Fig. 2. The biconically tapered single-mode optical fiber was centered between the poles of a high field electromagnet. The 25- $\mu\text{m}$ -diameter ferromagnetic sphere was amorphous  $\text{Fe}_{7.5} \text{Co}_{67.5} \text{Si}_{15} \text{B}_{10}$  with a saturation moment of  $3.7 \times 10^{-6} \text{ emu}$ . The light source was a He-Ne laser and the detector was a silicon diode. The detector output was fed into a lock-in amplifier tuned to the optical fiber resonance frequency of 1.378 kHz. The gradient coil was driven at this same frequency. The gradient field at the sample was approximately 20 Oe/cm. The force on the ferromagnetic sphere along the x-direction from the interaction of the gradient field ( $dh_x/dx$ ) and the magnetic moment ( $m_x$ ) is

$$F_x = m_x dh_x/dx,$$

where  $m_x$  depends on the applied dc field  $H_x$ . The gradient coil was rigidly attached to the pole face to avoid coil motion and the associated noise.

A plot of the optical power output at 1.378 kHz from the biconically tapered single-mode optical fiber vs. dc magnetic field is shown in Fig. 3. The ac modulation signal arises from the displacement of the fiber waist at the 1.378 kHz frequency. For these small displacements the output is linear. A calculation of the response of the system as a function of the force on the fiber waist has not been done to date; however, the measured response appears to be linear. Therefore, the plot in Fig. 3 also represents the magnetization of the ferromagnetic sphere as a function of dc magnetic field. Measurements were made on the same sphere at a signal-to-noise ratio of several hundred; this corresponds to a sensitivity of at least  $2 \times 10^{-8}$  emu. This technique is about 1000 times more sensitive than a conventional vibrating sample magnetometer and it is comparable to a recently developed piezoelectric technique.<sup>3</sup>

### References

1. L. C. Bobb, P. M. Shankar and H. D. Krumboltz, J1. Lightwave Technol 8, 1084 (1990).
2. P. M. Shankar, L. C. Bobb and H. D. Krumboltz, J1. Lightwave Technol 9, 832 (1991).
3. P. J. Flanders, J. Appl. Phys. 63, 3940 (1988).

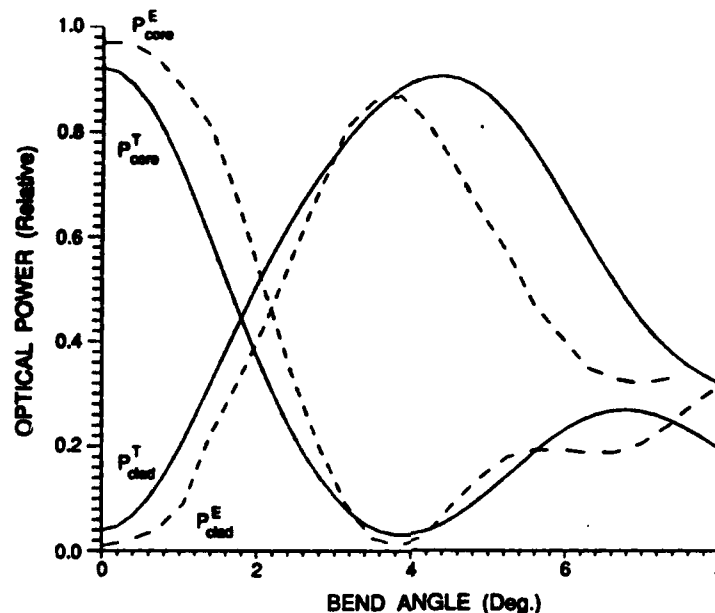


Fig. 1. The relative power in the core ( $P_{core}$ ) and cladding ( $P_{clad}$ ) are plotted as a function of the bend angle. The dashed curve is experimentally derived and the solid is theoretically derived.



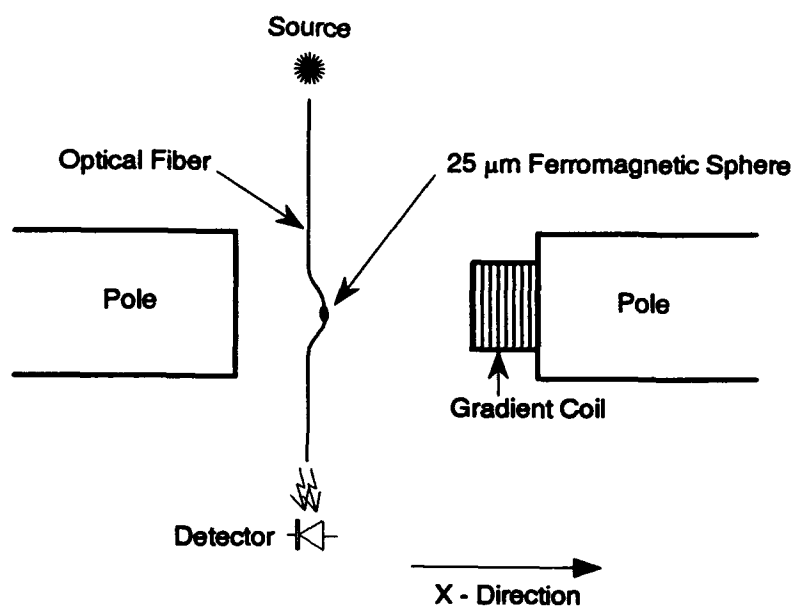


Fig. 2. The optical fiber alternating-gradient magnetometer is shown schematically.

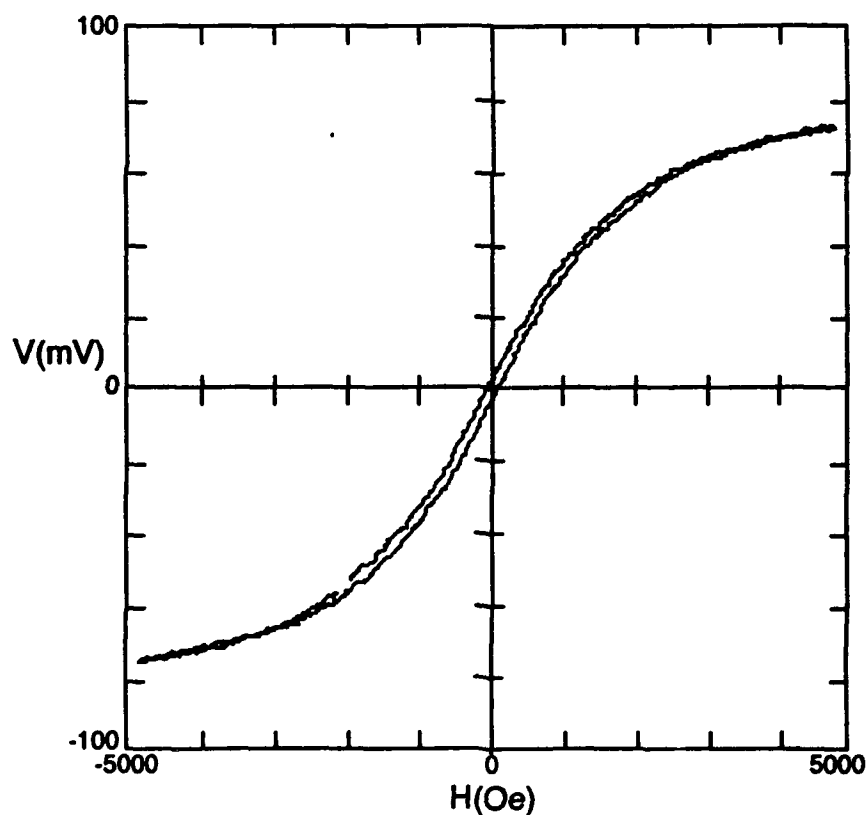


Fig. 3. The magnetization curve of the 25- $\mu\text{m}$ -diameter amorphous  $\text{Fe}_{7.5}\text{Co}_{67.5}\text{Si}_{15}\text{B}_{10}$  sphere with a saturation moment of  $3.7 \times 10^{-6} \text{ emu}$  is displayed.

### F4.3

## Remote Fiber Optic AC Magnetometer A.R. Davis, S.S. Patrick, A. Dandridge, F. Bucholtz

Naval Research Laboratory Code 6570 Washington DC 20375

\* Permanent Address: University Research Foundation, Greenbelt MD 20770

\*\* Permanent Address: Virginia Polytechnic Institute, Blacksburg VA 24061

Fiber optic AC magnetic field sensors have been reported utilizing the Faraday effect [1], the magnetostrictive effect [2] and the Lorentz force effect [3]. In general, these sensors have exhibited either large bandwidth and low resolution or medium-to-high resolution but with strong in-band variations in the frequency response. In some cases active elements were required in the transducer either for magnetic biasing or for interferometer stabilization. In this paper we describe a magnetostrictive sensor for the measurement of AC magnetic fields. The transducer is totally passive in nature, shows flat ( $\pm 3$  dB) response over the frequency range 1 kHz - 45 kHz, and exhibits resolution of  $1.8 \times 10^{-7}$  G/ $\sqrt{\text{Hz}}$  over the entire frequency range.

The magnetostriction of metallic glasses,  $e$ , for small fields is given by  $e = C_{\text{eff}} H^2$  [4] where  $H$  is the total applied magnetic field and  $C_{\text{eff}}$  is a material parameter. If a DC magnetic field,  $H_o$ , is applied to a sensor made of magnetostrictive glass via a permanent magnet, the applied field becomes  $H = H_o + H_\omega$  where  $H_\omega$  is the AC field of interest at some frequency  $\omega$ . Substituting this for  $H$ , the magnetostriction becomes

$$e = C_{\text{eff}} (H_o^2 + 2H_o H_\omega + H_\omega^2). \quad (1)$$

A fiber optic interferometric sensor constructed of magnetostrictive material would have a phase shift at the frequency  $\omega$  of  $\phi_\omega = 2l\alpha C_{\text{eff}} H_o H_\omega$  where  $l$  is the length of fiber wound on the sensor,  $\alpha = 2\pi n(0.78)/\lambda$ ,  $n$  is the optical index of the fiber and  $\lambda$  is the optical wavelength. This phase shift is the signal of interest.

The phase shift induced at DC is irrelevant in an AC interferometric sensor system; however, the signal at  $2\omega$  will cause harmonic distortion with a level of

$$\text{H.D.} = 20 \log[H_\omega^2 / 2H_o H_\omega] = 20 \log[H_\omega / 2H_o]. \quad (2)$$

Thus, for a harmonic distortion of -60 dB, the largest AC field which can be measured must be below 0.2% that of the DC "bias" field. For a bias field of 10 Gauss, this corresponds to a signal of 20 milli-Gauss.

In order to achieve remote operation, one of several interferometric phase retrieval techniques must be employed. These include, but are not limited to Phase Generated Carrier [5], and active homodyne feedback to source wavelength [6].

The sensors were fabricated from unannealed Allied Metglas 2605 S2 ( $\text{Fe}_{78}\text{B}_{13}\text{Si}_9$ ) strips 25 mm wide and 25  $\mu\text{m}$  thick. These were wound into cylinders 12 mm in diameter. The cylinders were tension wound with 80  $\mu\text{m}$  diameter payout fiber which covered 90% of the cylinder's length with a single layer. A permanent magnet 3 mm square by 30 mm long was mounted such that it was coaxial to the sensor. Two sensors were made and tested.

Figure 1 shows the experimental set-up used to characterize the sensors. Light from a Nd:YAG laser was launched into one arm of a 50/50 fiber optic coupler. This coupler split the light into two legs of a path-length mismatched Mach Zehnder (MZ): one leg contained the sensor to be tested, the other made up the reference leg. The two legs were combined in a second coupler and the interferometer outputs were fused to pigtailed InGaAs photodetectors. The photodiode outputs were differentially amplified and sent to an active homodyne demodulator whose output was fed to the laser to control its wavelength and thus hold the interferometer in quadrature. A solenoid 45 mm in diameter by 100 mm long with 250 turns was used to create the AC test magnetic fields. The sensor was positioned approximately in the center of the solenoid.

The  $C_{\text{eff}}$  value was measured by combining a low frequency field  $H_{\Omega}$  (10 Hz) with a high frequency field  $H_{\omega}$  (16 kHz). Thus, from equation (1), there will be optical signals at 16 kHz with side bands of 10 Hz having a value proportional to the product of the amplitudes of the two magnetic fields

$$\varphi = l \alpha C_{\text{eff}} H_{\Omega} H_{\omega} . \quad (3)$$

The sensor was wound with 7 meters of fiber having an index of 1.458 and the laser output was at 1.3  $\mu\text{m}$ , giving a value for  $\alpha = 5.5 \times 10^6/\text{m}$ . A known phase shift was created at 16.040 kHz and the side band response scaled from this. The magnetically induced phase shift was  $8.2 \times 10^{-4}$  radians for field levels of 17.3 milli-Gauss ( $\Omega$ ) and 97 milli-Gauss ( $\omega$ ), thus  $C_{\text{eff}} = 1.27 \times 10^{-8}/\text{G}^2$ .

The response of the sensor to DC bias field levels was measured. Figure 2 shows the induced

phase shift for an applied field at 16 kHz as a function of applied DC field. The sensor exhibits near flat response between approximately 15 and 30 Gauss. This implies that if the sensor is biased between these limits, it will have an AC response scale factor virtually independent of its orientation in Earth's field. The figure also shows the response of the sensor with the permanent magnet in place. The zero applied DC field shows the magnet to be biasing the sensor into this region of high AC field sensitivity and low DC field susceptibility.

Figure 3 shows the frequency response and the corresponding noise floor of the magnetic sensor system. This signal-to-noise ratio gives a minimum detectable of  $1.8 \times 10^{-7} \text{ G}/\sqrt{\text{Hz}}$ . The antenna pattern of the sensor is shown in Figure 4. The isolation for fields perpendicular to the sensitive axis was 48 dB down. It is believed that a more meticulous alignment of the permanent magnet to the sensor could improve this null.

We have reported on a fiber optic AC magnetometer which has been operated in a remote fashion. It is shown to have a minimum detectable signal of  $1.8 \times 10^{-7} \text{ G}/\sqrt{\text{Hz}}$  and to have flat real-time response to 45 kHz. The transducer is made from unannealed Allied Metglas 2602 S2 and requires no active components. The sensor is light weight and can be packaged with a small form factor.

## ACKNOWLEDGMENT

The authors would like to thank J.A. McVicker for fabricating the transducers used in this study.

## REFERENCES

- 1 DEETER, M. N., ROSE, A. H. AND DAY, G.W. 'Fast sensitive magnetic-field sensors based on the Faraday effect in YIG'; *J. Lightwave Technol.*, 8, pp. 1838-1842
- 2 BUCHOLTZ, F., DAGENAIS, D. M. AND KOO, K.P. 'High-frequency fibre-optic magnetometer with 70 fT/(Hz) resolution'; *Electron. Lett.*, 1989, 25, pp. 1719-1720
- 3 OKAMURA, H., AND FUJII, Y.: 'Lorentian force type fibre-optic AC magnetic sensor realizing frequency independent sensitivity'; *Electron. Lett.*, 1988, 24, pp. 1090-1091
- 4 LIVINGSTON, J.D., 'Magnetomechanical properties of amorphous metals', *Phys. Stat. Sol.*, 1982, 70, pp. 591-596
- 5 DANDRIDGE, A., TVETEN, A.B. AND GIALLORENZI, T. G. 'Homodyne demodulation scheme for fiber optic sensors using phase generated carrier'; *J. Quantum Electron.*, 1982, QE-18, pp. 1647-1653
- 6 DANDRIDGE, A. AND TVETEN, A.B. 'Phase compensation in interferometric fiber-optic sensors'; *Opt. Letters*, 1982, 7, pp. 279-281

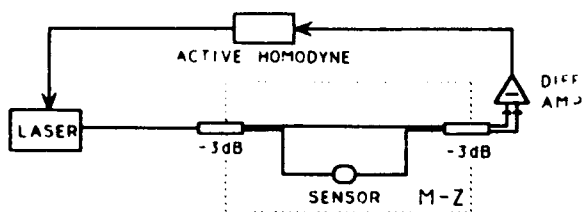


**FIGURE 1**  
**EXPERIMENTAL SET-UP**

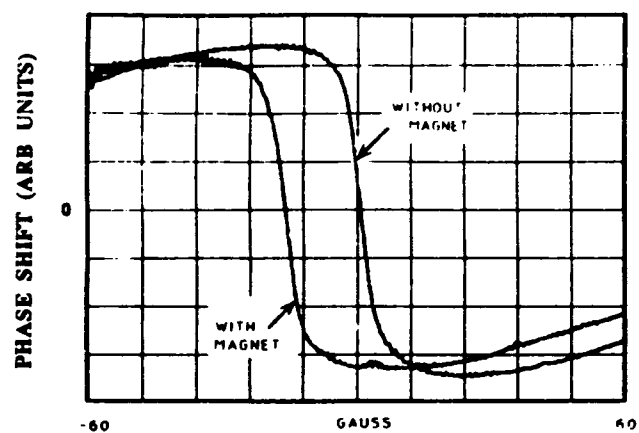


**FIGURE 2**  
**RESPONSE OF SENSOR VERSUS DC BIAS FIELD**

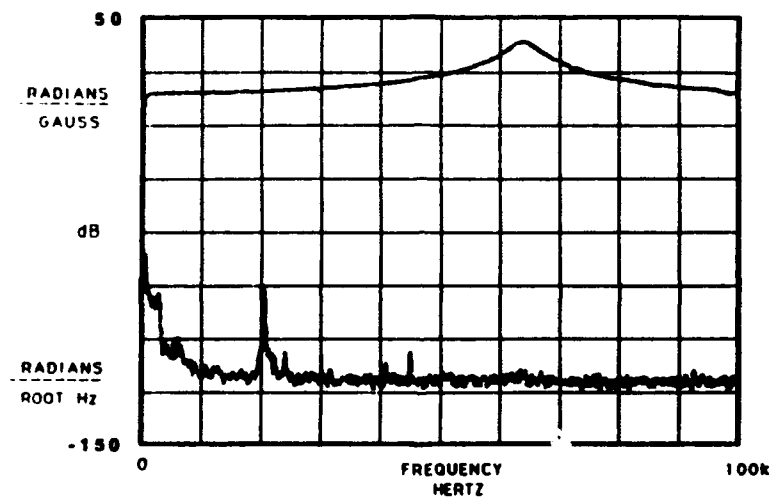


**FIGURE 3** **FREQUENCY RESPONSE AND NOISE FLOOR OF SENSOR**

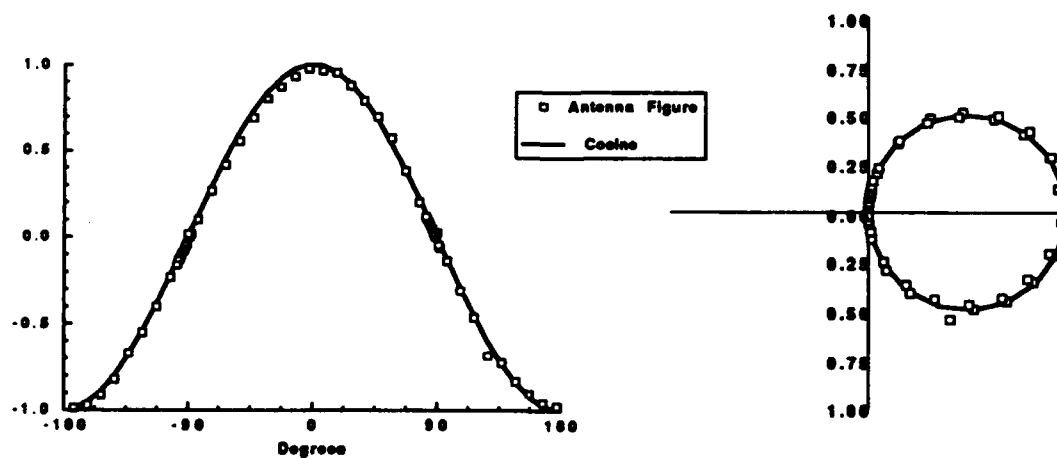


**FIGURE 4** **SENSOR ANTENNA PATTERN**

## F4.4 A Fiber Optic DC And Low Frequency Electric Field Sensor

S.T. Vohra, F. Bucholtz and A.D. Kersey  
Naval Research Laboratory  
Optical Science Division, Code 6570  
Washington, D.C. 20375

### Abstract

We demonstrate a novel fiber-optic interferometric dc and low frequency electric field sensor based on the electrostrictive effect in a Ba:PZT transducer. The sensor exhibits a minimum detectable electric field of  $0.01 \text{ V/m}/\sqrt{\text{Hz}}$  at 1 Hz using 9 cm of fiber.

### 1. Introduction :

Fiber optic (FO) interferometric electric field sensors reported so far have utilized piezoelectric materials (e.g.  $\text{PVF}_2$ ) in the transducing element [1]. The primary disadvantage of using a piezoelectric linear transducer in an fiber-optic electric field sensor is that the noise spectrum generally exhibits  $1/f$  dependence which severely limits dc and low frequency resolution. Reported values for the minimum detectable field for a FO electric field sensor using a  $\text{PVF}_2$  sensing element and 60 cm of fiber are in the range of  $80\text{--}90 \text{ V/m}/\sqrt{\text{Hz}}$  at 10 Hz [1]. We report a novel low frequency FO electric field sensor which utilizes a nonlinear transducing element containing an electrostrictive ceramic, Ba:PZT, to attain electric field resolution of  $0.01 \text{ V/m}/\sqrt{\text{Hz}}$  and a voltage resolution of  $10 \mu\text{V}/\sqrt{\text{Hz}}$  at 1 Hz for 9 cm of fiber.

Nonlinear transducers overcome the  $1/f$  noise problem by mixing the signal at frequency  $\Omega$  with a carrier or "dither" at a much higher frequency  $\omega$ , thereby upconverting the information of interest to a frequency region  $(\omega \pm \Omega)$  where  $1/f$  noise is not significant. Nonlinear transducing elements such as Metglas 2605S-2 magnetostrictive alloys have been successfully utilized in FO interferometers to detect low frequency magnetic signals, attaining resolution of  $10 \text{ pT}/\sqrt{\text{Hz}}$  at 1 Hz [2]. The induced strain in such materials is quadratically related to the applied field. An electrostrictive ceramic is a second example of a nonlinear transducer in which the induced strain  $e$  depends nonlinearly on the applied electric field  $E$ ,  $e = ME^2$ , where  $M$  is the electrostrictive coefficient [3].

Although the electrostrictive effect occurs in a variety of materials it is usually too small ( $M \leq 10^{-20} \text{ m}^2/\text{V}^2$ ) to be useful in sensors. However, in certain materials (e.g. Ba:PZT, PLZT,  $\text{PbMnNbO}_3$  etc.) the effect is large enough ( $M \geq 10^{-16} \text{ m}^2/\text{V}^2$ ) to render useful devices such as

actuators, relays etc. [3,4]. We exploit the nonlinear transducing properties of the electrostrictive material  $[(\text{Pb}_{0.73}\text{Ba}_{0.27})_{0.97}\text{Bi}_{0.02}(\text{Zr}_{0.7}\text{Ti}_{0.3})\text{O}_3]$  ("Ba:PZT"), to measure dc and low frequency electric fields with a FO interferometer. The electric field resolution of the FO sensor reported here displays a 30 dB improvement over previously reported results [5].

## 2. Experiment :

The FO electric field sensor comprised a 3 cm x 0.75 cm x 1 mm electrostrictive ceramic (Ba:PZT) bonded to a 9 cm section of fiber in 3 fiber passes in one arm of a Mach-Zehnder fiber-optic interferometer. A 300 Å gold film on each facet of the ceramic allowed for electrical contacts. The phase shift of light propagating in the fiber attached to the ceramic plate is a direct measure of the electric field generated strain. A schematic of the experimental setup is shown in Fig. 1

An electrostrictive ceramic excited by an E-field given by  $E = E_{\text{dc}} + E_{\omega}\cos\omega t + E_{\Omega}\cos\Omega t$ , where  $E_{\omega}$  is amplitude of the carrier,  $E_{\Omega}$  is amplitude of the low frequency field and  $E_{\text{dc}}$  is the dc bias, produces strains (using  $e = ME^2$ ),

$$e_{\omega} = (2ME_{\text{dc}}E_{\omega})\cos\omega t \quad (1a)$$

$$e_{\omega\pm\Omega} = ME_{\omega}E_{\Omega}\cos(\omega\pm\Omega)t \quad (1b)$$

along with strains  $e_{\text{dc}}$ ,  $e_{\Omega}$  and higher harmonics. The amplitude of the optical phase shift due to the strain component  $e_{\omega\pm\Omega}$  is given by

$$\phi_{\omega\pm\Omega} = KMLE_{\omega}E_{\Omega} \quad (2)$$

where L is the length of the fiber interacting with the electrostrictive element, M is the electrostrictive parameter and  $K = (2\pi n/\lambda)\xi$  where  $\lambda$ , n and  $\xi$  are the free space wavelength, core refractive index and strain-optic factor, respectively. DC electric fields are measured by monitoring the phase shift at the fundamental ( $\omega$ ) :

$$\phi_{\omega} = 2KMLE_{\omega}E_{\text{dc}} \quad (3)$$

## 3. Results :

The power spectrum of the output near  $\omega/2\pi = 9.5$  kHz is shown in Fig. 2. A 1 Hz signal added to the drive appears as expected (eq. 1b) as the sidebands of  $\omega$ . Figure 2 shows the spectrum for  $E_{\omega} = 20$  kV/m and  $E_{\Omega} = 10$  V/m, corresponding to applied voltages  $V_{\omega} = 20$  V and  $V_{\Omega} = 0.01$  V. The measured M value was  $4 \times 10^{-16} \text{ m}^2/\text{V}^2$  which agrees well with the values reported in the literature [3]. The signal-to-noise ratio of the sideband signal was 60 dB (BW = 1 Hz), corresponding to a minimum detectable field of  $0.01 \text{ V/m}/\sqrt{\text{Hz}}$ . This result shows an improvement in resolution of greater than 30 dB over previously reported results [5]. The corresponding voltage resolution of the sensor reported here is  $10 \mu\text{V}/\sqrt{\text{Hz}}$  at 1 Hz. Large strain at  $2\omega$  limits the

signal-to-noise ratio of the sidebands imposed by the 80dB dynamic range of the spectrum analyzer. The minimum detectable field at 1 Hz for a FO E-field sensor utilizing a nonlinear transducer (Ba:PZT) is several orders of magnitude better than for a device using a linear transducer (90 V/m/ $\sqrt{\text{Hz}}$  at 10 Hz [1]).

A simple calculation (from eq. 1b and eq. 2) predicts that for a phase noise limited sensor ( $\phi_{\text{noise}} = 1 \mu\text{rad}/\sqrt{\text{Hz}}$ ) with 10 m of fiber attached to a electrostrictive ceramic it should be possible to achieve a minimum detectable field of  $\leq 10 \mu\text{V}/\text{m}/\sqrt{\text{Hz}}$ . The calculation assumes a dither of 100 volts on a 100  $\mu\text{m}$  thick electrostrictive plate and a electrostrictive coefficient  $M = 10^{-15} \text{ m}^2/\text{V}^2$ . The predicted low frequency voltage resolution is  $\leq 1 \text{ nV}/\sqrt{\text{Hz}}$ .

Finally, the dc field sensing capability of the electrostrictor was measured. From eq. (1a) and eq. (3) it is clear that for a fixed dither field the strain at  $\omega$  is linearly dependent on the dc field. Fig. 3 shows the dependence of the strain component  $e_{\omega}$  on the dc field for a fixed dither amplitude  $E_{\omega} = 20 \text{ kV}/\text{m}$  at  $\omega/2\pi = 9.5 \text{ kHz}$ . The linearity of the strain component  $e_{\omega}$  as a function of dc E-field depicted in Fig. 3 demonstrates the ability of the device to function as a dc field sensor.

#### 4. Conclusions:

In conclusion, we have demonstrated a fiber optic dc and low frequency electric field sensor based on the electrostrictive effect. The electrostrictive nonlinear transducer (Ba:PZT) allows detection of low frequency signals as sidebands of a high frequency carrier thereby avoiding the 1/f noise problem limiting low frequency resolution in FO E-field sensors based on the piezoelectric effect. Preliminary characterization of the device has yielded a minimum detectable field of 0.01 V/m/ $\sqrt{\text{Hz}}$  at 1 Hz for 9 cm fiber which is two orders of magnitude better than for FO sensor based on piezoelectric materials. The projected low frequency electric field and voltage resolution are  $\leq 10 \mu\text{V}/\text{m}/\sqrt{\text{Hz}}$  and  $\leq 1 \text{ nV}/\sqrt{\text{Hz}}$ , respectively.

We are greatly indebted to J. Kyonka for supplying the electrostrictive ceramics. We acknowledge the Office of Naval Research for partial financial support.

#### References

1. See e.g. K.P. Koo and G.H. Sigel, IEEE J. of Quant. Electrn., QE-18 (4), 67 (1982).
2. D.M. Dagenais, F. Bucholtz and K.P. Koo, Appl. Phys. Lett. 53 (16), 1474 (1988).
3. See e.g. G.H. Haertling, Ferroelectrics 75, 25 (1987).
4. L.M. Levinson ed., Electronic Ceramics. Properties, Devices and Applications, Marcel Dekker (1988).
5. S.T. Vohra, F. Bucholtz and A.D. Kersey, Opt. Lett. (to appear September 1991).



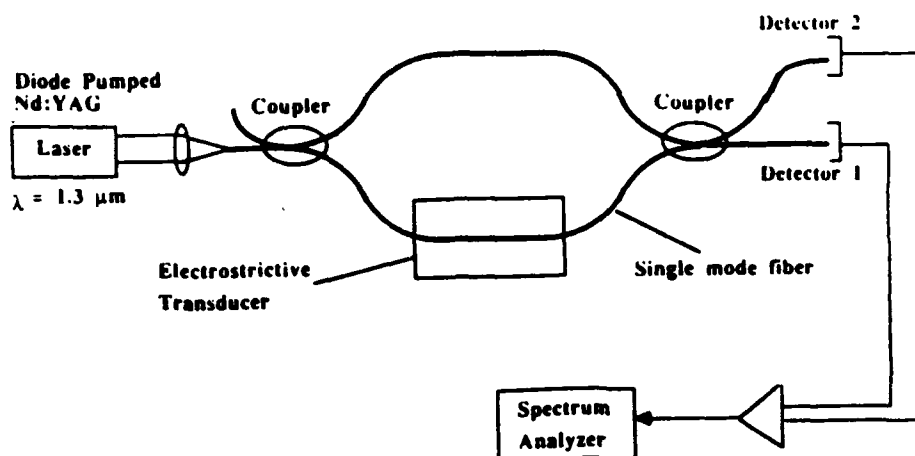


**Fig. 1** A schematic of the fiber-optic interferometer used for measuring low frequency and dc electric fields.

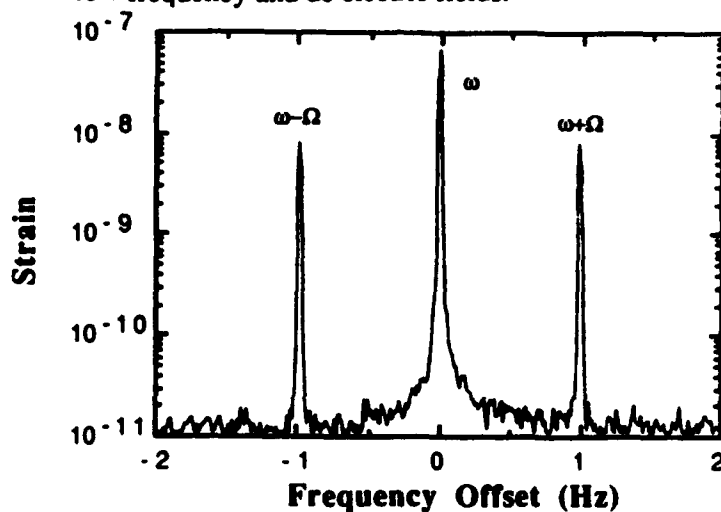


**Fig.2** Power spectrum of the E-field sensor output. The electrostrictive ceramic was driven by  $E = E_{dc} + E_{\omega} \cos \omega t + E_{\Omega} \cos \Omega t$ . Zero frequency offset corresponds to (a)  $\omega/2\pi = 9.5$  kHz and (b)  $\Omega/2\pi = 1$  Hz appear as sidebands of  $\omega$ .

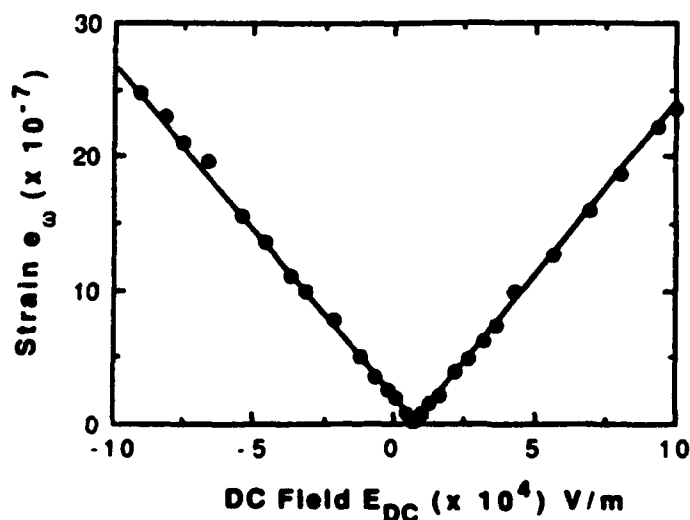


**Fig. 3** Dependence of  $e_{\omega}$  on applied dc field for  $E_{\omega} = 20$  kV/m.

## F4.5 A New Scheme Of Fiber Optic Light Sensor For Detection Of Corona Discharges In Gas Insulated Power Apparatus

K. Kurosawa and W. Watanabe

Tokyo Electric Power Company, Engineering Research Center  
2-4-1 Nishi-Tsutsujigaoka Chofu-shi Tokyo 182, Japan

A sensitive scheme has been proposed and demonstrated for detection of weak corona discharge light in gas insulated power apparatus. The sensor is fabricated with a fluorescent plastic fiber and a light concentrator.

### 1. Introduction

When there is a small region of high electric field in electric power apparatus insulated by the  $\text{SF}_6$  gas (GIS), weak corona discharge occurs at the point. If the phenomenon is permitted to stand, the insulation may will break down. Therefore it is necessary to monitor the discharge. Presently, devices to detect currents or voltages or acoustic waves generated by the discharge are used for the monitoring (1). However it is a serious problem for them to eliminate influences of external severe electrical or acoustical noises.

On the other side, a method to detect the light radiated from the discharge point has been studied (2,3,4), using an optical fiber containing fluorescent materials, inserted in the GIS. The principle of it is that the incident light to the side of the fiber is converted into fluorescence in it. This method has following advantages.

- \*No influences of electrical or acoustical noises
- \*No background light noise because of darkness in the GIS
- \*Light from any direction to the sensor can be detected.
- \*The discharge light can be transformed into longer wavelength light whose loss in optical fiber is lower.

A problem of this method is that the radiated discharge light hardly be concentrated effectively in the fiber because the cross-sectional area for detection is restricted by the diameter of it.

The authors have studied a method using fluorescent plastic fiber made from polycarbonate (PC) (4). The PC fiber was chosen for following reasons.

- \*Effective concentration of light is possible with a thick or special shape fiber.

\*The material has high heat resistant property, within plastic.

In this paper we propose a sensitive scheme in which a fluorescent fiber is combined with plates for the concentration of light.

### 2. Principle

Fig.1 shows the structure of primitive fluorescent fiber. When light is incident to the core, the fluorescent substance absorbs the light, then emits fluorescence of longer wavelength isotropically. Component of the fluorescence satisfying the total reflection condition is guided along the fiber. The light is, then, transmitted to a photo-detector with a normal fiber.

To obtain higher sensitivity, a method has been studied by the authors, using a PC fiber doped with two different fluorescent substances  $F_g$  and  $F_r$ . In the method, firstly, the short wavelength incident corona discharge light  $l^g$  (as described later) of the fiber is converted into fluorescence by  $F_g$  whose absorption band agrees with the spectrum of the discharge light. Then the fluorescence is transformed into light of still longer wavelength by  $F_r$  whose absorption band agrees with the spectrum of the light emitted by  $F_g$ . Wavelength of the emitted light of  $F_r$  is about 650nm, and is in the lowest

loss band of the fiber.

Fig.2 shows the new scheme proposed here. The concentrator is made of plastic plates doped with the fluorescent substance  $F_c$ . The fluorescent fiber is doped with both  $F_c$  and  $F_g$ . The incident corona discharge light to the concentrator is transformed into fluorescence. Component of the fluorescence radiated in the region of direction satisfies the condition of total reflection is guided in the plate, and is emitted from the side of it. Both the light emitted from the concentrator and light from the discharge point illuminate the fluorescent fiber. The incident light to the fiber is, finally, converted into light whose wavelength is about 650nm by  $F_g$ . Then a part of the light is guided along the fiber. By this combination of the concentrator of wide cross-sectional area and the fluorescent fiber, the radiated weak discharge light is expected to be detected sensitively.

To evaluate the critical sensitivity of the proposed scheme, the output light power was compared theoretically with that of the another scheme using only the fiber containing two kinds of fluorescent substances. Following assumptions were set for the evaluation.

\*The corona discharge light illuminates the sensors uniformly.

\*Area of the concentrator and length of the fibers are infinite.

\*Light emitted by a fluorescent substance is not absorbed by the same kind of substance again.

In each case, output power from the fluorescent fiber can be calculated by integration of the fluorescence generated along the fiber and guided to the end. The output power from the side of concentrator per unit length can be calculated by integrating the guided fluorescence to the side from each points of the plate. The effectiveness of the concentrator can be evaluated by the ratio of the output powers. From the above consideration the ratio can be expressed as follows.

$$P_2/P_1 = 1 + (2A_c A_{cf} B_{cg} T_c) / (A_f B_{fg} w_f \alpha_g) \quad (1)$$

Where,  $P_1$ : output power without the concentrator

$P_2$ : output power in case of using the concentrator

$A_c$ : efficiency that the light illuminating the concentrator enters it.

$A_{cf}$ : efficiency that the output light of the concentrator enters the fiber

$A_f$ : efficiency that the discharge light illuminating the fiber enters it.

$T_c$ : efficiency that the fluorescence is trapped in the concentrator

$(= (1 - n^2)^{-1/2} = 0.76, \text{ refractive index } n = 1.54)$

$B_{cg}$ : efficiency that the incident light is absorbed by  $F_c$  in the concentrator

$B_{fg}$ : efficiency that the discharge light is absorbed by  $F_g$  in the fiber

$w_f$ : diameter of the fluorescent fiber

$\alpha_g$ : attenuation coefficient of the fluorescence in concentrator (1/m)

Assuming realistic conditions that  $B_{cg} = B_{fg}$ ,  $A_c T_c = 0.7$ ,  $w_f = 1\text{mm}$ ,  $\alpha_g = 1.5(1/\text{m})$ ,

eq.(1) is changed into  $P_2/P_1 = 1 + 300(A_{cf}/A_c)$ .

### 3. Experiment

To design the sensors, spectrums of the corona discharge light generated by DC voltage in a closed vessel filled with  $\text{SF}_6$  gas were measured(5). The measurement were done under several different conditions, changing the shape of electrode, polarity and magnitude of applied voltage and discharge current. The results showed that principal component of spectrum of the discharge light is in the region of wavelength 300-500nm. Fig.3 shows one of the measured spectrum when negative voltage is applied to a needle electrode.

Referring the measurement results, the fluorescent substances  $F_c$  and  $F_g$  were chosen within the organic material of perylene dye. Then the fluorescent PC fiber and plates for the concentrator made from a copolymer of methyl methacrylate and styrene doped with the fluorescent materials were produced.

The absorption band of  $F_6$  is in the region of 480-520nm (peak;520nm), and the emission band of it is 520-570nm (peak;520nm). The absorption band of  $F_7$  is 500-620nm (peak;620nm), and the emission band is 630-670nm (peak;650nm).

For investigating the effectiveness of the concentrator, the output powers of the both schemes were measured, illuminating them uniformly with a light source composed with a xenon lamp, a filter and a glass fiber(Fig.4). The wavelength of the source is 471nm and the half width of the spectrum is about 10nm and the output power is about 2mW. 8 pieces of plates for the concentration were set in touch with the fiber as shown in the figure. The dimensions of a plate are 1.5mm thickness, 100mm length and 54mm width. The plate is doped with  $F_6$  of 6%. The fiber has a diameter of 1.0mm and is doped with  $F_6$  of 0.02% and  $F_7$  of 0.04%.

The results showed that the output power from the fiber was -52.3dBm when the plates were not used. On the other hand, when the plates were attached, the output power was -45.8dBm, about 4.5 times as much as that of the another case. The power increased to -44.0dBm when water was poured into the space between the plates and the fiber. The value is approximately 7 times as much as that of the case without using the plates. The effect of water is considered to be due to a rise of the efficiency  $A_{cf}$ . Higher sensitivity is feasible by improvement of the efficiency  $A_{cf}$ , because the thickness of plates for the experiment was larger than the diameter of the fiber, and the fiber of cylindrical shape was contacted with the plates of plane surfaces.

To confirm the effect of the concentrator, experiment for detecting the real corona discharge light emitted in  $SF_6$  gas was done with the two different schemes. The discharge was generated in the same way as the measurement of the spectrum of discharge light. The sensors were set at about 10cm distance from the point of discharge. 10 pieces of plates were attached to one of the fibers. The fibers are doped with  $F_6$  of 0.02% and  $F_7$  of 0.02% respectively. The diameter of the fibers is 1.0mm. The output light of the fluorescent fibers were guided to photomultipliers with 1m PMMA fibers. The output of photomultipliers were observed with a oscilloscope. The synthetic frequency response band of the photo detecting circuit is about 140MHz.

Fig.5 shows the output of the photomultipliers when the sensors detected the corona discharge light pulses. Generally the corona discharge occurs in the state of short pulsation. Fig.6(a) shows the output of the system without using the plates, and (b) shows that of the system using the plates. The area between the output voltage and the ground line of the Fig.6(b) is about 3 times as extensive as that of (a). Because of the wide band of the photodetecting circuit, fluctuation of the output voltages due to the irregularity of photoelectrons is observed. Fig.6(a) and (b) show the outputs corresponding different discharge pulses each other. However from the result of comparing averaged values of many areas of the two kinds of output pulses, the ratio was 3.1 too. In this experiment the plates were not be in contact with the fiber. So it is considered that the effect of the plates can be enhanced more by improvement of the efficiency  $A_{cf}$ .

#### 4. Conclusion

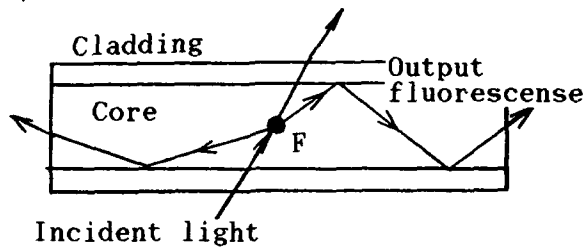
It has been confirmed that the sensitivity of the light sensor for detection of corona discharge light in  $SF_6$  gas can be enhanced by using a new scheme in which plates doped with fluorescent material were attached to the fluorescent optical fiber.

#### Acknowledgement

The authors wish to thank Fujitsu Limited and Fuji Electric Corporate R&D Ltd for their assistance in this work.

## References

- (1)(for example)S.Kusumoto, et al, IEEE T. PAS, Vol.99 NO.4, 1980
- (2)T.Yoshino, et al, Japan Soc. of Appl. Phys. Autumn Meeting, 29p-K-9, 1982
- (3)K.Muto, IEEE J. Light Wave Tech., Vol.7 NO.7, 1989
- (4)K.Kurosawa, et al, SPIE Vol.1368, pp150-156, 1990
- (5)W.Watanabe, et al, IEEJ 1991 Power/Energy Div. Meeting, NO.44
- (6)K.Sakuta, Bulletin of The E.T.L, Vol50 NO.8, pp.787-796



F:Fluorescent substance

Fig.1 Principle of light detection of primitive fluorescent fiber

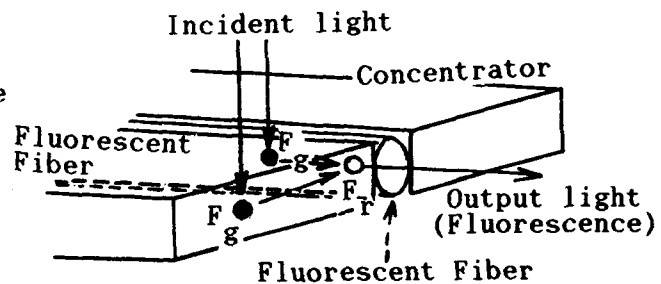


Fig.2 Principle of light detection of the proposed scheme

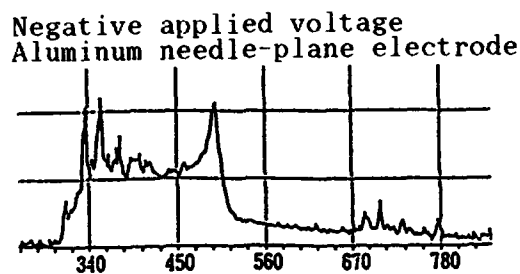


Fig.3 Emission spectrum of corona discharge in  $\text{SF}_6$  gas

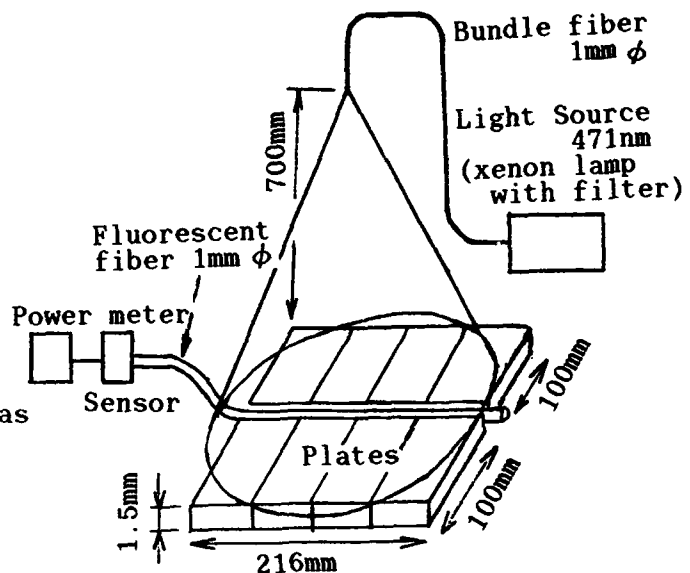
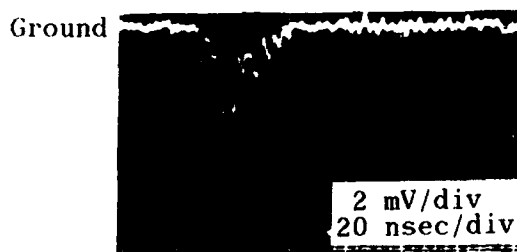
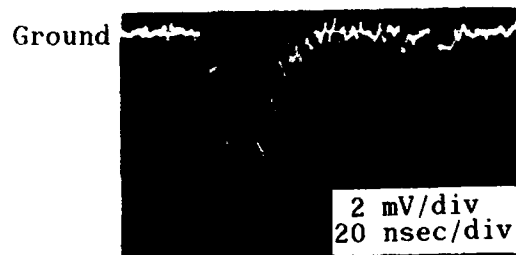


Fig.4 Experimental set up for investigation of effect of the concentrator



(a)Fluorescent fiber only



(b)Being attached the plates

Fig.5 Outputs of the photomultiplier tubes when the two kinds of fluorescent sensors detected the corona discharge light

## **F4.6 Three Phase Current Measurement Using A Hybrid Current Sensing Technique**

D. A. Jackson, Y. N. Ning, C. McGarrity, and J. L. Santos\*

Applied Optics Group, Physics Laboratory  
University of Kent, Canterbury, Kent. CT2 7NR, UK

\* Physics Laboratory, University of Porto,  
Praca Gomes Teixeira, 4000 Porto, Portugal

### **1. Introduction:**

In the power generation industry it is important to measure the amplitude, frequency and phase of the generated currents in electricity distribution networks. This measurement is required for fiscal reasons and also to establish if there are faults in the network. The conventional method of current measurement is based upon a 'current transformer' which is deployed around the current carrying wire commonly termed a 'bus bar'. As the bus bar is normally at very high potential, for example, 440,000 volts, insulation between the current transformers secondary and the permeable core which surround the bus bar must be extremely high as the signals generated by the current transformer are monitored in the central control unit of the power station. Hence the current transformer is both large and extremely expensive. Although considerable effort has been devoted to the development of optical fibre current sensors based upon the Faraday effect, the performance of these sensors is often limited by problems associated with bend-induced birefringence, temperature and wavelength sensitivity of the Verdet constant and the high sensitivity to vibrational noise [1].

We have recently shown that it is possible to use a new hybrid current sensing technique [2] to measure the signal appearing at the output of the current transformer's secondary and to simultaneously transfer the information concerning the amplitude, frequency and phase of the current safely to ground potential for subsequent processing. The new measuring system is based upon a fibre optic interferometric sensor which is conditioned such that the current signal from the secondary of the C.T. induces a strain in the fibre optic interferometer which, with suitable signal processing, means is converted to an output which is linearly related to the current. As the optical fibre is an insulator both the size and hence cost of the CT can be greatly reduced.

### **2. Theoretical background:**

The operation of the CT is based upon Ampere's law where the line integral of the magnetic field  $H$  along any closed path equals the enclosed current  $I$ :

$$\oint \vec{H} \cdot d\vec{l} = I \quad (1)$$

hence the position of the current within the closed path is not important and the presence of magnetic fields associated with currents external to the closed loop do not affect the measurement. Thus, three CTs may be grouped together to independently measure each current in a typical three phase electricity distribution network.

When a current passes through a bus bar to be measured, the action of the current is to induce a magnetic flux change  $\Delta\Phi$  in the medium constituting the core of the CT, given by

$$\Delta\Phi = \frac{\mu SI}{l} \quad (2)$$

where  $S$  is the cross-sectional area of the core,  $\mu$  its permeability, and  $l$  its length. A solenoid is wound around the CT's core hence if  $\Delta\Phi$  is time dependent an alternating current is generated in the solenoid (the secondary of the CT) which may be converted into a voltage signal by placing a resistor across the CT's secondary. This voltage signal is then applied to a cylinder made from piezo-electric material. The dimensions of the piezo-electric cylinder vary as a linear function of the voltage generated across the resistor and can be measured by a fibre optic Michelson interferometer with its sensing arm wrapped under tension around the PZT.

### 3. Experimental arrangement and its performance:

In order to measure three phase currents, a time division multiplexing scheme with a binary tree topology was employed. The experimental arrangement is illustrated schematically in figure 1. A four sensor network multiplexed in the time domain was used to measure three independent currents simultaneously. The fourth sensor is required as a reference sensor to monitor extraneous noise signals at 50Hz as the signal being measured is at the line frequency of 50Hz.

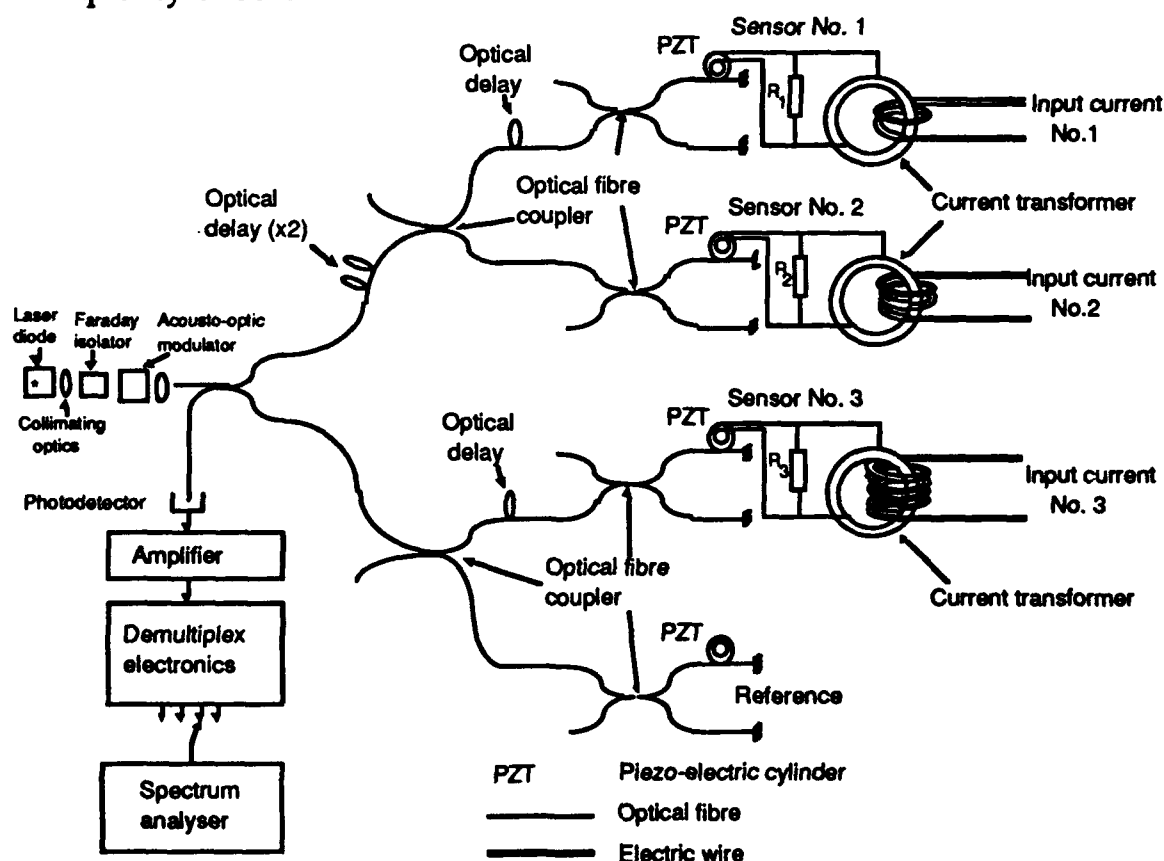
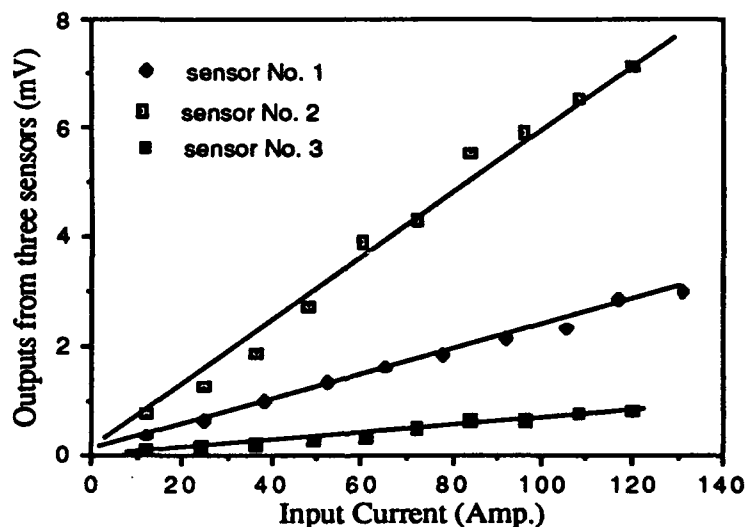


Figure 1. Experimental arrangement

A Sharp LT024 laser diode operating at 780 nm was used. An acousto-optic modulator is used to convert the continuous output of the laser into a stream of narrow light pulses [3]. The topology is reflective and is designed to return pulses from the 4 sensors at a spacing of 1  $\mu$ s. The four Michelson interferometers had optical path differences of 4cm and the ends of the fibre were silvered to achieve high power returns on the optical bus. The detected signals are amplified, electronically demultiplexed and displayed on a spectrum analyser.

The current source used in the experiment comprised a variable transformer in series with a step-down transformer capable of generating a maximum output power of 6 kVA. The output currents from the transformer were carried by a 100 Amp copper wire which passed sequentially through the 3 CT's, the number of turns deployed on each CT being different to simulate different input currents.

Ten measurements of the outputs of each of the sensing interferometers in the linear regime were taken in the range 10mrad to 100mrad and the average interferometric sensitivities of the three sensing interferometers in quadrature were 424 $\mu$ rad/ $\sqrt{\text{Hz}}$ , 348 $\mu$ rad/ $\sqrt{\text{Hz}}$  and 402 $\mu$ rad/ $\sqrt{\text{Hz}}$ . The difference in sensitivities between the interferometers is primarily due to differences in the returned light power. The experimental data obtained with this new system are summarized in figure 2, where the variation of the output signals for each sensing interferometer as a function of the input current are shown. The slopes of the figures are 0.023mV/Amp, 0.076mV/Amp and 0.019mV/Amp respectively.



**Figure 2.** *Output signals as a function of input current at 50Hz in the 0 to 140 Amp regime.*

The measured values of  $d\phi/dI$  of the three sensors are 0.8287mrad/Amp, 0.7809mrad/Amp and 0.8253mrad/Amp, which correspond to measurand sensitivities of 0.51A/ $\sqrt{\text{Hz}}$ , 0.45A/ $\sqrt{\text{Hz}}$  and 0.49A/ $\sqrt{\text{Hz}}$  in the 0 to 120 Amp regime. Both the measurement sensitivity and the operating regime of these sensors are determined by the number of turns of fibre wrapped on the PZT, the value of the load resistor, and the sensitivity of the interferometer. The operating regime of each sensor can be adjusted by simply changing the value of the load resistor across the PZT in the interferometer. This was done for the



second sensor and the experiment repeated over the maximum range the apparatus would allow. Figure 3 shows the results of this experiment. In this case the measured sensitivity of the sensor was of  $1.6\text{A}/\sqrt{\text{Hz}}$ , in the 0 to 500 Amp regime.

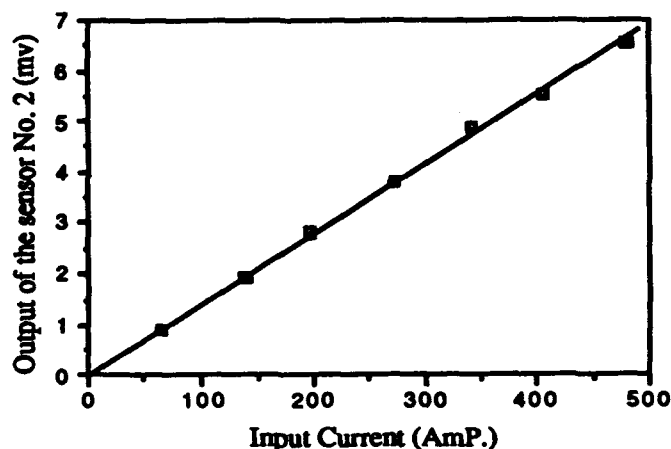


**Figure 3.** *Output signal as a function of input current at 50Hz in the 0 to 500 Amp regime.*

An estimate of the quality of these measurements is required due to the frequency of the measurand being at the line frequency where electrical pickup will be at a maximum. Standard deviations of the interferometric sensitivities in the experiment are typically less than  $10\mu\text{rad}/\sqrt{\text{Hz}}$ .

#### 4. Discussion and conclusion:

Although this new measurement system performs well in the laboratory further development is necessary before it can be deployed in the field. One major problem is that if ordinary monomode fibre is used for the interferometers as was the case here, polarisation fading will inevitably occur leading to a reduction in the visibility of the interferometric sensors severely degrading the signal being returned on the optical bus. This can be overcome either by the use of polarisation maintaining fibre and couplers or through active polarisation control at the optical input. More stringent problems are that the interferometric signals are sensitive to the temperature and vibration perturbations which may be induced if the system is deployed in the power distribution industry. Further investigations to reduce the impact of such perturbations are currently in progress.

In conclusion we have demonstrated a new hybrid current sensor system via a TDM fibre network for the measurement of three phase currents at high potential. The resolution and dynamic range of the system is well within the requirements of the standard specification quoted for a conventional current transformer.

#### References:

- [1] A. J. Rogers, J. of Optoelectronics, 3, 391, (1988).
- [2] Y.N. Ning, B.C.B. Chu and D.A. Jackson, to be published in Optics Letters.
- [3] A.D. Kersey and A. Dandridge, Vol. 44 of Springer Proc. in Physics. Springer-Verlag, Berlin. 1989. pp486-490.

# INDEX OF AUTHORS

Alcoz, J.J. ....	368	Donald, D.K. ....	61
Anderson, D.J. ....	22	Duffy, C.J. ....	181
Artigaud, S. ....	262	Duling I.N., III ....	10
Ashizuka, N. ....	38		
Askautrud, J.O. ....	101	Engan, H.E. ....	101
Atcha, H. ....	217		
Atkins, R.A. ....	368,105	Falco, L. ....	254
		Ferguson, B.A. ....	145
Bacci, M. ....	325	Fevrier, H. ....	262
Baldini, F. ....	313,325	Fogg, B.R. ....	376,129
Barel, A.R.F. ....	205	Fratello, V.J. ....	390
Barton, J.S. ....	73,346	Frosio, G. ....	53
Berkey, G.E. ....	121	Fuhr, P.L. ....	380
Berwick, M. ....	117	Fujii, S. ....	297
Berkoff, T.A. ....	372	Fürstenau, N. ....	113
Bibby, Y.W. ....	161		
Blake, J. ....	125	Gaouditz, O. ....	362
Blodgett, J.A. ....	241	Gibler, W.N. ....	368,105
Bløtekjaer, K. ....	6,189	Glaesemann, G.S. ....	279
Bobb, L.C. ....	410,161	Goetting, H.C. ....	113
Bohm, M. ....	90	Graindorge, P. ....	57
Borthwick, W.K.D. ....	346	Grattan, K.T.V. ....	358,93,209,237
Bouilleret, D. ....	262	Greene, J.A. ....	376
Boyle, W.J.O. ....	358,237	Guerin, J.J. ....	288
Brenci, M. ....	313,97	Gunther, M.F. ....	193
Brevignon, M. ....	362	Gyorgy, E.M. ....	390
Brown, D.A. ....	342		
Bucholtz, F. ....	406,418,225,414	Haldar, D. ....	165
Burns, W.K. ....	42,82	Handerek, V.A. ....	250
		Hartog, A. ....	246
Carolan, T. ....	346	Hattori, Y. ....	305
Carrara, S.L.A. ....	125	Hawk, R.M. ....	279
Cernosek, R.W. ....	398	Heffner, B.L. ....	61
Chao, Y.Y. ....	350	Hervo, J. ....	262
Chen, C.L. ....	145	Hotate, K. ....	34
Cho, K. ....	157	Huang, W.P. ....	233
Chu, W. ....	165	Huggins, R.W. ....	149
Chu, B.C.B. ....	169	Huston, D.R. ....	380
Claus, R.O. ....	376,129,193		
Cokgor, I. ....	250	Iizuka, K. ....	297
Collins, S.F. ....	209	Imaeda, M. ....	386
Cosi, F. ....	325	Iwatsuki, K. ....	309
Culshaw, B. ....	270,86,197,221		
Culverhouse, D.O. ....	185	Jackson, D.A. ....	426,117,169,185
		Jaeger, N.A.F. ....	153
Dagenais, D.M. ....	406,177,225	Jedrzejewski, K.P. ....	2
Dändliker, R. ....	53	Jin, W. ....	86
Dandridge, A. ....	69,266,350,177,225,414	Johnson, M. ....	201
Davis, M.A. ....	266,292,141	Johnstone, W. ....	197
Davis, C.C. ....	157	Jones, J.D.C. ....	22,73,346
Davis, A.R. ....	414	Jurczynsyn, M. ....	262
Day, G.W. ....	390,394		
Deeter, M.N. ....	390,394	Kajioka, H. ....	38
Del Bianco, A. ....	325	Kalli, K. ....	185
Derossis, A. ....	262	Katagiri, Y. ....	229
Desforges, F.X. ....	57,205	Kersey, A.D. ....	69,266,292,372,418,141
Ding, J.Y. ....	321	Kidd, S.R. ....	73

# INDEX OF AUTHORS

Kim, B.Y. ....	368	Pacitti, M.C. ....	125
Kobayashi, M. ....	65	Palmer, A.W. ....	358,93,209,237
Koltveit, E. ....	189	Pannell, C.N. ....	201
Koo, K.P. ....	406,177,225	Parriaux, O. ....	254
Kozuka, Y. ....	386	Patrick, S.S. ....	414
Kringlebotn, J.T. ....	6	Pauschke, J.M. ....	109
Krumboltz, H.D. ....	410	Payne, D.N. ....	2
Kubo, Y. ....	284	Pierrat, J.L. ....	262
Kumagai, T. ....	38	Poole, S.B. ....	258,274
Kurnyavko, Y.V. ....	78	Porter, C.R. ....	149
Kurosawa, K. ....	422		
Kuzmenko, P.J. ....	354	Rahmatian, F. ....	153
Kwong, N.S. ....	14	Rao, Y.J. ....	270
		Robert, P. ....	402
Lang, S.R. ....	109	Rogers, A.J. ....	250,165
Larson, D.C. ....	161	Rose, A.H. ....	394
Le Pesant, J.P. ....	362	Ryan, D.J. ....	109
Lee, C.E. ....	368,105		
Lefèvre, H.C. ....	57	Saddow, S. ....	157
Licht, S.J. ....	390	Safin, S.A. ....	78
Lieberman, R.A. ....	320,390	Sanders, G. ....	26
Liu, R.-Y. ....	26	Sansonetti, P. ....	288
Liu, T.Y. ....	117	Santos, J.L. ....	426
Lutz, D. ....	133	Sasaoka, E. ....	284,137
		Sceats, M.G. ....	258
MacDonald, R.I. ....	301	Scheggi, A.M. ....	325
Mágari, K. ....	18	Schmidt, W. ....	113
Maillard, J.M. ....	288	Semenov, A.T. ....	78
Marrone, M.J. ....	69,141	Shahriari, M.R. ....	321
Matano, M. ....	329	Shankar, P.M. ....	410
Mazzoni, D.L. ....	157	Shaw, H.J. ....	213
McBride, R. ....	346	Shidlovski, V.R. ....	78
McCallion, K. ....	197	Shigehara, M. ....	305
McGarrity, C. ....	426	Shigemori, K. ....	329
McStay, D. ....	165	Sigel, G.H. Jr. ....	321
Measures, R. ....	366	Sinha, P.G. ....	73
Meggitt, B.T. ....	209,237	Snitzer, E. ....	42
Mencaglia, A. ....	97	Sohlström, H. ....	173
Mermelstein, M.D. ....	241	Sorin, W.V. ....	61
Mignani, A.G. ....	97	Spillman, W.B. Jr. ....	380
Mikami, O. ....	18	Strandjord, L.K. ....	22
Moeller, R.P. ....	42,82	Suchoski, P.G. ....	296
Moodie, D. ....	197	Suganuma, H. ....	284,137
Morkel, P.R. ....	2	Sugimura, M. ....	329
Motohara, S. ....	30	Suzuki, Y. ....	18,229
Murphy, K.A. ....	376,129,193	Svantesson, K. ....	173
Nakai, H. ....	38	Tai, H. ....	333
Nathan, A. ....	233	Takagi, M. ....	284,137
Nicati, P.A. ....	402	Takiguchi, K. ....	34
Ning, Y.N. ....	426,169	Tanaka, H. ....	229
Noda, J. ....	65	Tardy, A. ....	262
Noguchi, Y. ....	18	Tatam, R.P. ....	181,217
Nychka, R. ....	301	Taylor, H.F. ....	65,368,105
Ohno, A. ....	30	Taylor, E.R. ....	2
Okamura, H. ....	309	Thorncraft, D.A. ....	258
Osawa, S. ....	333		

# INDEX OF AUTHORS

Thursby, G. ....	197
Trouchet, D. ....	57
Tur, M. ....	213
Turpin, M. ....	362
Tveten, A.B. ....	350
Tyagi, S. ....	161
Uchida, M. ....	333
Uehara, K. ....	333
Uttamchandani, D. ....	270
Vadekar, A. ....	233
Vengsarkar, A.M. ....	376,129
Venkatesh, S. ....	61
Voet, M.R.H. ....	205
Vohra, S.T. ....	418
Walsh, D. ....	221
Wang, A. ....	193
Wang, W.M. ....	358
Wanser, K.H. ....	292
Watanabe, W. ....	422
Weir, K. ....	237
Weis, R.S. ....	10
Wolfe, R. ....	390
Yamamoto, K. ....	333
Yoshida, M. ....	329
Yoshino, T. ....	46
Yurek, A.M. ....	338,350
Zhang, Z. ....	93
Zhuchov, N.A. ....	78
Zimmerman, E. ....	53